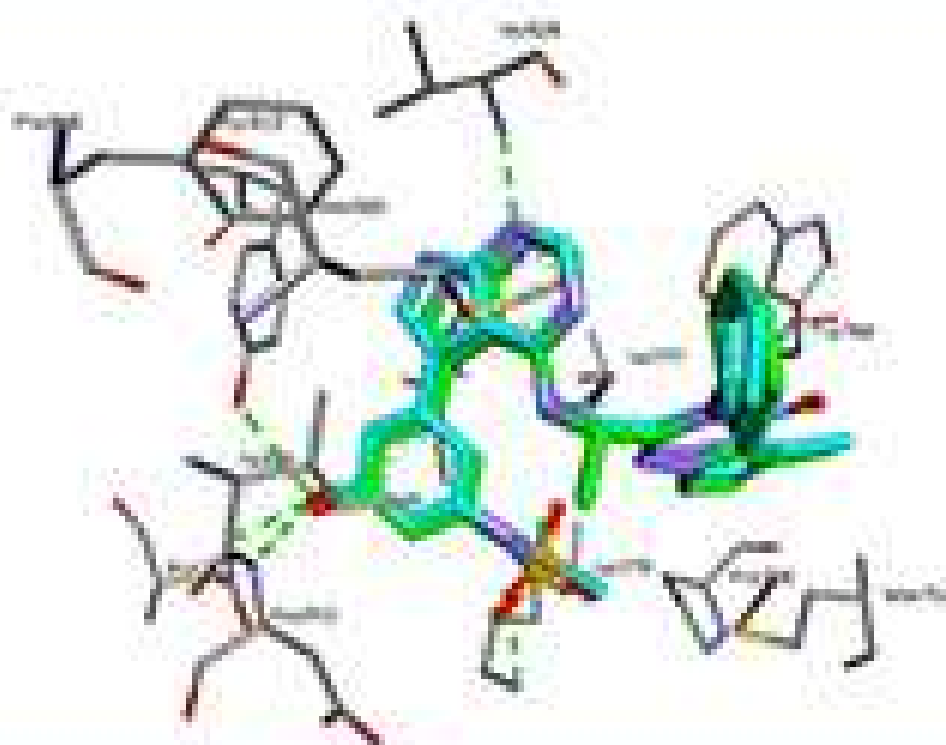
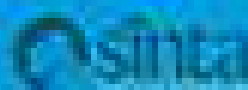


Indonesian Journal of Chemistry

Vol. 20, No. 5, October 2020



Google Scholar



Accepted by journal editor
on 09/08/2020

Study of the Mechanical Properties of Natural Rubber Composites with Synthetic Rubber Using Used Cooking Oil as a Softener

Nasruddin* and Tri Susanto

Palembang Institute for Industrial Research and Standardization, Ministry of Industry,
Jl. Perindustrian II No. 12 Km. 9, Palembang 30152, Indonesia

* **Corresponding author:**

email: nas.bppi@gmail.com

Received: January 2, 2019

Accepted: March 12, 2020

DOI: 10.22146/ijc.42343

Abstract: This research aims to study the mechanical properties of natural rubber composites with nitrile butadiene rubber and ethylene propylene diene monomer rubber. Composite fillers consisted of kaolin, and softener using used cooking oil. The study was carried out by the method of mastication, vulcanization, and maturation of the compound into rubber vulcanizates. The vulcanization and mastication process is carried out in the open mill. The maturation of the compound into rubber vulcanizates from the results of mastication and vulcanization was carried out using semi-automatic heat press and press at a temperature of $130\text{ }^{\circ}\text{C} \pm 2\text{ }^{\circ}\text{C}$ for 17 min. Based on data from testing the mechanical properties of five samples from five formulas, the mechanical properties of composite rubber are affected by the ratio of natural rubber, synthetic rubber, kaolin, and used cooking oil as a softener. The difference in the results of vulcanizates rubber testing of natural rubber composites with synthetic rubber is not only influenced by the ratio of the composite, but also by the degree of cross-linking between the material molecules.

Keywords: properties; natural rubber; synthetic rubber; used cooking oil

■ INTRODUCTION

The composite material consists of two or more mixtures, each of which has different mechanical characteristics and properties. Composite materials with different mechanical properties have the advantage of being used as technical goods. Differences in the mechanical properties of materials in a mixture can complement each other to form a mixture that is better than the original material. Polymer matrix composites in the last decade have been widely used for various engineering goods applications in order to improve the mechanical properties of the products produced [1-4].

Natural rubber with the general formula cis-1,4-polyisoprene has high double bond and elasticity but is not resistant to heat, and ozone attack [5-6]. According to Linos et al. [7], oxygen attacks can reduce the number of double bonds by cutting the polymer chain on cis-1,4, which causes a biodegradation process that produces carbonyl groups with one-sided aldehydes and ketones. Composite natural rubber with various materials for technical goods needs has various advantages, including

its mechanical properties. Composite natural rubber with carbon fill material from several studies can improve the mechanical properties of rubber vulcanization better [8-9].

Natural rubber composites are examples that produce mechanical properties that are better than the original material [10]. Composite natural rubber with various materials for technical goods needs has various advantages, including its mechanical properties. Composite natural rubber with carbon fill material from several studies can improve the mechanical properties of rubber vulcanization better [11-12]. Natural rubber (NR) composites with nitrile butadiene rubber (NBR), and ethylene propylene diene monomer rubber (EPDM) from several studies that have been done can improve ozone resistance [13-14]. Reclaimed rubber composites with styrene butadiene rubber can improve the properties of styrene-butadiene [15-16]. NBR in silica composites, as reinforcement fillers, can improve the dynamic properties of rubber vulcanizates [17-18]. According to Wu and Tian [19], composites of natural

rubber, synthetic rubber (SBR, BR, NBR, EPDM, and CR) with kaolin fillers as a substitute for silica can improve properties of rubber vulcanizates better. Composites of SBR, carbon black, and nano clay modified with organo (MMT Closite-20A) can increase the properties of rubber vulcanizates produced [20-21].

Natural rubber composites carried out on this study by adding NBR and EPDM. The added ingredients include silica and kaolin. The added filler aims to improve the tensile strength, modulus, tear strength, abrasion resistance [22-25]. EPDM, as a composite material, has the advantages of heat resistance, ozone resistance, and moisture resistance [26]. Besides, the addition of silica as an active filler can improve the mechanical properties of a rubber vulcanizate. According to Ahmad et al. [27], natural rubber with silica fillers can increase tensile strength, modulus, tear strength, hardness, and cross bond density, and elongation at break. According to Wang and Chen [28], silica is a reinforcing filler that is widely used to improve the mechanical properties of rubber composites. According to Da Costa et al. [29], the addition of silica from rice husk ash on composite rubber can increase the tensile strength and abrasion resistance.

The filler added to the polymer matrix will need to be added to the softener so that it can be evenly distributed. The development of softening materials for vegetable oil-based rubber compounds has been carried out [30]. Vegetable oils have the advantage of being environmentally friendly and renewable. *Jatropha* oil [31-32], and palm oil [33-34] have been used as a softener. Castor oil as a softener to improve the mechanical properties of rubber compounds has been developed [35-36]. According to Song [37], palm oil can be used as a softener in the manufacture of rubber compounds.

In this study, natural rubber composites used cooking oil softener from palm oil. Used cooking oil from palm oil in natural rubber composites with synthetic rubber aims to increase the distribution of additives and fillers into natural rubber composite molecules with synthetic rubber. Used cooking oil softener from palm oil contains saturated fatty acids [38]. The addition of used cooking oil as a softener is intended to stretch polymer matrix molecules so that the added ingredients can be

distributed evenly. During vulcanization, complex chemical reactions occur between molecular matrix polymers with process materials such as sulfur and other materials [39-40]. This research studies the mechanical properties of rubber vulcanizates from natural rubber composites, synthetic rubber, with filler (silica and kaolin), with softeners from used cooking oil.

■ EXPERIMENTAL SECTION

Materials

The material used for this study consisted of natural rubber (NR) type SIR-20, and nitrile butadiene rubber (NBR-N.2205), ethylene propylene diene monomer rubber (EPDM), zinc oxide purity 95% for rubber tire application, stearic acid CAS No: 57-114-4 purity 99% min, 2,2,4-trimethyl-1,2-dihydroquinoline (TMQ-RD) TMQ 26780-96-1, pigment yellow 83 (PL-PY 83 product code HRO₂, chemical class dis azo pigment color Index No: 21108 CAS No: 5567-15-7), silicon dioxide (SiO₂) CAS No: 112945-52-5 purity 99.8%, kaolin 400 mesh from Tanjung Pandan Belitung Indonesia, 2-mercaptobenzothiazole (MBTS-CAS: 120-78-5), titanium dioxide CAS No: 13463-67-7 with purity 98%, polyethylene glycol (PEG-4000) CAS No: 25322-68-3 purity 99%, diphenylguanidine (DPG) CAS No: 102-06-7 purity 99%, used cooking oil (UCO) derived from palm oil as a softener, sulfur CAS No: 7704-34-9 purity 99%, and paraffin wax with a melting point of 37 °C (99 °F; 310 K).

Instrumentation

The tools used for this study consisted of rubber mixing mill Model No. XK 160-450 origin China (Mainland), analytical balance capacity of 3.200 g (Mettler Toledo ME30020), platen rubber vulcanizing press rubber machine Model Number: SKZ401, infrared thermometer (Brand KRISBOW-KW08-280), and molding (equipment for making test samples).

Experimental Design

Studies on the effects of natural rubber composites and synthetic rubbers were carried out by varying natural rubber (NR) type SIR-20, and nitrile butadiene rubber (NBR-N.2205), ethylene propylene diene rubber

monomer (EPDM). The ratio of additional ingredients used, such as accelerators, color pigments, activators, fillers, anti-oxidants, anti-ozone, softeners, and conditioned vulcanization. This experiment consisted of five treatments with three replications. Discussion is taken from the average of experiments. The ratio of ingredients used in this study for each formula is shown in Table 1.

Procedure

Compound preparation

The natural rubber is ground with an open mill until it becomes soft (15 min). While continuing grinding, nitrile butadiene rubber is added, and at the same time, EPDM is added as well (3 min), then followed by the addition of titanium oxide until the rubber composite color turns white when pounded for 2 min. The next yellow pigment is added until the rubber composite color turns yellow within 2 min while continuing to add ZnO and stearic acid for 2 min. Next, silica, paraffin wax, kaolin, PEG, TMQ, and UCO were added together in grinding for 4 min. MBTS and DPG were added together to the rubber mixture with a grinding time of 2 min. Sulfur is added when all the mixture is homogeneous, and

it took 2 min of grinding. The total grinding time was 32 min. The ratio of each ingredient added is shown in Table 1.

Making vulcanizate rubber

The resulting rubber compound is then placed in a molding tool, then vulcanized at a temperature of 130 ± 2 °C for 17 min using a hot press.

Test method

The five formulas of vulcanizate rubber were tested for parameters as follows the hardness testing before and after aging (ASTM D.2240-15), tensile strength before and after aging (ASTM D.412-16), modulus 300% (ASTM 412.16), elongation at break (ASTM D.412-16), tear strength (ASTM D.624-00, ra2012), the specific gravity (ASTM D.297-15), abrasion resistance (ASTM D.5963-04, ra2015), compression set, 25% defl, 70 °C, 22 h (ASTM D.395-16e1), and abrasion resistance (to ASTM D.5963-04, ra20150).

RESULTS AND DISCUSSION

Hardness

The hardness test of natural rubber composites with synthetic rubber from five formulas (Table 1) shows different results, as shown in Fig. 1. Formula A has the lowest hardness value (73 Shore A) compared to the other formulas (B, C, D, and E). Meanwhile, the highest hardness test result (78 Shore A) is seen in formula D (Fig. 1).

The hardness value of rubber vulcanizates is influenced by the ratio of filler, additives, softeners (Table 1), and the density of bonds between molecules of the material. Other than that fillers material kaolin, and silica, according to their respective, its characteristics influence the rubber vulcanizates hardness. The distribution of additives and fillers to rubber composites (natural rubber and synthetic rubber) is influenced by the softener and bond density between composite molecules. Softener material serves to stretch the bond between the composite rubber molecules so that the added material can be distributed evenly into the composite matrix molecule. The hardness value of rubber

Table 1. Rubber composite formula

Ingredients	Formula				
	A*	B*	C*	D*	E*
NR-SIR 20	100	80	75	75	80
NBR	0	10	10	15	20
EPDM	0	10	15	10	0
TiO ₂	4.15	4.15	4.15	4.15	4.15
Pigment Yellow	5	5	5	5	5
ZnO	4.75	4.75	4.75	4.75	4.75
Stearic Acid	2.25	2.25	2.25	2.25	2.25
Silica	50.25	50.25	50.25	50.25	50.25
Paraffin Wax	1.25	1.25	1.25	1.25	1.25
Kaolin	4	4	4	4	4
UCO	6.55	6.55	6.55	6.55	6.55
MBTS	1.85	1.85	1.85	1.85	1.85
PEG	2.75	2.75	2.75	2.75	2.75
TMQ	1.25	1.25	1.25	1.25	1.25
DPG	0.95	0.95	0.95	0.95	0.95
Sulfur	2.75	2.75	2.75	2.75	2.75

annotation: *phr

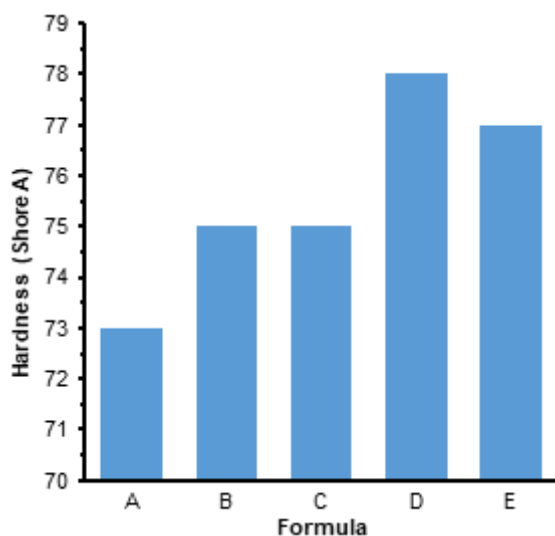


Fig 1. Hardness of the composites

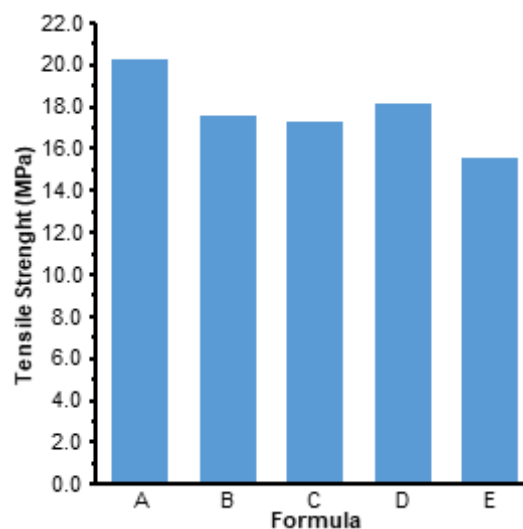


Fig 2. Tensile strength of the composites

vulcanizates indirectly illustrates the strength of the bond between a material molecule against pressure by another object [41]. Rubber vulcanizates (Formula A) with kaolin fillers and silica (Table 1) without composition with synthetic rubber (NR and EPDM) hardness value is lower than the value of the hardness of other formulas (Fig. 1). According to Johns and Rao [42], natural rubber that is not mixed with synthetic rubber has a lower hardness value than natural rubber mixed with synthetic rubber.

This shows that the hardness of rubber vulcanizates is influenced by the interaction between natural rubber molecules and synthetic rubber molecules. Additives and fillers with the help of softener to stretch the molecular structure of matrix composites have contributed to the hardness value. In addition, the bonding between molecules of materials and the formation of cross-link reactions by sulfur affect the value of hardness.

Tensile Strength

The tensile strength describes the strength of a bond between material molecules when pulled in the opposite direction. When a material is pulled, there is a shift between molecules following the direction of withdrawal. The tensile strength of a material is influenced by the type of material used, the ratio of the material, and the process of its formation.

The test data in Fig. 2 shows that the lowest tensile strength value is 15.6 MPa in the formula E. The tensile

strength value is influenced by the density of cross bonds between the material molecules. In addition, the tensile strength that is influenced by the ratio of the mixture of natural rubber and synthetic rubber is also influenced by additives, softeners, and fillers (Table 1). The results of the tensile strength test are inversely proportional to the value of the hardness test (Fig. 2). This shows that there is an inverse relationship between the tensile strength with hardness. Tensile strength is related to the degree of elasticity, while hardness is related to the degree of density of the broad unity of the material. Rubber elasticity affects the value of hardness, where the elasticity value of natural rubber is a synthetic rubber. Natural rubber naturally has high elasticity, but its hardness value is low.

The addition of additives to the composite rubber causes interactions between molecules that form strong bonds, which results in increased tensile strength [43]. The addition of additives to natural rubber composites with synthetic rubber, in addition, to increase the density of cross-linking between molecules, also reduces elasticity [44]. Besides, cross-linking density is also influenced by the ratio of material and temperature during the vulcanization process. Natural rubber without composite with synthetic rubber has a higher elasticity (Formula A) compared to composite rubber formulas B, C, D, and E. The differences in elasticity of

natural rubber and rubber composites cause differences in tensile strength (Fig. 2).

Modulus 300%

The modulus test results of 300% natural rubber and synthetic rubber composites (Fig. 3) show that the modulus values of formulas B and C are lower (4.9 MPa) than other formulas (Table 1). Modulus describes the strength needed to stretch the sample to a certain state. According to Dahham et al. [45], the increase in modulus occurs due to an increase in bonds between rubber molecules with additive molecules and filler molecules. According to Chaturvedi et al. [46], differences in modulus values indicate differences in cross-linking density and differences in material ratios.

The combination of several molecules of filler and softener in natural rubber composites with synthetic rubber can improve thermal performance. Improved thermal performance causes a synergistic effect between material molecules [47]. Bonds between material molecules affect the modulus value. The difference in strain strength in products from rubber composite materials, as shown in Fig. 3, is influenced by the strength of the cross-linking between the molecules and the difference in the ratio of natural rubber and synthetic rubber (Table 1).

The difference in the ratio of ingredients causes differences in reactions between molecules and affects the nature of the product formed. Formula A, as a

comparison formula without addition synthetic rubber, has lower modulus value than formula D, and E. However, the value is higher than formula B and Formula C. This is caused by differences in the degree of cross-linking formed from each ratio of the formula. The difference in the formation of the degree of cross-linking is influenced by the interaction between the rubber molecule and the filler [48-50].

In addition, fillers (kaolin, and silica) and softeners added to this study had a significant effect on the vulcanization process. Silica, as a reinforcing filler added to rubber composites, aims to improve modulus and other properties [51]. According to Setyowati et al. [52], the addition of active fillers to rubber compounds can improve the properties of rubber vulcanizates better. The difference in modulus values is caused by differences in the cross-linking that is formed from each formula. Silica can gradually increase interactions between fillers and rubber matrices [53]. The speed cross-linking interaction that is formed is influenced by sulfur, additives, fillers, softeners, the ratio of natural rubber, and synthetic rubber used. The difference in the ratio of natural rubber and synthetic rubber (Table 1) determines the difference in modulus values (Fig. 3).

Elongation at Break

The elongation at break test results of the five formulas (Table 1) shows that there are differences (Fig. 4).

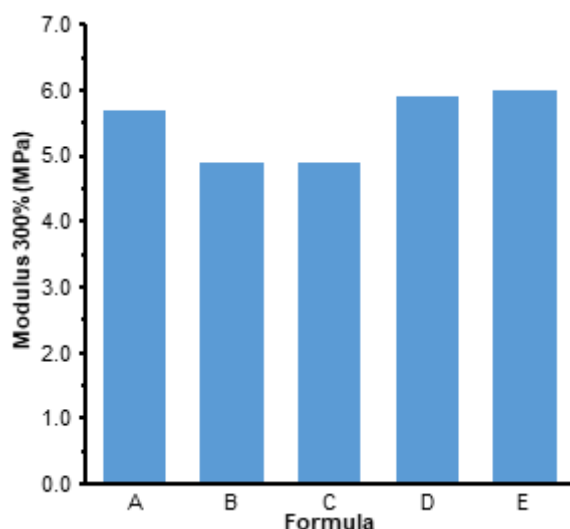


Fig 3. Modulus of the composites

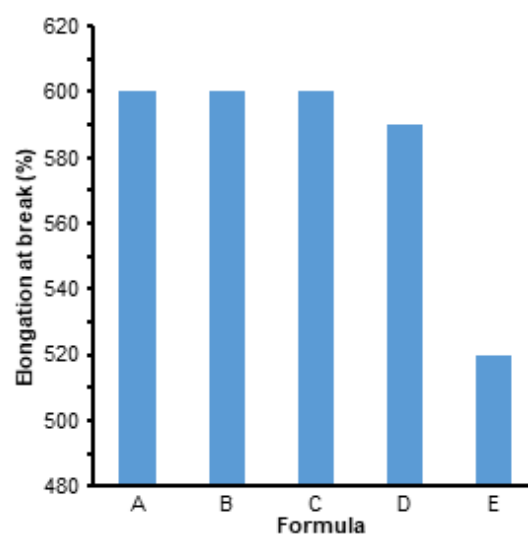


Fig 4. Elongation at break of the composites

The difference in the value of elongation at break is due to the difference in the ratio of natural rubber with synthetic rubber used. The difference in the ratio of natural rubber and synthetic rubber causes differences in the speed of interaction between the additive, sulfur, and filler molecules. In addition, with the difference in the ratio of natural rubber and synthetic rubber, the softener's performance to stretch the molecules of the composite material follows the ratio of the material used. The elongation at break is directly related to the bond between the molecules, the density of the cross-linking formed, and the degree of elasticity of natural rubber with synthetic rubber composites.

Elongation at break occurs because energy is used to stretch the bond between the vulcanizates molecules to break. Elongation at break is influenced not only by the ratio of natural rubber and synthetic rubber (Table 1) but also by the interaction of fillers and softening that form bonds between the molecular. Additives are added to natural rubber composites with synthetic rubber with the help of sulfur forming a cross-linked network. According to Delchev et al. [54], the addition of active fillers and softeners to rubber composites can increase elongation at break, modulus, hardness, tensile strength.

The interaction between the materials used (Table 1), which forms natural rubber and synthetic rubber composites, greatly determines the value of elongation at break. In addition, the value of elongation at break is also influenced by softening material used to stretch composite molecules. The test results show that, for natural rubber formula A without synthetic rubber, the elongation at break value is the same as formula B and formula C, but higher than formula D and formula E (Fig. 4). For formula A, interactions occur between natural rubber molecules and molecules of additives. For formulas B, C, D, and E, the interactions occur between molecules of natural rubber, synthetic rubber, and additives.

The elongation at break test results for formula D (590%) is lower than formulas A, B, C (600%), but their values are higher than formula E (520%). The ratio of EPDM and NBR in natural rubber molecules affects the bond between molecules of rubber composite compounds. EPDM and NBR at optimal ratios can

produce strong bonds because of their interactions with rubber fillers [55]. Increasing the NBR ratio and decreasing the EPDM ratio in rubber composites (Table 1) affects the cross-link density and the elongation at break value. According to Kim et al. [56], the difference in the EPDM ratio of rubber composites can affect breakout extension values. In formulas B and C, NBR and EPDM produce an elongation at break value that is equal to the value of the elongation at break formula A (Fig. 4). This illustrates, in formulas B and C, the density of bonds between molecules is the same as formula A. For formulas B, C, D, and E, the interaction that occurs is influenced by the speed of the reaction between molecules of natural rubber composites and synthetic rubber. In addition, additives, fillers, softeners, and sulfur are added to accelerate the vulcanization process to form vulcanizate rubber. When viewed from the ratio of natural rubber and synthetic rubber, it affects the value of elongation at break.

Tear Strength

The tear strength value, as shown in Fig. 5, showed that formula E is higher (63.6 kN/m) than other formulas, and formula D has the lowest tear strength value (54.8 kN/m). The added softener material (Table 1) affects the bond between the rubber composite molecules. At the same time, the movement of the filler and the additive occupy the rubber composite chamber. The amount of additives and fillers that occupy the space between the rubber composite molecules influences the difference in tear strength values.

Formula A, as a comparison formula without synthetic rubber, has a tear strength value equal to formula B but is lower than formula E (Fig. 5). The difference in the value of tear strength from each formula was caused by the ratio of natural rubber and synthetic rubber, while for the addition of softener material and filler material affected the mechanical properties of rubber, especially against the value of tear strength. Tear strength is directly related to the bonds between molecules, cross-linking, and the level of density of molecules that form rubber vulcanizates. In addition, the ratio of natural rubber and synthetic rubber

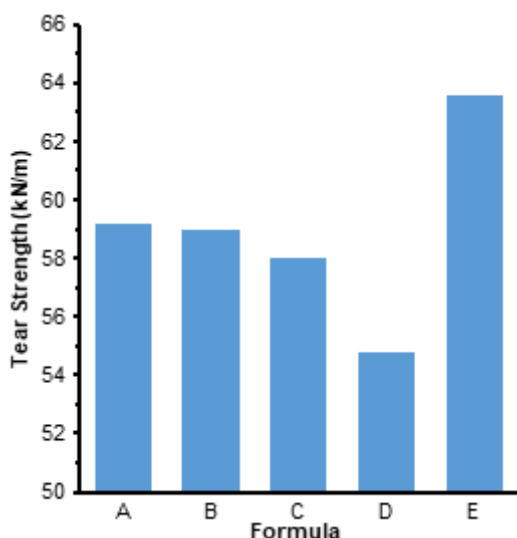


Fig 5. Tear strength of the composites

and fillers greatly determines the binding capacity between molecules, which ultimately determines the nature of the rubber vulcanizates. The ratio of the ingredients added (Table 1) influences the intensity of the polymer chain in the form of bonds. It increases the functional groups associated with the Van der Waals style to the polymer chain in a composite of natural rubber with synthetic rubber.

Specific Gravity

The results of testing the specific gravity of the five samples before and after aging, as shown in Fig. 6, have a significant difference. The specific gravity value of formula B before aging and after aging is 1.160 g/cm^3 , lower than formulas A, C, D, and E. The specific gravity values for formula E before aging and after aging of 1.18 g/cm^3 are higher than formulas A, B, C and D (Fig. 6). The aging process causes damage to the elastomeric tissue [55]. Elastomeric tissue damage due to an increase in temperature during the aging process. During the aging process, there is a movement of bonds between the material molecules. The movement of bonds between molecules can damage the molecular structure of the material. The occurrence of molecular expansion or constriction due to the aging process depends on the mechanical properties of the ingredients and the ratio of the constituent materials.

The difference in the value of specific gravity is not

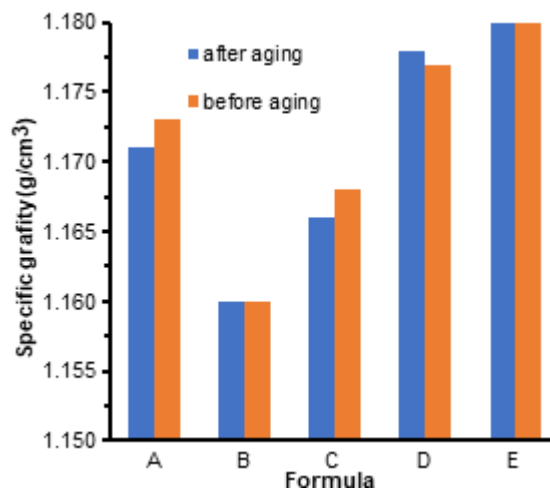


Fig 6. Specific gravity of the composites

only influenced by the level of density between the molecules of the material. However, it is also affected by the compound milling process. The distribution of material into the rubber vulcanizate molecule, the time of vulcanization, and the change in temperature at the time of compound maturation also affect specific gravity.

The ability of softener to stretch the molecular structure of the rubber composite during grinding also influences the speed of the additive and filler to enter the molecular structure of the rubber composite. The speed of distribution of the material into the rubber composite molecule at the time of compound milling and the speed of the vulcanization reaction that forms a three-dimensional network have an effect on the density of cross bonds and the level of density of the rubber composite. In addition, differences in material ratios and material types also affect differences in specific gravity values. According to Hashim et al. [57], changes in the value of specific gravity are influenced by the ingredients used. Increasing the specific gravity of rubber can be caused by an increase in cross-link between rubber and filler material, where cross-linking density causes reduced pores formed [15]. The number of pores formed affects molecular density and specific gravity values.

Abrasion Resistance

Rubber vulcanizates test results for abrasion resistance before and after aging in Fig. 7 show a significant difference.

Testing after aging is carried out at 70 °C for 24 h and aimed to determine the loss of the surface after abrasion. Loss of surface part of rubber vulcanizates occurs due to friction/touch with the object in its path or can be expressed by losing the volume of rubber vulcanizates during friction. The lowest abrasion test results are 169.0 mm³ and 175 mm³ for after aging and before aging in formula C, respectively. Meanwhile, the highest abrasion resistance after aging of 188.2 mm³ was obtained from treatment A. The lowest abrasion resistance before aging is 208.7 mm³ in the formula E (Fig. 7).

The surface loss of rubber vulcanizates is affected by the cross-linking formed during vulcanization, where the strength of the cross-linking is influenced by the ratio of the material used (Table 1). Abrasion resistance is related to the strength of bonds between molecules characterized by the formation of mono-sulfide and disulfide structures. Sulfur, which forms cross-linking with densities between molecules, determines abrasion resistance [58].

Compression Set

The results of the compression set test of the five formulas (Table 1) for vulcanizates show significant differences. The lowest compression set test result of 45.3% was found in formula A, and for the highest test result of 54.91% was obtained from sample D (Fig. 7). Tests of compression set of rubber vulcanizates were carried out at 25% defl, the temperature of 70 °C, for 22 h.

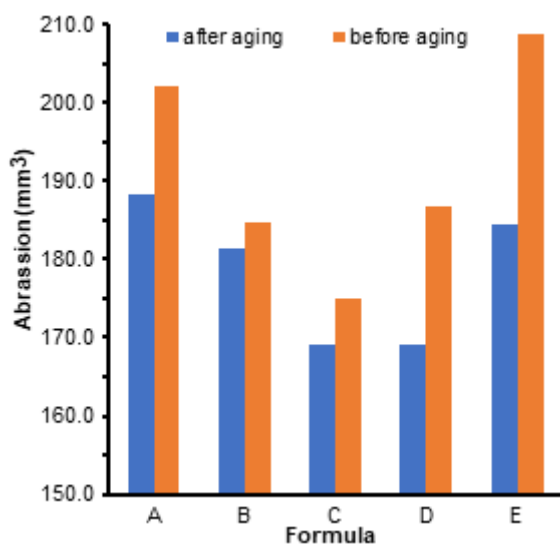


Fig 7. Abrasion resistance of the composites

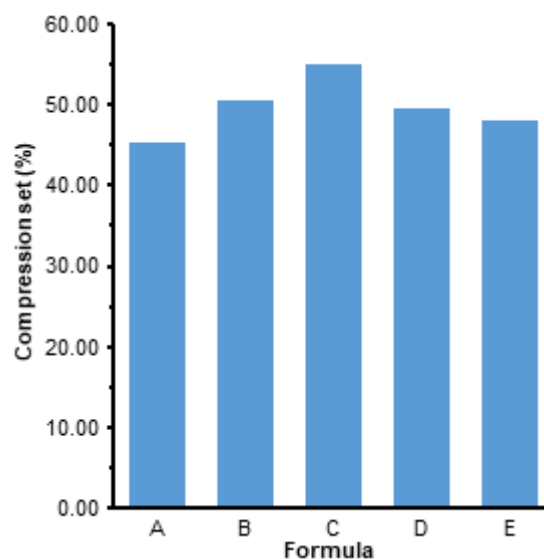


Fig 8. Compression set of the composites

The difference in the value of compression sets is influenced by the interaction between materials and material ratios (Table 1). Based on the test data, Fig. 8 illustrates the bond strength between composite rubber molecules influenced by the strength of the cross-linking formed from the reaction of sulfur with rubber molecules and additives. The strength of cross-linking is influenced by the vulcanization process and the ratio of the material used. The mechanical properties of vulcanization composites are influenced by composite compounds, material distribution, and material homogeneity [59]. Homogeneity and the specific gravity of materials affect the resistance of rubber vulcanizates when under pressure. In addition, the value of the compression set is related to the mass specific gravity, which is illustrated by the values of specific gravity, elongation at break, and other properties.

CONCLUSION

The study of natural rubber composites with synthetic rubber (NBR, and EPDM) using used cooking oil softeners has an effect on differences in the mechanical properties of the resulting rubber vulcanizate. The difference in the ratio of natural rubber and synthetic rubber affects the performance of the softener to stretch the molecular structure of the composite material (natural rubber with synthetic rubber) and affects the bond between the molecular, as well as the

formation of the cross-link reaction by the sulfur. The test results of mechanical properties such as A formula, as a comparative formula without composites with synthetic rubber, have a value of 73 Shore A hardness, which is lower than B, C, D, and E formulas. The tensile strength value of 20.3 MPa is higher than the B, C, D, and E formulas. Modulus 300% with a value of 5.7 MPa is higher than B, and C formulas but lower than D, and E formulas. The Elongation at break with a value of 600% is the same as B and C formulas. However, the value is higher than D, and E formulas. Tear strength of 59.2 kN/m is higher than B, C, and D formulas but lower than E formula. The specific gravity value before aging of 1.173 g/cm³, and after aging of 1.171 g/cm³, is higher than B, and C formulas, but lower than D, and E formulas. The abrasion resistance before the aging of 202.2 mm³ is higher than B, C, and D formulas but lower than E formula. The abrasion resistance after aging of 188.2 mm³ is higher than B, C, D, and E formulas. The compression set with a value of 45.3% is lower than B, C, D, and E formulas.

■ ACKNOWLEDGMENTS

Thanks to the Head of Palembang Institute for Industrial Research and Standardization for providing research facilities, Director of PT Shima Prima Utama, which has provided information regarding the use of rubber for medical equipment and provides research facilities, and technicians. PT. Shima Prima Utama who has helped research activities. Thank you to Prof. Dr. Ir. Dedik Budianta, MS, who has deigned to correct this manuscript.

■ REFERENCES

- [1] Masłowski, M., Miedzianowska, J., and Strzelec, K., 2019, Natural rubber composites filled with crop residues as an alternative to vulcanizates with common fillers, *Polymers*, 11 (6), 972.
- [2] Sawere, B.T., and Igbuku, A.U., 2016, Evaluation of some mechanical properties of composites of natural rubber with egg shell and rice husk, *Int. Res. J. Adv. Eng. Sci.*, 1 (3), 71–75.
- [3] Koumoulos E.P., Trompeta, A.F., Santos, R.M., Martins, M., dos Santos, C.M., Iglesias, V., Böhm, R., Gong, G., Chiminelli, A., Verpoest, I., Kiekens, P., and Charitidis, C.A., 2019, Research and development in carbon fibers and advanced high-performance composites supply chain in Europe: A roadmap for challenges and the industrial uptake, *J. Compos. Sci.*, 3, 86.
- [4] Pandian, J.J., and Govindan, T., 2015, Comparative studies on the mechanical properties of natural rubber and natural rubber carbon black composites, *IJETCSE*, 13 (2), 48–52.
- [5] Krishnan, Y., Chandran, S., Usman, N., Smitha, T.R., Parameswaran, P.S., and Prema, K.H., 2015, Processability, mechanical and magnetic studies on natural rubber- ferrite composites, *Int. J. Chem. Stud.*, 3 (1), 15–22.
- [6] Yahya, Y.S.R., Azura, A.R., and Ahmad, Z., 2011, Effect of curing systems on thermal degradation behaviour of natural rubber (SMR CV 60), *J. Phys. Sci.*, 22 (2), 1–14.
- [7] Linos, A., Berekaa, M.M., Reichelt, R., Keller, U., Schmitt, J., Flemming, H.C., Kroppenstedt, R.M., and Steinbüchel, A., 2000, Biodegradation of *cis*-1,4-polyisoprene rubbers by distinct actinomycetes: Microbial strategies and detailed surface analysis, *Appl. Environ. Microbiol.*, 66 (4), 1639–1645.
- [8] Mente, P., Motaung, T.E., and Hlangothi, S.P., 2016, Natural rubber and reclaimed rubber composites-A systematic review, *Polym. Sci.*, 2 (1), 7.
- [9] Aguele, F.O., Madufor, C.I., and Adekunle, K.F., 2014, Comparative study of physical properties of polymer composites reinforced with uncarbonised and carbonised coir, *Open J. Polym. Chem.*, 4, 73–82.
- [10] Egwaikhide, P.A., Akporhonor, E.E., and Okieimen, F.E., 2007, Effect of coconut fibre filler on the cure characteristics physico-mechanical and swelling properties of natural rubber vulcanisates, *Int. J. Phys. Sci.*, 2 (2), 039–046.
- [11] Pornprasit, R., Pornprasit, P., Boonma, P., and Natwichai, J., 2016, Determination of the mechanical properties of rubber by FT-NIR, *J. Spectro.*, 2016, 4024783.
- [12] Arayapranee, W., and Rempel, G.L., 2013, Effects of polarity on the filler-rubber interaction and

- properties of silica filled grafted natural rubber composites, *J. Polym.*, 2013, 279529.
- [13] Ajam, A.M., Al-Nesrawy, S.H., and Al-Maamori, M., 2016, Effect of reclaim rubber loading on the mechanical properties of SBR composites, *Int. J. Chem. Sci.*, 14 (4), 2439–2449.
- [14] Ismail, H., Ahmad, H.S., and Rashid, A.A., 2015, Fatigue, resilience, hardness, and swelling behaviour of natural rubber/recycled acrylonitrile-butadiene rubber (NR/NBRr) blends, *Polym. Polym. Compos.*, 23 (8), 583–588.
- [15] Kapgate, B.P., Das, C., Basu, D., Das, A., and Heinrich, G., 2013, Rubber composites based on silane-treated stöber silica and nitrile rubber: Interaction of treated silica with rubber matrix, *J. Elastomers Plast.*, 47 (3), 248–261.
- [16] Mousavi, M., Arjmand, O., Mostajabi, H., and Shooli, H., 2013, Investigation of physical, mechanical and biodegradation properties of nitrile butadiene rubber by natural polymers and nano-silica particles, *AIJRFANS*, 5 (1), 110–117.
- [17] Suzuki, N., Ito, M., and Ono, S., 2005, Effects of rubber/filler interactions on the structural development and mechanical properties of NBR/Silica composites, *J. Appl. Polym. Sci.*, 95 (1), 74–81.
- [18] Singh, R., Shah, M.D., Jain, S.K., Shit, S.C., and Giri, R., 2013, Elastomeric composite: Mechanical and thermal properties of styrene butadiene rubber (SBR) based on carbon black and nanoclay, *J. Inf. Knowl. Res. Mech. Eng.*, 02 (02), 515–521.
- [19] Wu, W., and Tian, L., 2013, Formulation and morphology of kaolin-filled rubber composites, *Appl. Clay Sci.*, 80–81, 93–97.
- [20] Setyorini, I., and Yuniari, A., 2017, Determination of vulcanization rate constant, crosslink density, and free sulfur content on carbon black filled EPDM, *MKKP*, 33 (2), 93–98.
- [21] Ugbaja, M.I., Onuoha, M.I., Ibeneme, U., Uzochukwu, M.I., Opara, H., and Mbada, I.N., 2016, Swelling and mechanical behaviour of natural rubber vulcanisate filled with leather wastes (buffing dust) and its modeling, *Am. J. Appl. Sci. Res.*, 2 (2), 6–11.
- [22] Okele, I.A., Mohammed, F., Agho, B.O., Marut, A.J., and Jekada, J.Z., 2015, Experimental study on particle size and filler loading reinforcement of sugarcane baggase on natural rubber compound, *RRPL*, 6 (4), 155–160.
- [23] Aguele, F.O., and Madufor, C.I., 2012, Effects of carbonised coir on physical properties of natural rubber composites, *Am. J. Polym. Sci.*, 2 (3), 28–34.
- [24] Mohammed, M.R., and Hadi, A.N., 2012, Effect of egg shells powder on some mechanical and physical properties of natural rubber (NR), *Iraqi J. Mech. Mater. Eng.*, 12 (3), 446–458.
- [25] Momoh, F.P., Mamza, P.A.P., Gimba, C.E., and Nkeonye, P., 2016, Morphological trends of modified coconut fibre in natural rubber reinforcement, *JETEAS*, 7 (4), 167–172.
- [26] Ahmed, K., Nizami, S.S., Raza, N.Z., and Shirin, K., 2012, Cure characteristics, mechanical and swelling properties of marble sludge filled EPDM modified chloroprene rubber blends, *Adv. Mater. Phys. Chem.*, 2 (2), 90–97.
- [27] Ahmed, K., Nizami, S.S., Raza, N.Z., and Habib, F., 2013, The effect of silica on the properties of marble sludge filled hybrid natural rubber composites, *J. King Saud Univ. Sci.*, 25 (4), 331–339.
- [28] Wang, J., and Chen, D., 2013, Mechanical properties of natural rubber nanocomposites filled with thermally treated attapulgite, *J. Nanomater.*, 2013, 496584.
- [29] Da Costa, H.M., Visconte, L.L.Y., Nunes, R.C.R., and Furtado, C.R.G., 2000, The effect of coupling agent and chemical treatment on rice husk ash-filled natural rubber composites, *J. Appl. Polym. Sci.*, 76, 1019–1027.
- [30] Samarth, N.B., and Mahanwar, P.A., 2015, Modified vegetable oil based additives as a future polymeric material-Review, *Open J. Org. Polym. Mater.*, 5, 1–22.
- [31] Song, F., Xia, H., Jia, P., Zhang, M., Hu, L., and Zhou, Y., 2018, The effects of epoxidized acrylated castor oil (EACO) on soft poly (vinyl chloride) films as a main plasticizer, *Pol. J. Chem. Technol.*, 20, (4), 13–19.

- [32] Pechurai, W., Chiangta, W., and Tharuen, P., 2015, Effect of vegetable oils as processing aids in SBR compounds, *Macromol. Symp.*, 354 (1), 191–196.
- [33] Puspitasari, S., and Cifriadi, A., 2014, Pembuatan bahan pelunak alami untuk kompon karet melalui reaksi hidrogenasi minyak jarak castor, *Indonesian J. Nat. Rubb. Res.*, 32 (1), 56–64.
- [34] Nasir, A.N.M., Romli, A.Z., Wahab, M.A., and Abidin, M.H., 2013, Effect of Epoxidized palm oil (EPO) on tensile properties and density of rubber compounding, *Adv. Mater. Res.*, 812, 216–220.
- [35] Syamin, Y.M., Azemi, S., and Dzaraini, K., 2017, Evaluation of cooking oil as processing additive for natural rubber, *ASEAN J. Sci. Technol. Dev.*, 34 (1), 17–25.
- [36] Puspitasari, S., and Cifriadi, A., 2013, Karakterisasi proses vulkanisasi minyak jarak kastor dan evaluasi mutu hasil faktis cokelat, *Buletin RISTRI*, 4 (2), 99–108.
- [37] Song, S.H., 2018, The effect of palm oil-based hybrid oils as green multifunctional oils on the properties of elastomer composites, *Polymers*, 10 (9), 1045.
- [38] Nasruddin, and Susanto, T., 2018, Thermal, morphological and physic-mechanical properties of natural rubber-CaCO₃ composites using jatropa oil as softener, *MATEC Web Conf.*, 156, 05016
- [39] Aprem, A.S., Thomas, S., Joseph, K., Barkoula, N.M., and Kocsis, J.K., 2003, Sulphur vulcanisation of styrene butadiene rubber using new binary accelerator systems, *J. Elastomers Plast.*, 35 (1), 29–55.
- [40] Joseph, R., Alex, R., Vinod, V.S., Premalatha, C.K., and Kuriakose, B., 2003, Studies on epoxidized rubber seed oil as plasticizer for acrylonitrile butadiene rubber, *J. Appl. Polym. Sci.*, 89 (3), 668–673.
- [41] Ramdja, A.F., Febrina, L., and Krisdianto, D., 2010, Pemurnian minyak jelantah menggunakan ampas tebu sebagai adsorben, *J. Teknik Kimia*, 17 (1), 7–14.
- [42] Johns, J., and Rao, V., 2009, Mechanical properties and swelling behavior of cross-linked natural rubber/chitosan blends, *Int. J. Polym. Anal. Charact.*, 14 (6), 508–526.
- [43] Mohamad, N., Sharafina, Z.N., Ab Maulod, H.E., Yuhazri, M.Y., and Jeefferie, A.R., 2013, Morphological and mechanical properties of polypropylene/epoxidized natural rubber thermoplastic vulcanizates treated with maleic anhydride-grafted polypropylene, *IJAME*, 8, 1305–1315.
- [44] Egwaikhide, A.P., Okieimen, F.E., and Lawal, U., 2013, Rheological and mechanical properties of natural rubber compounds filled with carbonized palm kernel husk and carbon black (N330), *Sci. J. Chem.*, 1 (5), 50–55.
- [45] Dahham, O.S., Noriman, N.Z., Kahar, A.W.M., Ismail, H., and Sam, S.T., 2015, The Effect of sawdust loading as natural short fiber on NBR/NRL-G compounds, *J. Appl. Sci. Agric.*, 10 (5), 33–39.
- [46] Chaturvedi, A., Chaturvedi, S., Rajkumar, K., and Patil, A.S., 2016, Experimental study of natural rubber based shock attenuation device, *Int. J. Eng. Stud.*, 8 (1), 63–71.
- [47] Zhang, H., Li, Y., Shou, J.Q., Zhang, Z.Y., Zhao, G.Z., and Liu, Y.Q., 2015, Effect of curing temperature on properties of semi-efficient vulcanized natural rubber, *J. Elastomers Plast.*, 48 (4), 331–339.
- [48] Valentini, L., Bon, S.B., Lopez-Manchado, M.A., Verdejo, R., Pappalardo, L., Bolognini, A., Alvino, A., Borsini, S., Berardo, A., and Pugno, N.M., 2016, Synergistic effect of graphene nanoplatelets and carbon black in multifunctional EPDM nanocomposites, *Compos. Sci. Technol.*, 128, 123–130.
- [49] Karaağaç, B., İnal, M., and Deniz, V., 2011, Predicting optimum cure time of rubber compounds by means of ANFIS, *Mater. Des.*, 35, 833–838.
- [50] Alemdar, A., and Sain, M., 2008, Biocomposites from wheat straw nanofibers: Morphology, thermal and mechanical properties, *Compos. Sci. Technol.*, 68 (2), 557–565.
- [51] Chuayjuljit, S., Imvittaya, A., Na-Ranong, N., and Potiyaraj, P., 2002, Effects of particle size and amount of carbon black and calcium carbonate on

- curing characteristics and dynamic mechanical properties of natural rubber, *JMMM*, 12 (1), 51–57.
- [52] Setyowati, P., Rahayu, S., and Supriyanto, 2004, Karakteristik karet ebonit yang dibuat dengan berbagai variasi rasio RSS I/Riklim dan jumlah belerang, *MKKP*, 20 (1), 10–14.
- [53] Norhafizah, Z., Noriman, N.Z., Kamarudin, H., Sam, S.T., Ismail, H., Omar, M.F., Ruzaidi, C.M., and Afiratul, A.A., 2015, Properties of ethylene propylene diene monomer/recycled acrylonitrile-butadiene rubber blends (EPDM/rNBR): Effect of the addition of bamboo fillers, *Appl. Mech. Mater.*, 815, 19–23.
- [54] Delchev, N., Malinova, P., Mihaylov, M., and Dishovsky, N., 2014, Effect of the modified solid product from waste tyres pyrolysis on the properties of styrene-butadiene rubber based composites, *J. Chem. Technol. Metall.*, 49 (6) 525–534.
- [55] Neuhaus, C., Lion, A., Johlitz, M., Heuler, P., Barkhoff, M., and Duisen, F., 2017, Fatigue behavior of an elastomer under consideration of ageing effects, *Int. J. Fatigue*, 104, 72–80.
- [56] Kim, Y.S., Kim, Y.T., and Jeon, E.S., 2019, Optimization of accelerator mixing ratio for EPDM rubber grommet to improve mountability using mixture design, *Appl. Sci.*, 9, 2640.
- [57] Hashim, F.S., Almaamori, M.H., and Hamood, F.J., 2016, Effect of silica on the mechanical properties of rubber reclaim composite, *Int. J. Chem Tech Res.*, 9 (4), 325–333.
- [58] El-Sabbagh, S.H., Ismail, M.N., and Yehia, A.A., 2001, Effect of the curing systems on the fatigue behavior of NR vulcanizates, *J. Elastomers Plast.*, 33, 263–281.
- [59] Ateia, E.E., El-Nashar, D.E., Hassan, H.H., and Abd El-Aziz, A.K., 2017, A comparative study of the cure characteristics, mechanical properties and abrasion resistance of silica and carbon black filled NBR/SBR blends, *Egypt. J. Chem.*, 60 (5), 769–777.

Pharmacokinetic Study and Incurred Sample Stability of Esomeprazole in Dried Blood Spot Sample Using High Performance Liquid Chromatography-Photodiode Array

Yahdiana Harahap^{1,*}, Anja Tamabri¹, Vicha¹, Herman Suryadi¹, Sunarsih², and Callista Andinie Mulyadi¹

¹Faculty of Pharmacy, Universitas Indonesia, Depok 16424, West Java, Indonesia

²Dea Medika Clinic, Jl. Bina Marga No. 7, Gunung Putri, Bogor 16961, West Java, Indonesia

* **Corresponding author:**

email: yahdiana03@yahoo.com

Received: January 7, 2019

Accepted: August 15, 2019

DOI: 10.22146/ijc.42404

Abstract: In the past years, Esomeprazole (EMP) was analyzed in human plasma samples, which still has stability issues; thus, the new biosampling technique known as Dried Blood Spot (DBS) might solve the issue. This research aims to evaluate the incurred sample stability of esomeprazole in dried blood spot using high performance liquid chromatography-photodiode array with lansoprazole as an internal standard. The analytical separation was performed on a C-18 column (Waters, Sunfire™ 5 μm; 250 × 4.6 mm) at 40 °C. The mobile phase used was acetonitrile–phosphate buffer pH 7.6 (40:60% v/v) with a flow rate of 1.00 mL/min; and was detected at 300 nm. The analyte was extracted from dried blood spot by methanol. Incurred sample stability was evaluated from 6 healthy subjects on day 0, 7, 14, and 28, respectively. This method was linear in the range concentration of 70–1400 ng/mL with $r > 0.98$. Pharmacokinetic study shows that the average of AUC_{0-t} of EMP in the DBS sample was 1765.41 ngh/mL. The highest percent difference value of esomeprazole's incurred samples stability on day 7, 14, and 28 from 6 healthy subjects were 9.81%. This result fulfilled the acceptance criteria, which is the percent difference should not be greater than 20%, and 67% of total samples have to fulfill the criteria. The incurred sample stability result showed that esomeprazole was stable in the DBS sample at least until 28 days with the highest value of percent difference is 9.81%.

Keywords: dried blood spot; esomeprazole; lansoprazole; HPLC; incurred sample

■ INTRODUCTION

Esomeprazole (EMP) is one of the proton pump inhibitors indicated for gastroesophageal reflux. Until now, the analysis of EMP was carried out in plasma samples, which has several disadvantages [1]. New biosampling method known as Dried Blood Spot (DBS) has several advantages, including easy and non-invasive sample collection; harmless and is easily transported; the price of DBS paper is also relatively cheap, easy to handle and store; analytes in the absorbed matrix on DBS paper are generally more stable; the process of collecting DBS samples minimizes the risk of infection; and less blood volume is needed compared to analysis in liquid or plasma blood [2-5]. Previous pharmacokinetic (PK) studies of EMP was done using human plasma sample [6].

The stability of EMP in human plasma is still an issue from the latest PK study of EMP [7]. Omeprazole's Red Blood Count (RBC) to plasma partitioning value is 5.25. Analysis of drugs with high RBC to plasma partitioning value (> 2) is better performed using the whole blood rather than in plasma or serum because it will generate a more sensitive and accurate result for *in vivo* pharmacokinetic studies [8]. With the advantages of the DBS technique and usage of the whole blood, as mentioned above, this method might solve the stability issue of EMP in the bioanalytical study.

Besides being unstable in an acidic media, EMP is also unstable against the light, moisture, and oxidation [8]. The Global CRO Council suggests evaluating the incurred sample stability if there is an instability issue in the analyte [9]. Incurred sample stability needs to be

done because the use of calibration standards and quality control (QC) samples when validating *in vitro* cannot describe the condition of *in vivo* sample stability due to metabolic processes in the body [10]. To conduct the incurred stability in the DBS sample, this study used 6 healthy subjects who had administered 40 mg EMP film-coated tablet. The pharmacokinetic parameters should be determined on the day the blood was collected (day 0), and the incurred stability was determined on 7, 14, and 28 days. This study had obtained ethical clearance from the Ethical Committee of Medical Faculty Universitas Indonesia No. 0036/UN2.F1/ETIK/2018.

■ EXPERIMENTAL SECTION

Materials

Esomeprazole (Esteve Quimica), Lansoprazole (Sigma-Aldrich), methanol HPLC grade, methanol, phosphoric acid, sodium hydroxide, formic acid, disodium hydrogen phosphate, sodium dihydrogen phosphate, acetonitrile, and dichloromethane were purchased from Merck (Darmstadt, Germany). The other materials used were Aqua pro injection was purchased from Ikapharmindo (Jakarta, Indonesia), and Perkin Elmer 226 papers were purchased Perkin Elmer (Waltham, Massachusetts, USA).

Instrumentation

The instruments used were HPLC equipped with pump (Shimadzu, LC-20AD), auto-sampler (Shimadzu, SIL-20A), column C-18 (Waters, Sunfire™; 5µm, 250 × 4.6 mm), photodiode array detector (Waters 2996), and data processor (Dell), pH meter (Eutech pH 510), analytical scales (Acculab), filter paper (Whatman), degasser (Elmasonic S60H), centrifuge (Digisystem DSC-300SCD), freezer (Biomedical Labtech Deep Freezer), vortex (Maxi Mix II), evaporator (TurboVap LV), micropipette Eppendorf (Socorex), blue tip, yellow tip, and glasses equipment.

Procedure

Chromatography system

The analytical separation used C-18 column (Waters, Sunfire™ 5µm; 250 × 4.6 mm) and acetonitrile –

phosphate buffer pH 7.6 (40:60) as mobile phase with a flow rate of 1.0 mL/min isocratically. The column temperature was set at 40 °C, and the injection volume was 20 µL. Detection was performed with Photodiode Array (PDA) with a wavelength of 300 nm [11].

Optimization of esomeprazole in dried blood spot sample preparation

Whole blood samples containing EMP were spotted on DBS paper and dried. The DBS paper was cut in accordance with the spot size, extracted using methanol, shaken with vortex, sonicated, and centrifuged. The supernatant was evaporated under a nitrogen gas flow at 40 °C for 15 min, and the residue was reconstituted using 100 µL of solvent. Then it was centrifuged for 5 min in the autosampler vial, and 20 µL of the aliquot was injected into the HPLC. The optimized parameters were blood volume spotting, duration of drying, extraction method, the volume of extracting solution, time of vortex shaking, sonication time, centrifugation time, evaporating treatment, and solvent type for reconstitution of residue.

Method validation of esomeprazole analysis in dried blood spot

This study referred to the European Medicines Agency (EMA) Guideline for Bioanalytical Method Validation 2011 and the Food and Drug Administration (FDA) Guidance for Bioanalytical Method Validation 2013 [12-13]. Validation parameters were selectivity, carry over, lower limit of quantification (LLOQ), the linearity of calibration curve, accuracy, precision, recovery, dilution integrity, and stability.

Blood sampling on healthy volunteers

This study was approved (no.: 0036UN2/F1/ETIK/2018) by the Ethics Committee of Faculty of Medicine, Universitas Indonesia. Prior to the study, all 6 subjects (age: 20–55 years old, BMI: 18.5–24.9 kg/m²) had been declared healthy based on the results of medical check-ups and had signed the informed consent. One day before blood sampling, healthy volunteers were quarantined and fasted for 8 h. About 150 µL blood was collected at 30 min before drug administration (pre-dose); 0.5, 1, 1.5, 1.75, 2, 2.5, 3, 4, 6, 8, and 10 h after

administration of 40 mg of esomeprazole tablet. Blood collection was done through the fingertip (finger prick) with a sterile lancet needle. The blood that had been collected was then stored in a 0.5 mL vacutainer and spotted on DBS paper as much as 30 μ L to be dried for approximately 2.5 h. Blood sampling was conducted in the Faculty of Pharmacy, Universitas Indonesia, Depok.

Pharmacokinetic study and incurred sample stability

Pharmacokinetic parameters were obtained based on the first-order equation of the rate of elimination, and the area under curve (AUC) was calculated by using the trapezoidal rule. Incurred sample stability was observed on DBS samples that represent both the high and low concentration range of results obtained, thereby analysis samples around the C_{max} and elimination phase. This test was done by storing the DBS sample that contains the analyte of the healthy subject for a certain time in a zip lock bag at room temperature. On day 0, 7, 14, and 28 at each selected sample concentration, the DBS paper was extracted and analyzed. The acceptance criteria from EMEA 2011 is the percent difference between the initial concentration and the concentration measured during the repeat analysis should not be greater than 20% of their mean for at least 67% of the repeats.

■ RESULTS AND DISCUSSION

Optimization of Esomeprazole in Dried Blood Spot Sample Preparation

Optimization of DBS sample preparation was carried out to afford the optimum extraction methods of esomeprazole from the DBS sample, thus could improve the analytical method sensitivity and recovery.

The purpose of blood volume spotting optimization is to obtain the maximum peak area with the smallest blood volume. These parameters relate to the application of methods on the subject. For the convenience of the subject, the blood volume was taken as small as possible. Optimized blood volume was 20, 25, and 30 μ L. The largest area was obtained at 30 μ L of blood spotted.

The purpose of drying time optimization is to obtain the fastest drying time with the largest area obtained. Drying time may affect recovery, so optimization is necessary [14]. The optimized drying time was 2, 2.5, and

3.5 h. The result showed that the largest area was obtained at 2.5 h of drying time.

The volume of methanol as an extracting solvent greatly affects the number of analytes that can be extracted from the DBS sample. This is related to methanol saturation by analytes and DBS samples, which are completely submerged during the extraction process by methanol. The purpose of methanol volume optimization is to obtain an efficient methanol volume with the largest area. The volume of methanol optimized is 500, 1000, and 1500 μ L. From the optimization results, a volume of 500 μ L of methanol shows a large and constant area compared to the volume of 1000 and 1500 μ L. The increasing volume of methanol requires longer evaporation time.

Vortex time needs to be optimized to get efficient time. If the vortex time is too fast, the extracting solvent will not penetrate completely into the DBS paper. However, if the vortex time is too long, the organic solvents will form emulsions. In this study, the optimized vortex time is 1, 3, and 5 min. The result showed that the largest area is obtained at the time of vortex for 3 and 5 min. Therefore, vortex for 3 min is the most efficient time.

Sonication is performed to improve the efficiency of extraction. Sonication is the agitation process of particles in a solution using ultrasonic sound waves [15]. In this study, the optimization of sonication time is 5, 15, and 25 min. Based on the results of the experiment, the largest area was obtained when the sonication was performed for 15 min. If sonication time is too short, the analyte will not completely be dissolved from the DBS paper. Whereas if the sonication time is too long, there will be problems in analyte stability due to the heat generated from the sonication process.

The centrifugation step is important to ensure the DBS paper is completely submerged by the extracting solvent and the impurities from the biological matrix and paper fibers that are removed from the DBS paper settle so that a clearer supernatant is obtained [16]. Clearer extraction results are expected to reduce the number of impurities and extend the life of the columns. In this study, the optimization of the centrifugation time

was 1, 3, and 5 min. The result showed that the largest area was obtained on centrifugation for 1 min. The longer centrifugation time allows the precipitation of the analytes in the sample together with the protein precipitated by methanol.

Evaporation of the sample is performed to get a larger sample concentration so that the sensitivity of the method will increase. Optimization was carried out in 2 types of treatment, the extraction result was directly injected into HPLC, and the extraction results were evaporated under a nitrogen gas flow for 15 min at 40 °C then reconstituted using 100 µL mobile phase. The larger and constant areas were obtained in the treatment, which was continued by evaporation.

The optimized type of reconstituting solvent is methanol and the mobile phase. The consideration of solvent type optimization for reconstitution is related to esomeprazole solubility. Based on the results, the larger area was obtained from the reconstitution using a mobile phase that is acetonitrile-buffer phosphate pH 7.6 (40:60) compared to methanol. Sampled extract chromatogram with optimum preparation method can be seen in Fig. 1.

Method Validation of Esomeprazole Analysis in Dried Blood Spot

Lower Limit of Quantification (LLOQ) and calibration curve

The LLOQ of this method was 70 ng/mL, with the coefficient of variation (CV) value of 10.60% and % diff between -17.14 to 8.88%. The calibration curve was linear, with the correlation coefficient $r > 0.98$ in the concentration range from 70 to 1400 ng/mL.

Selectivity

Selectivity test was performed by analyzing esomeprazole at LLOQ concentration of 70 ng/mL and blood blank from 6 different sources every 2 replicas. The study results showed no interference in the retention time of the analyte and the internal standard.

Carry-over

The Carry-over test was performed by analyzing esomeprazole at the concentrations of the upper limit of quantification (ULOQ), blank, and LLOQ, respectively. The results of the carry-over test in this study showed that

the interference value of the LLOQ esomeprazole area was obtained by 12.69 and 13.50%, while the interference value of the internal standard area was 0.60 and 0.58% so that the results meet the requirement.

Accuracy, precision, and recovery

The accuracy, precision, and recovery tests were performed by analyzing the analyte at concentrations lower limit of quantification (LLOQ, 70 ng/mL), quality control low (QCL, 200 ng/mL), quality control middle (QCM, 700 ng/mL), and quality control high (QCH, 1000 ng/mL). There are 2 types of accuracy and precision tests performed, namely within-run and between-run. In testing the accuracy and precision within-run, there were 5 replicas analyzed in the one continue analysis time. Meanwhile, the test of accuracy and precision between-run is done by doing 3 times analysis of each 5 replicas at each concentration within a period of at least 2 different days. The results of the test are shown in Table 1.

Dilution integrity

Dilution integrity tests are performed to ensure that dilution does not affect the accuracy and precision of measurement results. Dilution integrity test was done by making a test solution at a concentration above ULOQ, which was 2000 ng/mL, and diluting the solution with whole blood so that a concentration of 1000 and 500 ng/mL were obtained. The result obtained shown in Table 2.

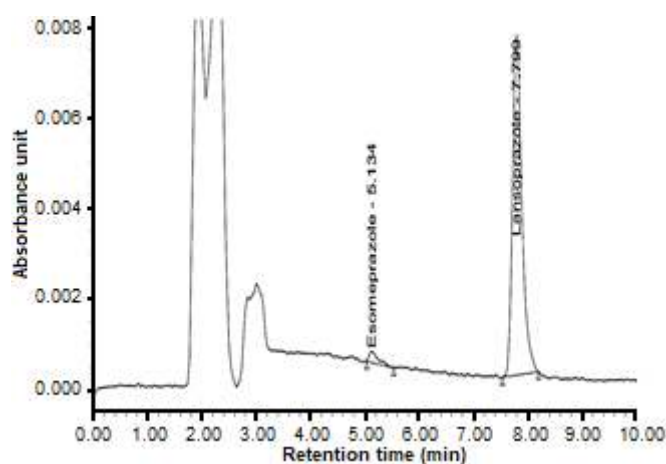


Fig 1. Chromatogram of esomeprazole at LLOQ (Lower Limit of Quantification)

Table 1. Within-run and between-run accuracy and precision

Actual Conc. (ng/mL)	Within-Run			Between-Run		
	Measured Conc. (Mean \pm SD; ng/mL)	CV (%)	Bias (%)	Measured Conc. (Mean \pm SD; ng/mL)	CV (%)	Bias (%)
70.0	68.49 \pm 4.70	6.86	5.41	68.49 \pm 3.86	5.64	8.66
200.0	208.93 \pm 23.08	11.04	8.07	201.05 \pm 9.16	4.55	6.55
700.0	708.27 \pm 31.95	4.51	3.49	729.35 \pm 19.95	2.74	5.06
1000.0	908.16 \pm 41.76	4.60	9.18	989.37 \pm 74.34	7.51	7.35

Table 2. Dilution integrity data

Dilution Factor	Actual Conc. (ng/mL)	Measured Conc. (Mean \pm SD; ng/mL)	CV	% Bias
1 \times	2000.00	1977.73 \pm 48.59	2.46	2.32
1/2 \times	1000.00	1018.42 \pm 67.63	6.64	5.92
1/4 \times	500.00	497.39 \pm 35.18	7.07	5.71

Stability

The stability test is performed to ensure that every step is taken, and storage conditions during the preparation do not affect the concentration of the analyte. In this study, the stability test carried out was the stock solution stability test, short-term stability, long-term stability, and autosampler stability.

The results of the stock solution stability test showed that esomeprazole was stable for 24 h at room temperature and protected from light storage and stable until day 14 at a storage temperature of -80 °C and protected from light. Whereas, the results of the stock solution stability test showed that the stock solution of lansoprazole was stable for 24 h at room temperature and protected from light storage, and stable for 14 days at -80 °C storage protected from light.

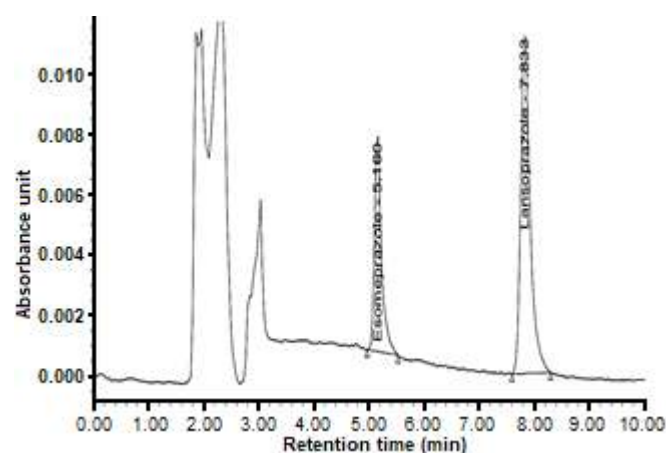
Short-term stability test results showed that the analyte contained in the DBS sample was stable at room temperature for 24 h. Whereas, the results of the long-term stability test showed that the analytes contained in the DBS sample were stable for 28 days with room temperature protected from light storage.

An autosampler stability test is carried out to ensure the injection process in autosampler does not affect the concentration of analytes within a certain period. This test needs to be done because often, the sample must be left in the autosampler for a certain duration before being injected into HPLC. The results of the autosampler

stability test showed that the sample in the autosampler could be left for 24 h before being injected into HPLC.

Pharmacokinetic Study

The pharmacokinetic study is essential to determine the C_{max} and elimination phase of esomeprazole in the DBS sample. The validated method was applied to the pharmacokinetic study in healthy subjects following an oral route of administration of 40 mg film-coated tablet of esomeprazole. From the results of sample analysis, data on the concentration of esomeprazole in blood per unit of time were obtained. This data was then plotted into the time vs. concentration curve of 6 subjects and can be seen in Fig. 2. From the data, several pharmacokinetic parameters

**Fig 2.** Chromatogram of ULOQ

obtained, including a maximum concentration in DBS sample (C_{max}), time to reach maximum concentration in DBS (t_{max}), half-life ($t_{1/2}$), and Area Under Curve (AUC). Based on the pharmacokinetic profile data, it can be seen that C_{max} obtained from all subjects ranged from 795.14–1135.73 ng/mL with an average of 916.65 ng/mL. The coefficient of variation of C_{max} from the six subjects was 14.59%. Time to reach maximum concentration in the six subjects ranged from 2–3 h with an average of 2.25 h and a coefficient of variation of 18.59%. There was a decrease in AUC value in the DBS sample when compared with plasma. Esomeprazole's AUC_{0-t} in the plasma sample was 3064.09 ngh/mL, while the mean AUC_{0-t} in DBS was 1765.41 ngh/mL. Sample concentration in DBS compared to the concentration in plasma are as follows: (1) analytes in DBS were not perfectly attracted during extraction, due to semi-polar analyte retained on polar DBS paper, and it was showed by recovery obtained only 67.13%; (2) blood samples for DBS are taken in peripheral blood vessels whose drug levels are lower than in the vein; (3) the blood volume for DBS samples is much smaller than plasma samples, so the concentration of analytes will also be smaller [17]. Besides that, ratio $AUC_{0-t}/AUC_{0-\infty}$ obtained in this study was 100% for all subjects as shown in Table 3, and its fulfilled EMEA criteria, which only requires greater than 80% [17-18].

Incurred Sample Stability

According to the EMEA 2011, samples taken for the incurred sample stability (ISS) test are samples whose blood-collection points that are in approximately C_{max} and the elimination phase. Because the t_{max} obtained

varies between subjects, the point in time that ISS also varies. The highest percent difference (% difference) value of esomeprazole's incurred samples stability on day 7, 14, and 28 days as shown in Table 4 from subject 1 to subject 6 were 9.81% as shown in Table 5. This result fulfilled the acceptance criteria of the validation method based on the EMEA Bioanalytical Guideline 2011, which is the % difference should not be greater than 20%, and 67% of total samples have to fulfill the criteria. So, the incurred sample stability result showed that esomeprazole was stable in the DBS sample at least until 28 days. Some factors can support this stability in the DBS sample, such as the analyte is in a solid/dry state, so that collisions between particles can be minimized, which can further maintain the stability of esomeprazole compared to liquid samples such as plasma [19-20].

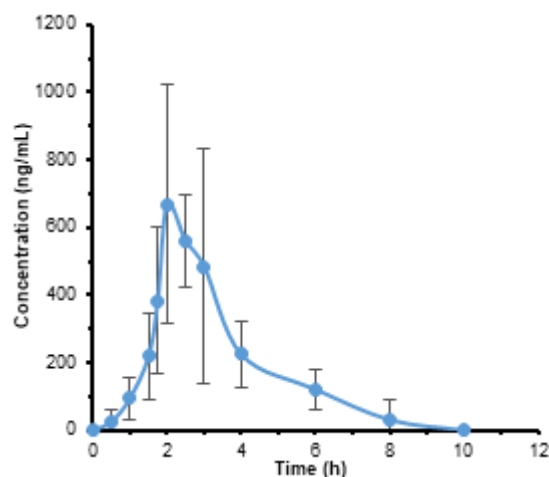


Fig 3. Mean concentration of esomeprazole in DBS sample from 6 healthy subjects after administration of 40 mg esomeprazole enteric coated tablet

Table 3. Summary of pharmacokinetic parameters of esomeprazole in DBS sample

No. Subject	C_{max} (ng/mL)	t_{max} (h)	$t_{1/2}$ (h)	AUC_{0-t} (ngh/mL)	$AUC_{0-\infty}$ (ngh/mL)	$AUC_{0-t}/AUC_{0-\infty}$ (%)
1	1135.73	3	2.93	2675.5	2675.5	100
2	931.79	2	1.69	1466.6	1466.6	100
3	837.97	2	1.62	1494.39	1494.39	100
4	800.33	2.5	1.65	1831.43	1831.43	100
5	795.14	2	1.84	1581.92	1581.92	100
6	998.93	2	1.89	1542.63	1542.63	100
Mean	917	2	2	1765	1765	100
SD	133.78	0.42	0.50	464.47	464.47	0
CV	14.59	18.59	25.73	26.31	26.31	0

Table 4. ISS data of esomeprazole in DBS sample of subject 1

Day 7					
Time (h)	Area ($\mu\text{V}\cdot\text{s}$)		PAR	Conc. Measured (ng/mL)	% diff
	Analyte	IS			
2.50	7362	198307	0.0371	582.49	0.04
3.00	13562	198672	0.0683	1107.65	-2.50
6.00	3268	206340	0.0158	223.51	0.51
Day 14					
2.50	6037	180675	0.0334	583.64	0.24
3.00	11205	175400	0.0639	1139.17	0.30
6.00	2758	207315	0.0133	216.98	-2.45
Day 28					
2.50	4993	143893	0.0347	527.81	-9.81
3.00	8448	125922	0.0671	1088.90	-4.21
6.00	2794	167170	0.0167	216.24	-2.80

Table 5. Mean ISS data of Esomeprazole in DBS sample from all 6 subjects

Day 7	
ISS Point	% diff
1	-0.84
2	-1.43
3	-0.08
Day 14	
1	-1.88
2	-0.48
3	-0.92
Day 28	
1	-2.88
2	-5.46
3	-5.32

■ CONCLUSION

Based on the incurred sample stability test results, esomeprazole was stable in DBS sample at least until 28 days, because it fulfilled the acceptance criteria of EMEA Bioanalytical Method Validation Guideline 2011, in which the percent difference of the initial analysis and the repeat analysis was not greater than 20% on all incurred sample stability samples.

■ ACKNOWLEDGMENTS

Directorate of Research and Community Engagement, Universitas Indonesia, for financial support with Grant No. 1241/UN2.R3.1/HKP.05.00/2018.

■ REFERENCES

- [1] Food and Drug Administration, 2014, *NEXIUM (esomeprazole magnesium) delayed-release capsules, for oral use*, Reference ID: 3675799, Food and Drug Administration, U.S. Department of Health and Human Services, USA.
- [2] Xu, Y., Fang, W., Zeng, W., Leijen, S., and Woolf, E.J., 2012, Evaluation of dried blood spot (DBS) technology versus plasma analysis for the determination of MK-1775 by HILIC-MS/MS in support of clinical studies, *Anal. Bioanal. Chem.*, 404 (10), 3037–3048.
- [3] Li, W., and Lee, M.S., 2014, *Dried Blood Spots: Applications and Techniques*, John Wiley & Sons, Inc., Hoboken, New York.
- [4] Zakaria, R., Allen, K.J., Koplín, J.J., Roche, P., and Greaves, R.F., 2016, Advantages and challenges of dried blood spot analysis by mass spectrometry across the total testing process, *EJIFCC*, 27 (4), 288–317.
- [5] Sharma, A., Jaiswal, S., Shukla, M., and Lal, J., 2014, Dried blood spots: Concepts, present status, and future perspectives in bioanalysis, *Drug Test. Anal.*, 6 (5), 399–414.
- [6] Hasselgren, G., Hassan-Alin, M., Andersson, T., Claar-Nilsson, C., and Röhss, K., 2001, Pharmacokinetic study of esomeprazol in the elderly, *Clin. Pharmacokinet.*, 40 (2), 145–150.

- [7] Harahap, Y., Baskara, A.E., and Harmita, 2017, Method validation of esomeprazol analysis in human plasma using high performance liquid chromatography–photodiode array, *J. Young Pharm.*, 9 (Suppl. 1), s24–s28.
- [8] Wen, Z., Huang, Y., Behler, N., Bambal, R., Bhoopathy, S., and Owen, A., 2010, *Determination of red blood cell partitioning and whole blood to plasma ratio using human, rat, and mouse blood: Methods, model-compounds, and specific differences*, Absorption Systems, Exton, Pennsylvania, USA.
- [9] Reddy, P., Sait, S., Vasudevurthy, G., Vishwanath, B., Prasad, V., and Reddy, S.J., 2011, Stability indicating simultaneous estimation of assay method for naproxen and esomeprazole in pharmaceutical formulations by RP-HPLC, *Der Pharma Chemica*, 3 (6), 553–564.
- [10] Lowes, S., LeLacheur, R., Shoup, R., Garofolo, F., Dumont, I., Martinez, S., Zimmer, J., Caturla, M.C., Couerbe, P., Awaiye, K., Fatmi, S., Farmen, R., Sheldon, C., Bower, J., Fiscella, M., Fast, D., Cape, S., Hulse, J., Kamerud, J., Zhang, T., Padas-Farmer, S., Garofolo, W., Moussallie, M., Rocci, M., Allinson, J., Gouty, D., Buonarati, M., Boudreau, N., Pellerin, B., Lin, J., Xu, A., Hayes, R., Bouhajib, M., Stipancic, M., Nicholson, R., Nehls, C., Warren, M., Karnik, S., Houghton, R., Stovold, C., Reuschel, S., Cojocar, L., Marcelletti, J., Fang, X., Smith, I., and Watson, A., 2014, Recommendations on incurred sample stability (ISS) by GCC, *Bioanalysis*, 6 (18), 2385–2390.
- [11] Es'haghi, Z., 2011, “Photodiode array detection in clinical applications: Quantitative analyte assay advantages, limitations, and disadvantages” in *Photodiodes—Communications, Bio-Sensings, Measurements and High-Energy Physics*, Chapter 9, Eds. Shi, J.W., InTechOpen, New York.
- [12] Committee for Medicinal Products for Human Use (CHMP), 2011, *Guideline on bioanalytical method validation*, European Medicines Agency London, UK.
- [13] United States Food and Drug Administration, 2013, *Guidance for industry. Bioanalytical method validation*, U.S. Department of Health and Human Services Food and Drug Administration, Center for Drug Evaluation and Research (CDER), and Center for Veterinary Medicine (CVM), USA.
- [14] Koster, R.A., Greijdanus, B., Alffenaar, J.W., and Touw, D.J., 2015, Dried blood spot analysis of creatinine with LC-MS/MS in addition to immunosuppressants analysis, *Anal. Bioanal. Chem.*, 407 (6), 1585–1594.
- [15] Hielscher Ultrasound Technology, 2018, *Probe-type sonication vs. ultrasonic bath: An efficiency comparison*, <https://www.hielscher.com/probe-type-sonication-vs-ultrasonic-bath-an-efficiency-comparison.html>, accessed on 7 December 2018.
- [16] Lad, R., 2010, Validation of individual quantitative methods for determination of cytochrome P450 probe substrates in human dried blood spots with KCKT–MS/MS, *Bioanalysis*, 2 (11), 1849–1861.
- [17] Wilhelm, A.J., den Burger, J.C., and Swart, E.L., 2014, Therapeutic drug monitoring by dried blood spot: Progress to date and future directions, *Clin. Pharmacokinet.*, 53 (11), 961–973.
- [18] Committee for Medicinal Products for Human Use (CHMP), 2010, *Guideline on the investigation of bioequivalence (Rev. 1)*, European Medicines Agency, London, United Kingdom.
- [19] Déglon, J., Thomas, A., Mangin, P., and Staub, C., 2011, Direct analysis of dried blood spots coupled with mass spectrometry: Concepts and biomedical applications, *Anal. Bioanal. Chem.*, 402 (8), 2485–2498.
- [20] Chunduri, R.H.B., and Dannana, G.S., 2016, Development and validation of a high throughput UPLC–MS/MS method for simultaneous quantification of esomeprazol, rabeprazole, and levosulpiride in human plasma, *J. Pharm. Anal.*, 6 (3), 190–198.

Selective Determination of Acidic Drugs in Water Samples Using Online Solid Phase Extraction Liquid Chromatography with Alginate Incorporated Multi-Walled Carbon Nanotubes as Extraction Sorbent

Nurzaimah Zaini @ Othman¹, Nor Suhaila Mohamad Hanapi^{1*}, Nor'ashikin Saim¹, Wan Nazihah Wan Ibrahim¹, and Ahmad Lutfi Anis²

¹Faculty of Applied Sciences, Universiti Teknologi MARA, 40450 Shah Alam, Selangor, Malaysia

²Faculty of Applied Sciences, Universiti Teknologi MARA, 94300 Kota Samarahan, Sarawak, Malaysia

* **Corresponding author:**

tel: +603-55435586

email: norsuhaila979@salam.uitm.edu.my

Received: February 20, 2019

Accepted: July 26, 2019

DOI: 10.22146/ijc.43703

Abstract: A rapid and effective method is developed for selective determination of five selected acidic drugs (salicylic acid, naproxen, diclofenac, ibuprofen and mefenamic acid) in water samples by using online solid phase extraction (Online-SPE) prior to liquid chromatography diode array detector (LC-DAD) analysis. In this study, Alginate incorporated multi-walled carbon nanotubes (Alg-MWCNT) beads were prepared and utilized as solid phase extraction sorbent. Optimization of online SPE-LC operating parameters such as valve switching time, composition of acetonitrile and buffer pH was conducted using Box-Behnken Design of Response Surface Methodology (RSM) to evaluate the interactive effects of these three variables. Under the optimized conditions (valve switching time: 1.5 min, composition of acetonitrile: MSA, 60:40 and buffer pH: pH 2), the method showed good linearity ($1-500 \mu\text{g L}^{-1}$) with coefficient of determination (R^2) of 0.9971–0.9996 and low limits of detection $\leq 0.018 \mu\text{g L}^{-1}$. The method showed high relative recoveries in the range of 75–110% for river water and tap water samples, respectively with RSDs of ≤ 7.8 ($n = 3$). This method was successfully applied to the determination of acidic drugs in river and tap water samples. In addition, Alg-MWCNT sorbent offered high degree of selectivity and efficiency for online SPE-LC-DAD analysis.

Keywords: online SPE-LC; alginate; MWCNTs; acidic drugs; water samples

■ INTRODUCTION

One of the trends in drug analysis nowadays is the development of rapid, highly efficient, as well as sensitive and reliable method for the identification and quantification of analytes in various matrices. Recent developments and improvements in analytical methodologies and advanced instruments have made the detection of pharmaceutical drugs at low concentration level possible. As a result of this advancement, pharmaceutical residues can be detected in various environmental samples and recognized as an 'emerging' contaminant [1].

In the last few decades, pharmaceutical drugs have played an increasingly important role in improving the

quality of human life. Thousand tonnes of pharmaceuticals are consumed each year to treat and prevent illnesses [2]. However, the increasing consumption may lead to an accumulation of unused medicines in the household area. Nearly one-third of the pharmaceuticals sold annually are unused [3]. This situation may put human and animal health at risk due to accidental ingestion or exploitation of unused medicine.

Non-steroidal anti-inflammatory drugs (NSAIDs) can be present in water supplies, either from domestic or industrial waste water discharges. The common method used for analyzing these pharmaceuticals in trace level is chromatography, either gas chromatography or liquid chromatography coupled with sensitive detection technique which is mass spectrometry [4-8]. However,

the matrix effects and the selection of internal standards should be taken into consideration [9]. Even though the concentrations of NSAIDs detected in a surface or ground water are in a range of ng L^{-1} , they persist for longer periods of time in soils and sediments [10]. Therefore, the challenge remains in reaching these levels of detection using a method that is affordable, simple and yields reliable results.

In this study, a method of using online solid phase extraction liquid chromatography (online SPE-LC) for the separation of five selected pharmaceutical drugs was proposed. Quantitative, non-destructive and time saving are some criteria of an ideal extraction system [11]. Solid phase extraction (SPE) is the most common method used for the extraction of pharmaceutical drugs in water samples. SPE has been claimed as an effective sample preparation method for removal of interfering compounds and enrichment of analytes [12]. Over time, the SPE technique not only can be performed in the off-line mode but also provides the possibility of online coupling to other analytical steps, such as chromatographic analysis. The application of online coupling with chromatographic analysis may shorten the analysis time, reduce sample contamination and analyte loss, as well as improve the precision and accuracy [13].

Carbon nanotubes (CNTs) possess advantages in adsorbent-adsorbate interactions. On the other hand, this potential sorbent has high production cost, involves non-biodegradable materials and leads to some environmental issues. Meanwhile, alginate is a potential bio-sorbent for the removal of pharmaceutical drugs from water sample. However, it is readily soluble in aqueous media due to its hydrophilic nature which limits its application as an adsorbent.

Hence, this research pursues the potential usage of MWCNTs incorporated with alginate as a promising material to overcome both weaknesses with the aid of online-SPE-LC which is a simpler, more rapid and efficient method compared to the traditional offline SPE.

■ EXPERIMENTAL SECTION

Materials

Ibuprofen, naproxen, diclofenac, mefenamic acid and salicylic acid were purchased from Sigma-Aldrich

(purity assay in range of 98–101%). Acetonitrile (ACN) and methanol (MeOH) of high performance liquid chromatography (HPLC) grade was obtained from Merck (Darmstadt, Germany). Calcium chloride (CaCl_2) was obtained from HmbG Chemicals (Germany) and methanesulfonic acid (MSA) was procured from Sigma-Aldrich (St. Louis, USA). Ultrapure water was produced by Barnstead Nanopure (Thermo Scientific). Sodium hydroxide and hydrochloric acid were obtained from Merck, Darmstadt, Germany and sodium alginate from Qrec (New Zealand). A multi-walled carbon nanotubes (MWCNTs) with specific surface area $> 233 \text{ m}^2/\text{g}$, purity of $> 95\%$, 8–15 nm outer diameter \times 50 μm in length was purchased from Sun Nanotech (Jiangxi, China).

Procedure

Preparation of standard and sample solutions

The individual stock solution (1000 mg mL^{-1}) of ibuprofen (IBU), naproxen (NAP), diclofenac (DIC), mefenamic acid (MEF) and salicylic acid (SAL) were prepared separately in methanol. All standard solutions were stored in the amber glass bottle at $4 \text{ }^\circ\text{C}$ when not in use. A series of working standard solutions were prepared in methanol by dilution prior to analysis to prevent from decomposition of analytes.

The water samples were collected in bottles, pre-cleaned with acetone and filtered through a nylon membrane filter to remove colloidal particles and stored in a freezer at $4 \text{ }^\circ\text{C}$ until analysis commenced. The tap water and river water samples (10 mL, pH 3) were spiked with the standard solution of five pharmaceuticals NSAIDs mixture to give a final concentration of $0.1 \mu\text{g mL}^{-1}$ for each analyte.

Preparation of Alg-MWCNT sorbent

The preparation method for composite beads was adapted and modified from literature [14-15]. The composite beads were formed by suspension technique. Initially, 3% (w/v) of sodium alginate solution was prepared under stirring at $60 \text{ }^\circ\text{C}$. Meanwhile, 0.3 g of MWCNT was dispersed in 30 mL deionized water under sonication for 30 min. Then, MWCNT was added into the sodium alginate solution and sonicated for another

1 h. The mixture solution was dripped through an injection needle into 1000 mL of 4% (w/v) of calcium chloride solution. The alginate-MWCNT beads were formed upon contact with calcium ions. After removal from the calcium chloride bath, the beads were rinsed thoroughly with deionized water using 11 μm filter paper and dried in an oven at 50 $^{\circ}\text{C}$ for 24 h. The dried Alg-MWCNT beads (0.3 g) were packed in an online SPE empty column, ready to be used for analysis.

The alginate-MWCNT beads were then characterized using Fourier Transformed Infrared (FTIR) spectroscopy (Thermo Fischer Scientific) in the range of 4000–400 cm^{-1} using Attenuated Total Reflection (ATR) technique with diamond as the ATR crystal. This method was used to determine the surface chemistry and components of the biopolymer composite beads. The functional groups were determined based on specific broad bands observed. Surface morphology of the Alg-MWCNT sorbent was analyzed using an ultra-high resolution field emission electron microscope (FESEM) model Zeiss Supra 40VP with 10K magnification. Nitrogen adsorption and desorption isotherm of the adsorbent were measured at -196 $^{\circ}\text{C}$ using BELSORP-mini II instrument (BEL, Japan Inc.). Prior to measurements, the samples were degassed at 70 $^{\circ}\text{C}$ for 24 h in a vacuum oven. The isotherm was further analyzed using Brunauer-Emmett-Teller (BET) method to determine the specific surface area, total pore volume and average pore diameter of the sorbent.

Online solid phase extraction system

All analyses were performed using an automated high performance liquid chromatography Dionex Ultimate 3000 (Sunnyvale, CA, USA) system. The system comprises of a large volume loop (10.2 mL) autosampler, dual gradient pump, left and right, a solvent rack with an integrated vacuum degasser, a thermostat column compartment, two columns (online SPE column and analytical column) and a diode array detector (DAD).

The analytical column was an Acclaim Polar Advantage II (5 μm , 120 \AA , 4.6 \times 150 mm) (Thermo Scientific USA) and the online SPE clean-up was performed using alginate incorporated multi-walled carbon nanotube biopolymer sorbent packed in an empty

online SPE column. The system was equipped with a programmable 6 port/2 position switching valve for several modes (loading, clean-up, elution and separation). Data were processed by the Chromeleon™ Software v.6.8 (Dionex). Fig. 1 shows the schematics of the online SPE-LC system.

The method comprises three steps which are sample loading, clean-up, elution and LC separation. Both pumps ran simultaneously. The flow rate was set at 1 mL min^{-1} throughout the analysis with a temperature of 40 $^{\circ}\text{C}$.

At equilibrium mode, 10 μL of spiked water sample was loaded onto the flow system using auto-sampler (fitted with a 100 μL syringe). SPE column was then positioned into the loading mode using the switching valve. The left pump was used to load sample from the sample loop onto the SPE column at 1 mL min^{-1} and simultaneously the analytical column was equilibrated with the right pump. Next, the co-retained sample matrix was flushed out using a washing composition of 10 mM MSA and ACN (95:5) while analytes were retained on the SPE column. During the cleanup process, the choice of mobile phases and time of switching valve are important factors that influence the extraction recovery [16]. After sample loading, the valve was switched to clean-up using the clean-up mobile phase (ACN: 10 mM MSA, 5:95 (v/v) and kept for 1.0 min to remove any possible impurities retained together with analytes.

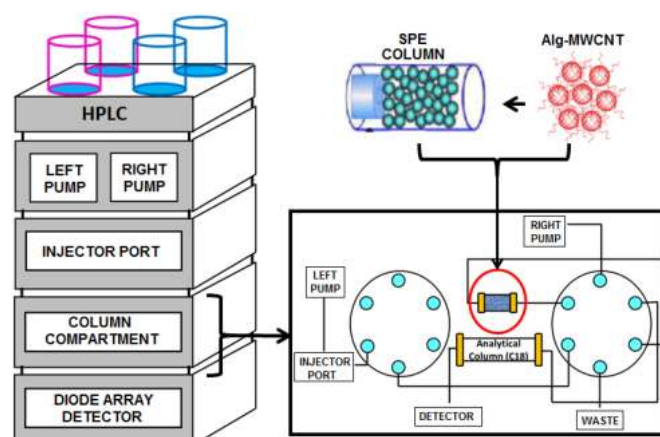


Fig 1. Schematic Diagram for Alg-MWCNT-Online-SPE-LC

In the elution step, the switching valve was switched into the elution position which couples the SPE column with the analytical column. The analytes were transferred using gradient elution mobile phase composition. Lastly, in the separation step the switching valve was switched back into equilibration mode and disconnected the SPE column from the analytical column. In this mode, analytes continued separating in the analytical column using the right pump. In the left pump, the SPE column was equilibrated prior to the next sample being loaded into the sample loop.

Detection method

All analytes were simultaneously analyzed using diode array detector (DAD) at various wavelengths. The DAD was set at 230 nm. Identification of NSAIDs was based on retention time and ultraviolet (UV) spectrum of each analyte.

RESULTS AND DISCUSSION

Physical Properties of the Prepared Alg-MWCNT Beads

Before the drying process, the shape of the composite beads formed were spherical with the turgidity

coming from the formation of bivalent ions when alginate comes in contact with calcium ions [17]. Approximated size of the bead was ~2 mm in diameter. After the drying process, the composite beads shrunk by half (~1 mm in diameter) from the original size of the beads before drying as the water content in the beads had been removed through evaporation.

Characterization of Alg-MWCNT Sorbent by FESEM Analysis

Fig. 2(a-c) show the FESEM images of alginate, MWCNTs and Alg-MWCNT. Surface structure of alginate (Fig. 2(a)) under the magnification of 10 K shows a very smooth and clear surface. Meanwhile, the structure of MWCNT (Fig. 2(b)) under the same magnification shows some ball-of-string-like structure clumping together in random manner. It was also noticed that there were numerous entangled carbon nanotubes observed. The structure of the synthesized Alg-MWCNT (Fig. 2(c)) under the same magnification showed that the clumps of MWCNTs have been deposited onto the surface of the alginate. From the micrograph, it can be suggested that the MWCNTs particles had bound around the alginate surface [18].

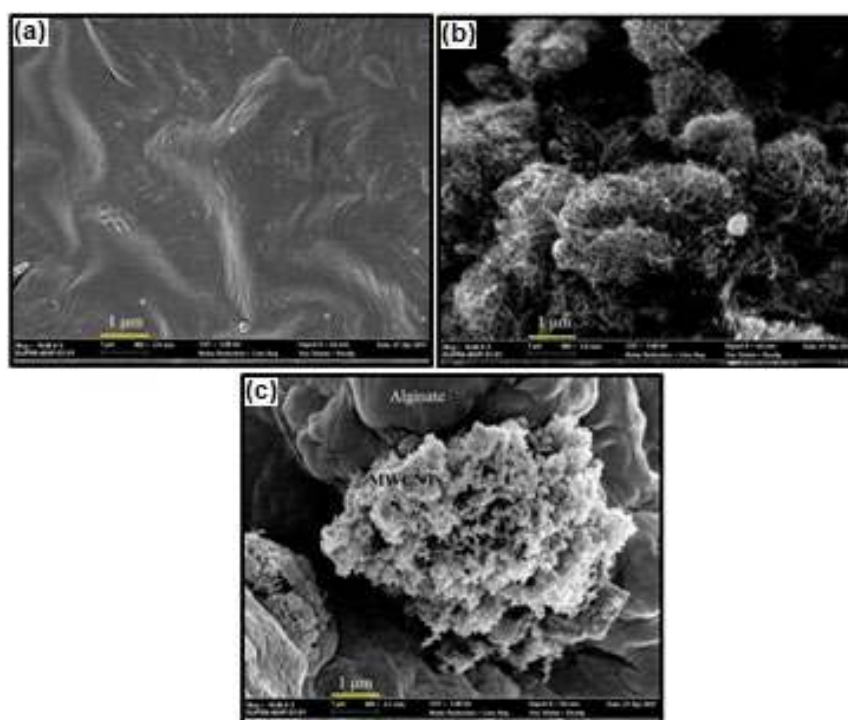


Fig 2. FESEM Micrographs of (a) Alginate (b) MWCNTs (c) Alg-MWCNT under 10 K Magnification

Characterization of Alg-MWCNT Sorbent by FTIR Analysis

Fourier Transform Infrared (FTIR) spectroscopy was used to investigate functionalized spectra of sodium alginate, multi-walled carbon nanotubes (MWCNTs) and alginate-MWCNTs. The results for FTIR spectroscopy were recorded and compared. Fig. 3(a) shows the spectra for the three compounds.

Spectrum of sodium alginate showed important absorption bands corresponding to hydroxyl, ether, and carboxylic functional groups. Stretching vibrations of O-H bonds of alginate appeared in a very broad band at 3258 cm^{-1} . Observed bands in 1594 and 1407 cm^{-1} were attributed to the stretching vibrations of carbon-oxygen double bond and carbon-carbon double bond, respectively. Meanwhile, the band at 1026 cm^{-1} could be attributed to the C-O stretching vibration.

On the other hand, the IR spectrum of carboxylated multi-walled carbon nanotubes (MWCNTs) displays some unresolved peaks due to the low transparency of CNT that caused it difficult for IR ray to penetrate and be absorbed into the sample. A broad peak appeared at 3305 cm^{-1} corresponding to the O-H bond stretch of carboxylic acid functional group of MWCNTs. A peak appeared at 1772 cm^{-1} which represents C=O from carboxylate group. Peaks at 1645 and 1405 cm^{-1} suggest that the compound has a benzene ring which is the main structure of MWCNTs.

The FTIR spectrum of alginate incorporated multi-walled carbon nanotube shows slightly different peaks as compared to the alginate spectrum. It is suggested that the hydroxyl group present at 3258 cm^{-1} in the alginate spectra had been shifted to 3353 cm^{-1} in the Alg-MWCNT spectra and the peak is broader than in the alginate spectra, indicating that the carboxyl group of MWCNT and the carboxyl group from sodium alginate were cross-linked synchronously with calcium ions [19]. Apart from that, this also shows that the alginate was cross-linked by the aid of calcium chloride solution [20].

The adsorption bands for carbon-oxygen double bond and carbon-carbon double bond were shifted from 1594 and 1407 cm^{-1} to 1601 and 1423 cm^{-1} , respectively. It was also observed that the carbon-oxygen single bond band at 1026 cm^{-1} in the alginate spectra was less intense in the Alg-MWCNT spectra, and the peak was shifted to 1010 cm^{-1} . This suggests that there could be substitution reaction that may have occurred during the formation of Alg-MWCNT [21].

Isotherm and Surface Area Analysis of Alg-MWCNT Sorbent

Nitrogen adsorption and desorption isotherm of the adsorbent were measured at $-196\text{ }^{\circ}\text{C}$ using BELSORP-mini II instrument (BEL, Japan Inc.). Prior to these measurements, the samples were degassed at $70\text{ }^{\circ}\text{C}$ for 24 h in a vacuum oven. The isotherm was further analyzed using Brunauer-Emmett-Teller (BET) method

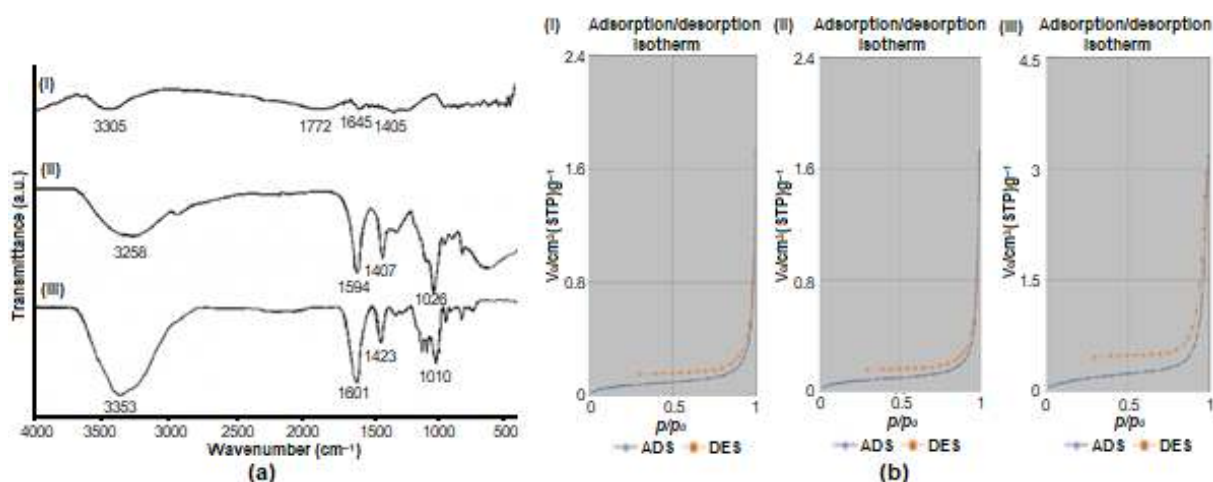


Fig 3. (a) Infrared spectra of (i) MWCNTs, (ii) Alginate and (iii) Alg-MWCNT and (b) Brunauer Emmet Teller (BET) analysis of (i) Alginate, (ii) MWCNTs and (iii) Alg-MWCNT bead

to identify the specific surface area, total pore volume, and average pore diameter of the adsorbent. The porosity and surface area of pristine alginate, MWCNTs and Alg-MWCNT beads were determined by BET. The BET analysis provides the value of specific surface area, total pore volume and average pore diameter while pore analysis provides information on the pore distribution of the adsorbents. Nitrogen adsorption-desorption isotherm of pristine alginate, MWCNTs and Alg-MWCNT (Fig. 3(b)) at 77 K shows that they possess Types IV hysteresis loop which indicates a mesoporous to macroporous adsorbent with strong affinities towards adsorbate [22].

Table 1 shows the specific surface area, total pore volume and average pore diameter obtained from BET analysis. The results show that the pristine alginate has lower surface value than MWCNTs. The results show that the incorporation of MWCNTs in alginate matrix increases the surface area, and total pore volume of the Alg-MWCNT beads. The low surface area for Alg-MWCNT is probably due to the low amount of MWCNTs used in the composition of beads (3%).

Sorbent-Sorbate Interactions between Alg-MWCNT with Target Analytes

The possible interaction between the sorbents (alginate and MWCNTs) and the interaction between the sorbent with the five target analytes were shown in Fig. 4. Strong hydrogen bonding interactions can occur between side chains of biopolymers alginate with other molecules either with the multi-walled carbon nanotubes or with the analytes. The highly associated interaction between blended Alg-MWCNT through hydrogen bonding helped improve swelling and gelation properties of alginate while imparting mechanical strength to agar. Meanwhile, the hydrogen bonding between alginate and target analytes can contribute to the extraction efficiency. On the other hand, π - π interaction may occur between the MWCNTs and the target analytes. At lower pH, strong interactions

between the non-polar aromatic bonds of targeted analytes towards the hexagonal array of graphene sheets of MWCNTs could be attributed to π - π and hydrophobic interactions [23-25].

Optimization of Online SPE-LC Parameters Using Box-Behnken Design (BBD)

Optimization for the extraction of five types of NSAIDs using online solid phase extraction yielded three optimized conditions, which are 1.5 min for valve switching time, 60% composition of acetonitrile in elution solvent composed of ACN: MSA and pH 2 for buffer with desirability 0.974. The regression equation of the fitted model is as shown in Eq. (1), where Y is the response (total peak area) of target analytes, A is the valve switching time, B is acetonitrile composition and C is buffer pH.

$$Y = 9.62 - 0.037A - 0.009B + 0.30C - 0.31A^2 - 0.30B^2 - 0.35C^2 - 0.062AB + 0.081AC - 0.060BC \quad (1)$$

The statistical significance of the terms used in the model was defined via ANOVA analysis. A multi-linear regression analysis was applied to the results of Box-Behnken design. Composition of mobile phase and valve

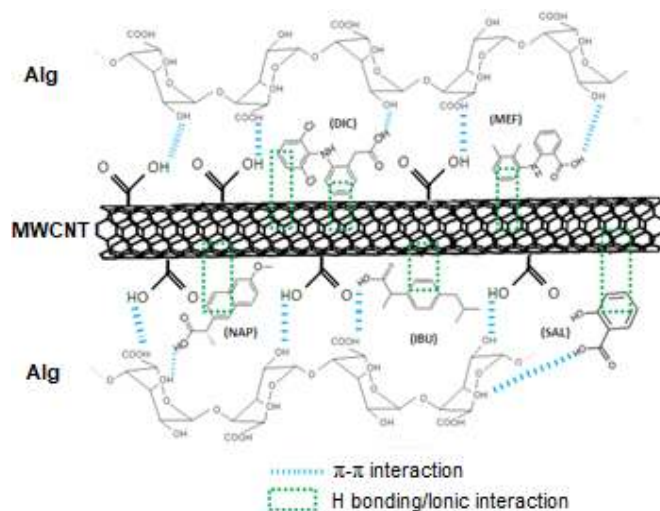


Fig 4. Sorbent-sorbate interactions between Alg-MWCNT with target analytes

Table 1. Results for BET analysis

Sample	Pristine alginate	MWCNTs	Alg-MWCNT
sBET (m^2g^{-1})	0.28363	134.14	0.62756
Total pore volume (cm^3g^{-1})	0.0024974	1.4358	0.0048269
Average pore diameter (nm)	35.221	42.817	30.766

switching time are two significant variables for the clean-up step [26]. The effect of independent variables, which are valve switching time, acetonitrile composition, and buffer pH were evaluated by second order (quadratic). Table 2 shows the analysis of variance (ANOVA) regression model for response quadratic model for salicylic acid, naproxen, ibuprofen, diclofenac and mefenamic acid. The reliability of the fitted model was proven by the high F-values and the low P-values.

The quality of fit on the quadratic polynomial model was presented by the coefficient of determination, R^2 [27]. The value of R^2 shows that there is an acceptable relationship between the predicted and actual values (Fig. 5(a)). The closer the value of R^2 to unity, the better is the empirical model fit to the actual data. Criteria for a good fit of a model, the R^2 should be at least 0.80 [28]. The R^2 value calculated for the extraction of five NSAIDs was 0.9052, indicating a significantly good fitted model.

The main effects of the variables were visualized by Pareto chart (Fig. 5(b)). According to this figure, the acetonitrile composition affects the extraction the most. This is because, among the three parameters being investigated, acetonitrile composition is very crucial to ensure that the analyte will be well-eluted. The most

commonly used organic solvents in HPLC are acetonitrile as it results in the lowest system backpressure in water mixtures and has a very low UV cut off for better UV/Vis detection sensitivity [29].

Effect of valve switching time on the peak of analytes

The right time to switch the valve is very important to ensure all the analytes have been fully extracted by the sorbent and ready for separation step. Effect of valve switching time depends on the step that has been done in the SPE column. For example, if the valve has been switched too early, the analyte would not have been fully extracted by the SPE column. Some analytes would have skipped the SPE column and directly flowed into the analytical column during the separation step. The result will either be low in recoveries or some analytes may not be eluted (Fig. 6(a)).

Effect of ACN:MSA composition on the peak of analytes

In optimizing solvent composition, various isocratic elution of acetonitrile and 10 mM MSA were studied. Each analyte were eluted by increasing the strength of elution solvent. The increase in acetonitrile composition means that the elution strength of the

Table 2. Summary of ANOVA analysis of NSAIDs

Transform	Model	Lack of fit	DF	R-square	Equation
Square Root	<u>Quadratic</u> Significant	Not significant	9	0.9052	$\text{Sqrt}(\text{Total Peak Area}) = 9.62 - 0.037A - 0.009B + 0.30C - 0.31A^2 - 0.30B^2 - 0.35C^2 - 0.062AB + 0.081AC - 0.060BC$

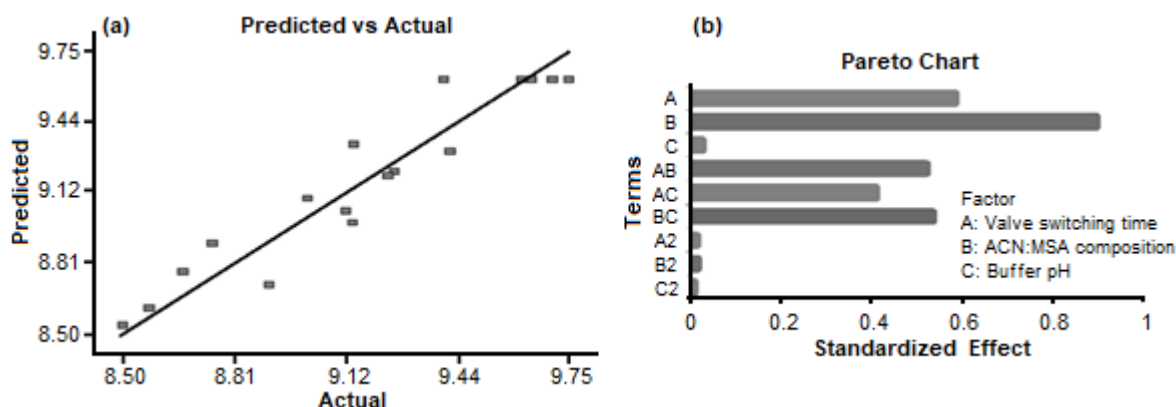


Fig 5. (a) The parity plot between predicted and actual (experimental) values for all analytes, (b) Pareto chart of the standardized effects in Alg-MWCNT online SPE-LC

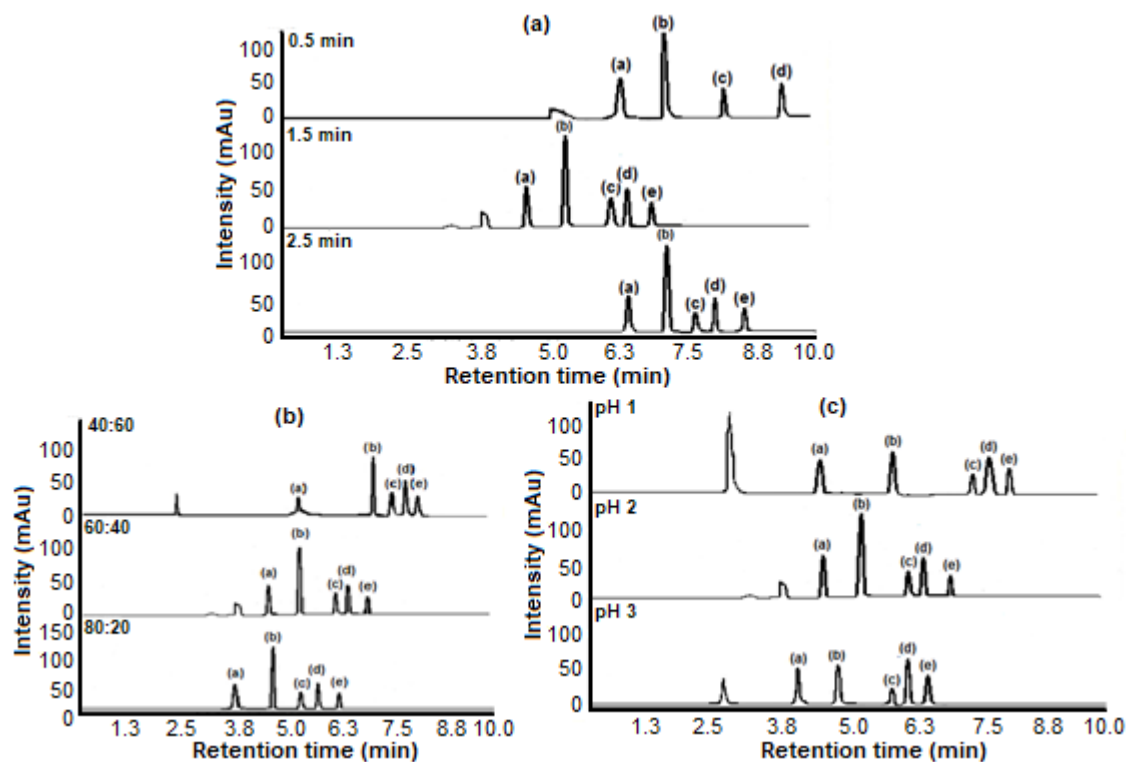


Fig 6. Effect of (a) Valve switching time, (b) ACN:MSA composition and (c) Buffer pH on the peak of analytes, (a) salicylic acid, (b) naproxen, (c) diclofenac, (d) ibuprofen and (e) mefenamic acid

retained analyte on the sorbent will be increased. All of the analytes were eluted from the column within 60–70% of ACN. A decrease in composition of 10 mM MSA with increasing ACN composition, improved the separation of the NSAIDs. Fig. 6(b) shows that the increase in the strength of the elution solvent (ACN:MSA) is proportional to the total peak area of the analytes.

Effect of buffer pH on the peak of analytes

Buffering is commonly needed when analyzing ionizable analytes with reversed phase LC. The ionized species always elute from the column earlier. Sometimes buffer is needed because some impurities are ionizable. The most suitable buffer pH for acidic analyte is at least two units below the pKa of the analyte. As shown in Fig. 6(c), at pH 2, the peak area of analytes were higher compared to pH 1. However, the peak area of analytes at pH 3 decreased as there could be some analytes that were still in ionized form and combined with the impurities [30].

Response Contour Plot

Fig. 7(a) shows the three-dimensional contour plot

for the valve switching time and the buffer pH against the total peak area of the analytes. Meanwhile, the third parameter, which is composition of acetonitrile were kept at a mid-constant level: 60%. As observed, the hyperbolic contour plot shows that both buffer pH and valve switching time were correlated to one another. The optimal extraction efficiencies were observed near the middle of the contour plot at medium buffer pH and valve switching time which was located within the experimental region.

Fig. 7(b) shows the three-dimensional graph plot for the composition of acetonitrile and the buffer pH against the total peak area of the analytes. The third parameter which was valve switching time was kept at a mid-constant level: 1.5 min. At lower pH, strong interaction between the non-polar aromatic bonds of the targeted analytes toward the hexagonal arrays of graphene sheets of MWCNT could be attributed to π - π and van hydrophobic interactions [31].

A three-dimensional graph was plotted for the valve switching time and acetonitrile composition against

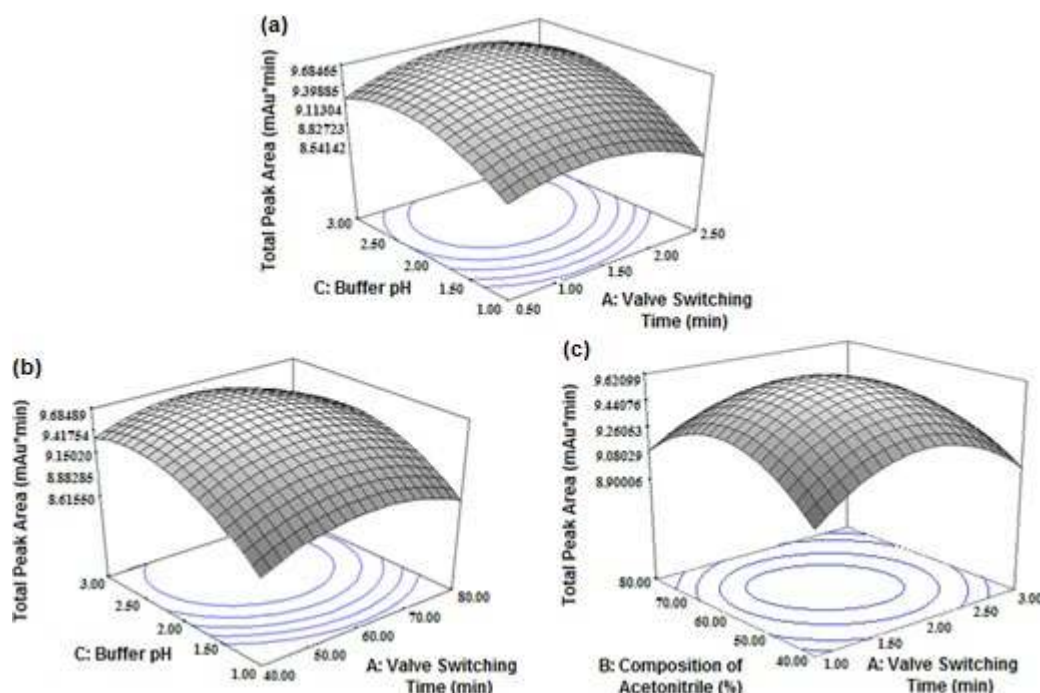


Fig 7. RSM 3-D contour plots for Alg-MWCNT-online SPE-LC. Legends: (a) pH buffer and valve switching time (b) pH buffer and ACN composition (c) ACN composition and valve switching time against peak area of analytes

the total peak area of the analytes, as shown in Fig. 7(c). The third parameter which was pH buffer was kept at a mid-constant level that is pH 2.0. It suggests that the optimum valve switching time is at 1.5 min and optimum acetonitrile composition is at 60%. With increase in the strength of the elution solvent, there is an increase in the total peak area of analytes. At one level, the high acetonitrile composition and the total peak area was maintained and gradually started to decrease. It could be due to the 60% acetonitrile composition which provides the most suitable

polarity strength for the analyte to be eluted.

Method Validation and Analytical Performance of Online SPE-LC

The optimization of online SPE-LC method was then validated for relative recoveries, sample calibration, and Limit of Detection (LOD). A calibration curve was generated using five concentrations of standard mixture in the range of 1 to 500 $\mu\text{g L}^{-1}$ with three replicates. Linear curves for each analyte were obtained with a good

Table 3. Validation data of Alg-MWCNT-online SPE-LC method of NSAIDs in tap and river water samples

Sample	Analytes	Linear range ($\mu\text{g L}^{-1}$)	Coefficient of determination, R^2	LOD ($\mu\text{g L}^{-1}$)	Precision (RSD, %) (n = 3)
Tap water	Salicylic acid	1–500	0.9993	0.0183	4.9
	Naproxen	1–500	0.9975	0.0118	5.0
	Diclofenac	1–500	0.9991	0.0062	1.4
	Ibuprofen	1–500	0.9996	0.0075	3.4
	Mefenamic acid	1–500	0.9971	0.0141	3.8
River water	Salicylic acid	1–500	0.9984	0.0152	0.9
	Naproxen	1–500	0.9992	0.0159	6.8
	Diclofenac	1–500	0.9978	0.0176	1.7
	Ibuprofen	1–500	0.9995	0.0144	2.5
	Mefenamic acid	1–500	0.9983	0.0095	2.1

correlation coefficient ($R^2 = 0.9971-0.9996$). The sensitivity of the method expressed as Limit of Detection (LOD) was calculated at a signal to noise ratio of 3 based on linear regression method and the results were in the range of $0.0062-0.0183 \mu\text{g L}^{-1}$ for LODs. This proved that LOD for online SPE-LC method is much lower than traditional SPE method [32]. Table 3 shows the validation data for online SPE-LC of NSAIDs from water sample.

Application of Online SPE-LC on River Water and Tap Water Samples

To investigate the practicality of the proposed method for the analysis of acidic drugs in real samples, the method was applied to analyze salicylic acid, ibuprofen, naproxen, diclofenac and mefenamic acid in the tap and river water samples (Fig. 8). However, there was no peak detected for naproxen, ibuprofen, diclofenac and mefenamic acid in the samples. Percentage recovery study

was conducted by spiking river water samples to give final concentration of 50 and $100 \mu\text{g L}^{-1}$. The results showed that good percentage recoveries were obtained in the range of 75 to 110% (Table 4) [33]. Thus, the online solid phase extraction method proved to be a simple, sensitive, and selective extraction method that complies to green chemistry, which could potentially be used in the chemical laboratory for routine analysis of water samples.

CONCLUSION

In this study, an online SPE-LC method by using Alg-MWCNT as sorbent has been successfully developed, for rapid analysis of five selected acidic drugs in water samples. Alg-MWCNT sorbent is expected to be an alternative green sorbent material that has a higher performance of extraction efficiency and higher selectivity rather than common SPE sorbent. An alternative online

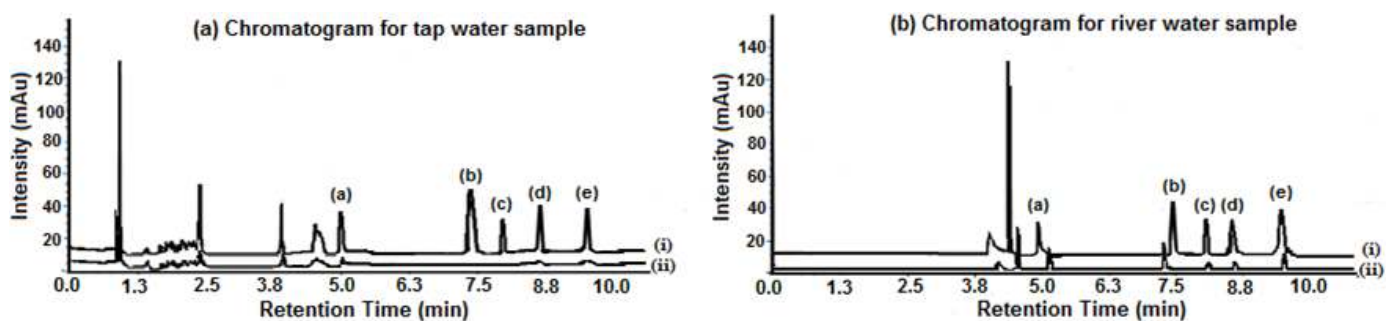


Fig 8. Chromatogram of online-SPE-LC of five NSAIDs in tap and river water samples; (i) spiked sample (ii) blank sample; (a) salicylic acid, (b) naproxen, (c) diclofenac, (d) ibuprofen and (e) mefenamic acid

Table 4. Relative recoveries (%) and method precisions (RSD %, $n = 3$) at two different concentrations of Alg-MWCNT-online SPE-LC in tap water and river water samples

Sample	Analyte	Average relative recovery, % (RSD, %)	
		Spiking level ($n = 3$)	
		$50 \mu\text{g L}^{-1}$	$100 \mu\text{g L}^{-1}$
Tap water	Salicylic acid	75 (4.5)	79 (4.6)
	Naproxen	91 (4.1)	96 (7.8)
	Diclofenac	76 (3.7)	78 (5.5)
	Ibuprofen	79 (4.1)	76 (3.8)
	Mefenamic acid	85 (3.2)	82 (5.3)
River water	Salicylic acid	91 (3.2)	104 (4.8)
	Naproxen	83 (3.9)	86 (2.7)
	Diclofenac	104 (4.3)	110 (0.9)
	Ibuprofen	79 (5.3)	83 (2.0)
	Mefenamic acid	87 (3.6)	103 (4.7)

solid phase extraction combined with liquid chromatography (SPE-LC) has shown to have improved the extraction efficiency as it shortens the extraction and analysis time. Several parameters were optimized in the online SPE method. The optimum conditions were as follows: buffer pH at pH 2, ACN: MSA composition at 60:40 and suitable valve switching time at 1.5 min. The optimum parameters were used in the analysis of real samples. All five analytes were successfully extracted using the same conditions in online SPE-LC. Good linearities were achieved for the analytes with coefficients of determination, R^2 , in the range of 0.9971–0.9996. The method was successfully applied for the analysis of river water and tap water samples, with good relative recoveries in the range of 75–110%. Online SPE-LC method by using Alg-MWCNT as sorbent proved to be a rapid, selective and efficient technique for the extraction and separation of acidic drugs in aqueous matrices.

■ ACKNOWLEDGMENTS

The authors would like to thank Universiti Teknologi MARA (UiTM), Shah Alam, Selangor for providing research facilities and the Ministry of Education Malaysia for financial support through the FRGS research grant 600-IRMI/FRGS 5/3 (010/2019).

■ REFERENCES

- [1] Białk-Bielińska, A., Kumirska, J., Borecka, M., Caban, M., Paszkiewicz, M., Pazdro, K., and Stepnowski, P., 2016, Selected analytical challenges in the determination of pharmaceuticals in drinking/marine waters and soil/sediment samples, *J. Pharm. Biomed. Anal.*, 121, 271–296.
- [2] Ji, Y., Du, Z., Zhang, H., and Zhang, Y., 2014, Rapid analysis of non-steroidal anti-inflammatory drugs in tap water and drinks by ionic liquid dispersive liquid–liquid microextraction coupled to ultra-high performance supercritical fluid chromatography, *Anal. Methods*, 6 (18), 7294–7304.
- [3] Hanapi, N.S.M., Sanagi, M.M., Ibrahim, W.A.W., Saim, N., Ismail, A.K., Ibrahim, W.N.W., and Tahiruddin, S., 2015, Analysis of some anti-depressant drugs in aqueous samples using agarose film micro-electro driven membrane extraction, *Der Pharma Chem.*, 7 (5), 235–242.
- [4] Kosjek, T., Heath, E., and Krbavčič, A., 2005, Determination of non-steroidal anti-inflammatory drug (NSAIDs) residues in water samples, *Environ. Int.*, 31 (5), 679–685.
- [5] Payán, M.R., López, M.Á.B., Torres, R.F., Navarro, M.V., and Mochón, M.C., 2011, Electromembrane extraction (EME) and HPLC determination of non-steroidal anti-inflammatory drugs (NSAIDs) in wastewater samples, *Talanta*, 85 (1), 394–399.
- [6] Zhang, Y., and Lee, H.K., 2012, Ionic liquid-based ultrasound-assisted dispersive liquid–liquid microextraction followed high-performance liquid chromatography for the determination of ultraviolet filters in environmental water samples, *Anal. Chim. Acta*, 750, 120–126.
- [7] Yao, C., Li, T., Twu, P., Pitner, W.R., and Anderson, J.L., 2011, Selective extraction of emerging contaminants from water samples by dispersive liquid–liquid microextraction using functionalized ionic liquids, *J. Chromatogr. A*, 1218 (12), 1556–1566.
- [8] Iuliani, P., Carlucci, G., and Marrone, A., 2010, Investigation of the HPLC response of NSAIDs by fractional experimental design and multivariate regression analysis. Response optimization and new retention parameters, *J. Pharm. Biomed. Anal.*, 51 (1), 46–55.
- [9] Hernando, M.D., Mezcuca, M., Fernández-Alba, A.R., and Barceló, D., 2006, Environmental risk assessment of pharmaceutical residues in wastewater effluents, surface waters and sediments, *Talanta*, 69 (2), 334–342.
- [10] Toledo-Neira, C., and Álvarez-Lueje, A., 2015, Ionic liquids for improving the extraction of NSAIDs in water samples using dispersive liquid–liquid microextraction by high performance liquid chromatography–diode array–fluorescence detection, *Talanta*, 134, 619–626.
- [11] Zhang, S.Q., Bi, H.M., and Liu, C.J., 2007, Extraction of bio-active components from *Rhodiola sachalinensis* under ultrahigh hydrostatic pressure, *Sep. Purif. Technol.*, 57 (2), 277–282.

- [12] Hennion, M.C., 1999, Solid-phase extraction: method development, sorbents, and coupling with liquid chromatography, *J. Chromatogr. A*, 856 (1-2), 3–54.
- [13] Chen, L., Wang, H., Zeng, Q., Xu, Y., Sun, L., Xu, H., and Ding, L., 2009, On-line coupling of solid-phase extraction to liquid chromatography—A review, *J. Chromatogr. Sci.*, 47 (8), 614–623.
- [14] Jeon, O., Powell, C., Ahmed, S.M., and Alsberg, E., 2010, Biodegradable, photocrosslinked alginate hydrogels with independently tailorable physical properties and cell adhesivity, *Tissue Eng. Part A*, 16 (9), 2915–2925.
- [15] Sahasathian, T., Praphairaksit, N., and Muangsin, N., 2010, Mucoadhesive and floating chitosan-coated alginate beads for the controlled gastric release of amoxicillin, *Arch. Pharmacol Res.*, 33 (6), 889–899.
- [16] Fernández-Ramos, C., Šatínský, D., Šmídová, B., and Solich, P., 2014, Analysis of trace organic compounds in environmental, food and biological matrices using large-volume sample injection in column-switching liquid chromatography, *TrAC, Trends Anal. Chem.*, 62, 69–85.
- [17] Sakai, S., and Kawakami, K., 2007, Synthesis and characterization of both ionically and enzymatically cross-linkable alginate, *Acta Biomater.*, 3 (4), 495–501.
- [18] Joddar, B., Garcia, E., Casas, A., and Stewart, C.M., 2016, Development of functionalized multi-walled carbon-nanotube-based alginate hydrogels for enabling biomimetic technologies, *Sci. Rep.*, 6, 32456.
- [19] Jie, G., Kongyin, Z., Xinxin, Z., Zhijiang, C., Min, C., Tian, C., and Junfu, W., 2015, Preparation and characterization of carboxyl multi-walled carbon nanotubes/calcium alginate composite hydrogel nano-filtration membrane, *Mater. Lett.*, 157, 112–115.
- [20] Pawar, S.N., and Edgar, K.J., 2012, Alginate derivatization: A review of chemistry, properties and applications, *Biomaterials*, 33 (11), 3279–3305.
- [21] Şolpan, D., and Torun, M., 2005, Investigation of complex formation between (sodium alginate/acrylamide) semi-interpenetrating polymer networks and lead, cadmium, nickel ions, *Colloids Surf., A*, 268 (1-3), 12–18.
- [22] Sangwichien, C., Aranovich, G.L., and Donohue, M.D., 2002, Density functional theory predictions of adsorption isotherms with hysteresis loops, *Colloids Surf., A*, 206 (1-3), 313–320.
- [23] Fugetsu, B., Satoh, S., Iles, A., Tanaka, K., Nishi, N., and Watari, F., 2004, Encapsulation of multi-walled carbon nanotubes (MWCNTs) in Ba²⁺-alginate to form coated micro-beads and their application to the pre-concentration/elimination of dibenzo-p-dioxin, dibenzofuran, and biphenyl from contaminated water, *Analyst*, 129 (7), 565–566.
- [24] Luo, Y.B., Zheng, H.B., Wang, J.X., Gao, Q., Yu, Q.W., and Feng, Y.Q., 2011, An anionic exchange stir rod sorptive extraction based on monolithic material for the extraction of non-steroidal anti-inflammatory drugs in environmental aqueous samples, *Talanta*, 86, 103–08.
- [25] Manzo, V., Honda, L., Navarro, O., Ascar, L., and Richter, P., 2014, Microextraction of non-steroidal anti-inflammatory drugs from waste water samples by rotating-disk sorptive extraction, *Talanta*, 128, 486–492.
- [26] Liu, L., Wen, Y.B., Liu, K.N., Sun, L., Wu, M., Han, G.F., Lu, Y.X., Wang, Q.M., and Yin, Z., 2013, Optimization of on-line solid phase extraction and HPLC conditions using response surface methodology for determination of WM-5 in mouse plasma and its application to pharmacokinetic study, *J. Chromatogr. B*, 923-924, 8–15.
- [27] Ahmad, M.A., and Alrozi, R., 2010, Optimization of preparation conditions for mangosteen peel-based activated carbons for the removal of Remazol Brilliant Blue R using response surface methodology, *Chem. Eng. J.*, 165 (3), 883–890.
- [28] Joglekar, A.M., and May, A.T., 1987, Product excellence through design of experiments, *Cereal Food World*, 32, 857–868.
- [29] Funari, C.S., Carneiro, R.L., Cavalheiro, A.J., and Hilder, E.F., 2014, A trade off between separation, detection and sustainability in liquid chromatographic fingerprinting, *J. Chromatogr. A*, 1354, 34–42.

- [30] LoBrutto, R., Jones, A., Kazakevich, Y.V., and McNair, H.M., 2001, Effect of the eluent pH and acidic modifiers in high-performance liquid chromatography retention of basic analytes, *J. Chromatogr. A*, 913 (1-2), 173–187.
- [31] Fugetsu, B., Satoh, S., Shiba, T., Mizutani, T., Lin, Y.B., Terui, N., Nodasaka, Y., Sasa, K., Shimizu, K., Akasaka, T., Shindoh, M., Shibata, K., Yokoyama, A., More, M., Tanaka, K., Sato, Y., Tohji, K., Tanaka, S., Nishi, N., and Watari, F., 2004, Caged multiwalled carbon nanotubes as the adsorbents for affinity-based elimination of ionic dyes, *Environ. Sci. Technol.*, 38 (24), 6890–6896.
- [32] Kot-Wasik, A., Dębska, J., Wasik, A., and Namieśnik, J., 2006, Determination of non-steroidal anti-inflammatory drugs in natural waters using off-line and on-line SPE followed by LC coupled with DAD-MS, *Chromatographia*, 64 (1-2), 13–21.
- [33] Paíga, P., Lolić, A., Hellebuyck, F., Santos, L.H.M.L.M., Correia, M., and Delerue-Matos, C., 2015, Development of a SPE–UHPLC–MS/MS methodology for the determination of non-steroidal anti-inflammatory and analgesic pharmaceuticals in seawater, *J. Pharm. Biomed. Anal.*, 106, 61–70.

Supplementary Data

This supplementary data is a part of paper entitled “Catalytic and Thermal Cracking of Bio-Oil from Oil-Palm Empty Fruit Bunches, in Batch Reactor”.

Appendix 1. Compounds in the upgrading bio-oil as identified through GC-MS analysis

Name of compound	% Area							
	Treatments							
	A ₁ B ₁	A ₁ B ₂	A ₂ B ₁	A ₂ B ₂	A ₃ B ₁	A ₃ B ₂	A ₄ B ₁	A ₄ B ₂
Aromatic								
Hexane	-	-	-	-	6.62	-	-	5.85
1-Methyl-Indan-2-one	-	-	-	2.05	-	-	-	-
1H-Indene, 2,3-dihydro-4,7-dimethyl-	-	-	-	-	0.53	-	-	-
Benzene, methoxy-	0.71	-	1.34	-	0.40	-	-	0.65
3,4-Dimethoxytoluene	-	0.14	-	-	0.22	-	0.21	0.31
Benzene, 1,2-dimethoxy	0.46	--	-	-	0.21	0.4	-	0.30
Benzeneethanol, 2-methoxy-.alpha.-methyl-	-	-	0.26	-	-	-	-	-
Benzene, 1-ethyl-4-methoxy-	-	-	-	-	-	-	-	0.32
Benzene, 1,4-dimethoxy-	-	-	-	-	-	-	-	0.36
2,3-Dimethoxytoluene	-	-	-	0.67	-	0.54	-	-
Benzaldehyde, 2-hydroxy-	-	-	-	-	-	0.31	-	-
Naphthalene, 2-methyl	-	-	-	-	-	0.34	-	-
Methyl-4-methoxybenzoate	-	1.05	-	1.71	0.32	1.12	0.56	0.53
	1.17	1.19	1.60	4.43	8.3	2.71	0.77	8.32
Phenols								
Phenol	38.8	23.0	62.59	33.06	55.62	30.48	34.16	29.26
Phenol, 2-methyl	2.44	-	-	-	-	-	-	-
Phenol, 4-methyl	1.26	-	-	-	-	-	-	-
Phenol, 2-methoxy	2.59	2.51	2.53	4.92	2.64	-	-	-
Phenol, 3-ethyl	0.61	-	-	-	-	-	-	-
Phenol, 4-methoxy-3-methyl	1.03	-	-	-	-	-	-	-
2-Methoxy-4-methylphenol	4.41	2.08	-	-	0.62	-	-	0.9
Phenol, 4-ethyl-2-methoxy-	-	1.40	-	-	-	-	-	-
2-methoxy-4-ethyl-6-methylphenol	-	-	-	-	-	0.24	-	-
	51.14	28.99	65.12	37.98	58.88	30.72	34.16	30.16
Aliphatic and Alicyclic								
Tridecane (CAS) n-Tridecane	-	0.17	0.62	0.68	0.37	-	1.45	-
Octadecane (CAS) n-Octadecane	-	0.98	-	-	-	-	2.4	-
Hexadecane (CAS) n-Hexadecane	-	1.78	0.21	1.08	-	2.28	0.76	0.26
Tetradecane (CAS) n-Tetradecane	-	-	0.133	-	0.29	0.92	0.71	2.54
Eicosane (CAS) n-Eicosane	-	-	1.22	-	-	-	-	-
Nonadecane (CAS) n-Nonadecane	-	-	-	-	1.09	-	-	2.06
Dodecane (CAS) n-Dodecane	-	-	-	-	-	3.09	4.07	2.74
Heptadecane, 2,6,10,15-tetramethyl-	-	-	-	-	-	2.59	-	-
Octane (CAS) n-Octane	-	-	-	-	-	-	0.28	-
Nonane (CAS) n-Nonane	-	-	-	-	-	-	0.61	-
Cyclododecane	-	-	-	-	-	-	0.51	-
Pentacosane (CAS) n-Pentacosane	-	-	-	-	-	-	1.61	-
Octacosane	-	-	-	-	-	-	-	0.86
Pentatriacontane	-	1.20	-	-	-	-	-	-
Cyclopentane, methyl	-	-	-	-	-	-	-	0.4

Appendix 1. Compounds in the upgrading bio-oil as identified through GC-MS analysis (*Continued*)

Name of compound	% Area							
	Treatments							
	A ₁ B ₁	A ₁ B ₂	A ₂ B ₁	A ₂ B ₂	A ₃ B ₁	A ₃ B ₂	A ₄ B ₁	A ₄ B ₂
9-Eicosene, (E)	-	-	-	-	0.27	-	-	-
1-Octene (CAS) Caprylene	-	-	-	-	-	-	0.21	-
3-Methylpentane	-	-	-	-	-	-	-	0.60
2-methylpentane	-	-	-	-	-	-	-	0.08
1-Hexadecene (CAS) Cetene	-	-	-	0.45	-	0.31	0.23	0.27
1-Octadecene	-	-	-	2.27	-	0.79	0.77	0.49
1-Nonadecene	0.59	-	-	1.72	-	1.08	1.03	-
	0.59	4.13	2.18	6.2	2.01	11.06	14.64	10.3
Ketone								
acetone-oxime	-	-	0.62	-	-	0.19	-	0.10
Ethanone, 1-(2-furanyl)	0.69	-	-	-	0.41	-	-	-
2-Cyclopenten-1-one, 2-methyl-	0.37	-	0.44	-	0.59	-	-	-
2,3-Dimethyl-2-cyclopenten-1-one	1.96	0.27	2.5	2.23	0.82	1.34	1.46	0.93
2-Undecanone	-	-	-	0.33	0.17	0.23	-	0.2
3-isopropylcyclopentyl-2-enone	-	-	-	-	0.21	-	-	-
	0.23	0.27	3.56	2.56	2.2	1.76	1.46	1.23
Ester								
Acetic acid, methyl ester	1.16	-	0.93	-	-	0.19	0.18	0.10
Butanoic acid, anhydride	1.97	-	-	-	-	0.69	-	-
Acetic acid, phenyl ester	1.06	-	0.4	0.25	1.75	0.66	0.30	1.06
Octanoic acid, methyl ester	1.45	0.23	2.29	-	0.42	3.13	2.49	5.64
Benzoic acid, methyl ester	-	-	2.75	-	3.06	-	2.64	7.4
Tetradecanoic acid, methyl ester	-	3.11	-	-	-	-	-	-
Dodecanoic acid, methyl ester	6.90	6.41	4.96	12.88	5.36	9.58	10.91	8.71
Decanoic acid, methyl ester	-	0.45	1.01	2.86	1.19	2.43	1.91	2.12
Dodecanoic acid, phenyl ester	-	0.72	-	1.18	-	0.8	0.78	2.63
9-Octadecenoic acid (Z)-, methyl ester	-	2.67	-	0.36	-	-	2.77	0.25
Heptadecanoic acid, 16-methyl- ester	-	0.74	-	-	-	-	-	-
Methyl propanoate	-	-	0.2	-	-	-	-	-
Hexanoic acid, methyl ester	-	-	0.74	-	0.29	-	-	2.08
Octadecoic acid methyl ester	-	-	-	1.84	-	-	-	-
octanoic acid, phenyl ester	-	-	-	0.4	-	0.31	-	0.15
Propanoic acid, phenyl ester	-	-	-	-	0.23	-	-	-
Methyl palmitate	-	-	-	1.7	0.42	1.07	3.00	1.13
Octadecanoic acid, 2-propenyl ester	-	1.88	-	-	-	-	-	-
Heptadecanoic acid, 16-methyl-, methyl ester	-	-	-	-	-	-	0.89	-
Pentanoic acid, 4-methyl-, methyl ester	-	-	-	-	-	-	-	0.13
Heptanoic acid, methyl ester	-	-	-	-	-	-	-	0.67
	12.54	16.21	13.28	21.47	12.72	18.86	25.87	31.94
Acid								
Acetic acid	5.40	-	10.87	1.91	9.71	-	3.32	4.53
Octanoic acid	4.87	2.04	-	0.75	-	4.28	-	1.28
Hexadecanoic acid	-	0.98	-	-	-	-	-	-
Decanoic acid (CAS) Capric acid	-	0.49	-	-	-	-	-	-
Tetradecanoic acid (CAS) Myristic acid	-	6.60	-	-	-	-	-	-
Dodecanoic acid, 1-(hydroxymethyl)-1,2-ethanediyl	-	0.25	-	-	-	-	-	-
Dodecanoic acid (CAS) Lauric acid	20.10	34.23	-	5.15	-	1.54	8.47	-

Appendix 1. Compounds in the upgrading bio-oil as identified through GC-MS analysis (*Continued*)

Name of compound	% Area							
	Treatments							
	A ₁ B ₁	A ₁ B ₂	A ₂ B ₁	A ₂ B ₂	A ₃ B ₁	A ₃ B ₂	A ₄ B ₁	A ₄ B ₂
Nonanoic acid (CAS) Nonoic acid	-	-	-	-	-	-	0.88	-
Propanoic acid (CAS) Propionic acid	-	-	-	-	1.62	-	-	-
Butanoic acid (CAS) n-Butyric acid	-	-	-	-	0.61	-	-	0.65
	30.37	44.59	10.87	7.81	11.94	5.82	12.67	6.46
Furan								
2-Furancarboxaldehyde (CAS) Furfural	-	-	-	-	-	-	-	0.34
2,3-Dimethylbenzofuran	-	-	0.59	0.32	0.19	0.29	-	0.82
2-Furanmethanol, tetrahydro-	-	-	-	0.70	-	-	1.00	-
Benzofuran, 2-methyl	0.81	-	0.62	-	0.34	1.12	-	1.36
2-Ethylbenzofuran	0.21	-	-	-	-	-	-	-
2,4-Dimethylfuran	-	-	-	-	-	0.26	-	-
	1.02		1.21	1.02	0.53	1.67	1.00	2.52
Alcohol								
1-Heptadecanol (CAS) n-Heptadecanol	-	0.48	-	-	-	-	-	-
1-Tridecanol (CAS) n-Tridecanol	-	-	-	0.65	-	-	-	-
1-Tetradecanol (CAS) Alfol 14	-	-	-	1.23	0.26	0.51	0.55	1.35
1-Nonanol (CAS) n-Nonyl alcohol	-	-	-	-	-	-	0.25	-
1-Dodecanol (CAS) n-Dodecanol	-	-	-	-	-	-	0.23	-
1-Undecanol (CAS) n-Undecanol	-	-	-	-	-	0.32	0.39	1.15
7-Dodecenol	-	-	-	-	-	-	-	0.49
	-	0.48		1.88	0.26	0.83	1.42	2.99
Other Compounds		3.84	0.31	3.49	0.41	23.49	3.95	2.08
Total	97.06	99.7	98.13	86.84	97.25	96.92	95.94	96

Catalytic and Thermal Cracking of Bio-Oil from Oil-Palm Empty Fruit Bunches, in Batch Reactor

Santiyo Wibowo*, Lisna Efiyanti, and Gustan Pari

Forest Product Research and Development Center, Ministry of Environment and Forestry Republic of Indonesia,
Jl. Gunung Batu No. 5, Bogor 16610, West Java, Indonesia

* **Corresponding author:**

tel: +62-251-8633378

email: santiyowibowo1973@yahoo.co.id

Received: March 11, 2019

Accepted: December 4, 2019

DOI: 10.22146/ijc.44076

Abstract: The world's potency of fossil-derived petroleum fuels has declined steadily, while its consumption continues to rise ominously. Therefore, several countries have started to develop renewable fuels like bio-oil from biomass. Relevantly, the aim of this research was to explore the technical feasibility of upgrading the qualities of crude bio-oil (CBO) produced from the pyrolysis on oil-palm empty fruit bunches (OPEFB) using Ni/NZA catalyst in a batch reactor. The natural zeolite (NZ) was activated by HCL 6 N and NH₄Cl (obtained sample NZA). Supporting Ni onto NZA was conducted with an impregnation method using a salt precursor of Ni(NO₃)₂·6H₂O followed by calcination with a temperature of 500 °C. Catalyst characterization includes determining the site of TO₄ (T = Si or Al) in zeolites, acidity, crystallinity, and catalyst morphology. Cracking reaction of CBO was carried out in batch reactor in varied temperatures of 250 and 300 °C with the variation of catalyst weight of 0, 4, 6, and 8% toward CBO. Several analyses of the liquid product such as product yield, specific gravity, pH, viscosity, calorific value, and chemical compound were conducted. The results showed that acidification and Ni loading on zeolite samples increased their acidity. The optimum CBO's cracking condition was judged to be the temperature of 300 °C with 6% Ni/NZA catalyst use, whereby the fuel yield reached 26.42% and dominated by particular compounds comprising phenol, octanoic acid, and alkane hydrocarbons. Under such conditions, the characteristics of fuel were pH 3.54, specific gravity 0.995, viscosity 14.3 cSt, and calorific value 30.85 MJ/kg.

Keywords: fossil fuels; renewable biomass-derived fuels; oil-palm empty fruit bunches; crude bio-oil (CBO); upgrading; catalyst cracking; CBO's fuel

■ INTRODUCTION

The fossil-derived fuels, particularly petroleum oils, cannot be renewed and might inflict harmful effects on the environment. Besides, their formation may take considerable ages. Recently, worldwide petroleum oil production, including in Indonesia, continues to decline steadily, while the need for such fuel oil increases almost every year. This situation requires the findings of alternative materials as the replacement for fossil fuels, which are almost limitless in supply and renewable, such as solar energy, water/marine energy, wind power, geothermal power, atomic/nuclear energy, and biomass.

Biomass is one of the promising and considered alternative energy materials as a natural resource that can

be renewed, which more environmentally friendly. The biomass also contains carbon (C) and hydrogen (H) elements, of which burning releases energy but exhibits unique characteristics and enacts the related interests, as among others exemplified in the following details. Biomass sources being renewable are abundantly available, especially from agricultural and forestry wastes in the form of woods and other lignocellulose matters [1].

One kind of the biomass-derived fuels which afford the potentiality to be developed prospectively and beneficially is bio-oil. Bio-oil could be in the shape of liquid fuels, and the biomass sources for such bio-oil are among other agricultural and forestry by-products, crops, and municipal wastes through further biochemical or thermochemical processes [2]. Bio-oil is

a thermally unstable mixture containing hundreds of oxygenated organic compounds [3]. This high content of such oxygenated matters increases the polar nature of the bio-oils, rendering their hygroscopicity and therefore limits its mixing ability with inherently less- or non-polar hydrocarbon fuels [4].

Some pathways that can be used to improve the qualities of crude bio-oil are through several various upgrading processes such as catalytic cracking, hydrocracking, or hydrodeoxygenation [5]. Liu et al. [6] reported that some researches had been conducted for the upgrading of bio-oil using Fe, Zn, Al, and Mg metal catalysts at ambient temperature under open atmospheric pressure. Results revealed that such metal catalysts improved the quality of resulting upgraded bio-oil (fuel), whereby its pH raised from 3.53 to 4.85, which could decrease the corrosive nature of bio-oil.

Another metal that is also often used in the cracking reaction is Ni because it has good results and selectivity for the desired product [7]. However, Ni metal has several disadvantages when it is used directly, considering the high price, low surface area, and sintering can occur during the reaction. Other materials, as support such as zeolite, are required to improve catalyst performance and make a bifunctional catalyst. Natural zeolite is a porous material whose availability is abundant so that it has a high potential and occupies a special place to be used as a catalyst support material [8]. The use of natural zeolite impregnated with Ni, Mo, and Co was conducted by Sriningsih et al. [9] on hydrocracking of LDPE plastics waste. In this research, the highest gasoline conversion percentage is reached about 71.49% at a temperature of 350 °C with H₂ flow of 20 mL/min for 1 h. It is also shown that the composition of the product is paraffins, olefins, and naphthenes.

Yang et al. [10] reported the working on the upgrading of bio-oil into fuel, which was produced from shrubs residues, through the cracking process using Zeolite H-ZSM-5 catalyst. Results showed that the quality of bio-oil-converted fuel improved after such catalytic cracking, whereby its oxygen content (w/w) decreased from 47.61 to 31.83% and its moisture content (w/w)

decreased from 33.23 to 22.15%.

Relevantly, the aim of this research was to investigate the technical feasibility of upgrading the qualities and characteristics of CBO previously produced from OPEFB, through the CBO's cracking into fuel, with Ni/NZA as a catalyst and entirely under open atmospheric pressure.

■ EXPERIMENTAL SECTION

Materials

The main material for bio-oil manufacture was fresh oil-palm empty fruit bunches (OPEFB). The OPEFB samples were obtained from the palm-oil factory, located in Lebak District, Banten Province. The natural zeolite was obtained from Bayah, Lebak-Banten. Meanwhile, the chemical matters used were AgNO₃ (Merck), hydrochloric acid (Merck), NH₄Cl (Merck), Na₂SO₄ (Merck), Ni(NO₃)₂·6H₂O (Merck).

Instrumentation

The FTIR spectra were recorded on a Shimadzu (FTIR-8201-FC) spectrophotometer; the XRD diffractograms were recorded on a Shimadzu XRD-7000. The GC-MS chromatogram and spectra were recorded on a Shimadzu QP-2010 Ultra. The SEM images were recorded on a Zeiss EVO 50, sieve shaker (Retsch), bomb calorimetry Toshniwal DT 100, viscometer (Brookfield LVF), fixed bed reactor, analytical balance (Ohaus), oven (Mettler), distillation apparatus, stirrer, desiccator, pH meter (Hanna), pycnometer, Erlenmeyer and other glassware.

Procedure

OPEFB pyrolysis

OPEFB samples were dried and cut into small pieces with a crusher. The resulting small-sized OPEFB were ready to use for fast pyrolysis process to obtain CBO product. For such, 500 g of sample OPEFB (moisture content, i.e., 10–15%, dry basis) was put into the pyrolysis reactor at a temperature of 550 °C [11]. After the pyrolysis, the mixed liquid (water and bio-oil) was collected as crude bio-oil (CBO).

Preparation of Ni/NZA

The preparation of the catalyst that incorporated zeolite referred to the procedure performed from the previous study [12]. The natural zeolite is crushed and then sieved using a sieve of 100 mesh, washed using distilled water, and then dried at a temperature of 120 °C (obtained sample is named as NZ). NZ was activated with 6 N hydrochloric acid for 30 min at reflux temperature. The resulting solid was filtered and washed with distilled water to neutral and showed a negative test for the presence of Cl⁻ ions using the AgNO₃ solution. The residue was dried at a temperature of 100–120 °C. The sample was refluxed in the NH₄Cl solution for 3 h at a temperature of 90 °C. The resulting solid was filtered and dried at a temperature of 100–120 °C to obtain activated natural zeolite (NZA).

Loading Ni onto NZA was conducted with the impregnation method using a salt precursor of 3% Ni(NO₃)₆H₂O to NZA (w/w) followed by calcination using the reactor with a temperature of 500 °C for 60 min (obtained sample Ni/NZA). Catalyst characterization includes determining the site of TO₄ (T = Si or Al) in zeolites observed with Fourier Transform Infrared Spectroscopy (FT-IR Shimadzu, Prestige-21), acidity using ammonia adsorption, crystallinity using X-ray diffraction (XRD Shimadzu 7000), and catalyst morphology using a scanning electron microscope (SEM Zeiss EVO 50).

Measurement of the catalyst acidity was carried out by flowing ammonia vapor for 24 h at room temperature on the catalyst sample. The acidity of the catalyst was calculated as the weight difference of the catalyst sample before and after adsorption, using the following equation:

$$\text{Acidity (A : \%w / w)} = \frac{W3 - W2}{(W2 - W1)M} \times 1000 \text{ mmol / g}$$

where A is the acidity of catalyst (mmol/g zeolite), W1 is the weight of an empty porcelain cup that has been heated (g), W2 is the weight of the cup aided of the catalyst before adsorption (g), W3 is the weight of cup and sample of the catalyst after adsorption (g), and M is the molecular weight of the base ammonia (g/mol).

Cracking CBO in a batch reactor

Cracking of CBO was performed in a batch reactor (reactor has a capacity of 500 mL, and is equipped with heater, condenser and thermocouple) with weight of Ni/NZA i.e. A₁ = 0% (control), A₂ = 4%, A₃ = 6% and A₄ = 8% toward CBO at temperature of B₁ = 250 °C and B₂ = 300 °C for 2 h and replicated 3 times, respectively. The physicochemical properties of the liquid products were analyzed to obtain yield gravimetrically, specific gravity by pycnometer method, pH by pH meter, viscosity by Brookfield LVF viscometer, calorific value by bomb calorimetry Toshniwal DT 100 and chemical component product by GCMS Shimadzu QP 2010 Ultra. As a comparison, the CBO from the OPEFB pyrolysis was also examined for its characteristics similarly.

RESULTS AND DISCUSSION

Characteristics of Zeolite-Related Catalyst

Table 1 discloses the results of total acidity analysis on the NZ, NZA, and Ni/NZA samples, which corresponded to 0.85, 1.20, and 1.70 mmol/g, respectively. It appears that the total acidity of Ni/NZA catalyst was the largest, followed in decreasing order by NZA, and NZ (the lowest).

Total acidity is calculated by the amount of chemically adsorbed NH₃ per unit weight of the sample. The amount of ammonia adsorbed on zeolite is obtained from the difference in weight of zeolite before and after the adsorption. Acidity measured in this research is the total acidity of the catalyst sample, namely Brønsted and Lewis acid. This is because ammonia has a small molecular size (molecular weight of 17 g/mol), so it can be adsorbed into the zeolite pore. Zeolites have small-pore sizes in the range of 0.30–0.45 nm [13]. Loading Ni onto NZA increased Brønsted and Lewis acid sites; therefore, Ni/NZA catalysts

Table 1. Total acidity of NZ, NZA and Ni/NZA

Sample	Acidity (mmol/g)
NZ	0.8494
NZA	1.1963
Ni/NZA	1.7006

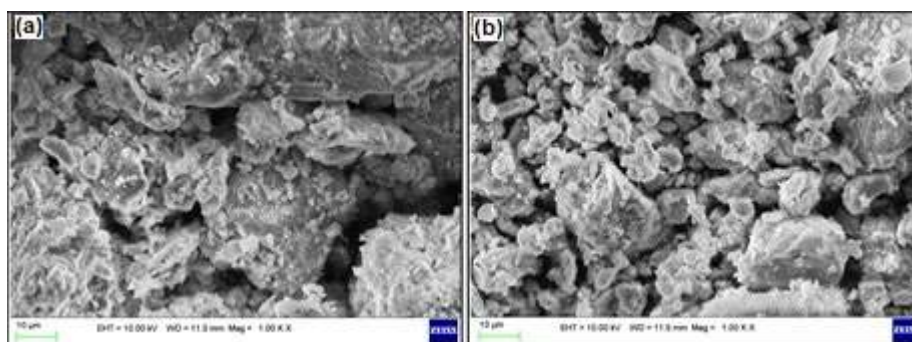


Fig 1. SEM results on the visual morphology image of (a) NZ and (b) Ni/NZA

had the greatest acidity. Ni metal is highly coordinated (has an ability to bind with ligand due to the arrangement of electron potential from unoccupied d-orbital), which has many low-energy orbitals and can act as a Lewis site. This result was in accordance with the result obtained by Trisunaryanti et al. [14], that loading of Co, Ni, and Pd metals onto mordenite could increase the number of both Brønsted and Lewis acid sites. According to Naqvi et al. [15], increasing acidity of catalysts can facilitate converting biomass into an organic compound with lower molecular weight. An almost similar situation occurred in this research, whereby the use of Ni/NZA catalyst during CBO cracking into fuel brought out more numerous the fragmented and lower molecular weight organic compounds in the product, thereby contributing greatly to the increased fuel yield, compared to the cracking without catalyst (Table 2).

Fig. 1(a) and 1(b) reveal the SEM images of NZ and Ni/NZA catalyst visually. From this figure, we can see the porous character and sphere-like crystals of the catalyst. Ni particles were less dispersed in catalyst because we can find the large Ni particles on the surface and Ni particle agglomeration tend to occur after the impregnation process.

The XRD results of NZ and Ni/NZA catalysts are disclosed in Fig. 2. From this figure, the 2θ that appears in the sample can be identified through comparison with mordenite and clinoptilolite type at JCPDS data. It strongly indicates that the NZ could be classified as mordenite (m) mineral, which constituted the NZ's main component and still contained clinoptilolite (kl) and quartz (k) (Fig. 2). Salim et al. [16] conducted zeolite-related research and came out with a similar conclusion that natural zeolite contained mordenite, clinoptilolite,

and quartz. Mordenite crystal is chemically a neutral basic structure and exhibits high resistance against high temperatures [17].

Metal impregnation into the zeolite causes decreasing of the crystallinity of NZA (crystallinity of NZA and Ni/NZA are 90.15 and 87.09%, respectively). It occurred because of the high temperature calcination process, making damage to the structure, and also less dispersed Ni on zeolite.

The successful Ni-metal loading onto the zeolite was shown by the obvious diffraction line at 29.68° (Fig. 2). This peak was sharp and strong enough, indicating that the active Ni sites were less dispersed on the support (also in line with SEM observation shown in Fig. 1). This is consistent with Yao et al. [18] research that the diffraction lines of Ni metal were weak and broad, indicating that the Ni was well dispersed in the support material.

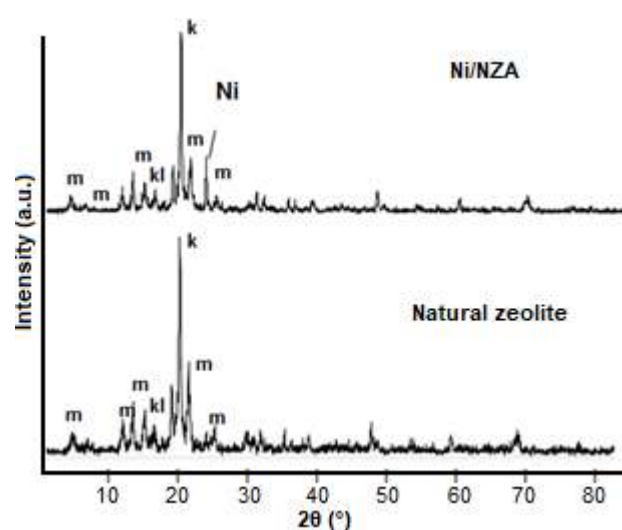


Fig 2. XRD's diffractogram of NZ and Ni/NZA catalyst

Fig. 3 depicts the comparison of the FTIR spectra between natural zeolite (NZ) and Ni/NZA catalyst. For a zeolite in common, the typical absorption band of its structure was found in the wavenumber at 795 cm^{-1} . Such a particular wavenumber was due to the bending absorption of the Si–O bond on the external zeolite framework. The vibration of Si–O/Al–O bonds at the area in the range of $420\text{--}500\text{ cm}^{-1}$ of FTIR spectra appeared at 465 and 463 cm^{-1} for the NZ and Ni/NZ, respectively.

The absorption bands at $3000\text{--}4000\text{ cm}^{-1}$ disclose the vibration of O–H hydroxyl inside the zeolite structure. The O–H group at 3449 cm^{-1} in the FTIR spectra was due to the adsorbed water molecule on the zeolite for the Ni/NZA catalyst. Further, the absorption bands at 1639 cm^{-1} reveal the vibration caused by the OH-group buckling in water molecules, which was adsorbed into the natural zeolite as well as into Ni/NZA catalyst.

From Fig. 3, it also can be seen that there was a peak shift at $1000\text{--}1100\text{ cm}^{-1}$, which showed the absorption due to the asymmetrical vibration of the TO_4 group to larger wavenumber. In NZ spectra, a vibrational region of TO_4 showed a peak of 1043 cm^{-1} whereas on Ni/NZA at 1051 cm^{-1} . In zeolite, this shift occurred due to decreasing of Al atoms in zeolite framework in the dealumination process by HCl; therefore, the distance between the Al atoms will be further away, and Al atoms interaction will decrease, and it can be easier to move. This is similar to Ichsan et al. [19] that the shift of asymmetric vibration occurred after the impregnation of Ni into zeolite, and the band at 1045.46 cm^{-1} shifted to 1092.72 cm^{-1} for zeolite and NiMO/ZA, respectively.

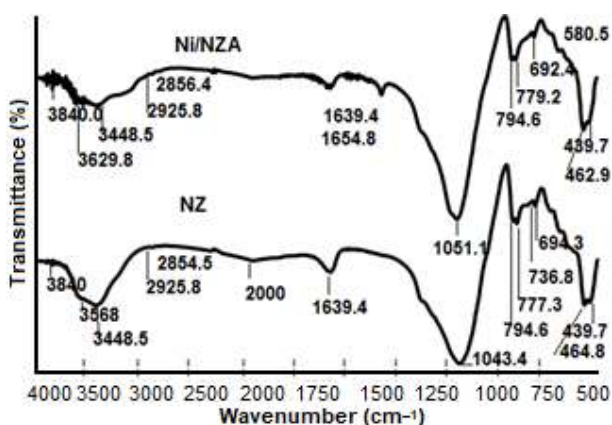


Fig 3. FTIR spectra of NZ and Ni/NZA

Characteristics of the Upgraded Crude Bio-Oil

The yield of the upgraded crude bio-oil

The yield of CBO derived fuel, which was free of water, ranged about 1.52–26.42% (Table 2). The highest yield (26.42%) was obtained with a 6% Ni/NZA catalyst at $300\text{ }^{\circ}\text{C}$. Meanwhile, the lowest fuel yield was obtained without a catalyst at $250\text{ }^{\circ}\text{C}$. The CBO's cracking at $250\text{ }^{\circ}\text{C}$, either with or without Ni/NZA catalyst, exhibited low fuel yield (1.52–3.91%). Accordingly, the CBO's cracking at $250\text{ }^{\circ}\text{C}$ did not run optimally. The possible explanation is that because the collision between the involved reactants during the cracking at such low temperatures might not proceed effectively.

On the other hand, the CBO's cracking at higher temperatures ($300\text{ }^{\circ}\text{C}$), either with Ni/NZA catalyst (4–8%) or without catalyst (0%), brought out the higher fuel yield (20.32–26.42%). This can be explained as because the CBO's cracking could occur more intensively at $300\text{ }^{\circ}\text{C}$, thereby converting more of CBO's high molecular-weight chemical components through degradation and other chemical breakdowns to numerously simpler and lower molecular weight compounds, all in produced fuel, increasing the fuel yield. The addition of Ni/NZA catalyst to the CBO's cracking could increase the fuel yield (1.92–26.42%) when compared with the cracking without catalyst (1.52–20.32%). According to Hessel et al. [20], the use of catalysts could decrease the reaction temperature, and hence, it was able to reduce the reaction's energy, and it could also provide more active sites for the reaction process.

A catalyst could accelerate the reaction rate and improves the quantity as well as the quality of the reaction product. Besides, the catalyst might also enhance the selectivity of the reaction course toward releasing the desired final products. Accordingly, such a situation will allow the reaction to take place rapidly or to decrease the temperature due to the changes otherwise triggered by the reagents. Relevantly, in this research results, it is indicated that the use of Ni/NZA catalyst indeed accelerated the CBO's cracking reaction and induced reaction selectivity, thereby intensifying the CBO's chemical conversion and increasing the yield of the desired product.

Table 2. Characteristics of the upgraded CBO into fuel

Code for treatment combination in the cracking (AB)	CBO's cracking results					Physical properties			
	Mixed liquid (%)	Water-free liquid (fuel) (%)	Water (%)	Residue (%)	Conversion (%)	pH	Specific gravity	Viscosity (cSt)	Calorific value (MJ/kg)
Raw bio-oil	-	-	-	-	-	2.70	1.072	57.7	-
A ₁ B ₁	6.67	1.52	5.15	84.19	15.81	2.86	1.001	11.5	17.22
A ₁ B ₂	24.87	20.32	4.55	62.36	34.64	3.16	0.999	21.3	22.24
A ₂ B ₁	9.43	1.92	7.51	83.29	16.71	3.15	0.998	9.5	18.94
A ₂ B ₂	30.72	25.62	5.10	57.15	42.85	3.53	0.994	11.17	29.49
A ₃ B ₁	10.06	3.90	6.16	81.69	18.31	3.43	0.996	9.7	22.65
A ₃ B ₂	30.65	26.42	4.23	56.59	43.40	3.54	0.995	14.3	30.85
A ₄ B ₁	8.88	3.56	5.32	80.81	19.19	3.31	0.992	9.8	27.46
A ₄ B ₂	30.65	26.12	4.53	59.29	40.71	3.53	0.990	15	28.59

Remarks:

Treatment combination (AB) implemented in the cracking, as follows:

A₁B₁ = Non catalyst, 250 °C temperature

A₃B₁ = 6% catalyst, 250 °C temperature

A₁B₂ = Non catalyst, 300 °C temperature

A₃B₂ = 6% catalyst, 300 °C temperature

A₂B₁ = 4% catalyst, 250 °C temperature

A₄B₁ = 8% catalyst, 250 °C temperature

A₂B₂ = 4% catalyst, 300 °C temperature

A₄B₂ = 8% catalyst, 300 °C temperature

In the upgrading of CBO qualities, it also ended up with the residue, which in portion ranged about 56.59–84.19%. The highest portion of residue from the CBO's cracking was obtained at 250 °C without a catalyst, while the lowest was at the 300 °C with a 6% Ni/NZA catalyst.

The possible explanation for such occurring phenomena above was that the residue from the CBO's cracking at 250 °C without catalyst was in greater part still in viscous form like tar, and could be cracked down at 300 °C, thereby cracking at 300 °C with the catalyst is able to convert the CBO to lower molecular weight fractions and less viscous form as a liquid. Meanwhile, the residues at 300 °C were initially in a very thick form like mud, and subsequently, when the heating was continued to the cracking completion, it would induce the CBO's cracking and carbonization more intensively. It is also generating more low molecular weight products and lower the residue portion in the form of mostly a solid charcoal.

From this research that at higher temperature with catalyst use, it could intensify the cracking action on converting the CBO's through degradation to simpler and lower molecular weight compounds, thereby lowering the residue portion and conversely increasing the product

yield. The situation was on the contrary at lower cracking temperature and especially without a catalyst.

The cracking process in this research was able to convert as much as 15.81–43.40% of the CBO (Appendix 1) into the mixed liquid forms (6.67–30.72%), and the rest escaped as non-condensable gases/vapors (7.28–12.75%). As much as 1.52–26.42% of those 6.67–30.72% mixed forms were as the CBO converted to fuel.

The pH of the upgraded CBO

The result showed that the pH of the upgraded CBO into fuel ranged from about 2.86–3.53 (Table 2). The lowest pH occurred to the fuel that resulted from CBO's cracking at 250 °C without catalyst use, while the highest pH was obtained at 300 °C with 6% Ni/NZA catalyst use. This result indicates that high temperature with Ni/NZA catalyst brought about the fuel with higher pH. These pH values are entirely still in the common pH range (2.8–4.0) of bio-oil chemically converted from most biomass materials [21].

Such low pH value indicates the presence of organic acids in CBO-derived fuel generated from the further degradation of the CBO's chemical compounds, which previously were already in degraded/depolymerized

forms (e.g., cellulose, hemicellulose, lignin, and extractives [especially residual palm oil/fat]) following the OPEFB's pyrolysis.

The CBO's cracking at 300 °C aided by 6% Ni/NZA catalyst brought about the situation that those organic acids might be broken down to non-acidic (neutral) or weak-acid compounds with much lower molecular weight (e.g., hydrocarbon, aldehyde, ketone, slightly acidic phenols, and neutral hydrocarbons), thereby rendering the produced fuel less acidic or increasing the fuel pH until it achieved the highest (3.54). This is in line with the data in Appendix 1 for the treatment using 6% Ni/NZA at 300 °C, 5.82% acid compound obtained, lower than the other treatments. In relevant, according to Wang [22], the pH value of bio-oil typically ranged about 2–3, due to the presence of carboxylic acids such as formic acid and acetic acid.

The overall pH of the fuel produced from the CBO's cracking was entirely greater than the pH of raw bio-oil or CBO that resulted from the OPEFB's pyrolysis (Table 2). This indicates that the organic acids in the CBO in part underwent further chemical breakdown during the CBO's cracking into numerous much lower molecular-weight compounds as among others neutral or rather neutral hydrocarbons in the cracking results (e.g., fuel). Bio-oil fuels with low pH value are less desirable, as they can lead to the corrosion of metal equipment such as conducting pipes, burner devices, and other metal-made apparatus.

The specific gravity of the upgraded CBO

The specific gravity of fuel ranged from about 0.990–1.001 (Table 2). The lowest specific gravity occurred to the fuel produced from the CBO's cracking at 300 °C with an 8% Ni/NZA catalyst. Meanwhile, the highest specific gravity was achieved at 250 °C without a catalyst.

These overall fuel's specific gravity values were entirely higher than the specific gravity of OPEFB's upgraded bio-oil into fuel, which reached 0.851, as conducted in another study [23]. As such, the upgraded bio-oil was produced through cracking of the bio-oil under high pressure by adding hydrogen (H₂) gas and using the ZSM-5 catalyst. Presumably, such high fuel's specific gravity achieved in this research could be attributed to the absence of high pressure and due to not

adding H₂ gas. In general, the specific gravity of the particular type of CBO produced from biomass pyrolysis reached as high as 1.2, and the specific gravity of bio-oil that resulted from the sawdust's biomass pyrolysis achieved even higher (1.3) [24].

The viscosity of the upgraded CBO

The measurement results on fuel's viscosity revealed the variation in the range of 9.5–21.3 cSt (Table 2). The lowest viscosity occurred at the fuel produced from CBO's cracking at 250 °C with a 4% Ni/NZA catalyst while the highest fuel viscosity was from the implementation of 300 °C temperature without a catalyst. The fuel viscosity (9.5–11.5 cSt) at 250 °C for CBO cracking tended to be smaller than the fuel viscosity (11.7–21.3 cSt) at 300 °C. On the contrary, at 250 °C as well as at 300 °C in the CBO's cracking, the fuel viscosity without catalyst (11.5–21.3 cSt) was greater than fuel viscosity with Ni/NZA catalyst (9.5–14.3 cSt).

It has been strongly confirmed that the use of Ni/NZA catalyst assisted in intensifying the conversion of CBO's to more numerous fragmented/simpler and low molecular weight compounds. It is also explained that the CBO's chemical breakdown brought about the produced fuel with low viscosity, due to the presence of Ni/NZA catalyst.

In general, according to Vispute [25], the high viscosity of CBO is due to a large number and high concentration of high molecular weight compounds inside. Long-chain molecule compounds tended to entangle with each other, creating viscous mass, increasing the fuel viscosity.

The fuel viscosity in these research results (9.5–21.3 cSt) was still much higher than the viscosity as experimented by Zhang et al. [26] who performed the upgrading of bio-oil through the pine wood's bio-oil cracking with 10% silica sulphuric acid (SSA) catalyst (w/w) in the reactor that was pressurized for 3 h at 120 °C. Such pressurized cracking brought about the upgraded bio-oil with low viscosity (5.5 cSt) and also low specific gravity (0.89). However, if compared to the viscosity of CBO (57.7 cSt) that resulted from OPEFB's pyrolysis, the overall viscosity of the upgraded CBO into fuel was still much lower. This again confirms that CBO's cracking at

elevated temperature (250 and 300 °C) aided by Ni/NZA catalyst (4–8%) could induce the conversion of CBO's compounds to numerous simpler and low molecular-weight compounds and lowering the fuel viscosity.

Although the fuel that resulted from the upgrading of OPEFB's CBO indicatively cannot be used as fuel for running vehicles or other transportation means that use piston-driven engines due to its still high viscosity, it seems still useful after being blended with petroleum's heavy fuel for operating fuel-fired boilers [27].

The heating value of the upgraded crude bio-oil

The calorific values from the CBO's cracking were ranged from about 17.22–30.85 MJ/kg (Table 2). The lowest calorific value was encountered at the fuel produced from the CBO's cracking at 250 °C without catalyst, while the highest was at 300 °C with a 6% Ni/NZA catalyst. These phenomena strongly confirm the previous indication that high cracking temperature (300 °C) aided by the Ni/NZA catalyst intensified more CBO's conversion and therefore generated fragmented and low molecular weight compounds.

When the fuel with such numerous fragmented low molecular-weight compounds was combusted, the heating potency of each compound would combine and add up to each other, accordingly released a considerable amount of energy, and hence, caused higher fuel's calorific value. The calorific values of CBO-derived fuel in these results were, in part, still in the range of calorific values for the upgraded bio-oil into fuel that resulted from the hydrocracking of bio-oil or hydrodeoxygenation (HDO) using zeolite catalyst, which reached 21–36 MJ/kg. Further, the calorific values of CBO-derived fuel were considerably lower than the calorific values of fuel that resulted from bio-oil's HDO process (42–45 MJ/kg) [28].

Such a high calorific value of the HDO's upgraded bio-oil into fuel was attributed to the HDO's cracking process, which used hydrogen gas and implemented high-pressure in a 1–10 MPa range [29]. It seems that such HDO's cracking intensified the bio-oil's cracking more severely, generating the amount of short-chain hydrocarbon alkanes such as octane (C₈H₁₈) and nonane (C₉H₂₀) in the produced fuel. Accordingly, when those numerous short-chain alkanes were combusted together,

their released energy could add up to each other and end up with high fuel's calorific value. High heating values of particular combustible materials or fuels are desired, because it can provide a considerable amount of energy or power for operating fuel-run devices, such as fuel-powered vehicles, electric generators, stoves, boilers, and furnaces.

Chemical Compounds in the Produced Fuel

Appendix 1 discloses the list of organic compounds present in the fuel that resulted from the upgrading of CBO, which was identified through the GC-MS analysis. It turns out that particular aromatic groups such as hydrocarbon, phenols, aliphatic, furan, ester, acids, ketones, and alcohols were identified, which contained significant amounts of phenolic compounds. These phenolic compounds, as identified, were due to the lignin degradation during the CBO's cracking process, which was responsible for the higher content of carbon and hydrogen fractions in the produced fuel and contributed to the fuel's higher heating values [30].

The cracking's liquid product also contained aromatic hydrocarbons (e.g., benzene and benzene derivatives) and aliphatic hydrocarbons (e.g., hexane, tridecane, octadecane, hexadecane, etc.). The most numerous aliphatic and aromatic hydrocarbons were encountered in the fuel resulted from CBO's cracking at 300 °C temperature with 8% Ni/NZA catalyst, compared to the number of which resulted from the cracking with the other treatment. On the other hand, more numerous hydrocarbons were found in the fuel from CBO's cracking at 300 °C temperature, aided by 8% Ni/NZA catalyst, compared to the number of hydrocarbons from CBO's cracking at 250 °C with also 8% Ni/NZA catalyst. This again confirms that the use of higher temperatures during the CBO's cracking brought out the produced fuel with more numerous hydrocarbon compounds inside and increasing the fuel heating/calorific value.

To improve such unsatisfactory fuel qualities, it is recommended that the modification of CBO's cracking process is necessary by implementing among others higher pressure, H₂-gas addition, and higher

temperature. Relevantly, according to Huber et al. [31] in the biomass's conversion through a cracking process into fuel which was suitable in use for transportation means that used piston engines, it necessitates the biomass cracking process at temperatures as high as 300–600 °C and implementing high pressure that reached 14 MPa (140 bar).

Frey et al. [32] suggested that implementing higher hydrogen gas pressure during the biomass' hydrocracking process would increase the production of alkane compounds. However, the hydrocracking process seems still an expensive way in an upgrading attempt to produce fuel with high energy and other improved qualities, because it requires the involvement of hydrogen-gas use and proper reactor equipment.

■ CONCLUSION

The optimum CBO's cracking condition was determined to be the temperature of 300 °C with 6% Ni/NZA catalyst use. The fuel yield product, calorific value, pH, specific gravity, and viscosity were 26.42%, 30.85 MJ/kg, 3.54, 0.995, 14.3 cSt, respectively. Several characteristics of fuel were regarded as satisfactory, except pH and viscosity.

■ REFERENCES

- [1] Luo, H., Bao, L., Kong, L., and Sun, Y., 2017, Low temperature microwave-assisted pyrolysis of wood sawdust for phenolic rich compounds: Kinetics and dielectric properties analysis, *Bioresour. Technol.*, 238, 109–115.
- [2] Dermibas, A., 2008, *Biodiesel: A Realistic Fuel Alternative for Diesel Engines*, Springer-Verlag London Limited, London, UK.
- [3] Choi, J.H., Woo, H.C., and Suh, D.J., 2014, Pyrolysis of seaweeds for bio-oil and bio-char production, *Chem. Eng. Trans.*, 37, 121–126.
- [4] Hassan, E.B., Abou-Yousef, H., Steele, P., and El-Giar, E. 2016, Characterization of bio-oils from the fast pyrolysis of white oak and sweetgum, *Energy Sources Part A*, 38 (1), 43–50.
- [5] Brown, R.C., and Holmgren, J., 2013, Fast pyrolysis and bio-oil upgrading, https://www.researchgate.net/profile/Robert_Brown31/publication/204979128_Fast_pyrolysis_and_bio-oil_upgrading/links/00b7d52b21146924c1000000.pdf.
- [6] Liu, W.J., Zhang, X.S., Qv, Y.C., Jiang, H., and Yu, H.Q., 2012, Bio-oil upgrading at ambient pressure and temperature using zero valent metals, *Green Chem.*, 14 (8), 2226–2233.
- [7] Wu, J., Shi, J., Fu, J., Leidl, J.A., Hou, Z., and Lu, X., 2016, Catalytic decarboxylation of fatty acids to aviation fuels over nickel supported on activated carbon, *Sci. Rep.*, 6 (1), 27820.
- [8] Hovhannisyanyan, V.A., Dong, C.Y., Lai, F.J., Chang, N.S., and Chen, S.J., 2019, Natural zeolite for adsorbing and release of functional materials, *J. Biomed. Opt.*, 23 (9), 091411.
- [9] Sriningsih, W., Saerodji, M.G., Trisunaryanti, W., Triyono, Armunanto, R., and Falah, I.I., 2014, Fuel production from LDPE plastic waste over natural zeolite supported Ni, Ni-Mo, Co and Co-Mo metals, *Procedia Environ. Sci.*, 20, 215–224.
- [10] Yang, H., Wang, Q., Sang, Y., Fan, G., and Xu, Q., 2014, Online upgrading of bio-oil pyrolyzed form by shrub residues, *Asian J. Chem.*, 26 (1), 247–250.
- [11] Singh, R.K., and Shadangi K.P., 2011, Liquid fuel from castor seeds by pyrolysis, *Fuel*, 90 (7), 2538–2544.
- [12] Bahri, S., Sunarno, Muhdarina, and Anugra, R.D., 2011, Catalytic pyrolysis using catalyst nickel-natural zeolite (Ni/NZA) on conversion of biomass to bio-oil, *2011 International Conference & Utility Exhibition on Power and Energy Systems: Issues and Prospects for Asia (ICUE)*, Pattaya City, Thailand, 28–30 September 2011.
- [13] Dusselier, M., and Davis, M.E., 2018, Small-pore zeolites: Synthesis and catalysis, *Chem. Rev.*, 118 (1), 5265–5329.
- [14] Trisunaryanti, W., Triyono, Armunanto, R., Hastuti, L.P., Ristian, D.D., and Ginting, R.V., 2018, Hydrocracking of α -cellulose using Co, Ni, and Pd supported on mordenite catalysts, *Indones. J. Chem.*, 18 (1), 166–172.
- [15] Naqvi, S.R., Uemura, Y., Yusup, S., Sugiur, Y., Nishiyama, N., and Naqvi, M., 2015, The role of zeolite structure and acidity in catalytic

- deoxygenation of biomass pyrolysis vapors, *Energy Procedia*, 75, 793–800.
- [16] Salim, I., Trisunaryanti, W., Triyono, and Arryanto, Y., 2016, Hydrocracking of coconut oil into gasoline fraction using Ni/modified natural zeolite catalyst, *Int. J. ChemTech Res.*, 9 (4), 492–500.
- [17] Houas, A., Lachheb, H., Ksibi, M., Elaloui, E., Guillard, C., and Herrmann, J.M., 2001, Photocatalytic degradation pathway of methylene blue in water, *Appl. Catal., B*, 31 (2), 145–157.
- [18] Yao, D., Yang, H., Chen, H., and Williams, P.T., 2018, Investigation of nickel-impregnated zeolite catalysts for hydrogen/syngas production from the catalytic reforming of waste polyethylene, *Appl. Catal., B*, 227, 477–487.
- [19] Ichsan, G.M., Nugrahaningtyas, K., Widjonarko, D., and Rahmawati, F., 2019, Structure and morphology of the (Ni, Co) Mo/Indonesian natural zeolite, *IOP Conf. Ser. Mater. Sci. Eng.*, 578, 012009.
- [20] Hessel, V., Anastasopoulou, A., Wang, Q., Kolb, G., and Lang, J., 2013, Energy, catalyst and reactor considerations for (near) -industrial plasma processing and learning for nitrogen-fixation reactions, *Catal. Today*, 211, 9–28.
- [21] Sadaka, S., and Boateng, A., 2009, Pyrolysis and bio-oil, *Agriculture and Natural Resources*, Cooperative Extension Service, University of Arkansas, United States Department of Agriculture and County Governments Cooperating.
- [22] Wang, S., 2013, “High-efficiency separation of bio-oil” in *Biomass Now: Sustainable Growth and Use*, Eds. Matovic, M.D., IntechOpen, Croatia, 401–418.
- [23] Hew, K.L., Tamidi, A.M., Yusup, S., Lee, K.T., and Ahmad, M.M., 2010, Catalytic cracking of bio-oil to organic liquid product (OLP), *Bioresour. Technol.*, 101 (22), 8855–8858.
- [24] Bardalai, M., and Mahanta, D.K., 2015, A review of physical properties of biomass pyrolysis oil, *Int. J. Renew. Energy Res.*, 5 (1), 277–286.
- [25] Vispute, T., 2011, Pyrolysis oils: Characterization, stability analysis, and catalytic upgrading to fuels and chemicals, *Dissertations*, University of Massachusetts, USA.
- [26] Zhang, Z., Sui, S., Wang, F., Wang, Q., and Pittman, C.U., 2013, Catalytic conversion of bio-oil to oxygen-containing fuels by acid-catalyzed reaction with olefins and alcohols over silica sulfuric acid, *Energies*, 6 (9), 4531–4550.
- [27] Hou, S.S., Huang, W.C., Rizal, F.M., and Lin, T.H., 2016, Co-firing of fast pyrolysis bio-oil and heavy fuel oil in a 300-kW_{th} furnace, *Appl. Sci.*, 6 (11), 326.
- [28] Mortensen, P.M., Grunwaldt, J.D., Jensen, P.A., Knudsen, K.G., and Jensen, A.D., 2011, A review of catalytic upgrading of bio-oil to engine fuels, *Appl. Catal., A*, 407 (1-2), 1–19.
- [29] Daudin, A., Bournay, L., and Chapus, T., 2010, Method of converting effluents of renewable origin into the fuel of excellent quality by using a molybdenum-based catalyst, *US Patent 20100163458A1*, 1 November 2010.
- [30] Nanda, S., Mohanty, P., Kozinski, J.A., and Dalai, A.K., 2014, Physico-chemical properties of bio-oils from pyrolysis of lignocellulosic biomass with high and slow heating rate, *Energy Environ. Res.*, 4 (3), 21–32.
- [31] Huber, G.W., Sara, I., and Corma, A., 2006, Synthesis of transportation fuels from biomass, *Chem Rev.*, 106 (9), 4044–4098.
- [32] Frety, R., da Rocha, M.G.C., Brandão, S.T., Pontes, L.A.M., Padilha, J.F., Borgesc, L.E.P., and Gonzalez, W.A., Cracking and hydrocracking of triglycerides for renewable liquid fuels: Alternative processes to transesterification, *J. Braz. Chem. Soc.*, 22 (7), 1206–1220.

The Effect of Bioactive Polyphenols from *Anacardium occidentale* Linn. Leaves on α -Amylase and Dipeptidyl Peptidase IV Activities

Nur Imanina Abdullah Thaidi¹, Hanapi Mat Jusoh², Ahmad Badruddin Ghazali³, Deny Susanti¹, and Normah Haron^{1,*}

¹Kulliyyah of Science, International Islamic University Malaysia, 25200, Kuantan, Pahang, Malaysia

²Kulliyyah of Allied Health Science, International Islamic University Malaysia, 25200, Kuantan, Pahang, Malaysia

³Kulliyyah of Dentistry, International Islamic University Malaysia, 25200, Kuantan, Pahang, Malaysia

* **Corresponding author:**

tel: +609-570 5037

email: normahh@iium.edu.my

Received: April 7, 2019

Accepted: July 26, 2019

DOI: 10.22146/ijc.44807

Abstract: *Anacardium occidentale* Linn. (*A. occidentale* L.) leaves possess bioactive polyphenols which are associated with antidiabetic potency for the management of type 2 diabetes mellitus (T2DM). In this study, free, soluble ester, and insoluble-bound phenolic fractions from young and mature leaves of *A. occidentale* L. were extracted. Subsequently, all fractions were investigated for their inhibitory effect on α -amylase and dipeptidyl peptidase IV (DPPIV) activities. Both free ($72.45 \pm 3.6\%$) and soluble ester ($83.40 \pm 4.7\%$) phenolic fractions in the mature leaves extracts had significantly demonstrated greater α -amylase inhibitors than the young leaves. Likewise, soluble ester ($4.09 \pm 0.34 \mu\text{g/mL}$) and insoluble-bound ($4.87 \pm 0.32 \mu\text{g/mL}$) phenolic fractions in the mature leaves extracts were significantly more effective in inhibiting DPPIV than the young leaves. As for fractions comparison, insoluble-bound derived from the young leaves extract was a more potent α -amylase inhibitor than free and soluble ester phenolic fractions ($p < 0.0001$). Besides, soluble ester and insoluble-bound phenolic fractions showed a stronger inhibitor of DPPIV than the free phenolic ($p < 0.001$), irrespective of the maturity of the leaves. In conclusion, this study showed that *A. occidentale* L. extracts possessed antidiabetic properties, which may potentially be used as an alternative treatment for T2DM management.

Keywords: *Anacardium occidentale* Linn; dipeptidyl peptidase IV; α -amylase; inhibitor

■ INTRODUCTION

Diabetes mellitus is one of the major health problems that affect millions of people worldwide. It is projected that 642 million people aged 20–79 years around the globe will suffer from diabetes by 2040 [1]. In Malaysia, since the first National Health Morbidity Survey (NHMS I) until recent NHMS V, the prevalence of diabetes mellitus among the adult population has markedly increased from 6.3% in 1986, 8.2% in 1996, 11.6% in 2006 and 15.2% in 2011 to 17.5% in 2015 [2-3]. Besides, diabetes also becomes one of the leading causes of death globally [1]. In 2012, it was reported that diabetes had caused 1.5 million (2.7%) deaths [4].

The management of diabetes involves continuous medical care with multifactorial risk reduction strategies, including lifestyle modifications and treatments with synthetic hypoglycemic drugs. Nevertheless, it is estimated that 70–80% of the world population still relies on traditional herbal medicine to meet their primary health care needs, including treatments for diabetes, especially in rural areas of developing nations [5]. For example, plants such as *Aloe vera*, *Andrographis paniculata*, *Centella asiatica*, *Curcuma longa*, and *Anacardium occidentale* have been demonstrated to possess antidiabetic properties [6-8], owing to the presence of bioactive compounds such as carotenoids and polyphenols that act as antidiabetic agents [9].

In the carbohydrate metabolism, polyphenols such as phenolic acids, flavonoids, and tannins play a role in inhibiting α -amylase, a glycoside hydrolase enzyme that, if attenuated can slow down the breakdown of long chain carbohydrates to glucose, thus preventing a sudden rise in postprandial blood glucose levels [10-12].

Polyphenols are also able to regulate postprandial glucose levels through the inhibition of dipeptidyl peptidase IV (DPP-IV), a serine protease that localizes on the cell surface of various tissues, including the small intestine [13]. By inhibiting DPP-IV, it prevents the rapid degradation of incretins such as glucagon-like peptide 1 (GLP-1) and gastric inhibitory peptide (GIP) that play a vital role in blood glucose control. GLP-1 and GIP actions include stimulating insulin secretion, lowering glucagon concentration and slowing gastric emptying [14-15].

Anacardium occidentale Linn. (*A. occidentale* L.) or commonly known as cashew tree, is a popular tropical plant among various ethnics in Malaysia for its leaves, shoots, the cashew seed, and the cashew apple. Its shoots or young leaves are especially one of the commonly consumed vegetables by various ethnics in Malaysia [16]. The leaves were noted to be petiolate, elliptic-obovate, measuring 4 to 22 cm long and 2 to 15 cm broad, have a cuneate base with obtuse tip, reticulate venation, entire and smooth edges, a spiral arrangement and have a notable leathery texture [17]. When young, the leaves are pliable and reddish (Fig. 1), and when the leaves mature, they turn to dark green and leathery with prominent yellow veins (Fig. 2).

As described earlier, the leaves of *A. occidentale* L. also possess an excellent source of bioactive compounds, including phenolic acids [8,18-19]. Alkali and water extracts of *A. occidentale* L. contained predominantly gallic acid as well as protocatechuic, *p*-hydroxybenzoic, cinnamic, *p*-coumaric, and ferulic acids [20]. Besides, flavonol glycosides were also identified from the extract of *A. occidentale* L. young leaves, with the highest constituent was kaempferol-3-*O*-glucoside, followed by kaempferol-3-*O*-arabinofuranoside and quercetin-3-*O*-glucoside [16]. For this reason, this study sought to determine whether *A. occidentale* L. leaves extracts to play a role in the inhibition of α -amylase and DPP-IV enzymes.

In nature, the insoluble-bound phenolics are one of the components of cell walls, while soluble ester phenolics compartmentalized within the plant cell vacuoles [21]. Therefore, the yield of extraction depended on the polarity of the compound to the solvent and method of extraction [22]. In this study, the soluble ester and insoluble-bound phenolic fractions were undergone extraction with acid-alkali treatments to release them from the bonded form. Here, we compared the enzyme-inhibitory activities of the extracts between free, soluble esters, and insoluble-bound phenolic fractions, as well as between the young and mature leaves. It is anticipated that these findings could provide some possible mechanisms by which they are used in the management and prevention of type 2 diabetes mellitus.



Fig 1. Young leaves of *A. occidentale* L.



Fig 2. Mature leaves of *A. occidentale* L.

■ EXPERIMENTAL SECTION

Materials

All chemicals used in this study were analytical grade and purchased either from Merck or Fisher Scientific Chemicals (Germany). Ultrapure water was obtained from Mili-Q system and was used in HPLC and enzyme assays. The recombinant DPPIV (human) enzyme was purchased from Enzo Life Sciences (USA). DPPIV-Glo (TM) Protease assay was purchased from Promega. α -Amylase enzyme and sodium potassium tartrate tetrahydrate were purchased from Nacalai Tesque. Acarbose (95%) and 3,5-dinitrosalicylic acid were purchased from Acros. Soluble starch, monosodium phosphate, disodium phosphate, and standards reference were purchased from Sigma Chemical Co. (Missouri, USA). Parts of young and mature leaves of *A. occidentale* L. (2.0 kg) were purchased from Taman Pertanian (Kuantan, Malaysia).

Procedure

Sample preparation for extraction

Young and mature leaves of *A. occidentale* L. (2.0 kg) were selected and washed under running water for several times. The leaves were chopped into small pieces. The leaves were then put into a freezer bag and kept frozen at $-20\text{ }^{\circ}\text{C}$ for 24 h. The frozen leaves were freeze-dried with conditions of 63 Pa vacuum pressures at $30\text{ }^{\circ}\text{C}$ for three days. Subsequently, the samples were ground and sieved to obtain a uniform size of fine powder ($< 1\text{ mm}$). The powdered samples were kept in a vacuum-sealed container and stored at $-20\text{ }^{\circ}\text{C}$ for further analysis.

Sample extraction

The fine powdered of *A. occidentale* L. young and mature leaves were extracted using the maceration method with three different phenolic fractions - free, soluble ester, and insoluble-bound phenolic fraction extracts. The samples were extracted using methanol according to the procedure described by Dvořáková et al. [23] and Singh et al. [24] with slight modifications.

Free phenolic fraction. Three grams of powdered sample was extracted three times, with 30 mL of methanol (80%) on an ultrasonic bath at $60\text{ }^{\circ}\text{C}$ for 1 h. The samples were centrifuged at $9000\times g$ for 15 min at $4\text{ }^{\circ}\text{C}$. The supernatant

was filtered using a no. 4 Whatman filter paper and evaporated until a semisolid residue was obtained using a Büchi rotary evaporator (Newcastle, DE). The semisolid residue was labeled as a crude extract. The crude extract was then extracted with diethyl ether ($3\times 30\text{ mL}$). The ether extracts were collected and evaporated to dryness using a Büchi rotary evaporator with 850 mbar at $35\text{ }^{\circ}\text{C}$. The dried sample was labeled as free phenolic and dissolved into two solvents, methanol, and DMSO. The free phenolic extract was stored at $-20\text{ }^{\circ}\text{C}$ for further analysis. The supernatant with esterified phenolic compounds was moved into a new Falcon tube.

Soluble ester phenolic fraction. The supernatant with esterified phenolic compounds was treated with 20 mL of 4 M sodium hydroxide (NaOH) for 2 h at room temperature. The treated supernatant was then acidified to pH 2 by adding 6 M hydrochloride acid (HCl) and was extracted with diethyl ether ($3\times 10\text{ mL}$). The ether extract was collected and evaporated to dryness using a Büchi rotary evaporator with 850 mbar at $35\text{ }^{\circ}\text{C}$. The dried sample was labeled as soluble ester phenolic and dissolved into two solvents, methanol, and DMSO. Soluble ester phenolic extract was stored at $-20\text{ }^{\circ}\text{C}$ for further analysis.

Insoluble-bound phenolic fraction. The residue obtained from free phenolic fraction extract was treated with 15 mL of 4 M sodium hydroxide (NaOH) for 1 h at room temperature. The treated residue was then acidified to pH 2 by adding 2 M hydrochloride acid (HCl) followed by centrifuged for 10 min at $5000\times g$. The layer of supernatant was collected and extracted with 15 mL of hexane to remove free fatty acid and other lipids contaminants. The liberated phenolic was extracted with diethyl ether ($3\times 10\text{ mL}$). The ether extracts were collected and evaporated to dryness using a Büchi rotary evaporator with 850 mbar at $35\text{ }^{\circ}\text{C}$. The dried sample was labeled as insoluble bound phenolic and dissolved into two solvents, methanol, and DMSO. The insoluble-bound phenolic extract was stored at $-20\text{ }^{\circ}\text{C}$ for further analysis.

High-performance liquid chromatography (HPLC) analysis

High-performance liquid chromatography (HPLC) analysis consists of HPLC equipped with an ultraviolet-visible (UV-Vis). Before injection, each

extracted sample was allowed to be filtered by a 0.45 μm PTFE filter (Millipore). The injection volume was 5 μL . A C-6 phenyl column (250 \times 4.6 mm i.d., particle size 5 μm , C-6 Phenyl, phenomenex, Torrance, CA, USA) was used for the separation of sample components at 25 $^{\circ}\text{C}$. For phenolic acid analysis, the mobile phase comprised of solvent A (methanol) and solvent B (a 1.5%, v/v, solution of formic acid in water). For flavonoids analysis, the mobile phase comprised of solvent A (methanol), solvent B (acetonitrile) and solvent C (0.5–1.0%, v/v, solution of formic acid in water). The flow rate was set at 1.0 mL/min for the compounds.

In vitro α -amylase inhibition study

α -Amylase enzyme activity was 3100 Unit/mg of protein (Nacalai Tesque). The α -Amylase enzyme was dissolved in sodium phosphate or phosphate buffer solution to give a concentration of 12 unit/mL solution. Soluble starch (1%, w/v) in water was used as a substrate solution. Briefly, 250 μL of extracted samples with DMSO were put into a screw-top Falcon tube. Then, 250 μL of the α -amylase enzyme in a phosphate buffer solution with pH 6.9 was added into the Falcon tube. The mixture was preincubated for 10 min at 25 $^{\circ}\text{C}$. Approximately 250 μL of the starch solution was mixed in the mixture as a substrate and incubated for another 10 min at 25 $^{\circ}\text{C}$. Next, 500 μL of DNS color reagent solution (96 mM 3,5-dinitrosalicylic acid, 5.31 M sodium potassium tartrate in 2 M NaOH) was added into the Falcon tube to terminate the reaction. The Falcon tube was then placed into boiling water for 10 min. The mixture was cooled down and diluted with 5 mL of distilled water.

The α -amylase activity was determined by measuring the absorbance of the mixture in a transparent 96-well plate at 540 nm. Control incubations that represent 100% enzyme activity were conducted in an identical fashion replacing plant extract with DMSO. The absorbance (A) due to maltose generated was calculated using the following calculation:

$$A\ 540\ \text{nm control or plant extract} = A\ 540\ \text{nm Test} - A\ 540\ \text{nm Blank}$$

The % of maltose generated was calculated from the linear equation obtained from the maltose standard calibration curve (0–0.25%, w/v, maltose). Percentage of inhibition = 100 - % of reaction, whereby:

$$\% \text{ reaction} = \frac{\text{Means Maltose in sample}}{\text{Means Maltose in negative control}} \times 100$$

In vitro dipeptidyl peptidase IV (DPPIV) inhibition study

The *A. occidentale* L. extracts were examined for inhibition bioactivities on DPPIV using the Promega DPPIV-Glo Protease Assay kit with a white 96-well plate. Before the inhibition test was performed, each sample was allowed to pass through a 0.45 μm PTFE filter (Millipore). The purified porcine DPPIV enzyme (88% homology to the human enzyme) from Sigma-Aldrich was used to determine the activity of DPPIV inhibitor. DPPIV enzyme activity was defined as 1 Unit produces 1 μmol free pNA/min, using standard DPPIV assay condition at 37 $^{\circ}\text{C}$. The DPPIV inhibitor activities were observed using a luminometer (Luminoskan Ascent 2.6) to detect luminescence on the white 96-well plate. IC_{50} values ($\mu\text{g/mL}$) were calculated from the quadratic formula generated from the log (concentration) and percentage inhibition. The protocols of analysis were based on the manufacturer specifications from Promega [25]. Kaempferol was used as a positive control.

Statistical analysis

Results were expressed as means \pm SEM. The analysis was analyzed using SPSS statistical software (SPSS version 20; SPSS Inc., Chicago, IL). T-test analysis was used to compare the means between young and mature leaves. One-way analysis of variance (ANOVA) and Tukey's Honestly Significant Difference test was used to compare means between fractions. The level of significance was set at $p < 0.05$, which corresponds to a 95% confidence level.

RESULTS AND DISCUSSION

High-Performance Liquid Chromatography (HPLC) Analysis

The presence of phenolic acid and flavonoids in *A. occidentale* L. leaf extracts were first determined by HPLC using external standards. In this analysis, it was found that all extracts contained phenolic acid and flavonoids. Free phenolic fraction had a higher

concentration of phenolic acid but a lower concentration of flavonoids compared to soluble ester and insoluble-bound phenolic fractions. Mature leaves of *A. occidentale* L. contained higher concentration in both phenolic acid and flavonoids than the young leaves. This trend was in line with a previous study where the presence of phenolic compounds varies in different parts of leaves. The variation of phenolic compounds concentration has also been reported at different stages of maturity of plants [26].

An *in vitro* Study of α -Amylase and DPPIV Inhibitory by Maturity

Phenolic compounds in three different fractions between the young and mature leaves of *A. occidentale* L. were further analyzed for their α -amylase inhibitory effect (Table 1). Free phenolic fraction ($72.45 \pm 3.6\%$) in the mature leaves demonstrated a higher inhibition percentage of α -amylase activities than that in the young leaves ($p < 0.05$). Similarly, soluble ester phenolic fraction ($83.40 \pm 4.7\%$) in the mature leaves also exhibited a greater α -amylase inhibitor as compared to the young leaves ($p < 0.001$). However, the α -amylase inhibitory effect of the insoluble-bound phenolic fraction was not significantly different between the matured and young leaves.

Table 2 shows the concentration of phenolic compounds fractions from the young and mature leaves of *A. occidentale* L. in the inhibition of DPPIV (IC_{50}). IC_{50} is defined as the concentration of an inhibitor (extracts of *A. occidentale* L. leaves) where the DPPIV enzyme activity is reduced by half (50%). A lower concentration indicates a more potent inhibitor. Regardless of fractions, the mature leaves were generally more effective in reducing the activity of DPPIV than the young leaves. Specifically, soluble ester ($4.09 \pm 0.34 \mu\text{g/mL}$) and insoluble-bound ($4.87 \pm 0.32 \mu\text{g/mL}$) phenolic fractions of the mature leaves were found to be significantly more potent inhibitors of DPPIV activities than the young leaves ($p < 0.001$). Nevertheless, no statistical difference was found between the mature and young leaves for the DPPIV inhibition activity by a free phenolic fraction.

In summary, it is clear that the mature leaves of *A. occidentale* L. are more potent inhibitors of both α -amylase

Table 1. The inhibition percentage of α -amylase activities in the presence of compounds extracted (0.6 mg/mL) from *A. occidentale* L. Results are expressed in means \pm SEM

Fraction ^a	Young (%)	Mature (%)
Free	54.92 ± 2.3	72.45 ± 3.6^b
Soluble ester	16.34 ± 1.5	83.40 ± 4.7^c
Insoluble-bound	69.04 ± 2.8	69.65 ± 1.9

^aFraction of phenolic compounds extracted from *A. occidentale* L. was used in the α -amylase inhibition study; ^bYoung and mature leaves were compared by t-test, p -value < 0.05 ; ^cYoung and mature leaves were compared by t-test, p -value < 0.001

Table 2. DPPIV inhibition activity for free, soluble ester and insoluble-bound phenolic compounds are tabulated by concentration (IC_{50}) = $\mu\text{g/mL}$. Results are expressed in means \pm SEM

Fractions ^a	Young	Mature
Free	156.6 ± 27.5	53.46 ± 6.49
Soluble ester	8.29 ± 0.33	4.09 ± 0.34^b
Insoluble-bound	11.48 ± 0.48	4.87 ± 0.32^b

^aFractions of phenolic compounds extracted from *A. occidentale* L. were used in the DPPIV inhibition study; ^bYoung and mature leaves were compared by t-test, p -value < 0.001

and DPPIV enzyme activities than the young leaves. Of relevance, our previous study had found that the concentration of phenolic acid and flavonoids were higher in *A. occidentale* L. mature leaves than in the young leaves (unpublished data). Therefore, it is believed that the higher phenolic content may proportionately increase its antioxidant capacity toward inhibiting both enzyme activity [12].

An *in vitro* α -Amylase and DPPIV Inhibitory Activity Study by Fractions

Fig. 3 shows the comparison between the free, soluble ester and insoluble-bound phenolic fractions in inhibiting α -amylase activity in the young and mature leaves, respectively. In the young leaf extracts, the insoluble-bound phenolic fraction ($69.04 \pm 2.8\%$) demonstrated a significantly more potent inhibitor than free ($54.92 \pm 2.3\%$, $p < 0.05$) and soluble ester phenolic fractions ($16.34 \pm 1.5\%$, $p < 0.0001$). Likewise, free

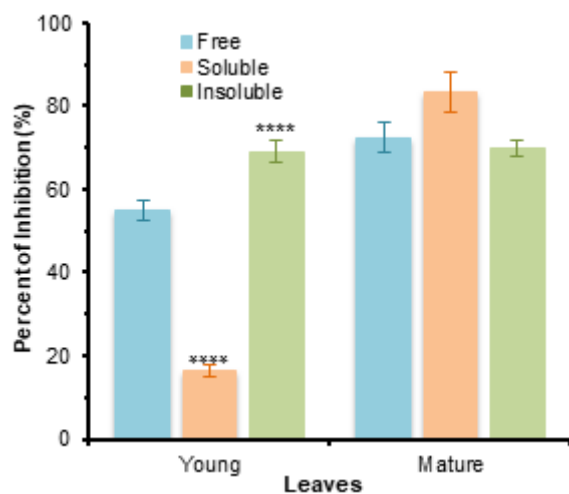


Fig 3. Comparison within phenolic fractions in inhibiting α -amylase activities using one-way ANOVA followed by Tukey's multiple comparison test analysis. Results are expressed in means \pm SEM. * $p < 0.05$ and **** $p < 0.0001$

phenolic had a greater capability in inhibiting α -amylase enzyme than soluble ester phenolic fraction ($p < 0.0001$). On the contrary, we found no significant differences in the α -amylase inhibitory effect between fractions of the mature leaves' extracts.

Fig. 4 indicates that in young leaf extracts, soluble ester (8.29 ± 0.33) and insoluble-bound (11.48 ± 0.48) phenolic fractions demonstrated a stronger inhibitor of DPPIV than free phenolic (156.6 ± 27.5 , $p < 0.001$). A similar trend for the mature leaves extracts was noted where soluble ester (4.09 ± 0.34) and insoluble-bound (4.87 ± 0.32) phenolic fractions also exhibited a lower IC_{50} than free phenolic (53.46 ± 6.49 , $p < 0.001$). No significant differences were found between the soluble ester and insoluble-bound phenolic fractions for both the young and mature leaves, respectively.

It appears that insoluble-bound fraction was the most potent inhibitor when compared to free and soluble ester phenolic fraction in both α -amylase and DPPIV inhibition activities. Although soluble ester phenolic fraction did not strongly inhibit the α -amylase activity, it was nevertheless effective in inhibiting DPPIV activity. We speculate that soluble ester and insoluble-bound phenolic fractions may contain a higher concentration of flavonoids than the free phenolic fraction. As indicated by a previous study, flavonoids were a strong inhibitor of α -amylase and DPPIV

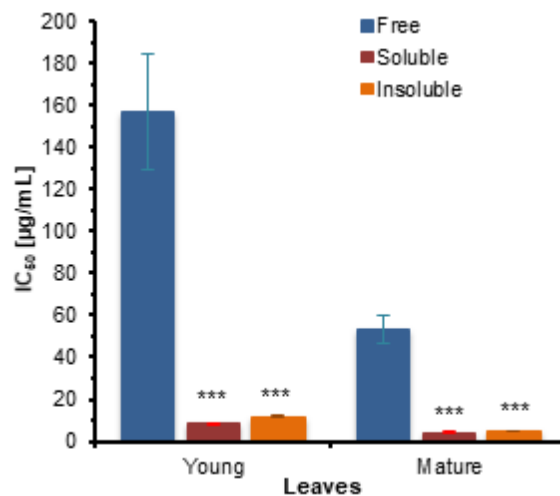


Fig 4. Comparison within phenolic fractions in DPPIV inhibition activities using one-way ANOVA followed by Tukey's multiple comparison test analysis. Results are expressed in means \pm SEM, *** $p < 0.001$

enzymes [27]. In another study, it was shown that the soluble ester and insoluble-bound phenolic extracts of *Moringa oleifera* seed flour were more effective with minimum inhibitory concentration against bacteria than free phenolic fractions [24].

CONCLUSION

Our findings indicated that the mature leaves of *A. occidentale* L. possessed better antidiabetic properties, as shown by a greater inhibition of both α -amylase and DPPIV enzymes when compared to young leaves. It was also observed that regardless of the maturity of the leaves, soluble ester and insoluble-bound phenolic fractions were a more potent inhibitor of α -amylase and DPPIV enzymes than free phenolic. Further studies of the elucidation and characterization methodologies are required in identifying specific phenolic compounds that are responsible for the inhibition of these enzymes.

ACKNOWLEDGMENTS

This work is part of a research project, RAGS15-058-0121, supported by the Ministry of Higher Education, Malaysia, and the International Islamic University Malaysia. The technical and editorial assistance for this manuscript was provided by Asst. Prof. Normah Haron, Ph.D., Department of Biotechnology,

Kulliyyah of Science, International Islamic University Malaysia.

■ REFERENCES

- [1] Ogurtsova, K., da Rocha Fernandes, J.D., Huang, Y., Linnenkamp, U., Guariguata, L., Cho, N.H., Cavan, D., Shaw, J.E., and Makaroff, L.E. 2017, IDF diabetes atlas: Global estimates for the prevalence of diabetes for 2015 and 2040, *Diabetes Res. Clin. Pract.*, 128, 40–50.
- [2] Institute for Public Health (IPH), 2015, *National Health and Morbidity Survey 2015. Vol. II: Non-Communicable Diseases, Risk Factors and Other Health Problems*, Ministry of Health Malaysia, Kuala Lumpur.
- [3] Institute for Public Health (IPH), 1997, *Report of the Second National Health and Morbidity Survey Conference*, Ministry of Health Malaysia, Kuala Lumpur.
- [4] World Health Organization, 2016, *Global Report on Diabetes*, World Health Organization, Geneva.
- [5] World Health Organization (WHO), 2002, *WHO Traditional Medicine Strategy 2002-2005*, World Health Organization, Geneva.
- [6] Esimone, C.O., Okonta, J.M., and Ezugwu, C.O., 2001, Blood sugar lowering the effect of *Anacardium occidentale* leaf extract in an experimental rabbit model, *J. Nat. Remedies*, 1 (1), 60–63.
- [7] Mustafa, F., Indurkar, J., Ali, N.I.M., Hanapi, A., Shah, M., Ismail, S., and Mansor, S.M., 2011, A review of Malaysian medicinal plants with potential antidiabetic activity, *J. Pharm. Res.*, 4 (11), 4217–4224.
- [8] Ojezele, M.O., and Agunbiade, S., 2013, Phytochemical constituents and medicinal properties of different extracts of *Anacardium occidentale* and *Psidium guajava*, *Asian J. Biomed. Pharm. Sci.*, 3 (16), 20–23.
- [9] Ali, M.S.M., Crozier, A., and Rahman, S.N.A., 2011, Polyphenols and antioxidant activities of selected traditional vegetables, *J. Trop. Agric. Food Sci.*, 39 (203), 69–83.
- [10] Jang, J.H., and Moon, K.D., 2011, Inhibition of polyphenol oxidase and peroxidase activities on fresh-cut apple by simultaneous treatment of ultrasound and ascorbic acid, *Food Chem.*, 124 (2), 444–449.
- [11] Nair, S.S., Kavrekar, V., and Mishra, A., 2013, *In vitro* studies on alpha amylase and alpha glucosidase inhibitory activities of selected plant extracts, *Eur. J. Exp. Biol.*, 3 (1), 128–132.
- [12] Ranilla, L.G., Kwon, Y.I., Apostolidis, E., and Shetty, K., 2010, Phenolic compounds, antioxidant activity and *in vitro* inhibitory potential against key enzymes relevant for hyperglycemia and hypertension of commonly used medicinal plants, herbs, and spices in Latin America, *Bioresour. Technol.*, 101 (12), 4676–4689.
- [13] Avila, J.A.D., García, J.R., Aguilar, G.A.G., and De la Rosa, L.A., 2017, The antidiabetic mechanisms of polyphenols related to increased glucagon-like peptide-1 (GLP1) and insulin signaling, *Molecules*, 22 (6), 903.
- [14] Barnett, A., 2006, DPP-4 inhibitors and their potential role in the management of type 2 diabetes, *Int. J. Clin. Pract.*, 60 (11), 1454–1470.
- [15] Nadkarni, P., Chepurny, O.G., and Holz, G.G., 2014, Regulation of Glucose Homeostasis by GLP-1, *Prog. Mol. Biol. Transl. Sci.*, 121, 23–65.
- [16] Ali, M.S.M., and Crozier, A., 2010, Analysis of phenolics in *Anacardium occidentale* shoot extracts using a reversed-phase high performance liquid chromatography tandem mass spectrometry (RP-HPLC-MS), *J. Trop. Agric. Food Sci.*, 38 (2), 221–230.
- [17] Jaiswal, Y., Naik, V., Tatke, P., Gabhe, S., and Vaidya, A. 2012, Pharmacognostic and preliminary phytochemical investigations of *Anacardium occidentale* (Linn.) leaves, *Int. J. Pharm. Pharm. Sci.*, 4 (3), 625–631.
- [18] Malviya, N., Jain, S., and Malviya, S., 2010, Antidiabetic potential of medicinal plants, *Acta Pol. Pharm.*, 67 (2), 113–118.
- [19] Nugroho, A.E., Malik, A., and Pramono, S., 2013, Total phenolic and flavonoid contents, and *in vitro* antihypertension activity of purified extract of Indonesian cashew leaves (*Anacardium occidentale* L.). *Int. Food Res. J.*, 20 (1), 299–305.

- [20] Kögel, I., and Zech, W., 1985, The phenolic acid content of cashew leaves (*Anacardium occidentale* L.) and of the associated humus layer, Senegal, *Geoderma*, 35 (2), 119–125.
- [21] Jähne, A., Fritzen, C., and Weissenböck, G., 1993, Chalcone synthase and flavonoid products in primary-leaf tissues of rye and maize, *Planta*, 189 (1), 39–46.
- [22] Krygier, K., Sosulski, F., and Hogge, L., 1982, Free, esterified, and insoluble-bound phenolic acids. 1. Extraction and purification procedure, *J. Agric. Food Chem.*, 30 (2), 330–334.
- [23] Dvořáková, M., Guido, L.F., Dostálek, P., Skulilová, Z., Moreira, M.M., and Barros, A.A., 2008, Antioxidant properties of free, soluble ester and insoluble-bound phenolic compounds in different barley varieties and corresponding malts, *J. Inst. Brew.*, 114 (1), 27–33.
- [24] Singh, R.S.G., Negi, P.S., and Radha, C., 2013, Phenolic composition, antioxidant and antimicrobial activities of free and bound phenolic extracts of *Moringa oleifera* seed flour, *J. Funct. Foods*, 5 (4), 1883–1891.
- [25] Promega, 2015, *DPPIV-GloTM Protease Assay, Technical Bulletin, TB339*, Promega Corporation, Madison, Wisconsin, USA.
- [26] Makkar, H.P.S., Dawra, R.K., and Singh, B., 1991, Tannins levels in leaves of some oak species at a different stage of maturity, *J. Sci. Food Agric.*, 54 (4), 513–519.
- [27] Fan, J., Johnson, M.H., Lila, M.A., Yousef, G., and de Mejia, E.G., 2013, Berry and citrus phenolic compounds inhibit dipeptidyl peptidase IV: Implications in diabetes management, *Evid.-Based Complementary Altern. Med.*, 2013, 479505.

Synthesis 1,1-Dibutoxybutane from Single Reagent of *n*-Butanol Using Cr/Activated Carbon Catalyst

Iip Izul Falah*, Mokhammad Fajar Pradipta, Alvan Luthfi Rinaldi, and Wega Trisunaryanti

Department of Chemistry, Faculty of Mathematics and Natural Sciences, Universitas Gadjah Mada, Sekip Utara BLS 21, Bulaksumur, Yogyakarta 55281, Indonesia

* **Corresponding author:**

email: iip_mipa@ugm.ac.id

Received: April 8, 2019

Accepted: May 16, 2019

DOI: 10.22146/ijc.44829

Abstract: Synthesis of 1,1-dibutoxybutane from the single reagent of *n*-butanol using Cr/Activated Carbon (Cr/AC) as a catalyst has been done. The aims of this research were to evaluate the effect of temperature, amount of catalyst, and alcohol flow rate towards the yield of 1,1-dibutoxybutane. Activated carbon (AC) was prepared by activating coconut shell carbon at 650 °C in the atmosphere of H₂ at a flow rate of 15 mL/min for 4 h. The product was washed using acetone in a Soxhlet for 15 rounds, washed 3 times by 1.0 M HCl, and finally, it was sieved at 60–80 mesh. Metal content was analyzed using atomic absorption spectrophotometry (AAS) for Na, Ca, and Fe. The AC was impregnated with Cr(VI) solution and reduced with H₂ at 650 °C. The acidity of Cr/AC catalyst was determined by the adsorption of ammonia vapor. Optimization of *n*-butanol conversion to 1,1-dibutoxybutane using Cr/AC catalyst was conducted in an oven using variations of temperature of 450, 500, and 550 °C, catalyst amount of 5, 10, and 15 g, under an alcohol flow rate of 0.10, 0.50, and 0.90 mL/min. The conversions of 1,1-dibutoxybutane were analyzed by GC-MS and ¹H-NMR. The results showed that after washing by acetone and 1.0 M HCl, the content of metals in the AC was significantly decreased. The AC and Cr/AC showed acidity of 2.49 and 8.27 mmol/g, respectively. The highest product of 1,1-dibutoxybutane (53.42%) was achieved at 450 °C using 5 g catalyst of Cr/AC under the alcohol flow rate of 0.10 mL/min.

Keywords: *n*-butanol; 1,1-dibutoxybutane; Cr/AC; catalyst

■ INTRODUCTION

The increase in the number of vehicles and industries causes the consumption of fuel oil has raised. This condition has caused the use of the fossil fuel to increase, and the world stock of this material is running low, and this condition will cause an energy crisis as it happened in 2008 [1].

In 2010, Europe consumed 12% energy from a renewable source, and 21% from electricity, wherein 2005, the consumption from renewable source had just reached 6.38% and 13.97% from electricity [2]. In Indonesia, the consumption of subsidizing petroleum oil in 2011 reached 41.79 × 10³ million Liter. To overcome the crisis due to the rare of the oil in the future, a lot of researchers have

studied the use of new materials of fatty animal [3-5] and vegetable oil [6-8], biomass, dissociated rubbish, roots, and fruits, as the source of bio-diesel and ethanol [9-10].

The cetane number is a measure of the quality of diesel fuel and can be increased by the addition of fuel additives. Primary alcohol and ether are known as a fuel additive, which has a burning temperature lower than diesel oil. These compounds can have a lower machine knock and lower unnecessary gas emission as carbon monoxide [11-14].

Fuel additives as a booster of ether compound could be produced from alcohol. In this case, Nord and Haupt [15] showed that the utilization of acetal such as 1,1-dietoxyethane as diesel fuel additive decreased

particulate matter emission and smoke, and lower burning temperature [16-18].

Acetal or diether could be produced from alcohol and aldehyde using an acid catalyst, as shown by Capelletti et al. [19] and Kaufhold and El-Chawawi [20]. It can be produced from a single reagent of ethanol using Cu/SiO₂ and H-Y-Zeolite as the catalyst [21] and from the conversion of butanol into dibutyl ether [22]. In addition, alcohol with C atoms more than 4 is non-hygroscopic and noncorrosive; hence, it was proposed to replace ethanol with *n*-butanol [23-25]. Research work of Falah and Triyono [26] reported that when the contact time between catalyst and feed is longer, and the temperature is higher, the diether compound as a product could be used as booster diesel oil. The catalytic reaction using Cu on activated carbon (AC) or the other metals for the conversion of alcohol to the diether is cheap because this reaction occurs in the gas phase; hence, it will not easily deactivate the catalyst.

The reaction between alcohols using a Cr/AC catalyst at high temperature (400–550 °C) is rarely discussed. The utilization of Cr/AC catalysts could convert the alcohol into H₂ and aldehyde, or react with another alcohol to produce ether and H₂O. Based on the above consideration, we undertook the evaluation of conversion of alcohol (*n*-butanol) to diether (1,1-dibutoxybutane) using the Cr/AC catalyst under variation of temperatures (450–550 °C) and a new route of 1,1-dibutoxybutane formation as a better fuel additive will be discussed.

■ EXPERIMENTAL SECTION

Materials

The chemical used in the experiment were purchased from Merck in p.a. quality. i.e., *n*-butanol, AgNO₃, HNO₃ 65%, HCl 37%, H₂O₂ 20%, CrO₃, NaCl, Ca(OH)₂, FeCl₃·6H₂O, acetone, and ammonia. Coconut shell, glass-wool, pH paper, aquabidest were also needed. H₂ and N₂ gases were from Surya Indotim Imex with a purity of 99.999%, while CO₂ was from Samator with a purity of 99.999%.

Instrumentation

The catalyst was prepared using 40–60 and 60–80 mesh sievers, Soxhlet extractor, electric oven, and Mettler electric balance (model AT200). The metals were determined using atomic absorption spectrophotometer (AAS Perkin Elmer Model 3110). Products of Hydrogenation were characterized by FTIR (Shimadzu Prestige 21), GC-MS (Shimadzu QP2010S) using HP-5MSUI column, GC148 (Shimadzu) using CBP1 column and FID detector, ¹H-NMR (JEOL JNM ECZ-500R).

Procedure

Synthesis of activated carbon and metal content analysis

The coconut shell was ground and sieved using 40–60 mesh siever. Then, it was activated at 650 °C for 4 h, while CO₂ gas flowed at 20 mL/min. The carbon was then put in a Soxhlet and extracted using acetone for 15 rounds, followed by drying in an open-air. Then it dipped 3 times in 1.0 M HCl solution for each 24 h. Finally, the carbon was sieved again using 60–80 siever.

Further, 0.20 g of the activated carbon was destructed in 100 mL round bottle by adding 10.0 mL of HNO₃ 65% and then refluxed for 1 h at 130 °C. As much as 1.0 mL of this solution was inserted into 50 mL volumetric flask, and 4 mL of 20% H₂O₂ was added. Finally, the solution was diluted until 50 mL. This solution was used for analyses of Na, Ca, and Fe using FES and AAS. This procedure was also used for the carbon after washing with 0.1 M HCl 1, 2, and 3 times.

Preparation of Cr/AC catalyst

Four grams of CrO₃ was put into 500 mL beaker glass, and 50 mL aquabidest was added. After all, CrO₃ was dissolved, 100 g of activated carbon was added. After 24 h, while it was stirred, the mixture was heated at 90 °C until all water evaporated, and then the temperature was increased to 110 °C for 3 h (until the mass was constant). Further, the obtained solid was reduced at 650 °C for 4 h by flowing H₂ at 15 mL/min. Before and after impregnated with Cr, the carbon was analyzed using FTIR.

Determination of catalyst acidity

Empty crucible porcelain was heated at 110 °C for 1 h, and then it was used as samples holder of (0.2 g) dry sample of activated carbon or (0.30 g) of the Cr/AC catalyst. The porcelain was placed in a desiccator, and then 20 mL ammonia was inserted. After 24 h, the ammonia was evaporated for 30 min. The acidity of the activated carbon (or the catalyst) was calculated as follow:

$$\text{Acidity} = \frac{W_3 - W_2}{(W_2 - W_1)M} \times 1000 \frac{\text{mmol}}{\text{g}}$$

where M is the molecular weight of ammonia (17.03 g/mol), W_1 and W_2 are the weight of empty crucibles, and crucible contains activated carbon (or the catalyst). W_3 is the weight of crucible after adsorbed ammonia.

Conversion of n-butanol to 1,1-dibutoxybutane

Five grams of Cr/AC catalyst was inserted into a reactor, where the lower part of this reactor was already closed by glass-wool, and then this reactor was inserted into an electric tube furnace. The upper part of this reactor was connected with Liebig cooler, and the lower part was connected with three necks bottles. The other necks bottle was used to insert a sample of n-butanol at a flow rate of 0.10 mL/min and insert H_2 gas at a flow rate of 15 mL/min, and this bottle was heated at 130 °C. The temperature of the electric furnace was varied at 450, 500, and 550 °C; the flow rate of n-butanol was varied at 0.10, 0.50, and 0.90 mL/min, while the amount of the catalyst was varied at 5, 10, and 15 g. The products were analyzed using GC-MS, FTIR, and 1H -NMR.

RESULTS AND DISCUSSION

Activated carbon from coconut shell is an excellent material for catalyst support because it has an abundance of micro-pore, low ash content, and low reactivity. The carbon is inert and stable in acid or base condition, and it

can be prepared in particle form; hence, this material is very good to be used as a support of a catalyst.

Determination of Na, Ca and Fe on the Carbon

As support of catalyst, activated carbon has to have a large surface area. This condition could be reached using a small particle, but it must not cause a gas flow to stop while it is used in the reaction system. Hence, the carbon particle used in this work was 60–80 mesh.

Table 1 showed the metal content in carbon after washing with acetone and HCl solution. It is shown that around 50% of metals could be washed out in this work, whereas metals ion was replaced by hydrogen ion, which then disappeared when heated. Hence, the content of the metals decreased in this work.

The Acidity of AC and Cr/AC Catalyst

From 3 experiments, it was known that the AC and Cr/AC catalyst acidity were 2.49 and 8.27 mmol/g, respectively. This data showed that the impregnation of Cr metal onto the AC significantly increased the acidity of AC.

Catalytic Conversion of 1,1-Dibutoxybutane from n-Butanol

Table 2 and Fig 1-4 showed the result of analyses using GC-MS, where the compound at a retention time (R_t) 16.29 min was predicted as 1,1-dibutoxybutane, at R_t of 2.98 min was n-butanol, and at R_t of 3.60 min was n-butanol. Table 2 also showed that the highest product of 1,1-dibutoxybutane was 53.42%. This product resulted at a temperature of 450 °C, the mass of catalyst 5 g, and the flow rate of n-butanol 0.10 mL/min, with the rest of n-butanol 25.46% and a total of other product was 16.60%.

In analyzing the conversion of n-butanol to 1,1-dibutoxybutane, the FTIR spectra of the reagent and

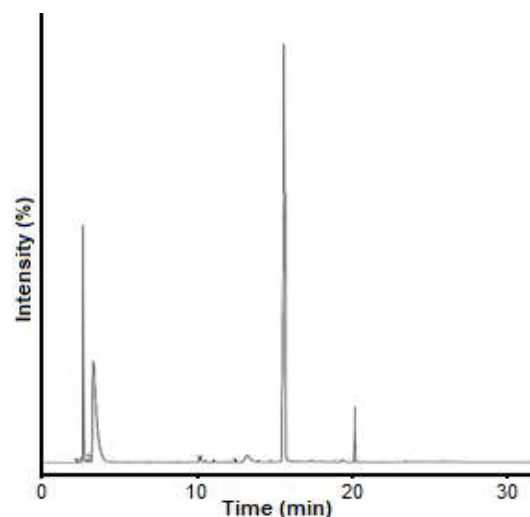
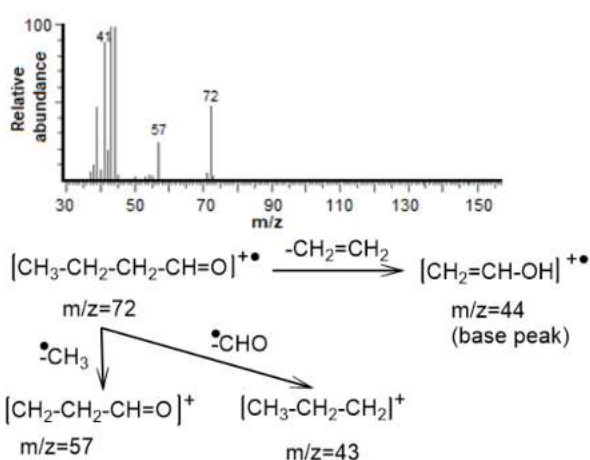
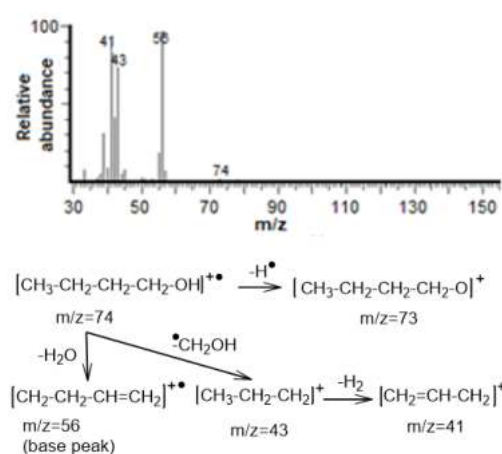
Table 1. Metals content in the activated carbon after washing

Liquid washing	Metal content in the carbon (ppm)		
	Na	Ca	Fe
Acetone	1.846	3.980	2.396
0.10 M HCl (the first)	1.022	3.205	1.316
0.10 M HCl (the second)	0.802	2.827	1.146
0.10 M HCl (the third)	0.692	2.569	1.052

Table 2. Result of conversion of *n*-butanol to 1,1-dibutoxybutane

Temperature (°C)	Weight of catalyst (g)	Flow rate of <i>n</i> -butanol (mL/min)	Product (% area GC)		
			<i>n</i> -butanol	1,1-dibutoxybutane	Other
450	5	0.10	25.46	53.42	16.60
450	10	0.50	79.43	9.21	1.08
450	15	0.90	92.74	6.43	0.81
500	5	0.10	95.61	0.39	3.81
500	10	0.50	33.40	47.74	13.58
500	15	0.90	62.45	33.32	3.27
550	5	0.10	58.45	29.55	10.45
550	10	0.50	89.31	2.03	8.39
550	15	0.90	78.75	9.46	11.35

product are showed in Fig. 5(a) and 5(b). Spectra of *n*-butanol (Fig. 5(a)) showed absorption with strong intensity at 3348 cm^{-1} due to the existence of $-\text{OH}$ group. This peak was significantly reduced in the product (Fig. 5(b)) because OH group has been converted into C–O–C of diether and C=O of aldehyde (butanal). The high peaks at 2932 and 2832 cm^{-1} were consistent due to these peaks related to the bond of C–H, which were not converted to the other bond. From Fig. 5(b), could be seen a strong peak at 1720 cm^{-1} whereas in Fig. 5(a), this peak did not appear. This peak is related to the formation of C=O bond of butanal as a side product. Another fact is that fingerprint at 1057 cm^{-1} from C–O alcohol changed to a broad peak at $1000\text{--}1150\text{ cm}^{-1}$ of C–O ether. These facts showed that most alcohols had been converted into 1,1-dibutoxybutane, and a small part has changed into an aldehyde.

**Fig 1.** Chromatogram of *n*-butanol conversion product at $450\text{ }^{\circ}\text{C}$, using 5 g catalyst of Cr/AC, a flow rate of the alcohol 0.10 mL/min and flow rate of H_2 15 mL/min**Fig 2.** Mass spectra and fragmentation of the first peak at R_t of 2.98 min**Fig 3.** Mass spectra and fragmentation of the second peak at R_t of 3.60 min

of OH and CH₂-O, respectively.

■ CONCLUSION

Preparation of activated carbon by washing with acetone and 1.0 M HCl consecutively, could significantly decrease the ions of Na, Ca, and Fe in the activated carbon. Impregnation of activated carbon with Cr metal could increase its acidity from 2.49 to 8.27 mmol/g. The GC-MS and ¹H-NMR analysis showed that dehydration of *n*-butanol at 450 °C using 5.0 g catalysts of Cr/AC and 0.10 mL/min of the alcohol could produce 1,1-dibutoxybutane in 53.42%.

■ ACKNOWLEDGMENTS

The authors thank the Indonesian Directorate General of Higher Education, who already supported this research under the contract no. 1969/UN1/DITLIT/DIT-LIT/LT/2018.

■ REFERENCES

- [1] Bencivenga, C., D'Ecclesia, R.L., and Triulzi, U., 2012, Oil prices and the financial crisis, *Rev. Manag. Sci.*, 6, 227–238.
- [2] Houdková, L., Boráň, J., Pěček, J., and Šumpela P., 2008, Biogas: A renewable source of energy, *Therm. Sci.*, 12 (4), 27–33.
- [3] Bhatti, H.N., Hanif, M.A., Qasim, M., and Rehman, A., 2008, Biodiesel production from waste tallow, *Fuel*, 87 (13-14), 2961–2966.
- [4] Nebel, B.A., and Mittelbach, M., 2006, Biodiesel from extracted fat out of meat and bone meal, *Eur. J. Lipid Sci. Technol.*, 108 (5), 398–403.
- [5] Lebedevas, S., Vaicekauskas, A., Lebedeva, G., Makareviciene, V., Janulis, P., and Kazancev, K., 2006, Use of waste fats of animal and vegetable origin for the production of biodiesel fuel: Quality, motor properties, and emissions of harmful components, *Energy Fuel*, 20 (5), 2274–2280.
- [6] Akoh, C.C., Chang, S.W., Lee, G.C., and Shaw, J.F., 2007, Enzymatic approach to biodiesel production, *J. Agric. Food Chem.*, 55 (22), 8995–9005.
- [7] Ooi, Y.S., Zakaria, R., Mohamed, A.R., and Bhatia, S., 2005, Catalytic conversion of fatty acid mixture to liquid fuels over mesoporous material, *React. Kinet. Catal. Lett.*, 84 (2), 295–302.
- [8] Twaiq, F.A., Zabidi, N.A.M., Mohamed, A.R., and Bhatia, S., 2003, Catalytic conversion of palm oil over mesoporous aluminosilicate MCM 41 for the production of liquid hydrocarbon fuels, *Fuel Process. Technol.*, 84 (1-3), 105–120.
- [9] Gopal, S., and Smirniotis, P.G., 2002, Deactivation behavior of bifunctional Pt/H-zeolite catalysts during cyclopentane hydroconversion, *J. Catal.*, 205 (2), 231–243.
- [10] Ma, D., Wang, D., Su, L., Shu, Y., Xu, Y., and Bao, X., 2002, Carbonaceous deposition on Mo/HMCM-22 catalysts for methane aromatization: A TP technique investigation, *J. Catal.*, 208, 260–269.
- [11] Ali, O.M., Abdullah, N.R., Mamat, R., and Abdullah, A.A., 2015, Comparison of the effect of different alcohol additives with blended fuel on cyclic variation in diesel engine, *Energy Procedia*, 75, 2357–2362.
- [12] Topgül, T., 2015, The effect of MTBE blends on engine performance and exhaust. Emission in a spark ignition engine, *Fuel Process. Technol.*, 138, 480–489.
- [13] Xing-Cai, L., Jian-Guang, Y., Wu-Gao, Z., and Zhen, H., 2014, Effect of cetane number improver on heat release rate and emissions of high speed diesel engine fueled with ethanol-diesel blend fuel, *Fuel*, 83 (14-15), 2013–2020.
- [14] Geng, P., Cao, E., Tan, Q., and Wei, L., 2017, Effects of alternative fuels on the combustion characteristics and emission products from diesel engines: A review, *Renewable Sustainable Energy Rev.*, 71, 523–534.
- [15] Nord, K.E., and Haupt, D., 2005, Reducing the emission of particles from a diesel engine by adding an oxygenate to the fuel, *Environ. Sci. Technol.*, 39 (16), 6260–6265.
- [16] Agirre, L., Güemez, M.B., Ugarte, A., Requies, J., Barrio, V.L., Cambra, J.F., and Arias, P.L., 2013, Glycerol acetals as diesel additives: Kinetic study of the reaction between glycerol and acetaldehyde, *Fuel Process. Technol.*, 116, 182–188.

- [17] Rahaman, M., Graça, N.S., Pereira, C.S.M., and Rodrigues, A.E., 2015, Thermodynamic and kinetic studies for synthesis of the acetal (1,1-diethoxybutane) catalyzed by Amberlyst 47 ion-exchange resin, *Chem. Eng. J.*, 264, 257–267.
- [18] Bueno, A.C., Goç Alves, J.A., and Gusevskaya, E.V., 2007, Palladium-catalyzed oxidation of primary alcohol: Highly selective direct synthesis of acetals, *Appl. Catal., A*, 329, 1–6.
- [19] Capeletti, M.R., Balzano, L., de la Puente, G., Laborde, M., and Sedran, U., 2000, Synthesis of acetal (1,1-diethoxyethane) from ethanol and acetaldehyde over acidic catalysts, *Appl. Catal., A*, 198 (1-2), L1–L4.
- [20] Kaufhold, M., and El-Chawawi, M., 1996, Process for preparing acetaldehyde diethyl acetal, *U.S. Patent*, US5527969A.
- [21] He, X., and Liu, H., 2014, Efficient synthesis of 1,1-diethoxyethane via sequential ethanol reaction on silica-supported copper and H-Y zeolite catalyst, *Catal. Today*, 233, 133–139.
- [22] Pérez, M.A., Bringué, R., Iborra, M., Tejero, J., and Cunnil, F., 2014, Ion exchange resins as catalysts for the liquid-phase dehydration of 1-butanol to di-n-butyl ether, *Appl. Catal., A*, 482, 38–48.
- [23] Siwale, L., Kristóf, L., Adam, T., Bereczky, A., Mbarawa, M., Penninger, A., and Kolesnikov, A., 2013, Combustion and emission characteristics of n-butanol/diesel fuel blend in a turbo-charged compression ignition engine, *Fuel*, 107, 409–418.
- [24] Zhang, Z.H., and Balasubramanian, R., 2016, Investigation of particulate emission characteristics of a diesel engine fueled with higher alcohols/biodiesel blends, *Appl. Energy*, 163, 71–80.
- [25] Zaharin, M.S.M., Abdullah, N.R., Najafi, G., Sharudin, H., and Yusaf, T., 2017, Effects of physicochemical properties of biodiesel fuel blends with alcohol on diesel engine performance and exhaust emissions: A review, *Renewable Sustainable Energy Rev.*, 79, 475–493.
- [26] Falah, I.I., and Triyono, 2010, Conversion of n-pentanol and n-butanol over Cu/AC catalyst, *J. Chem. Chem. Eng.*, 4 (6), 22–28.

Chemical Investigation and Antimicrobial Activity of Medicinal Plant *Toddalia asiatica* Lam

Wilmar Maarisit^{1,*} and Misran Lawani²

¹Department of Pharmacy, Faculty of Mathematics and Natural Sciences, Christian University of Indonesia Tomohon, Jl. Raya Talete II Kuranga Tomohon, P.O. Box 112, Tomohon 95441, South Sulawesi, Indonesia

²Department of Agricultural Product Technology, Faculty of Agriculture, Khairun University, Jl. Raya Kampus Unkhair Gambesi Ternate, Ternate 97719, North Maluku, Indonesia

* **Corresponding author:**

tel: +62-85242613749

email: wmaarisit@yahoo.com

Received: June 15, 2019

Accepted: February 20, 2020

DOI: 10.22146/ijc.46643

Abstract: Medicinal plants have become important sources of natural products, which have been used in the development of therapeutic agents. Four new coumarins (**1-4**) have been isolated together with five known metabolites (**5-9**) from the medicinal plant *T. asiatica*. The structures of **1-9** were assigned based on their spectroscopic data. Compounds (**1-9**) inhibited the growth of the Gram-negative bacteria *E. coli* and Gram-positive bacteria *S. aureus* at a concentration of 25 and 50 µg/disc. Compounds (**2-4**) inhibited the phytopathogenic fungus *C. cucurbitarum* at 50 µg/disc.

Keywords: natural products; *Toddalia asiatica*; antimicrobial activity; NMR

■ INTRODUCTION

Toddalia asiatica Lam is a well-recognized medicinal plant in India, China, East Africa, Europe, and Okinawa [1-4]. Three main parts of this plant; fruits, roots, and leaves have been used to cure the same diseases like malaria, coughs, influenza, lung disease, rheumatism, bronchial pains, stomachache, snake bites [1,5]. From the fact above, it is noted that many people already have traditional medical treatments using *T. asiatica*.

Previous phytochemical studies reported the isolation from *T. asiatica* that contain the following compounds like coumarins, few polyphenolic, triterpenoids, flavonoids, lignans, and alkaloids [6-10]. Crude extracts and isolated compounds from this plant are reported to have pharmacological activities such as antioxidant, cytotoxic [11-14], anti-leukemic [15], antiparasitic [16-17] antidiabetic [18], analgesic [19], phosphodiesterase-4 (PDE 4) inhibitory [20], and antibacterial activities [21-22].

During our screening for new bioactive metabolites from terrestrial and marine natural resources [23-25], we found that the acetone extract of the stems of *T. asiatica* collected in Okinawa, Japan inhibited the growth of microorganisms. The aim of this study was to investigate

chemical constituents of the traditional medicinal plant *T. asiatica* from Okinawan Island.

This part describes the isolation, structure elucidation, and bioactivities of the four new coumarins class **1-4** together with five known compounds, toddalo lactone (**5**), toddaculin (**6**), toddanol (**7**), dihydrochelerythrine (**8**), and 6-Acetyldihydrochelerythrine (**9**) from the medicinal plant *T. asiatica* [4,6,15,26].

■ EXPERIMENTAL SECTION

Materials

The materials used were the stems of *T. asiatica* (collected from Okinawa Island Japan), and Merck silica gel 60 (particle size 0.063–0.200 mm, 70–230 mesh, 250 µm). Analytical TLC was performed using Kieselgel 60 F254 DC-fertigplatten (Merck). Microbial strains used were *E. coli*, *S. aureus*, *A. niger*, *Cladosporium* sp., and *C. cucurbitarum* (supplied by Natural Product Laboratory, Faculty of Science, University of the Ryukyus).

Instrumentation

The ¹H (500 MHz) and ¹³C (125 MHz) NMR spectra were measured on a JEOL α-500 spectrometer, HPLC was performed on a HITACHI L-6000 pump

equipped with a water RI detector (R401), using Nacalai tesque COSMOSIL packed column (5C18, 10 × 250 mm and 55 L, 10 × 250 mm), Merck Hibar pre-packed column (RT 250-10 RP-18, 7 μm). Chemical shifts were referenced to residual solvent signals (CDCl₃; δ_H 7.26, δ_C 77.0).

Procedure

Collection, extraction, and isolation

The stems of *T. asiatica* were collected from Mibaru, Okinawa Island, in July 2008. The specimen was deposited at the University of the Ryukyus. The stems of *T. asiatica* (10 kg) was soaked in acetone and methanol three times at room temperature and filtered. The acetone and methanol extracts were combined and partitioned between water and ethyl acetate to yield a brown organic fraction.

The ethyl acetate extract (159 g) was suspended in methanol and water (1:1) and then successively extracted with hexane, chloroform, and 1-BuOH. The hexane extract showed strong inhibition against bacteria *E. coli* and *S. aureus* at 100 μg/disc. Hexane extract (36 g) was washed with hexane then purified by PTLC to give compound **5** (13 mg/0.0001% dry weight), **1** (2 mg/0.00002% dry weight), and **2** (2.0 mg/0.00002% dry weight).

The hexane fraction (26 g) was subjected to column chromatography on silica gel using hexane-EtOAc-MeOH solvent system to give 15 fractions. Fraction 12 (850 mg) was washed with hexane then purified by recrystallization to give compound **9** (2 mg/0.00013% dry weight). Fraction 3 was subjected to further purification by PTLC using EtOAc: hexane (1:2) to afford compound **6** (2 mg/0.00002% dry weight). Compounds **8** (2 mg/0.00002% dry weight), **9** (1.7 mg/0.000017% dry weight) and **2** (1.5 mg/0.00015% dry weight) were isolated from fraction 12-3-2 (50 mg) by HPLC using EtOAc:hexane (1:2). Fraction 14 (133.8 mg) was subjected to open column chromatography on silica gel using hexane-EtOAc-MeOH solvent system to give 10 fractions. Fraction 14-2 (18 mg) yielded compound **3** (2.2 mg/0.00022% dry weight) by HPLC on S_i-60 using EtOAc:hexane (1:2). Finally, compounds **7** (2.2 mg/0.000022% dry weight) and **4** (2.2 mg/0.000022%) were isolated from fraction 14-5 (90 mg) by HPLC using EtOAc:hexane (1:2).

Microbial test cultures and growth conditions

Gram-negative bacteria *E. coli* and Gram-positive bacteria *S. aureus* were used for antibacterial tests and fungi *A. niger*, *Cladosporium* sp., and *C. cucurbitarum* were used for antifungal tests. Bacterial strains were maintained on bacteria medium agar (meat extract 0.05 g, peptone 0.1 g, NaCl 0.05 g, and agar 3 g in 100 mL dH₂O) petri dishes at 4 °C, while fungi were maintained on fungi medium agar (malt extract 1.48 g, glucose 1.4 g, peptone 0.08 g, and agar 3 g in 100 mL dH₂O). Antimicrobial in-vitro assays were done using the disc diffusion method. The fresh cultures were obtained by growing the test strains overnight at 37 °C for bacteria, while fungi were grown at 28 °C for 48 h.

Antimicrobial activity assay

The crude extracts and pure compounds were tested for antimicrobial activity against bacteria; *E. coli*, *S. aureus*, and phytopathogenic fungi; *A. niger*, *C. cucurbitarum*, and *Cladosporium* sp. Single colonies of the microorganisms used in the bioassay were sub-cultured in 5 mL of bacteria and fungus liquid medium and incubated for 24 h. Aliquots of the test solution were applied to sterile paper discs (8 mm diameter) using a final disc loading concentration of 25, 50, and 100 μg/disc for the crude extracts and 25 and 50 μg/disc for the pure compounds. The plates were incubated at 37 °C for 24 h, and antimicrobial activities were determined by measuring the diameter of the inhibitory zones in millimeters.

RESULTS AND DISCUSSION

The stems of *T. asiatica* were collected from Mibaru, Okinawa Island, in July 2008. The sample (10 kg wet weight) was extracted with methanol and acetone. The combined extracts were partitioned between water and EtOAc. The EtOAc extract was suspended in MeOH and water (1:1) and then successively extracted with hexane, chloroform, and 1-BuOH. Separation of the hexane extract by a series of chromatographic processes, including silica gel CC, PTLC, and HPLC, led to the isolation of four new compounds **1-4** together with five known compounds **5-9**.

Compound **1** was isolated as a yellow crystalline solid, and the molecular formula $C_{16}H_{20}O_6$ was elucidated on the basis of NMR spectral data (Table 1 and 2). NMR spectra were similar to those of the known aculeatin [4]. 1H and ^{13}C -NMR spectra of compound **1** showed 16 carbon resonances including signals for two methoxy groups [δ_H 2.92 (3H, s), δ_C 56.0 (CH₃); δ_H 3.83 (3H, s), δ_C 63.1 (CH₃)], two methyls [δ_H 1.23 (3H, s), δ_C 18.9 (CH₃); δ_H 1.38 (3H, s), δ_C 23.5 (CH₃)], one epoxide δ_H 2.92 (H, s), δ_C 56.0 (CH), δ_C 63.6], one sp^3 methylene [δ_H 2.84 (2H, dd, $J = 5.8, 9.7$ Hz), δ_C 24.7 (CH₂)], three sp^2 methines [δ_H 6.22 (1H, d, $J = 9.5$ Hz), δ_C 112.4 (CH); δ_H 7.85 (1H, d, $J = 9.5$ Hz), δ_C 138.9 (CH); [δ_H 6.61 (1H, s), δ_C 95.4 (CH)], six quaternary carbons [δ_C 107.2 (C), 161.1 (C), 156.0 (C), 116.7 (C), 155.1 (C), 161.7 (C)]. The 1H and ^{13}C -NMR correlations were demonstrated by the HMQC. The

extensive 1D and 2D NMR analysis (Fig. 2) coupled with a comparison of spectral data with those of aculeatin allowed us to define the structure of **1**. Compounds **1** and **5** were positional isomers for a methoxyl group.

Compound **2** was isolated as a yellow crystalline solid, and the molecular formula $C_{16}H_{18}O_4$ was elucidated based on NMR spectral data (Table 1 and 2). 1H and ^{13}C -NMR spectra of **2** were similar to those toddaculin (**6**). 1H and ^{13}C -NMR spectra of compound **2** showed the presence of two methoxy groups [δ_H 3.83 (3H, s), δ_C 63.1 (CH₃); δ_H 2.92 (3H, s), δ_C 56.0 (CH₃)], two methyl [δ_H 1.68 (3H, s), δ_C 17.8 (CH₃); δ_H 1.74 (3H, s), δ_C 22.8 (CH₃)], one sp^3 methylenes [δ_H 3.31 (2H, d, $J = 6.8$ Hz), δ_C 25.7 (CH₂)], four sp^2 methines [δ_H 6.18 (1H, d, $J = 9.5$ Hz), δ_C 112.2 (CH); δ_H 7.82 (1H, d, $J = 9.7$ Hz), δ_C 139.0 (CH); δ_H 6.58 (1H, s), δ_C 95.3 (CH); δ_H 5.10 (1H, m),

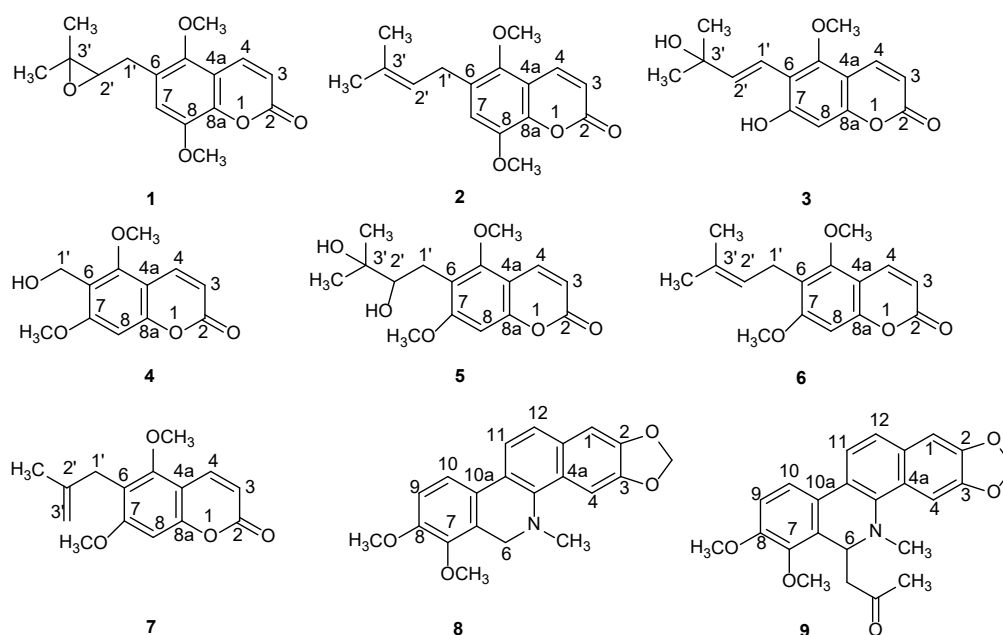


Fig 1. Structures of compounds **1-9** isolated from medicinal plant *T. asiatica*

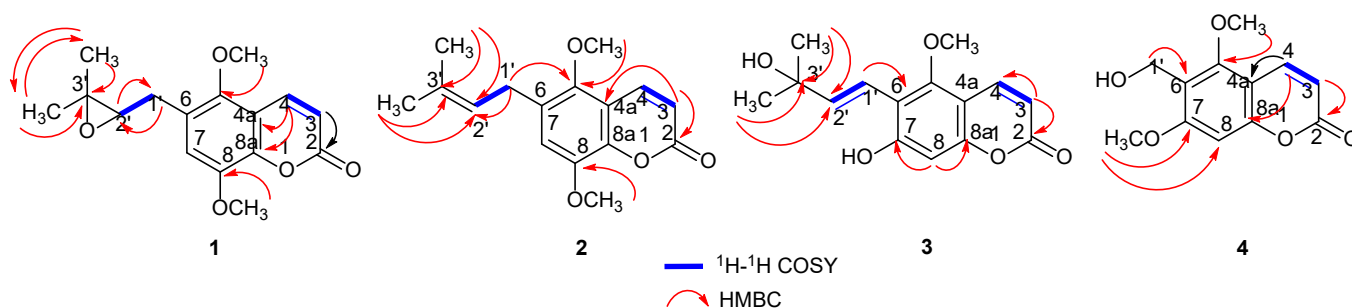


Fig 2. 1H - 1H COSY and key HMBC correlations for **1-4**

Table 1. ^{13}C -NMR data for compounds **1-4**

Position	δ_{C} (mult.) ^a			
	1	2	3	4
1				
2	161.7 (s)	161.6 (s)	163.0 (s)	160.9 (s)
3	112.4 (d)	112.2 (d)	113.2 (d)	112.2 (d)
4	138.9 (d)	139.0 (d)	130.8 (d)	138.8 (d)
4a	107.2 (s)	107.1 (s)	111.4 (s)	104.2 (s)
5	161.1 (s)	161.2 (s)	161.2 (s)	156.1 (s)
6	156.0 (s)	155.2 (s)	145.8 (s)	148.7 (s)
7	95.4 (d)	95.3 (d)	143.7 (s)	138.8 (s)
8	116.7 (s)	120.2 (s)	108.5 (d)	91.3 (d)
8a	155.1 (s)	155.1 (s)	143.7 (s)	152.3 (s)
5-OCH ₃	63.1 (q)	63.1 (q)	56.5 (q)	56.5 (q)
8-OCH ₃	56.0 (q)	56.0 (q)		56.5 (q)
1'	24.7 (t)	25.7 (t)	115.2 (d)	61.6 (t)
2'	56.0 (d)	122.1 (d)	130.8 (d)	
3'	63.6 (s)	132.0 (s)	78.0 (s)	
CH ₃	18.9 (q)	17.8 (q)	28.0 (q)	
CH ₃	23.5 (q)	22.6 (q)	28.0 (q)	

^a Data recorded at 125 MHz**Table 2.** ^1H -NMR data for compounds **1-4**

Position	δ_{H} (mult., J/Hz) ^a			
	1	2	3	4
1				
2				
3	6.22 (d, 9.5)	6.18 (d, 9.7)	6.23 (d, 9.5)	6.13 (d, 9.7)
4	7.85 (d, 9.5)	7.82(d, 9.7)	7.55 (d, 9.5)	7.97 (d, 9.7)
4a				
5				
6				
7	6.61 (s)	6.58 (s)		
8			6.75 (s)	6.32 (s)
8a				
5-OCH ₃	3.83 (s)	3.83 (s)	3.87 (s)	3.87 (s)
8-OCH ₃	2.92 (s)	2.92 (s)		3.85 (s)
1'	2.84 (dd, 5.8, 9.7)	3.31 (d, 6.8)	6.86 (d, 10.0)	3.93 (t, 1.7)
2'	2.92 (s)	5.10 (m)	5.72 (d, 10.0)	
3'				
CH ₃	1.23 (s)	1.68 (s)	1.54 (s)	
CH ₃	1.38 (s)	1.74 (s)	1.53 (s)	

^a Data recorded at 500 MHz

δ_{C} 122.1 (CH)], seven quaternary carbons [δ_{C} 161.6 (C), 107.2 (C), δ_{C} 107.2 (C), 155.2 (C), 161.2 (C), 120.2 (C), 132.0 (C)]. ^1H and ^{13}C -NMR correlations were

demonstrated by the HMQC. The structure of **2** was elucidated to be as depicted in the formula **2** by the extensive analysis of 1D and 2D NMR data (Fig. 2), and

by comparison of the NMR data with those of **6**. Compound **2** differed from **6** only in the position of a methoxyl group.

Compound **3** was isolated as a yellow crystalline solid, and the molecular formula $C_{15}H_{17}O_5$ was established by NMR spectra (Table 1 and 2). ^{13}C -NMR spectra of compound **3** showed 15 carbons resonances and 1H and ^{13}C -NMR data indicated the presence of a methoxy group [δ_H 3.87 (3H, s), δ_C 56.5 (CH₃)], two methyls [δ_H 1.54 (3H, s), δ_C 28.0 (CH₃); δ_H 1.53 (3H, s), δ_C 28.0 (CH₃)], one oxygenated quaternary carbon [δ_C 78.0 (C)], five sp^2 methines [δ_H 6.23 (1H, d, $J = 6.2$ Hz), δ_C 113.2 (CH); δ_H 5.72 (1H, d, $J = 10.0$ Hz), δ_C 130.8 (CH); δ_H 6.78 (1H, s), δ_C 108.5 (CH); δ_H 6.86 (1H, d, $J = 10.0$ Hz), δ_C 115.2 (CH)], six quaternary carbons [δ_C 163.0 (C), 111.4 (C), δ_C 161.2 (C), 145.8 (C), 143.7 (C)], and three oxygenated sp^2 carbon [δ_C 143.7 (C), 143.7 (C), 161.2 (C)]. 1H and ^{13}C -NMR correlations were demonstrated by the HMQC experiment. The 1H -NMR spectrum of **3** was similar to that of toddalolactone (**5**). The main differences were the

presence of two olefinic protons in **3** instead of a hydroxyl group in **5** and the lack of three protons for a methoxyl group in **3**. The extensive 1D and 2D NMR analysis and comparison of the spectral data with those of **5** led to the structure determination for **3**. The *Z* geometry of the Δ^2 double bond was established by the large coupling constant observed between H-1' and H-2' ($J = 10.0$ Hz) [27-28].

Compound **4** was isolated as a yellow crystalline solid, and the molecular formula was $C_{12}H_{12}O_6$ deduced from NMR spectral data (Table 1 and 2). ^{13}C -NMR spectra of compound **4** showed 12 carbon resonances. 1H and ^{13}C -NMR data indicated the presence of two methoxy groups [δ_H 3.87 (3H, s), δ_C 56.5 (CH₃), δ_H 3.85 (3H, s), δ_C 56.5 (CH₃)], two methyls [δ_H 1.54 (3H, s), δ_C 28.0 (CH₃); δ_H 1.53 (3H, s), δ_C 28.0 (CH₃)], one hydroxyl group [δ_H 3.93 (1H, t, $J = 1.7$ Hz), δ_C 61.6 (CH₂)], three sp^2 methines [δ_H 6.13 (1H, d, $J = 6.2$ Hz), δ_C 112.2 (CH); δ_H 7.97 (1H, d, $J = 9.7$ Hz), δ_C 138.8 (CH); δ_H 6.32 (1H, s), δ_C 91.3 (CH)], six quaternary carbons [δ_C 160.9 (C),

Table 3. Antibacterial and antifungal activity of crude extracts of *T. asiatica*

Crude extract	<i>E. coli</i>			<i>S. aureus</i>			<i>A. niger</i>			<i>Cladosporium sp.</i>			<i>C. cucurbitarum</i>		
	25	50	100	25	50	100	25	50	100	25	50	100	25	50	100
CHCl ₃	+	+	++	+	+	++	-	-	-	-	-	-	-	-	-
Hexane	+	+	++	+	+	++	-	-	-	-	-	-	-	+	++

Diameter of inhibition zone (mm); + (11–12.5), ++ (13–15.5), - no activity

Diameter of a paper disc; 8 mm

Concentration: (μ g/disc)

Table 4. Antibacterial and antifungal activity of compounds (**1-9**) isolated from the stems of the plant *T. asiatica*

Compounds	<i>E. coli</i>		<i>S. aureus</i>		<i>A. niger</i>		<i>Cladosporium sp.</i>		<i>C. cucurbitarum</i>	
	25	50	25	50	25	50	25	50	25	50
1	+	++	+	++	-	-	-	-	-	-
2	+	++	+	++	-	-	-	-	-	+
3	+	++	+	++	-	-	-	-	-	+
4	+	++	+	++	-	-	-	-	-	+
5	+	++	+	++	-	-	-	-	-	-
6	+	++	+	++	-	-	-	-	-	-
7	+	++	+	++	-	-	-	-	-	-
8	+	++	+	++	-	-	-	-	-	-
9	+	++	+	++	-	-	-	-	-	-

Diameter of inhibition zone (mm); + (11–12.5), ++ (13–15.5), - no activity

Diameter of a paper disc; 8 mm

Concentration: (μ g/disc)

104.2 (C), 156.1 (C), 138.8 (C), 152.3 (C)]. The ^1H and ^{13}C -NMR correlations were demonstrated by the HMQC experiment. An extensive analysis of 2D NMR spectra (Fig. 2) led to the planar structure of **4**. HMBC correlations between $\text{H}_3\text{-5-OCH}_3/\text{C-5}$ and $\text{H}_3\text{-7-OCH}_3/\text{C-7}$ and C-8 confirmed the location of the methoxy groups.

Antibacterial and Antifungal Assays

The antibacterial and antifungal assays were carried out at the concentration of 25 and 50 $\mu\text{g}/\text{disc}$ for pure compounds and 25, 50, and 100 $\mu\text{g}/\text{disc}$ for crude extracts. The results are tabulated in Tables 3 and 4.

The two extracts (chloroform and hexane) from *T. asiatica* showed activity against *E. coli* and *S. aureus* at 25, 50, and 100 $\mu\text{g}/\text{disc}$, only hexane extract showed activity against *C. cucurbitarum* at 100 $\mu\text{g}/\text{disc}$. Compounds **1-9** showed strong antibacterial activity at 25 and 50 $\mu\text{g}/\text{disc}$. Compounds **2-4** showed activity against the phytopathogenic fungi *C. cucurbitarum* at 50 $\mu\text{g}/\text{disc}$.

CONCLUSION

Chemical investigation of the stems of *T. asiatica* led to the isolation of four new metabolites **1-4**, along with five known metabolites **5-9**. Compounds **1-9** were active against the bacteria *E. coli* and *S. aureus* at 25 and 50 $\mu\text{g}/\text{disc}$. Compounds **2-4** showed activity against *C. cucurbitarum* at 50 $\mu\text{g}/\text{disc}$ in disc diffusion antimicrobial assay.

ACKNOWLEDGMENTS

This work was supported by The Japanese Ministry of Education, Culture, Sports, Science, and Technology of Japan (Monbukagakusho).

REFERENCES

- [1] Orwa, J.A., Jondiko, I.J.O., Minja, R.J.A., and Bekunda, M., 2008, The use of *Toddalia asiatica* (L) Lam. (Rutaceae) in traditional medicine practice in East Africa, *J. Ethnopharmacol.*, 115 (2), 257–262.
- [2] Hirunwong, C., Sukieum, S., Phatchana, R., and Yenjai, C., 2016, Cytotoxic and antimalarial constituents from the roots of *Toddalia asiatica*, *Phytochem. Lett.*, 17, 242–247.
- [3] Hu, J., Shi, X., Chen, J., Mao, X., Zhu, L., Yu, L., and Shi, J., 2014, Alkaloids from *Toddalia asiatica* and their cytotoxic, antimicrobial and antifungal activities, *Food Chem.*, 148, 437–444.
- [4] Ishii, H., Kobayashi, J.I., Sakurada, E., and Ishikawa, T., 1992, The absolute stereochemistries of (+)-toddalolactone and its related chiral coumarins from *Toddalia asiatica* (L.) Lam. (*T. aculeata* Pers.) and their optical purities, *J. Chem. Soc., Perkin Trans. 1*, 13, 1681–1684.
- [5] Kokwaro, J.O., 1993, *Medical Plants of East Africa*, Kenya Literature Bureau, Nairobi, 212.
- [6] Ishii, H., Kobayashi, J., Ishikawa, M., Haginiwa, J., and Ishikawa, T., 1991, Studies on the chemical constituents of rutaceae++ plants LXVI. The chemical constituents of *Toddalia asiatica* l. Lam. *Toddalia aculeata* (L.) Lam. (*T. Aculeata* Pers.) (1). Chemical constituents of the root bark, *Yakugaku Zasshi*, 111 (7), 365–375.
- [7] Combes, G., and Gaignault, J.C., 1984, The coumarins in *Toddalia asiatica*, *Fitoterapia*, 55 (3), 161–170.
- [8] Zhang, X., Sun, W., Yang, Z., Liang, Y., Zhou, W., and Tang, L., 2017, Hemostatic chemical constituents from natural medicine *Toddalia asiatica* root bark by LC-ESI Q-TOF MS, *Chem. Cent. J.*, 11, 55.
- [9] Li, W., Zhang, J.S., Huang, J.L., Jiang, M.H., Xu, Y.K., Ahmed, A., Yin, S., and Tang, G.H., 2017, New prenylated coumarins from the stems of *Toddalia asiatica*, *RSC Adv.*, 7 (49), 31061–31068.
- [10] Liu, Y., Guo, J., Xiao, Z., Peng, D., and Song, K., 2020, Adsorption of chelerythrine from *Toddalia asiatica* (L.) Lam. by ZSM-5, *Adv. Polym. Technol.*, 2020, 9408921.
- [11] Irudayaraj, S.S., Sunil, C., Durairamian, V., and Ignacimuthu, S., 2013, *In vitro* antioxidant and antihyperlipidemic activities of *Toddalia asiatica* (L) Lam. leaves in Triton WR-1339 and high fat diet induced hyperlipidemic rats, *Food Chem. Toxicol.*, 60, 135–140.
- [12] Thirugnanasampandan, R., Jayakumar, R., and Prabhakaran, M., 2012, Analysis of chemical composition and evaluation of antigenotoxic, cytotoxic and antioxidant activities of essential oil

- of *Toddalia asiatica* (L.) Lam., *Asian Pac. J. Trop. Biomed.*, 2 (3), S1276–S1279.
- [13] Balasubramaniam, A., Manivannan, R., Paramaguru, R., Mazumder, P.M., and Vijayakumar, M., 2012, Evaluation of anti-inflammatory and antioxidant activities of Stem Bark of *Toddalia asiatica* (L.) Lam. using different experimental models, *Pharmacologia*, 3 (5), 144–149.
- [14] Ceballos, R., Sankoli, S.M., Ramnath, S., Venkataramgowda, S., Murthy, G.S., and Ceballos R.M., 2013, Evaluation of phytochemicals and in vitro antioxidant studies of *Toddalia asiatica* leaf, *J. Med. Plants*, 5 (4), 202–205.
- [15] Vázquez, R., Riveiro, M.E., Vermeulen, M., Mondillo, C., Coombes, P.H., Crouch, N.R., Ismail, F., Mulholland, D.A., Baldi, A., Shayo, C., and Davio, C., 2012, Toddaculin, a natural coumarin from *Toddalia asiatica*, induces differentiation and apoptosis in U-937 leukemic cells, *Phytomedicine*, 19 (8-9), 737–746.
- [16] Shan, X.F., Meng, Q.F., Kang, Y.H., Bian, Y., Gao, Y.H., Wang, W.L., and Qian, A.D., 2011, Isolation of active compounds from methanol extracts of *Toddalia asiatica* against *Ichthyophthirius multifiliis* in goldfish (*Carassius auratus*), *Vet. Parasitol.*, 199 (3-4), 250–254.
- [17] Borah, R., Kalita, M.C., Kar, A., and Talukdar, A.K., 2010, Larvicidal efficacy of *Toddalia asiatica* (Linn.) Lam against two mosquito vectors *Aedes aegypti* and *Culex quinquefasciatus*, *Afr. J. Biotechnol.*, 9 (16), 2527–2530.
- [18] Stephen, I.S., Sunil, C., Duraipandiyan, V., and Ignacimuthu, S., 2012, Antidiabetic and antioxidant activities of *Toddalia asiatica* (L.) Lam. leaves in Streptozotocin induced diabetic rats, *J. Ethnopharmacol.*, 43 (2), 515–523.
- [19] Kimang'a, A., Gikunku, J., Kariuki, D., and Ogutu, M., 2015, Safety and analgesic properties of ethanolic extracts of *Toddalia asiatica* (L) Lam. (Rutaceae) used for central and peripheral pain management among the East African ethnic communities, *Ethiop. J. Health Sci.*, 26 (1), 55–64.
- [20] Lin, T.T., Huang, Y.Y., Tang, G.H., Cheng, Z.B., Liu, X., Luo, H.B., and Yin, S., 2014, Prenylated coumarins: Natural phosphodiesterase-4 inhibitors from *Toddalia asiatica*, *J. Nat. Prod.*, 77 (4), 955–962.
- [21] He, N., Wang, P., Wang, P., Ma, C., and Kang, W., 2018, Antibacterial mechanism of chelerythrine isolated from root of *Toddalia asiatica* (Linn) Lam, *BMC Complement Altern. Med.*, 18, 261.
- [22] Karunai, R.M., Balachandran, C., Duraipandiyan, V., Agastian, P., and Ignacimuthu, S., 2012, Antimicrobial activity of Ulopterol isolated from *Toddalia asiatica* (L.) Lam. A traditional medicinal plant, *J. Ethnopharmacol.*, 140 (1), 161–165.
- [23] Roy, P.K., Maarisit, W., Roy, M.C., Taira, J., and Ueda, K., 2012, Five new diterpenoids from an Okinawan soft coral, *Cespitularia* sp., *Mar. Drugs*, 10 (12), 2741–2748.
- [24] Maarisit, W., and Ueda, K., 2013, Antimicrobial Metabolites from a marine-derived fungus, *Indonesian J. Pharm.*, 24 (3), 163–169.
- [25] Maarisit, W., Yano, K., Miyazato, T., Roy, P.K., Taira, J., and Ueda, K., 2015, Structures and bioactivities of xenicanes from an Okinawan soft coral *Xenia* sp., *Heterocycles*, 91 (3), 505–514.
- [26] Watanabe, A., Kumagai, M., Mishima, T., Ito, J., Otoki, Y., Harada, T., Kato, T., Yoshida, M., Suzuki, M., Yoshida, I., Fujita, K., Watai, M., Nakagawa, K., and Miyazawa, T., 2015, Toddaculin, isolated from *Toddalia asiatica* (L.) Lam., inhibited osteoclastogenesis in RAW 264 cells and enhanced osteoblastogenesis in MC3T3-E1 cells, *PLoS ONE*, 10 (5), e0127158.
- [27] Morrison, R.T., and Boyd, R.N., 1992, *Organic Chemistry*, 6th Ed., Prentice Hall, New Jersey.
- [28] Silverstein, R.M., Webster F.X., and Kiemle, D.J., 2005, *Spectrometric Identification of Organic Compounds*, 7th Ed., John Wiley & Sons, Inc., New York.

Atmospheric Corrosion Behavior of Carbon Steel and Galvanized Steel after Exposure in Eretan and Ciwaringin, West Java Province, Indonesia

Gadang Priyotomo^{1,*}, Lutviasari Nuraini¹, Siska Prifiharni¹, Ahmad Royani¹, Sundjono¹, Hadi Gunawan², and Meng Zheng³

¹Research Center for Metallurgy and Materials-Indonesian Institute of Sciences, Kawasan PUSPIPTEK, Serpong, Tangerang Selatan 15314, Banten, Indonesia

²Research Center and Development of Roads and Bridge, Indonesia's Ministry of Public Works and Housing, Jl. A.H. Nasution No. 264, Bandung 40294, West Java, Indonesia

³Key Laboratory of Marine Environmental Corrosion and Bio-fouling, Institute of Oceanology, Chinese Academy of Sciences, Qingdao, 266071, China

* **Corresponding author:**

email: gadangp@gmail.com

Received: June 18, 2019

Accepted: October 8, 2019

DOI: 10.22146/ijc.46755

Abstract: The investigation of corrosion for carbon steel and galvanized steel has been conducted in the marine atmosphere of Eretan and Ciwaringin Districts, West Java Province. The exposure time of the field test was up to 200 days, and their corrosion rates are determined according to the weight loss method. The objective of the work is to elucidate the corrosion behavior of those alloys, which is affected by distances from the coastline and environmental conditions. The magnitude of the corrosion rate for carbon steel was 20 times as high as that for galvanized steel in both districts. The distance from coastline has significantly affected the magnitude of corrosion rate, where that both alloys in Ciwaringin are lower than that in Eretan. The deposition of chloride ion in Eretan and Ciwaringin Districts were 4.305 mg/m² day and 1.863 mg/m² day, respectively, where the higher chloride ion can tend to increase the corrosion rates. Relative humidity (RH), which is over 60%, has an essential role in the corrosion process as well as rainfall. The uniform corrosion attack was observed both alloys after exposure. The corrosion product phases of galvanized steel exhibit zincite, hydrozincite, and simonkolleite as the typical coastline atmosphere phases in Eretan, but not in Ciwaringin. The formation of rust product for both metals lead the decrease of further corrosion attack due to the barrier between metal and environment. The usage of galvanized steel is remarkable to minimize corrosion attack compared to that of carbon steel in the tropical coastline.

Keywords: carbon steel; galvanized steel; atmospheric corrosion; coastline; corrosion product

■ INTRODUCTION

Carbon steel, alloyed steel, and galvanized steel are the most generally utilized metallic material in open-air structures, being used to build a variety of metallic structures due to their good mechanical strength, reasonable cost, and easy manufacture in marine and coastal environment. Atmospheric corrosion phenomena could contribute a detrimental effect significantly for various metallic constructions, where 80% of all

degradations made by its corrosion in the constructions due to the atmospheric corrosion [1]. The magnitude of atmospheric corrosion depends upon the time of wetness (TOW) that the metal surface tends to become wet conditions. TOW defines the duration of the electrochemical process, which is associated with the water vapor content of the atmosphere, such as the relative humidity (RH) at a certain temperature. The presence of RH and temperature variations could lead to cyclic wet and dry periods [2], where on the wet surface

of a metal, the corrosion process occurs spontaneously, comparing with the dry surface [3]. The degree of corrosion attack also depends on the length of the wet time. Furthermore, generally, the atmospheric corrosion conditions are complicated for holistic investigation, which considers the corrosion behavior of metals in the function of geographic regions, various climates, and seasons. The alteration of those functions can vary the magnitude of corrosion rates for metals. On the other hand, the other complications of atmospheric corrosion are related to the presence of several parameters, such as air temperature, relative humidity, wind speed, and wind direction, various airborne pollutants, and so on [4]. However, it is very difficult to simulate the real condition with many factors into a laboratory scale. The vulnerability of atmospheric corrosion to steel structures in the coastal environment has been reported by many researchers, where metal degradation is major concern [5-7]. In addition, the severity of atmospheric corrosion depends on the location of the environment, including inland (rural), urban, industry and marine regions, where marine region is one of the most severe locations. One of the main environmental factors is the presence of certain pollutants as airborne chloride salt in marine region [8], which mainly decreases the corrosion resistances of metals.

Furthermore, the mitigation of corrosion must be conducted to minimize the severity of metal degradation. Corrosion protection methods commonly used to alter electrochemical reaction of metals from surrounded environment in which consists of inhibitors, cathodic protection, and organic and metallic coatings [9]. Galvanized steel is one of metallic coated steel, where subtract of steel has been coated in zinc to increase corrosion resistance. Galvanized steel is applied widely in infrastructure and construction both onshore and offshore. The corrosion protection of that steel mostly

depends on the porosity, thickness, and the adherence of zinc coated on steel. In preceding work, the effect of galvanized steel significantly reduces the corrosion rate up to 20 times compared to structural plain steel in Limbangan area, Indramayu, West Java, where the deleterious effect of chloride ion increases the magnitude of corrosion rate by degrading the formation of protected oxide layer without zinc coating [10]. However, with regard to atmospheric corrosion subject, there is no or little investigation on the corrosion in the Eretan and Ciwaringin Districts, as a representative of tropical regions in Indonesia, even though carbon steel and galvanized steel were investigated systemically in the other regions of West Java [10]. Therefore, the objective of the present work is to investigate and elucidate the corrosion behavior of mild steel and galvanized steel as representative of infrastructural metals in the tropical atmosphere in Eretan and Ciwaringin Districts, West Java Province, Indonesia.

■ EXPERIMENTAL SECTION

The Specimen Preparation

In this recent work, a plate shape of as-received carbon steel was employed for atmospheric corrosion specimens. This alloy was cut into 15 cm × 7.5 cm × 0.3 cm. A pickling processing was carried out in the specimen in which refers to the standard of ASTM G-1 before exposure. During the field test, the observation of corrosion behavior was only on one side of the upper specimen surface, while the bottom side was covered fully with black adhesive tape. The duration of test exposure was up to 200 days. All specimens were set up at a 45° angle from a horizontal axis and oriented to face toward to open sea. The chemical composition of the specimen is shown in Table 1 as well as the preceding work from Nuraini and co-workers [10].

Table 1. Chemical composition of specimen employed in the recent study (wt.%) [10]

Fe	Si	P	Mn	Ni	Cr	Cu	Ti	C	Zn	Al
99.00	0.11	0.02	0.29	0.01	0.30	0.01	0.01	0.13	-	-



Fig 1. (a) Location of two field sites in West Java Province; test racks of atmospheric corrosion in (b) Eretan District and (c) Ciwaringin District

The Location of Field Test

The magnitude of atmospheric corrosion leads to varying in different geographic regions, where the distance of specimens to the coastal lines is the primary factor. With regards to the recent study, two exposure sites, such as Eretan and Ciwaringin District, were located in 50 m and 2000 m from the sea, respectively, as shown in Fig. 1(a). The value of chloride deposition rate was specified by a wood rectangular collector, which contains cross stitch cloth in the dimension of 10 cm × 10 cm, as shown in Fig. 1(b) and Fig. 1(c). The airborne salt, which contains chloride ion, was trapped and precipitated in that collector during exposure. The measurement of chloride ion was conducted by the HACH chloride titrator strips kit. In addition, local data of relative humidity (RH), air temperature, wind direction, and daily rainfall was officially obtained from Meteorological, Climatological and Geophysical Agency, Indonesia.

Characterization and Analysis of Corroded Specimens after Exposure

After a certain exposure time in both sites, the corroded specimens were retrieved, analyzed, and characterized in a laboratory. The procedure of cleaning and pickling processes was carried out to remove rust products which refer to the standard of ASTM G-1. The

method of measurement of the corrosion rate was conducted based on weight loss. The measurements of the loss of weight of the materials are related to a function of exposure time. Moreover, the weight loss in each specimen before and after exposure was calculated using the following formula:

$$CR = \frac{\Delta W \cdot K}{d \cdot A \cdot t}$$

where CR = corrosion rate in mills per year (mpy); ΔW = weight loss in grams; K = constant; d = metal density in g/cm³; t = exposure time (day). The morphology of the surface of corroded materials, the distribution of elemental composition for rust products, and various phases of corrosion products were observed and identified by Scanning Electron Microscopy (SEM), Energy Dispersive Spectroscopy (EDS), and X-Ray Diffraction (XRD) respectively.

RESULTS AND DISCUSSION

Corrosion Rates of Metals

Fig. 2 shows the corrosion rate of carbon steel as a function of exposure time in Eretan and Ciwaringin District, West Java Province, Indonesia. The corrosion rates for these materials tend to increase and decrease up to final exposure time initially. It was found that the magnitude of the corrosion rate for carbon steel in the

Eretan region becomes higher than that in the Ciwaringin region. Moreover, Fig. 3 also shows the corrosion rate of galvanized steel as a function of exposure time in Eretan District and Ciwaringin District, West Java Province, Indonesia. The magnitude of the corrosion rate of galvanized steel in the Ciwaringin region initially was higher than that in the Eretan region. After 142 days of exposure, the opposite of its behavior took place up to 200 days.

On the basis of the result, the magnitude of corrosion rates for carbon steel is 20 times higher than those for galvanized steels in both regions of a field test. The major factor of distance from coastline to test site affects the corrosion rate of metals, where the closer test site from the coast line could increase the corrosion attack on metals [11]. In present work, the corrosion rate of exposed carbon steel at a test station near the sea shore line has the highest corrosion rate at the Eretan region, but not at the Ciwaringin region. The same behavior of distance factor is also the same on galvanized steel.

On the other hand, the corrosion resistance of galvanized steel is not only considered from the distance factor but also the thickness of zinc coating on subtract. The increase in thickness of zinc coating could enhance the corrosion resistance of galvanized steel [12]. The average thickness of as-received galvanized steel is around 55 μm (2.2 mils). In tropical environment, the prediction

of service life of galvanized steel, which defined to be occurred 5% red rusting of the steel surface, is estimated 25 years [13]. In a recent study, the estimated service life of galvanized steel in Eretan and Ciwaringin Districts is 21 and 35 years, respectively. However, the difference in the service life of this investigated atmospheric corrosion subject may take place due to the complexity of environmental factors. Prifiharni and co-workers reported the role of distance from sea line to site test in Limbangan and Karangsong region, where the magnitude of atmospheric corrosion rate of carbon steel and galvanized steel raise in getting closer from sea line [14]. Therefore, it implies that the service of life of galvanized steel increase in increasing the distance from the sea coastline to the metal structures. In addition, the estimated service life of carbon steel in the Ciwaringin District is also longer than that in the Eretan District.

The susceptibility of atmospheric corrosion of metal structure is related to the duration of exposure time and essential climatic variables such as air temperature (T), relative humidity (RH), airborne salinity, and sulfur content [6]. The other factors that may be considered are wind direction and precipitation. The electrochemical process initiates on the surface of a metal to corrode gradually at a critical level humidity (RH_{crit}) of 60% [5], then the corrosion rate increases

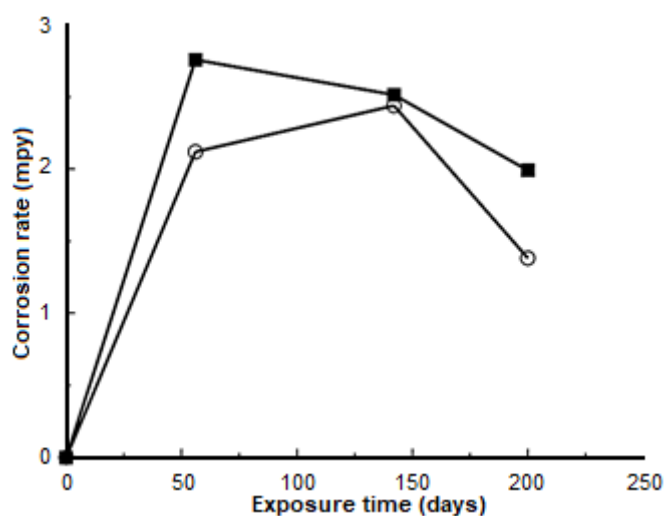


Fig 2. Corrosion rate of carbon steel as function of exposure time in ■ Eretan region and ○ Ciwaringin region, West Java Province, Indonesia

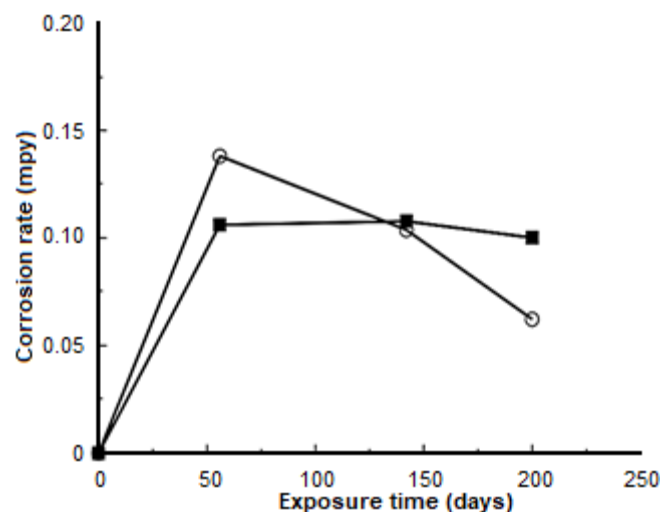


Fig 3. Corrosion rate of galvanized steel as a function of exposure time in ■ Eretan region and ○ Ciwaringin region, West Java Province, Indonesia

drastically at 80% RH [15]. The existence of a thin electrolyte layer spreads on the metallic surface takes place when reached to RH_{crit} [8].

Fig. 4 shows a representative relative humidity (RH) variation as a function of time exposure at Eretan and Ciwaringin Districts, which was retrieved and carried out a subsequent data processing from a raw database of Meteorological, Climatological and Geophysical Agency, Indonesia [16]. Based on the current result, it was more than 80% of the percentage from all-time exposure, which is categorized as average daily RH_{crit} . The highest of RH tends to initiate the electrochemical process on the surface of a metal, which allows a longer time of wetness (TOW). TOW is defined as the time during wetness (condensation process) that took place on the exposed surface to the environment when RH is greater than 80% at a temperature greater than 0 °C [5]. In addition, both Ciwaringin and Eretan Districts are located in tropical regions, which have warm temperatures, ranges from 23

to 33 °C during field tests [16]. On the other hand, the condensation of humidity is regarded as a major cause of corrosion attack of metal and alloys, which depends on RH and the alteration of air temperature. Based on the results of corrosion rates in Fig. 2 and 3, the effect of high RH, which tends to increase corrosion attack, has no or little impact on galvanized steel due to low corrosion rate, but not on carbon steel.

Fig. 5 shows daily rainfall as a function of time exposures at Eretan and Ciwaringin Districts, West Java Province, which was retrieved and carried out a subsequent data processing from a raw database of Meteorological, Climatological and Geophysical Agency, Indonesia [16]. The daily rainfall frequently occurs in all exposure time, where the highest peak of rainfall was in 30 days of exposure or the beginning of the first month of the year. Condensation (dew) could not wash the surface of the metal, so the precipitated pollutant (chloride content) on it increases and could be more severe than

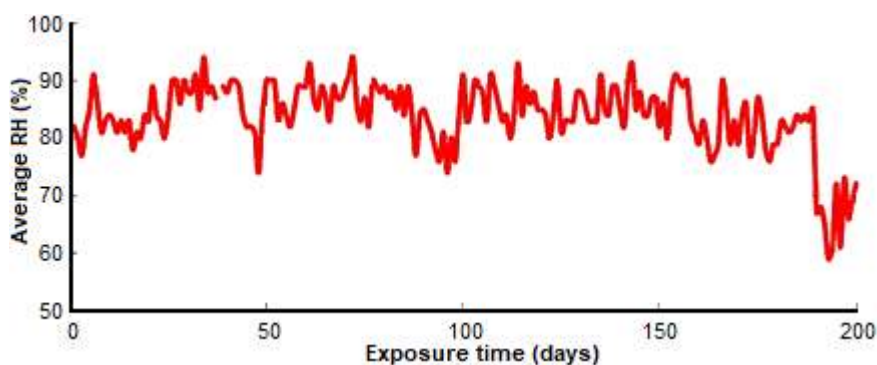


Fig 4. A representative relative humidity (RH) variation as a function of exposure time at Eretan and Ciwaringin Districts, West Java province

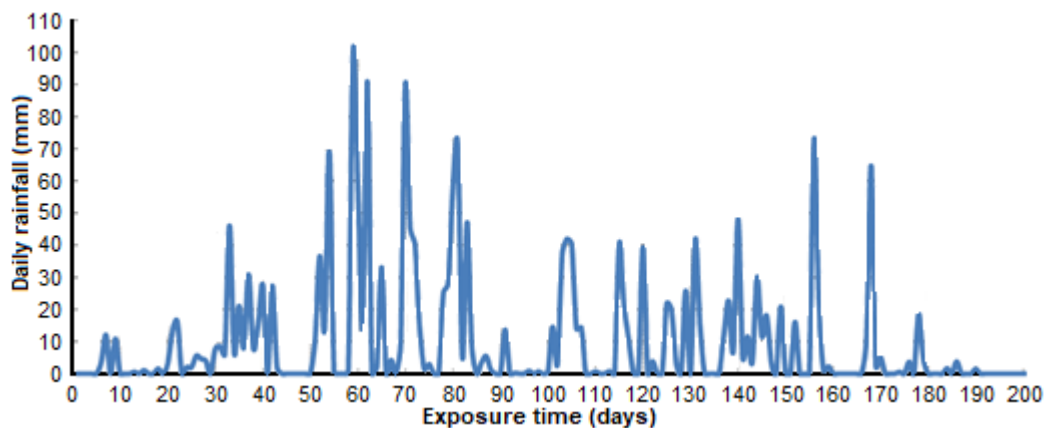


Fig 5. Daily rainfall as a function of exposure time at Eretan and Ciwaringin Districts, West Java province

rain. However, high intensity of duration of rainfall could lead to washing away the contaminant of pollutants on the surface of the metal. In addition, rainfall also contributes to increasing the formation of a thick layer of water and also absorbs corrosion agents such as H^+ and SO_4^{2-} [17] but depending on the duration of daily dry sessions and types of pollutant in a different environment. Therefore, it is difficult to elucidate only the role of precipitation towards the corrosion rates of both alloys. The presence of chloride in airborne salt is predominantly to take responsibility to increase the severity of corrosion attack compared to the presence of other corrosion agents such as H^+ and SO_4^{2-} in the marine environment.

Airborne salinity refers to the content of suspended salt in the atmosphere, which is predominantly chloride ion in the coastal region. The airborne salt that contains chloride ion was dissolved in a thin electrolyte layer on the metallic surface during the condensation process, where the conductivity of it increases significantly. The higher conductivity of electrolytes could contribute to accelerating the corrosion process of metals [18-19]. In current work, the airborne salinity level was represented by the deposition rate of chloride refers to International Standard Organization (ISO) 9223:2012 [20]. On the basis of results, the deposition of chloride rate values in Eretan and Ciwaringin Districts were $4.305 \text{ mg/m}^2\cdot\text{day}$ and $1.863 \text{ mg/m}^2\cdot\text{day}$, respectively, which are classified into S1 for the coastal region (Eretan) and S0 for Non-Coastal (Ciwaringin). It was assumed that there are no variables influencing the transport inland of airborne sea salt such as wind velocity and local topography. The distance factor of the field test site to the sea and wind direction was also

considered to the magnitude of atmospheric corrosion. In addition, according to raw database service of Meteorological, Climatological and Geophysical Agency, Indonesia for wind direction [16], it is more than 51% of wind direction toward to north side. It implies that airborne salt contaminant prefers to flow to sea than to inland. The deposition of chloride rate was $117 \text{ mg/m}^2\cdot\text{day}$ in Limbangan District, Northern West Java at 100 meters from coastline [10], but its less rate in the Eretan District. However, the magnitude of corrosion rates for carbon steel and galvanized steel in Eretan are lower than those in Limbangan. Based on results, the lower corrosion rate in Eretan District may be caused by wind direction toward the north side, the higher intensity of rainfall, and lower airborne salinity during the exposure of field tests. Therefore, the less magnitude of corrosion rate in the Ciwaringin District comparing with that in Eretan is caused by the difference of distance from the sea.

Fig. 6 shows the highest and lowest air temperatures as a function of time exposure, which was obtained and conducted a subsequent data processing from a raw database of Meteorological, Climatological and Geophysical Agency, Indonesia [16]. The lowest air temperature occurs at night, increasing in the morning, and then raising drastically after midday. This condition took place if there is no high intensity of rainfall. The possibility of fluctuated temperature magnitude is related to solar radiation in which contributes to the corrosion rate of metals due to the semiconducting behavior of the oxidative corrosion processes [21].

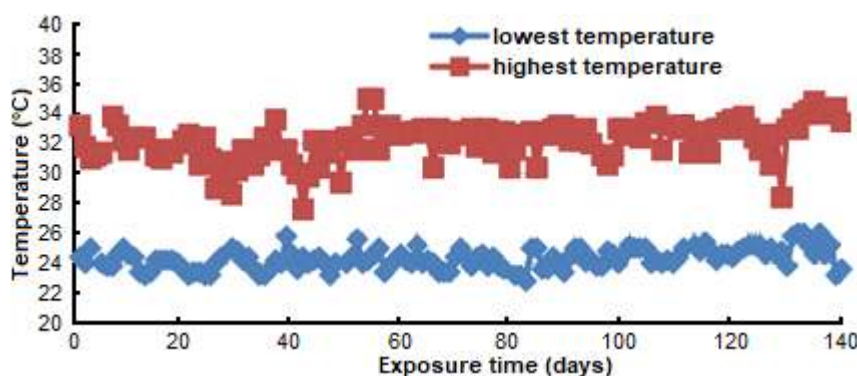


Fig 6. The highest air temperature and the lowest air temperature as function of exposure time during test

Morphology of Corroded Metals after Exposure

Fig. 7 shows macro surface appearances before exposure and after exposure up to 142 days in both Eretan and Ciwaringin Districts. The rust products were uniformly distributed on the entire surface of specimens. The abundance of rust product is denser with increasing exposure time. It implies that in the initial stage, the higher corrosion rate of steel made the rust product on steel. On the other hand, the corrosion rate decreases when a dense, thick rust product forms on the surface. Fig. 8 shows surface appearances of galvanized steel before and after exposure in both Eretan and Ciwaringin Districts up to 142 days. Before exposure, the visual results of newly galvanized steel are bright and shiny, where it has visible spangle clearly, as shown in Fig. 8(a). Within 142 days of exposure, the surface appearance of galvanized steel changes to a uniform dull gray in both

Eretan and Ciwaringin Districts. The crystallization pathway of the spangle was increasingly unclear during the exposure time.

Fig. 9 shows a representative morphology of rust products for corroded steel after 200 days of exposure in Eretan and Ciwaringin Districts. On the basis of the result, the specimens were fully covered by rust products after exposure. The identification of the various types of morphologies such as grain, flakes, powdery rust particles, and easy peel-off of lamination is possible to identify after exposure in the atmosphere visually [22]. In Fig. 9(a) and 9(b), there are various shapes of rust product morphology. In Eretan, the types of rust products were cracked and flaked, which has mostly a flowery structure and cotton ball structure. In Ciwaringin, those were also the same where a cotton ball structure is predominantly. There are many flaky and cracks that lead

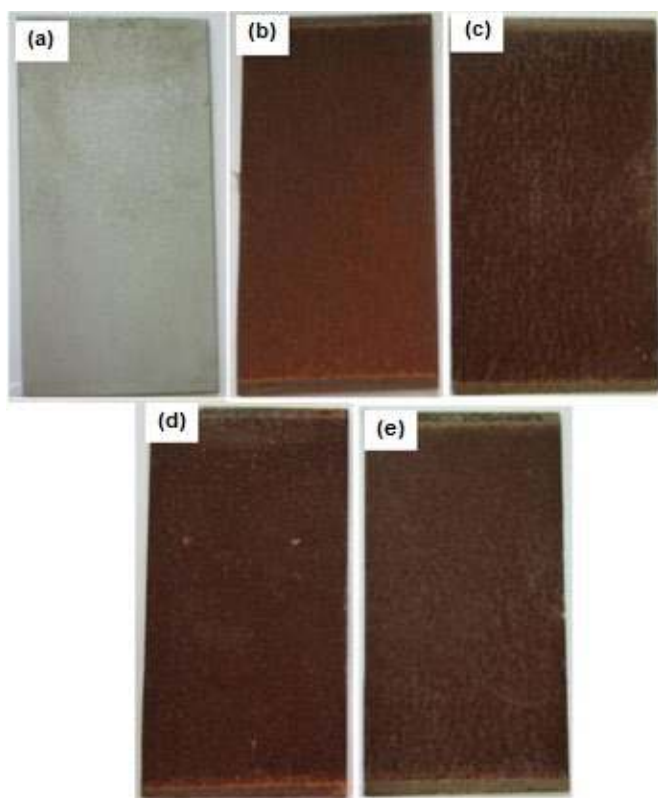


Fig 7. Photos of carbon steel (a) before exposure and after (b) 56 days of exposure and (c) 142 days exposure in Eretan; (d) 56 days of exposure and (e) 142 days exposure in Ciwaringin

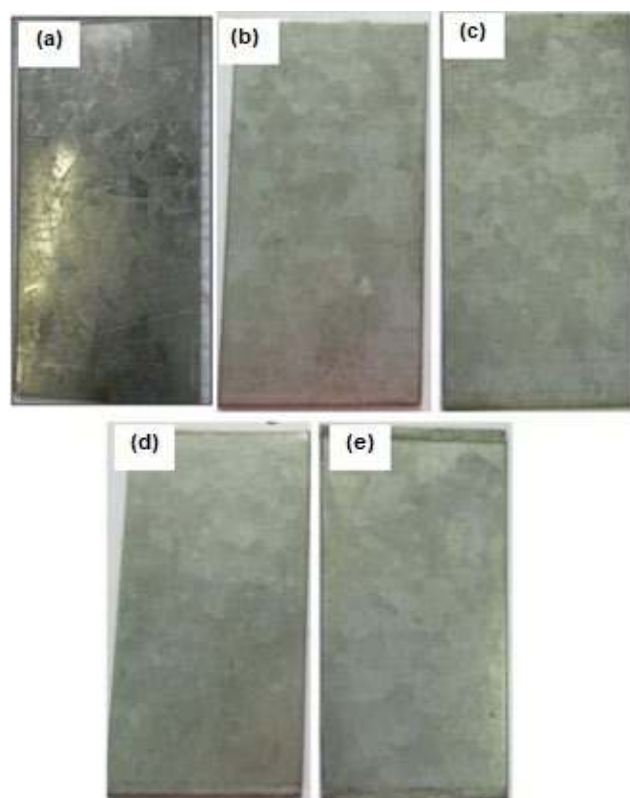


Fig 8. Photos of galvanized steel (a) before exposure and after (b) 56 days of exposure and (c) 142 days exposure in Eretan; (d) 56 days of exposure and (e) 142 days exposure in Ciwaringin

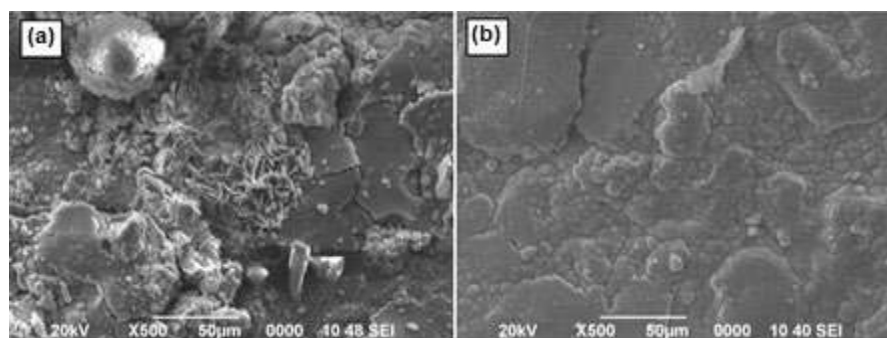


Fig 9. Representative morphology of rust product for corroded steel of exposure in (a) Eretan and (b) Ciwaringin Districts

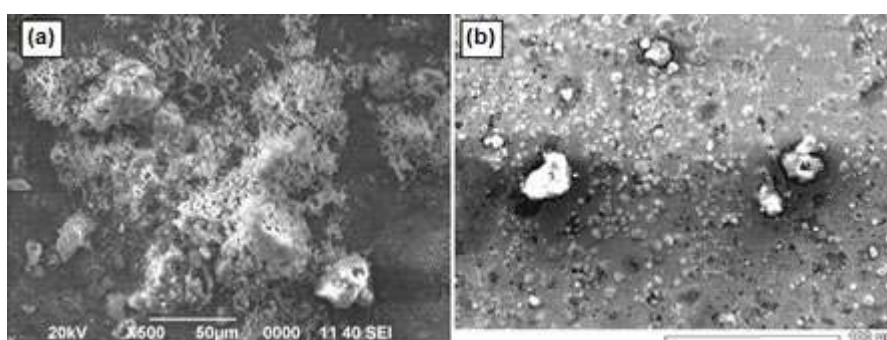


Fig 10. Representative morphology of galvanized steel after exposure in (a) Eretan and (b) Ciwaringin Districts

to the diffusion of chloride ion into the rust product from airborne salts. Morcillo and co-workers reported that the formation of coarse flakes and layered sheets on rust products in the marine atmosphere due to the presence of chloride [23] as well as the present results.

Fig. 10 shows a representative morphology of galvanized steel after 200 days of exposure in Eretan and Ciwaringin Districts. The visual observation of galvanized steel surface after exposure shows that corrosion products adhere to the metal surfaces in both districts. The morphology of the corrosion products shows deposits of granulates formed due to RH and its interaction with oxygen and the presence of a pollutant in the atmosphere, such as chloride ion [24], as shown in Fig. 10(a) and 10(b). In Fig. 10(a), certain areas on the surface were fine flake-like crystals structure observed in Eretan, where Chen and co-workers also had observed the same crystal structure as simonkolleite for galvanized steel [25]. Ciwaringin District also shows that the type of corrosion product was less dense fine cotton ball structure, as in Fig. 10(b).

Fig. 11 shows XRD of corrosion products for steel after exposure in Eretan Districts. On the basis of results, its corrosion products are identified as Magnetite (Fe_3O_4) and Lepidocrocite ($\gamma\text{-FeOOH}$). In Ciwaringin District, the corrosion products of steel surface are identified as goethite ($\alpha\text{-FeOOH}$) and Lepidocrocite ($\gamma\text{-FeOOH}$), as shown in Fig. 12. Furthermore, the initial stage of the steel rusting forms ferrous hydroxide ($\text{Fe}(\text{OH})_2$), which

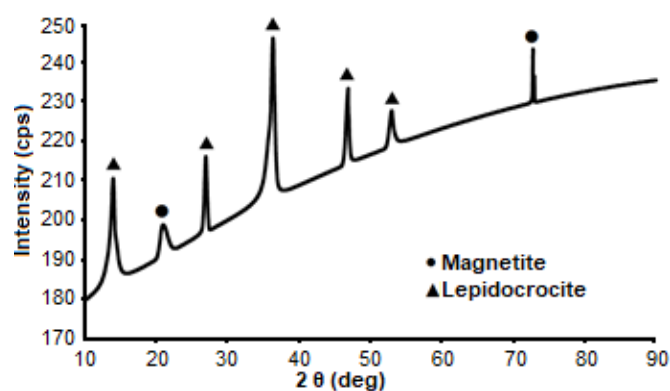


Fig 11. X-Ray Diffraction of various corrosion products for carbon steel after exposure in Eretan Districts

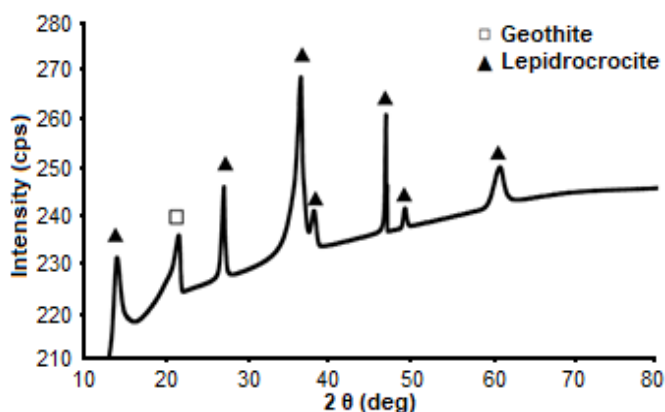


Fig 12. X-Ray Diffraction of various corrosion products for carbon steel after exposure in Ciwaringin Districts

oxidizes to lepidrocrocite (γ -FeOOH). The formation of magnetite (Fe_3O_4) took place by the reduction process inside the flaked rust layer, where the diffusion of oxygen is restricted from the outside rust layer. The magnetite was formed in the presence of chloride ion by the transformation of lepidrocrocite [7]. Moreover, the existence of akaganeite phase (β -FeOOH) is common as a primary phase in the severe marine environment [26]. The presence of the magnetite phase is also found in atmospheres with a lower airborne salinity [23]. However, in present work, there is no evidence of akaganeite phase, where the magnetite phase was identified. It implies that there is less severe of the marine environment due to lower airborne salinity levels ($4.305 \text{ mg/m}^2\cdot\text{day}$). In Ciwaringin District, the lepidrocrocite phase was predominantly as major phases compared to the Geothite phase. There are no akaganeite and magnetite phases on steel due to the lowest concentration of airborne salinity ($1.865 \text{ mg/m}^2\cdot\text{day}$). In the previous description, the concentration of chloride ion (airborne salinity) depends on the distance from the sea line.

Generally, in marine environment corrosion product of galvanized steel consists of simonkolleite ($\text{Zn}_5(\text{OH})_8\text{Cl}_2\cdot(\text{H}_2\text{O})$), hydrozincite ($\text{Zn}_5(\text{CO}_3)_2(\text{OH})_6$), zinc (Zn) and sodium hydroxyl-chlorosulfate ($\text{NaZn}_4\text{Cl}(\text{OH})_6\text{SO}_4\cdot 6\text{H}_2\text{O}$) [27]. In present results, those are identified as zinc, zincite, hydrozincite, and simonkolleite after 200 days of exposure in Eretan District, as shown in Fig. 13. Many studies reveal that the formation of simonkolleite increased by the presence of

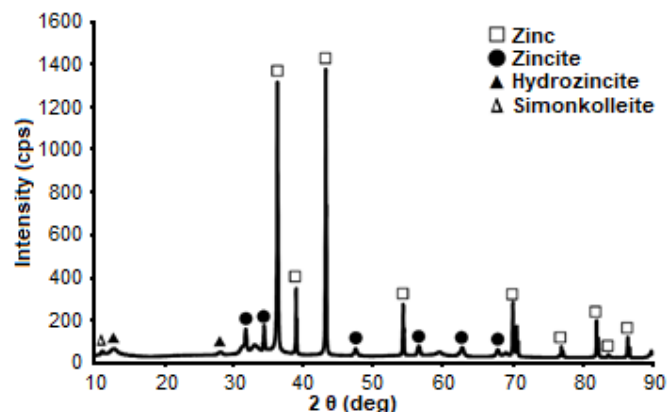
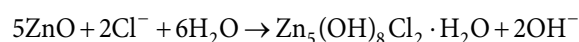


Fig 13. X-Ray Diffraction of various corrosion product for galvanized steel after exposure in Eretan Districts

chloride ion in the atmosphere [25-27]. In thermodynamic stability, zinc metal is easy to react with oxygen, forming an oxide film (ZnO) at ambient temperature. This oxide has good adhesion and compactness, which may protect subtract of steel from corrosion process. The presence of hydrozincite is also predominantly at the marine sites [28], where the surfaces of zinc exposed to the air at the RH range of 85%–100% [25]. On the basis of results, within 200 days of exposure, there is 45% of the percentage that reach or exceed RH 85%. In addition, the presence of CO_2 gas dissolved into a thin layer of electrolytes on the surface of the metal, which leads to the formation of zinc carbonate and hydrozincite in long-term outdoor exposure with little contaminants in open air [29]. However, in the existence of chloride as a marine pollutant, zincite will subsequently react with chloride to form insoluble simonkolleite [25] as follows



In Ciwaringin District, the distance of the site from the coastline is around 2000 meters, which the airborne salinity level decreases. In this location, the XRD result shows phases of galvanized steel as Zinc and zinc chloride (ZnCl_2), as shown in Fig.14. However, there are no zincite, simonkolleite, and hydrozincite phases. It presumes that the XRD apparatus was difficult to detect those phases due to the less amount of the products. In the initial stage of exposure, the magnitude of corrosion rate in Ciwaringin is higher than that in Eretan, in which is possible to be caused by no those protective phases on the

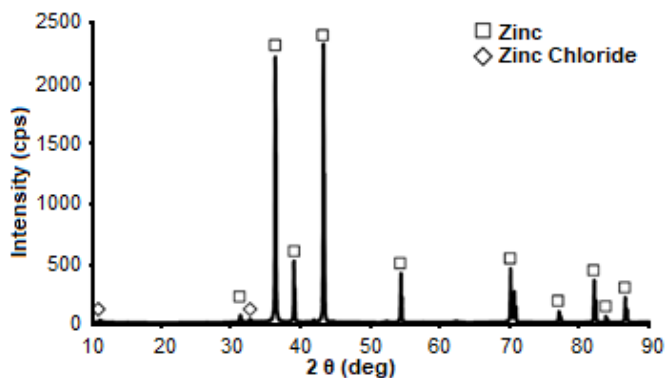


Fig 14. X-Ray Diffraction of various corrosion product for galvanized steel after exposure in Ciwaringin Districts

Table 2. The elemental semi-quantitative composition of corrosion product on steel after exposure

Element	Mass %	
	Ciwaringin District	Eretan District
O	18.75	19.22
S	0.14	0.29
Cl	0.05	0.49
Fe	81.06	80.01

Table 3. The elemental semi-quantitative composition of corrosion product on galvanized steel after exposure

Element	Mass %	
	Ciwaringin District	Eretan District
O	5.12	14.36
Si	0.06	0.90
S	0.20	0.37
Cl	0.04	0.90
Ca	0.01	0.59
Fe	0.41	0.32
Zn	98.18	82.56

surface of galvanized steel. Furthermore, without those protective corrosion products, it could be elucidated by the fact that the chloride ion directly reacts with metallic zinc to form soluble zinc chloride, which would offer no protection from the marine environment [25]. Zinc chloride can be physically removed from the surface of galvanized steel or dissolved by rain or condensation [27] during exposure over RH 85%. Furthermore, there is the fact that the lower magnitude of corrosion rate in Ciwaringin District took place after occurrence of the initial stage. However, it could not be explained by the

presence of recent salt products on the metal surface. On the other hand, the alteration of surface appearance from shiny to dull could be considered to be the indication for the form of zincite and hydrozincite phases on the metal surface during exposure.

Table 2 shows the major elements in the semi-quantitative composition of steel after exposure. On the basis of results, the elemental concentration of both Cl and O in Eretan District is higher than those in Ciwaringin District, which related to the formation of corrosion products. Table 3 also shows the principal elements in the semi-quantitative composition of galvanized steel after exposure, which the concentration of both Cl and O in Eretan District is higher compared to those in Ciwaringin. Furthermore, the main role of chloride ion has been already described in previous section, where the magnitude of corrosion rates of both metals was higher with the closeness to the coastline. In addition, the effect of environmental parameters such as RH, rainfall, and air temperature could vary the severe behavior of corrosion each metal.

■ CONCLUSION

The magnitude of corrosion rate for steel was much higher than that for galvanized steel in both Eretan and Ciwaringin Districts due to no protection of zinc coating on the surface of the steel. The distance from coastline has a significant impact on the magnitude of corrosion rate, where both metals in Ciwaringin are lower than that in Eretan because of the presence of chloride ion. The high relative humidity and the intensity of rainfall also contribute to the severity of corrosion rates. A uniform corrosion attack was observed for both metals during exposure. The morphology of phases found in the corrosion product of steel in both districts is predominantly of lepidocrocite (γ -FeOOH). In Eretan, the typical phase from the marine environment was also found as magnetite (Fe_3O_4), but it was found as goethite (α -FeOOH) in Ciwaringin. The corrosion products of galvanized steel are identified as zincite, hydrozincite, and simonkolleite in Eretan, which are the characteristic of coastline atmosphere phases, but not in Ciwaringin. The

formation of rust products for both metals can lead to a decrease of further corrosion attacks due to the barrier between the metal and corrosive environments. The galvanized steel is outstanding to mitigate the severity of atmospheric corrosion compared to that of carbon steel.

■ REFERENCES

- [1] Badea, G.E., Cret, P., Lolea, M., and Setel, A., 2011, Studies of carbon steel corrosion in atmospheric conditions, *Acta Tech. Corviniensis*, 4, 25–28.
- [2] Hoerlé, S., Mazaudier, F., Dillmann, Ph., and Santarini, G., 2004, Advances in understanding atmospheric corrosion of iron. II. Mechanistic modelling of wet-dry cycles, *Corros. Sci.*, 46 (6), 1431–1465.
- [3] Chico, B., De la Fuente, D., Díaz, I., Simancas, J., and Morcillo, M., 2017, Annual atmospheric corrosion of carbon steel worldwide. An integration of ISOCORRAG, ICP/UNECE and MICAT databases, *Materials*, 10 (6), 601.
- [4] Xu, N., Zhao, L., Ding, C., Zhang, C., Li, R., and Zhong, Q., 2002, Laboratory observation of dew formation at an early stage of atmospheric corrosion of metals, *Corros. Sci.*, 44 (1), 163–170.
- [5] Castro-Borges, P., and Veleva, L., 2015, Time of wetness and HR-T complex as tools for corrosion risk evaluation in a concrete block exposed to a humid tropical environment, *Rev. Constr.*, 14 (2), 65–71.
- [6] Feliu, S., Morcillo, M., and Chico, B., 1999, Effect of distance from sea on atmospheric corrosion rate, *Corrosion*, 55 (9), 883–891.
- [7] Jaén, J.A., Iglesias, J., and Hernández, C., 2012, Analysis of short-term steel corrosion products formed in tropical marine environments of Panama, *Int. J. Corros.*, 2012, 162729.
- [8] Roberge, P.R., 2000, *Handbook of Corrosion Engineering*, 2nd Ed., McGraw-Hill, New York.
- [9] Parisot, R., Forest, S., Pineau, A., Grillon, F., Demonet, X., and Maigne, J.M., 2004, Deformation and damage mechanisms of zinc coatings on hot-dip galvanized steel sheets: Part 1, Deformation modes, *Metall. Mater. Trans. A*, 35 (3), 797–811.
- [10] Nuraini, L., Prifiharni, S., Priyotomo, G., Sundjono, Gunawan, H., and Purawardi, I., 2018, Atmospheric corrosion performance of different steels in early exposure in the coastal area region West Java, Indonesia, *AIP Conf. Proc.*, 1964, 020040.
- [11] Okonkwo, P.C., Shakoor, R.A., and Mohamed, A.M.A., 2015, Environmental factors affecting corrosion of pipeline steel: A review, *IJMPERD*, 5 (5), 57–70.
- [12] Sen, A., and Tareq, M.S.H., 2016, Effect of zinc coating thickness on the corrosion behavior of galvanized corrugated iron sheets in fresh water, brine (3.5% NaCl) and sea water environments, *Int. J. Sci. Eng. Invest.*, 5 (54), 134–137.
- [13] Saravanan, P., and Srikanth, S., 2019, Post treatment of hot dip galvanized steel sheet-chromating, phosphating and other alternative passivation technologies, *J. Mater. Sci. Appl.*, 3, 1–22.
- [14] Prifiharni, S., Nuraini, L., Priyotomo, G., Sundjono, Gunawan, H., and Purawardi, I., 2018, Corrosion performance of steel and galvanized steel in Karangsong and Limbangan sea water environment, *AIP Conf. Proc.*, 1964, 020038.
- [15] Li, Z.W., Marston, N.J., and Jones, M.S., 2013, *Update of New Zealand's atmospheric corrosivity map*, BRANZ Study Report 288, BRANZ Ltd., Judgeford, New Zealand.
- [16] BMKG, 2019, *Data Online Pusat Database-BMKG*, http://dataonline.bmkg.go.id/dashboard_user.
- [17] Corvo, F., Pérez, T., Reyes, J., Dzib, L., González-Sánchez, J., and Castañeda, A., 2009, "Atmospheric corrosion in tropical humid climates" in *Environmental Degradation of Infrastructure and Cultural Heritage in Coastal Tropical Climate*, 1st Ed., Eds. González-Sánchez, J., Corvo, F., and Acuña-González, N., Transworld Research Network, Kerala, India, 1–34.
- [18] Priyotomo, G., Nuraini, L., Prifiharni, S., and Sundjono, 2018, Corrosion behavior of mild steel in seawater from Karangsong and Eretan of West Java Region, Indonesia, *Indones. J. Mar. Sci. Technol.*, 11 (2), 184–191.
- [19] Sundjono, Priyotomo, G., Nuraini, L., and Prifiharni, S., 2017, Corrosion behavior of mild steel in seawater from northern coast of Java and

- southern coast of Bali, Indonesia, *J. Eng. Technol. Sci.*, 49 (6), 770–784.
- [20] International Organization for Standardization, 2012, *Corrosion of metals and alloys - Corrosivity of atmospheres - Classification, determination and estimation*, International Standard of ISO 9223, Switzerland, 12.
- [21] Sica, Y.C., Kenny, E.D., Portella, K.F., and Filho, D.F.C., 2007, Atmospheric corrosion performance of carbon steel, galvanized steel, aluminum and copper in the North Brazilian coast, *J. Braz. Chem. Soc.*, 18 (1), 153–166.
- [22] Raman, A., 1987, "Atmospheric corrosion problems with weathering steels in Louisiana bridges" in *STP965-EB Degradation of Metals in the Atmosphere*, Eds. Dean, S., and Lee, T., ASTM International, West Conshohocken, PA, 16–29.
- [23] Morcillo, M., Chico, B., Alcántara, J., Díaz, I., Simancas, J., and de la Fuente, D., 2015, Atmospheric corrosion of mild steel in chloride-rich environments. Questions to be answered, *Mater. Corros.*, 66 (9), 882–892.
- [24] Del Angel, E., Vera, R., and Corvo, F., 2015, Atmospheric corrosion of galvanised steel in different environments in Chile and Mexico, *Int. J. Electrochem. Sci.*, 10, 7985–8004.
- [25] Chen, Y.Y., Chung, S.C., and Shih, H.C., 2006, Studies on the initial stages of zinc atmospheric corrosion in the presence of chloride, *Corros. Sci.*, 48 (11), 3547–3564.
- [26] Rodríguez, J.J.S., Hernández, F.J.S., and González-González, J.E., 2002, XRD and SEM studies of the layer of corrosion products for carbo steel in various different environments in the province of Las Palmas (The Canary Islands, Spain), *Corros. Sci.*, 44 (11), 2425–2438.
- [27] Vera, R., Guerrero, F., Delgado, D., and Araya, R., 2013, Atmospheric corrosion of galvanized steel and precipitation runoff from zinc in a marine environment, *J. Braz. Chem. Soc.*, 24 (3), 449–458.
- [28] Persson, D., Thierry, D., and Karlsson, O., 2017, Corrosion and corrosion products of hot dipped galvanized steel during long term atmospheric exposure at different sites world-wide, *Corros. Sci.*, 126, 152–165.
- [29] Saarimaa, V., Kaleva, A., Nikkanen, J.P., Heinonen, S., Levänen, E., Väisänen, P., Markkula, A., and Juhanoja, J., 2017, Supercritical carbon dioxide treatment of hot dip galvanized steel as a surface treatment before coating, *Surf. Coat. Technol.*, 331, 137–142.

Determination of Total Flavonoid Content in Medicinal Plant Leaves Powder Using Infrared Spectroscopy and Chemometrics

Lestyo Wulandari*, Bayu Dwi Permana, and Nia Kristiningrum

Pharmaceutical Analysis and Chemometrics Research Group, Faculty of Pharmacy, University of Jember, Jl. Kalimantan 37, Jember 68121, East Java, Indonesia

* **Corresponding author:**

email: lestyowulandari@unej.ac.id

Received: June 26, 2019

Accepted: April 30, 2020

DOI: 10.22146/ijc.47047

Abstract: Flavonoid is phenolic compounds consisting of fifteen carbon atoms and is commonly found in plants. Infrared (IR) spectroscopy combined with chemometrics, has been developed for a simple analysis of flavonoid in the medicinal plant leaves powder. IR spectra of selected medicinal plant powder were correlated with flavonoid content using chemometrics. The chemometric methods used for calibration analysis were Partial Least Square (PLS), Principal Component Regression (PCR), and Support Vector Regression (SVR). After the calibration model was formed, it was then validated using Leave-One-Out-Cross-Validation (LOOCV) and 2-fold cross-validation. In this study, the PLS of the Near-infrared (NIR) calibration model showed the best calibration with R-Square and RMSEC values of 0.9676524 and 0.0978202, respectively. The LOOCV of PLS of the NIR calibration model has the R-square and RMSE values of 0.9850164 and 0.067663, respectively. The 2-fold cross-validation gave the R-square and RMSE values of 0.9857071 and 0.2104665, respectively. PLS of the NIR calibration model was further used to predict unknown flavonoid content in commercial samples. The significance of flavonoid content that has been measured by NIR and UV-Vis spectrophotometry was evaluated with paired samples T-test. The flavonoid content that has been measured with both methods gave no significant difference.

Keywords: medicinal plant leaves powder; total flavonoid content; NIR; FTIR; chemometric

■ INTRODUCTION

Traditional medicine is a mixture of ingredients from plants, animals, and minerals that have been used for generations in accordance with the prevailing norms in society [1]. The use of traditional medicines in the past decade has increased along with the development of lifestyle called “back to nature” and rising prices of modern medicines. Indonesia, according to Torri [2], is a country with a biodiversity rank 3rd in the world where there are around 30,000 species out of a total of 40,000 species of plants. However, only 25% or about 7,500 plant species have been known or examined for their potential use as medicinal plants. This shows that there are still many species of plants in Indonesia that have no known potential as a medicinal plant, so that the research about active chemical compounds in plants needs to be done.

Parts of the plant that are often used for medicines and research materials are the leaves. This is related to some advantages of leaves, such as ease of use, more productivity, and readily available than other parts of the plant [3]. One of the active chemical compounds that are often found in plants, especially in parts of the leaves is flavonoid [4]. Flavonoid is phenolic compounds consisting of 15 carbon atoms and is commonly found in plants [5]. Flavonoid has several pharmacological activities, such as antioxidants, hepatoprotective, antibacterial, anti-inflammatory, anticancer, antiviral and vasodilator [4].

Several analytical techniques have been developed for determining flavonoid content such as UV spectrometry, mass spectrometry, gas chromatography (GC), thin-layer chromatography, high-performance liquid chromatography (HPLC) and capillary

electrophoresis [6]. These methods can measure accurately, but the process is too long and requiring various reagents or solvents that are quite expensive [6]. Based on this case, a simple, selective, and eco-friendly method is required.

Infrared (IR) spectroscopy method is an analytical method that has several advantages, such as non-destructive (does not damage the sample), does not cause pollution, does not require chemical reagents (without solvents) and can analyze at high speed [7]. On the other side, infrared spectroscopy has the disadvantage that the data formed from the results of the analysis are quite complicated and with overlapping spectra [8], therefore multivariate chemometrics analysis is needed to analyze data from the infrared spectra. The chemometric calibration model is a statistical and mathematical analysis technique for processing, evaluating, and interpreting

relevant information from (Near-infrared) NIR and (Fourier Transform-infrared) FTIR spectra data. This method can be used to analyze NIR and FTIR spectrum data, which have overlapping absorption bands [9]. The functions of chemometrics are to find good statistical correlations between spectral data and chemical parameter data for the model development process. Chemometric methods are often applied to a condition where no theory can solve or describe a problem that uses many variables (multivariate). The purpose of forming a chemometric calibration model is to describe a system that has a hidden relationship between available data and the information generated [8]. The quantitative multivariate models that are often used are Partial Least Square (PLS), Principal Component Regression (PCR), and Support Vector Regression (SVR) [10].

The objective of this research is to develop a simple, rapid and validated model of infrared spectroscopy at different altitudes by NIR and FTIR spectroscopies with chemometrics for the determination of the flavonoid content. Furthermore, the selected infrared spectroscopy calibration model with chemometrics methods was applied for determining the flavonoid content in commercial samples.

■ EXPERIMENTAL SECTION

Materials

The materials used in this study were twenty-five (25) samples of medicinal plant leaves with varieties of flavonoid content taken from the residential areas and plantation areas in Jember city, East Java, Indonesia (Table 1). Reagents used were ethanol 96% (Brataco, Indonesia), quercetin (Sigma-Aldrich), 10% aluminum chloride, potassium acetate (Merck), and filter paper. Five commercial samples were purchased from a pharmacy department store in Jember city (Chinese Teak®, Meniran®, Sambiloto®, Gotu Kola®, and Soursop®).

Instrumentation

The instruments used were NIR spectrometer (Brimrose Corporation Luminar 3070) Brimrose Software (Brimrose corp.), The Unscrambler X 10.2 software (CAMO), computer (Intel Core 2 Duo), FTIR

Table 1. Plant species used in this research

No	Scientific name (Species)	Code
1.	<i>Ocimum basilicum</i>	A
2.	<i>Cosmos caudatus</i>	B
3.	<i>Coffea canephora</i>	C
4.	<i>Nepheliumpulpaceum</i>	D
5.	<i>Persea americana</i>	E
6.	<i>Averrhoa bilimbi</i>	F
7.	<i>Pluchea indica</i>	G
8.	<i>Magnolia liliifera</i>	H
9.	<i>Moringa oleifera</i>	I
10.	<i>Morinda citrifolia</i>	J
11.	<i>Syzygium polyanthum</i>	K
12.	<i>Psidium guajava</i>	L
13.	<i>Clidemia hirta</i>	M
14.	<i>Sauropus androgynus</i>	N
15.	<i>Lunasia amara</i>	O
16.	<i>Aleurites moluccana</i>	P
17.	<i>Artocarpus heterophyllus</i>	Q
18.	<i>Diplazium esculentum</i>	R
19.	<i>Piper betle</i>	S
20.	<i>Annona muricata</i>	T
21.	<i>Syzygium aqueum</i>	U
22.	<i>Leucaena leucocephala</i>	V
23.	<i>Chrysophyllum cainito</i>	W
24.	<i>Pandanus sp</i>	X
25.	<i>Carica papaya</i>	Y

spectrometer (Bruker Alpha) and UV-Vis spectrophotometer (Hitachi U 1800), moisture analyzer (PMB 53), grinding Machine (Philips HR2116), stainless steel sieves 100 mesh (Advantech), analytical balance (Sartorius), and oven (Memmert).

Procedure

Preparation and testing of the water percentage content of the leaves powder

The leaves that had been collected were then pulverized using a grinding machine and sieved using a 100 mesh sieve. The concentration of water content was tested using a moisture analyzer until the water content was less than 10% [11]. If the water content of the sample was greater than 10%, the powder was dried again in an oven at 50 °C until the water content of the sample was less than 10%.

Analysis using NIR and FTIR spectrophotometers

All samples were scanned on both infrared spectroscopy instruments (NIR and FTIR). Each sample was examined five replications by NIR spectrometer with five shots for each replication and three replications by the FTIR spectrometer [12]. The NIR and FTIR spectra data were obtained through Acquire Brimrose (NIR) and OPUS (FTIR) software, and each spectra data were coded.

Determination of the total flavonoid content

In this research, total flavonoid content was determined by UV-Vis spectroscopy as a reference method. This method used aluminum chloride as the reagent and quercetin as the reference compound [13]. The sample was prepared by mixing 0.5 mL of 10 mg/mL sample extract in ethanol with 3 mL of ethanol, 0.2 mL of AlCl₃ 10%, 0.2 mL of 1 M potassium acetate and then diluted to 10 mL in distilled water. After incubation at room temperature for 30 min, the absorbance of the mixture solution was measured at 428 nm by using a UV-Vis spectrophotometer. Various standard solutions of quercetin (2.0, 4.0, 6.0, 8.0, 10.0, 12.0 and 15.0 µg/mL) were also prepared.

Determination and validation of the calibration model

Spectral data of the samples that had been scanned using NIR and FTIR spectrophotometers were analyzed

using the Unscrambler X 10.2 (Camo Analytics, Norway) software. The spectral data of the training sets were correlated with the flavonoid concentration of the samples to form the calibration model. The calibration models used were PLS (partial least square), PCR (principal component regression), and SVR (support vector regression).

PLS model is a multivariate projection method for modeling a relationship between dependent variables (Y) and independent variables (X). The principle of PLS is to find the component in the input matrix (X) that describe as much as possible the relevant variations in the input variables and at the same time have a maximal correlation with the target value in Y, given less weight to the variations that are irrelevant or noisy [14]. Therefore, PLS models, both X and Y, simultaneously to find the latent variables in X that will predict the latent variables in the Y model. The PCR model has a principle like PLS, but the difference is that PCR can eliminate several predictors by using several major components [15]. The SVR model is a result of the development of a regression method that can be used to predict the regression method in a statistical approach. The SVR principle is based on the calculation of linear regression functions in high-dimensional spaces where the input data is mapped through nonlinear functions [16].

The concentration of flavonoid of samples determined using UV-Vis spectroscopy as a response (variable y) and absorbance value of infrared spectra as a predictor (variable x). The assessment criteria in forming a calibration model were the value of R², RMSEC (root mean square error of calibration), and RMSECV (root mean square error of cross-validation). The calibration model was stated to be good and has the best prediction if the correlation value R² is greater (greater than 0.91 or close to 1), and the RMSEC and RMSECV values were getting smaller [15].

The calibration model selected was then validated using a Leave-One-Out-Cross-Validation (LOOCV), and 2-Fold-Cross-Validation (2-FCV) approaches. LOOCV was evaluated by omitting a data point, or a sample from the training data set one at a time. Then, the remaining data sets or samples were used to build a

new calibration model, which was then used to predict the omitted data set or sample. The second validation method was 2-fold cross-validation. In this research, validation with 2-fold cross-validation used 5 independent samples (test sets) with known concentrations. The calibration model formed were used to predict the concentration of flavonoid in the test set samples [17].

Applications of the selected and validated model for commercial samples

The selected and validated calibration models were applied for the determination of the total flavonoid content in the commercial samples. A spectrum of commercial samples was scanned then was analyzed by a chemometric calibration model in order to predict the concentration of the total flavonoid content [12].

Analysis of data

The results of the determination of the total flavonoid content in the commercial samples by infrared spectroscopy and UV-Vis spectrophotometry methods were compared using the Two Paired Samples t-Test with SPSS Ver. 22 (IBM, USA). Data analysis was carried out at a confidence level of 95% with significance or Sig. (2-tailed) > 0.05 [18-19].

■ RESULTS AND DISCUSSION

Preparation and Testing of Water % Content

Each of the samples was given a unique code, and its moisture content of < 10% was presented in Table 2. The

water content of sample powder has to prepared below 10% in order to reduce the interfere of spectra measurements of the sample and to stop the process enzymatic reactions of microbial that can reduce the quality of sample powder [12]. The results of NIR and FTIR spectra data are shown in Fig. 1 and the spectral data of all samples were used as predictors on the calibration models.

Total Flavonoid Content in the Sample

Total flavonoid content in the sample was determined in mg quercetin equivalent (QE). Quercetin is used as a standard (comparison) because it belongs to the largest groups of flavonol that are often found in plants, where its amount is between 60–75% of flavonoids. In addition, quercetin also has keto groups on C-4 atoms and hydroxyl groups on C-3 or C-5 atoms, which can react to form acidic complexes with $AlCl_3$ [13]. The results of the total flavonoid content are as shown in Table 3. The range of total flavonoids is 3–30 mg QE/g powder. The samples were then divided into two categories, namely training sets (used in forming the calibration models) and test sets (used for validation on selected calibration models).

NIR and FTIR Calibration Models

The calibration model was formed by correlating NIR and FTIR spectra of the samples with the total flavonoid content that was determined by spectroscopy

Table 2. Code name and % water content of the sample

No	Code	% of water content \pm SD	No	Code	% of water content \pm SD
1.	A	4.633% \pm 0.0764	14.	N	5.250% \pm 0.1000
2.	B	5.650% \pm 0.0500	15.	O	3.500% \pm 0.0866
3.	C	4.767% \pm 0.1041	16.	P	4.200% \pm 0.0500
4.	D	5.217% \pm 0.0289	17.	Q	3.233% \pm 0.0764
5.	E	4.217% \pm 0.0764	18.	R	4.750% \pm 0.2000
6.	F	4.300% \pm 0.0500	19.	S	5.183% \pm 0.1528
7.	G	4.150% \pm 0.0500	20.	T	4.750% \pm 0.1323
8.	H	4.250% \pm 0.1000	21.	U	3.133% \pm 0.0764
9.	I	3.883% \pm 0.0764	22.	V	4.500% \pm 0.0500
10.	J	4.783% \pm 0.0764	23.	W	4.233% \pm 0.1041
11.	K	4.483% \pm 0.1258	24.	X	4.500% \pm 0.1000
12.	L	2.867% \pm 0.0764	25.	Y	4.133% \pm 0.0764
13.	M	3.567% \pm 0.0289			

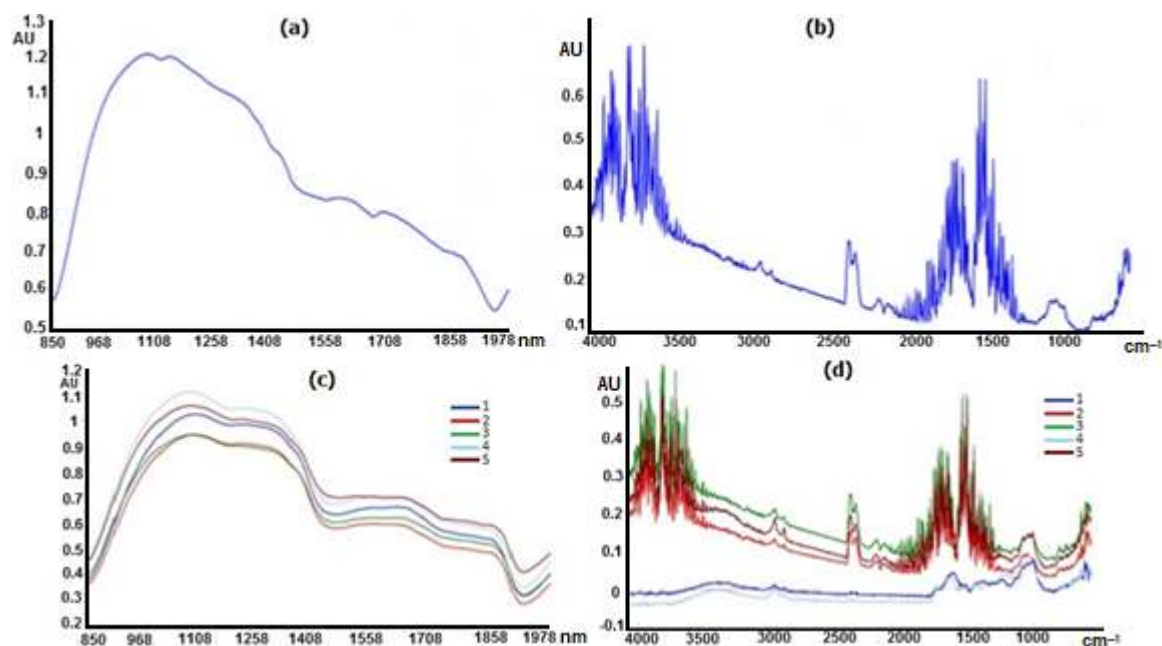


Fig 1. (a) NIR spectra of quercetin (b) FTIR spectra of quercetin (c) NIR spectra of samples (d) FTIR spectra of samples, 1) *Ocimum basilicum*, 2) *Nephelium lappaceum*, 3) *Coffea canephora*, 4) *Cosmos caudatus*, 5) *Persea americana*

Table 3. The results of the total flavonoid content in the training set and test sample

Code	Category sample	Average mg QE/g \pm SD	Code	Category sample	Average mg QE/g \pm SD
A	Training Set	13.22 \pm 0.0273	N	Training Set	15.11 \pm 0.0479
B	Training Set	29.93 \pm 0.0136	O	Training Set	10.39 \pm 0.0118
C	Training Set	8.108 \pm 0.0236	P	Training Set	7.361 \pm 0.0136
D	Training Set	9.439 \pm 0.0295	Q	Training Set	7.985 \pm 0.0277
E	Training Set	14.93 \pm 0.0236	R	Training Set	9.017 \pm 0.0518
F	Training Set	13.24 \pm 0.0174	S	Training Set	11.46 \pm 0.0236
G	Training Set	12.49 \pm 0.0177	T	Training Set	14.47 \pm 0.0169
H	Training Set	9.176 \pm 0.0192	U	Test Set	8.139 \pm 0.0236
I	Training Set	16.35 \pm 0.0320	V	Test Set	26.30 \pm 0.0459
J	Training Set	8.688 \pm 0.0086	W	Test Set	3.726 \pm 0.0115
K	Training Set	10.57 \pm 0.0136	X	Test Set	4.048 \pm 0.0216
L	Training Set	12.91 \pm 0.0107	Y	Test Set	17.92 \pm 0.0123
M	Training Set	5.350 \pm 0.0136			

UV-Vis as the reference method. In order to create a calibration model, 362 data were used as the training set in the NIR, while 60 data were used as the training set in the FTIR. The calibration models used were PLS, PCR, and SVR. The results of the calibration model are as shown in Table 4.

In this research, the calibration model selected and used in determining the total flavonoid content was the PLS model in the NIR. The PLS model in the NIR was chosen because it has the R-square value that is close to 1

(0.9676524) and the smallest RMSEC value (0.0978202). A calibration model is considered optimum or has a good correlation if it has an R-square value close to 1 and the smallest RMSEC value [20].

The selected PLS model was then validated with Leave-One-Out-Cross-Validation (LOOCV) and 2-Fold-Cross-Validation (2-FCV). The cross-validation was carried out for determining the accuracy and predictive ability of the models that have been formed [21]. The results of the LOOCV of PLS for the NIR calibration

Table 4. The results of PLS, PCR and SVR calibration models from NIR and FTIR spectra

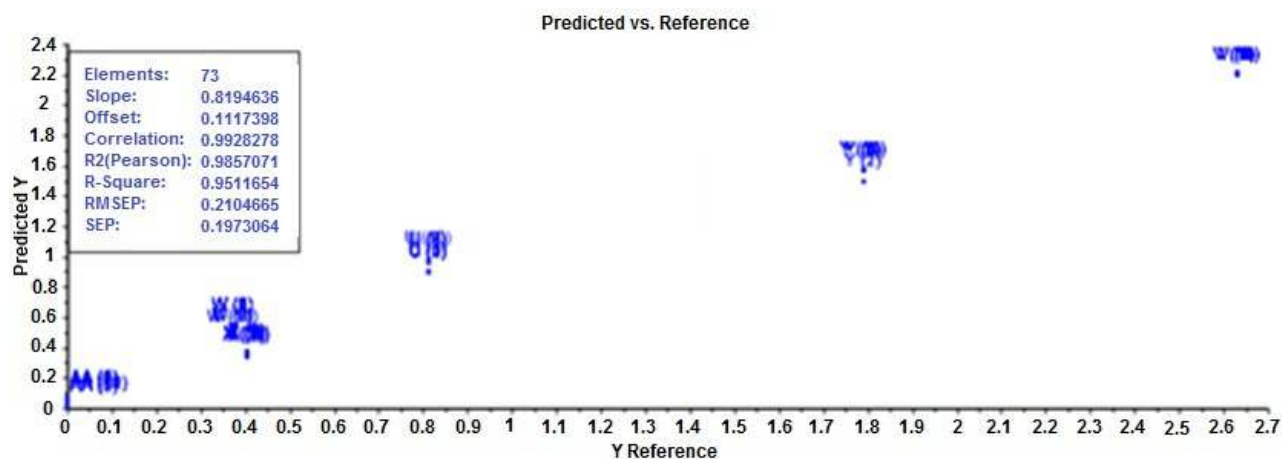
Spectra	Model	R-square Calibration	R-square Validation	RMSEC	RMSECV
NIR	PLS	0.9676524	0.9628204	0.0978202	0.1050252
	PCR	0.9592377	0.9526183	0.1098087	0.1189304
	SVR	0.5125262	0.4877062	0.4065073	0.4067137
FTIR	PLS	0.9240598	0.7372873	0.1384766	0.2625193
	PCR	0.8064864	0.6212984	0.2626473	0.3743665
	SVR	0.9136168	0.5951188	0.1674283	0.3239591

model show the R-square and RMSE values are 0.9850164 and 0.067663, respectively. The 2-fold cross-validation results show the R-square and RMSE values are 0.9857071 and 0.2104665, respectively (Fig. 2). Based on the results of LOOCV and 2-fold cross-validation, it can be concluded that the PLS calibration model formed has good predictability and accuracy. The model can be applied to commercial samples.

Selected and Validated Model Applications in the Commercial Samples

The commercial samples were scanned using a NIR

spectrophotometer five times with five replicates each time, and as a result, 125 data were obtained. All of the collected data were analyzed by being included in the Unscrambler X 10.2 software to determine the total flavonoid content of the sample. Furthermore, all of the data of the total flavonoid content of the samples (mg QE/g powder) obtained using NIR spectroscopy were compared with the results of the sample content obtained using UV-Vis spectrophotometry and the SPSS software. The results of the determination of the total flavonoid content in the commercial samples are as shown in Table 5.

**Fig 2.** The result of a 2-fold cross-validation PLS model**Table 5.** The results of the determination of the total flavonoid content in the commercial samples

Real Sample	Average of total flavonoid content (mg QE/g) \pm SD	
	NIR Spectroscopy	UV-Vis Spectrophotometry
Chinese Teak [®]	17.95 \pm 0.4119	18.12 \pm 0.0136
Meniran [®]	12.14 \pm 0.0503	12.26 \pm 0.0136
Sambiloto [®]	12.48 \pm 0.0964	12.58 \pm 0.0307
Gotu Kola [®]	11.25 \pm 0.1350	11.09 \pm 0.0307
Soursop [®]	13.98 \pm 0.0973	14.15 \pm 0.0545

The results of total flavonoid content in the commercial samples using NIR spectroscopy and UV-Vis spectrophotometry were compared using the "Paired Sample T-test". The purpose was to find out whether there was a significant difference between the total flavonoid content in the commercial samples determined using the NIR spectroscopy over UV-Vis spectrophotometry. In the paired sample T-test, decision forming is based on its significance value, if the significance (Asymp. Sig) < 0.05, then Ho (no significant difference) is rejected and Ha (there are significant differences) accepted. Conversely, if the significance (Asymp. Sig) > 0.05, then Ho is accepted, and Ha is rejected. The results of the paired sample T-test showed that there were no significant differences in the determination of the total flavonoid content in the commercial samples with the two methods, where the p-value obtained was 0.249 with a 95% confidence level.

■ CONCLUSION

The NIR spectroscopy, combined with multivariate calibrations methods, can be used to determine the total flavonoid content in medicinal plant leaf powder. The selected calibration model was PLS (Partial Least Square) with R-square, and RMSE calibration values were 0.9676524 and 0.0978202, respectively. The suggested method is simple, selective, validated, and eco-friendly.

■ REFERENCES

- [1] Yuan, H., Ma, Q., Ye, L., and Piao, G., 2016, The traditional medicine and modern medicine from natural products, *Molecules*, 21 (5), 559.
- [2] Torri, M.C., 2013, Traditional jamu versus industrial jamu: Perceptions and beliefs of consumers in the city of Yogyakarta: What future for traditional herbal medicine in urban Indonesia?, *IJESB*, 19 (1), 1–20.
- [3] Yusro, F., Mariani, F., Diba, F., and Ohtani, K., 2014, Inventory of medicinal plants for fever used by four Dayak sub ethnic in West Kalimantan, Indonesia, *Kuroshio Sci.*, 8 (1), 33–38.
- [4] Kumar, S., and Pandey. A.K., 2013, Chemistry and biological activities of flavonoids: An overview, *Sci. World J.*, 2013, 162750.
- [5] Brodowska, K.M., 2017, Natural flavonoids: Classification, potential role, and application of flavonoid analogues, *Eur. J. Biol. Res.*, 7 (2), 108–123.
- [6] Siddiqui, M.R., AlOthman, Z.A., and Rahman, N., 2017, Analytical techniques in pharmaceutical analysis: A review, *Arabian J. Chem.*, 10 (Suppl. 1), S1409–S1421.
- [7] Haas, J., and Mizaikoff, B., 2016, Advances in mid-infrared spectroscopy for chemical analysis, *Annu. Rev. Anal. Chem.*, 9, 45–68.
- [8] Gad, H.A., El-Ahmady, S.H., Abou-Shoer, M.I., and Al-Azizi, M.M., 2013, Application of chemometrics in authentication of herbal medicines: A review, *Phytochem. Anal.*, 24 (1), 1–24.
- [9] Ozaki, Y., 2012, Near-infrared spectroscopy-its versatility in analytical chemistry, *Anal. Sci.*, 28 (6), 545–563.
- [10] Morellos, A., Pantazi, X.E., Moshou, D., Alexandridis, T., Whetton, R., Tziotziou, G., Wiebensohn, J., Bill, R., and Mouazen, A.M., 2016, Machine learning based prediction of soil total nitrogen, organic carbon and moisture content by using VIS-NIR spectroscopy, *Biosyst. Eng.*, 152, 104–116.
- [11] Hunt Jr., E.R., Daughtry, C.S.T., and Li, L., 2016, Feasibility of estimating leaf water content using spectral indices from worldview-3's near-infrared and shortwave infrared bands, *Int. J. Remote Sens.*, 37 (2), 388–402.
- [12] Wulandari, L., Retnaningtyas, Y., and Lukman, H., 2016, Analysis of flavonoid in medicinal plant extract using infrared spectroscopy and chemometrics, *J. Anal. Methods Chem.*, 2016, 4696803.
- [13] Mathur, R., and Vijayvergia, R., 2017, Determination of total flavonoid and phenol content in *Mimusops elengi*, *Int. J. Pharm. Sci. Res.*, 8 (12), 5282–5285.
- [14] Mantanus, J., 2012, New pharmaceutical applications involving near-infrared spectroscopy as a pat compliant process analyzer, *Dissertation*, Faculty of Medicine, University of Liege, Belgium.

- [15] Lengkey, L.C.E.C., Budiastira, I.W., Seminar, K.B., and Purwoko, B.S., 2013, Determination of chemical properties in *Jatropha curcas* L. seed IP-3P by partial least-squares regression and near-infrared reflectance spectroscopy, *Int. J. Agric. Innov. Res.*, 2 (1), 41–48.
- [16] Gu, B., Sheng, V.S., Wang, Z., Ho, D., Osman, S., and Li, S., 2015, Incremental learning for ν -support vector regression, *Neural Networks*, 67, 140–150.
- [17] Ritz, M., Vaculikova, L., and Plevova, E., 2011, Application of infrared spectroscopy and chemometric methods to identification of selected minerals, *Acta Geodyn. Geomater.*, 8 (1), 47–58.
- [18] Vasishth, S., and Nicenboim, B., 2016, Statistical methods for linguistic research: Foundational ideas – Part I, *Lang. Linguist. Compass*, 10 (8), 349–369.
- [19] Kumar, R., and Kumar, V., 2015, Discrimination of various paper types using diffuse reflectance ultraviolet–visible near-infrared (UV-Vis-NIR) spectroscopy: Forensic application to questioned documents, *Appl. Spectrosc.*, 69 (6), 714–720.
- [20] Georgieva, M., Nebojan, I., Mihalev, K., Yoncheva, N., Kljusurić, J.G., and Kurtanjek, Z., 2013, Application of NIR spectroscopy and chemometrics in quality control of wild berry fruit extracts during storage, *Croatian J. Food Technol. Biotechnol. Nutr.*, 8 (3-4), 67–73.
- [21] Cheng, H., Garrick, D.J., and Fernando, R.L., 2017, Efficient strategies for leave-one-out cross-validation for genomic best linear unbiased prediction, *J. Anim. Sci. Biotechnol.*, 8, 38.

Varietal Discrimination of Pineapple (*Ananas comosus* L.) Using Chromatographic Fingerprints and Chemometrics

Almie Amira Munaras Khan^{1,*}, Norashikin Saim¹, Rossuriati Dol Hamid¹,
Rozita Osman¹, and Siti Raihan Zakaria²

¹Faculty of Applied Sciences, Universiti Teknologi MARA (UiTM), Shah Alam 40450, Selangor, Malaysia

²Faculty of Applied Sciences, Universiti Teknologi MARA Pahang, Jengka 26400, Pahang, Malaysia

* **Corresponding author:**

tel: +60-173398547

email: almie.amiramk@yahoo.com

Received: July 1, 2019

Accepted: December 8, 2019

DOI: 10.22146/ijc.47159

Abstract: Online solid-phase extraction-liquid chromatography (online SPE-LC) with diode array detector (DAD) was used to obtain the chromatographic fingerprint of bioactive compounds of pineapple (*Ananas comosus* L.). The extracts from 40 samples of three different varieties of pineapple (Morris, MD2, and Josaphine) were obtained using pressurized liquid extraction (PLE) prior to separation using online SPE-LC. The SPE-LC method was optimized and validated and applied to 40 pineapple samples of those three varieties. Seven bioactive compounds identified include catechin, epicatechin, chlorogenic acid, ferulic acid, quercetin, myricetin, and bromelain. For varietal discrimination, the relative areas of 16 selected peaks were subjected to chemometric techniques. The three pineapple varieties were successfully discriminated using cluster analysis (CA) and principal component analysis (PCA).

Keywords: online SPE-LC; pineapple; bioactive compounds; chromatographic fingerprint; chemometrics

■ INTRODUCTION

Pineapple (*Ananas comosus* L.) is widely cultivated in tropical countries, including Malaysia [1-2]. Pineapple is known to contain a significant amount of bioactive compounds such as anthocyanins, polyphenols, and bromelain, a health-inducing enzyme. Many studies have reported on the biological properties of pineapple such as anti-oxidative [3], anti-browning [4], anti-inflammatory, and anti-platelet activities [5]. Food policies such as stated in General Food Law Regulation No.178/2002 gives the right to the consumers to obtain truthful information about the fruit they purchased, and the data includes the composition, types, grades, and origin of the food [6]. The current quality control of fruits in Malaysia is based solely on the morphological traits and with the manual inspection done by the agricultural officer [7]. This approach depends on the human's perception and judgment, which may be biased and inconsistent.

The World Health Organization (WHO) has recommended chromatographic fingerprint analysis as a

quality control strategy for foods with medicinal values [8-9]. The chromatographic fingerprint of phenolic compounds has been successfully used by researchers in the authentication of honey [10], olive oil [11-12], and herbal medicines [13]. The development of a valuable chromatographic fingerprint requires efficient extraction, cleanup, and separation methods. Pressurized liquid extraction (PLE) has been successfully applied for the extraction of thermal-sensitive bioactive compounds, including phenolic compounds from plants and fruits [14-15]. It involves extraction using solvents in a liquid state at elevated temperature and pressure to enhance the extraction process. For plant extracts, removal of interference and analyte concentration, known as the cleanup step, is usually required prior to analysis [2]. Solid-phase extraction (SPE) usually consists of 4 steps: conditioning/equilibration, loading, washing, and elution. This technique has been largely applied and proved to be a good alternative to traditional liquid-liquid extraction. Due to the laborious steps in SPE, an

online SPE-LC is getting more attention. The SPE process in both approaches follows the same steps and is governed by the same principles. However, using online SPE-LC, the eluted analytes are directly transferred into the analytical column for separation and quantitation. Thus, online SPE-LC approach has the advantages of a significant reduction in sample preparation time and less human handling.

In this study, an online SPE-LC was developed to obtain a chromatographic fingerprint of selected bioactive compounds as an alternative to traditional quality control of pineapple. The developed method was used to analyze three common varieties of pineapple in Malaysia (MD2, Morris, and Josaphine). These varieties were selected because seventy percent of the fresh pineapple fruit produced in Malaysia is from Morris variety. Josaphine pineapple is the most common variety cultivated on an annual cycle in Malaysia, while MD2 variety is listed as major export crop under Malaysia National Key Economic Agenda (NKEA). Chemometric methods such as cluster analysis (CA) and principal component analysis (PCA) were applied to the dataset of the chromatographic fingerprints to discriminate the selected pineapple varieties.

■ EXPERIMENTAL SECTION

Materials

Forty samples of ripened fruits of three pineapple varieties (Moris, MD2, and Josaphine) were purchased from local traders. The fruits were peeled, cut into thin pieces, and dried for 48 h at 45 °C in an oven (Memmert UN110). The dried flesh was stored in a dark-covered container prior to extraction. The standards for selected bioactive compounds (epicatechin, catechin, quercetin, chlorogenic acid, ferulic acid, myricetin, and bromelain) were purchased from Merck (Darmstadt, Germany). Acetonitrile (HPLC grade), methanol (HPLC grade), and acetic acid were purchased from Merck Schuchardt (Hohenbrunn, Germany).

Instrumentation

Pressurized liquid extraction

PLE was performed using Dionex ASE 350 accelerated solvent extractor (Thermo Scientific Ltd.

Surrey, UK). The extracts from 40 pineapple samples were obtained using the PLE method. Dried flesh of pineapple (60 g) was accurately weighed, mixed with an equal amount of diatomaceous earth, and transferred to a 100 mL PLE stainless steel extraction cell with cellulose filter at the bottom end to eliminate particles in the extracts. The sample cell was then closed to medium tightness and placed into the carousel of the ASE 350 system. Extraction was performed using single cycle mode with 100% of methanol as the solvent. The extracted analyte was purged from the sample cell using pressurized nitrogen. The PLE parameters were: static cycle, 1; flush volume, 100%; purge time, 120 sec; and the optimized PLE parameters were: extraction temperature, 105 °C; extraction time, 20 min. After PLE, each extract was transferred into online SPE-LC vials before analysis [16].

Online SPE-LC

Analysis of bioactive compounds was done using online SPE-LC (Dionex Ultimate 3000 Liquid Chromatography system) with diode array detector (DAD) using two C18 columns, a 5 µm, 4.6 mm × 50 mm for SPE cleanup and a 5 µm, 4.6 mm × 250 mm for separation of compounds. The column temperature was maintained at 40 °C in an oven, and the injection volume was 100 µL. Eluted compounds were monitored at the optimized detection wavelength of 280 nm. Data acquisition was performed by Chromeleon software. The mobile phase consisted of ultrapure water (A), methanol (B), and acetonitrile (C). The separation done with application of gradient elution 0–19 min: 50% A: 20% B: 30% C; 20–25 min: gradient elution 15% A: 40% B: 45% C; 25–40 min: gradient elution 10% A: 80% B: 10% C. The flow rate was set at 1 mL/min throughout the analysis [17]. Fig. 1 shows the chromatogram of selected bioactive compounds obtained using the optimized online SPE-LC method.

Procedure

Calibration and linearity

The standard solution of all bioactive compounds was prepared in HPLC grade methanol. The concentration of standards of bioactive compounds was

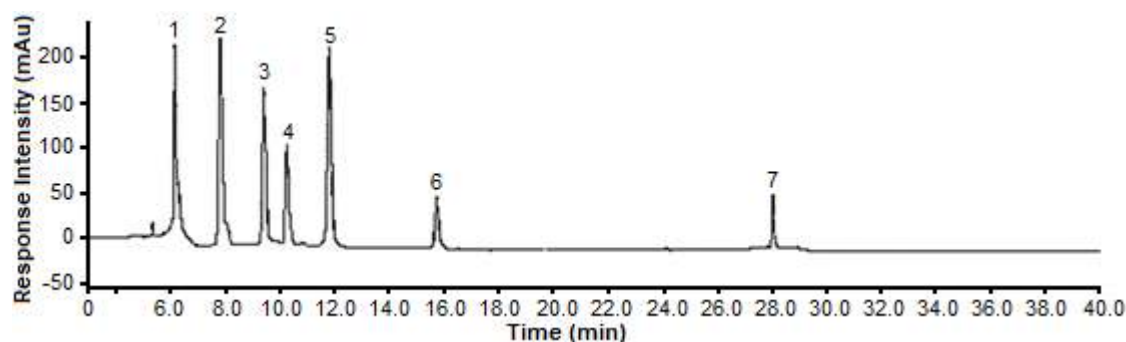


Fig 1. Chromatogram of selected bioactive compounds standards (100 mg/L), 1) catechin; 2) epicatechin; 3) chlorogenic acid; 4) ferulic acid; 5) myricetin; 6) quercetin; 7) bromelain

prepared between 5–200 mg/L for quantification in pineapple samples. Linearity was determined as (R^2) of the calibration graph. The coefficient of determination showed good linearity ($R^2 > 0.997$) as shown in Table 1.

Precision

The repeatability of this method was conducted using three replicates of the standard mixture (50 mg/L) to give low percent RSD ranging between 2.1-4.6% (Table 1).

Limit of detection and limit of quantitation

The limit of detection (LOD) and quantification (LOQ) were determined based on the signal-to-noise ratio (S/N) of about 3 and 10, respectively. The LOD values were between 2.4 and 5.2 mg/L, while the LOQ values were between 8.2 and 17.1 mg/L for each standard compound (Table 1).

Data analysis

Chemometric analysis applied on the dataset of chromatographic fingerprints was done using XLSTAT 2013 software (Addinsoft, New York, NY). Peak areas of

16 selected peaks were utilized as variables to evaluate the similarities and differences in CA and PCA.

RESULTS AND DISCUSSION

Identification of selected bioactive compounds in pineapple samples was performed by comparing their retention times and UV spectra with that of the standard compounds. Fig. 2 shows the chromatograms of representative samples from the three pineapple varieties and Table 2 tabulates the amount of selected bioactive compounds in all pineapple samples. Bromelain, epicatechin and chlorogenic acid existed in all pineapple varieties. The amount of catechin was found highest in Josaphine pineapple (5.23 mg in 100 g of dried pineapple), but not detected in most MD2 samples. The presence of catechin and epicatechin was reported by a study on the Bali pineapple [18]. Catechin was also reported in grapes and teas in high amount [19]. Epicatechin, however, showed a higher amount in MD2 varieties than in other varieties.

Table 1. Coefficients of determination, precision, limit of detection (LOD) and limit of quantification (LOQ) of selected bioactive compounds

Compounds	Correlation coefficient (R^2)	LOD (mg L^{-1})	LOQ (mg L^{-1})	Precision (% RSD)
Catechin	0.997	4.2	14.1	3.2
Epicatechin	0.975	4.5	15.3	2.1
Chlorogenic acid	0.994	5.2	17.1	3.9
Ferulic acid	0.997	3.4	11.2	2.8
Quercetin	0.994	2.4	8.2	4.6
Myricetin	0.995	3.6	12.0	4.3
Bromelain	0.995	3.1	9.6	2.6

Table 2. Quantitative determination of bioactive compounds in pineapple samples (mg/100 g dried pineapples \pm RSD (n = 3), ND: not detected)

Samples	Catechin	Epicatechin	Chlorogenic acid	Ferulic acid	Myricetin	Quercetin	Bromelain
J1	4.483 \pm 0.002	1.799 \pm 0.002	1.343 \pm 0.032	1.077 \pm 0.001	0.222 \pm 0.021	0.635 \pm 0.011	7.345 \pm 0.003
J2	4.827 \pm 0.012	1.873 \pm 0.003	1.392 \pm 0.001	0.833 \pm 0.064	0.155 \pm 0.011	0.744 \pm 0.002	7.637 \pm 0.005
J3	4.601 \pm 0.041	1.947 \pm 0.011	1.445 \pm 0.002	1.109 \pm 0.011	0.302 \pm 0.001	0.619 \pm 0.004	7.762 \pm 0.029
J4	3.552 \pm 0.029	2.058 \pm 0.052	1.705 \pm 0.001	1.267 \pm 0.003	0.237 \pm 0.005	0.249 \pm 0.001	6.476 \pm 0.063
J5	4.459 \pm 0.011	2.080 \pm 0.033	1.004 \pm 0.031	0.956 \pm 0.022	0.329 \pm 0.006	0.674 \pm 0.083	7.707 \pm 0.041
J6	4.769 \pm 0.005	1.915 \pm 0.041	1.415 \pm 0.011	0.835 \pm 0.015	0.217 \pm 0.006	0.421 \pm 0.002	8.001 \pm 0.011
J7	4.824 \pm 0.003	2.048 \pm 0.001	1.101 \pm 0.015	1.315 \pm 0.021	0.279 \pm 0.003	0.436 \pm 0.016	8.058 \pm 0.002
J8	3.388 \pm 0.010	1.908 \pm 0.006	1.335 \pm 0.048	1.151 \pm 0.002	0.325 \pm 0.017	0.593 \pm 0.003	11.443 \pm 0.001
J9	5.166 \pm 0.001	2.085 \pm 0.008	1.419 \pm 0.001	1.242 \pm 0.001	0.270 \pm 0.002	0.625 \pm 0.002	7.002 \pm 0.004
J10	4.450 \pm 0.005	1.985 \pm 0.022	1.742 \pm 0.017	1.283 \pm 0.003	0.248 \pm 0.039	0.754 \pm 0.001	8.155 \pm 0.042
J11	4.858 \pm 0.012	1.843 \pm 0.061	1.219 \pm 0.002	1.023 \pm 0.046	0.137 \pm 0.003	0.358 \pm 0.023	9.284 \pm 0.002
J12	3.794 \pm 0.009	1.853 \pm 0.002	1.459 \pm 0.048	1.362 \pm 0.003	0.307 \pm 0.054	0.470 \pm 0.004	7.948 \pm 0.014
J13	4.883 \pm 0.018	2.077 \pm 0.002	1.536 \pm 0.033	1.402 \pm 0.021	0.218 \pm 0.012	0.828 \pm 0.024	11.590 \pm 0.013
J14	5.233 \pm 0.009	2.238 \pm 0.008	1.302 \pm 0.012	1.455 \pm 0.001	0.146 \pm 0.003	0.884 \pm 0.001	7.838 \pm 0.007
J15	3.992 \pm 0.071	1.867 \pm 0.032	1.429 \pm 0.038	1.008 \pm 0.003	0.196 \pm 0.029	0.663 \pm 0.003	10.323 \pm 0.005
M1	2.399 \pm 0.002	0.235 \pm 0.001	0.651 \pm 0.071	ND	ND	0.080 \pm 0.031	2.898 \pm 0.048
M2	2.176 \pm 0.016	0.104 \pm 0.006	0.751 \pm 0.001	ND	ND	ND	3.425 \pm 0.025
M3	2.571 \pm 0.003	0.261 \pm 0.003	0.716 \pm 0.006	ND	ND	ND	3.251 \pm 0.032
M4	2.789 \pm 0.006	0.278 \pm 0.019	0.761 \pm 0.008	ND	ND	ND	2.908 \pm 0.011
M5	2.781 \pm 0.002	0.604 \pm 0.008	0.639 \pm 0.025	ND	ND	ND	3.583 \pm 0.002
M6	2.544 \pm 0.038	0.450 \pm 0.013	0.578 \pm 0.043	ND	ND	ND	4.077 \pm 0.006
M7	2.925 \pm 0.004	0.202 \pm 0.064	0.549 \pm 0.002	ND	ND	ND	2.878 \pm 0.002
M8	2.363 \pm 0.006	0.154 \pm 0.002	0.668 \pm 0.005	ND	ND	ND	6.371 \pm 0.015
M9	2.781 \pm 0.036	0.124 \pm 0.042	0.483 \pm 0.011	ND	ND	ND	3.376 \pm 0.004
M10	2.544 \pm 0.062	0.086 \pm 0.011	0.620 \pm 0.035	ND	ND	ND	4.032 \pm 0.001
M11	2.925 \pm 0.021	0.275 \pm 0.017	0.577 \pm 0.001	ND	ND	ND	3.349 \pm 0.026
M12	2.363 \pm 0.003	0.462 \pm 0.043	0.643 \pm 0.007	ND	ND	ND	2.332 \pm 0.001
M13	2.200 \pm 0.005	0.214 \pm 0.061	0.560 \pm 0.005	ND	ND	ND	2.990 \pm 0.002
M14	1.529 \pm 0.007	0.313 \pm 0.011	0.669 \pm 0.018	ND	ND	ND	7.021 \pm 0.011
M15	1.886 \pm 0.002	0.284 \pm 0.004	0.555 \pm 0.012	ND	ND	ND	5.074 \pm 0.043
MD 1	ND	5.449 \pm 0.011	3.157 \pm 0.032	0.597 \pm 0.004	1.963 \pm 0.044	1.629 \pm 0.009	4.473 \pm 0.016
MD 2	ND	5.480 \pm 0.032	3.402 \pm 0.022	0.653 \pm 0.008	1.825 \pm 0.002	1.436 \pm 0.021	4.718 \pm 0.001
MD 3	ND	4.372 \pm 0.049	2.785 \pm 0.021	0.616 \pm 0.001	1.793 \pm 0.005	2.128 \pm 0.032	4.149 \pm 0.001
MD 4	ND	3.171 \pm 0.002	3.648 \pm 0.001	0.628 \pm 0.006	1.721 \pm 0.001	2.287 \pm 0.028	4.835 \pm 0.006
MD 5	0.047 \pm 0.001	4.239 \pm 0.049	3.675 \pm 0.071	0.504 \pm 0.012	1.695 \pm 0.011	1.921 \pm 0.025	3.575 \pm 0.019
MD 6	ND	5.579 \pm 0.024	3.717 \pm 0.001	0.661 \pm 0.008	1.639 \pm 0.025	2.061 \pm 0.066	4.915 \pm 0.022
MD 7	ND	3.603 \pm 0.052	3.429 \pm 0.003	0.531 \pm 0.005	1.969 \pm 0.039	1.655 \pm 0.004	4.568 \pm 0.001
MD 8	ND	2.456 \pm 0.011	3.406 \pm 0.004	0.637 \pm 0.001	1.731 \pm 0.041	1.373 \pm 0.011	5.590 \pm 0.021
MD 9	ND	6.547 \pm 0.002	2.995 \pm 0.012	0.709 \pm 0.011	1.687 \pm 0.032	1.672 \pm 0.031	7.210 \pm 0.004
MD 10	ND	5.517 \pm 0.038	3.151 \pm 0.019	0.651 \pm 0.024	1.7540 \pm 0.004	2.005 \pm 0.002	5.935 \pm 0.006

Quercetin was present in MD2 and Josaphine samples except in Morris samples. This may be due to MD2 as a hybrid or genetically modified seedlings derived from Josaphine by the Malaysian Agriculture Research and Development Institute (MARDI) [20]. Even though the similarities and differences among the three varieties of

pineapple can be observed in the chromatographic fingerprints obtained, a more systematic approach in varietal discrimination was further evaluated using chemometric techniques as this approach will help to discriminate even the slightest variation of bioactive compounds [21].

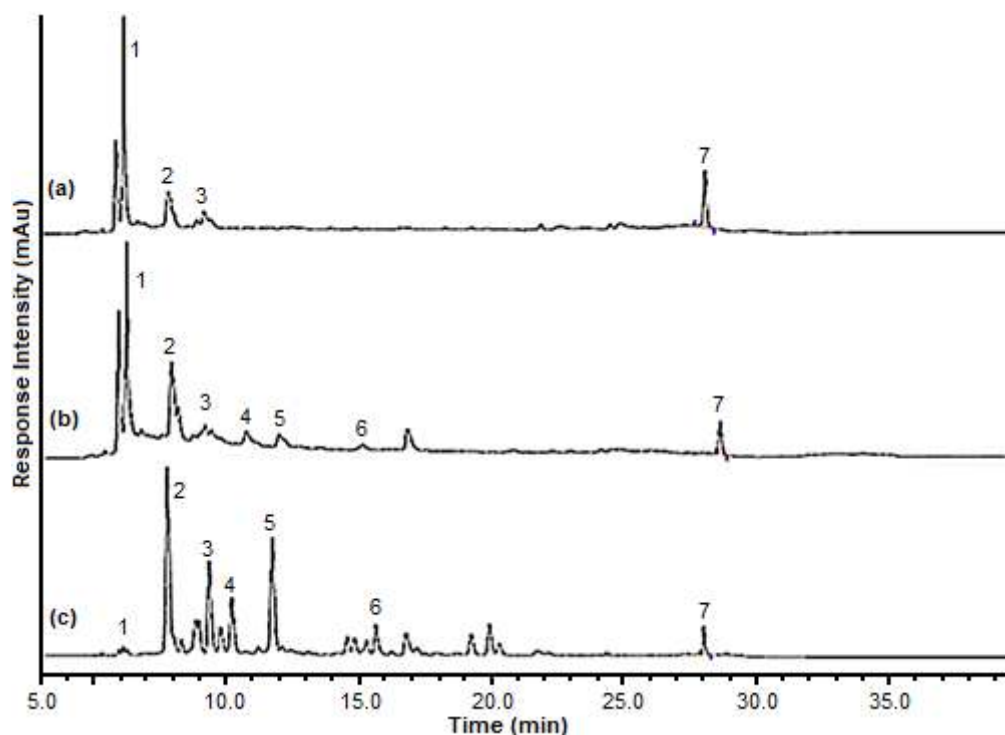


Fig 2. Representative chromatographic fingerprints of three different varieties of pineapples obtained at 280 nm (a) Morris (b) Josaphine (c) MD2. 1) catechin; 2) epicatechin; 3) chlorogenic acid; 4) ferulic acid; 5) myricetin; 6) quercetin; 7) bromelain

Chemometric Analysis

For chemometric analysis, relative peak areas of 16 peaks were selected inclusive of 7 identified bioactive compounds and 9 unknown compounds. A larger number of variables were needed to perform thorough varietal discrimination.

Cluster Analysis (CA)

Cluster analysis is a multivariate method that aims to classify a sample of subjects (or objects) on the basis of a set of measured variables into a number of different groups such that similar subjects are placed in the same group [22]. The dataset was grouped using Ward's linkage with squared Euclidean distance as a measure of similarity [23]. Fig. 3 shows the dendrogram obtained. The three pineapple varieties were clearly grouped in individual clusters. However, within each cluster, subgroups could be observed due to the origin (location) and maturity of samples. Maturity can affect significantly the different composition of bioactive compounds in fruits [24].

Principle Component Analysis (PCA)

PCA has been implemented in many recent studies for authentication and classification in food [25-28]. It was also used in a recent study to determine the seasonal and regional variation in food authentication based on chromatographic fingerprinting [29]. The variation in the chromatographic fingerprints of each pineapple varieties analyzed by PCA (Fig. 4) yielded 3 principal components (PCs) also known as varimax factors analyzed with some of them consist of strong factor loading as shown in Table 3.

Data variance was explained in the first two PCs with a cumulative variability of 75.28%. Chlorogenic acid and ferulic acid possessed a strong loading in PC1. Other significant variables in PC1 could not be identified. In PC2, epicatechin and bromelain gave strong loadings. Fig. 5 shows the PCA score plot of the pineapple samples. The groupings in the score plot were in good agreement with the result obtained from CA whereby the three varieties existed in different axes. Our

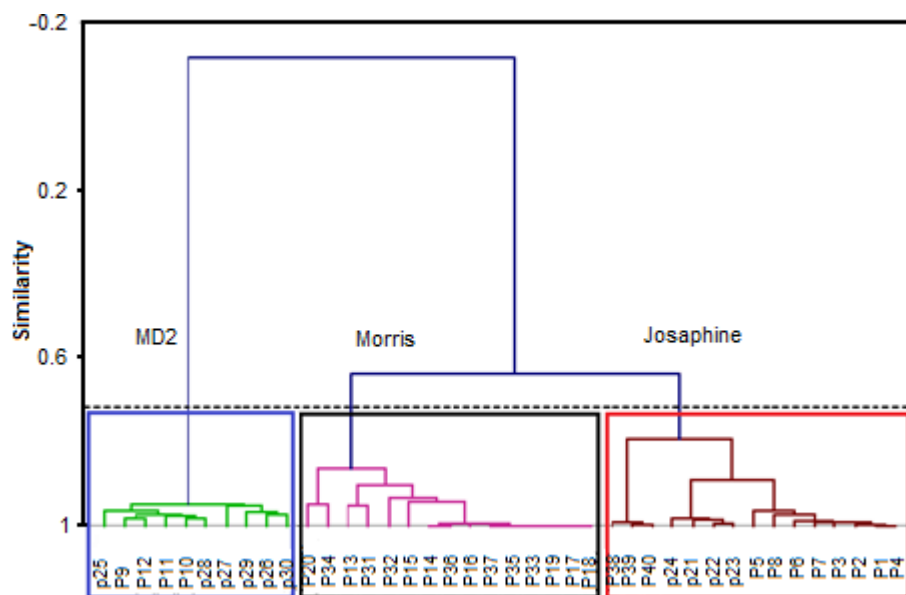


Fig 3. Dendrogram of three varieties of pineapple

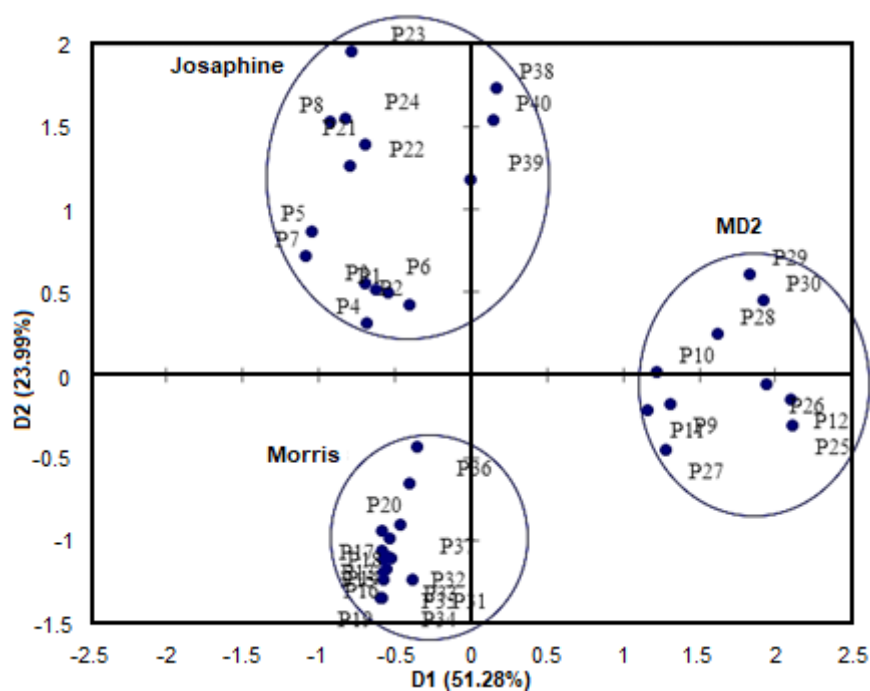


Fig 4. PCA score plot of pineapple samples. Observation was done after varimax rotation

previous studies had successfully applied CA and PCA on the authentication of Harumanis mango [30] and the clustering of Tongkat Ali roots [17].

With the aids of chemometric techniques such as PCA and CA, significant parameters, chlorogenic acid and ferulic acid concentration in each pineapple variety were further analyzed. Fig. 5 shows a graph of the ratio of

the two major bioactive compounds. The ratio of these two compounds in the three varieties of pineapple differed from each other. In Josaphine variety, the ratio of chlorogenic acid and ferulic acid concentration in the samples has only small differences where the concentration of chlorogenic acid is higher than ferulic acid. However, in MD2 variety, large differences can be

Table 3. Factor loadings for bioactive compounds detected in pineapple samples. (Strong loadings > 0.75 are shown in bold)

Parameters	PC1	PC2	PC3
X1	0.165	0.294	0.038
Catechin	0.655	0.196	0.009
Epicatechin	0.020	0.805	0.077
X4	0.102	0.737	0.074
Chlorogenic acid	0.816	0.074	0.053
X6	0.088	0.542	0.030
Ferulic acid	0.899	0.004	0.043
X8	0.854	0.009	0.095
X9	0.824	0.037	0.062
X10	0.337	0.109	0.470
X11	0.910	0.000	0.037
Quercetin	0.209	0.136	0.603
X13	0.845	0.023	0.028
Myricetin	0.564	0.044	0.342
X15	0.890	0.000	0.024
Bromelain	0.027	0.831	0.000
Eigenvalue	9.838	4.132	0.693
Variability (%)	51.28	23.99	12.41
Cumulative (%)	51.28	75.28	87.69

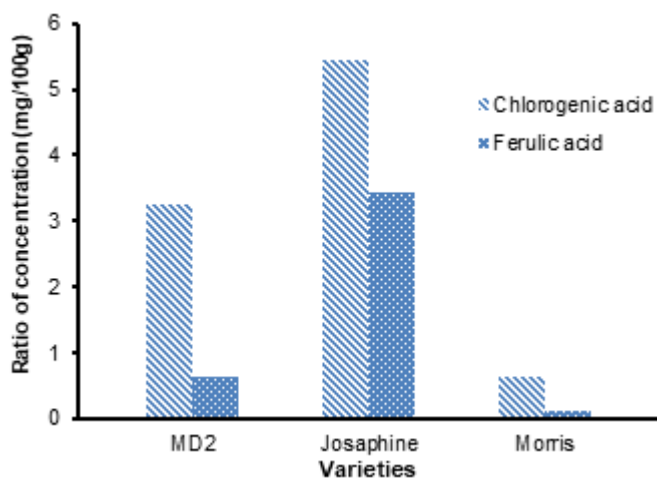


Fig 5. Ratio of concentration (mg/100 g) of chlorogenic acid and ferulic acid for three varieties of pineapples

observed in the ratio of the two compounds whereby, the concentration of chlorogenic acid is almost six times higher than that of ferulic acid. Similar to MD2 variety, chlorogenic acid in Morris variety is higher than ferulic acid. However, the total amount of these two compounds was very much lower than those in Josaphine variety. Due

to the differences in the ratio of these two compounds, the amount of chlorogenic acid and ferulic acid could be promising marker compounds to distinguish these three varieties.

■ CONCLUSION

A comprehensive and reliable chromatographic fingerprint of pineapple was obtained using PLE followed by the online SPE-LC method. The complex data of 16 compounds from 40 samples were interpreted using multivariate data analyses (CA and PCA) which successfully discriminated the three pineapple varieties. This study suggested that chromatographic fingerprints with chemometric evaluation can provide a systematic approach in quality control and authentication of fruit varieties.

■ ACKNOWLEDGMENTS

The authors would like to acknowledge the financial support obtained from Ministry of Education Malaysia for this project (Project number: FRGS 1/2018/STG01/UiTM/02/8) and Universiti Teknologi MARA.

■ REFERENCES

- [1] Yapo, E.S., Kouakou, H.T., Kouakou, L.K., Kouadio, J.Y., Kouamé, P., and Mérillon, J., 2011, Phenolic profiles of pineapple fruits (*Ananas comosus* L. Merrill) influence of the origin of suckers, *Aust. J. Basic Appl. Sci.*, 5 (6), 1372–1378.
- [2] Wen, L., 2001, *Pineapple juice: Phenolic composition and enzymatic browning inhibition*, Dissertation, Oregon State University, United States.
- [3] Larrauri, J.A., Rupérez, P., and Saura-Calixto, F., 1997, Pineapple shell as a source of dietary fiber with associated polyphenols, *J. Agric. Food Chem.*, 45 (10), 4028–4031.
- [4] Chaisakdanugull, C., Theerakulkait, C., and Wrolstad, R.E., 2007, Pineapple juice and its fractions in enzymatic browning inhibition of banana, *J. Agric. Food Chem.*, 55 (10), 4252–4257.
- [5] Hale, L.P., Greer, P.K., Trinh, C.T., and Gottfried, M.R., 2005, Treatment with oral bromelain decreases colonic inflammation in the IL-10-

- deficient murine model of inflammatory bowel disease, *Clin. Immunol.*, 116 (2), 135–142.
- [6] Reid, L.M., O'Donnell, C.P., and Downey, G., 2006, Recent technological advances for the determination of food authenticity, *Trends Food Sci. Technol.*, 17 (7), 344–353.
- [7] Saad, A.M.A., 2016, An investigation into the implementation of total quality environmental management (TQEM) for sustainability in Libyan food industry, *Dissertation*, Nottingham Trent University, United Kingdom.
- [8] Gong, F., Liang, Y.Z., Xie, P.S., and Chau, F.T., 2003, Information theory applied to chromatographic fingerprint of herbal medicine for quality control, *J. Chromatogr. A*, 1002 (1-2), 25–40.
- [9] Chun, M.H., Kim, E.K., Yu, S.M., Oh, M.S., Moon, K.Y., Jung, J.J., and Hong, J., 2011, GC/MS combined with chemometrics methods for quality control of *Schizonepeta tenuifolia* Briq: Determination of essential oils, *Microchem. J.*, 97 (2), 274–281.
- [10] Stanek, N., and Jasicka-Misiak, I., 2018, HPTLC phenolic profiles as useful tools for the authentication of honey, *Food Anal. Methods*, 11, 2979–2989.
- [11] Bajoub, A., Bendini, A., Fernández-Gutiérrez, A., and Carrasco-Pancorbo, A., 2018, Olive oil authentication: A comparative analysis of regulatory frameworks with especial emphasis on quality and authenticity indices, and recent analytical techniques developed for their assessment. A review, *Crit. Rev. Food Sci. Nutr.*, 58 (5), 832–857.
- [12] Bengana, M., Bakhouch, A., Lozano-Sánchez, J., Amir, Y., Youyou, A., Segura-Carretero, A., and Fernández-Gutiérrez, A., 2013, Influence of olive ripeness on chemical properties and phenolic composition of Chemlal extra-virgin olive oil, *Food Res. Int.*, 54 (2), 1868–1875.
- [13] Fan, X.H., Cheng, Y.Y., Ye, Z.L., Lin, R.C. and Qian, Z.Z., 2006, Multiple chromatographic fingerprinting and its application to the quality control of herbal medicines, *Anal. Chim. Acta*, 555 (2), 217–224.
- [14] Petersson, E.V., Liu, J., Sjöberg, P.J.R., Danielsson, R., and Turner C., 2010, Pressurized hot water extraction of anthocyanins from red onion: A study on extraction and degradation rates, *Anal. Chim. Acta*, 663 (1), 27–32.
- [15] Hartonen, K., Parshintsev, J., Sandberg, K., Bergelin, E., Nisula, L., and Riekkola, M.L., 2007, Isolation of flavonoids from aspen knotwood by pressurized hot water extraction and comparison with other extraction techniques, *Talanta*, 74 (1), 32–38.
- [16] Khan, A.A.M., Saim, N., and Hamid, R.D., 2017, Optimisation of pressurised liquid extraction of bioactive compounds from *Ananas comosus* (pineapple) fruit, *Pertanika J. Sci. Technol.*, 25 (S), 175–182.
- [17] Zaini, N.N., Osman, R., Juahir, H., and Saim, N., 2016, Development of chromatographic fingerprints of *Eurycoma longifolia* (Tongkat Ali) roots using online solid phase extraction-liquid chromatography (SPE-LC), *Molecules*, 21 (5), E583.
- [18] Li, T., Shen, P., Liu, W., Liu, C., Liang, R., Yan, N., and Chen, J., 2014, Major polyphenolics in pineapple peels and their antioxidant interactions, *Int. J. Food Prop.*, 17 (8), 1805–1817.
- [19] Fine, A.M., 2000, Oligomeric proanthocyanidin complexes: History, structure, and phytopharmaceutical applications, *Altern. Med. Rev.*, 5 (2), 144–151.
- [20] Mazalan, M.F., and Yusof, Y., 2017, Natural pineapple leaf fibre extraction on Josapine and Morris, *MATEC Web Conf.*, 135, 00043.
- [21] Bevilacqua, M., Bro, R., Marini, F., Rinnan, Å., Rasmussen, M.A., and Skov, T., 2017, Recent chemometrics advances for foodomics, *TrAC, Trends Anal. Chem.*, 96, 42–51
- [22] Gad, H.A., El-Ahmady, S.H., Abou-Shoer, M.I., and Al-Azizi, M.M., 2013, Application of chemometrics in authentication of herbal medicines: A review, *Phytochem. Anal.*, 24 (1), 1–24.
- [23] Perestrelo, R., Barros, A.S., Rocha, S.M., and Câmara, J.S., 2014, Establishment of the varietal profile of *Vitis vinifera* L. grape varieties from different geographical regions based on HS-SPME/GC-qMS combined with chemometric tools, *Microchem. J.*, 116, 107–117.
- [24] Soifoini, T., Donno, D., Jeannoda, V., Rakotoniaina,

- E., Hamidou, S., Achmet, S.M., Solo, N.R., Afraitane, K., Giacoma, C., and Beccaro, G.L., 2018, Bioactive compounds, nutritional traits, and antioxidant properties of *Artocarpus altilis* (Parkinson) fruits: Exploiting a potential functional food for food security on the Comoros Islands, *J. Food Qual.*, 2018, 5697928.
- [25] Belmonte-Sánchez, J.R., Gherghel, S., Arrebola-Liébanas, J., González, R.R., Vidal, J.L.M., Parkin, I., and Frenich, A.G., 2018, Rum classification using fingerprinting analysis of volatile fraction by headspace solid phase microextraction coupled to gas chromatography-mass spectrometry, *Talanta*, 187, 348–356.
- [26] Efenberger-Szmechtyk, M., Nowak, A., and Kregiel, D., 2018, Implementation of chemometrics in quality evaluation of food and beverages, *Crit. Rev. Food Sci. Nutr.*, 58 (10), 1747–1766.
- [27] Neto, S., 2018, Classification and authentication of plants by chemometric analysis of spectral data, *Compr. Anal. Chem.*, 80, 105–125.
- [28] Rafi, M., Jannah, R., Heryanto, R., Kautsar, A., and Septaningsih, D., 2018, UV-Vis spectroscopy and chemometrics as a tool for identification and discrimination of four *Curcuma* species, *Int. Food Res. J.*, 25 (2), 643–648.
- [29] Wang, Y., and Jin, Y., 2017, Development and distinction of *Rhizoma rodgersiae* with HPLC-DAD fingerprint analysis combined with chemical pattern recognition techniques, *Am. J. Anal. Chem.*, 8, 681–689.
- [30] Zakaria, S.R., Saim, N., Osman, R., Abdul Haiyee, Z., and Juahir, H., 2018, Combination of sensory, chromatographic, and chemometrics analysis of volatile organic compounds for the discrimination of authentic and unauthentic Harumanis mangoes, *Molecules*, 23 (9), E2365.

Cellulose Acetate of Rice Husk Blend Membranes: Preparation, Morphology and Application

Meri Suhartini^{1*}, Engela Evy Ernawati², Anisa Roshanova², Haryono², and June Mellawati³

¹CIRA, National Nuclear Energy Agency, Lebak Bulus Raya No. 49, Pasar Jumat, PO Box 7002, JKSKL, South of Jakarta, Jakarta 12070, Indonesia

²Department of Chemistry, Faculty of Mathematics and Natural Sciences, Padjadjaran University, Jatinangor 45363, West Java, Indonesia

³CTRSM, National Nuclear Energy Agency, Lebak Bulus Raya No. 49, Pasar Jumat, PO Box 7043 JKSKL, South of Jakarta, Jakarta 12070, Indonesia

* Corresponding author:

tel: +62-151657145

email: meri@batan.go.id

Received: July 1, 2019

Accepted: August 30, 2019

DOI: 10.22146/ijc.47185

Abstract: Cellulose acetate blend membranes in this study was synthesized from cellulose acetate (CA) of rice husk and NaA zeolites (Z) with N,N'-Methylene bis acrylamide (MBA) as the cross-linker agent and gamma-rays from cobalt-60 source as the reaction initiator. Application of the membrane was carried out to increase the concentration of vetiverol in vetiver oil. The steps in this study were isolation of the cellulose rice husk with alkali treatment, delignification, acetylation, preparation of the cellulose acetate-NaA zeolites NaA-membrane by inverse phase technique, addition of N,N'-Methylene bis acrylamide, and irradiation by gamma-rays. Swelling degree, crosslinking yield, tensile strength, membrane performance, FTIR, and SEM analysis were observed. The results showed that the optimal irradiation dose for the synthesis the CA-Z-MBA membrane was 20 kGy. The CA-Z-MBA membrane had a swelling degree of 4.44%, tensile strength of 656.40 kg/cm², and crosslinking yield of 6.61%. Performance of the CA-Z-MBA membrane reached the flux of 60.58 g/m².h, permeate concentration (CP) of 11.67%, and the CP increase 5 times from 2.40% to 11.67%.

Keywords: cellulose acetate membrane; NaA zeolites; gamma-rays; vetiver oil

■ INTRODUCTION

The cellulose acetate membrane is one of the hydrophilic membranes. A hydrophilic membrane has an active polar side, which interacts with a polar molecule or compound. The interaction between the penetrant and the membrane can occur through a chemical bond, the hydrogen bond. The hydrophilic property of the cellulose acetate membrane affects the ease of interaction and diffusion of molecules or penetrant compounds in the membrane if each membrane and solute has similarities or differences in polarity or charge [1]. Cellulose acetate membranes have high water absorption rates, weak electrical resistance, and limited heat and chemical resistance. The properties of water resistance increase with the increasing degree of acetylation and its strength

can last up to 60 °C. Besides that, the cellulose acetate membrane has a specific gravity ranging from 1.27–1.34 [2]. Cellulose acetate membranes have a high degree of bloat, low chemical resistance, weak electrical resistance, and small mechanical strength [2-4]. This causes the cellulose acetate membrane to have high flux but low selectivity. The selectivity of cellulose acetate membranes can be increased by zeolite addition [4-6]. An essential criterion for determining membrane effectiveness is to observe permeation and selectivity rates. The rate of permeation or flux is the rate of mass transfer per unit of membrane surface area per unit of time. This statement is formulated in Eq. 1 [7].

$$J = \frac{1}{A} \left(\frac{dm}{dt} \right) \quad (1)$$

where J = total flux value ($\text{g}/\text{m}^2\cdot\text{h}$), A = membrane surface area (m^2), dm/dt = slope of the permeate mass curve over time.

Selectivity can be expressed by separation factor (α) Eq. 2 [7],

$$\alpha = \frac{(Y_W/Y_A)}{(X_W/X_A)} \quad (2)$$

where, Y_W , Y_A = molar fractions of water (W) and vetiverol (A) at the vapor phase in the permeate, $Y_W + Y_A = 1$; and X_W , X_A = molar fractions of water (W) and vetiverol (A) at the liquid phase in the feed, $X_W + X_A = 1$.

Previous studies of modified cellulose acetate membranes with hydrophilic NaA zeolite fillers resulted in membranes that were densified that could increase membrane selectivity to hydrophilic materials [8-10]. Gamma irradiation of the cellulose acetate membrane by the addition of glutaraldehyde as a cross-linker can improve both physical and mechanical properties [11] evidenced by decreasing degrees of swelling and increased tensile strength. The addition of a stable N,N'-Methylene bis acrylamide as a cross-linker agent with crosslinking techniques can avoid degradation of irradiated membranes [12]. Modification of the membrane increases the membrane selectivity for pervaporation of hydrophilic materials. Pervaporation is a process of separating a volatile mixture by using a tight membrane regulated by a vacuum pump or carrier gas [7]. Pervaporation by using cellulose acetate membrane for extraction and separation of essential oils with the main component of hydrophilic compound (vetiverol) has been carried out, but the essential oil produced from vetiver has not had vetiverol level that meets SNI quality standard, so it needs to be improved [7]. The purpose of this research is to improve the physical and chemical characteristic of the membrane by increasing the polarity by adding NaA zeolite and the crosslinking between the bond of the cellulose acetate by adding N,N'-Methylene bis acrylamide. Based on that, in this research, modified cellulose acetate membrane of rice husk with zeolite NaA and N,N'-Methylene bis acrylamide were irradiated by gamma-rays in the hope of producing a tight and selective membrane to vetiverol compound in vetiver oil by pervaporation methods. NaA zeolite has a high affinity [13]. Vetiver oil is one of the essential oils that contain a

mixture of sesquiterpene alcohol and a very complex hydrocarbon. The main components of vetiver oil composition consist of sesquiterpene hydrocarbons (γ -cadinene, cloven, α -amorphine, aromadendrene, juniper, and alcohol derivatives), vetiverol (khusimol, epiglobulol, spathulenol, khusinol, and carbonyl derivatives), and vetivone (α -vetivone, β -vetivone, khusimon and ester derivatives). Increased levels of vetiverol in vetiver oil can improve the quality of vetiver oil [14].

■ EXPERIMENTAL SECTION

Materials

The rice husk used was from Cileles Village, Jatiningor District, vetiver oil was from Garut Regency. Glacial acetic acid, sulfuric acid, acetone, ethanol, hexane, chloride peroxide, methylene chloride, sodium hydroxide, sodium carbonate, potassium hydroxide, magnesium sulfate were obtained from Merck with p.a grade. Sodium chloride and Liquid nitrogen, N,N'-Methylene bis acrylamide were from Merck and NaA zeolites were from Wiko (No. 267-00595).

Procedure

Synthesis of CA-zeolite NaA-MBA membrane (CA-Z-MBA)

Five percent w/v of CA polymer was dissolved in methylene chloride until homogeneous. Five percent w/v NaA zeolite of 5% w/v CA acetate weight was incorporated into the membrane solution while continuously stirring for 24 h. It was then stored in the refrigerator for 24 h to avoid solvent evaporation and bubble removal. Then the membrane solution was printed on a glass plate. The membrane on the glass plate was stored in the desiccator until the membrane was detached from the glass plate. The formed membrane was soaked with MBA 1% for 10 min and stored in an air tight plastic [10].

Irradiation of CA-Z-MBA membrane

The CA-Z-MBA membranes in the airtight plastic was irradiated with various doses of 10, 20, 30 and 40 kGy. Irradiation was carried out by gamma rays from cobalt-60 as the source [11].

Pervaporation

Pervaporation is a separation process by contacting

the feed solution on the active side of one membrane surface. The result is a permeate in the form of vapor emitted on the other side of the membrane. The membrane was placed over the support horizontally on the apparatus of pervaporation. Into a flask, 100 g of vetiver oil was placed and heated to 40 °C. The pervaporation process was carried out at a vacuum pressure (0.5 mbar). Before and after the pervaporation process, the feed solution was taken slightly. Permeate was taken every one hour. Then the feed and permeate solution was calculated [4].

Determination of ash content

Samples were weighed as much as 1 g and fed into the already known weight plate, then inserted in the kiln and heated to a temperature of 600 °C for 4 h. Then the samples were cooled in a desiccator and weighed. Ash content calculation was performed according to Eq. 3 [15].

$$\text{Ash\%} = \frac{\text{Ash_Mass}}{\text{Sample_Mass}} \times 100 \quad (3)$$

The degree of swelling

The 3 × 2 cm of CA membrane was weighed by dry weight, immersed in 10 mL of water at room temperature for 24 h. The membrane surface was then dried with absorbent paper to remove excess water attached to the membrane surface. The wet membrane was weighed again several times until a constant weight (M_b) was obtained, then the degree of swelling was calculated. Swelling degree (DS) of membrane can be determined by Eq. 4 [16].

$$\text{DS\%} = \frac{M_s - M_d}{M_d} \times 100 \quad (4)$$

where M_s and M_d are the mass of the swollen and dry membranes respectively.

Membrane flux value

The flux value determines the permeate obtained from the pervaporation process (Eq. 1) [7].

Fourier-transform infra-red (FTIR)

Membrane characterization using FTIR was conducted to determine functional groups present in the resulting membrane [2]. Cellulose acetate modified membrane with a weight of 1–2 mg was mashed mixed with 300–400 mg of potassium bromide powder and put in a stainless steel cup. The infrared light absorption of the samples was measured in the region of wave numbers

4000–500 cm^{-1} . The IR spectra produced were compared with CA spectra before the copolymerization process.

Scanning electron microscope (SEM)

Membrane characterization using SEM was conducted to determine the morphological structure of the membrane and to perform cross-sectional analysis [2]. The samples were coated with Au then placed in a sample container on the SEM device, and afterwards the samples were closed and made airtight. The surface of the samples was then measured.

Tensile strength (Ts)

The modified CA membrane was cut to a plate with a width of 0.3 cm and its thickness was measured several times in the section of the cut membrane. After that, the membrane was tested for its tensile strength with the Stograph-RJ tool. The value of Ts was determined based on Eq. 5 [3].

$$T_s = \frac{m}{t \times l} \quad (5)$$

where m , t , and l are mass of tensile strength (kg), thickness (cm), and width (cm) of the membranes, respectively.

Crosslinking yield

The crosslinking yield (CY) was determined by Eq. 6 [17].

$$\text{CY\%} = \frac{M_x - M_y}{M_y} \times 100 \quad (6)$$

where M_y and M_x are the mass of the membrane before and after crosslinking, respectively.

Vetiverol in vetiver oil

Concentration of vetiverol in the permeate (CP) and vetiverol in the feed (CF) were calculated from ester numbers before acetylation and ester numbers after acetylation according to SNI 06-2386-2006. The ester number of CA before acetylation was determined by the addition of 25 mL of 0.5 N KOH to each sample and blank, which was then refluxed for 1 h. Phenolphthalein was added to the mixture solution then titrated with 0.5 N HCl to a color change. The ester number before acetylation was calculated according to Eq. 7.

The ester number after acetylation was determined by adding 10 mL acetic anhydride and 2 g sodium silicate

anhydride to 10 mL of sample. The solution mixture was refluxed for 2 h, cooled, and added with 50 mL of water. The mixture solution was heated at 40 °C for 15 min, stirred and inserted into a separating funnel and washed with 10 mL of water. The oil layer was separated by a layer of water. 50 mL of sodium chloride, 50 mL of Na₂CO₃/NaCl, 20 mL of water and 3 g MgSO₄ were then added to the oil layer. The essential oil was weighed and added with 2 mL of water and phenolphthalein. Then 25 mL of ethanol/KOH 0.5 M was added to the solution mixture, refluxed for 1 h, then cooled by adding 20 mL of water. The solution mixture was titrated with 0.5 M HCl and the ester number after acetylation was calculated according to the equation E₂. Vetiverol concentration was determined by Eq. 9 [11].

$$E_1 (\text{The ester number before acetylation}) = \frac{56.1(V_1 - V_0)N}{m} \quad (7)$$

$$E_2 (\text{The ester number after acetylation}) = \frac{28.05(a - b)}{c} \quad (8)$$

$$\text{Vetiverol concentration} = \frac{M(E_2 - E_1)}{561 - 0.42 \times E_2} \quad (9)$$

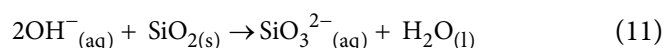
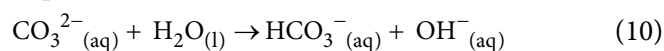
where: m = mass of sample before acetylation/g, V₁ = volume of 0.5 N HCl for the blank titration/mL, V₀ = 0.5 N HCl volume for sample titration/mL, N = acidity of HCl, a = volume of 0.5 N HCl for the blank titration/mL, b = volume of 0.5 N HCl for sample titration/mL, c = sample mass after acetylation/g, M = molecular mass of vetiverol/g, E₁ = ester number after acetylation, E₂ = ester number before acetylation.

■ RESULTS AND DISCUSSION

Cellulose Isolation from Rice Husk

Cellulose isolation was carried out through 3 stages: 1) Dissolving with potassium carbonate, 2) alkali treatment (1.5% hydrogen peroxide and 5 N sodium hydroxide pH 11), and 3) delignification (70% nitric acid and 80% acetic acid). At the dissolving process using potassium carbonate, the cellulose content increased from 46.50 to 77.03%, but

the silica content decreased from 20.20 to 2.02%. The dissolution process with potassium carbonate in water resulted in the bonding of hydroxide ion (Eq. 10) to silica (Eq. 11).



The decrease in lignin levels and hemicellulose levels (Table 1) was due to the potassium carbonate solution [18]. However, at this stage the lignin production was still high (16.98%), which can disturb the cellulose isolation process, so it was necessary to perform alkali treatment [19]. At the alkali treatment stage, the cellulose content increased up to 77.08% but there was a decrease in lignin reaching 6.02% as well as a decrease in hemicellulose and silica levels (Table 1).

Alkali treatment was done to separate cellulose, lignin, and hemicellulose because of the presence of hydroxide ions (Eq. 12, 13). At this stage, the lignocellulose bonds degraded and caused a decrease in lignin and hemicellulose levels, but increased the cellulose levels. The addition of sodium hydroxide at pH 11 caused the degree of polymerization and crystallization properties of lignocellulose bond to decrease. The reaction in alkaline conditions can extract the silica [20-21].



Delignification with 70% nitric acid and 80% acetic acid (catalyst) protected the cellulose, but broke the lignin bond, and reduced the silica and hemicellulose levels reaching close to 0%. The resulting lignin content (2.02%) did not affect the process of cellulose isolation [22].

Type of Cellulose Acetate (CA)

The preparation of CA from rice husk was conducted through the activation, the acetylation process, and the hydrolysis process. The activation stage

Table 1. Content of silica, cellulose, hemi-cellulose and lignin in rice husk at each stage

Stages	Content (%)			
	Silica	Cellulose	Hemicellulose	Lignin
Rice Husk	20.20	46.50	10.24	22.52
Dissolution with Potassium Carbonate 1:3.5	2.02	77.03	0.17	16.98
Alkali treatment	1.62	77.08	0.08	6.21
Delignification	0.62	93.32	0.07	2.20

was carried out by the addition of glacial acetic acid which inflated the cellulose structure and enlarged the surface area on the cellulose which lead to increased reactivity to the acetyl group, causing the acetylation process to take place quickly [2]. The acetylation process was carried out by addition of acetic acid anhydride and sulphuric acid as a catalyst. Acetic acid anhydride serves to substitute acetyl groups in hydroxyl groups of the cellulose. The acetylation process is an exothermic reaction, so it was carried out at room temperature to keep the cellulose structure from being degraded. The homogeneous mixture of the solution successfully characterized the acetylation reaction. The hydrolysis process discontinued the acetylation reaction by the addition of 80% acetic acid [2]. The hydrolysis process was carried out in order to release the acetyl group and to remove the residual unreacted acetic acid anhydride. The acetyl content of CA was 43.87%, which indicated that the type of cellulose was cellulose triacetate [2]. The cellulose triacetate was used as the base material of the CA membrane.

The Crosslinking Yield and Degree of Swelling

Fig. 1 and 2 show the crosslinking yield and degree of swelling of the irradiated CA-Z-MBA membrane. The density of the membrane was determined from the crosslinking yield of CA-Z-MBA membrane [3]. Fig. 1 shows that the crosslinking yield of CA-Z-MBA increased up to 14.28% at doses of 0–30 kGy indicating the number of bonds formed –between the cross-linkers and the CA

causing the membrane to become closer [23]. Fig. 2 shows that the CA-Z membrane had the degree of swelling of 8.57%, then decreased to 4% by adding 1% MBA at an irradiation dose of 30 kGy.

The crosslinking occurred after irradiation in the presence of MBA. As a result, water absorption capacity of the membrane was less due to the smaller pores formed [12,24]. The degree of swelling of CA-Z-MBA increased at an irradiation dose of 40 kGy from 4 to 7.14% (Fig. 2) due to the CA degradation. At irradiation dose of 40 kGy, the CA started degradation which opened the membrane pores, causing the water to diffuse more. The phenomena can be seen from the result of cross-linking which decreased (14.28 to 8.22%) at Fig. 1. High radiation energy resulted in the breaking of the bond of the CA polymer [12].

Mechanical Properties

The mechanical properties of modified CA-Z-MBA membrane can be seen by the results of the tensile strength test (Ts) shown in Fig. 3.

The Ts of CA-MBA and CA-Z-MBA increased at a dose of 10 to 30 kGy. Up to irradiation dose of 30 kGy the CA-MBA-membrane gave high Ts. The increase in Ts was due to the formation of polymer bonds between CA with the cross-linkers MBA as the binding bridge, which caused the membrane to become tighter. However, the Ts of CA-Z-MBA-membrane at a dose of 10 to 30 kGy was higher than that of the CA-MBA membrane. The high

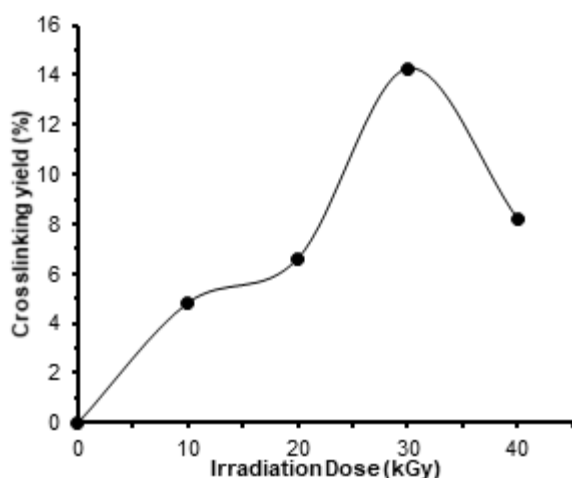


Fig 1. Crosslinking yield of CA-Z-MBA membrane at different irradiation dose

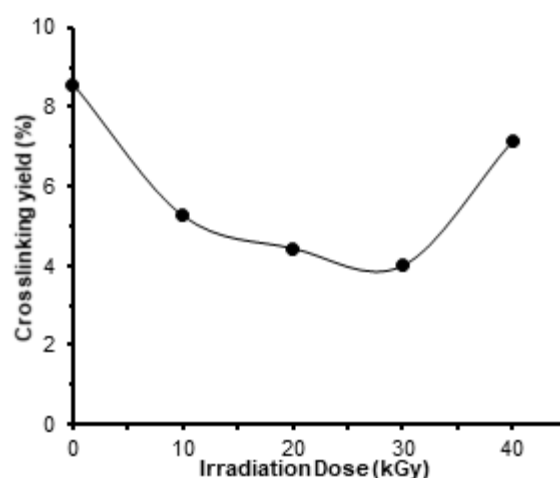


Fig 2. Degree of swelling of CA-Z-MBA membrane at different irradiation dose

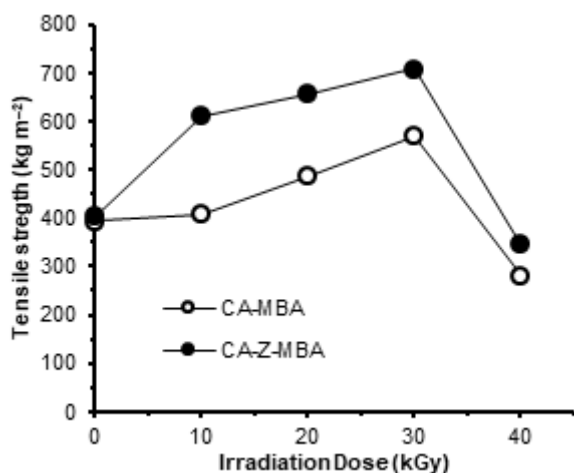


Fig 3. The tensile strength of CA-MBA and CA-Z-MBA membranes

Ts of the CA-Z-MBA membrane indicated the effect of the NaA zeolite filler on the void of the membrane that improved the mechanical properties. The presence of MBA increased the tensile strength of the membrane due to the bonds formed between the polymer matrix and the cross-linker [23]. Based on the data, it can be said that the irradiated CA-Z-MBA membrane at irradiation dose up to 30 kGy improved the mechanical properties. At irradiation dose of 40 kGy, the Ts decreased due to the degradation on the backbone of CA caused by high irradiation dose.

The Functional Group Analysis

The FTIR spectra of CA and irradiated CA-Z-MBA membrane at irradiation dose of 20 kGy is shown in Fig. 4. There is no significant difference between the spectra of the CA membrane and the CA-Z-MBA membrane. The results of FTIR spectra show that there is shifting of the wavenumber in the typical region of absorption of the O-H group from 3488 to 3487 cm^{-1} . The wavenumber shifted due to the location of the O-H group on the CA that resulted from the reaction of free radical formation in the group O, which binds to the C=O group of MBA. The wavenumber shift also occurred in the C=O uptake region derived from the acetyl group on the SA matrix from 1638 to 1670 cm^{-1} . The shift of C=O happened because of environmental changes (adjacent neighboring groups) of the acetyl groups. Also amplified by the number of waves at 1527 cm^{-1} which is characteristic of the N-H group on the MBA. The absorption of the N-H (1527 cm^{-1}) group in addition to C=O (1670 cm^{-1}) group uptake is characteristic of the amide compound from the MBA [23]. From the FTIR spectra analysis of the CA membrane and irradiated CA-Z-MBA membrane the formation of a bond between MBA with the CA matrix can be observed.

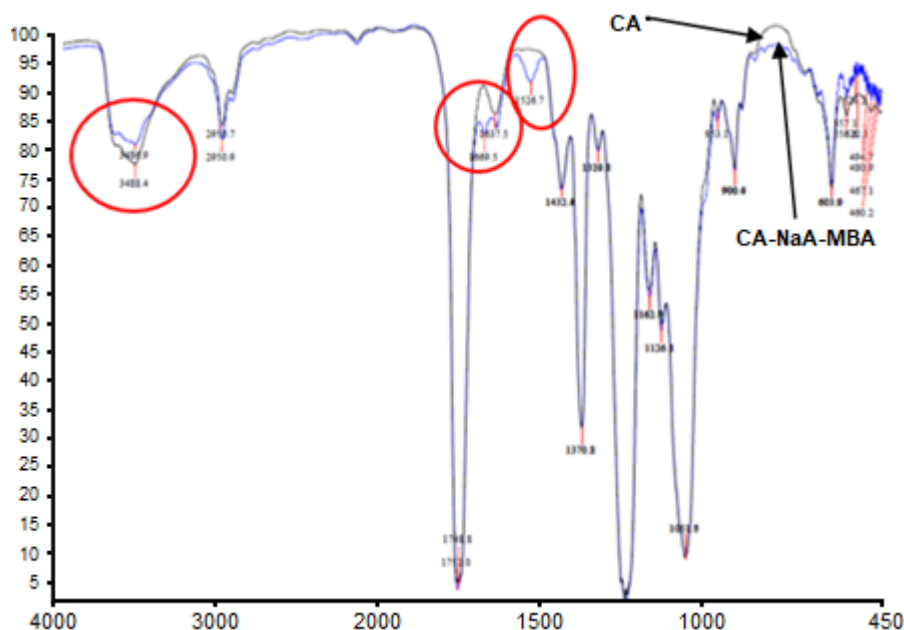


Fig 4. The FTIR spectra of CA membrane and irradiated CA-Z-MBA membrane (Irradiation dose of 20 kGy)

Fig. 5 shows the description of the reaction between the CA as a polymer matrix and MBA as a cross-linking agent irradiated by gamma-rays. The MBA functions as a cross-linker between two cellulose acetate bonds, which replaced the H⁺ on the cellulose acetate.

The Morphology Analysis

The SEM analysis of the cross-section of the CA membrane and the CA-Z-MBA membrane is shown in Fig. 6. The CA-Z-MBA membrane (Fig. 6(b)) has a dense and orderly structure morphology compared to the CA membrane (Fig. 6(a)). The dense and orderly structure is due to the presence of NaA zeolites and the addition of MBA as a cross-linker agent to the CA membrane, causing closer and stronger bonding of the CA polymer [10,24]. The statement mentioned above is supported by the data

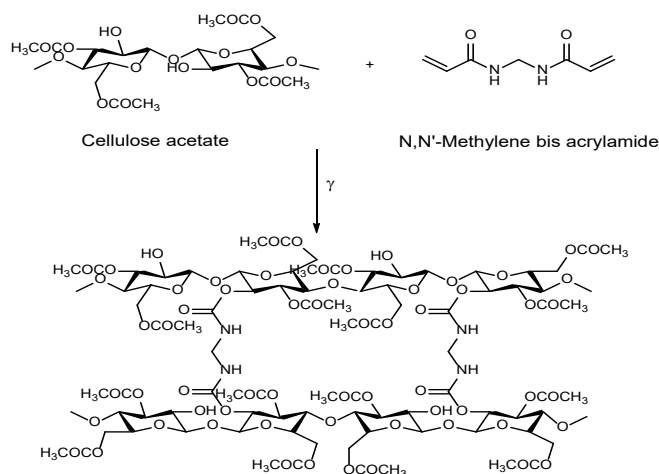


Fig 5. The reaction of cellulose acetate as polymer matrix with N,N'-Methylene bis acrylamide as cross-linker

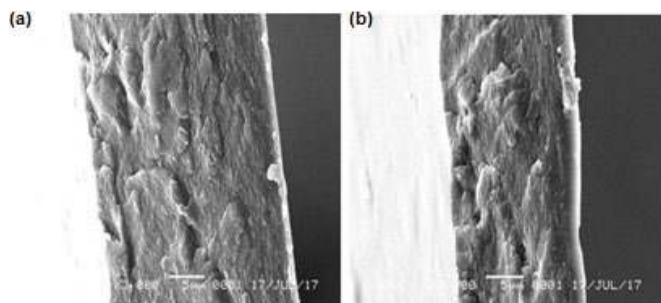


Fig 6. (a) Cross section of the CA membrane, and (b) the irradiated CA-Z-MBA membrane (irradiation dose of 20 kGy)

of crosslinking yield and degree of swelling of irradiated CA-Z-MBA membrane at an irradiation dose of 20 kGy (Fig. 1 and 2). The irradiated CA-Z-MBA membrane has a higher crosslinking yield and a lower degree of swelling compared to the CA membrane. Furthermore, it is supported by the higher tensile strength data of the irradiated CA-Z-MBA membrane compared to the CA membrane (Fig. 3). However, the CA-Z-MBA membrane is denser than the CA membrane.

Pervaporation of Vetiverol in Vetiver Oil

Pervaporation is a separation process done by contacting the feed solution on the active side on one of the membrane surfaces, while the result is a permeate released in the form of a vapor on the other side of the membrane [24]. The pervaporation process is conducted at a temperature of 40 °C because this temperature is the optimal temperature of the pervaporation process. The membrane is placed on the supporting module, resulting in a flow of cross flow, so the non-via membrane feed returns into the flask [24]. The interaction between a hydrophilic vetiverol compound and a hydrophilic CA-Z-MBA-membrane show that separation takes place through the diffusion of the membrane with hydrophilic properties. The resulting permeate turns into a gas phase due to the different pressures, atmospheric pressure at the feed side and 0.5 mbar vacuum pressure on the permeate side so that liquid nitrogen is required to convert the gas phase into a solid phase so as not to be missed to the pump on the device leading to the silica pile. The permeate is accommodated 4 times every hour and measured [3]. The CA-Z-MBA-membrane that had been characterized was analyzed using a pervaporation device to determine its performance (flux value) and the resulting permeate concentration (CP). The flux and CP of the membrane in the pervaporation process can be seen in Fig. 7.

It can be seen that the CP value of the irradiated CA-Z-MBA membrane increased by increasing the irradiation dose. The highest CP value obtained on the CA-Z-MBA membrane was at irradiation dose of 30 kGy (13.47%) evidenced by the highest crosslinking yield (14.28%) with the smallest degree of swelling (4%), but the

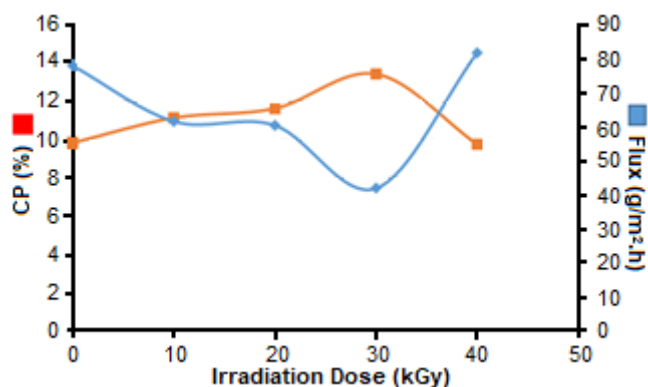


Fig 7. The effect of irradiation dose-on flux and Cp of irradiated CA-Z-MBA membrane

resulting flux dropped dramatically as the membrane becomes denser compared to the CA-Z-MBA membrane irradiated at dose of 20 kGy, evidenced by the increased tensile strength of the CA-Z-MBA membrane at irradiation dose of 30 kGy (Fig. 3). The decrease of flux causes the pervaporation to take place slowly. The pervaporation process is optimal if permeate concentration (CP) rises gradually but the flux does not decrease drastically. The CA-Z-MBA membrane irradiated at a dose of 20 kGy reached the flux of 60.58 g/m²·h and CP of 11.67%. The CP increased 5 times from 2.40 to 11.67%.

CONCLUSION

Radiation induced crosslinking of CA-Z-MBA membranes using gamma rays, decreased the degree of swelling, and increased the tensile strength of the membrane. The optimum dose of irradiation of the modified membrane was 20 kGy with crosslinking yield of 6.61%, degree of swelling of 4.44%, and a tensile strength of 656.40 kg/m². The addition of zeolite NaA stimulated vetiverol in vetiver oil using pervaporation methods. Performance of the CA-Z-MBA membrane resulted in flux of 60.58 g/m²·h and CP of 11.67% where the vetiverol level increased 5 times from 2.40 to 11.67%.

ACKNOWLEDGMENTS

The authors would like to thank CIRA-National Nuclear Energy Agency (NNEA) and Faculty of Mathematics and Natural Sciences, Padjadjaran University for funding this study. We also thank Mr. Santoso Prayitno, and Mr. Supandi from CIRA-NNEA

for experimental help in this work and Dr. Mardiyanto from AMC-NNEA for the suggestions.

REFERENCES

- [1] Kusworo, T.D., Soetrinanto, D., Widayat, Budiyono, and Utomo, D.P., 2018, Study of polymeric, membranes potential for eugenol purification from crude clove leaf oil, *ASEAN J. Chem. Eng.*, 18 (2), 81–92.
- [2] Etemadi, H., Yegani, R., Seyfollahi, M., and Rabiee, M., 2018, Synthesis, characterization, and anti-fouling properties of cellulose acetate/polyethylene glycol-grafted nanodiamond nano composite membranes for humic acid removal from contaminated water, *Iran. Polym. J.*, 27 (6), 381–393.
- [3] Das, A.M., Ali, A.A., and Hazarika, M.P., 2014, Synthesis and characterization of cellulose acetate from rice husk: Eco-friendly condition, *Carbohydr. Polym.*, 112, 342–349.
- [4] Zheng, P.Y., Zhang, W.H., Li, C., Wang, N.X., Li, J., Qin, Z.P., and An, Q.F., 2019, Efficient bio-ethanol recovery by non-contact vapor permeation process using membranes with tailored pore size and hydrophobicity, *Chem. Eng. Sci.*, 207, 448–455.
- [5] Ernawati, E., 2014, Pembuatan membran selulosa asetat termodifikasi zeolit alam Lampung untuk pemisahan etanol-air secara pervaporasi, *Chimica at Natura Acta*, 2 (1), 101–104.
- [6] Fu, Y.J., Lai, C.L., Chen, J.T., Liu, C.T., Huang, S.H., Hung, W.S., Hu, C.C., and Lee, K.R., 2014, Hydrophobic composite membranes for separating of water-alcohol mixture by pervaporation at high temperature, *Chem. Eng. Sci.*, 111, 203–210.
- [7] Jyoti, G., Keshav, A., and Anandkumar, J., 2015, Review on pervaporation: Theory, membrane performance, and application to intensification of esterification reaction, *J. Eng.*, 2015, 927068.
- [8] Sarialp, G., 2012, Dehydration of aqueous aprotic solvent mixtures by pervaporation, *Thesis*, Department of Engineering, Middle East Technical University, Turkey.
- [9] Iryani, D.A., Wulandari, N.F., Cindradewi, A.W., Ginting, S., Ernawati, E., and Hasanudin, E., 2018,

- Lampung natural zeolite filled cellulose acetate membrane for pervaporation of ethanol-water mixtures, *IOP Conf. Ser.: Earth Environ. Sci.*, 141, 012013.
- [10] Wee, S.L., Tye, C.T., and Bhatia, S., 2008, Membrane separation process – Pervaporation through zeolite membrane, *Sep. Purif. Technol.*, 63 (3), 500–516.
- [11] Suhartini, M., and Ernawati, E.E., 2014, Karakteristik kopolimer radiasi selulosa asetat-ko-glutaraldehida, *Jusami*, 15 (4), 214–220.
- [12] Becker, W., and Schmidt-Naake, G., 2002, Proton exchange membranes by irradiation induced grafting of styrene onto FEP and ETFE: Influences of the crosslinker N,N-methylene-bis-acrylamide, *Chem. Eng. Technol.*, 25 (4), 373–377.
- [13] Kristóf, T., 2017, Selective removal of hydrogen sulphide from industrial gas mixture using zeolite NaA, *Hung. J. Ind. Chem.*, 45 (1), 9–15.
- [14] Mulyono, E., Sumangat, D., and Hidayat, T., 2012, Peningkatan mutu dan efisiensi produksi minyak akar wangi melalui teknologi penyulingan dengan tekanan uap bertahap, *Buletin Teknologi Pascapanen Pertanian*, 8 (1), 35–47.
- [15] Sluiter, A., Hames, B.V., Ruiz, R., Scarlata, C., Sluiter, J., and Templeton, D., 2008, Determination of ash in biomass – Laboratory analytical procedure (LAP), *Technical Report NREL/TP-510-42622*, National Renewable Energy Laboratory, U.S. Department of Energy, Colorado, USA.
- [16] Gierszewska-Drużyńska, M., and Ostrowska-Czubenko, J., 2015, Structural and swelling properties of hydrogel membranes based on chitosan crosslinked with glutaraldehyde and sodium tripolyphosphate, *Prog. Chem. Appl. Chitin Deriv.*, 20, 43–53.
- [17] Suleman, M.S., Lau, K.K., and Yeong, Y.F., 2016, Characterization and performance evaluation of PDMS/PSF membrane for CO₂/CH₄ separation under the effect of swelling, *Procedia Eng.*, 148, 176–183.
- [18] Rosa, S.M.L., Rehman, N., de Miranda, M.I.G., Nachtigall, S.M.B., and Bica, C.I.D., 2012, Chlorine-free extraction of cellulose from rice husk and whisker isolation, *Carbohydr. Polym.*, 87 (2), 1131–1138.
- [19] Bazargan, A., Gebreegziabher, T., Hui, C.W., and McKay, G., 2014, The Effect of alkali treatment on rice husk moisture content and drying kinetics, *Biomass Bioenergy*, 70, 468–473.
- [20] Watkins, D., Nuruddin, M., Hosur, M., Tcherbi-Narteh, A., and Jeelani, S., 2015, Extraction and characterization of lignin from different biomass resources, *J. Mater. Res. Technol.*, 4 (1), 26–32.
- [21] Ab Ghani, M.H., Royan, N.R.R., Kang, S.W., Sulong, A.B., and Ahmad, S., 2015, Effect of alkaline treated rice husk on the mechanical and morphological properties of recycled HDPE/RH Composite, *J. Appl. Sci. Agric.*, 10 (5), 138–144.
- [22] Wang, Z., Li, J., Barforf, J.P., Hellgrandt, K., and McKay, G., 2016, A comparison of chemical treatment methods for the preparation of rice husk cellulosic fibers, *Int. J. Environ. Agric. Res.*, 2 (1), 67–77.
- [23] Muñoz-García, R.O., Hernandez, M.E., Ortiz, G.G., Fernández, V.V.A., Arellano, M.R., and Sánchez-Díaz, J.C., 2015, A novel polyacrylamide-based hydrogel crosslinked with cellulose acetate and prepared by precipitation polymerization, *Quím. Nova*, 38 (8), 1031–1036.
- [24] Hunger, K., Schmeling, N., Jeazet, H.B.T., Janiak, C., Staudt, C., and Kleinermanns, K., 2012, Investigation of cross-linked and additive containing polymer materials for membranes with improved performance in pervaporation and gas separation, *Membranes*, 2 (4), 727–763.

Supplementary Data

This supplementary data is a part of paper entitled “Identification of Phosphatidylinositol 3-Kinase δ (PI3K δ) Inhibitor: Pharmacophore-based Virtual Screening and Molecular Dynamics Simulation”.

Table S1. The hydrogen bonds summary

LASW1976				
Acceptor	Donor	Occupancy (%)	Distance	Angle
LIG@O4	LYS_779@HZ1: LYS_779@NZ	19.38	2.8321	154.2841
LIG@O11	TYR_813@HH: TYR_813@OH	19.00	2.8056	151.4145
LIG@O4	LYS_779@HZ2: LYS_779@NZ	18.96	2.8288	154.4780
LIG@O4	LYS_779@HZ3: LYS_779@NZ	17.17	2.8309	154.1194
ASP_787@OD1	LIG@H22: LIG@O11	12.75	2.7040	163.9481
LIG@O11	ASP_911@H: ASP_911@N	10.98	2.9121	147.4844
TYR_813@OH	LIG@H22: LIG@O11	10.77	2.8217	158.2042
ASP_787@OD2	LIG@H22: LIG@O11	9.10	2.7047	164.5774

Lig25/ZINC253496376				
Acceptor	Donor	Occupancy (%)	Distance (Å)	Angle
ASN_836@OD1	LIG@H10: LIG@N1	18.17	2.8508	161.7049
LIG@O2	ASN_836@HD21: ASN_836@ND2	12.58	2.8665	161.3705
ASP_897@OD1	LIG@H11: LIG@O1	6.14	2.705	157.9328
LIG@O4	LYS_779@HZ1: LYS_779@NZ	6.08	2.834	153.6269
LIG@O4	LYS_779@HZ3: LYS_779@NZ	4.59	2.8385	153.1854
LIG@O4	LYS_779@HZ2: LYS_779@NZ	4.29	2.8376	152.9561
LIG@O4	SER_754@HG: SER_754@OG	4.1	2.7551	160.871
ASP_897@OD2	LIG@H11: LIG@O1	2.55	2.6948	157.8535
ASP_753@O	LIG@H11: LIG@O1	1.21	2.7306	155.9408

Lig199/ZINC12638303				
Acceptor	Donor	Occupancy (%)	Distance (Å)	Angle
LIG@O3	ASP_911@H: ASP_911@N	29.37	2.8572	155.433
LIG@O	LYS_779@HZ2: LYS_779@NZ	17.73	2.8494	158.0609
LIG@O	LYS_779@HZ3: LYS_779@NZ	17.27	2.8509	158.3119
LIG@O	LYS_779@HZ1: LYS_779@NZ	17.03	2.8488	158.1917
LIG@O3	PHE_912@H: PHE_912@N	8.48	2.9122	161.5461
LIG@O3	TYR_813@HH: TYR_813@OH	0.56	2.8	157.2852

Lig449/ZINC85878047				
Acceptor	Donor	Occupancy (%)	Distance (Å)	Angle
LIG@N	SER_754@HG: SER_754@OG	12.56	2.8348	161.0314
LIG@O2	ASP_911@H: ASP_911@N	3.98	2.8956	149.7736
LIG@O5	ASN_836@HD21: ASN_836@ND2	3.61	2.8949	155.151
LIG@O2	TYR_813@HH: TYR_813@OH	0.94	2.7947	151.3205

Lig554/ZINC253389510

Acceptor	Donor	Occupancy (%)	Distance (Å)	Angle
GLU_826@O	LIG@H49: LIG@O2	17.43	2.7683	149.2093
ASP_832@OD2	LIG@H49: LIG@O2	15.99	2.6771	164.9243
ASP_911@OD1	LIG@H54: LIG@O4	15.4	2.6663	163.5248
ASP_911@OD1	LIG@H73: LIG@O14	12.8	2.6889	160.5992
ASP_753@O	LIG@H75: LIG@O15	12.5	2.7488	152.2243
LIG@O2	VAL_828@H: VAL_828@N	11.6	2.9046	154.3873
ASP_911@OD2	LIG@H54: LIG@O4	8.32	2.6839	162.1231
ASP_911@OD2	LIG@H52: LIG@O3	7.74	2.7059	162.2474
ASP_911@OD1	LIG@H71: LIG@O13	7.47	2.7205	162.0516
ASP_832@OD1	LIG@H49: LIG@O2	5.3	2.6716	164.6396
LIG@O15	SER_754@HG: SER_754@OG	5.07	2.7794	162.2276
ASP_911@OD1	LIG@H52: LIG@O3	4.66	2.7094	162.4811
VAL_828@O	LIG@H49: LIG@O2	4.1	2.7805	158.1816
SER_749@O	LIG@H49: LIG@O2	4.02	2.7497	158.3409
ASP_753@O	LIG@H65: LIG@O11	3.98	2.729	158.5985
LIG@O6	LYS_779@HZ2: LYS_779@NZ	3.85	2.8663	155.1535
LIG@O11	ASP_753@H: ASP_753@N	3.84	2.9079	161.8676
LIG@O6	LYS_779@HZ3: LYS_779@NZ	3.73	2.8534	154.9095
ASP_753@OD2	LIG@H65: LIG@O11	3.05	2.7129	155.0601
ASP_753@OD2	LIG@H63: LIG@O10	2.93	2.6682	163.9365
ASP_911@OD2	LIG@H73: LIG@O14	2.8	2.7502	159.7989
LIG@O13	LYS_779@HZ1: LYS_779@NZ	2.57	2.8804	156.8394
LIG@O6	LYS_779@HZ1: LYS_779@NZ	2.46	2.8665	155.2725
ASP_897@OD1	LIG@H54: LIG@O4	1.74	2.6572	163.4485
ASP_753@OD1	LIG@H63: LIG@O10	1.58	2.6847	164.1326
ASP_753@OD1	LIG@H65: LIG@O11	1.46	2.7115	152.5103
ASP_753@O	LIG@H63: LIG@O10	1.41	2.7781	158.6556
ASP_897@OD2	LIG@H54: LIG@O4	1.11	2.6637	162.7398
LIG@O13	LYS_779@HZ3: LYS_779@NZ	1.05	2.8727	156.1291
ASP_911@OD2	LIG@H71: LIG@O13	1.03	2.6941	161.9972

Lig682/ZINC98047241

Acceptor	Donor	Occupancy (%)	Distance (Å)	Angle
ASP_832@OD1	LIG@H1: LIG@O1	96.26	2.5762	160.8423
LIG@O	THR_751@HG1: THR_751@OG1	52.23	2.8151	160.591
ASP_832@OD2	LIG@H1: LIG@O1	2.89	2.5814	161.5876
LIG@O	THR_751@H: THR_751@N	2.22	2.9229	146.8994
LIG@O	ASN_836@HD22: ASN_836@ND2	1.35	2.8636	151.0019
LIG@F	TRP_760@HE1: TRP_760@NE1	1.35	2.8948	143.8625
LIG@O3	ASP_753@H: ASP_753@N	0.24	2.9288	157.3903

Identification of Phosphatidylinositol 3-Kinase δ (PI3K δ) Inhibitor: Pharmacophore-based Virtual Screening and Molecular Dynamics Simulation

Muhammad Arba^{1*}, Malindo Sufriadin¹, and Daryono Hadi Tjahjono²

¹Faculty of Pharmacy, Halu Oleo University, Jl. Kampus Hijau Bumi Tridharma, Anduonou, Kendari 93132, Southeast Sulawesi, Indonesia

²School of Pharmacy, Institut Teknologi Bandung, Jl. Ganesa No. 10, Bandung 40132, West Java, Indonesia

* **Corresponding author:**

email: muh.arba@uho.ac.id

Received: July 5, 2019

Accepted: July 27, 2019

DOI: 10.22146/ijc.47327

Abstract: Phosphatidylinositol 3-kinase δ (PI3K δ) is a validated drug target for the treatment of cancer. The present study aims to search for new inhibitors of PI3K δ by employing pharmacophore modelling using LigandScout Advanced 4.3 software. The three hydrogen bond acceptors and two hydrophobic features were proposed as a pharmacophore model using LASW1976 structure. The model was then validated using the Area Under Curve (AUC) of Receiver Operating Characteristic (ROC) and GH score. It was used to screen new molecules in the ZINC database, which resulted in 599 hits. All 599 hits were then docked into PI3K δ protein, and five best hits were submitted to 50 ns molecular dynamics simulations. Each hit complexed with PI3K δ underwent minor conformational changes as indicated by the values of Root Mean Square Deviation (RMSD) and Root Mean Square Fluctuation (RMSF). Furthermore, prediction of the binding free energy using Molecular Mechanics-Poisson Boltzmann Surface Area (MM-PBSA) method showed that five hits, i.e., Lig25/ZINC253496376, Lig682/ZINC98047241, Lig449/ZINC85878047, Lig554/ZINC253389510, and Lig199/ZINC12638303, had lower binding energy compared to LASW1976. This result indicated their potentials as new inhibitors of PI3K δ .

Keywords: PI3K; molecular docking; pharmacophore modeling; molecular dynamics simulation

■ INTRODUCTION

The phosphoinositide 3-kinases (PI3Ks) are a family of key enzymes that regulate numerous intracellular signal transduction pathways. The PI3K family is subdivided into three classes, i.e., Class I, Class II, and Class III. The Class-I PI3K family catalyzes the phosphorylation of phosphatidylinositol (4,5)-bisphosphate (PIP₂) to produce phosphatidyl-inositol(3,4,5)-trisphosphate (PIP₃) [1-2]. PIP₃ is a membrane-bound second messenger that activates downstream signaling pathways and crucial for cellular processes, such as proliferation, metabolism, and survival [3-4]. Class I, which bears regulatory and catalytic subunits, is subdivided into Class IA and Class IB. Class IA comprises of PI3K α , PI3K β , and PI3K δ , while Class IB includes PI3K γ [5].

Class-IA PI3K is activated by protein tyrosine kinase-coupled receptors, while Class IB is activated downstream by G-protein-coupled receptors. While PI3K α and PI3K β are ubiquitously expressed in all tissues, both PI3K δ and PI3K γ are predominantly found in hematopoietic cells, such as myeloid cells, B cells, and T cells [1,6]. The confined expression profile of PI3K δ suggests that its selective inhibition may be an interesting approach for the treatment of immune cell-related diseases, such as rheumatoid arthritis (RA), asthma, and hematological malignancies [5].

Idelalisib is the first inhibitor of PI3K δ , which is approved by Food and Drug Administration (FDA) to treat relapsed follicular B-cell non-Hodgkin's lymphoma (FL) and relapsed chronic lymphocytic leukemia (CLL) [7].

Another PI3K inhibitor, Copanlisib, has been recently approved for the treatment of follicular lymphoma [8-10]. Despite those facts, the finding of a new inhibitor of PI3K δ is urgently needed due to the side effects of the two agents, such as hepatic toxicity, diarrhea, colitis, and intestinal perforation [11]. However, the design of PI3K δ isoform has not been straightforward due to the similar ATP binding pockets between the isoforms. With the increasingly important role of computational drug design [12-13], the present study combines structure-based pharmacophore modeling with molecular docking to identify a potent inhibitor of PI3K δ . Furthermore, the combined molecular dynamics simulation and the molecular mechanics-Poisson Boltzmann Surface Area (MM-PBSA) methods were applied to explore the conformational change of ligand-receptor complex and to predict the binding affinity of the ligand to PI3K δ .

■ Computational Methods

Pharmacophore Modeling and Database Screening

The pharmacophore model was built by employing LigandScout Advanced 4.3 software [14] based on the 3D structure of PI3K δ -LASW1976 complex, which was retrieved from the Protein Data Bank (www.rcsb.org) with the PDB ID 6G6W [11]. The model was then validated by performing screening against 27 actives taken from BindingDB [15] and 1455 decoys retrieved from the Directory of Useful Decoys-Enhanced (DUD-E) [16].

Furthermore, Pharmit web server (<http://pharmit.csb.pitt.edu/>) [17] was used to screen hit molecules against the ZINC database using the validated pharmacophore [18]. The radius of each hydrogen bond donor/acceptor and hydrophobic features was 0.5 Å and 1 Å, respectively.

Molecular Docking and Molecular Dynamics Studies

Each hit molecule was docked into the active site of PI3K δ using iDock software [19]. The PI3K δ structure in complex with LASW1976 was retrieved from the Protein Data Bank (PDB ID: 6G6W) [11]. The receptor was prepared by using AutoDockTools 1.5.6., including adding polar hydrogen and assigning Kollman charges. The grid box for docking was set to the center of LASW1976

coordinates with a size of 22.5 × 22.5 × 22.5 Å in XYZ dimensions. The LASW1976 was redocked into PI3K δ to validate the docking protocol. Analysis and visualization of docked molecules were performed by using Discovery Studio Visualizer 2016. Five top molecules having the best binding affinities with good interaction were subjected to molecular dynamics simulation.

Molecular dynamics (MD) simulation was used to study the conformational changes in the interaction of ligands with PI3K δ . Five best docked ligands and native inhibitor (LASW1976), each complexed with PI3K δ , were chosen for MD simulation employing AMBER16 package [20-21]. Leap module of AMBER16 was used to prepare each ligand-protein complex. The ff14SB force field [22] was used to process protein, while GAFF force field [23] and AM1-BCC [24] were used to treat ligands. Each complex was immersed in a truncated octahedron TIP3P water box with a 10 Å radius. Counterions were added to the neutralized complex.

Each prepared complex underwent minimization using the sander program of AMBER16. The minimization was performed by 500 cycles of steepest descents and 5500 cycles of conjugate gradients methods in three steps: i) the protein was restrained with a force constant of 500 kcal mol⁻¹ Å⁻²; ii) the backbone atoms of protein were restrained with a force constant of 500 kcal mol⁻¹ Å⁻²; iii) minimization without restraint.

Furthermore, each system was gradually heated from 0 to 100, 100 to 200, and 200 to 300 K, respectively, for every 50 ps with a time step of 0.0005 ps and backbone atoms of protein were restrained with a force constant 5 kcal mol⁻¹ Å⁻². The system was then equilibrated at 300 K in three steps over a period of 200 ps. First and second equilibrations were performed for every 50 ps with force constants of 5 and 3 kcal mol⁻¹ Å⁻². Final 100 ps equilibration was conducted without restraint. A full production step was performed for 50 ns in NPT ensemble without any restraint employing pmemd.cuda module of AMBER16.

All bonds involving hydrogen atoms were constrained using SHAKE algorithm [25] with 2 fs integration time step. The particle-mesh Ewald

algorithm method was used to treat long-range electrostatics interactions [26] of a periodic box with a non-bonding cutoff distance of 9.0 Å. The Langevin thermostat was used to control Langevin thermostat with a collision rate of 1.0 ps⁻¹. The coordinate files were saved every 1 ps. Analyses were performed with the CPPTRAJ module of AMBER16 [27], while visualization was conducted using the Visual Molecular Dynamics software [28].

Binding Free Energy Calculation

The binding affinity of ligands to PI3Kδ was assessed through the binding free energy calculation using the Molecular Mechanics-Poisson Boltzmann solvent accessible surface area (MM-PBSA) method [29-30] of AMBER16 [31]. Trajectories with two hundred snapshots were taken from 30–50 ns MD simulation. The binding free energy (ΔG_{bind}) is calculated using the following equations:

$$\Delta G_{\text{bind}} = G_{\text{complex}} - G_{\text{rec}} - G_{\text{ligand}} \quad (1)$$

$$\Delta G_{\text{bind}} = \Delta E_{\text{MM}} + \Delta G_{\text{sol}} - T\Delta S \quad (2)$$

$$\Delta E_{\text{MM}} = \Delta E_{\text{bond}} + \Delta E_{\text{angle}} + \Delta E_{\text{torsion}} + \Delta E_{\text{vdw}} + \Delta E_{\text{EEL}} \quad (3)$$

$$\Delta G_{\text{sol}} = \Delta G_{\text{PB}} + \Delta G_{\text{SA}} \quad (4)$$

where G_{complex} , G_{rec} , and G_{lig} refer to the free energy of the complex, receptor, and ligand, respectively. The ΔG_{bind} consists of the binding energy in the vacuum/gas phase (ΔE_{MM}), the solvation free energy (ΔG_{sol}), and the conformational entropy change upon ligand binding at temperature T ($T\Delta S$). The ΔE_{MM} is the sum of bond energy (ΔE_{bond}), the angle energy (ΔE_{angle}), the torsion energy ($\Delta E_{\text{torsion}}$), the van der Waals energy (ΔE_{vdw}), and the electrostatic energy (ΔE_{EEL}). Meanwhile, ΔG_{sol} includes polar contribution to solvation free energy (ΔG_{PB}) calculated by solving the Poisson-Boltzmann (PB) equation using a grid size of 0.5 Å, and the non-polar contribution (ΔG_{SA}), which was calculated using the solvent accessible surface area (SASA) with the solvent-probe radius set to 1.4 Å.

RESULTS AND DISCUSSION

The pharmacophore model development resulted in a hypothesis consisting of three hydrogen bond acceptors and two hydrophobic features. Fig. 1 shows the

pharmacophore model generated on LigandScout 4.3 Advanced software.

Validation of the model against 27 actives and 1455 decoys resulted in Area Under Curve (AUC) of Receiver Operating Characteristic (ROC) of 0.67. The calculation of Goodness of Hit Score (GH-score) gave a result of 0.64. Both parameters indicated that the pharmacophore model was able to differentiate the actives from the decoy molecules. Fig. 2 displays the Area Under Curve (AUC) of Receiver Operating Characteristic (ROC) curve.

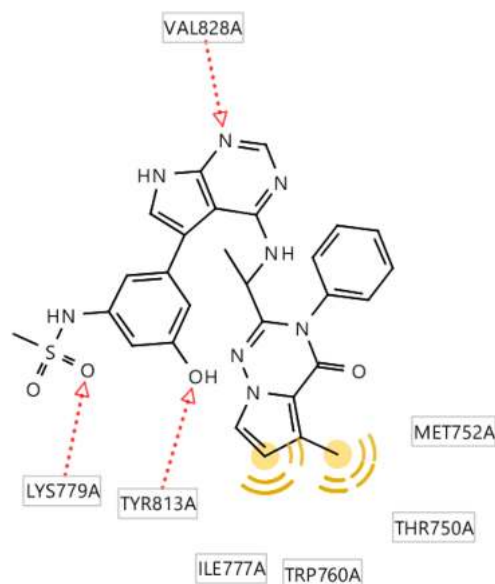


Fig 1. 3D pharmacophore model consisting of three hydrogen bond acceptors (red dotted lines) and two hydrophobic (yellow sphere) features

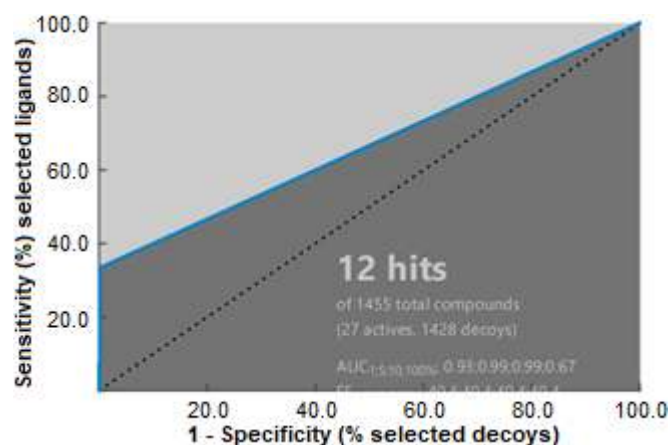


Fig 2. The Area Under Curve (AUC) of Receiver Operating Characteristic (ROC) curve

Furthermore, screening for hit molecules against the ZINC database by using the built pharmacophore model in Pharmit (<http://pharmit.csb.pitt.edu/>) retrieved 599 hit molecules. All 599 hits were then docked into PI3K δ using iDock, which gave conformations and binding energies ranging from -3.26 to -10.68 kcal/mol. Meanwhile, redocking of LASW1976 produced a similar conformation to the X-ray pose (root mean square deviation, RMSD=1.04 Å) and binding energy of -10.99 kcal/mol, which indicated that the docking protocol was valid [32]. All hydrogen bonds (Hbonds) of X-ray experiment were reproduced in a docked pose such as those with Lys779, Asp787, Tyr813, and Val828. Additional Hbond interaction of docked conformation was found between LASW1976 and Asp911. Fig. 3 shows the superimposed LASW1976 conformations of both experimental and docked experiments.

Based on the binding energies and conformations, five best docked hit molecules were selected. They were Lig25/ZINC253496376 ($E=-10.68$ kcal/mol), Lig682/ZINC98047241 ($E=-10.68$ kcal/mol), Lig449/ZINC85878047 ($E=-10.54$ kcal/mol), Lig554/ZINC253389510 ($E=-10.29$ kcal/mol), and Lig199/ZINC12638303 ($E=-10.28$ kcal/mol).

Fig. 4 shows the chemical structures of the five best docked hit molecules.

In the meantime, the binding of hit molecules occurred through several Hbond and hydrophobic interactions. Lig25/ZINC253496376 formed two Hbond interactions with Lys779 through oxygen atoms of

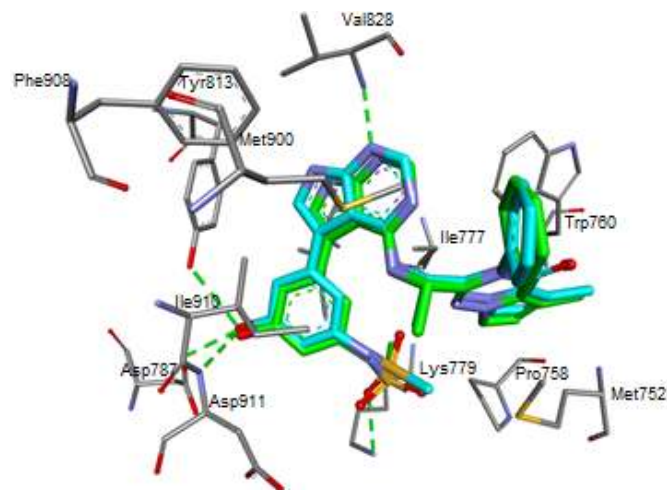


Fig 3. The superimposed LASW1976 conformations of both experimental (green) and docked (blue) experiments. The hydrogen bonds are represented in green colored dashed lines

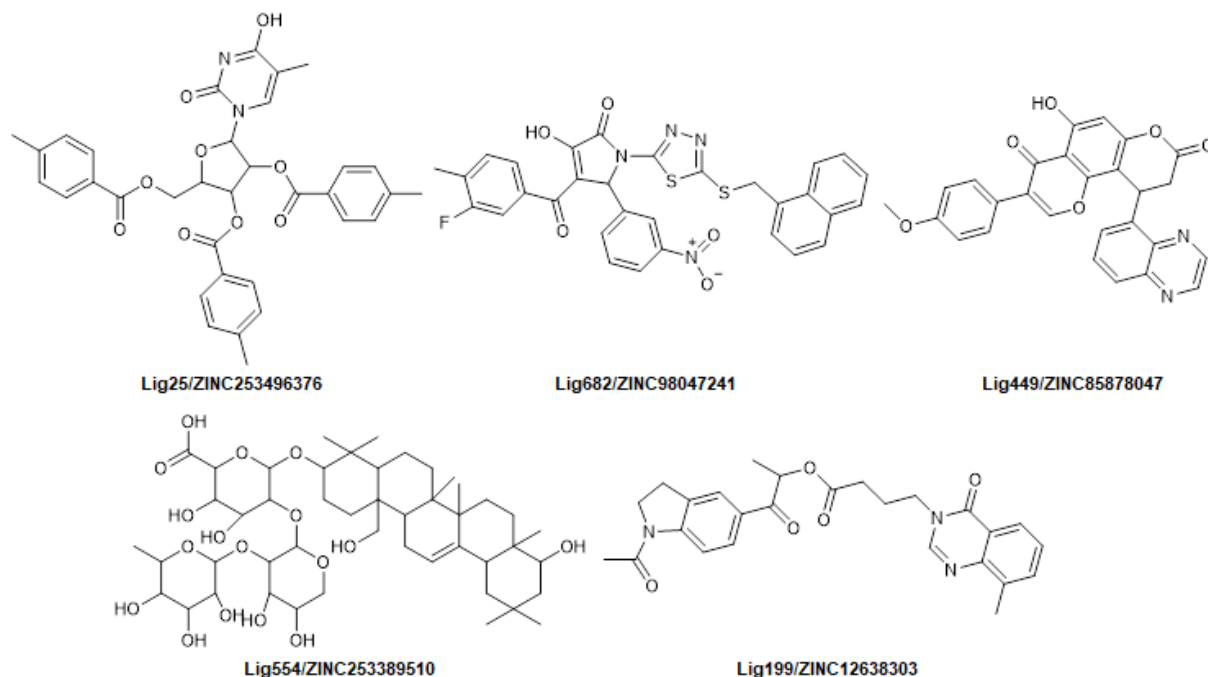


Fig 4. The chemical structures of the five best docked hit molecules

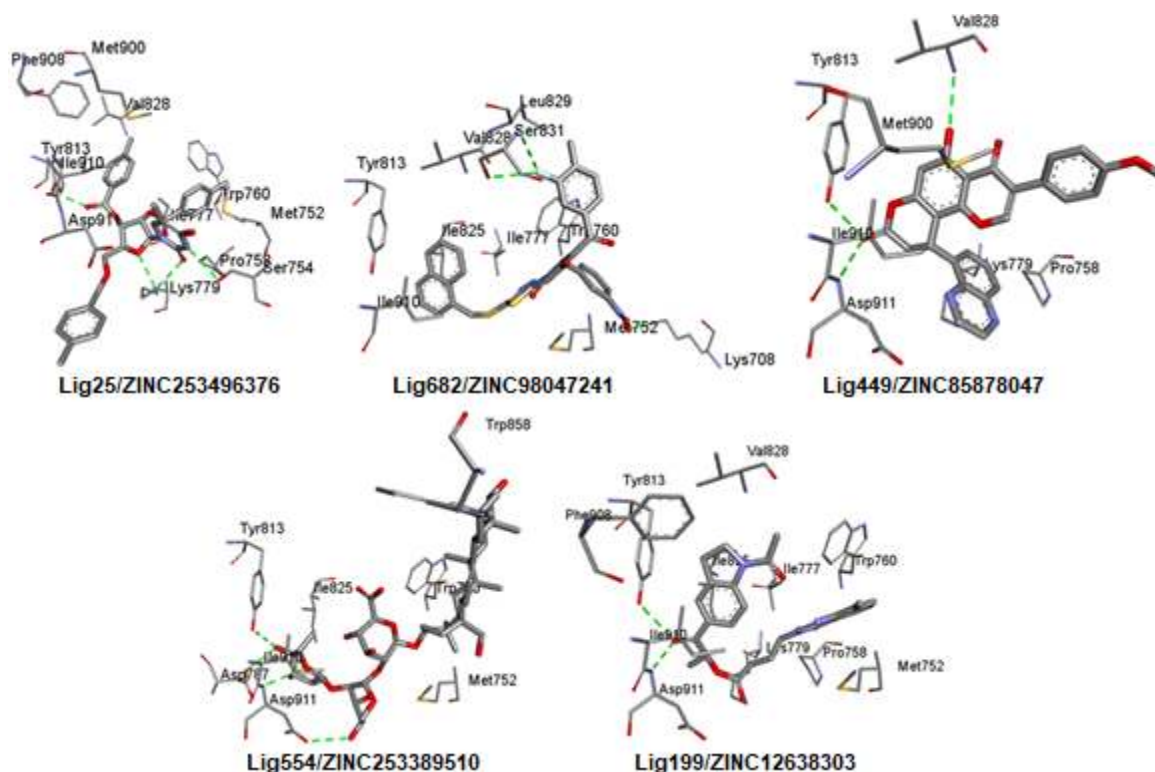


Fig 5. The binding modes of each hit molecules, i.e., Lig25/ZINC253496376, Lig682/ZINC98047241, Lig449/ZINC 85878047, Lig554/ZINC253389510, Lig199/ZINC12638303, into the active site of PI3K δ . The hydrogen bonds are represented in green colored dashed lines

pyrimidine and oxolane groups. The nitrogen atom of the pyrimidine group also formed Hbond with Ser754, while Tyr813 formed Hbond with the oxygen atom of the carbonyl group. Lig682/ZINC98047241 formed Hbond interaction through an oxygen atom of phenylnitroso oxidanol group with Lys708 and two Hbond interactions between the fluorine atom of the ligand with Ser831 were also established. Amino acid residues Tyr813 along with Asp911 also formed Hbonds with Lig449/ZINC85878047 through an oxygen atom of pyran group, in addition to Val828 which formed Hbond interaction with the oxygen atom of the phenyl group. Tyr813 and Asp911 were both found to establish two Hbond interactions in the binding of Lig554/ZINC 253389510, in addition to the one with Asp787. The binding of Lig199/ZINC12638303 was also corroborated with Hbond interactions between oxygen atoms of two carbonyl groups and Tyr813 and Asp911, as well as Lys779. Fig. 5 displays the binding modes of each hit molecules into the active site of PI3K δ .

Molecular Dynamics Simulations

Five best docked hit molecules to PI3K δ were subjected to MD simulation for 50 ns to assess their conformational changes in a physiological condition. The values of root mean square deviation (RMSD), which is considered as a parameter for the stability of complex during dynamics runs, were calculated. Fig. 6 shows the RMSD values of heavy atoms (Ca, C, N, O) of the protein. There was a sudden increase in the early stage of simulation (0–20 ns) for all ligands, but it soon became stable throughout the simulation. The Lig682/ZINC98047241 (pink) and Lig554/ZINC253389510 (purple) displayed lower RMSD values than the cognate ligand (LASW1976, red) did, indicating their more stable conformational changes. On the other hand, although Lig25/ZINC253496376 (green), Lig449/ZINC 85878047 (blue), and Lig199/ZINC12638303 (cyan) showed more fluctuated changes than LASW1976 (red), their movements tended to be stable in the rest simulation.

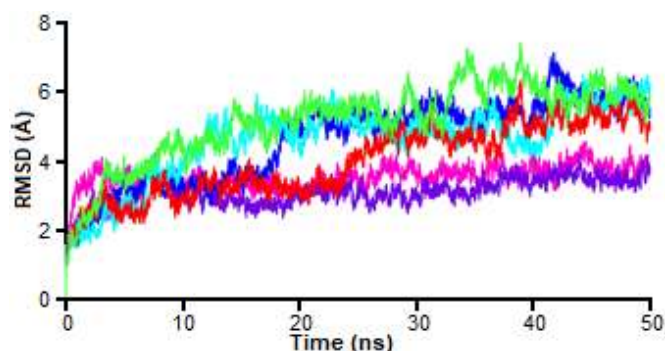


Fig 6. RMSD value of protein heavy atom of each ligand-PI3K δ complex during 50 ns MD calculated for LASW1976 (red), Lig25/ZINC253496376 (green), Lig682/ZINC98047241 (pink), Lig449/ZINC85878047 (blue), Lig554/ZINC253389510 (purple), and Lig199/ZINC12638303 (cyan)

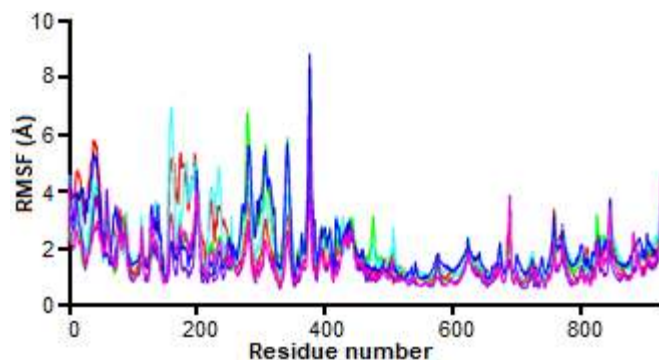


Fig 7. RMSF change during 50 ns MD simulation for LASW1976 (red), Lig25/ZINC253496376 (green), Lig682/ZINC98047241 (pink), Lig449/ZINC85878047 (blue), Lig554/ZINC253389510 (purple), and Lig199/ZINC12638303 (cyan)

In addition to the RMSD plot, atomic fluctuation along amino acid residues of the PI3K δ during dynamics runs were monitored in root mean square fluctuation (RMSF) plot (Fig. 7). It shows that amino acid residues fluctuated in a similar pattern in all regions of the protein, indicating the similar binding modes of hit molecules. Higher values of RMSF were found at peaks of Tyr39 (Tyr55), Asp279 (Asp336), Val308 (Val365), Glu376 (Glu448), and Ser688 (Ser770), which were attributable to the loop regions. In addition, Pro160 (Pro186) and Glu342 (Glu399) were also dominant and corresponded to the ends of beta-helix. On the other hand, amino acid residues involved in the Hbond interactions over all ligands, such as Lys708, Ser754, Lys779, Asp787, Tyr813, Val828, Ser831, and Asp911, appeared to be more rigid, indicating that ligand binding induced stability over the protein fluctuation.

Monitoring the conformation of each hit after 50-ns MD simulation revealed several changes were noted in the poses of hit molecules. Hit molecule Lig25/ZINC253496376 formed conventional Hbond interaction with Asn754, C—H \cdots O hydrogen bond interaction with Ser672, as well as pi-alkyl interactions with Tyr731, Met670, and Ile815. Lig682/ZINC98047241 formed conventional Hbond interactions with Lys626, Thr751, Asn754, and Asp750, as well as C—H \cdots O hydrogen bond interaction with Met670. In addition, pi-sulfur contact occurred with Met670. Pi-alkyl interaction was observed

with Met680, Trp678, Met805, Ile695, Ile743, and Ile815, while pi-pi interaction occurred with Trp678. Pi-alkyl interactions were also noted between Lig449/ZINC85878047 with Ile815, Met670, Val745, and Met805, while pi-pi interaction was observed with Trp678. Meanwhile, Lig554/ZINC253389510 established conventional Hbond interactions with Lys697, Val746, and Glu744, as well as pi alkyl interactions with Trp678 and Tyr731. Conventional Hbond interaction was also formed between Lig199/ZINC12638303 and Asp816. While pi-alkyl interactions were noted between Lig199/ZINC12638303 and Trp678, Met670, Ile695, and Ile815. The binding of Lig199/ZINC12638303 was also corroborated by pi-pi interaction with Trp678. Fig. 8 showed each mode of interaction of each hit molecule after 50 ns MD simulation.

Monitoring of the Hbonds during dynamics run showed that the Hbonds interactions showed fair occupancies during molecular dynamics simulation. For example, the Hbonds of Lig199/ZINC12638303 with Asp911 and Lys779 showed fair occupancies of 29.37% and 17.73%, respectively. Meanwhile, the Hbond with Tyr813 showed very low occupancy which was only 0.56%. In the Lig554/ZINC253389510 binding, several Hbonds between ligand atoms and Asp911 were found with occupancies ranging from 1.03% to 15.4%. Whereas, Hbonds between Lig554/ZINC253389510 and Val828 had 4.10% and 11.6% occupancies. The Lig449/ZINC85878047

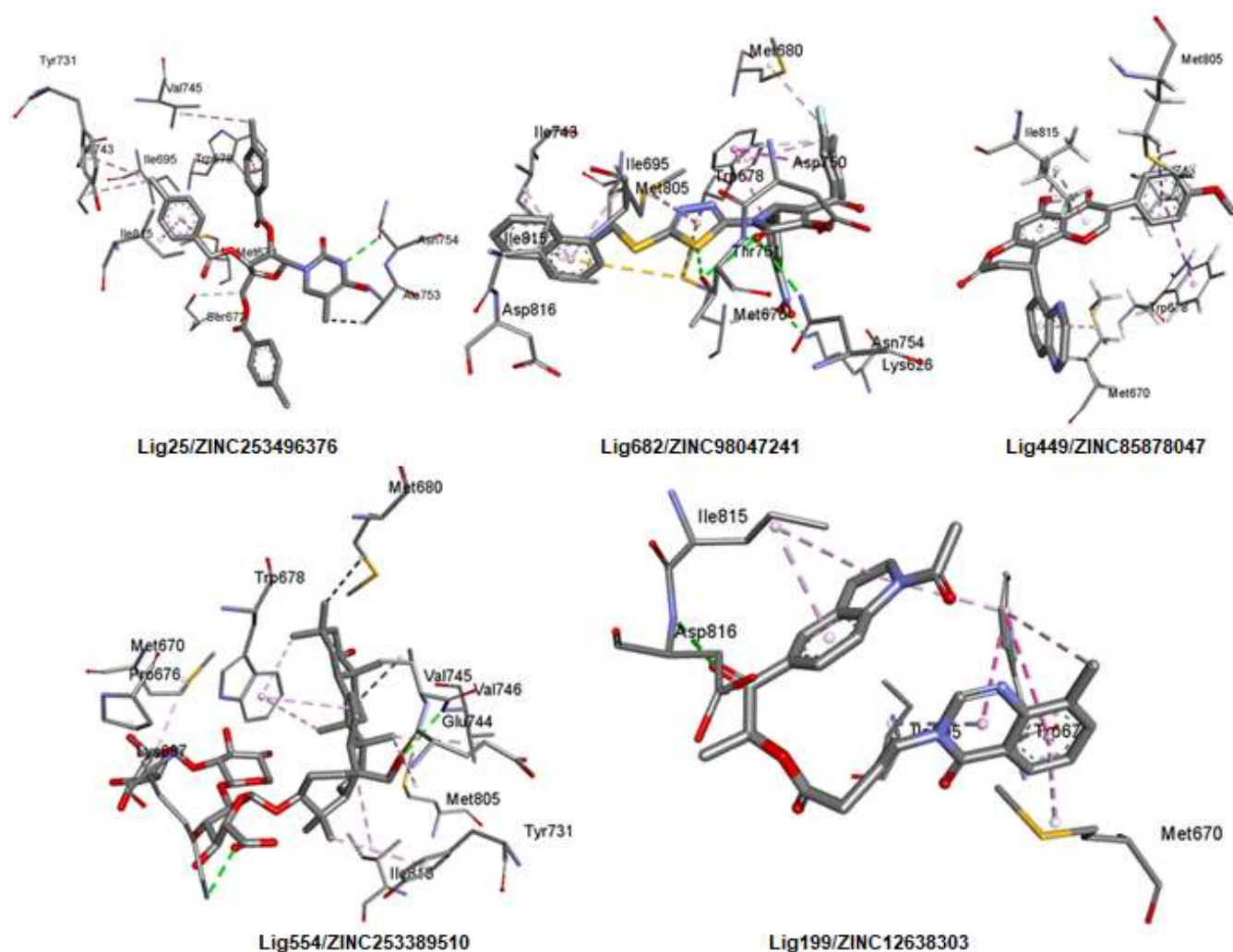


Fig 8. Conformation of each hit molecule after 50 ns MD simulation. The hydrogen bond, C—H···O hydrogen bond, pi-alkyl, pi-pi, pi-sulfur interactions are represented in green, pale blue, pink, magenta, and yellow colored dashed lines, respectively

showed that the Hbonds with Ser754, Asp911, and Tyr813 had the occupancies of 12.56, 3.98, and 0.94%, respectively. While Lig25/ZINC253496376 had several Hbonds with Lys779 with the occupancies of 4.29 to 6.08%, while that with Ser754 showed very low occupancies of 4.1%.

On the other hand, several new Hbonds were found during MD simulation. The new Hbonds were, for example, Hbonds between Lig682/ZINC98047241 and Asp832 and Thr833 with occupancies of 96.26 and 52.23%, respectively. The Hbond with Asp832 was also found in the binding of Lig554/ZINC253389510 with occupancy of 15.99%. In addition, Hbond with Asn836 was found

doubly in the binding of Lig25/ZINC253496376 with occupancies of 18.17 and 12.58%. Meanwhile, that with Lig449/ZINC85878047 showed 3.61% occupancy. On the other hand, Hbond with Glu826 was found with 17.43% occupancy in the binding of Lig554/ZINC253389510. Table S1 shows the Hbond occupancies during the 50 ns simulation.

Free Binding Energy Calculations

The five best docked hit molecules were subjected to free binding energy calculation using the MM-PBSA method. The MM-PBSA method is widely considered to be more accurate compared to the docking scoring. Table 1

Table 1. The binding free energy and their individual energy contributions

Ligand	ΔE_{ELE} (kcal/mol)	ΔE_{VDW} (kcal/mol)	ΔE_{PBCAL} (kcal/mol)	ΔE_{PBSUR} (kcal/mol)	ΔE_{PBTOT} (kcal/mol)
LASW1976	-15.54±6.17	-49.03±3.84	53.15±7.99	-4.84±0.18	-16.27±4.54
Lig25/ZINC253496376	-29.24±13.14	-44.58±5.50	54.01±12.75	-5.24±0.41	-25.05±4.96
Lig199/ZINC12638303	-24.79±4.33	-56.99±2.99	53.38±4.54	-5.25±0.11	-33.64±3.69
Lig449/ZINC85878047	2.96±7.43	-38.78±3.83	23.73±6.95	-4.49±0.21	-16.58±5.96
Lig554/ZINC253389510	-32.85±21.38	-52.19±6.04	58.56±20.15	-5.63±0.41	-38.27±8.90
Lig682/ZINC98047241	-32.96±4.96	-45.14±4.60	53.67±5.41	-5.37±0.22	-29.80±3.97

displays the binding free energy and their individual energy contributions. The hit molecule Lig554/ZINC 253389510 had the lowest predicted binding free energy ($\Delta E_{PBTOT} = -38.27 \pm 8.90$ kcal/mol), about 2 times more negative than that of LASW1976 ($\Delta E_{PBTOT} = -16.27 \pm 4.54$ kcal/mol). The binding energy value for a good inhibitor was considered in the range of -9 to -12 kcal/mol, however, the much lower binding energy value obtained in the present study corresponded to the excluded entropy term in the calculation [30]. Furthermore, the hit molecule Lig199/ZINC12638303 scored the second best binding free energy ($\Delta E_{PBTOT} = -33.64 \pm 3.69$ kcal/mol), followed by the molecule hits Lig682/ZINC98047241 ($\Delta E_{PBTOT} = -29.80 \pm 3.97$ kcal/mol), Lig25/ZINC253496376 ($\Delta E_{PBTOT} = -25.05 \pm 4.96$ kcal/mol), and Lig449/ZINC85878047 ($\Delta E_{PBTOT} = -16.58 \pm 5.96$ kcal/mol). The major favorable contributions to ligand binding at PI3K δ were originated from electrostatic (ΔE_{ELE}), van der Waals (ΔE_{VDW}), and non-polar solvation energy (ΔE_{PBSUR}), except for Lig449/ZINC85878047 which had positive electrostatic energy. Overall, all hit molecules displayed stronger affinities than LASW1976 did.

CONCLUSION

Structure-based pharmacophore modelling was performed based on PI3K δ -LASW1976 interaction. The pharmacophore model was built and validated based on the Area Under Curve of Receiver Operating Characteristic and GH-score. It was then used to identify hit molecules in the ZINC database. Five hundred and ninety-nine hit molecules were retrieved and then docked to the active site of PI3K δ to reveal their binding modes. Hit molecules maintained their interactions with the PI3K δ through important Hbond and hydrophobic interactions. Five

best hits were selected and subjected to MD simulation, which showed good stability during 50 ns. Prediction of binding free energy using the MM-PBSA method showed that the five hit molecules displayed stronger affinities than LASW1976 did. The van der Waals, electrostatic, and nonpolar contribution to the solvation energy interactions were favorable for most hit molecules. The present work suggests five hit molecules that might serve as potential inhibitors of PI3K δ .

ACKNOWLEDGMENTS

The present research was partly funded by the Ministry of Research and the Higher Education Republic of Indonesia through Hibah Penelitian Dasar 2019.

REFERENCES

- [1] Ameriks, M.K., and Venable, J.D., 2009, Small molecule inhibitors of phosphoinositide 3-kinase (PI3K) delta and gamma, *Curr. Top. Med. Chem.*, 9 (8), 738–753.
- [2] Hoegenauer, K., Soldermann, N., Hebach, C., Hollingworth, G.J., Lewis, I., von Matt, A., Smith, A.B., Wolf, R.M., Wilcken, R., Haasen, D., Burkhart, C., and Zécric, F., 2016, Discovery of novel pyrrolidineoxy-substituted heteroaromatics as potent and selective PI3K delta inhibitors with improved physicochemical properties, *Bioorg. Med. Chem. Lett.*, 26 (23), 5657–5662.
- [3] Vanhaesebroeck, B., Stephens, L., and Hawkins, P., 2012, PI3K signalling: The path to discovery and understanding, *Nat. Rev. Mol. Cell Biol.*, 13 (3), 195–203.
- [4] Ma, C.C., Zhang, C.M., Tang, L.Q., and Liu, Z.P., 2018, Discovery of novel quinazolinone derivatives

- as high potent and selective PI3K δ and PI3K δ / γ inhibitors, *Eur. J. Med. Chem.*, 151, 9–17.
- [5] Hoegenauer, K., Soldermann, N., Stauffer, F., Furet, P., Graveleau, N., Smith, A.B., Hebach, C., Hollingworth, G.J., Lewis, I., Gutmann, S., Rummel, G., Knapp, M., Wolf, R.M., Blanz, J., Feifel, R., Burkhart, C., and Zécéri, F., 2016, Discovery and pharmacological characterization of novel quinazoline-based PI3K delta-selective inhibitors, *ACS Med. Chem. Lett.*, 7 (8), 762–767.
- [6] Rowan, W.C., Smith, J.L., Affleck, K., and Amour, A., 2012, Targeting phosphoinositide 3-kinase δ for allergic asthma, *Biochem. Soc. Trans.*, 40 (1), 240–245.
- [7] Nair, K.S., and Cheson, B., 2016, The role of idelalisib in the treatment of relapsed and refractory chronic lymphocytic leukemia, *Ther. Adv. Hematol.*, 7 (2), 69–84.
- [8] Göckeritz, E., Kerwien, S., Baumann, M., Wigger, M., Vondry, V., Neumann, L., Landwehr, T., Wendtner, C.M., Klein, C., Liu, N., Hallek, M., Frenzel, L.P., and Krause, G., 2015, Efficacy of phosphatidylinositol-3 kinase inhibitors with diverse isoform selectivity profiles for inhibiting the survival of chronic lymphocytic leukemia cells, *Int. J. Cancer*, 137 (9), 2234–2242.
- [9] Bashash, D., Safaroghli-Azar, A., Dadashi, M., Safa, M., Momeny, M., and Ghaffari, S.H., 2017, Anti-tumor activity of PI3K- δ inhibitor in hematologic malignant cells: Shedding new light on resistance to Idelalisib, *Int. J. Biochem. Cell Biol.*, 85, 149–158.
- [10] Flinn, I.W., Patel, M., Oki, Y., Horwitz, S., Foss, F.F., Allen, K., Douglas, M., Stern, H., Sweeney, J., Kharidia, J., Kelly, P., Kelly, V.M., and Kahl, B., 2018, Duvelisib, an oral dual PI3K- δ , γ inhibitor, shows clinical activity in indolent non-Hodgkin lymphoma in a phase 1 study, *Am. J. Hematol.*, 93 (11), 1311–1317.
- [11] Erra, M., Taltavull, J., Bernal, F.J., Caturla, J.F., Carrascal, M., Pagès, L., Mir, M., Espinosa, S., Gràcia, J., Domínguez, M., Sabaté, M., Paris, S., Maldonado, M., Hernández, B., Bravo, M., Calama, E., Miralpeix, M., Lehner, M.D., and Calbet, M., 2018, Discovery of a novel inhaled PI3K δ inhibitor for the treatment of respiratory diseases, *J. Med. Chem.*, 61 (21), 9551–9567.
- [12] Arba, M., Nur-Hidayat, A., Surantaadmaja, S.I., and Tjahjono, D.H., 2018, Pharmacophore-based virtual screening for identifying β 5 subunit inhibitor of 20S proteasome, *Comput. Biol. Chem.*, 77, 64–71.
- [13] Arba, M., Yamin, Ihsan, S., and Tjahjono, D.H., 2018, Computational approach toward targeting the interaction of porphyrin derivatives with Bcl-2, *J. Appl. Pharm. Sci.*, 8 (12), 60–66.
- [14] Wolber, G., and Langer, T., 2005, LigandScout: 3-D pharmacophores derived from protein-bound ligands and their use as virtual screening filters, *J. Chem. Inf. Model.*, 45 (1), 160–169.
- [15] Gilson, M.K., Liu, T., Baitaluk, M., Nicola, G., Hwang, L., and Chong, J., 2016, BindingDB in 2015: A public database for medicinal chemistry, computational chemistry and systems pharmacology, *Nucleic Acids Res.*, 44 (D1), D1045–D1053.
- [16] Mysinger, M.M., Carchia, M., Irwin, J.J., and Shoichet, B.K., 2012, Directory of useful decoys, enhanced (DUD-E): Better ligands and decoys for better benchmarking, *J. Med. Chem.*, 55 (14), 6582–6594.
- [17] Sunseri, J., and Koes, D.R., 2016, Pharmit: interactive exploration of chemical space, *Nucleic Acids Res.*, 44 (W1), W442–W448.
- [18] Irwin, J.J., Sterling, T., Mysinger, M.M., Bolstad, E.S., and Coleman, R.G., 2012, ZINC: A free tool to discover chemistry for biology, *J. Chem. Inf. Model.*, 52 (7), 1757–1768.
- [19] Li, H., Leung, K.S., and Wong, M.H., 2012, Idock: A multithreaded virtual screening tool for flexible ligand docking, 2012 *IEEE Symposium on Computational Intelligence in Bioinformatics and Computational Biology (CIBCB)*, San Diego, California, USA, 9–12 May 2012, 77–84.
- [20] Case, D.A., Cheatham, T.E., Darden, T., Gohlke, H., Luo, R., Merz, K.M., Onufriev, A., Simmerling, C., Wang, B., and Woods, R.J., 2005, The Amber biomolecular simulation programs, *J. Comput. Chem.*, 26 (16), 1668–1688.

- [21] Salomon-Ferrer, R., Götz, A.W., Poole, D., Le Grand, S., and Walker, R.C., 2013, Routine microsecond molecular dynamics simulations with AMBER on GPUs. 2. Explicit solvent particle mesh Ewald, *J. Chem. Theory Comput.*, 9 (9), 3878–3888.
- [22] Maier, J.A., Martinez, C., Kasavajhala, K., Wickstrom, L., Hauser, K.E., and Simmerling, C., 2015, ff14SB: Improving the accuracy of protein side chain and backbone parameters from ff99SB, *J. Chem. Theory Comput.*, 11 (8), 3696–3713.
- [23] Wang, J., Wolf, R.M., Caldwell, J.W., Kollman, P.A., and Case, D.A., 2004, Development and testing of a general amber force field, *J. Comput. Chem.*, 25 (9), 1157–1174.
- [24] Jakalian, A., Jack, D.B., and Bayly, C.I., 2002, Fast, efficient generation of high-quality atomic charges. AM1-BCC model: II. Parameterization and validation, *J. Comput. Chem.*, 23 (16), 1623–1641.
- [25] Ryckaert, J.P., Ciccotti, G., and Berendsen, H.J.C., 1977, Numerical integration of the Cartesian equations of motion of a system with constraints: Molecular dynamics of *n*-alkanes, *J. Comput. Phys.*, 23 (3), 327–341.
- [26] Darden, T., York, D., and Pedersen, L., 1993, Particle mesh Ewald: An $N \cdot \log(N)$ method for Ewald sums in large systems, *J. Chem. Phys.*, 98 (12), 10089.
- [27] Roe, D.R., and Cheatham III, T.E., 2013, PTRAJ and CPPTRAJ: Software for processing and analysis of molecular dynamics trajectory data, *J. Chem. Theory Comput.*, 9 (7), 3084–3095.
- [28] Humphrey, W., Dalke, A., and Schulten, K., 1996, VMD: Visual molecular dynamics, *J. Mol. Graphics*, 14 (1), 33–38.
- [29] Kollman, P.A., Massova, I., Reyes, C., Kuhn, B., Huo, S., Chong, L., Lee, M., Lee, T., Duan, Y., Wang, W., Donini, O., Cieplak, P., Srinivasan, J., Case, D.A., and Cheatham, T.E., 2000, Calculating structures and free energies of complex molecules: Combining molecular mechanics and continuum models, *Acc. Chem. Res.*, 33 (12), 889–897.
- [30] Arba, M., Kartasasmita, R.E., and Tjahjono, D.H., 2016, Molecular docking and dynamics simulations on the interaction of cationic porphyrin-anthraquinone hybrids with DNA G-quadruplexes, *J. Biomol. Struct. Dyn.*, 34 (2), 427–438.
- [31] Miller, B.R., McGee, T.D., Swails, J.M., Homeyer, N., Gohlke, H., and Roitberg, A.E., 2012, MMPBSA.py: An efficient program for end-state free energy calculations, *J. Chem. Theory Comput.*, 8 (9), 3314–3321.
- [32] Morris, G.M., Goodsell, D.S., Halliday, R.S., Huey, R., Hart, W.E., Belew, R.K., and Olson, A.J., 1998, Automated docking using a Lamarckian genetic algorithm and an empirical binding free energy function, *J. Comput. Chem.*, 19 (14), 1639–1662.

Spectrophotometric Determination of Cu(II) in Analytical Sample Using a New Chromogenic Reagent (HPEDN)

Esraa Raafid¹, Muneer A. Al-Da'amy¹, and Salih Hadi Kadhim^{2,*}

¹Department of Chemistry, College of Education for Pure Science, University of Kerbala, Kerbala, Iraq

²Department of Chemistry, College of Science, University of Babylon, Babylon, Iraq

* Corresponding author:

email: hadi197019@yahoo.com

Received: July 19, 2019

Accepted: September 12, 2019

DOI: 10.22146/ijc.47894

Abstract: A sensitive, accurate and rapid spectrophotometric method that can be used for the determination of Cu(II) in analytical samples using a new chromogenic reagent azo-Schiff base 1-((4-(1-(2-hydroxyphenylimino)ethyl)-phenyl)diazanyl) naphthalene-2-ol (HPEDN) was studied. The synthesized new (azo-Schiff base) ligand was complexed with copper(II) and characterized using UV/Vis spectroscopy, IR spectra, ¹H-NMR, ¹³C-NMR spectra, Molar electrical conductivity, and measuring of their melting points. The obtained complex showed a brown color with maximum absorption at $\lambda_{max} = 500$ nm at pH = 9. Beer's law was obeyed in the concentration range of 1.7 to 5.4 $\mu\text{g/mL}$. The molar absorption and Sandell's sensitivity values of the Cu(II) complex were found to be $0.5038 \times 10^4 \text{ L mol}^{-1} \text{ cm}^{-1}$ and $0.0039 \mu\text{g cm}^{-2}$, respectively. The structure of the prepared complex was investigated by using the continuous variation, mole ratio method and slope analysis method. The obtained results showed that the complex has (1:2) (M:L) molar ratio and these results showed that this method was more sensitive, more precise and accurate through the calculation of (Re, Erel, R.S.D)%. The most important interferences were Co^{2+} , Cd^{2+} , Zn^{2+} , Ni^{2+} , Mn^{2+} , Pd^{2+} , Fe^{3+} , thus suitable masking agents were used. This method was applied for the determination of Cu(II) in alloy. The obtained results were compared with flame atomic absorption spectrometry method and showed that results of both methods were in good agreement.

Keywords: azo-Schiff base compounds; 2-amino phenol Schiff base; precise and accuracy

■ INTRODUCTION

Copper is a reddish-colored metal and a heavy metal that changes color and properties when it is combined with other elements forming different compounds [1-2]. Copper is a soft material that can be reacted chemically [3] or physically with external source [4]. In addition to that, its advantages include a slow rate of reaction with diluted acids [5-6]. Copper is a fundamental supplementary element to plants and other living species [7].

Copper has electrical conductivity, thermal conductivity, is oxidative and can undergo hydrolysis [8] and has the ability to be used in the manufacturing of alloys [9-10], including biscuit alloy with zinc. Copper compounds are also used in analytical chemistry, such as the Vlnk solution which is used in the detection of sugars [11]. Copper can enter the composition of the skin and

hair, for example in the form of Batali that is responsible for coloring hair and skin. In addition, copper can enter the formation of joints and nerves, which is responsible for the sense of taste. Copper is also involved in the synthesis of many enzymes, thus maintaining the activity and health of the heart.

Many techniques can be used to determine copper percentage in its compounds. Some of these are atomic absorption spectrometry [12-14], inductive coupled plasma-emission spectrometry [15], potentiometry [16], derivative potentiometric stripping analysis [17], flow injection catalytic photometric method [18-19], and inductive coupled plasma-mass spectrometry [19]. Several studies were published for spectral estimation of Cu(II).

Rao [20] was able to estimate copper(II) spectrophotometrically by using an organic detector (4-

HBTS), where the yellow colored complex that was formed showed a maximum absorption peak at 370 nm, in pH = 6.5, with absorption coefficient of $(2.85 \times 10^4) \text{ L mol}^{-1} \text{ cm}^{-1}$, sandal sensitivity of $0.00032 \mu\text{g cm}^{-1}$, and value of % R.S.D equal to (0.025). A colorimetric method was used for the determination of Cu(II) by using chromogenic reagent (CDSAII) in a neutral medium at 588 nm with concentration range of $6\text{--}0.25 \mu\text{g mL}^{-1}$ and D.L = $0.15 \mu\text{g mL}^{-1}$ [21].

The aim of this work is to prepare a new reagent to be used in a new method, that is more sensitive, easy and have low cost for the extraction and determination of copper(II) ion from industrial samples, and to study all the conditions that affects the determination process, such as the pH of reaction solution, the time needed to complete the reaction of the complex formation, and the optimum concentration of reagent that will result in complete complexation reaction with copper ions.

EXPERIMENTAL SECTION

Materials

All solvents and chemical Reagents used in this study have high purity and are supplied by B.D.H, Fluka and Merck companies without any additional purification

processes. The materials used were ethanol absolute, glacial acetic acid, *p*-aminoacetophenone, 2-naphthol, sodium nitrite, hydrochloric acid, sodium hydroxide, and *o*-aminophenol.

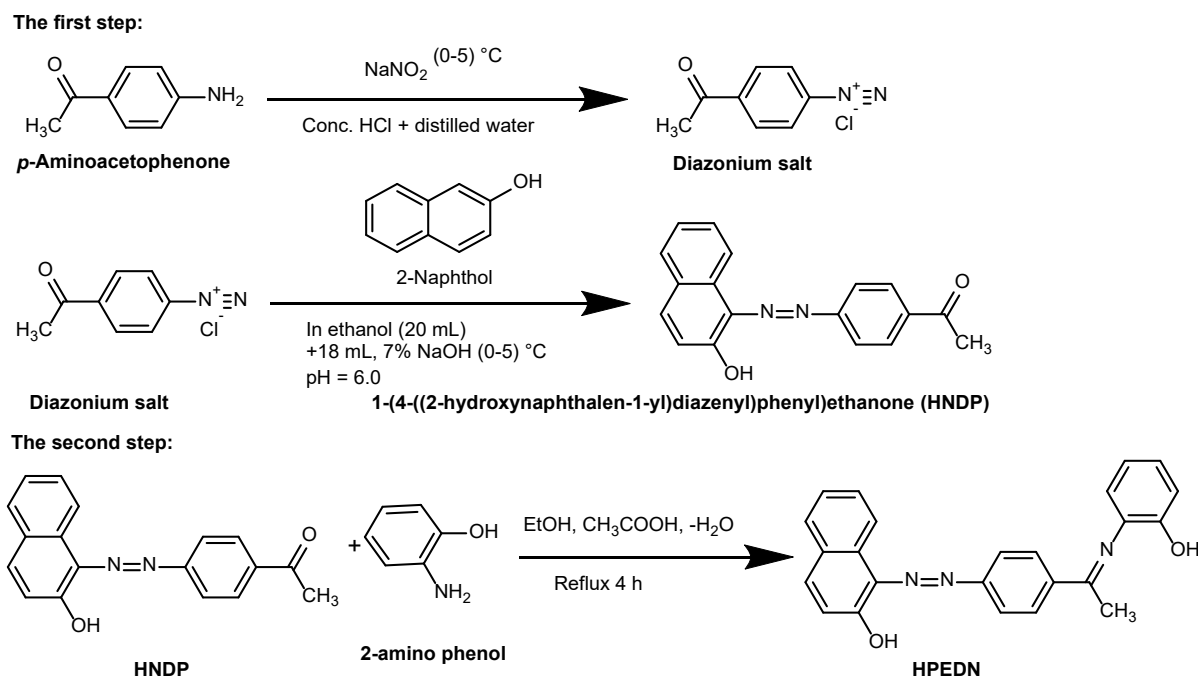
Instrumentation

All techniques that were used in the characteristic study of the new synthesized ligand and its complexes were a-UV-6100 PC Double beam Spectrophotometer (EMCLAB, Germany), FT-IR Spectrophotometer 8400S (Shimadzu, Japan), pH-meter (InoLab, WTW, 135i, Germany), Conductivity meter (Digital, InoLab, Germany), Melting point instrument (SMP 30, Stuart, England), Balance BL 2105 (Sartorius, Germany), Mova 400 MHz, $^1\text{H-NMR}$, and $^{13}\text{C-NMR}$ spectrophotometer.

Procedure

Synthesis of the new ligand (HPDN)

The ligand 1-((4-(1-(2-hydroxyphenylimino)ethyl)phenyl)diazenyl)naphthalene-2-ol (HPDN) was synthesized in two steps (Scheme 1). The first step was to prepare the azo derivative by reacting *p*-aminoacetophenone with 2-naphthol in controlled conditions and the addition of azo which was conducted



Scheme 1. Pathway of synthesis of 1-((4-(1-(2-hydroxyphenylimino)ethyl)phenyl)diazenyl)naphthalene-2-ol (HPEDN) ligand (step one and two)

in a snowy environment due to the exothermic process of the reaction. The obtained precipitate showed a dark red color with a yield of 75.37% and melting point of 145–147 °C.

The second step includes the reaction of the Azo derivative 1-(4-((2-hydroxynaphthalen-1-yl)diazenyl)phenyl)ethanone (HNPD) with 2-aminophenol, by refluxing of the mixture for 4 h which was later cooled to room temperature, dried and recrystallized with absolute ethyl alcohol. The resultant precipitate yield was 72.51% of reddish brown crystals and the melting point was 178–180 °C.

Preparation of buffer solution

The buffer solution was prepared by dissolving 0.7708 g, 0.01 mole of ammonium acetate in 1000 mL of distilled water. Different pH values were obtained by adding certain amounts of concentrated ammonia solution or concentrated acetic acid in order to prepare solutions with pH range between 4 and 12.

Synthesis of the divalent copper(II) complex

The metal complexes were prepared by the molar ratio (1:2) (M:L) by dissolving (1 mmol) of the metal chloride salt in 10 mL of buffer solution in optimal acidic function. Chlorides were selected as good leaving groups and to prevent interference with negative ions and for ease of use in the buffer solution with optimum acid function and 2 mmol of ligand was dissolved in 20 mL of ethanol absolute. The metal ligand mixture solution was then

heated at (50–60 °C) for 1 h, and the precipitate was washed and recrystallized with ethanol absolute and later dried in air. Table 1 shows the physical properties of the ligand and its complexes.

RESULTS AND DISCUSSION

UV-Visible Spectrophotometry

The absorption spectra of the (HPEDN) ligand solution in ethanol was recorded at wavelengths from 200–800 nm. The maximum absorption peak of the ligand was at 326 nm. The maximum absorption of the Cu²⁺ complex was at 500 nm after the application of optimal conditions. This observation confirms the formation of stable complexes as shown in Fig. 1 and Table 2.

When comparing absorption spectra of the ligand with that of the complex, a clear difference can be observed in the value of the maximum absorption peak which indicates a red shift and the formation of a complex with higher absorption in comparison with the ligand [22].

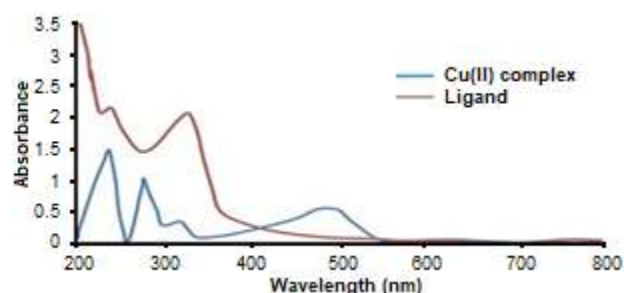


Fig 1. Electronic spectra for HPEDN ligand and its Cu(II) complex

Table 1. Physical properties of the azo-Schiff base ligand and its complexes

No.	Molecular formula	Color	m.p (°C)	Yield (%)	Am/Ohm ⁻¹ mol ⁻¹ cm ²			Reaction time
					DMF	Ethanol	DMSO	
1	C ₂₄ H ₁₉ N ₃ O ₂	Reddish brown	178–180	72.51	-	-	-	4 h
2	[Cu(C ₂₄ H ₁₉ N ₃ O ₂) ₂ Cl ₂]	Brown	196–198	63.11	16.5	11.3	10.3	1 h

Table 2. The electronic transitions for HPEDN ligand and complex

Molecular formula of ligand	λ (nm)	Wave number (cm ⁻¹)	Transition type
C ₂₄ H ₁₉ N ₃ O ₂	326	30674	n→π*
	237	42194	π→π*
[Cu(C ₂₄ H ₁₉ N ₃ O ₂) ₂ Cl ₂]	500	20000	CT
	314	31840	n→π*
	285	35087	π→π*
	226	44247	π→π*

Study of the Optimal Conditions for the Formation of the Complex

Effect of pH solution on the formation of the complex

A series of copper ions solutions with ligand (HPEDN) were prepared at pH ranges of 4–12, and were each measured for their absorbance at the maximum wavelength of the copper complex. The results showed that the best pH was 9, which gave the highest absorbance for the metal complex. It was also observed that the absorption values were varied with variation of pH values of the solution. This may be due to the change in chemical nature of the ligand or the competition between hydroxyl ions in the ligand with metal ions. It was also found that absorption values of the complex decreased with increasing value of pH, and this can be attributed to the deposition of ions of the element and the formation of an unstable complex [23], as shown in Fig. 2.

Effect of the concentration of ligand on the complex formation

To investigate the effect of the concentration of ligand on the complex formation, a series of solutions containing different concentrations of ligand (HPEDN) ranging from 0.5×10^{-4} – 4×10^{-4} M were mixed with constant concentration (1×10^{-4} M) of copper(II) ion solution. The pH of solution was adjusted to 9, and then the absorbance was measured against water and ethanol as a blank solution. The obtained results showed that the optimal concentration of ligand was 1.5×10^{-4} M, which gave the highest absorption of the complex. Higher

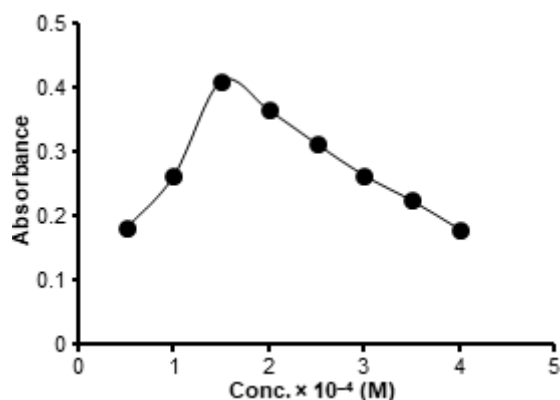


Fig 3. Effect of ligand concentration

concentrations of ligand, caused a decrease in absorption intensity this may be due to the formation of new species in the solution that are absorbed at different wavelengths and possibility to the condensation of the ions or the solubility of the reagent with the solvent completely. As shown in Fig. 3.

Effect of time on the formation of the Cu(II) complex

Fig. 4 shows that the formed complex gave high absorbance after 15 min of reaction time and remained constant for 48 h at optimal conditions. The results of this study showed that the prepared ligand can be used to estimate the concentration of copper by forming a stable complex, similar to other reagents that have been used to estimate the concentration of other ions spectrally [24].

The effect of additive sequencing of ligand, metal ion and buffer solution on the absorption intensity of the

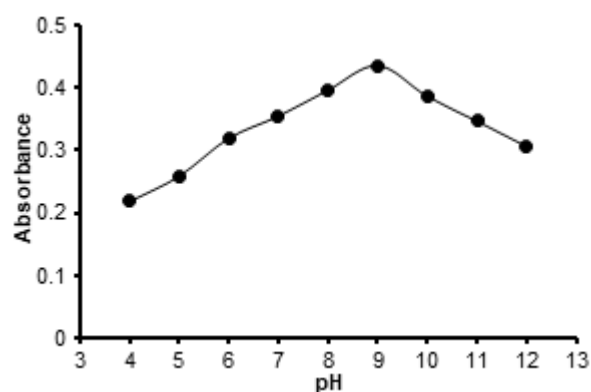


Fig 2. Effect of pH values of solution on complex formation

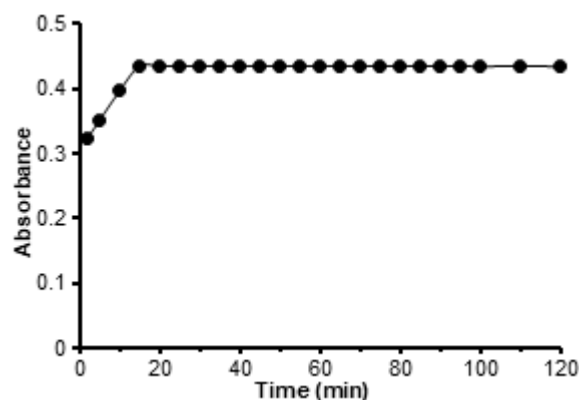


Fig 4. Effect of time on the stability of the copper(II) complex

formed complex was investigated in this part. The obtained results showed first and second sequential succession which exhibited low absorption values. This is due to positive and negative completion of ions of the acid and base in the metal bonding, that leads to low absorption values. Therefore, the third sequencing was used to determine the absorption values and to prepare the complex as shown in Table 3.

Effect of temperature

The effect of temperature on the stability of the synthesized complex was investigated in temperatures ranging between 5 and 50 °C. The obtained results showed that the copper complex absorbance remained almost constant at 15–30 °C. After that, the absorption decreased. This result may be due to the decomposing of the complex at temperatures above 30 °C, so it is preferable to study copper complex within this range of temperature. The results are shown in Fig. 5.

Mole Ratio Method

The possible compositions for the preparation of the complex were determined using the molar ratio method. The method was conducted by taking different volumes of ligand and a constant volume of the metal ion at the same concentration. The results showed that the complex

has the mole ratio of (1:2) (Metal:Ligand) as shown in Fig. 6.

The Continuous Variation Method (Job Method)

In this method, different volumes of both the ligand and the metal were selected with the same concentration at the optimal acid function and the absorbance of each solution was measured at the maximum wavelength of the copper complex. When drawing the absorbance values against $\frac{V_m}{V_m+V_l}$, V_m represents the volume of metal and V_l is the volume of ligand. The ratio was found to be (1:2), one mole of metal to 2 moles of the ligand as shown in Fig. 7.

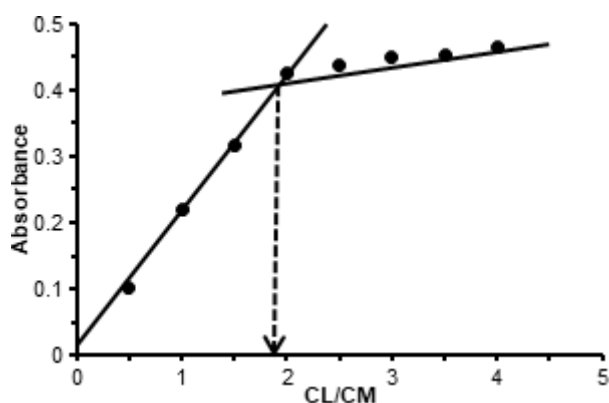


Fig 6. Molar ratio method of copper(II) complex

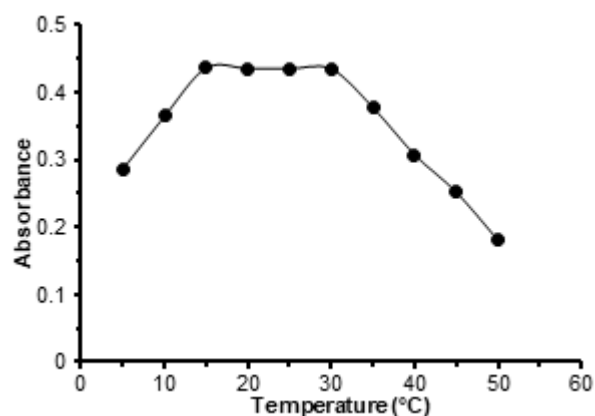


Fig 5. Effect of temperature on the stability of the complex

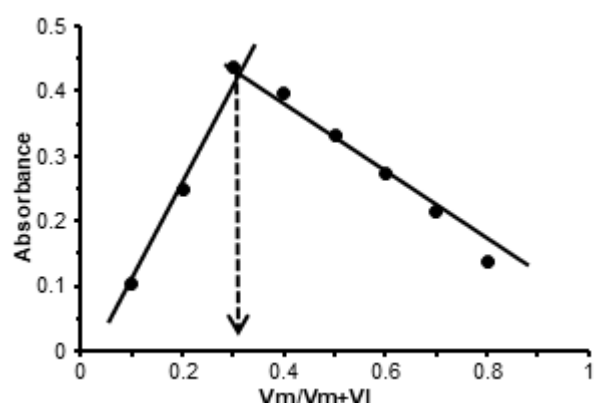
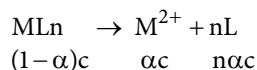


Fig 7. Continuous variation method of copper(II) complex

Table 3. Effect of Sequence of addition on the formation of Cu^{2+} complex with HPEDN ligand at pH = 9

The sequence of addition number	Sequence of addition	Absorbance
1	Metal + buffer solution to adjusting pH + ligand	0.3166
2	Ligand + Metal + buffer solution to adjusting pH	0.3325
3	Metal + Ligand + buffer solution to adjusting pH	0.4357

The values of the stability constant of the complex were calculated according to the following equations and the value of stability and instability constants are shown in Table 4.



$$K_{inst} = \frac{(ac)(nac)^n}{c(1-a)} \quad (1)$$

$$K_{st} = \frac{1}{K_{inst}} \quad (2)$$

The results of the stability constants showed that the copper complex is more stable. The reason is that the

higher the atomic number, the higher the nuclear charge, causing it to have more ability to attract ligands compared to other ions in the same period of the periodic table, which leads to more electric field absorbed by the positive ions of the ligand, which increases the stability of the complex [26].

Effect of Interference and Masking Reagent on the Absorption of the Copper(II) Complex

The effect of interference on the absorption of the copper complex with ligand was studied by selecting several positive and negative ions as shown in Table 5.

Table 4. Absorption values (A_s) and (A_m) as well as values of each (α) and (K_{st}) and (K_{inst}) of the copper complexes

Metal complex	A_s	A_m	α	K_{inst}	K_{st}	Log K_{st}
CuL	0.3922	0.4536	0.1353	1.145×10^{-10}	8.728×10^9	9.956

Table 5. Effect of addition of positive and negative ions on the absorption values of the divalent copper complex

Foreign ions	$1 \times 10^{-4}M$		d	E%	% Re
	Absorbance after addition of ions				
Cation					
Without Cation	0.4374		-----	-----	-----
Ni ⁺²	0.4266		-0.012	-2.46	97.54
Co ⁺²	0.4305		0.00069	-1.57	98.43
Cd ⁺²	0.3992		0.0382	-8.73	91.26
Pd ⁺²	0.4564		0.019	4.34	104.34
Mn ⁺²	0.4428		0.0054	1.23	101.34
Fe ⁺²	0.3197		-0.1207	-27.5	72.41
Zn ⁺²	0.2872		-0.1512	-34.3	65.66
Anion					
Without anion	0.4374		-----	-----	-----
CO ₃ ⁻²	0.3958		-0.041	-9.51	90.48
SO ₄ ⁻²	0.4283		-0.009	-2.08	97.91
C ₂ O ₄ ⁻²	0.4207		-0.016	-3.81	96.18
CH ₃ COO ⁻²	0.3984		-0.039	-8.91	91.08
NO ₂ ⁻¹	0.4092		-0.028	-5.95	94.04
SCN ⁻¹	0.4163		-0.021	-0.99	99.00
Cl ⁻¹	0.3995		-0.072	-3.49	96.50
Masking agent					
Without masking agent	0.4374		-----	-----	-----
Ascorbic acid	0.2793		-0.158	-36.14	63.85
Potassium Thiocyanate	0.4368		-0.0006	-0.137	99.862
EDTA	0.1806		-0.2568	-58.71	41.28
Thiourea	0.3512		-0.0862	-24.81	75.187
Potassium chloride	0.4084		-0.029	-6.63	93.36
Tartaric acid	0.2347		-0.2027	-46.34	53.65
Salicylic acid	0.3095		-0.1279	-29.24	70.75

The positive ions were found to decrease or increase the absorbance. This is due to the competition of these ions with the copper ion on the bonding with the reagent to form the complex, where part of the reagent is taken to be a new complex. The low absorbance values after the addition of the negative ions were due to their use as a masking reagent, where KSCN was used as a masking reagent to eliminate the effect of the interference by returning the absorption values to the original calculated output without interference [29].

FTIR Spectra of the Ligand and the Complex

Fig. 8 shows the IR FTIR spectra of the ligand and its complex, in which the ligand appeared as a narrow, weak-intensity band at 3416 cm^{-1} due to the stretching vibrations of the hydroxide group in the ligand. When compared with the complex at 3454 cm^{-1} , there was a change in the intensity, and location of the peak due to the bonding

of the carboxyl group, after they lost their proton [30].

The ligand spectrum showed a medium-intensity absorption at 1666 cm^{-1} attributed to $\nu(\text{C}=\text{N})$ and this site suffered less displacement when aligned with copper as well as a change in intensity and shape in the complex spectra.

The ligand spectra have shown to have a strong absorption at 1413 cm^{-1} , which is attributed to the vibration band of $\nu(\text{N}=\text{N})$, that had undergone a shift toward a lower wavelength when it was associated with the metal. The consistency of copper and the ligand was observed by the nitrogen atom of the azo group.

The low frequency region is limited to 593 cm^{-1} absorption bands for the metal-oxygen bonds and 473 cm^{-1} due to metal-nitrogen bonds. This result is due to the formation of a homogeneous bond between the deposited atoms with the central copper ion [31]. All these bands are summarized in Table 6.

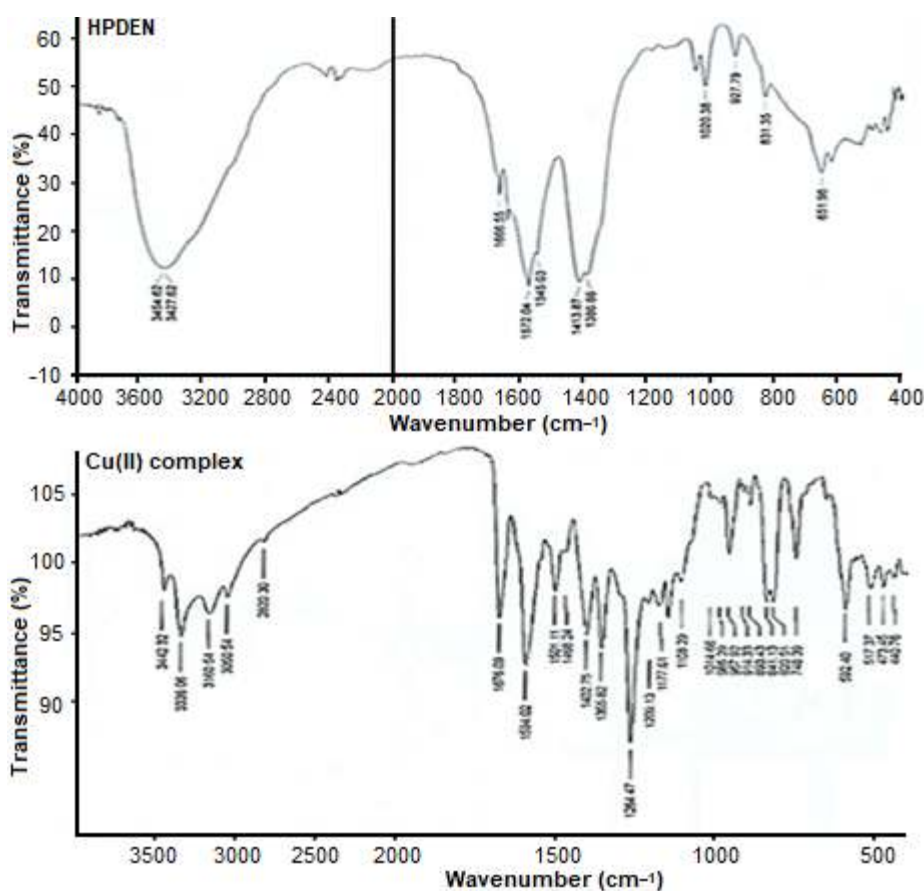


Fig 8. FT-IR spectrum of the ligand (HPDEN) and its complex with Cu(II)

Table 6. Typical FT-IR absorption frequencies for reagent and complexes

Compound	OHv	N=Cv	N=Nv	M-Nv	M-Ov
Ligand HPEDN	3454(s.)	1666(m.)	1413(s.)	-	-
Cu(II) complex	3442(w.)	1676(w.)	1468(w.)	473(w.)	593(w.)

w.: weak s.: strong m.: medium comp.: complex

¹H-NMR and ¹³C-NMR Spectra of Ligand (HPEDN)

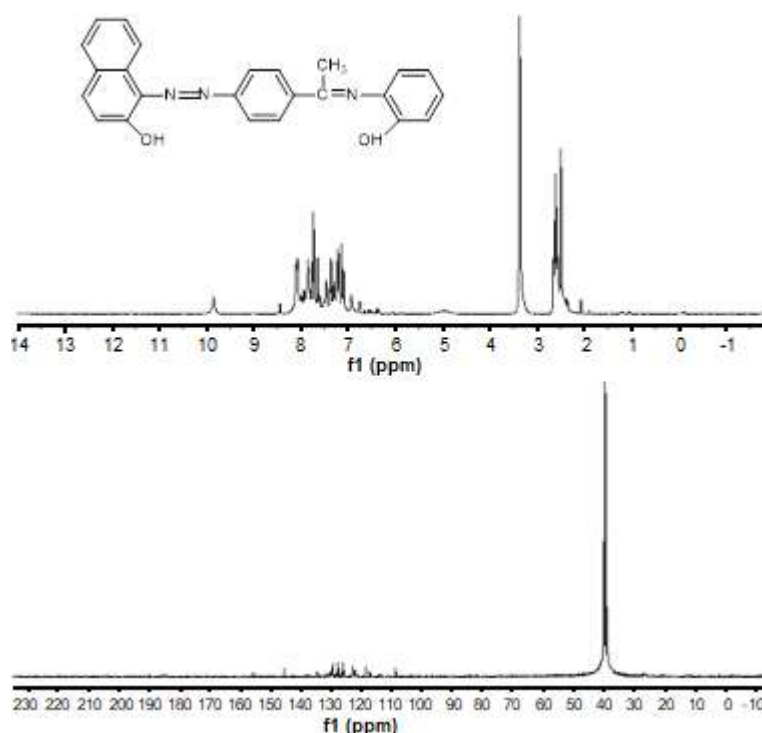
The ¹H-NMR Spectra of the ligand shows the chemical displacements of aromatic and elliptical protons. The single band at 9.8491 ppm belong to the proton of the hydroxyl group (OH), the three single bands at 2.5895, 2.6189 and 2.6471 ppm are attributed to the protons of the methyl group (CH₃), the multiple bands at 6.7574 to 8.4526 ppm belong to the nine protons of the aromatic rings, while the band at (2.500 ppm) relates to (DMSO d₆) [32]. Proton NMR spectra of the ligand are shown in Fig. 9. ¹³C-NMR spectra of the ligand, shows the appearance of a single band at 39.520 ppm which belongs to the carbon of the methyl group (CH₃), the single band at 155.3790 ppm belongs to the carbon of azomethine (-C=N-), and the multiple bands at 108.6402 to 145.3493 ppm belong to the 22 carbons of the aromatic rings [32].

The Suggested Structures of the Copper(II) Complex

From the results of the electrical conductivity, molar ratios and continuous variation methods and also all the spectral methods applied for the study of the copper(II) complex [33-34], we concluded that the complex structure consists of 2 moles of ligand and one mole of metal and the complex was uncharged, therefore the shape of the complex must be octahedral with the hybridization of d²sp³ as shown in Fig. 10.

Construction of the Calibration Curve

In order to construct a calibration curve, a series of different concentrations of the metal ion were prepared ranging from 1.7–8.4 μg mL⁻¹ with constant concentration of the ligand (1.5 × 10⁻⁴ M) using absolute ethanol as the

**Fig 9.** ¹H-NMR and ¹³C-NMR spectra of ligand (HPEDN)

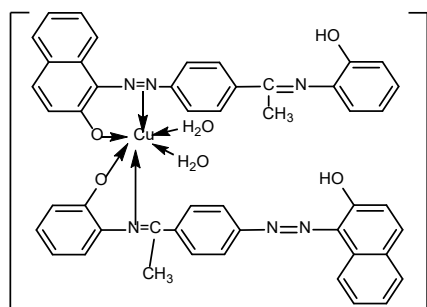


Fig 10. The suggested structures of copper(II) complex

solvent, where the results showed that the calibration curve follows the Lambert Beer's law for a range of concentrations 1.7–5.4 $\mu\text{g mL}^{-1}$. The Sandell's Sensitivity was equal to 0.0039, while the limit of detection (LOD) and limit of quantification (LOQ) was equal to 0.2217 and 0.7385, respectively. This shows that the method is highly sensitive and can be used to determine metals with low concentrations with agreeable accuracy and precision under the optimal conditions of the reaction [25]. These results were calculated by Eq. 3, 4 and 5 as shown in Table 7 and Fig. 11.

$$\text{LOD} = \frac{3\text{SD}}{\text{Slop}} \quad (3)$$

$$\text{LOQ} = \frac{10\text{SD}}{\text{Slop}} \quad (4)$$

$$\text{SD} = \sqrt{\frac{\sum (X_i - \bar{X})^2}{n-1}} \quad (5)$$

where x_i is the absorbance, \bar{x} is the mean of the absorbance, and n is the number of the measurement.

Precision

The precision of the analytical method was determined by calculating the amount of standard deviation (SD) for five measurements of absorbance, and the relative standard deviation (% RSD) by dividing the SD with the mean of the absorbance (\bar{x}) of the complex in optimal conditions as shown in Table 8. The sensitivity of this method was calculated using the detection limit (DL) and the limit of appreciation. This method is therefore

used to estimate metal ions [27]. These values were calculated by using Eq. 3, 4, 5 and 6. The result showed that this method is able to be used to determine Cu(II) concentrations with high precision compared with other spectrophotometric methods.

$$\text{RSD}\% = \text{SD}/\bar{x} \quad (6)$$

Accuracy

Accuracy means the closeness of the practical value from the theoretical value to determine if the results of an analytical method are accurate. The accuracy of the analytical method in this research was calculated by using the percentage relative error and the pre-processing ratio of the previously prepared complexes as shown in Table 9. The results show that the method that

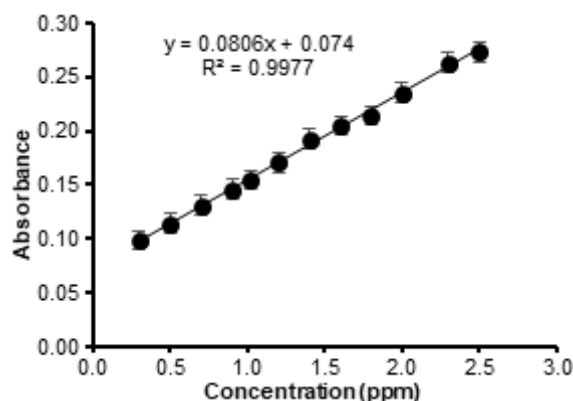


Fig 11. Calibration curve of the copper complex

Table 7. Construction of calibration curve of metal complexes

λ max (nm)	500
Beer's Law limit ($\mu\text{g mL}^{-1}$)	1.7–5.4
Molar Absorptivity ($\text{L mol}^{-1} \text{cm}^{-1}$)	0.5038×10^4
Sandell's Sensitivity ($\mu\text{g cm}^{-2}$)	0.0039
Limit of Detection ($\mu\text{g mL}^{-1}$)	0.2217
Limit of Quantification ($\mu\text{g mL}^{-1}$)	0.7385
Regression Equation	$y = 0.2519x + 0.0043$
Slope	0.2520
Correlation coefficient (R)	0.9994

Table 8. Values of standard deviation, percentage standard deviation

No.	1	2	3	4	5	Average \bar{x}	Sum $(x_i - \bar{x})^2$	SD	% RSD
Complex of Cu(II)	0.4378	0.4377	0.4377	0.4376	0.4376	0.4377	3×10^{-7}	0.00086	0.1964

Table 9. The relative percentage error and the pre-processing ratio of the complex

Complex ion	Analytical value (mol L ⁻¹)	d	% E _{real}	% Re
Cu(II)	0.971 × 10 ⁻⁴	-0.029 × 10 ⁻⁴	-2.9	97.1

Table 10. The percentages of copper determination by ligand in a copper alloy using an atomic absorption method

Sample	Content %	By Spectrophotometric method %	% E _{rel}	% Re	By Flame atomic absorption %	% E _{rel}	% Re
Alloy copper	70	69.4	0.6	100.6	68.8	1.2	101.2

was used to measure the metal concentration using ligand (HPDN) was highly accurate [28].

$$\%E_{\text{real}} = \frac{d}{\mu} \times 100 \quad (7)$$

where μ = analytical value, d = analytical value - theoretical value

Applications

The prepared ligand was used as a reagent to determine copper in an alloy that contains 70% copper and 30% zinc, using the UV-Vis method, and the results were compared to the flame atomic absorption method as shown in Table 10.

From Table 10 we can observe the compatibility between the UV-Vis method and the atomic absorption method, so we can conclude that the UV-Vis method can be widely used in the determination of copper in different models with precision, selectivity and high sensitivity.

CONCLUSION

The current study showed the success of the preparation of a reagent and the possibility of its use in determining micro amounts of copper in different models with high accuracy and sensitivity by forming a color complex. The optimal conditions to obtain the copper(II) complex were: pH = 9, temperature = 0–50 °C, the ratio of ligand to metal(1:2), SD = 0.00086, % RSD = 0.1964, DL (μg mL⁻¹) = 0.2217. According to this study, we can suggest that the shape of the complex must be an octahedral shape with the hybridization of d²sp³.

ACKNOWLEDGMENTS

The authors would like to thank Department of Chemistry, College of Education for Pure Science, University of Kerbala and College of Science, Babylon University in Iraq for funding this work.

REFERENCES

- [1] Wells, A.F, 1945, *Structural Inorganic Chemistry*, 4th Ed., Clarendon Press-Oxford, London, 439, 811, 954–973.
- [2] Greenwood, N., and Earnshaw A., 1997, *Chemistry of the Elements*, 2nd Ed., Elsevier, Oxford, 1174.
- [3] Fouad, H.K., Atrees, M.S., and Badawy, W.I., 2016, Development of spectrophotometric determination of beryllium in beryl minerals using chrome Azurol S, *Arabian J. Chem.*, 9 (Suppl. 1), S235–S239.
- [4] Supong, K, and Usapein, P., 2019, Reliable determination of copper complex ions in synthetic wastewater using flame atomic absorption spectrophotometry, *Water Sci. Technol.*, 79 (5), 833–841.
- [5] Mohammed, S.F., and Musa, F.H., 2014, Synthesis and characterization of Co(II), Ni(II), Cu(II), Cd(II) and Hg(II) complexes with a new derivative of L-ascorbic acid, *J. Kerbala Univ.*, 7 (4), 42–50.
- [6] Li, M., and Zinkle, S.J., 2012, “Physical and mechanical properties of copper and copper alloys in *Comprehensive Nuclear Materials*, Vol. 4, Elsevier, Amsterdam, 667–690.
- [7] Shiyab, S., 2018, Phytoaccumulation of copper from irrigation water and its effect on the internal structure of lettuce, *Agriculture*, 8(2), 29.
- [8] Li, M., and Zinkle, S.J., 2012, “Physical and mechanical properties of copper and copper alloys” in *Comprehensive Nuclear Materials*, Vol. 4, Eds. Konings, R.J.M., Elsevier, Oxford, 667–690.
- [9] Saranya, R., Rajasekaran, J., and Selvaraj, S.J., 2017, Synthesis and characterization of biologically important Zn(II), Cu(II) and Co(II) metal complexes in the 3D- series, *J. Chem. Pharm. Sci.*, 1, 64–73.

- [10] Ahuja, B., Karg, M., Nagulin, K.Y., and Schmidt, M., 2014, Fabrication and characterization of high strength Al-Cu alloys processed using laser beam melting in metal powder bed, *Physics Procedia*, 56, 135–146.
- [11] Chaudhary, N.K., and Mishra, P., 2017, Metal complexes of a novel Schiff bases on penicillin: Characterization, molecular modeling, and antibacterial activity study, *Bioinorg. Chem. Appl.*, 2017, 6927675.
- [12] Khdeeja, J.A., Layla, A.M., Fatima, J.A., and Haider, N.R., 2015, New spectrophotometric determination of copper(II) using an organic reagent derived from imidazole and 4-aminoantipyrine and applied onto different samples, *J. Chem. Pharm. Sci.*, 8 (2), 201–207.
- [13] Seidi, S., and Alavi, L. 2019, Novel and rapid deep eutectic solvent (DES) homogeneous liquid–liquid micro-extraction (HLLME) with flame atomic absorption spectrometry (FAAS) detection for the determination of copper in vegetables, *Anal. Lett.*, 52 (13), 2092–2106.
- [14] Yang, Q., Tang, G.P., Tian, L.F., Wei, Q.L., and Wang, C., 2015, Determination of trace copper in vanadium alloy by flame atomic absorption spectrometry, *Adv. Mater. Res.*, 1120-1121, 1395–1398.
- [15] Karadjov, M., Velitchkova, N., Veleva, O., Velichkov, S., Markov, P., and Daskalova, N., 2016, Spectral interferences in the determination of rhenium in molybdenum and copper concentrates by inductively coupled plasma optical emission spectrometry (ICP-OES), *Spectrochim. Acta, Part B*, 119, 76–82.
- [16] Pięk, M., Fendrych, K., Smajdor, J., Piech, R., and Paczosa-Bator, B., 2017, High selective potentiometric sensor for determination of nanomolar concentration of Cu(II) using a polymeric electrode modified by graphene/7,8,8-tetracyanoquinodimethane nanoparticles, *Talanta*, 170, 41–48.
- [17] Scarano, G., Morelli, E., Seritti, A., and Zirino, A., 1990, Determination of copper in seawater by anodic stripping voltammetry using ethylenediamine, *Anal. Chem.*, 62 (9), 943–948.
- [18] Ohno, S., Tanaka, M., Teshima, N., and Sakai, T., 2004, Successive determination of copper and iron by a flow injection-catalytic photometric method using a serial flow cell, *Anal. Sci.*, 20 (1), 171–175.
- [19] Al-Abachi, M.Q., Abed, S.S., and Al-Najjar, N.A., 2017, A new chromogenic reagent for determination of copper(II) in water samples using flow injection-technique, *Iraqi J. Sci.*, 58 (1), 201–210.
- [20] Satheesh, K.P., Ravichandran, S., and Rao, V.S., 2011, Spectrophotometric determination of Cu (II) and Ni (II) using 4-hydroxybenzaldehyde thiosemicarbazone, *Int. J. ChemTech Res.*, 3 (4), 2062–2065.
- [21] Ali, A.A.M., AL-Da'amy, M.A., and Kadhier, A.F., 2010, Synthesis of 2-[(3-chloro-4,6-disulfanamide phenyl) azo] -4,5-diphenyl imidazole (Cdsai) as a new analytical reagent for the determination of Cu(II), *Iraqi Nat. J. Chem.*, 37, 66–73.
- [22] Kadhim, S.H., Abd-Alla, I.Q., and Hashim T.J., 2017, Synthesis and characteristic study of Co(II), Ni(II) and Cu(II) complexes of new Schiff base derived from 4-aminoantipyrine, *Int. J. Chem. Sci.*, 15 (1), 107–114.
- [23] Aswar, A., Bansod, A.D., Aswale, S.R., and Mandlik, P.R., 2004, Synthesis, characterization, electrical and biological studies of Cr(III), Mn(III), Fe(III), Ti(III), VO(IV), Th(IV), Zr(IV) and UO₂(VI) polychelates with bis-bidentate Schiff base, *Indian J. Chem.*, 43A, 1892–1896.
- [24] Reiss, A., Samide, A., Ciobanu, G., and Dăbuleanu, I., 2015, Synthesis, spectral characterization and thermal behavior of new metal(II) complexes with Schiff base derived from amoxicillin, *J. Chil. Chem. Soc.*, 60 (3), 3074–3079.
- [25] Funk, W., Dammann, V., Donnevert, G., Ianelli, S., Ianelli, E., and Gray, A., 2007, *Quality Assurance in Analytical Chemistry: Applications in Environmental, Food, and Materials Analysis, Biotechnology, and Medical Engineering*, 2nd Ed., Wiley-VCH Verlag GmbH & Co. KGaA, Weinheim, 35.

- [26] Tirmizi, S.A., Wattoo, M.H.S., Sarwar, S., Anwar, W., Wattoo, F.H., Memon, A.N., and Iqbal, J., 2009, Spectrophotometric study of stability constants of famotidine-Cu(II) complex at different temperatures, *Arabian J. Sci. Eng.*, 34 (2), 43–48.
- [27] Yousif, E., Adil, H., and Aziz, Y.F.A., 2010, Synthesis and characterization of some metal ions with 2-amino acetate benzothiazole, *J. Appl. Sci. Res.*, 6 (7), 879–882.
- [28] Skorik, N.A., Filippova, M.M., Bukhol'tseva, E.I., Mal'kov, V.S., and Kurzina, I.A., 2015, *Russ. J. Inorg. Chem.*, 60 (6), 729–735.
- [29] Mihelj, T., Tomašić, V., Biliškov, N., and Liu, F., 2014, Temperature-dependent IR spectroscopic and structural study of 18-crown-6 chelating ligand in the complexation with sodium surfactant salts and potassium picrate, *Spectrochim. Acta, Part A*, 124, 12–20.
- [30] Varga, G., Csendens, Z., Peintler, G., Berkesi, O., Sipos, P., and Palinko, I., 2014, Using low-frequency IR spectra for the unambiguous identification of metal ion–ligand coordination sites in purpose-built complexes, *Spectrochim. Acta, Part A*, 122, 257–259.
- [31] Silverstein, R.M., Webster, F.X., and Kiemle, D., 1996, *Spectrometric Identification of Organic Compound*, 6th Ed, John Wiley & Sons, Inc., New York, 180.
- [32] Al-Adilee, K.J., and Hesson, H.M., 2015, Synthesis, identification, structural, studies and biological activity of some transition metal complexes with novel heterocyclic azo-Schiff base ligand derived from benzimidazole, *J. Chem. Pharm. Res.*, 7 (8), 89–103.
- [33] Sugiyarto, K.H., Kusumawardani, C., and Wulandari, K.E., 2018, Synthesis and structural analysis of powder complex of tris(bipyridine) cobalt(II) trifluoromethanesulfonate octahydrate, *Indones. J. Chem.*, 18 (4), 696–701.
- [34] Al-Shareefi, A.N., Kadhim, S.H., and Jawad, W.A., 2013, Synthesis and study of Fe(III), Co(II), Ni(II) and Cu(II) complexes of new Schiff's base ligand derived from 4-amino antipyrine, *J. Applicable Chem.*, 2 (3), 438–446.

Coating of Pd and Co on Mordenite for a Catalyst of Hydrotreating of Cashew Nut Shell Liquid into Biofuel

Maya Tri Hapsari, Wega Trisunaryanti*, Iip Izul Falah, and Media Laila Permata

Department of Chemistry, Faculty of Mathematics and Natural Sciences, Universitas Gadjah Mada, Sekip Utara, Yogyakarta 55281, Indonesia

* **Corresponding author:**

tel: +62-811256055

email: wegats@ugm.ac.id

Received: August 8, 2019

Accepted: January 29, 2020

DOI: 10.22146/ijc.48633

Abstract: The catalytic activity of Co and Pd loaded on mordenite (MOR) was evaluated in the hydrotreatment of cashew nut shell liquid (CNSL) into biofuel. Metals were loaded into MOR as support via wet impregnation process. The Co content was varied as 2, 4, and 6 wt.% to produce Co(1)/MOR, Co(2)/MOR, Co(3)/MOR catalysts. The micro-mesoporous structures of the catalyst were confirmed by XRD, SEM, TEM, FTIR, and N₂ adsorption-desorption measurement. AAS were used to analyze the amount of metal that is successfully loaded in the catalysts. Hydrotreating of the CNSL was conducted in a semi-batch reactor at 450 °C with hydrogen flow (20 mL/min) for 2 h. The liquid product was analyzed using GC-MS. The activity of Co/MOR was compared with the activity of Pd/MOR as a noble metal. The result of the hydrotreatment process showed a decrease of liquid product in the sequence of Co(3)/MOR > Co(2)/MOR > Pd/MOR > Co(1)/MOR > MOR. The Co(3)/MOR catalyst exhibited the highest conversion of liquid hydrocarbon than the others (61.8 wt.%), comprising predominantly by gasoline compounds with over 25.21 wt.% conversion.

Keywords: cobalt; CNSL; mordenite; palladium

■ INTRODUCTION

Fossil fuels are a major energy source widely used in various countries. However, depletion of petroleum is now deeply concerned and heavy consumption will cause environmental pollution. Thus, there is an urgent need to find suitable alternate fuels [1]. Nowadays, the world is confronted with two major problems, such as the limited supply of fossil fuels and its increasing demand with the growth of the population over the years. The gas emitted from the use of petroleum fuels, also contributes to environmental air pollution and global warming. These issues have led to the continuous search of a new clean and renewable energy source as an alternative [2]. One of the most attractive energy alternatives that have been studied these days is the use of biomass converted from renewable sources.

The cashew plant (*Anacardium occidentale* L.) is one commodity that has high economic value [3] and one of the largest plantations in Indonesia with over 547,000 ha [4]. The main product of the cashew plant is nuts. During

the production of cashew nuts, its shell is usually disposed of as waste for it has no economic value. Previous research reported that cashew nut shell contains a high percentage of oils (50%) called CNSL [5], making it a potential source to be used as a fuel alternative. The use of this oil as fuel has the benefit of its renewability, and its utility as non-edible oil does not cause any competition with food production. However, the character of cashew nut shell oil that has a high viscosity, high density, and low volatility is inefficient to be directly used as biofuel [6].

Various methods have been developed to convert CNSL into a more suitable compound as fuel. Previous studies focused more on converting CNSL into biodiesel via transesterification. This process requires a considerable amount of chemical ingredients including base as a homogenous catalyst which is difficult to separate. Therefore, we develop a new idea to convert CNSL directly into hydrocarbon compounds through a hydrotreatment process. In this method, we utilize

mordenite as a heterogeneous catalyst which is easier to separate. This method requires fewer chemical ingredients exhibiting more benefits to environmental conservation. In addition, the production of hydrocarbon compounds as a fuel is more desirable than biodiesel that contained FAME (Fatty Acid Methyl Ester) due to high energy density.

Mordenite is a well-known zeolite used in many catalytic reactions such as cracking, hydrotreatment, isomerization, etc. [7]. It is one of the six most abundant zeolites with high silica content which contributes to its high thermal stability. However, the major drawback of mordenite lies in its limited channel and pore size, which is limiting its activity, selectivity and stability [8-9]. One way to improve the activity of mordenite is by adding metal, either on its surface or in its pore, to give a more active site to the catalyst. Previously scientific reports were published concerning on the influence of metal on the activity of the mordenite catalyst. The previous research has proven that the presence of metal has a positive effect in the hydrogenation process, exhibiting higher selectivity [10].

The use of transition metal, such as nickel, in the hydrotreatment process, has been continuously studied as a replacement of noble metals (Pt and Pd) due to its high availability and activity. However, the low selectivity of nickel and its tendency to deposit coke have urged a modification to be proposed. Commonly, to improve its activity and selectivity for hydrotreating, Nickel is paired with Molybdenum in the bimetallic system (NiMo). Hydrotreating CNSL oil using bimetallic NiMo loaded in ZAA was done previously producing over 58.32% of hydrocarbon compounds [11]. The use of NiMo requires two types of metals will need a higher cost to synthesize. Therefore, in this study, Cobalt is employed to replace Nickel. Cobalt has a more unpaired electron in d orbital which can be used as a site for hydrogen splitting in hydrocracking reaction. Due to these unpaired electrons, it is expected that higher activity during the hydrogenation of CNSL will be obtained. In previous research [12], hydrocracking of α -cellulose using Co/MOR catalyst obtained liquid product of 90.48 wt.% at 450 °C. However, the effect of metal concentration

loaded in the pore of mordenite has not been discussed before. In this study, the activity of Co/MOR and the effect of metal concentration in hydrotreatment of CNSL oil will be evaluated. The result will also be compared with the liquid product obtained from the hydrotreatment using noble metals like Pd to evaluate significant differences of activity by both metals at its respective concentration.

■ EXPERIMENTAL SECTION

Materials

Zeolite mordenite (HSZ 640-HOA) was purchased from Catalyst & Chemical Ind.Co.Ltd., PdCl₂ (with 59% Pd), Co(NO₃)₂·6H₂O were purchased from Merck, methanol 98% were purchased from Sigma-Aldrich, Cashew Nut Shell Liquid (CNSL) was collected from Karang Tengah Village, Bantul, Yogyakarta.

Instrumentation

The functional groups of MOR and catalysts were determined using Fourier Transform Infrared spectrometer (FTIR, Shimadzu Prestige-21) equipped with data station in the range of 400–4000 cm⁻¹ with a KBr disc technique. X-Ray Diffraction (XRD, Philips X'Pert MPD) was used to observe the crystallinity of the catalysts. The pore images were taken using a Transmission Electron Microscope (TEM, JEM-1400). The surface parameters (surface area, pore volume, and pore diameter) of the sample were analyzed using Surface Area Analyzer (SAA, Quantachrome NOVAYouch 4LX), the surface area was calculated by the Brunauer-Emmett-Teller (BET) method, and the pore size distribution was calculated by the Barret-Joyner-Halenda (BJH) method. The amount of metals content of all samples was determined using Atomic Absorption Spectrophotometer (AAS, PERKIN ELMER 5110 PC). The surface morphology of catalyst was analyzed using Scanning Electron Microscopy (SEM, JEOL SM-6510). The liquid products obtained from the hydrotreating of CNSL were analyzed using gas chromatography-mass spectrometry (GC-MS, Shimadzu QP2010S).

Procedure

Catalysts preparation and characterization

The Co/MOR and Pd/MOR catalysts were prepared by impregnation method [22]. Metals (Co and Pd) were loaded into MOR by wet impregnation using a salt precursor of $\text{Co}(\text{NO}_3)_2 \cdot 6\text{H}_2\text{O}$ and PdCl_2 .

An amount of 6.6 mg PdCl_2 was dissolved in 50 mL methanol and the solution was then mixed with 2 g of MOR and stirred for another 7 h.

The Co concentration was varied in 2, 4, and 6 wt.% towards the MOR using the $\text{Co}(\text{NO}_3)_2 \cdot 6\text{H}_2\text{O}$ and diluted in 50 mL of methanol, then stirred for 7 h to produce Co(1)/MOR, Co(2)/MOR and Co(3)/MOR respectively. The solutions were evaporated at 70 °C, then calcined with N_2 flow for 3 h at 450 °C. Finally, the Pd/MOR and Co/MOR catalysts were produced by reduction with H_2 flow for 3 h at 450 °C.

Hydrotreating of CNSL

The CNSL and catalyst in a weight ratio of 50:1 were loaded in a semi-batch reactor. In this study, 0.1 g of catalyst was used to convert 5 g of CNSL oil into biofuel. The reaction temperature was 450 °C for 2 h with 20 mL/min of hydrogen flow. The reactor was connected with a condenser and the liquid product was collected and identified by GCMS analysis.

RESULTS AND DISCUSSION

Catalysts Characterization

The X-ray diffractogram of MOR, Co/MOR, and Pd/MOR were shown in Fig. 1. The peaks found in Co(1)/MOR, Co(2)/MOR, Co(3)/MOR and Pd/MOR were proved to be similar to those found in MOR. Each catalyst exhibited sharp peaks at Bragg angle 9.7, 13.5, and 22.3°. However, the intensity of each peak was shown to be slightly decreased after the impregnation of Co 2, 4, and 6 wt.%, indicating the decrease of crystallinity of MOR structure [13]. On the other hand, several peaks intensity increased for Pd/MOR catalyst, suggesting the loading of a small amount Pd (0.5 wt.% towards the MOR) did not cause blockage in the pores nor damage the crystalline sites of MOR. Instead, Pd appeared to donate its crystalline phase which contributes to the increase of

crystallinity in the Pd/MOR catalyst. Fig. 1 also revealed that the metals did not give any additional peak to the XRD pattern, which suggests the presence of small metal particles with high dispersion and low crystallinity [14].

The FTIR spectrum of the MOR and catalysts were investigated to investigate the effect of metal loaded on TO_4 sites. FTIR spectra of Co/MOR with various metal concentrations were shown in Fig. 2. Before impregnation, FTIR spectra of MOR revealed vibration band at 1080 and 3749 cm^{-1} which correspond to the asymmetric stretching vibration of T-O (where T=Si or Al) and the stretching of O-H hydroxyl group, respectively [15-16]. The band appeared at 640 and 462 cm^{-1} respectively refer to symmetric stretching and bending vibration of T-O. The metal addition caused the band to appear at 1635 cm^{-1} due to the increase of the Brønsted acid site. Fig. 2(a) and 2(d) showed FTIR spectra of MOR before and after the impregnation of Pd. Overall, FTIR spectra between Pd/MOR and Co/MOR do not have differences. As the vibration bands revealed to similar, metal impregnation does not cause any alteration to the functional group in MOR structure. This result is in accordance with XRD characterization.

The textural properties of the catalyst were shown in Table 1. After the metals were loaded, the pore volume, as well as the surface area, are shown to significantly

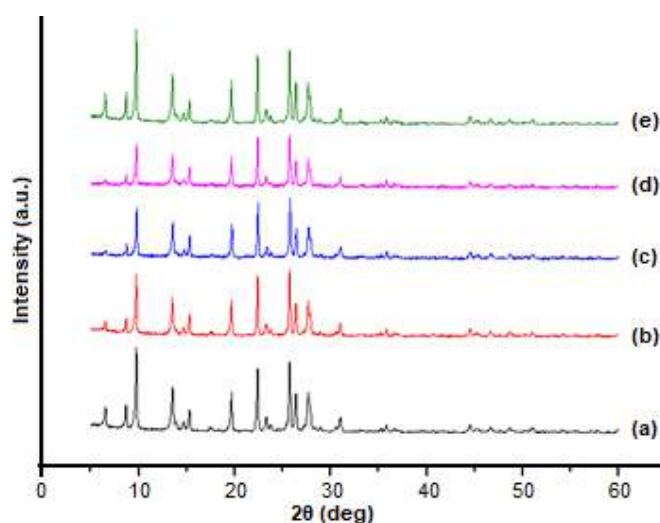


Fig 1. XRD pattern of the catalysts: (a) mordenite, (b) Co(1)/MOR, (c) Co(2)/MOR, (d) Co(3)/MOR, and (e) Pd/MOR

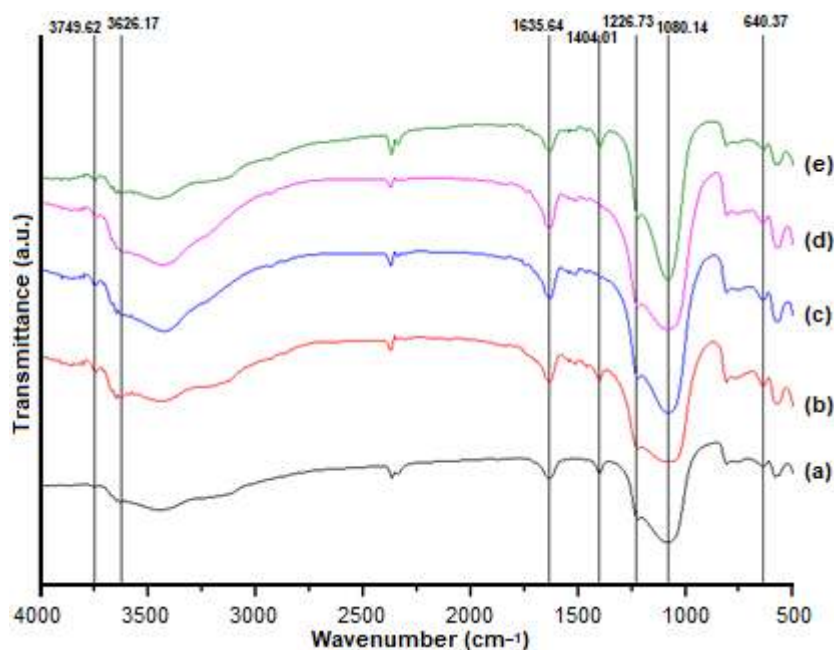


Fig 2. FTIR spectra of: (a) MOR, (b) Co(1)/MOR, (c) Co(2)/MOR, (d) Co(3)/MOR and (e) Pd/MOR

Table 1. Summary of textural properties of catalyst

Sample	Surface area (m ² /g)	Pore volume (cc/g)	Pore diameter (nm)	Total pore volume (cc/g)	Metal loading	Acidity (mmol/g)
MOR	280.38	0.02	3.56	0.17	-	5.87
Co(1)/MOR	592.62	0.27	3.20	0.52	1.11	8.80
Co(2)/MOR	233.75	0.02	3.22	0.14	2.46	12.06
Co(3)/MOR	192.90	0.01	3.21	0.11	4.14	15.67
Pd/MOR	407.62	0.02	3.23	0.23	0.41	11.29

decrease for Co(2)/MOR and Co(3)/MOR catalysts. The decrease was caused by the metal aggregations deposited in the pores leading to a blockage [17-19]. Meanwhile, the impregnation of 1% Co and Pd for Co(1)/MOR as well as Pd/MOR exhibited a different behavior where they seemed to increase the pore volume and the surface area of MOR instead. This result suggests that due to the low quantity of metals in both catalysts, an aggregation that leads to blockage was barely formed. Instead, the small-sized metal particles are generated and distributed fairly distributed on the surface of MOR, contributing to its roughness which increases the surface area [20-21]. Total pore volumes of Co/MOR catalysts are significantly decreased with more metal addition. The pore diameter of catalysts was shown to remain unchanged before and after impregnation.

Fig. 3 showed the pore distribution of the catalysts. The pore distribution ranges from 3–18 nm, which again confirms the mesoporous characteristic of each catalyst [22]. The quantities of some pores with various diameters were shown to decrease after metal impregnation, which suggests the occurrence of pore blockage by metal aggregation as previously discussed [23].

The surface of the catalyst was captured in SEM images (Fig. 4). Although no major morphological difference was observed after the impregnation of metal, EDX analysis was able to detect the addition of a new metal particle as shown in Table 2. The Co appeared in EDX becomes more prominent with the increase of metal concentration loaded inside the pore of MOR as there would be more metal particles giving off its X-Ray light during the analysis process. Pd was also shown to

appear in the EDX analysis for the Pd/MOR catalyst, which confirms the success of the impregnation process.

The Si/Al ratio of MOR that was quantitatively determined using AAS revealed to be 1.46 (mole/mole). AAS analysis was also used to determine the concentration of metal presence in each catalyst prepared as listed in Table 1. The concentration of cobalt loaded in the pore of Co(1)/MOR, Co(2)/MOR and Co(3)/MOR catalysts were found to be 1.11, 2.46, and 4.14 wt.%, respectively. Meanwhile, Pd/MOR catalyst revealed to contain 0.42 wt.% of Pd metal. The amount of metal being successfully loaded was found to slightly differ from the intended. This suggested that not all Co and Pd metals added were fully impregnated into the pore of MOR due to the interaction between metal cations and an aqueous solvent. Therefore, the interaction between salts and MOR as support was slightly hindered.

The acidity test was done gravimetrically by exposing each catalyst material with the flow ammonia gas [18]. The results were stated in Table. 1. The addition

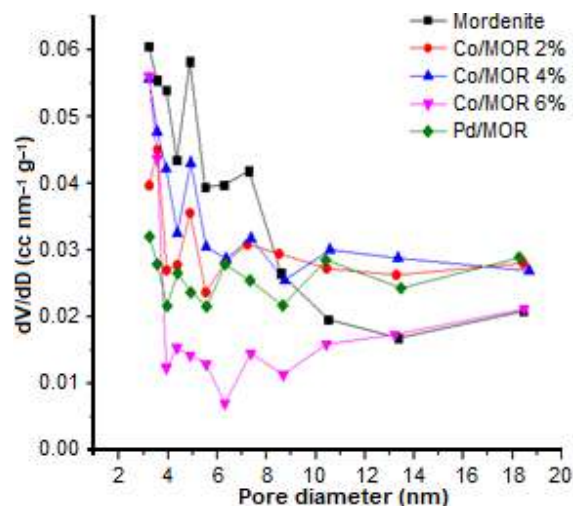


Fig 3. Pore distribution of catalyst

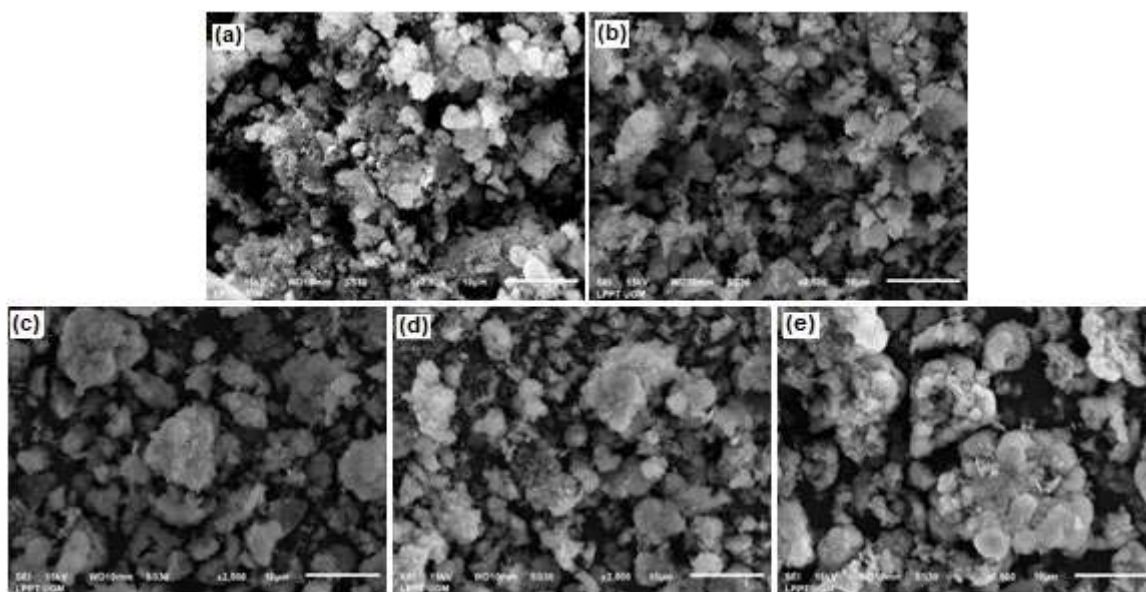


Fig 4. SEM images of (a) mordenite, (b) Co(1)/MOR, (c) Co(2)/MOR, (d) Co(3)/MOR, (e) Pd/MOR

Table 2. Chemical composition of catalysts based on EDX analysis

Element	Mass (%)				
	O	Si	Al	Co	Pd
MOR	56.04	39.53	4.42	-	-
Co(1)/MOR	47.5	46.52	4.96	1.01	-
Co(2)/MOR	58.94	35.22	4.06	1.78	-
Co(3)/MOR	51.76	38.05	4.24	5.95	-
Pd/MOR	58.27	37.21	4.25	-	0.17

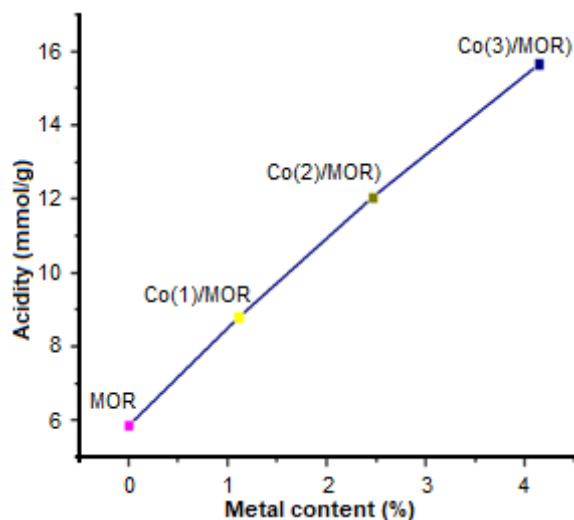


Fig 5. Correlation curve of acidity versus metal content of Co/MOR catalysts

of Co and Pd on the MOR was shown to increase the catalyst acidity. This is related to the empty orbital presence in both Co and Pd metals which contributes as Lewis acid site, therefore increase the total amount of ammonia absorption. Table 1 shows that acidity level of the catalyst decreased with the trend of Co(3)/MOR (15.67 mmol/g) > Co(2)/MOR (12.07 mmol/g) > Pd/MOR (11.29 mmol/g) > Co(1)/MOR (8.80 mmol/g) > the MOR (5.87 mmol/g). The linear correlation between acidity and metal content was depicted by a graph as shown in Fig. 5, where total acidity increased significantly with higher metal concentration.

TEM images of MOR, Co(3)/MOR and Pd/MOR are shown in Fig. 6. Two regions were captured by TEM in MOR material. The dark spots region refers to the pore wall of parent material, while the bright region represents the pores of MOR. After impregnation was done, dark

particles representing the agglomeration of added metal were appeared in the pore of MOR. This finding confirms that the metals are successfully impregnated. The nature of metal particles in the support material is also observed in TEM image. As shown in Fig. 6(b), Co, which formed smaller size agglomerates, would be deposited inside the pore of MOR, leading to the decrease of surface area as mentioned in Table 1. On the other hand, as shown in Fig. 6(c), Pd formed larger size agglomerates that it may not fit the pore provided by MOR, causing some of its particles to be deposited outside of the material pore instead. The Pd metal aggregation on the surface of MOR would add to its roughness which contributes to the increase of surface area as stated in Table 1.

Hydrotreatment of CNSL

The activities of the MOR, Co(1)/MOR, Co(2)/MOR, Co(3)/MOR and Pd/MOR were evaluated in the hydrotreatment of Cashew Nut Shell Liquid (CNSL). The results of each activity are shown in Table 3, the products are divided into 3 phases containing liquid fraction, gas fraction, and coke. Thermal hydrotreatment was revealed to exhibit the lowest production of liquid products with only a 40.01% conversion. The use of catalyst was shown to improve the liquid product consistently. The liquid product using non-loaded MOR catalyst was 49.64 wt.% and it gradually increased with the addition of metal to the support. The use of Co(1)/MOR, Co(2)/MOR, Co(3)/MOR was shown to exhibit 58.9, 60.5 and 61.8 wt.% conversion, respectively. The result implies that the conversion value increases with more metal particles present in the catalyst. This is

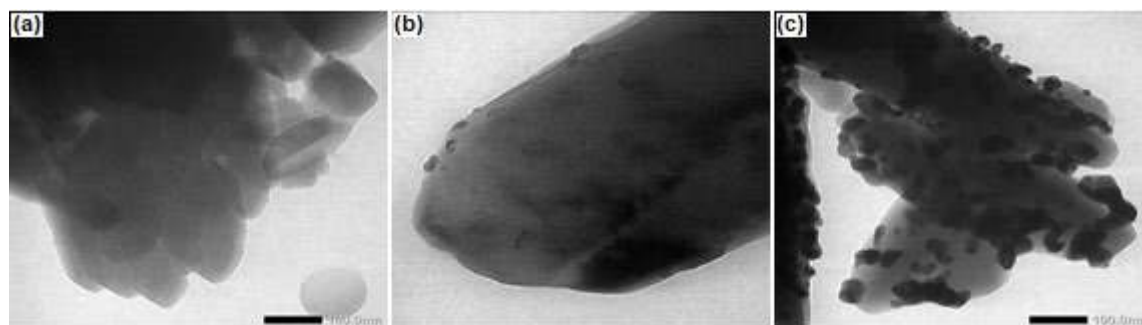


Fig 6. TEM images of (a) mordenite, (b) Co(3)/MOR, and (c) Pd/MOR

Table 3. Product distribution hydrotreating of the CNSL

Catalyst	Conversion (wt.%)			Residue	Total conversion (wt.%)
	Liquid	Gas	Coke		
Thermal	40.01	59.99	0	12.30	87.69
MOR	49.64	42.91	7.44	14.78	85.21
Co(1)/MOR	58.9	38.16	2.94	4.99	95.00
Co(2)/MOR	60.5	32.6	6.84	2.52	97.47
Co(3)/MOR	61.8	36.89	1.26	1.95	98.04
Pd/MOR	58.55	41.4	0.41	2.97	97.02

because metal particles provide empty p orbital that can act and add more acid sites to the catalyst, as referred to the total acidity value data shown in Table 1. These sites facilitate cracking mechanisms during hydrotreatment which leads to the production of more liquid products. Hydrotreating of CNSL oil using natural zeolite was done previously producing over 31.08 wt.% conversion [11]. Co/MOR and Pd/MOR catalysts give the better result of the conversion. The correlation between acidity value and conversion level is illustrated in Fig. 7.

We also compared the activity of Pd as noble metal with Co. In this study, it was revealed that 6% Co-loaded MOR (Co(3)/MOR) was able to exhibit higher liquid conversion than 0.5% Pd-loaded MOR (Pd/MOR). The result indicates the possibility to use Co as a noble metal substitute. Although the quantity of Co metal required for the optimum result was higher compared to Pd, it was compensated with the high availability and lower price. Due to its characteristics as a noble metal, the small amount of Pd produce more liquid products. Moreover, Pd remains in metallic state much longer and can preserve its role as catalyst during the hydrotreatment process. A strong correlation between metal content, acidity and total conversion was observed in Co/MOR catalyst. At the higher concentrations of metals, the acidity of the catalyst will increase, resulting in an increase of total conversion.

TEM images of Co(3)/MOR before and after the hydrotreatment process were shown in Fig. 8. The picture showed coke deposition after the catalytic performance as indicated by the darker shade in Fig. 8(b). However, as reported in Table 1, Co(3)/MOR produced the least coke formation compared to the other Co-loaded MOR studied in this work. It shows that the catalyst exhibits good stability towards coke deposition. It was expected

that Co(3)/MOR may have longer lifetime. Table 4 listed all compounds found in the liquid products obtained from this work. Pd/MOR catalyst exhibits the highest selectivity for gasoline fraction, followed by Co(3)/MOR, Co(2)/MOR, Co(1)/MOR, MOR, and thermal, respectively. Gasoline compounds were shown to be predominantly produced compared to the other compounds. This is correlated to the small size of gasoline

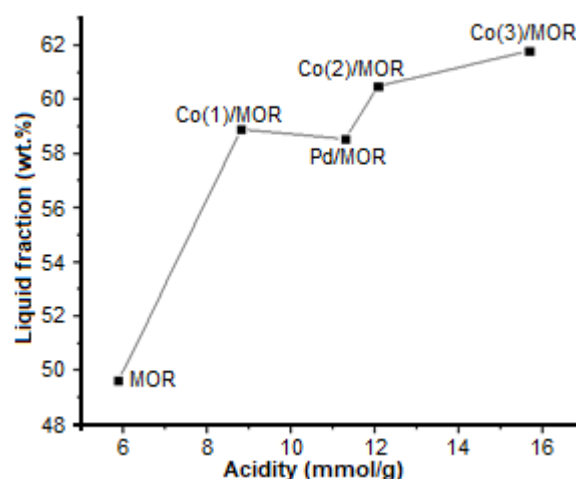
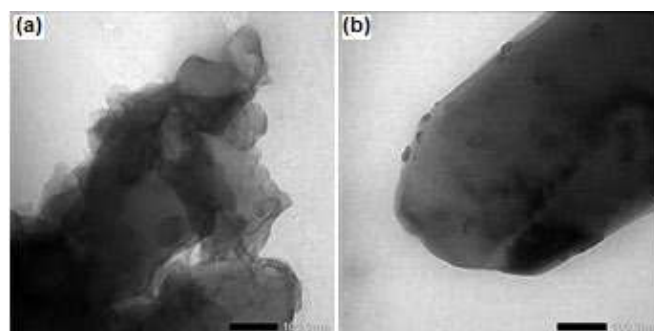
**Fig 7.** Correlation curve of liquid fraction product versus catalyst acidity**Fig 8.** TEM images of Co(3)/MOR: (a) before, and (b) after hydrotreating

Table 4. Distribution of compound in liquid product

Catalyst	The compound in the liquid product				
	C ₅ -C ₁₂	C ₁₃ -C ₁₇	C > 18	Alcohols	Organics
Thermal	13.67	11.18	1.44	11.48	2.24
MOR	16.53	15.60	0.89	12.84	3.78
Co(1)/MOR	16.34	6.18	0.00	19.36	17.05
Co(2)/MOR	23.47	7.55	0.00	20.55	9.01
Co(3)/MOR	25.21	10.48	0.00	19.18	6.96
Pd/MOR	34.50	0.50	0.00	13.88	9.68

compound which contributes to its accessibility in entering and leaving the pore of MOR.

■ CONCLUSION

The preparation of catalysts *via* the wet-impregnation method was successfully applied for Co/MOR and Pd/MOR catalysts. Each catalyst exhibited good activity in converting CNSL oil into fuel compounds. The characterization result showed that metal addition to MOR does not alter the crystallinity and morphology of the support material. The catalytic activity in producing liquid fraction showed a decrease with the sequence of Co(3)/MOR > Co(2)/MOR > Pd/MOR > Co(1)/MOR > MOR. The highest liquid fraction was produced by Co(3)/MOR was 61.8 wt.% at 450 °C.

■ ACKNOWLEDGMENTS

The authors thank Universitas Gadjah Mada for financial support of this work under the scheme of RTA 2019 (Contract no.: 3188/UNI/DITLIT/DIT-LIT/LT/2019).

■ REFERENCES

- [1] Kumari, A.S., Penchalayya, Ch., Raju, A.V.S.R., and Kumar, P.R., 2011, Experimental investigations of IC engine with Pongamia diesel blends, *IJAET*, 2 (4), 54–58.
- [2] Ong, H.C., Masjuki, H.H., Mahlia, T.M.I., Silitonga, A.S., Chong, W.T., and Talal, Y., 2014, Engine performance and emissions using *Jathropa curcas*, *Ceiba pentrada* and *Calophyllum inophyllum* biodiesel in a CI diesel engine, *Energy*, 69, 427–445.
- [3] Astuti, R.B., Suyati, L., and Nuryanto, R., 2012, Pirolisis kulit biji jambu mete (cashew nut shell) dengan katalis Ag/zeolit, *JKSA*, 15 (3), 100–104.
- [4] Listiyati, D., and Sujarmoko, B., 2011, Nilai tambah ekonomi pengolahan jambu mete Indonesia, *Buletin RISTRI*, 2 (2), 231–238.
- [5] Idah, P.A., Simeon, M.I., and Mohammed, M.A., 2014, Extraction and characterization of cashew nut (*Anacardium occidentale*) oil and cashew shell liquid oil, *Acad. Res. Int.*, 5 (3), 50–54.
- [6] Prasada, R., 2014, A review on CNSL biodiesel as an alternative fuel for diesel engine, *IJSR*, 3 (7), 2028–2038.
- [7] Cicziszwili, G.W., Andronikaszwili, T.G., Kirov, G.N., and Filizowa, L.D., 1990, *Zeolity Naturalne*, Wydawnictwa Naukowo-Techniczne, Warszawa.
- [8] Pastvova, J., Kaucky, D., Moravkova, J., Rathousky, J., Sklenak, S., Vorovkhita, M., Brabec, L., Pilar, R., Jakubec, I., Tabor, E., Klein, P., and Sazama, P., 2017, Effect of enhanced accessibility of acid sites in micromesoporous mordenite zeolites on hydroisomerization of *n*-hexane, *ACS Catal.*, 7 (9), 5781–5795.
- [9] Shi, J., Wang, Y., Yang, W., Tang, Y., and Xie, Z., 2015, Recent advances of pore system construction in zeolite-catalyzed chemical industry processes, *Chem. Soc. Rev.*, 44 (24), 8877–8903.
- [10] Trisunaryanti, W., Triyono, Rizki, C.N., Saptoadi, H., Alimuddin, Z., Syamsiro, M., and Yoshikawa, K., 2013, Characteristics of metal supported-zeolite catalysts for hydrocracking of polyethylene terephthalat, *IOSR-JAC*, 3 (4), 29–34.
- [11] Santi, D., and Efiyanti, L., 2014, Hidrorengkah minyak laka menggunakan katalis NiO/zeolit alam aktif dan NiOMoO/zeolit alam aktif menjadi fraksi berpotensi energi, *JPHH*, 32 (2), 93–102.
- [12] Trisunaryanti, W., Triyono, T., Armunanto, R.,

- Hastuti, L.P., Ristiana, D.D., and Ginting, R.V., 2018, Hydrocracking of α -cellulose using Co, Ni, and Pd supported on mordenite catalysts, *Indones. J. Chem.*, 18 (1), 166–172.
- [13] Triyono, Trisunaryanti, W., Ristiana, D.D., and Hastuti, L.P., 2019, Kinetic study of α -cellulose hydrocracking using Ni and Pd supported on mordenite catalysts, *Orient. J. Chem.*, 35 (2), 643–647.
- [14] Inoue, M., and Hiraswa, I., 2013, The relationship between crystal morphology and XRD peak intensity on $\text{CaSO}_4 \cdot 2\text{H}_2\text{O}$, *J. Cryst. Growth*, 380, 169–175.
- [15] Trisunaryanti, W., Syoufian, A., and Purwono, S., 2013, Characterization and modification of Indonesian natural zeolite for hydrocracking of waste lubricant oil into liquid fuel fraction, *J. Chem. Chem. Eng.*, 7 (2), 175–180.
- [16] Lu, M., Liu, X., Li, Y., Nie, Y., Lu, X., and Deng, D., 2016, Hydrocracking of bio-alkanes over Pt/Al-MCM-41 mesoporous molecular sieves for bio-jet fuel production, *J. Renewable Sustainable Energy*, 8, 053103.
- [17] Abdullah, Triyono, Trisunaryanti, W., and Haryadi, W., 2013, The optimum reaction time, activation energy and frequency factor of methyl ricinoleate nitration, *Indones. J. Chem.*, 13 (1), 36–40.
- [18] Xu, Y., Suzuki, Y., and Zhang, Z.G., 2013, Comparison of the activity stabilities of nanosized and microsized zeolites based Fe-Mo/HZSM-5 catalysts in the non-oxidative CH_4 dehydroaromatization under periodic CH_4 - H_2 switching operation at 1073 K, *Appl. Catal., A*, 452, 105–116.
- [19] Masiero, S.S., Marcilio, N.R., and Perez-Lopez, O.W., 2009, Aromatization of methane over Mo-Fe/ZSM-5 catalysts, *Catal. Lett.*, 131, 194–202.
- [20] Nishi, Y., and Inagaki, M., 2016, “Gas adsorption/desorption isotherm for pore structure characterization” in *Materials Science and Engineering of Carbon: Characterization*, Eds. Inagaki, M., and Kang, F., Butterworth-Heinemann, Oxford, UK, 227–247.
- [21] Trisunaryanti, W., Suarsih, E., Triyono, and Falah, I.I., 2019, Well-dispersed nickel nanoparticles on the external and internal surfaces of SBA-15 for hydrocracking of pyrolyzed α -cellulose, *RSC Adv.*, 9 (3), 1230–1237.
- [22] Gregg, S.J., and Sing, K.S.W., 1982, *Adsorption, Surface Area, and Porosity*, 2nd Ed., Academic Press, London.
- [23] Kostyniuk, A., Key, D., and Mdleleni, M., 2019, Effect of Fe-Mo promoters on HZSM-5 zeolite catalyst for 1-hexane aromatization, *J. Saudi Chem. Soc.*, 23 (5), 612–626.

Microwave-Assisted Preparation of Magnetic Citric Acid-Sugarcane Bagasse for Removal of Textile Dyes

Nguyen Thi Hong Anh¹, Tran Thanh Phuc², Tran Nguyen Minh An²,
Pho Quoc Hue², and Nguyen Van Cuong^{2,*}

¹Faculty of Chemical Engineering, Ho Chi Minh City University of Food Industry,
140 Le Trong Tan, Tay Thanh Ward, Tan Phu District, Ho Chi Minh City, Vietnam

²Faculty of Chemical Engineering, Industrial University of Ho Chi Minh City,
12 Nguyen Van Bao, Ward 4, Go Vap District, Ho Chi Minh City, Vietnam

* **Corresponding author:**

email: nvc@iuh.edu.vn

Received: August 13, 2019

Accepted: October 27, 2019

DOI: 10.22146/ijc.48713

Abstract: Wastewater from industries has been a serious issue that both manufactures and authorities raise concerns since it brings tremendous demerits to the surrounding environment and human well-being. Therefore, an appropriate treatment method should be applied before being discharged into the environment. In this paper, sugarcane bagasse was modified with citric acid and then used to load the suspension of Fe₃O₄ nanoparticles to form a nanocomposite of magnetic citric acid-modified sugarcane bagasse. The properties of prepared materials were investigated by a variety of modern methods such as X-ray diffraction (XRD), Fourier transforms infrared spectroscopy (FT-IR), Scanning electron microscopy (SEM), Transmission electron microscopy (TEM) and a Vibrating sample magnetometer (VSM). The adsorptive capacity of prepared materials was investigated with methylene blue as the typical adsorbate. The decolonization effectiveness was increased with increasing contact time and declined with rising initial dye concentration. The higher removal efficiency was observed for the basic medium in comparison with the acidic medium. Additionally, the results showed that more than 12.42 mg/g (98%) of cationic yellow 51, and basic red 46 dyes were removed after 30 min.

Keywords: sugarcane bagasse; adsorption; microwave; nanocomposites; textile dyes

■ INTRODUCTION

Industrial wastewater is defined as water that has been utilized for making commercial goods before treatment, which consists of plenty of toxic contaminants and usuch as indecomposable organic dyes and heavy metals [1]. Annually, it is estimated that more than 80 percent of the world's wastewater is released into the environment without preliminary treatment or recycling [2]. Apart from that, it is believed that most of the industrial sectors concentrate nearby coastal areas where sewage can be leaked into the ocean with ease and that the exploitation of fossil fuels has recently witnessed a dramatic increase due to global economic growth. As a result, the water, environment from surface water to groundwater in these areas, is investigated to be severely

polluted. Therefore, in addition to raising the awareness of people about environment protection, tightening the management of the environment, finding an effective way to eliminate pollutants has a great significance.

Among industrial sectors, textile industries have been considered to be one of the sources of water pollution as they consume large quantities of water and chemicals, especially in dyeing and finishing processes [3]. An approximation of 10–15% of the used dyes have vanished during the dyeing processes [4-5]. Current methods have been used for the treatment of this type of dye-related wastewater, which comprises precipitation, coagulation/flotation, sedimentation, flotation, filtration, membrane processes, electrochemical techniques, advanced oxidation, ion exchange, biological treatment, chemical reactions, and adsorption [6-8]. In particular,

biological treatment methods are preferable due to their treatment efficiency in the long run, but they also have drawbacks such as the uncontrollable process of ventilation, ease of smell [9]. Physical or chemical processes are often used, but the high cost of these processes is disadvantageous. The combination of various methods is usually used to treat real textile wastewater [10]. Meanwhile, among wastewater treatment methods, adsorption is one of the most applicable techniques used to remove pollutants from sewage because of several reasons related to cost-efficiency, easy-to-fabricate, eco-friendliness, and the ability to recycle. It is reported that there have various types of materials being used to remove contaminants from wastewater, among which are activated charcoal, chitosan, orange peels, porous materials, etc [11-15]. One of the disadvantages that make activated carbon less useful is the capability to recycle. From this perspective, a cost-efficient adsorbent that derives from agricultural residues combined with magnetic nanoparticles is used to remove pollutants in water with feasible recyclable ability, namely a nanocomposite of magnetic citric acid-modified sugarcane garbage [16-18].

It is reported that microwave irradiation was used in the chemical process due to the simple and clean method with high-efficiency energy. Nanoparticle materials have been prepared by microwave-assisted methods with uniform, small, narrow size distributions and high crystalline orders in comparison with nanoparticle synthesized by the conventional heating method [19-21]. Acid modification of material is usually conducted under a reflux condition with high temperature and long reaction time under an oil bath. However, the usage of microwave-assisted modification of materials was reported to reduce the reaction time and high modification efficiency.

In this research, the sugarcane bagasse is used as a matrix in the nanocomposite, which is a by-product of the sugar production process. The sugarcane bagasse and its modification were used as an environmentally friendly adsorbent for the elimination of textile dyes and heavy metals from aqueous solutions [22-23]. With a porous structure, sugarcane bagasse can function as a trap in order to attract dye molecules into its matrix through

physical and chemical interaction. There is a limitation in terms of the small particle size of sugarcane bagasse powders, which means that the small particle size of bagasse powders results in the difficulty of collecting after usage. Therefore, it is a huge attractive work to increase the separation property of the adsorbents with tiny size. In recent times, magnetic separation technologies have been giving interests. Magnetic materials can be recovered from an aqueous solution efficiently with an external magnet. Therefore, the magnetic nanoparticles loaded in bagasse matrix has a promising potential to overcome this issue. In addition, the surface of sugarcane bagasse was modified with citric acid under microwave irradiation and also increased the capacity of adsorbing metals and dye molecules.

■ EXPERIMENTAL SECTION

Materials

Clean sugarcane bagasse was provided from a local sugar mill with a low grade of impurities. Then, the sugarcane bagasse was dried in an oven at a temperature of 105 °C for 4 h to remove the water. The resulting material was ground into powders with a particle size of 0.5–1 mm and kept for further experiments. Reactive red 198 (RR198) ($M_w = 983.5$, $\lambda_{max} = 554$ nm), Cationic yellow 51 (CY51) ($M_w = 403.5$, $\lambda_{max} = 410$ nm), Basic red 46 (BS46) ($M_w = 401.312$, $\lambda_{max} = 532$ nm) and Methylene blue (MB) ($M_w = 319.86$, $\lambda_{max} = 664$ nm) were provided from Thanh Cong Textile Garment Investment Trading Joint Stock Company. Synthetic industrial wastewater was prepared by dissolving these dyes in distilled water.

Procedure

Sugarcane bagasse preparation

Preparation of citric acid-modified sugarcane bagasse (CAS). Sugarcane bagasse (RS, 10 g) was modified with 250 mL citric acid at various concentrations, including 0.1, 0.3, and 0.5 mol L⁻¹ under microwave radiation for 10 min. The resulting samples were washed by distilled water until reaching the pH value of 7. Afterward, the washed mixture was dried in an oven at a constant temperature of 70 °C for 12 h to obtain dried citric acid modified sugarcane (CAS).

Preparation of magnetic sugarcane bagasse (MCAS).

Magnetic sugarcane bagasse was fabricated by adding the citric acid-modified sugarcane bagasse to a suspension of Fe₃O₄ nanoparticles with a ratio of 9:1. Briefly, in order to synthesize Fe₃O₄ nanoparticles, a given amount of 5.41 g of FeCl₃·6H₂O and 1.99 g of FeCl₂·4H₂O were transferred into 150 mL of distilled water under mechanical stirrer for 30 min. Later on, 4.5 g of CAS was added to the resulting solution and heated up at 80 °C. Next, magnetic sugarcane bagasse was obtained by adding a dropwise NaOH solution (0.1 mol L⁻¹) and the pH value of the solution was adjusted to around 11 using NaOH to obtain nanocomposite. The obtained mixture was stirred mechanically for 6 h. An external magnet was applied in order to collect the nanocomposite. The final nanocomposite was washed with water and ethanol for 5 times and dried in a vacuum oven for 24 h.

Analytical methods

Fourier transform infrared (FT-IR) analysis of the samples was performed on Tensor 27 –Bruker, Germany in order to determine functional groups of nanocomposites with the scanning wave numbers ranging 400–4000 cm⁻¹. The structural properties of magnetic nanocomposites were investigated using X-ray powder diffraction (XRD) (D8 Advance–Bruker System, Germany). Morphological examination of the nanocomposites was evaluated by using scanning electron microscopy (SEM) (HITACHI-S-4800, Tokyo, Japan). In order to examine the existence of Fe₃O₄ nanoparticles in the nanocomposites by characterizing the magnetic properties of materials, a vibrating sample magnetometer (DMS-880) was used with a magnetic field from –15k Oe to 15k Oe at room temperature.

Adsorption experiments

To investigate the adsorption properties of the prepared materials, batch adsorption studies were prepared using 0.2 g of adsorbents and 50 mL various dye solutions at a wide range of initial concentrations of MB from 30 to 75 mg L⁻¹. At different time intervals, the dye solution was separated using a permanent magnet. The dye concentration at a certain time was determined using a UV-Vis spectrophotometer at a wavelength of 664 nm. In addition, to examine the influence of pH medium on

the adsorption capacity of the prepared materials, the batch adsorption was carried at various pH values from 3 to 9 with a 50 mL MB solution (50 mg L⁻¹). The impact of the mass of adsorbents used (0.05, 0.1, 0.2, and 0.5 g) was also determined by carrying out the experiments in the 50 mL dye solution (concentration of 50 mg L⁻¹) for 30 min. Finally, the effect of various dye structures, including RR198, CY51, BS46 (50 mg L⁻¹) on the adsorption capacity of the prepared materials, was performed in a set of 250 mL Erlenmeyer flasks containing 0.2 g adsorbent and 50 mL various dye solutions for 30 min. All of the adsorption experiments were repeated triplicate for the average value and its standard deviation. The yield of adsorption capacity was determined by the following Eq. (1):

$$(C_0 - C_e) / C_0 \times 100 \quad (1)$$

where C₀ and C_e are the initial and equilibrium concentration of dye solution (mg L⁻¹).

RESULTS AND DISCUSSION

Characteristic of the Materials

Fig. 1 represents the FT-IR spectra of samples RS, CAS, and MCAS. The result showed that in three samples, there are three typical absorption bands at 896, 1160, and 1031 cm⁻¹, which are assigned to β-(1-4) glycosidic bond of cellulose, C–O–C stretching, and C–O stretching, accordingly. The absorption bands that represent for C=O stretching were observed at 1714 and 1720 cm⁻¹. More interesting, the intensity of these peaks is higher in CAS and MCAS in comparison with RS. It is feasible that the acetylation reaction of carboxylic groups of citric acid and to the hydroxyl group of RS to generate an ester bond could have taken place. Meanwhile, bands at 1320 and 1370 cm⁻¹ in the FT-IR spectrum were attributed to the presence of C–H groups. In addition, the lignin associated bands were also depicted at 1511 and 1600 cm⁻¹. Importantly, the band at 580 cm⁻¹ representing the Fe–O stretching was found only in the MCAS sample, which means that magnetic nanoparticles exist in the bagasse powders.

XRD results of MCAS and Fe₃O₄ nanoparticles were revealed in Fig. 2. As a result, the diffraction spectrum at 16 and 22° showed the existence of cellulose

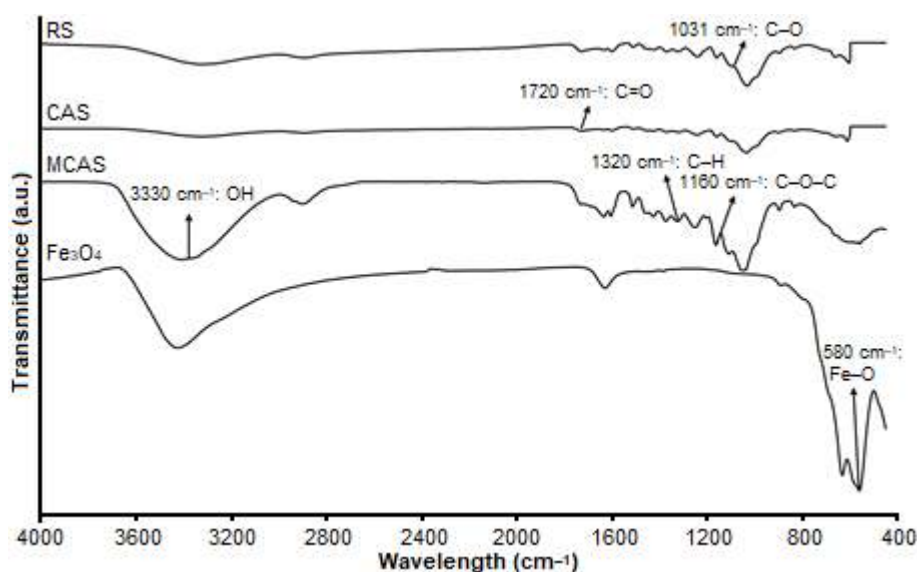


Fig 1. FTIR spectrum of the prepared materials RS, CAS, and MCAS

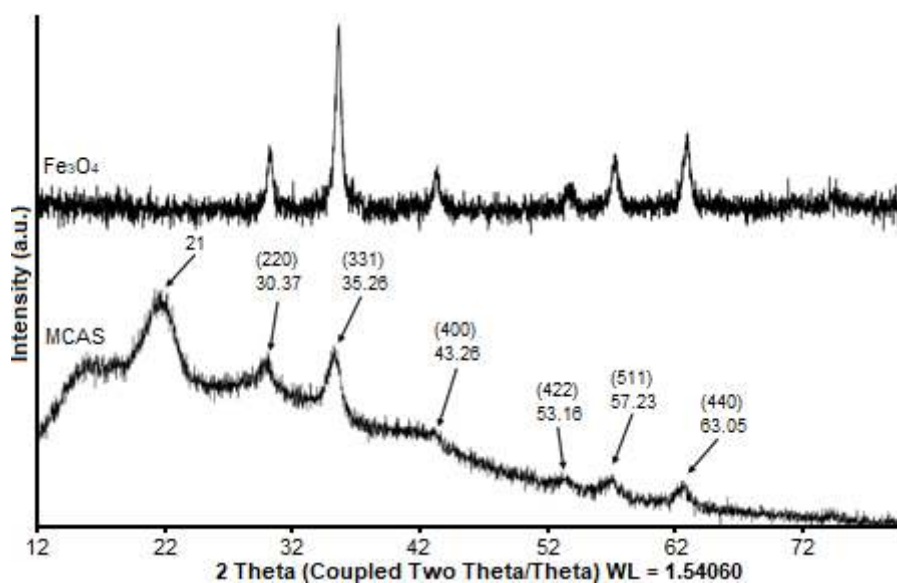


Fig 2. X-ray diffraction (XRD) pattern of Fe_3O_4 nanoparticles and MCAS

in MCAS samples. The peaks at 30, 35, 43, 53, 57, and 63° are corresponding to Fe_3O_4 nanoparticles [24]. Moreover, the TEM and SEM images in Fig. 3 confirmed that Fe_3O_4 nanoparticles adhered to the bagasse surface. The EDS result of the MCAS sample was also shown in Fig. 4, which depicted that the presence of iron was indicated by two peaks K of about 6.4 and 7.0 keV and a peak L of 0.78 keV. There was also the existence of other factors of sugarcane bagasse, such as Si at 1.80 keV. Additionally, the magnetization curve (VSM) of MCAS and Fe_3O_4 samples

were revealed in Fig. 5. The VSM shows that the magnetic saturation of MCAS ($M_s = 7.26$ emu/g) was lower than that of Fe_3O_4 nanoparticles ($M_s = 71.0$ emu/g) due to the presence of nonmagnetic organic matter of bagasse. Though Fe_3O_4 nanoparticles were dispersed into the bagasse matrix, the magnetic saturation of MCAS was still available with a smaller value. From this result, it is believed that our materials can be recovered from an aqueous solution with an external magnet [12].

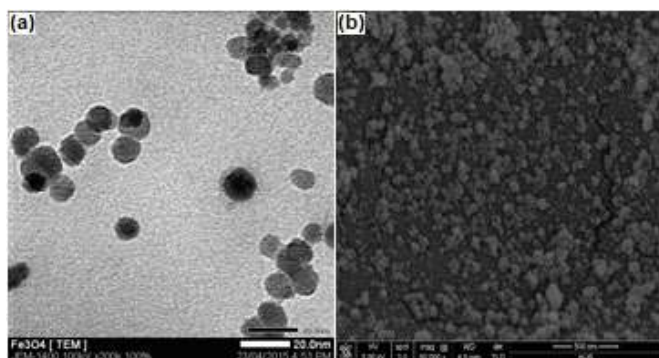


Fig 3. The TEM image of (a) Fe_3O_4 nanoparticles and (b) morphological SEM image of the prepared MCAS

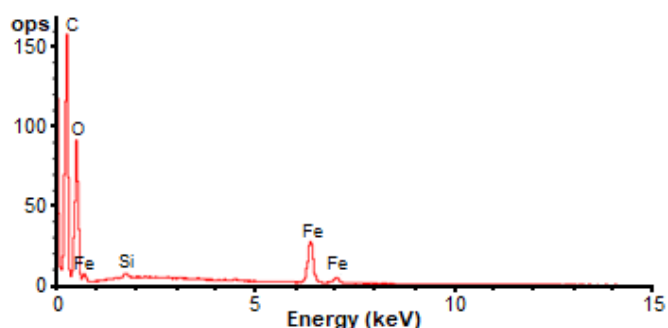


Fig 4. EDS spectra of MCAS

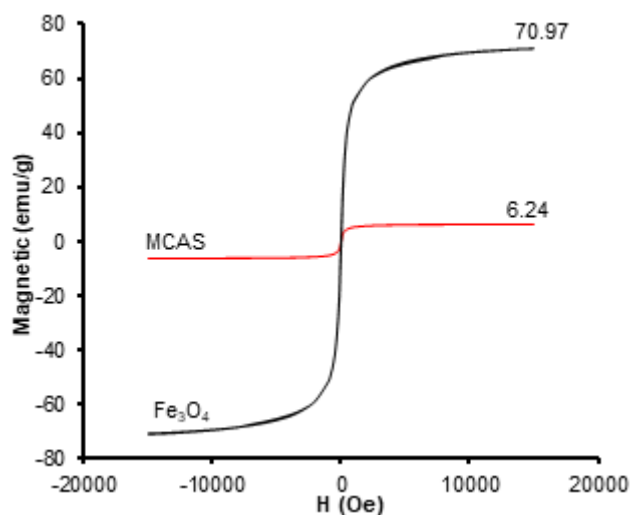


Fig 5. VSM spectra of MCAS and Fe_3O_4

Influence of Citric Acid Concentration on MB Adsorption of CAS

Fig. 6 shows the influence of citric acid concentration on the removal of MB. The results indicated that removal efficiency increased with rising citric acid concentration. The highest adsorption efficiency for MB was 99% was observed for the

concentration of citric acid 0.5 M. The crude sugarcane bagasse gave a much lower adsorption efficiency (66%) in comparison with citric acid-treated sugarcane bagasse (CAS). This could be explained due to CAS containing more $-\text{COO}-$ groups than that of crude sugarcane bagasse [25].

Effect of MCAS Dosage on Adsorption Efficiency of MB

Fig. 7 showed how the dosage factor of MCAS influenced the adsorption efficiency of MB. As observed,

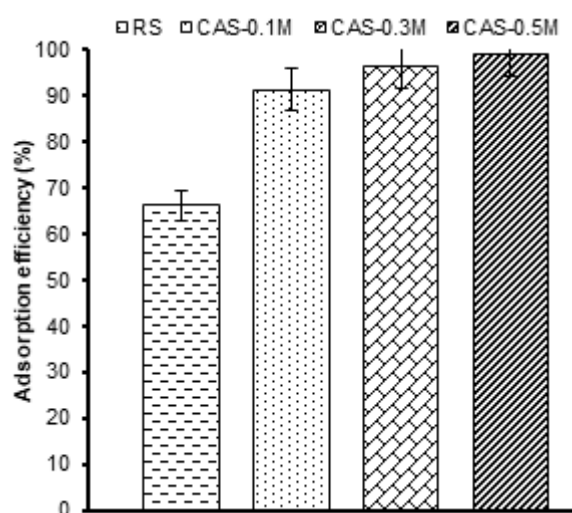


Fig 6. Adsorption efficiency of MB onto various materials (0.2 g materials; and solution volume: 50 mL with a concentration of 50 mg L^{-1})

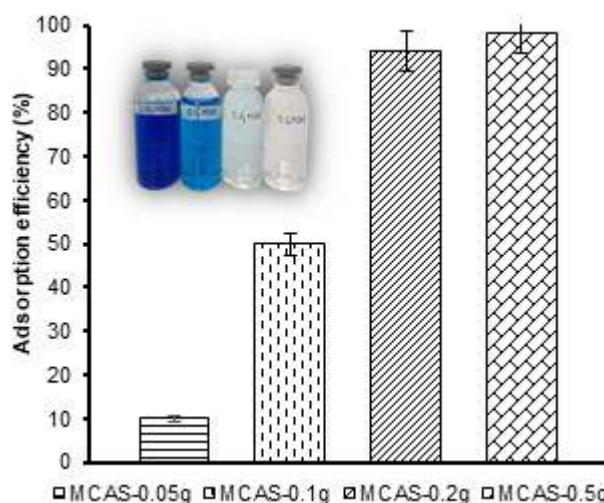


Fig 7. Adsorption kinetics of MB onto MCAS at different amounts of adsorbent (solution volume: 50 mL; time: 30 min; and MB concentration of 50 mg L^{-1})

the results indicated that the higher the mass of the adsorbent used, the greater the adsorption capacity of MB was. Particularly, the adsorption efficiency increased from 18 to 98% for MB with an increment of the amount of MCAS from 0.05 to 0.2 g. This could be due to the adsorption ability is influenced by the external surface of the prepared nanocomposite. Therefore, an increase in the amount of the nanocomposite ascribed to an increase in surface region and availability of adsorption sites.

Effect of Initial Concentration and Contact Time

The results showed that the rate of the MB decolorization was faster at the initial stages of the contact time, and then slowed down gradually before reaching equilibrium. As observed, the adsorption efficiency declined when the dye concentration rose. Particularly, the adsorption efficiencies were almost 100% for the concentration of 30 to 50 mg L⁻¹ and decreased to 87% for the concentration of 75 mg L⁻¹ (Fig. 8). After the first 10 min, the adsorption efficiency was fairly high owing to a large number of adsorption sites at the beginning. When contact time increased gradually, the number of MB molecules being accumulated or trapped on the surface of the prepared nanocomposite. Consequently, there was a decline in the adsorption rate at the later stages [26]. In particular, the MB could be adsorbed completely onto the MCAS surface within 15 min. Fig. 9 revealed the decrease in the UV-Vis spectra of MB for adsorption time from

initial to 90 min. Additionally, In order to examine the sorption isotherms, the Langmuir model was used. The results exhibited that a very high correlation coefficient ($R^2 > 0.9771$) was found, representing that the isotherm obtained for the adsorption of MB effluent followed the Langmuir model (Fig. 8).

Effect of pH Value on the Removal of MB

The effect of initial pH on the adsorption capacity of MB onto MCAS was carried out at various pH values in the range of 3–9. These results expressed that at lower pH, the existence of excess H₃O⁺ ions resulted in a high capacity to protonate carboxylate functional group (–COO⁻) on the adsorbent to form more the protonated form (–COOH), leading to a decline in the number of negative charges. Therefore, there might be fewer possibilities to favor positively charged dyes in the acidic medium [27]. When the pH is increased, the surface area of materials with negative charge significantly increased so that it is more likely to attract more positively charged dyes like MB, (Fig. 10).

Effect of Dye Structure

It has been reported that the chemical structure of dyes also influences directly on the adsorption capacity of the nanocomposite. Fig. 11 showed that MCAS performed high adsorption capacity with MB, CY51, BS46 and low adsorption capacity with RR198. It is believed that the

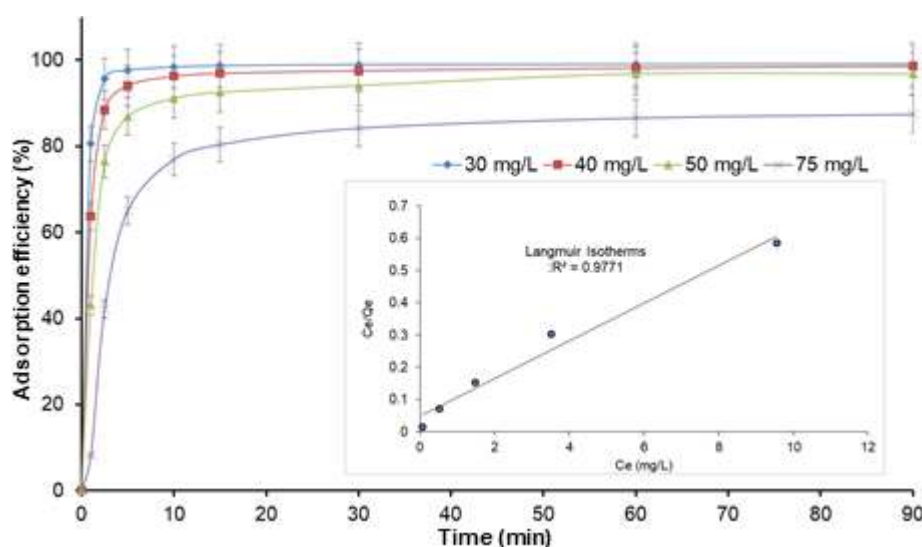


Fig 8. Adsorption kinetics of MB onto MCAS at different initial concentrations (0.2 g MCAS; solution volume: 50 mL)

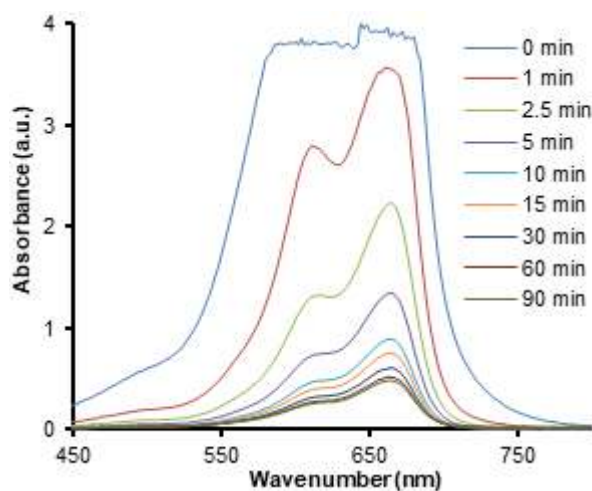


Fig 9. Time-dependent UV-Vis absorption spectra of MB (0.2 g of MCAS, solution volume: 50 mL, initial MB concentration: 75 mg L⁻¹)

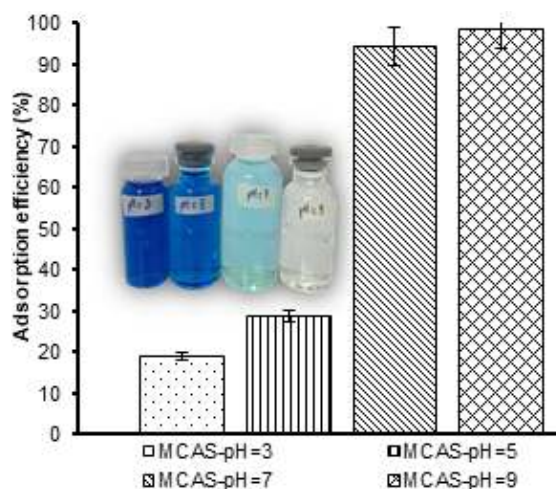


Fig 10. Effect of initial pH on the adsorption of MB onto MCAS (0.2 g MCAS; solution volume: 50 mL and concentration of 50 mg L⁻¹)

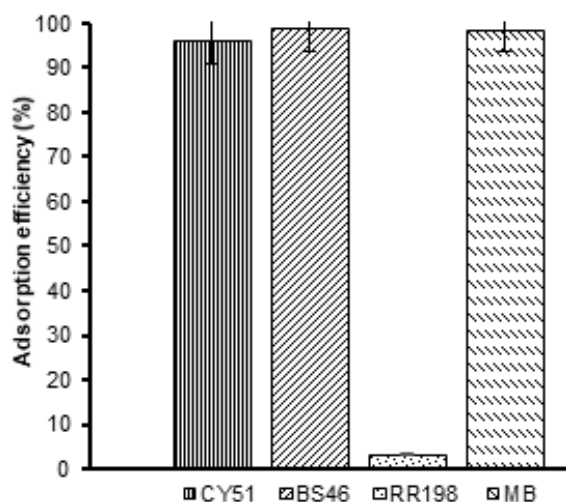


Fig 11. Effect of various dyes structure on adsorption efficiency of MCAS (0.2 g MCAS; solution volume: 50 mL, and concentration of 50 mg L⁻¹)

phenomenon could be explained due to the difference in the structure of dye molecules. RR198 is an anionic dye with a great number of negative charges while MB, CY51, and BS46 are cationic dyes with the positively charged surface. For this reason, three types of dye molecules MB, CY51 and BS46 can be trapped to the negatively charged surface of the nanocomposite.

CONCLUSION

In this present study, acid-treated sugarcane bagasse was prepared with the assistance of microwave irradiation,

and then a novel magnetic sugarcane bagasse nanocomposite was successfully synthesized by a simple precipitation method. The results indicated that 12.42 mg/g (98%) of the methylene blue was removed after 30 min. Additionally, MCAS exhibited a much better capacity in the removal of MB in alkaline milieu than in acidic milieu. Moreover, the higher removal capacity was also observed for MB, CY51, and BS46 dyes in comparison with RR198. The magnetic citric acid-modified sugarcane bagasse showed a much better performance in adsorbing MB than that of natural sugarcane bagasse.

ACKNOWLEDGMENTS

The authors would like to thank the Industrial University of Ho Chi Minh City, Vietnam for financial support in 2019 (code: 19.2H01).

REFERENCES

- [1] Chung, K.T., 2016, Azo dyes and human health: A review, *J. Environ. Sci. Health., Part C Environ. Carcinog. Ecotoxicol. Rev.*, 34 (4), 233–261.
- [2] United Nations World Water Assessment Programme, 2017, *Wastewater: The untapped resource*, The United Nations World Water Development Report, UNESCO, Paris.
- [3] Sivaram, N.M., Gopal, P.M., and Barik, D., 2019, “Toxic Waste from Textile Industries” in *Energy*

- from *Toxic Organic Waste for Heat and Power Generation*, 1st Ed., Eds. Barik, D., Woodhead Publishing, United Kingdom, 43–54.
- [4] Tahir, H., Sultan, M., Akhtar, N., Hameed, U., and Abid, T., 2016, Application of natural and modified sugar cane bagasse for the removal of dye from aqueous solution, *J. Saudi Chem. Soc.*, 20 (Suppl. 1), S115–S121.
- [5] Ozturk, E., Karaboyacı, M., Yetis, U., Yigit, N.O., and Kitis, M., 2015, Evaluation of integrated pollution prevention control in a textile fiber production and dyeing mill, *J. Cleaner Prod.*, 88, 116–124.
- [6] Karamah, E.F., and Nurcahyani, P.A., 2018, Degradation of Blue KN-R dye in batik effluent by an advanced oxidation process using a combination of ozonation and hydrodynamic cavitation, *Indones. J. Chem.*, 19 (1), 41–47.
- [7] Holkar, C.R., Jadhav, A.J., Pinjari, D.V., Mahamuni, N.M., and Pandit, A.B., 2016, A critical review on textile wastewater treatments: Possible approaches, *J. Environ. Manage.*, 182, 351–366.
- [8] Katheresan, V., Kansedo, J., and Lau, S.Y., 2018, Efficiency of various recent wastewater dye removal methods: A review, *J. Environ. Chem. Eng.*, 6 (4), 4676–4697.
- [9] Singh, R.L., Singh, P.K., and Singh, R.P., 2015, Enzymatic decolorization and degradation of azo dyes – A review, *Int. Biodeterior. Biodegrad.*, 104, 21–31.
- [10] Bazrafshan, E., Alipour, M.R., and Mahvi, A.H., 2016, Textile wastewater treatment by application of combined chemical coagulation, electrocoagulation, and adsorption processes, *Desalin. Water Treat.*, 57 (20), 9203–9215.
- [11] Salgot, M., and Folch, M., 2018, Wastewater treatment and water reuse, *Curr. Opin. Environ. Sci. Health*, 2, 64–74.
- [12] Nguyen, V.C., Hieu, T.Q., Thien, P.T., Vu, L.D., and Tan, L.V., 2017, Reusable starch-graft-polyaniline/Fe₃O₄ composite for removal of textile dyes, *Rasayan J. Chem.*, 10 (4), 1446–1454.
- [13] Ahmad, T., and Danish, M., 2018, Prospects of banana waste utilization in wastewater treatment: A review, *J. Environ. Manage.*, 206, 330–348.
- [14] Ahsan, M.A., Katla, S.K., Islam, M.T., Hernandez-Viezcas, J.A., Martinez, L.M., Díaz-Moreno, C.A., Lopez, J., Singamaneni, S.R., Banuelos, J., Gardea-Torresdey, J., and Noveron, J.C., 2018, Adsorptive removal of methylene blue, tetracycline and Cr(VI) from water using sulfonated tea waste, *Environ. Technol. Innovation*, 11, 23–40.
- [15] De Gisi, S., Lofrano, G., Grassi, M., and Notarnicola, M., 2016, Characteristics and adsorption capacities of low-cost sorbents for wastewater treatment: A review, *Sustainable Mater. Technol.*, 9, 10–40.
- [16] Said, A.A., El-Wahab, M.M.M.A., Soliman, S.A., and Aly, A.A.M., 2010, Potential application of propionic acid modified sugarcane bagasse for removal of basic and acid dyes from industrial wastewater, *International Conference on Environmental Engineering and Applications*, Singapore, 10–12 September 2010, 154–156.
- [17] Ekpete, O.A., Kpee, F., Amadi, J.C., and Rotimi, R.B., 2010, Adsorption of chromium(VI) and zinc(II) ions on the skin of orange peels (*Citrus sinensis*), *J. Nepal Chem. Soc.*, 26, 31–39.
- [18] Zhang, J., Li, Y., Zhang, C., and Jing, Y., 2008, Adsorption of malachite green from aqueous solution onto carbon prepared from *Arundo donax* root, *J. Hazard. Mater.*, 150 (3), 774–782.
- [19] Hasanpoor, M., Aliofkhaezaei, M., and Delavari, H., 2015, Microwave-assisted synthesis of zinc oxide nanoparticles, *Procedia Mater. Sci.*, 11, 320–325.
- [20] Valdez, J., and Gómez, I., 2016, One-step green synthesis of metallic nanoparticles using sodium alginate, *J. Nanomater.*, 2016, 9790345.
- [21] Prasiwi, A.D., Trisunaryanti, W., Triyono, T., Falah, I.I., Santi, D., and Marsuki, M.F., 2019, Synthesis of mesoporous carbon from Merbau wood (*Intsia* spp) by microwave method as Ni catalyst support for α -cellulose hydrocracking, *Indones. J. Chem.*, 19 (3), 575–582.
- [22] Fideles, R.A., Ferreira, G.M.D., Teodoro, F.S., Adarme, O.F.H., da Silva, L.H.M., Gil, L.F., and Gurgel, L.V.A., 2018, Trimellitated sugarcane bagasse: A versatile adsorbent for removal of cationic dyes from aqueous solution. Part I: Batch

- adsorption in a monocomponent system, *J. Colloid Interface Sci.*, 515, 172–188.
- [23] Elias, M.M.C., Ferreira, G.M.D., de Almeida, F.T.R., Rosa, N.C.M., Silva, I.A., Filgueiras, J.G., de Azevedo, E.R., da Silva, L.H.M., Melo, T.M.S., Gil, L.F., and Gurgel, L.V.A., 2019, Synthesis and application of sugarcane bagasse cellulose mixed esters. Part I: Removal of Co^{2+} and Ni^{2+} from single spiked aqueous solutions in batch mode using sugarcane bagasse cellulose succinate phthalate, *J. Colloid Interface Sci.*, 533, 678–691.
- [24] Zheng, Y., Cheng, Y., Bao, F., and Wang, Y., 2006, Synthesis and magnetic properties of Fe_3O_4 nanoparticles, *Mater. Res. Bull.*, 41 (3), 525–529.
- [25] Begum, H.A., and Bin Mahbub, M.K., 2013, Effectiveness of carboxymethyl cellulose for the removal of methylene blue from aqueous solution, *Dhaka Univ. J. Sci.*, 61 (2), 193–198.
- [26] Uddin, M.T., Islam, M.A., Mahmud, S., and Rukanuzzaman, M., 2009, Adsorptive removal of methylene blue by tea waste, *J. Hazard. Mater.*, 164 (1), 53–60.
- [27] Sartape, A.S., Mandhare, A.M., Jadhav, V.V., Raut, P.D., Anuse, M.A., and Kolekar, S.S., 2017, Removal of malachite green dye from aqueous solution with adsorption technique using *Limonia acidissima* (wood apple) shell as low cost adsorbent, *Arabian J. Chem.*, 10 (Suppl. 2), S3229–S3238.

Improved Maleic Anhydride Grafting to Linear Low Density Polyethylene by Microencapsulation Method

Iman Rahayu^{1,*}, Achmad Zainuddin¹, and Sunit Hendrana²

¹Department of Chemistry, Faculty of Mathematics and Natural Sciences, Universitas Padjadjaran, Jl. Raya Bandung-Sumedang km. 21, Jatinangor, Sumedang 45363, West Java, Indonesia

²Laboratory of Applied Physics, Indonesian Institute of Sciences, Jl. Sangkuriang, Kompleks LIPI, Bandung 40135, West Java, Indonesia

*** Corresponding author:**

tel: +62-89672184591

email: iman.rahayu@unpad.ac.id

Received: August 16, 2019

Accepted: January 8, 2020

DOI: 10.22146/ijc.48785

Abstract: A common graft copolymerization method usually results in a low degree of grafting due to its poor inter-component interactions. A monomer microencapsulation method should be useful to enhance the current graft copolymerization technique. The maleic anhydride (MAH) grafted with linear low-density polyethylene (LLDPE) was successfully synthesized by monomer microencapsulation without using a direct method in order to find a high degree of grafting. The results showed that the degree of grafting of the LLDPE synthesized by microencapsulation (5.9%) was higher than that achieved with the direct method (5.0%).

Keywords: grafting; LLDPE; maleic anhydride; microencapsulation

■ INTRODUCTION

The functionalization of polyolefin can increase its chemical and physical properties, leading to its wider application. Several methods that are widely used for functionalization are blending [1], surface treatment [2], and grafting [3-6]. There are several known types of the latter method, namely grafting in the aqueous phase [7], ultrasonic initiation [8], solid phase, photoionization [9], and free radical in the melting phase [10]. Among those methods, grafting by free radical in the melting phase using a polar monomer is one of the most frequently applied techniques due to its potential and wide applications [10-12].

To best of our knowledge, the functionalization of polyolefin through the free radical copolymerization by maleic anhydride (MAH) as the polar monomer is very popular in commercial applications due to its high activity [10, 13-14]. The use of MAH in the grafting process is preferable since it produces small oligomers, and no homopolymerization occurs [15-16]. Polyethylene-graft-maleic anhydride (PE-g-MAH) has been commercially used as fiberglass, anti-corrosive coating for metal pipes, paper for food containers, adhesives, and is compatible as

PE for polar polymers such as polyamide and polyester [13,17-19].

The functionalization of MAH to polyolefin is conducted to homogenize the graft reactions of MAH-polyolefin with a high degree of grafting. This method is used to avoid the non-favorable side-product resulting from crosslink and chain-breaking reactions [10]. Rosales et al. investigated the graft of LLDPE with diethyl maleate (DEM) in different extrusion conditions, which resulted in a maximum degree of grafting at 0.5 moles [14]. Moreover, the grafting degree (GD) of LLDPE-g-MAH by ultrasonic initiator was 0.54% [8]. So far, the grafting process using MAH remains unsatisfactory, as indicated by the low grafting degree and heterogeneous functionalization of the chemical group. To overcome this problem, several techniques have been developed through the modification of the monomer, initiator, and synthesis method or graft copolymerization. The graft copolymerization of MAH to the LLDPE using the monomer microencapsulation method is a relatively new approach. Theoretically, it is based on the directed-diffusion of the termination step where monomer molecules are trapped inside the pore

of the polymer. Thus, the closer segmental-diffusion would improve the interaction between the polymer and the monomer.

In the present study, the graft copolymerization of MAH to LLDPE using the monomer microencapsulation method was developed and compared to the direct method. The grafting degree in the process of graft copolymerization of MAH to the polyolefin was also investigated. This study was aimed to synthesize the maleic anhydride (MAH) grafted with low-density polyethylene (LLDPE) using the monomer microencapsulation method and to determine its degree of grafting and crosslink.

■ EXPERIMENTAL SECTION

Materials

The materials used in this study included LLDPE (melt flow rate (MFR) 1 g.10 min⁻¹ and $\rho = 0.920 \text{ g.cm}^{-3}$) from Bassel, Inc., Indonesia, dicumyl peroxide/DCP (Aldrich), acetone (Merck), chloroform (Merk), maleic anhydride (Merk, p.a grade), and xylene (Merk, p.a grade).

Instrumentation

The instruments employed in this experiment involved Oven 6PHP-200 (Tabai), Haake Reomix 600p Roller Rotors R600, analytical balance, vacuum oven DP 33 (Yamato), soxhlet extraction apparatus, hot and pressure (Gonno), MFR (Dynisco Polymer Test), FT-IR spectrophotometer (Perkin Elmer), Nuclear Magnetic Resonance (Bruker Avance III 300 MHz), Differential Scanning Calorimetry (Mettler Toledo 1 Star), and Thermal Gravimetric Analysis (Mettler Toledo 1 Star).

Procedure

Synthesis of LLDPE by monomer microencapsulation

To a container holding 2 kg LLDPE (MFR 1 g/10 min and density 0.920 g.cm⁻³), 100 mL of 5% MAH in acetone was added. The mixture was mixed thoroughly, and the container tightly closed. It was opened and stirred to evaporate the acetone every day for a week. Furthermore, the process was continued until 6 days in, at which point came the addition of 100 mL of 10% MAH in acetone. The sample was homogenized weekly for six months. Successful microencapsulation is indicated by a cloudy

solution. The microencapsulated polymer was named mLLDPE.

Synthesis of mLLDPE-g-MAH and LLDPE-g-MAH

To a mixing container, 50 g of mLLDPE and DCP, as an initiator with a concentration of 40% mol, was added and blended using Haake Rheomix 600p at 200 °C and a mixing speed of 40, 60, 80, and 100 rpm for 4 min. During the blending, the torsion value was recorded over time. Torsion is defined as the energy of rotation (Nm), which is used throughout the polymer blending process.

Analysis of grafting degree of LLDPE-g-MAH using titration

The sample was refluxed with xylene for 30 min before the temperature was lowered to 80 °C, which was followed by the addition of 0.2 M potassium hydroxide in ethanol. Reflux was carried out for another 15 min. Phenolphthalein was added to the reflux product, followed by the titration using 0.2 M of hydrochloric acid/isopropyl alcohol until the color changed from magenta to colorless. The grafting degree was calculated from the volume of hydrochloric acid/isopropyl alcohol employed in titration using Eq. (1) [7].

$$GD(\% \text{mass}) = \frac{N(V_o - V) \times 98.06}{2000W} \times 100\% \quad (1)$$

N = concentration of HCl/isopropyl alcohol (mol.L⁻¹)

V_o = volume of HCl/isopropyl alcohol used as a blank (mL)

V = volume of HCl/isopropyl alcohol used in titration (mL)

W = mass of sample (g)

98.06 = relative molecular mass of MAH

■ RESULTS AND DISCUSSION

Synthesis and Characterization of Grafted LLDPE

The change of torsion during the blending process using 40% of DCP at 80 rpm rotation rate indicated the different interactions of mLLDPE-g-MAH and LLDPE-g-MAH (Fig. 1). An obvious change of torsion between mLLDPE-g-MAH and LLDPE-g-MAH was observed from 0.3 up to 0.4 min, indicated by a sharp change of torsion value. At the beginning of the reaction, the first peak showed that the plasticization of LLDPE had occurred [10].

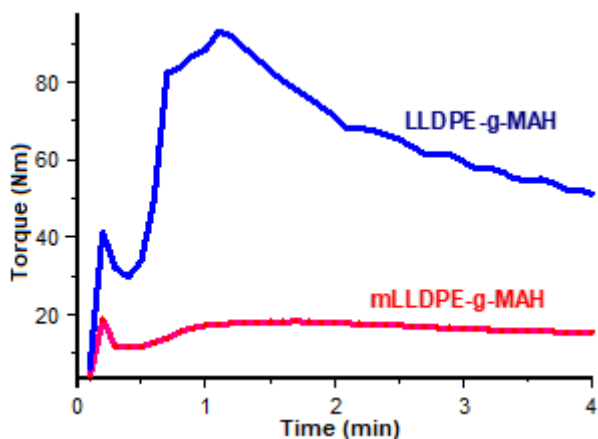


Fig 1. The plot of torsion over time for samples of mLLDPE-g-MAH and LLDPE-g-MAH (fabricated using 40% of DCP at 80 rpm rotation rate)

The second maximum peak or “cure peak” from LLDPE-g-MAH was higher than that of mLLDPE-g-MAH. This peak is known to be related to the viscosity [20]. Therefore, the high peak of LLDPE-g-MAH is indicating the formation of crosslinks within the sample. The results were supported by the torsion data (Fig. 1), where the torsion of mLLDPE-g-MAH was stable under 20 Nm, while that of LLDPE-g-MAH reached 50 Nm. Thus, it is suggested that the monomer encapsulation method could decrease the occurrence of the crosslink. The reason behind this observation is related to the theory of directed-diffusion, in which the polymer-monomer interaction is independent of the reactivity, but affected by the distance or physical interaction between the two. After the diffusion-translation occurred between the two propagated radicals, the diffusion-segmental between radicals of the polymer and monomer took place. Lastly, the chemical interaction between radicals would result in graft copolymerization of the monomer to the polymer.

Further evidence of the occurrence of crosslink in

LLDPE-g-MAH is presented in Table 1. The MFR value of mLLDPE-g-MAH was higher than LLDPE-g-MAH, which was immeasurable. A higher value of MFR reflects low viscosity of the sample, and hence it is diluted and flows easily [20]. In fact, LLDPE-g-MAH did not flow easily, indicating the gel formation due to the crosslink reaction. A high number of crosslinks in LLDPE-g-MAH is shown by the result of Soxhlet extraction (Table 1). The higher quantity of crosslinks in LLDPE-g-MAH was predicted to be formed at the “cure peak” (Fig. 1). This observation is in agreement with the theory of the mechanism of directed-diffusion. In a thick liquid, the reaction between polymer radicals is higher than the reaction between radicals of polymer and MAH, thus increasing the number of crosslinks in the product. Several analyses were performed to provide a better explanation of this phenomenon.

Fig. 2 shows the FT-IR spectra of mLLDPE-g-MAH and LLDPE-g-MAH after the extraction with acetone. The presence of maleic anhydride, which is attached to the LLDPE, is confirmed by the absorbance at wavenumber of 1720 and 1780 cm^{-1} for C=O stretching; at 1260 cm^{-1} for asymmetrical C–O–C stretching, and at 960 cm^{-1} for five-membered ring anhydride stretching [16].

Fig. 3 shows the FTIR spectra of the soluble fractions of mLLDPE-g-MAH and LLDPE-g-MAH. The successful maleation process is confirmed by the peaks at wavenumber between 1700 and 1800 cm^{-1} , i.e., 1720 and 1780 cm^{-1} . These absorptions are higher in mLLDPE-g-MAH than those in LLDPE-g-MAH. It indicates that the formation of succinic anhydride was higher than the maleic anhydride. However, the gel fraction showed a contrast result compared to the soluble fraction (Fig. 4).

Table 1. Values of MFR, monomer conversion, gel fraction, and grafting degree of mLLDPE-g-MAH and LLDPE-g-MAH (at 40% of DCP and 80 rpm rotation rate)

Parameter	mLLDPE-g-MAH	LLDPE-g-MAH
MFR (g/10 min)	0.89	Not detected
Monomer conversion (%)	59.7	53.3
Gel fraction (%)	68.3	79.8
Grafting degree (%)	5.92	4.98

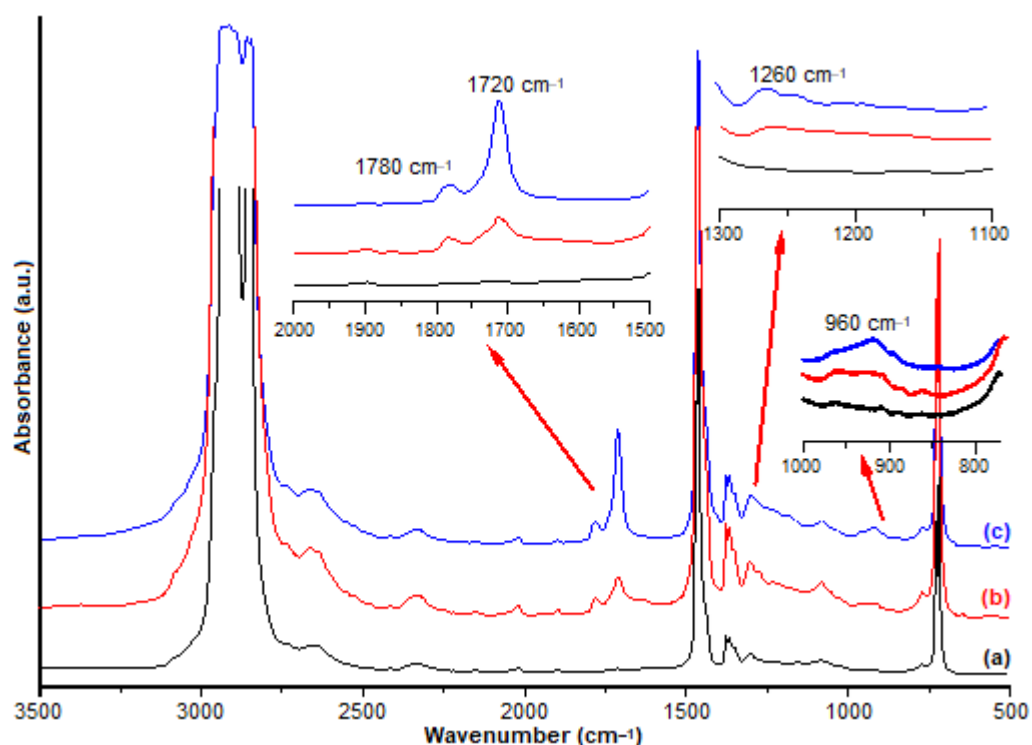


Fig 2. The FTIR spectra of acetone extract of (a) LLDPE, (b) mLLDPE-g-MAH, and (c) LLDPE-g-MAH (fabricated using 40% of DCP at 80 rpm rotation rate)

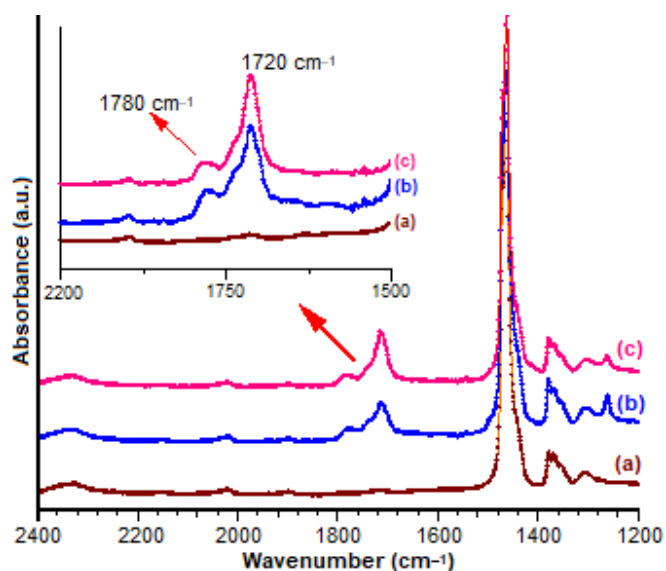


Fig 3. FTIR spectra of xylene soluble fraction extract of (a) LLDPE, (b) mLLDPE-g-MAH, and (c) LLDPE-g-MAH (fabricated using 40% of DCP at 80 rpm rotation rate)

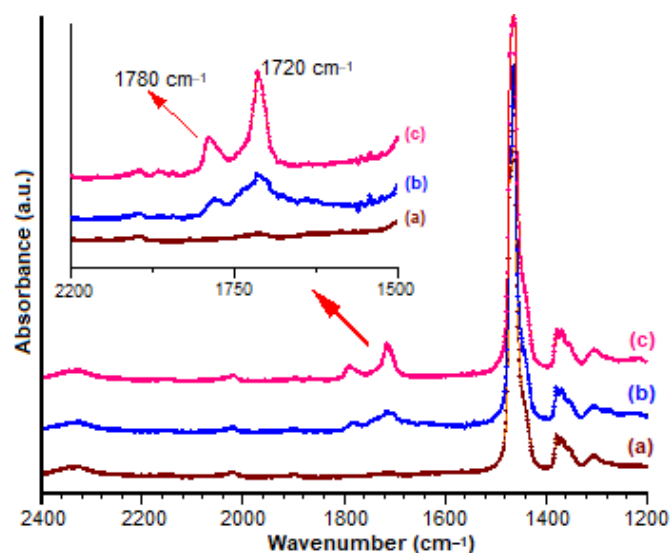


Fig 4. FTIR spectra of xylene extract gel fraction of (a) LLDPE, (b) mLLDPE-g-MAH, and (c) LLDPE-g-MAH (fabricated using 40% of DCP at 80 rpm rotation rate)

Thermal Properties

The DSC thermogram of glass transition temperature (T_g) and melting point (T_m) from both soluble and gel fractions

of mLLDPE-g-MAH and LLDPE-g-MAH are shown in Fig. 5. Fig. 5 and Table 2 illustrate that in both fractions, the T_g of mLLDPE-g-MAH is higher than that of

LLDPE-g-MAH. In the soluble fraction, the T_m of mLLDPE-g-MAH is lower than that of LLDPE-g-MAH, while in the gel fraction mLLDPE-g-MAH has a higher value. The presence of MAH and gel formation in the polymer lead to sturdier material, and lower crystallinity and T_m [21].

Fig. 5 shows the gel fraction of the LLDPE samples, as indicated by the width of the DSC thermogram. In general, there are no significant differences in T_g , T_m , and T_c values. However, the thermogram of the gel fraction of LLDPE-g-MAH shows a wide endothermic absorption.

Fig. 6 shows the DSC thermogram of the crystallization temperature (T_c) of mLLDPE-g-MAH and LLDPE-g-MAH in both fractions. T_c values are shown in Table 2. The T_c of the soluble fraction of mLLDPE-g-MAH is higher than that of LLDPE-g-MAH, while the T_c values of both samples in the gel fraction are similar. The presence of MAH and gel formation increase the rigidity of polymer, decrease the mobility of the chain, lower the crystallinity, and eventually increase the T_c value.

Fig. 7 shows the TGA thermogram of mLLDPE-g-MAH and LLDPE-g-MAH in both fractions in the range of decomposition temperature from 300 to 550 °C. To observe a clearer change of decomposition percentage, a first derivative of the decomposition thermogram is

drawn and is presented in Fig. 8. It is clear that the gradients of mLLDPE-g-MAH and LLDPE-g-MAH in the soluble fractions changed between 200 and 350 °C, whereas both samples in the gel fractions are not. Interestingly, the decomposition of mLLDPE-g-MAH in the soluble fraction is faster than the decompositions in the other samples. This might be related to the non-carbon decomposition, which probably derived from the maleic anhydride group.

Table 3 shows that between 325 and 425 °C, the percentage decomposition of mLLDPE-g-MAH in both fractions is higher than that of the LLDPE-g-MAH. Meanwhile, at 425 °C, decomposition of the gel fraction of mLLDPE-g-MAH is smaller than that of the LLDPE-g-MAH. We then compared this to the T_c of LLDPE

Table 2. Values of T_g , T_m , and T_c of the gel fractions (g) and solvated fractions (s) of mLLDPE-g-MAH and LLDPE-g-MAH (fabricated using 40% of DCP at 80 rpm rotation rate)

Sample	T_g (°C)	T_m (°C)	T_c (°C)
LLDPE-g-MAH (g)	64	118	107
mLLDPE-g-MAH (g)	65	122	107
LLDPE-g-MAH (s)	65	122	105
mLLDPE-g-MAH (s)	65.5	122	107

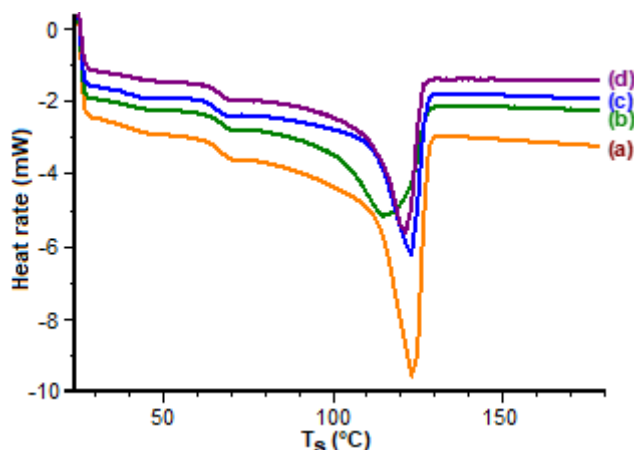


Fig 5. DSC thermogram of (a) mLLDPE-g-MAH gel fraction, (b) LLDPE-g-MAH gel fraction, (c) mLLDPE-g-MAH soluble fraction, and (d) LLDPE-g-MAH soluble fraction (fabricated using 40% of DCP at 80 rpm rotation rate)

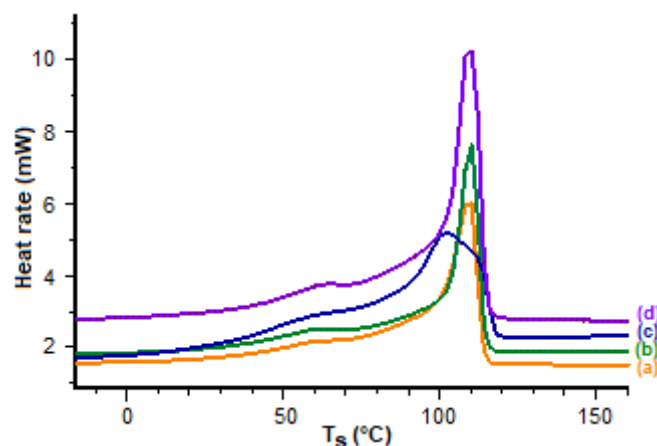


Fig 6. DSC thermogram of T_c of solvated fractions of (a) LLDPE-g-MAH, (b) mLLDPE-g-MAH, and gel fractions of (c) LLDPE-g-MAH, (d) mLLDPE-g-MAH (fabricated using 40% of DCP at 80 rpm rotation rate)

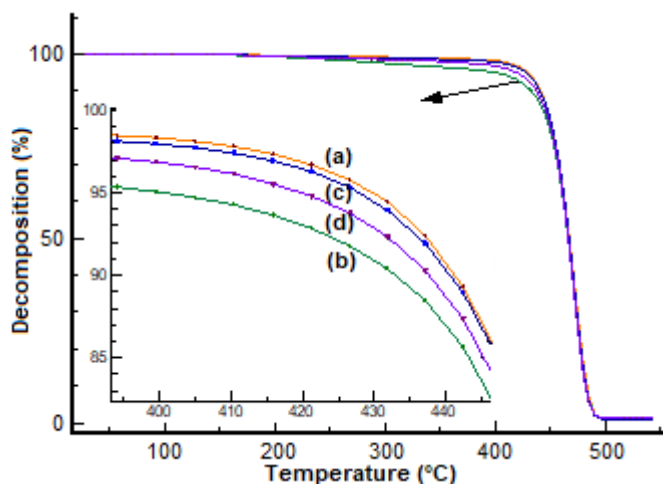


Fig 7. TGA thermogram of the soluble fractions of (a) mLLDPE-g-MAH, (b) LLDPE-g-MAH, and gel fractions of (c) mLLDPE-g-MAH, (d) LLDPE-g-MAH (fabricated using 40% of DCP at 80 rpm rotation rate)

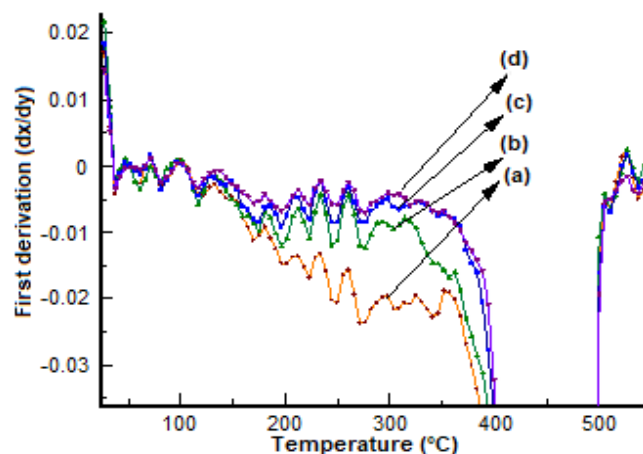


Fig 8. The first derivative of the TGA thermogram of samples decomposition of the soluble fractions: (a) mLLDPE-g-MAH (b) LLDPE-g-MAH, and that of gel fractions: (c) mLLDPE-g-MAH, (d) LLDPE-g-MAH (fabricated using 40% of DCP at 80 rpm rotation rate)

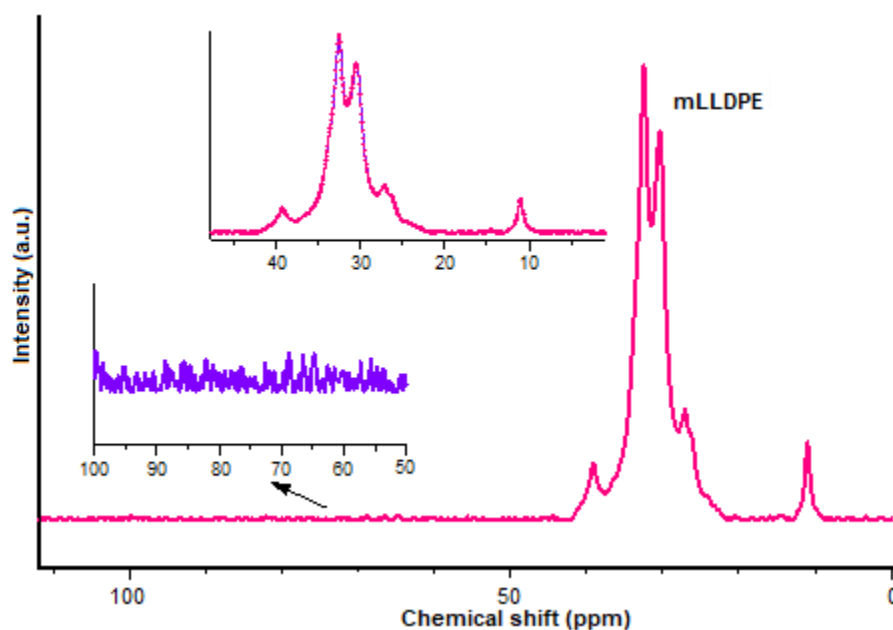


Fig 9. ^{13}C -NMR spectrum of mLLDPE-g-MAH

based on the reference, which shows a TG value of 360 °C. The T_c of LLDPE-g-MAH is much higher than the T_c of irradiated and non-irradiated LLDPE, which shows a range value of 380 to 340 °C [21].

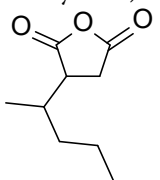
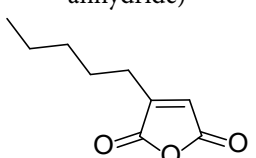
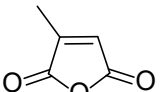
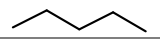
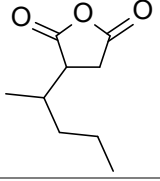
The decomposition between 325 and 425 °C indicates the removal of MAH from the LLDPE. The high decomposition percentage corresponded to the high number of MAH that were attached to the LLDPE. After

425 °C, the mass decreased due to the removal of the attached group, which mostly derived from the backbone of LLDPE. As can be seen in the diagram, LLDPE was completely decomposed after 550 °C. It is suggested that the number of MAH that attached to the microencapsulated sample was higher than the LLDPE-g-MAH. To confirm the MAH attached to LLDPE, the NMR analysis was deployed.

Table 3. Percentage decomposition of mLLDPE-g-MAH and LLDPE-g-MAH in the soluble fraction (s), and gel fraction (g) (fabricated using 40% of DCP at 80 rpm rotation rate)

Sample	Percentage of decomposition (%)	
	325 °C	425 °C
LLDPE-g-MAH (g)	0.88	4.21
mLLDPE-g-MAH (g)	1.14	4.64
LLDPE-g-MAH (s)	1.58	6.22
mLLDPE-g-MAH (s)	2.93	8.21

Table 4. Chemical shift and predicted carbon type/functional group of mLLDPE-g-MAH

Chemical shift (ppm)	Carbon type
173	C (C=O from succinic anhydride) 
166	C (C=O from maleic anhydride) 
132 and 142	C (C=C from maleic anhydride) 
29-35	C (CH ₂) from the polymeric chain 
28 and 39	C (CH ₂) from the ring of succinic anhydride 
11	C (CH ₃)

The ¹³C-NMR was used to determine the structure of MAH that attached to the LLDPE structure (Fig. 9).

Each chemical shift represents the carbon type from a particular functional group. The interpretations of each chemical shift are presented in Table 4 [22].

It is noted that the intensity of the chemical shift at 173 ppm indicates succinic anhydride. This result signifies that the number of MAH attached to the LLDPE is higher in the form of succinic anhydride than MAH. This result is also supported by the presence of a chemical shift at 28.6 ppm, which showed the (CH₂) from succinic anhydride.

CONCLUSION

The graft copolymerization of MAH to LLDPE using monomer microencapsulation and DCP as initiator increase the grafting degree compared to the direct method. The product of the monomer microencapsulation method, mLLDPE-g-MAH, has a grafting degree of 5.9%, while that of the direct method has a 5.0% degree. The microencapsulation process improves the T_g, T_m, and T_c of mLLDPE-g-MAH compared to the direct method based on DSC analysis. We suggest that the microencapsulation could be a novel method in the polymerization process to attach MAH to LLDPE, which can increase the degree of grafting to enhance the physical properties of LLDPE.

ACKNOWLEDGMENTS

This work was partially funded by the Indonesian Institute of Sciences through the Program Unggulan LIPI and I-MHERE project for Universitas Padjadjaran from the Directorate General of Higher Education, Ministry of National Education Republic of Indonesia. Characterization by DSC and TGA from the Australian Institute for Bioengineering and Nanomaterials (AIBN), University of Queensland, Brisbane Australia. Therefore, we would like to acknowledge their support.

REFERENCES

- [1] Valente, T., Ferreira, J.L., Henriques, C., Borges, J.P., and Silva, J.C. 2019, Polymer blending or fiber blending: A comparative study using chitosan and poly (ε-caprolactone) electrospun fibers, *J. Appl. Polym. Sci.*, 136 (1), 47191.

- [2] Sato, A., Kabusaki, D., Okumura, H., Nakatani, T., Nakatsubo, F., and Yano, H., 2016, Surface modification of cellulose nanofibers with alkenyl succinic anhydride for high-density polyethylene reinforcement, *Compos. Part A Appl. Sci. Manuf.*, 83, 72–79.
- [3] Wang, W., Zhang, X., Mao, Z., and Zhao, W., 2019, Effects of gamma radiation on the impact strength of polypropylene (PP)/high density polyethylene (HDPE) blends, *Results Phys.*, 12, 2169–2174.
- [4] Khani, M.M., Woo, D., Mumpower, E.L., and Benicewicz, B.C., 2017, Poly (alkyl methacrylate)-grafted silica nanoparticles in polyethylene nanocomposites, *Polymer*, 109, 339–348.
- [5] Khanonkon, N., Yoksan, R., and Ogale, A.A., 2016, Effect of stearic acid-grafted starch compatibilizer on properties of linear low density polyethylene/thermoplastic starch blown film, *Carbohydr. Polym.*, 137, 165–173.
- [6] Mandal, D.K., Bhunia, H., Bajpai, P.K., and Bhalla, V.K., 2017, Thermal degradation kinetics and estimation of lifetime of radiation grafted polypropylene films, *Radiat. Phys. Chem.*, 136, 1–8.
- [7] Campos, P.G.S., Fantini, M.C.A., and Petri, D.F.S., 2004, Grafting of tetrahydrophthalic and maleic anhydride onto polyolefins in solution, *J. Braz. Chem. Soc.*, 15 (4), 532–540.
- [8] Zhang, Y., Chen, J., and Li, H., 2006, Functionalization of polyolefins with maleic anhydride in melt state through ultrasonic initiation, *Polymer*, 47 (13), 4750–4759.
- [9] Deng, J.P., and Yang, W.T., 2001, Self-initiating performance of maleic anhydride on surface photografting polymerization, *J. Polym. Sci., Part A: Polym. Chem.*, 39 (19), 3246–3249.
- [10] Aghjeh, M.K.R., Nazockdast, H., and Assempour, H., 2006, Parameters affecting the free-radical melt grafting of maleic anhydride onto linear low-density polyethylene in an internal mixer, *J. Appl. Polym. Sci.*, 99 (1), 141–149.
- [11] Chang, M.K., 2015, Mechanical properties and thermal stability of low-density polyethylene grafted maleic anhydride/montmorillonite nanocomposites, *J. Ind. Eng. Chem.*, 27, 96–101.
- [12] Kahar, A.W.M., Ismail, H., and Othman, N., 2012, Effects of polyethylene-grafted maleic anhydride as a compatibilizer on the morphology and tensile properties of (thermoplastic tapioca starch)/(high-density polyethylene)/(natural rubber) blends, *J. Vinyl Add. Tech.*, 18 (1), 65–70.
- [13] Majid, R.A., Ismail, H., and Taib, R.M., 2010, Effects of polyethylene-g-maleic anhydride on properties of low density polyethylene/thermoplastic sago starch reinforced kenaf fibre composites, *Iran. Polym. J.*, 19 (7), 501–510.
- [14] Jantanasakulwong, K., Leksawasdi, N., Seesuriyachan, P., Wongsuriyasak, S., Techapun, C., and Ougizawa, T., 2016, Reactive blending of thermoplastic starch and polyethylene-graft-maleic anhydride with chitosan as compatibilizer, *Carbohydr. Polym.*, 153, 89–95.
- [15] Roumeli, E., Terzopoulou, Z., Pavlidou, E., Chrissafis, K., Papadopoulou, E., Athanasiadou, E., Triantafyllidis, K., and Bikiaris, D.N., 2015, Effect of maleic anhydride on the mechanical and thermal properties of hemp/high-density polyethylene green composites, *J. Therm. Anal. Calorim.*, 121, 93–105.
- [16] Saini, A., Yadav, C., Bera, M., Gupta, P., and Maji, P.K., 2017, Maleic anhydride grafted linear low-density polyethylene/waste paper powder composites with superior mechanical behavior, *J. Appl. Polym. Sci.*, 134 (31), 45167.
- [17] Colbeaux, A., Fenouillot, F., Gérard, J.F., Taha, M., and Wautier, H., 2005, Compatibilization of a polyolefin blend through covalent and ionic coupling of grafted polypropylene and polyethylene. I. Rheological, thermal, and mechanical properties, *J. Appl. Polym. Sci.*, 95 (2), 312–320.
- [18] Guzmán, M., and Murillo, E.A., 2015, The properties of blends of maleic-anhydride-grafted polyethylene and thermoplastic starch using hyperbranched polyester polyol as a plasticizer, *Polym. Eng. Sci.*, 55 (11), 2526–2533.

- [19] Hernandez-Ortiz, J., Van Steenberge, P.H.M., Duchateau, J.N., Toloza, C., Schreurs, F., Reyniers, M.F., Marin, G.B., and D'hooge, D.R., 2019, A multi-scal tool for functionalization of polyolefins through radical grafting, *Autex 2019 –The 19th World Textile Conference on Textiles at the Crossroads*, 11-15 June 2019, Ghent, Belgium.
- [20] Oliveira, A.C.F., Parra, D.F., Ferreto, H.F.R., and Lugão, A.B., 2013 Characterization of injected linear low density polyethylene (LLDPE) irradiated by gamma-ray, *The 6th International Nuclear Atlantic Conference – INAC 2013*, 24-29 November 2013, Recife, Brazil.
- [21] Saade-Caballero, H., and Martínez-Colunga, J.G., 2009, Reactive extrusion process for the grafting of maleic anhydride onto linear low-density polyethylene with ultraviolet radiation, *J. Appl. Polym. Sci.*, 113 (5), 3125–3129.
- [22] Dartora, P.C., Marlene, R., Santana, C., Cristina, A., and Moreira, F., 2015, The influence of long chain branches of LLDPE on processability and physical properties, *Polimeros*, 25 (6), 531–539.

Synthesis of Activated Carbon/Chitosan/Alginate Beads Powder as an Adsorbent for Methylene Blue and Methyl Violet 2B Dyes

Margaretha Aditya Kurnia Purnaningtyas, Sri Sudiono, and Dwi Siswanta*

Department of Chemistry, Faculty of Mathematics and Natural Sciences, Universitas Gadjah Mada, Sekip Utara, Yogyakarta 55281, Indonesia

* **Corresponding author:**

tel: +62-274-454188

email: dsiswanta@ugm.ac.id

Received: August 26, 2019

Accepted: January 20, 2020

DOI: 10.22146/ijc.49026

Abstract: The activated carbon-chitosan-alginate (KKA) beads powder was synthesized to form an adsorbent for the cationic dyes, methylene blue (MB) and methyl violet 2B (MV 2B). The aims of this research were to determine the optimum composition of KKA beads powder for the adsorption of cationic dyes and to investigate the effect of pH, adsorbent mass, contact time, and initial concentration of MB and MV 2B dyes. A desorption study was also implemented to predict the adsorption mechanisms of MB and MV 2B dyes. The KKA beads powder was prepared by mixing chitosan, Na-alginate with various variation of masses (0.6; 0.8; 1.0; and 1.2 g) and activated carbon. The KKA beads were immersed in a CaCl₂ solution. The KKA beads powder was characterized using FTIR spectroscopy and SEM. The desorption study was conducted in NaCl (0.1 M and 1.0 M), ethanol (40 and 60%), and pH 4 solution. The result showed that the KKA beads powder had been successfully created, with maximum adsorption capacities of 1.34 mmol g⁻¹ for MB and 1.23 mmol g⁻¹ for MV 2B. The kinetics and isotherms of MB and MV dyes adsorption on the KKA beads powder followed pseudo second order kinetics model and Freundlich isotherm. The desorption study showed that 60% ethanol was the most effective desorption solution for cationic dyes.

Keywords: activated carbon; alginate; chitosan; methylene blue; methyl violet 2B

■ INTRODUCTION

The dyeing process in the textile industry produces 10–15% of the dyes released to the environment [1]. Synthetic dyes have brightness, high color sharpness, and are clearly visible even in very low concentrations [2-3]. MB and MV 2B are cationic synthetic dyes. The presence of synthetic dyes in the environment can disrupt the stability of the organism in the environment due to their carcinogenic, mutagenic, and toxic effects. Therefore, the removal of dyes before being released into the water is very important.

The treatment of dye waste has been carried out by various methods such as biological processes [4], electrochemistry [5], ozonation [6], oxidation [7], photocatalyst [8], membrane filtration [9], and adsorption [10-13]. Adsorption became the most popular and widely used method due to its low operational costs, simple and easy procedure, requires less energy, non-

toxic effects, and because it is highly effective for the degradation of waste [10].

Activated carbon is a porous material that has potential in the removal of chemical species by adsorption [14]. The mesopores and macropores of activated carbon can be used to remove large pollutants such as dyes [15]. According to previous studies, activated carbon is able to adsorb MB [16-18] and MV 2B [3,19]. Modification of activated carbon with biopolymers such as chitosan [12] and alginate [11,13] can also be used as an alternative to remove cationic dyes.

Currently, there is no report about the fabrication of a composite material consisting of activated carbon, chitosan, and alginate to be used as an adsorbent for the removal of cationic dyes. Chitosan and alginate are polycationic and polyanionic natural polymers, respectively. The combination of both polymers will form a polyelectrolyte complex (PEC) due to the

interaction between the carboxyl groups of alginates and the amino groups of chitosan [20]. The formation of PEC enriches the active sites on the surface of the adsorbent.

Therefore, the main objective of this research was to explore the potential of activated carbon-chitosan-alginate (KKA) beads powder as an adsorbent for MB and MV 2B dyes. The aims of the research were to determine the optimum composition of KKA beads powder, to investigate the effect of contact time and initial concentration on the adsorption of MB and MV 2B, and to study the desorption of MB and MV 2B dyes.

■ EXPERIMENTAL SECTION

Materials

Chitosan (%DD c.a. 80%), activated carbon (technical), sodium alginate (MW 120–190 g/mol, G/M = 1.56), and other materials of analytical grade were supplied by Merck including calcium chloride, sodium hydroxide, acetic acid, hydrochloric acid, sodium chloride, ethanol absolute, MB, and MV 2B.

Instrumentation

The equipment used in this research were pH meter (SI Analytics Lab 860), magnetic stirrer, shaker (Memmert), and centrifuge (Thermo Scientific SL 16R). Characterization of the functional groups of the KKA beads powder was detected by Fourier transform infrared spectroscopy (FTIR) (Prestige-21 Shimadzu) at 4000–500 cm^{-1} wavelength. The morphology of the KKA beads powder was characterized by Scanning Electron Microscopy (SEM) (JSM-6510LV). The concentration of dyes was analyzed by Spectrophotometer UV-Vis (Thermoscientific 20D).

Procedure

Synthesis of the activated carbon/chitosan/alginate (KKA) beads powder

Chitosan (1 g) in 30 mL of acetic acid (2.0% v/v) was mixed with sodium alginate (1 g) in 30 mL of acetic acid (2.0% v/v). After the suspension had mixed completely, activated carbon (1 g) was added into the suspension. The suspension of KKA was stirred using a magnetic stirrer for 24 h. Then, the KKA beads were formed by dripping the solution into a CaCl_2 (2.5% b/v) solution. The KKA

beads were washed, dried, and crushed into powder. The same procedure was made for the synthesis of KKA beads powder with mass variations of sodium alginate (0.6; 0.8; and 1.2 g).

The optimum composition of KKA beads powder

The optimum composition of the KKA beads powder was determined by mixing mass variations of sodium alginate (0.6; 0.8; and 1.2 g) during the synthesis of the powder. The resulting KKA beads powder (20 mg) was added into 20 mL of MB or MV 2B dyes solution with concentration of 100 mg L^{-1} and the adsorption was carried out for 60 min. Afterwards, the solid material was separated, and the filtrate was analyzed by spectrophotometry UV-Vis. The adsorption capacity of the adsorbent towards MB and MV 2B dyes were calculated using Eq. (1).

$$\text{Adsorption capacity}(q_t) = \frac{(C_o - C_t)V}{m} \quad (1)$$

where C_o (mg L^{-1}) is the initial concentration of dyes, C_t (mg L^{-1}) is the concentration of dyes after adsorption, m (g) is the mass of the adsorbent, and V (mL) is the volume of the dyes.

Effect of pH

A series of solutions containing 20 mL of 100 mg L^{-1} MB or MV 2B dyes were prepared with pH of 4, 5, 6, 7, 8, and 9. pH adjustment was carried out by adding 0.1 M NaOH and 0.1 M HCl. Into the series of dyes solution, 20 mg of KKA beads powder with optimum composition was added as obtained from the previous experiment. Then the adsorption was carried out for 60 min. The solid material was then separated, and the filtrate was analyzed by spectrophotometry UV-Vis.

Effect of adsorbent dose

The effect of adsorbent dose was investigated by using 10, 20, 30, 40, and 50 mg of KKA beads powder. The varied adsorbent doses were added into 20 mL of 100 mg L^{-1} MB or MV 2B dyes solution. The solution was adjusted to the optimum pH obtained from the previous experiment. Then the adsorption was carried out for 60 min. The solid material was then separated, and the filtrated dyes were analyzed by spectrophotometry UV-Vis.

Effect of contact time

The effect of contact time was determined within the time range of 5–180 min. The optimum adsorbent dose of the KKA beads powder obtained from the previous experiment was added into 20 mL of 100 mg L⁻¹ MB or MV 2B dyes solution at the optimum pH. The adsorption was conducted for 5, 10, 15, 30, 45, 60, 90, 120, 150, and 180 min. The solid material was then separated, and the filtrated dyes were analyzed by spectrophotometry UV-Vis.

Effect of initial concentration

The optimum dose of the KKA beads powder was added into 20 mL of MB or MV 2B dyes solution at optimum pH. The effect of initial concentrations was investigated in 25, 50, 75, 100, 150, 200, 300, 400, 500, 600, 800, and 1000 mg L⁻¹. The adsorption was carried out for the duration of the optimum time as obtained from the previous experiment. The solid material was then separated, and the filtrated dyes were analyzed by spectrophotometry UV-Vis.

Adsorption Selectivity of MB and MV 2B dyes

The adsorption selectivity test between MB and MV 2B dyes was determined in comparison to the mole of MB: MV 2B dyes (1:0, 0:1, and 1:1). The adsorption was investigated in the optimum condition of MB or MV 2B.

Study of desorption

The process of desorption was investigated in NaCl (0.1 and 1.0 M), ethanol (40 and 60%) and pH 4 solution. The time of desorption was carried out for 1, 3, 18, and 24 h. The percentage of desorption was calculated using Eq. (2).

$$\% \text{Desorption} = \frac{C_e}{C_o} \times 100\% \quad (2)$$

where C_e (mg L⁻¹) is the concentration of dyes after desorption and C_o (mg L⁻¹) is the concentration of dyes in the adsorbent.

Isotherm models for the adsorption of MB and MV 2B dyes

The isotherms for the adsorption of MB and MV 2B dyes were determined using two models according to Eq. (3) and (4).

$$\text{Langmuir isotherm: } \frac{C_e}{q_e} = \frac{1}{K_L q_{\max}} + \frac{C_e}{q_{\max}} \quad (3)$$

$$\text{Freundlich isotherm: } \ln q_e = \ln K_F + \frac{1}{n} \ln C_e \quad (4)$$

where K_L (L mg⁻¹) is the Langmuir constant, q_{\max} (mg g⁻¹) represents the monolayer capacity, K_F and n are Freundlich constants, C_e (mg L⁻¹) is the equilibrium concentration, and q_e (mg g⁻¹) is the amount adsorbed at equilibrium.

Kinetics model for the adsorption of MB and MV 2B dyes

The kinetics model for the adsorption of MB and MV 2B dyes was determined using four models according to the following equations:

$$\text{First - order kinetics model: } \ln C_e = \ln C_0 - k_1 t \quad (5)$$

$$\text{Second - order kinetics model: } \frac{1}{C_e} = \frac{1}{C_0} + k_2 t \quad (6)$$

$$\text{Pseudo first - order kinetics model: } \ln(q_e - q_t) = \ln q_e - k_1 t \quad (7)$$

$$\text{Pseudo first - order kinetics model: } \frac{t}{q_t} = \frac{1}{k_2 q_e^2} + \frac{t}{q_e} \quad (8)$$

where k (min⁻¹) is the rate constant, t (min) is time, C_0 (mg L⁻¹) is the initial concentration, C_e (mg L⁻¹) is the equilibrium concentration, and q_e (mg g⁻¹) is the amount adsorbed at equilibrium.

RESULTS AND DISCUSSION

FTIR Spectra of KKA Beads Powder

FTIR analysis was used to identify several characteristic functional groups of the KKA beads powder. The FTIR spectra of the KKA beads powder before and after the dyes adsorption-desorption are shown in Fig. 1. Fig. 1 shows that activated carbon has characteristic peaks at 1628, 3425, also 2855 and 2924 cm⁻¹ due to stretching vibrations of -C=O, -OH, and -CH. Modified activated carbon peaks shifted from 1628 to 1605 cm⁻¹. This data represented the electrostatic interactions between the -NH₃⁺ of chitosan and -COO⁻ of alginates that form PEC in KKA beads powder. Additional peaks at 1400 and 1034 cm⁻¹ are identical to stretching vibrations of -CH amines from chitosan structures and stretching vibrations of -CO from chitosan and alginate structures.

FTIR spectra after MB and MV 2B dyes adsorption-desorption showed shifting of peaks that occurred due to the interaction between adsorbents and

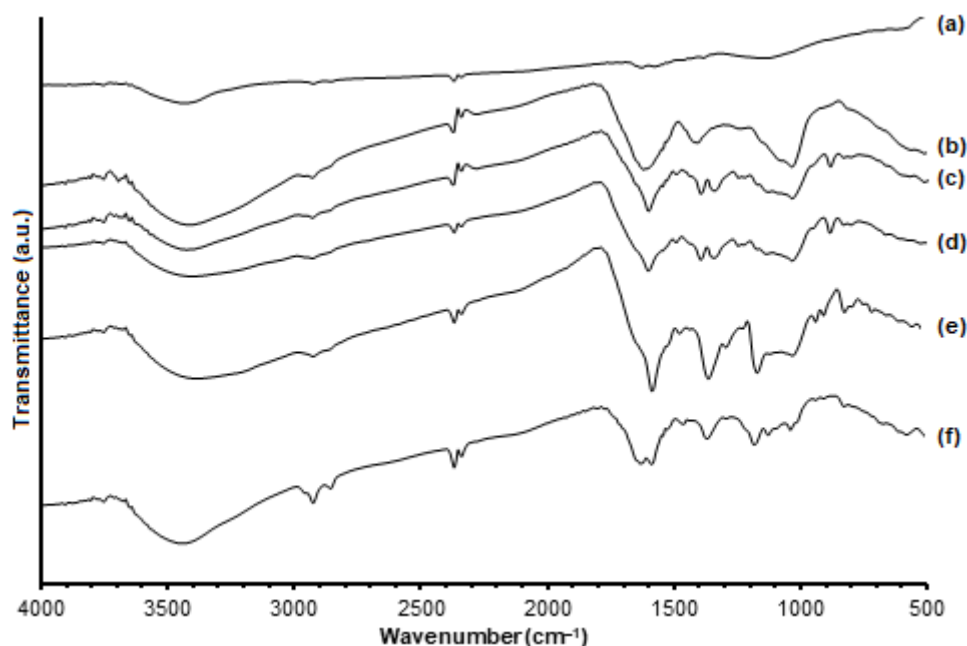


Fig 1. FTIR spectra for (a) activated carbon, (b) KKA beads powder 0.8, KKA beads powder 0.8: (c) after adsorption of MB, (d) after desorption of MB, (e) after adsorption of MV 2B, and (f) after desorption of MV 2B, respectively.

MB/MV 2B dyes [12-13]. After the MB adsorption and desorption, there were new peaks at 1342 and 802 cm^{-1} which show stretching vibrations of $-\text{N}=\text{O}$ and $-\text{CS}$, respectively [18]. The additional peak between 1134 to 1180 cm^{-1} is identical to stretching vibrations of $-\text{CN}$ of the dyes on the surface of the adsorbent [21]. Decreased peak intensity at 1034 cm^{-1} is due to the interaction of dyes and the KKA beads powder [13].

SEM Analysis of KKA Beads Powder

The surface morphology of the KKA beads powder was characterized by SEM analysis. The SEM photograph for activated carbon and the KKA beads powder before and after adsorption-desorption of MB and MV 2B under the same magnifications is given in Fig. 2. Fig. 2 shows that activated carbon has an irregular surface and various pore sizes. The pore size of the KKA

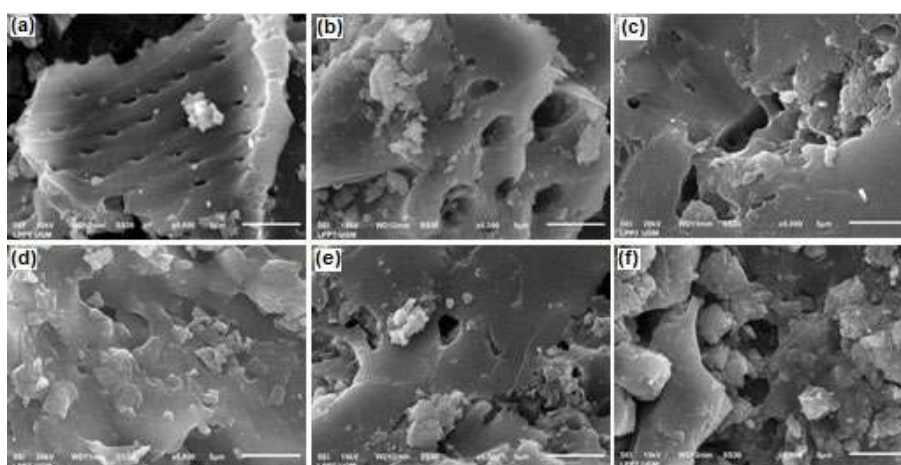


Fig 2. SEM images at 5000 magnifications for – (a) activated carbon, (b) KKA beads powder 0.8, KKA beads powder 0.8: (c) after adsorption of MB, (d) after adsorption of MV 2B, (e) after desorption of MB, and (f) after desorption of MV 2B, respectively

beads powder looks larger than that of the activated carbon. Chemical modification with chitosan and alginate through PEC can increase the pore size of activated carbon, potentially increasing the adsorption capacity of the dyes [13].

According to Fig. 2, the adsorption of dyes caused the surface of the KKA beads powder to be rough with lumps covering the pore of the activated carbon. These lumps indicate the presence of interaction between adsorbent and adsorbate, as well as showing the adsorbates which are trapped in the pores [22]. The SEM image of the KKA beads powder after desorption with 60% ethanol also shows the rough and lumpy surface. It shows that the desorption process is also followed by the removal of the adsorbent material from the surface of the KKA beads powder.

The Optimum Composition of KKA Beads Powder

Fig. 3 shows that the adsorption capacity of dyes decreased as an increasing amount of alginate was added. The formation of the KKA beads was carried out in a solution of CaCl_2 that acted as an agent to form and strengthen the physical properties of the beads. Increasing the amount of alginate increased the $-\text{COO}^-$ group and also increased the risk of the group reacting with Ca^{2+} during the beads formation process. This caused the amount of $-\text{COO}^-$ available to bind with dyes reduced, leading to the decrease of the adsorption capacity. The composition of the KKA beads powder that had maximum adsorption capacity was observed at 0.8 g alginate with $0.284 \text{ mmol g}^{-1}$ (MB) and $0.213 \text{ mmol g}^{-1}$ (MV 2B).

Effect of pH

The effect of pH on the dye adsorption of the KKA beads powder was studied at the pH range of 4–9. The relationship curve between the amount of dyes adsorbed and various pH is shown in Fig. 4. Fig. 4 shows that the dyes adsorption capacity increased along with the increase in pH. The KKA beads powder adsorption capacity tended to decrease after pH 7. The maximum adsorption capacity was observed at pH 7. Therefore, pH 7 was selected as the optimal pH for the dyes removal from aqueous solution using KKA beads powder. The

adsorption capacity of the KKA beads powder at pH 7 was $0.285 \text{ mmol g}^{-1}$ (MB) and $0.216 \text{ mmol g}^{-1}$ (MV 2B).

Chitosan in acidic medium will be protonated to $-\text{NH}_3^+$. The carboxylic group of alginate will maintain its protons thereby reducing the possibility of bonding with other positively charged ions [23]. The presence of an excess amount of free protons in an acidic solution competes with the dyes molecules for adsorption sites on the surface of the adsorbent [24]. At pH close to neutral, the dominant form of chitosan is $-\text{NH}_2$. The presence of $-\text{NH}_2$, $-\text{OH}$, and $-\text{COO}^-$ on the surface of the KKA beads powder can increase interactions with cationic dyes, so the capacity of adsorption increases. Adsorption capacity tends to decrease at basic medium, despite the high availability of $-\text{COO}^-$ on the surface of the adsorbent. This is due to the interaction between OH^- ions and cationic dyes in the solution. [25].

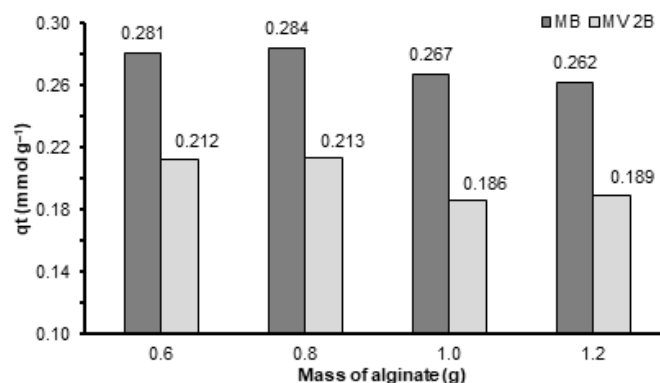


Fig 3. Effect of alginate on MB and MV 2B dyes adsorption onto the KKA beads powder

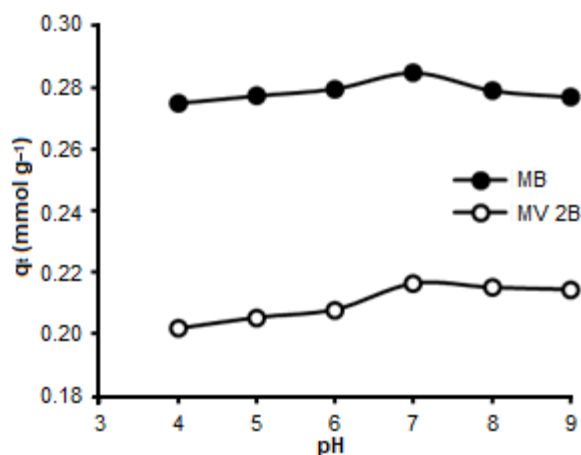


Fig 4. Effect of pH on MB and MV 2B dyes adsorption onto the KKA beads powder

Effect of Adsorbent Dosage

Fig. 5 shows the adsorption capacity and removal percentage of dyes against the adsorbent dosage. The percentage of adsorption increased with increasing amount of adsorbent dosage. As the adsorbent dose increase, the amount of active sites on the surface of the adsorbent also increases, so more dye molecules can adsorb to the surface of the adsorbent. Higher adsorbent dosage however, caused the adsorbent to aggregate reducing the surface area thus decreasing the adsorption capacity [25]. The KKA beads powder optimum dosage in this study was 30 mg with an adsorption percentage of more than 80% for both MB and MV 2B.

Effect of Contact Time

Fig. 6 shows the effect of contact time on the adsorption capacity of the KKA beads powder towards dyes. High adsorption capacity occurs at the beginning of the contact time because the active sites in the adsorbent is still empty, causing the dye molecules to be easily attached to the surface of the adsorbent. The adsorption capacity of the adsorbent towards the MV 2B dye increased gradually with increasing contact time, but the adsorption capacity towards the MB dye decreased after 60 min. The decrease in adsorption capacity is due to the decrease in the number of active sites on the adsorbent.

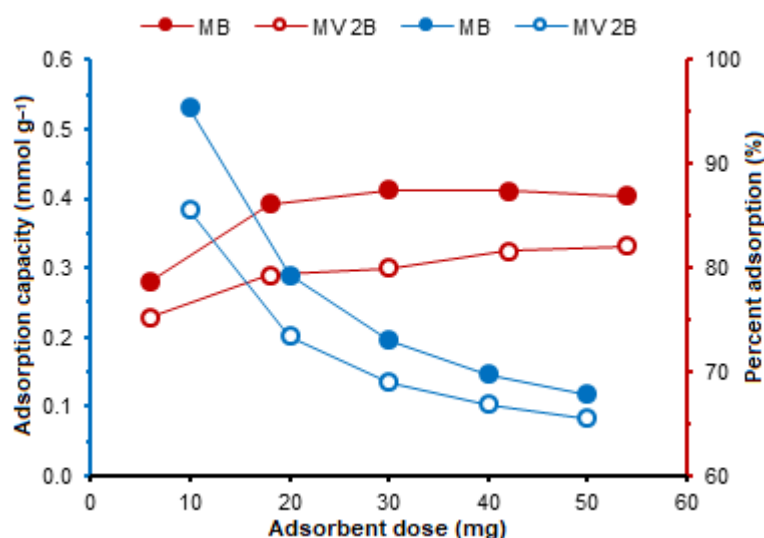


Fig 5. Effect of adsorbent dose of KKA beads powder on adsorption of MB and MV 2B dyes

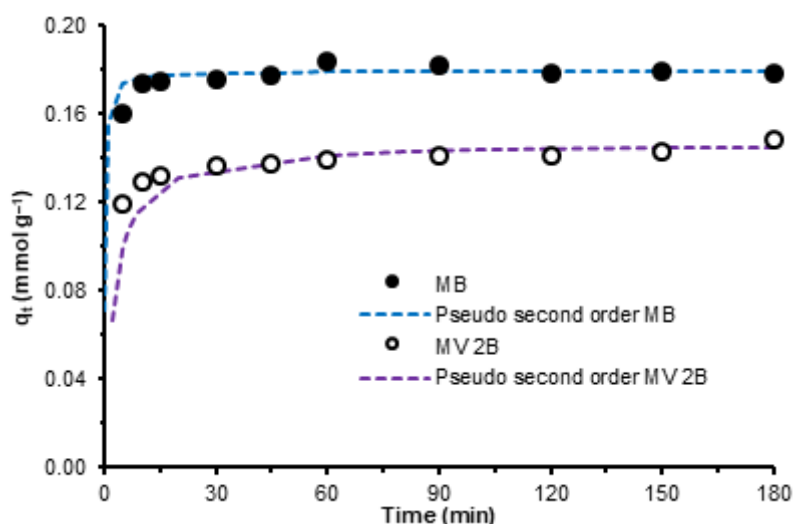


Fig 6. Effect of time on adsorption of MB and MV 2B dyes onto the KKA beads powder

The kinetics model for the KKA beads powder was described using four models, which consisted of the first-order, second-order, pseudo first-order, and pseudo second-order kinetic models. The kinetics data for the KKA beads powder in the various models are shown in Table 1. The R^2 value in the pseudo second-order kinetics model was closer to one, so it can be assumed that the pseudo second-order kinetics model best expressed the adsorption of the KKA beads powder. Theoretically, the pseudo second-order kinetics model describes the adsorption of more than one active sites of the adsorbent.

The dyes had $0.115 \text{ mg g}^{-1} \text{ min}^{-1}$ (MB) and $0.007 \text{ mg g}^{-1} \text{ min}^{-1}$ (MV 2B) of k value. These results illustrate that the adsorption rate of the MB dye was greater than the adsorption rate of MV 2B. Smaller

molecule size are more easily distributed, thus equilibrium would be achieved faster [26]. The MB dye have smaller molecular sizes compared to the MV 2B dye, which explains why higher adsorption rate of MB dye had a larger adsorption rate.

Effect of Initial Concentration

Fig. 7 shows that the adsorption capacity of the dye increased with increasing initial concentration. The adsorption limit which describes the saturation of the adsorbent against the adsorbate is not visible. The chance of the adsorbate interaction with the activated site of the adsorbent will increase with an increasing number of dye molecules in the solution. In this study, the maximum adsorption capacity of the KKA beads was

Table 1. Adsorption kinetics parameters of the adsorption on MB and MV 2B dyes onto the KKA beads powder

Kinetics model	Parameter	MB	MV 2B
	Molecular weight (g mol^{-1})	319.86	393.96
	q_e experiment (mmol g^{-1})	0.183	0.148
First-order	R^2	0.2953	0.8316
	k_1 (min^{-1})	0.001	0.004
Second-order	R^2	0.2845	0.8817
	k_2 (min^{-1})	0.026	0.083
Pseudo first-order	R^2	0.4367	0.9435
	k_1 (min^{-1})	0.007	0.061
	q_e cal (mmol g^{-1})	0.011	0.020
Pseudo second-order	R^2	0.9998	0.9991
	k_2 ($\text{g mmol}^{-1} \text{ min}^{-1}$)	36.8	2.79
	k_2 ($\text{g mg}^{-1} \text{ min}^{-1}$)	0.115	0.007
	q_e cal (mmol g^{-1})	0.179	0.147

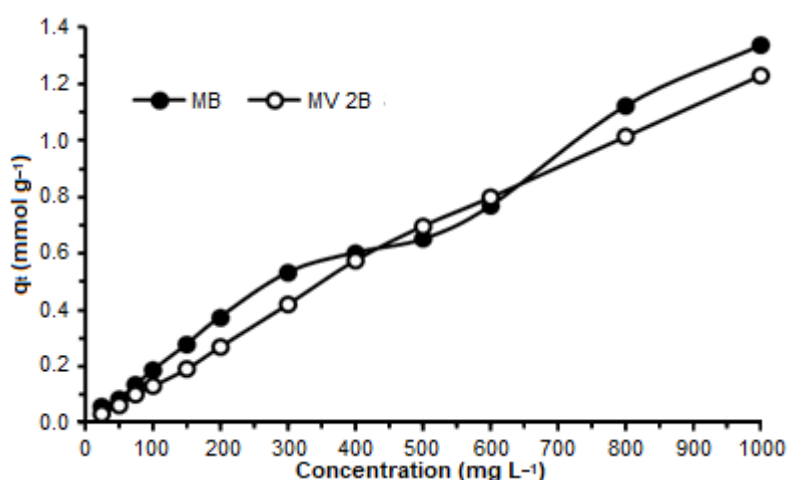


Fig 7. Effect of concentration on adsorption of MB and MV 2B dyes on the KKA beads powder

obtained at 1000 mg L⁻¹, with 1.34 mg g⁻¹ (MB) and 1.23 mg g⁻¹ (MV 2B) adsorption capacity.

The adsorption isotherms studied in this research are Langmuir and Freundlich isotherms. A summary of the adsorption isotherms calculation can be seen in Table 2. Table 2 shows that the R² value in the Freundlich isotherm is closer to one compared to the Langmuir isotherm which means that the MB and MV 2B dye adsorption on the KKA beads powder follow the Freundlich isotherm. Adsorption of MB dyes with zeolite-activated carbon/chitosan beads [12] and activated-alginate beads [13] also followed the Freundlich isotherm. The Freundlich isotherm describes the process of adsorption on heterogeneous surfaces. The heterogeneity factor (1/n) is a characteristic of the Freundlich model. In this study, n values were 1.64 (MB) and 1.16 (MV 2B). The higher n value represents the higher heterogeneity of the

site on the adsorbent.

Selectivity Adsorption of MB and MV 2B Dyes

Fig. 8 shows that the maximum adsorption of dyes are smaller if they are in a multicomponent solution, which proves that there is a competitive effect between the dyes. Under optimum conditions of MB adsorption, the presence of MV 2B reduced MB adsorption by 11.7%. Meanwhile, under the optimum conditions of MV 2B dye adsorption, the presence of MB reduced MV 2B adsorption by 12.3%. These results indicate that the reduction of MV 2B adsorption is greater in multicomponent solutions. In multicomponent solutions, smaller molecules will occupy the pores in the adsorbent structure first [27]. The MB dye have a smaller molecular weight compared to MV 2B causing the molecules of the MB dye to fill the pores of the adsorbent earlier than the MV 2B dye.

Table 2. The Langmuir and Freundlich isotherm parameters for MB and MV 2B dyes

Isotherms model	Parameter	MB	MV 2B
q _e experiment (mmol g ⁻¹)		1.34	1.23
Langmuir isotherm	q _{max} (mmol g ⁻¹)	1.36	2.42
	K _L (L mol ⁻¹)	3135	1552
	E (KJ/mol)	20.1	18.3
	R ²	0.8212	0.8789
Freundlich isotherm	K _F	1.17	2.14
	n	1.64	1.16
	R ²	0.9035	0.9820

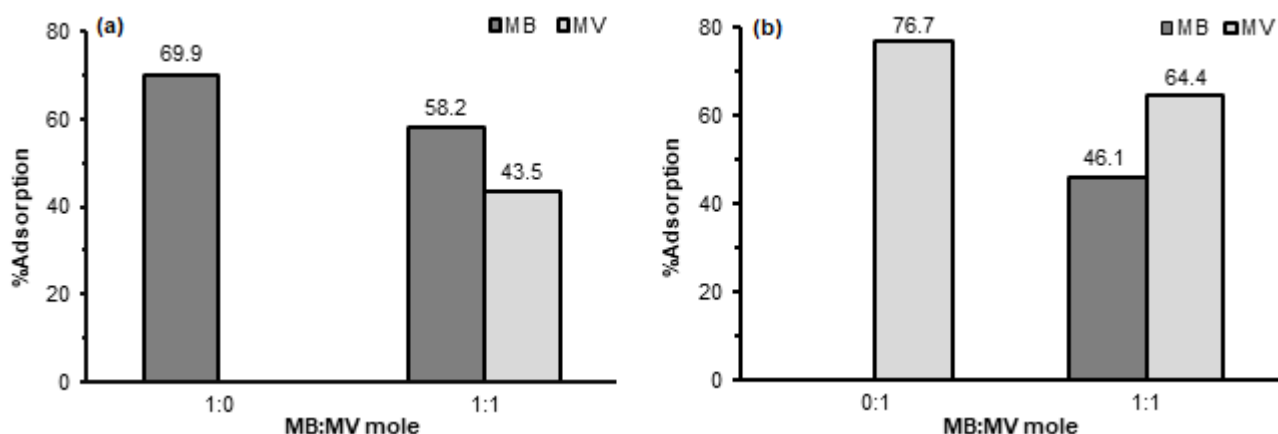


Fig 8. Effect of percentage adsorption of MB and MV 2B dyes under optimum conditions of (a) MB and (b) MV 2B adsorption

MB and MV 2B Dyes Adsorption

Table 3 shows that activated carbon has adsorption capacities of 0.151 mmol g⁻¹ (MB) and 0.171 mmol g⁻¹ (MV 2B) under optimum conditions, while the adsorption capacities of the KKA beads powder are 1.34 mmol g⁻¹ and 1.23 mmol g⁻¹ for MB and MV 2B, respectively. The results showed that the adsorption ability of activated carbon after modification into KKA beads powder increased by 787 and 621% for MB and MV 2B dyes, respectively. The increased adsorption ability of the activated carbon is due to the presence of activated sites on the surface of the adsorbent from chitosan and alginate modification.

Desorption Study

Desorption solution (NaCl) was found to have an influence in the process of releasing cationic dyes -N⁺(CH₃)₂ (MB) and -N⁺HCH₃ (MV 2B) from the adsorbent. The strength of Na⁺ ions was able to release the electrostatic cationic dyes which had been bound to the KKA beads powder. The greater the amount of Na⁺ ions in the solution, the greater amount of MB and MV 2B molecules that was released. pH 4 solution was used as the medium for desorption because it has an acidic strength that can protonate the activated site of chitosan from -NH₂ to -NH₃⁺. Protonated amino groups was able to

increase the hydrophilicity of the adsorbent causing the MB or MV 2B dyes to be released. Ethanol solution in water can also act as a medium of desorption because it can attract MB or MV 2B dyes through hydrogen bonds and hydrophobic interactions [31].

Fig. 9 shows that prolonging the desorption time increased the amount of MB and MV 2B released from the adsorbent. The desorption order for MB and MV 2B dyes were 60% ethanol > pH 4 solution > 40% ethanol > 1.0 M NaCl > 0.1 M NaCl. Therefore, 60% ethanol solution was the most effective desorption medium. This points to the tendency for hydrogen bonds and hydrophobic interactions. The existence of double bonds and benzene rings in the structure of dyes that are hydrophobic gives the possibility that hydrophobic interactions will be more dominant than electrostatic interactions [28].

The percentage of desorption for MB and MV 2B dyes in various solvents were less than 22%. This is likely because only the dye molecules on the surface of the adsorbent were able to be released. The porous structure of the KKA beads powder caused the adsorbed dyes to be trapped and difficult to escape. Similarly, MB desorption studies on carbon monolith (CM) adsorbents using ethanol were only able to adsorb MB dyes attached to the CM surfaces, not in macro and mesoporous adsorbent structures [32].

Table 3. Comparison of MB and MV 2B dye adsorption capacity in various adsorbents

Adsorbent	Dyes	Capacity adsorption		pH	Mass (mg)	Time (min)	Concentration (mg L ⁻¹)	Isotherm model	Reference
		mmol g ⁻¹	mg g ⁻¹						
Activated carbon	MB	0.151	48.2	7	30	60	1000	Freundlich	This work
	MV 2B	0.171	67.2	7	30	180	1000	Freundlich	
KAA beads powder	MB	1.34	428	7	30	60	1000	Freundlich	This work
	MV 2B	1.23	484	7	30	180	1000	Freundlich	
Activated carbon sunflower seed hulls	MV 2B	0.253	92.6	4.5	30	105	300	Freundlich	[3]
Activated carbon-alginate beads	MB	0.719	230	9.5	10	1200	100	Freundlich	[13]
Composite HNT-Fe ₃ O ₄	MV 2B	0.052	20.4	7	15	360	90	Langmuir	[25]
Activated carbon	MB	2.39	742	7	25	1440	3000	Langmuir	[28]
Activated carbon-clay	MB	0.560	179	9	20	1560	400	Langmuir	[29]
Polyglycerol magnetic gel	MB	1.44	459	7	20	120	1600	Langmuir	[30]
	MV 2B	1.01	400	7	20	120	2000	Langmuir	

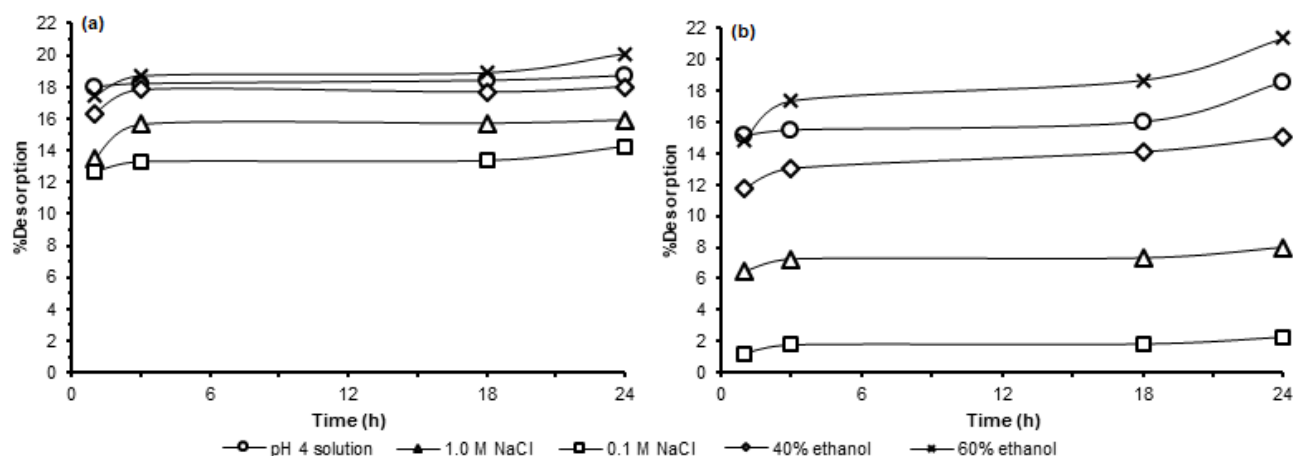


Fig 9. Percentage of desorption for (a) MB and (b) MV 2B dyes

CONCLUSION

The optimum adsorbent composition for adsorption of MB and MV 2B dyes was found in KKA beads powder with 0.8 g of alginate. The optimum contact time was 60 min for the MB dye and 180 min for MV 2B. Both dyes followed a pseudo second-order kinetics model with an adsorption rate of $0.115 \text{ g mg}^{-1} \text{ min}^{-1}$ for MB and $0.007 \text{ g mg}^{-1} \text{ min}^{-1}$ for MV 2B. The optimum initial concentration for both dyes was 1000 mg L^{-1} . Both dyes followed the Freundlich isotherm with K_F and n values of 1.17 and 1.64, respectively for MB, and 2.14 and 1.16 respectively for MV 2B. The most effective desorption medium for MB and MV 2B dyes in the KKA beads powder was 60% ethanol.

ACKNOWLEDGMENTS

This research was financially supported by the Master Thesis Research Program of the Director General of Higher Education, Ministry of Education and Culture, Republic of Indonesia (contract number 2858/UN1.DIT LIT/DIT-LIT/LT/2019).

REFERENCES

- [1] Zhou, L., Huang, J., He, B., Zhang, F., and Li, H., 2014, Peach gum for efficient removal of methylene blue and methyl violet dyes from aqueous solution, *Carbohydr. Polym.*, 101, 574–581.
- [2] Aksu, Z., 2005, Application of biosorption for the removal of organic pollutants: A review, *Process Biochem.*, 40 (3-4), 997–1026.
- [3] Hameed, B.H., 2008, Equilibrium and kinetic studies of methyl violet sorption by agricultural waste, *J. Hazard. Mater.*, 154 (1-3), 204–212.
- [4] Lucas, M.S., Dias, A.A., Sampaio, A., Amaral, C., and Peres, J.A., 2007, Degradation of a textile reactivated Azo dye by a combined chemical-biological process: Fenton's reagent-yeast, *Water Res.*, 41 (5), 1103–1109.
- [5] Orts, F., del Río, A.I., Molina, J., Bonastre, J., and Cases, F., 2018, Electrochemical treatment of real textile wastewater: Trichromy Procion HEXL®, *J. Electroanal. Chem.*, 808, 387–394.
- [6] Al jibouri, A.K.H., Wu, J., and Upreti, S.R., 2015, Continuous ozonation of methylene blue in water, *J. Water Process Eng.*, 8, 142–150.
- [7] Mohod, A.V., Hinge, S.P., Raut, R.S., Bagal, M.V., and Pinjari, D., 2018, Process intensified removal of methyl violet 2B using modified cavity-bubbles oxidation reactor, *J. Environ. Chem. Eng.*, 6 (1), 574–582.
- [8] Liu, H., Zhong, L., Govindaraju, S., and Yun, K., 2019, ZnO rod decorated with Ag nanoparticles for enhanced photocatalytic degradation of methylene blue, *J. Phys. Chem. Solids*, 129, 46–53.
- [9] Zhao, R., Li, Y., Sun, B., Chao, S., Li, X., Wang, C., and Zhu, G., 2019, Highly flexible magnesium silicate nanofibrous membranes for effective removal of methylene blue from aqueous solution, *Chem. Eng. J.*, 359, 1603–1616.

- [10] Rafatullah, M., Sulaiman, O., Hashim, R., and Ahmad, A., 2010, Adsorption of methylene blue on low-cost adsorbents: A review, *J. Hazard. Mater.*, 177 (1-3), 70–80.
- [11] Hassan, A.F., Abdel-Mohsen, A.M., and Fouda, M.M.G., 2014, Comparative study of calcium alginate, activated carbon, and their composite beads on methylene blue adsorption, *Carbohydr. Polym.*, 102, 192–198.
- [12] Khanday, W.A., Asif, M., and Hameed, B.H., 2017, Cross-linked beads of activated oil palm ash zeolite/chitosan composite as a bio-adsorbent for the removal of methylene blue and acid blue 29 dyes, *Int. J. Biol. Macromol.*, 95, 895–902.
- [13] Nasrullah, A., Bhat, A.H., Naeem, A., Isa, M.H., and Danish, M., 2018, High surface area mesoporous activated carbon-alginate beads for efficient removal of methylene blue, *Int. J. Biol. Macromol.*, 107 (Part B), 1792–1799.
- [14] Corcho-Corral, B., Olivares-Marín, M., Fernández-González, C., Gómez-Serrano, V., and Macías-García, A., 2006, Preparation and textural characterisation of activated carbon from vine shoots (*Vitis vinifera*) by H₃PO₄-Chemical activation, *Appl. Surf. Sci.*, 252 (17), 5961–5966.
- [15] Gao, Y., Yue, Q., Xu, S., and Gao, B., 2015, Activated carbons with well-developed mesoporosity prepared by activation with different alkali salts, *Mater. Lett.*, 146, 34–36.
- [16] Hameed, B.H., Din, A.T.M., and Ahmad, A.L., 2007, Adsorption of methylene blue onto bamboo-based activated carbon: Kinetics and equilibrium studies, *J. Hazard. Mater.*, 141 (3), 819–825.
- [17] Li, W., Yue, Q., Tu, P., Ma, Z., Gao, B., Li, J., and Xu, X., 2011, Adsorption characteristics of dyes in columns of activated carbon prepared from paper mill sewage sludge, *Chem. Eng. J.*, 178, 197–203.
- [18] Pathania, D., Sharma, S., and Singh, P., 2017, Removal of methylene blue by adsorption onto activated carbon developed from *Ficus carica* bast, *Arabian J. Chem.*, 10 (Suppl. 1), S1445–S1451.
- [19] Chafidz, A., Astuti, W., Augustia, V., Novira, D.T., and Rofiah, N., 2018, Removal of methyl violet dye via adsorption using activated carbon prepared from *Randu* sawdust (*Ceiba pentandra*), *IOP Conf. Ser.: Earth Environ. Sci.*, 167, 012013.
- [20] Wasupalli, G.K., and Verma, D., 2018, Molecular interactions in self-assembled nano-structures of chitosan-sodium alginate based polyelectrolyte complexes, *Int. J. Biol. Macromol.*, 114, 10–17.
- [21] Xu, R.K., Xiao, S.C., Yuan, J.H., and Zhao, A.Z., 2011, Adsorption of methyl violet from aqueous solutions by the biochars derived from crop residues, *Bioresour. Technol.*, 102 (22), 10293–10298.
- [22] Nitayaphat, W., 2014, Utilization of chitosan/bamboo charcoal composite as reactivated dye adsorbent, *Chiang Mai J. Sci.*, 41 (1), 174–183.
- [23] Vijaya, Y., Popuri, S.R., Boddu, V.M., and Krishnaiah, A., 2008, Modified chitosan and calcium alginate biopolymer sorbents for removal of nickel (II) through adsorption, *Carbohydr. Polym.*, 72 (2), 261–271.
- [24] Li, P., Su, Y.J., Wang, Y., Liu, B., and Sun, L.M., 2010, Bioadsorption of methyl violet from aqueous solution onto Pu-erh tea powder, *J. Hazard. Mater.*, 179 (1-3), 43–48.
- [25] Bonetto, L.R., Ferrarini, F., de Marco, C., Crespo, J.S., Guégan, R., and Giovanela, M., 2015, Removal of methyl violet 2B dye from aqueous solution using a magnetic composite as an adsorbent, *J. Water Process Eng.*, 6, 11–20.
- [26] Chiou, M.S., and Chuang, G.S., 2006, Competitive adsorption of dye metanil yellow and RB15 in acid solutions on chemically cross-linked chitosan beads, *Chemosphere*, 62 (5), 731–740.
- [27] Noroozi, B., and Sorial, G.A., 2013, Applicable models for multi-component adsorption of dyes: A review, *J. Environ. Sci.*, 25 (3), 419–429.
- [28] Iriarte-Velasco, U., Chimeno-Alanís, N., González-Marcos, M.P., and Álvarez-Uriarte, J.I., 2011, Relationship between thermodynamic data and adsorption/desorption performance of acid and basic dyes onto activated carbons, *J. Chem. Eng. Data*, 56 (5), 2100–2109.
- [29] Marrakchi, F., Bouaziz, M., and Hameed, B.H., 2017, Activated carbon–clay composite as an

- effective adsorbent from the spent bleaching sorbent of olive pomace oil: Process optimization and adsorption of acid blue 29 and methylene blue, *Chem. Eng. Res. Des.*, 128, 221–230.
- [30] Song, Y., Duan, Y., and Zhou, L., 2018, Multi-carboxylic magnetic gel from hyperbranched polyglycerol formed by thiol-ene photopolymerization for efficient and selective adsorption of methylene blue and methyl violet dyes, *J. Colloid Interface Sci.*, 529, 139–149.
- [31] Samiey, B., and Ashoori, F., 2012, Adsorptive removal of methylene blue by agar: Effects of NaCl and ethanol, *Chem. Cent. J.*, 6, 14.
- [32] He, X., Male, K.B., Nesterenko, P.N., Brabazon, D., Paull, B., and Luong, J.H.T., 2013, Adsorption and desorption of methylene blue on porous carbon monoliths and nanocrystalline cellulose, *ACS Appl. Mater. Interfaces*, 5, 8796–8804.

Metals Accumulation in Muscle Tissues and Digestive Contents of *Periglypta reticulata* (Kerang Geton) from Lancang Island, Jakarta

Suratno^{1*}, Rachma Puspitasari², Zahriza Purnadayanti³, and Novita Sandra⁴

¹Research Division for Natural Product Technology, Indonesian Institute of Sciences, Jl. Jogja-Wonosari Km 31.5, Gading, Yogyakarta 55861, Indonesia

²Research Center for Oceanography, Indonesian Institute of Sciences, Pasir Putih I, Ancol Timur, Jakarta 14430, Indonesia

³Department of Fisheries and Marine Science, Brawijaya University, Jl. Veteran, Ketawanggede, Malang 65145, Indonesia

⁴Toxicology Laboratory, Jakarta Public Health Laboratory, Jl. Rawasari Selatan No. 2, Cempaka Putih, Jakarta 10510, Indonesia

* **Corresponding author:**

tel: +62-274-392570

email: nanosan80@gmail.com

Received: September 2, 2019

Accepted: February 3, 2020

DOI: 10.22146/ijc.49219

Abstract: The concentration of nineteen metals (Hg, As, Cd, Co, Cr, Cu, Fe, Li, Mg, Mn, Mo, Ni, Pb, Se, Sr, Ti, Tl, V, and Zn) were determined in muscle tissues and digestive contents of *Periglypta reticulata* (Kerang Geton), collected from Lancang Island part of Seribu Islands, Jakarta. An interaction between toxic and essential metal in a clam is also studied. The results showed high concentrations of As (4.56), V (1.20), and Zn (4.91) mg/kg wet weight in muscle tissues and As (7.16), Ti (2.53), and Zn (8.68) mg/kg wet weight in digestive contents. Average concentrations of metals in muscle tissues and digestive contents were below regulation limit from permissible standard National Agency of Drug and Food Control except for Arsenic (As). The average concentration of metals in muscle tissues was significantly ($P < 0.05$) lower than in digestive contents except As, Co, Cr, Mg, and Tl, respectively. Toxic metals (Pb, Hg, Cd, and As) showed a strong correlation with several essential metals so that these metals can be a threat to the main function of a particular metal. The present study showed digestive contents could accumulate in higher metals; therefore, we suggested removing it before consuming this clam.

Keywords: *Periglypta reticulata*; heavy metals; Lancang Island

■ INTRODUCTION

Heavy metals contamination is one of the complex problems in an aquatic environment and raising concern over their potential in the risk of human health [1]. Some heavy metals (Co, Cr, Cu, Fe, Mn, Mo, Ni, Se, Zn) are essential elements for the organism being constituents of several key enzymes and playing important roles in various oxidation-reduction reactions [2]. However, an excess amount of metals may produce cellular and tissue damage [3]. Metals such as Hg, Pb, Cd, and As have no established biological functions and are considered as non-essential and potentially toxic at relatively low concentrations [4]. The heavy metals concentration may be attributed to sewage and agricultural drainage. Besides, the corrosion of the ship's hull coating and antifouling

paints at the ship can cause a high concentration of copper in the lake [5].

Marine bivalves could accumulate metals presented at undetectable levels from environmental to very high concentrations in tissues [6]. Bivalves are known to feed on suspended particles in the water column, which could be contaminated by various contaminants derived from either anthropogenic activities or natural emissions [7]. The primary source of heavy metals contamination in the natural environment is the run-off from agricultural activities [8]. Bivalves are known to filter between twenty and one hundred liters of surrounding waters a day. In doing so, they accumulate natural or anthropogenic contaminants [9].

Furthermore, since the bivalves have high nutritional and economic values, eating bivalves contain

high concentrations of heavy metals is dangerous and threats to human health [10]. The present study was aimed to investigate the concentration of toxic metals (As, Pb, Cd, and Hg) and essential metals (Co, Cr, Cu, Fe, Li, Mg, Mn, Mo, Ni, Se, Sr, Ti, Tl, V, and Zn) in muscle tissues and digestive content of *Periglypta reticulata* from Lancang Island, part of Seribu Islands, Jakarta. The other goal was to study the interaction between toxic and essential metals in the clam. Lancang Island located 30 km North-West from Jakarta Bay and 9 km from Cisadane estuary in Tangerang. Jakarta Bay receives enormous amounts of municipal discharges from the Jakarta metropolis [11] that caused marine pollution with various pollutants, especially heavy metals.

■ EXPERIMENTAL SECTION

Materials

Periglypta reticulata were purchased from fisherman in Lancang Island and directly placed in a zip-lock plastic bag and freeze until further analysis. All reagents used were analytical-reagents grade. The solutions were prepared using ultra-pure water (Milli-Q), Nitric acid (65% HNO₃ Suprapur, Merck), HCl 37% (Merck), Hg standard solution 1.000 mg/L (Merck) and L-Cysteine (Nacalai Tesque Inc. Japan).

Instrumentation

Caliper and analytical balance (Sartorius BP 210 S) were used for morphometric analysis. Dried samples were prepared using oven (Heraeus Instrument), petri dish, spatula, mortar, and pestle. ICP-OES 7400 Thermo and Mercury Analyzer NIC MA-3000 were used for concentrations analysis.

Procedure

Sample collection

In the laboratory, bivalves were cleaned to remove dirt attached to the bivalve and were separated from muscle tissues and digestive contents. Morphometric analysis of the total weight of the wet tissues was measured with Sartorius analytical balance, while the length and width of bivalves were measured with a digital caliper. Samples were dried in an oven at 60 °C for 24 h for heavy metals analysis. Moisture contents of muscle tissues and

digestive contents were measured with oven-dried at 105 °C for 24 h [12]. Muscle tissues (MT) and digestive contents (DC) were ground into a fine powder with mortar and pestle for the subsequent analysis.

Metal analysis

Three replicates of dried MT and DC samples were individually weighed approximately 10–20 mg directly in the sample boat and analyzed with mercury analyzer for total mercury concentration. The modified method from USEPA 3051a for total metals analysis was utilizing a mixture of concentrated HNO₃ and HCl and a microwave oven [13]. In brief, the mixture of acid (9 mL HNO₃ and 3 mL HCl) was drop-added into 0.5 g of samples then the mixture was heated using microwave oven CEM MARS 5 Express at 185 °C for 15 min and hold for 30 min. Then the solution was filtered using Whatman filter paper No. 41, and the filtrate was diluted to 25 mL using deionized water. Three replicates of dried MT and DC samples were also applied for a non-Hg measurement. The samples were measured using ICP-OES 7400 Thermo for metals analysis.

Data analysis

Statistical correlation analysis was based on IBM SPSS Statistics 22. Pearson's correlation coefficient analysis was used to determine the significant relationship between metal accumulation in muscle tissues and digestive contents with two-tailed *p*-value < 0.05 and *p*-value < 0.01 were considered significant. All graphical plot was based on the R program.

■ RESULTS AND DISCUSSION

Details of metals concentration MT and DC in *P. reticulata* are shown in Fig. 1 and Fig. 2. Bivalves (n = 10 individual samples) collected in this study displayed similar-sized of 8.00±0.53 cm (Length) × 8.65±0.85 cm (Width). The average wet weights of total tissues were 32.40±8.83 g, and the moisture content for MT and DC were 81.38% and 75.64%, respectively. Concentrations of As, Co, Cr, Mg, and Tl were not statistically significantly different between MT and DC. Concentrations of toxic metals (Hg, Pb, and Cd) except As were lower than the permissible limit from *Badan Pengawas Obat dan Makanan* or National Agency of

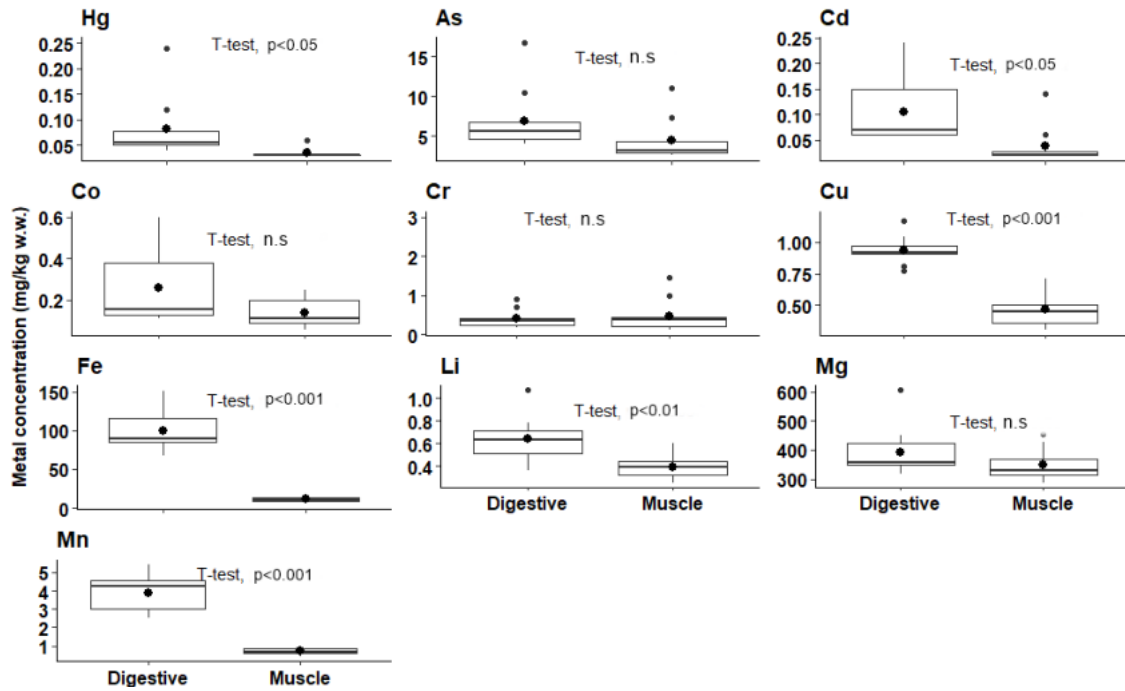


Fig 1. Metals concentrations (mg/kg w.w.) in digestive contents and muscle tissues of *P. reticulata* (“•” represents mean value)

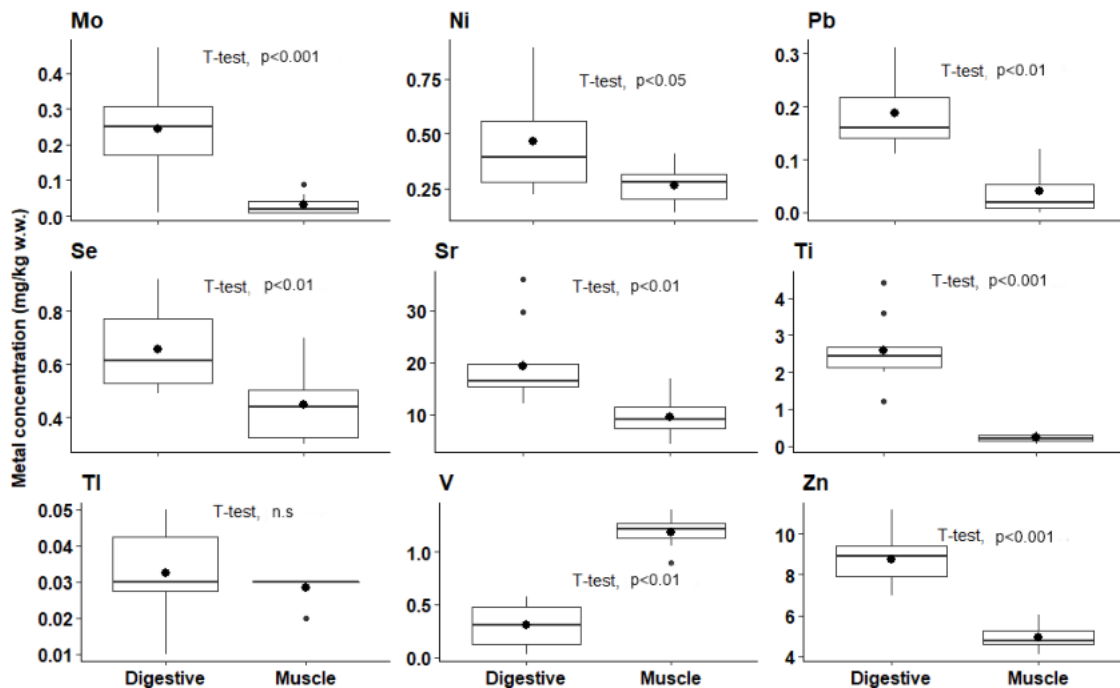


Fig 2. Metals concentrations (mg/kg w.w.) in digestive contents and muscle tissues of *P. reticulata* (“•” represents mean value)

Drug and Food Control (NADFC) in muscle tissues and digestive contents. Concentrations of As, Co, Cr, Mg and Tl in MT and DC were 2.58–11.04 (4.41±2.71) and 4.03–

16.74 (6.93±3.93); 0.06–0.25 (0.14±0.07) and 0.11–0.60 (0.26±0.18); 0.14–1.45 (0.49±0.42) and 0.18–0.90 (0.41±0.23); 288.86–454.28 (349.70±53.58) and 318.90–

605.27 (393.56±85.98); 0.06–0.37 (0.22±0.11) and 0.014–0.053 (0.033±0.014) mg/kg w.w., respectively. In this study, the concentration of Arsenic (As) in MT and DC (2.58–11.04 (4.41±2.71) and 4.03–16.74 (6.93±3.93) mg/kg w.w. were higher compared to study that reported by Copat et al. [14] in *Donax trunculus* from Catalina Gulf, Italia (1.53 mg/kg w.w.), Sivaperumal et al. [15] in *Villorita cyprinoides* from Cochin area, India (0.69 mg/kg w.w.), Lei et al. [16] in *Macra chinensis* from Shanghai (0.20 mg/kg d.w.) and Li et al. [17] in *Macra veneriformis* from Bohai Bay, China (1.44–2.51 mg/kg w.w.). These facts showed an As enrichment in *P. reticulata* that was not fully understood because of sediment, as the main factor, was not examined in this study. Enrichment As could be attributed to the natural and anthropogenic sources. Natural sources mostly related to phosphate deposits and anthropogenic As can be driven As-rich pesticides in the past and phosphorite processing activities [17].

Concentrations of Hg, Cd, and Ni were statistically significant ($p < 0.05$); Li, Pb, Se, Sr, and V statistically significant ($p < 0.01$) different between MT and DC.

Concentrations of Cu, Fe, Mn, Mo, Ti, and Zn were statistically highly significant ($p < 0.001$) different between MT and DC in *P. reticulata*. Copper, iron, manganese, molybdenum, and zinc were known as cofactors of many enzymes that play an important role in aquatic organisms [17]. Iron is an essential element for biological function, but in excess, it is related to heart disease, cancer, and impaired insulin sensitivity [18]. Mn is an essential micronutrient for many biochemical reactions in living beings [19]. Zinc has generally been considered to be non-toxic and a minor nutrient required for growth and development [20].

Accumulation of heavy metals in marine mollusks can be affected by many factors, including endogenous and exogenous factors. Endogenous factors such as body size, growth, fitness, reproductive condition and genotypes [21], the differences in biokinetic uptake, depuration rate, and other physiological processes could contribute to the variations in the heavy metal concentration in tissues [22]. Meanwhile, the exogenous factors could be salinity, metal bioavailability [23], alkalinity, and others [19].

Table 1. Pearson correlation R between metals concentration (mg/kg w.w.) in muscle tissues of *P. reticulata*

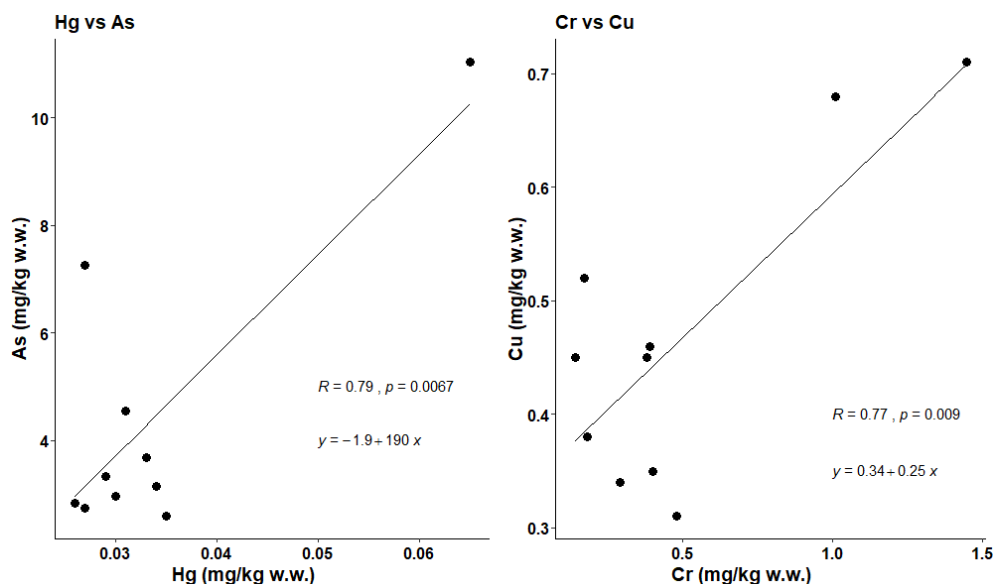
Element	Hg	As	Cd	Co	Cr	Cu	Fe	Li	Mg	Mn	Mo	Ni
Hg		0.783^a				-0.252		0.480	-0.351	0.440	-0.202	0.652^b
As			0.648^b						-0.466	0.255	0.323	0.603
Cd					0.425	0.440	0.585		-0.294	-0.446	0.475	-0.231
Co						-0.441		0.370		0.358	0.350	0.761^b
Cr						0.769^a	0.684^b		-0.257		0.234	
Cu								-0.286	-0.509	-0.299	0.409	-0.479
Fe								0.448				0.263
Li									0.495	0.382	-0.472	0.575
Mg											-0.314	
Mn											-0.466	0.716^b
Mo												
Ni												
Pb												
Se												
Sr												
Ti												
Tl												
V												
Zn												

Table 1. Pearson correlation R between metals concentration (mg/kg w.w.) in muscle tissues of *P. reticulata* (Continued)

Element	Pb	Se	Sr	Ti	Tl	V	Zn
Hg			-0.297		0.279		-0.537
As	-0.260						
Cd	-0.201	0.674^b			-0.353		
Co						0.430	
Cr	-0.224	0.427		0.329	-0.627		-0.212
Cu	-0.423	0.512		0.416	-0.737^b		
Fe		0.246			-0.305		
Li		-0.511	-0.512		0.406		
Mg	0.355	-0.565		-0.334	0.398		0.424
Mn				0.201		-0.204	-0.439
Mo	-0.370	0.477	0.354		0.719^b	0.625	0.449
Ni	0.225	-0.337				-0.206	-0.237
Pb		-0.480			0.416	-0.716^b	
Se			0.500		-0.603	0.400	-0.344
Sr				0.216	-0.536	0.287	
Ti					-0.417	-0.334	
Tl						-0.404	
V							0.417
Zn							

Only meaningful $|R| > 0.2$ correlation is shown; Bold is significant correlation value of > 0.4

^a Correlation is significant at the 0.01 level (2-tailed); ^b Correlation is significant at the 0.05 level (2-tailed)

**Fig 3.** Elemental relationship in the muscle tissues of *P. reticulata* (wet weight)

Pearson correlation between metals in muscle tissues in *P. reticulata* showed in Table 1 and a significantly positive linear correlation ($p < 0.05$) were observed between concentrations of some metals (As-Co, Cr-Fe,

Hg-Ni, Co-Ni, Mn-Ni, Cd-Se, Mo-Tl) and significantly negative linear correlation ($p < 0.05$) (Cu-Tl and Pb-V). A significant positive correlation ($p < 0.01$) between Hg-As ($r^2 = 0.79$) and Cr-Cu ($r^2 = 0.77$) is shown in Fig. 3.

Table 2. Pearson correlation R between metals concentration (mg/kg w.w.) in digestive contents of *P. reticulata*

Element	Hg	As	Cd	Co	Cr	Cu	Fe	Li	Mg	Mn	Mo
Hg											
As	0.976^a										
Cd	0.895^a	0.895^a									
Co	0.676^b	0.684^b	0.923^a								
Cr			0.226	0.350							
Cu	-	-0.529	-0.255								
	0.411										
Fe			0.298	0.431	0.622	0.601					
Li	0.202		0.411	0.534	0.319	0.459	0.813^a				
Mg		-0.220	0.209	0.487		0.631	0.686^b	0.701^b			
Mn	-	-0.574	-0.374		0.373	0.477	0.605	0.547	0.388		
	0.575										
Mo	0.477	0.478	0.724^b	0.770^a			0.480	0.509	0.443		
Ni	0.716^b	0.701^b	0.910^a	0.969^a	0.272		0.395	0.558	0.500	-0.222	0.753^b
Pb	0.411	0.420	0.707^b	0.793^a	0.546	0.223	0.654^b	0.500	0.475		0.606
Se	0.534	0.577	0.594	0.618		-0.556		0.255			0.660^b
Sr	0.709^b	0.656^b	0.741^b	0.735	0.360	-0.236	0.424	0.628	0.337		0.426
Ti	-0.207	-0.294		-0.257		0.733^b	0.560	0.226		0.404	
Tl	-0.293	-0.408		0.218		0.499	0.355		0.775^b		
V	0.467	0.554	0.525	0.578	0.614	-0.998^a		-0.288	-0.824	-0.331	0.910
Zn	-0.285	-0.283		0.286	0.277	0.675^b	0.705^b	0.683^b	0.653^b	0.681^b	0.387

Table 2. Pearson correlation R between metals concentration (mg/kg w.w.) in digestive contents of *P. reticulata* (Continued)

Element	Ni	Pb	Se	Sr	Ti	Tl	V	Zn
Hg								
As								
Cd								
Co								
Cr								
Cu								
Fe								
Li								
Mg								
Mn								
Mo								
Ni								
Pb	0.663^b							
Se	0.690^b							
Sr	0.806^a	0.395	0.606					
Ti	-0.330	0.270	-0.575	-0.334				
Tl		0.338	-0.236					
V	0.567		0.987^b	0.251	-0.660	-0.891		
Zn		0.604			0.507	0.330	-0.624	

Only meaningful $|R| > 0.2$ correlation is shown; Bold is significant correlation value of > 0.4

^a Correlation is significant at the 0.01 level (2-tailed); ^b Correlation is significant at the 0.05 level (2-tailed)

Pearson correlation between metals in digestive contents in *P. reticulata* showed in Table 2 and a

significantly positive linear correlation ($p < 0.05$) were observed between concentrations of some metals (Hg-Co,

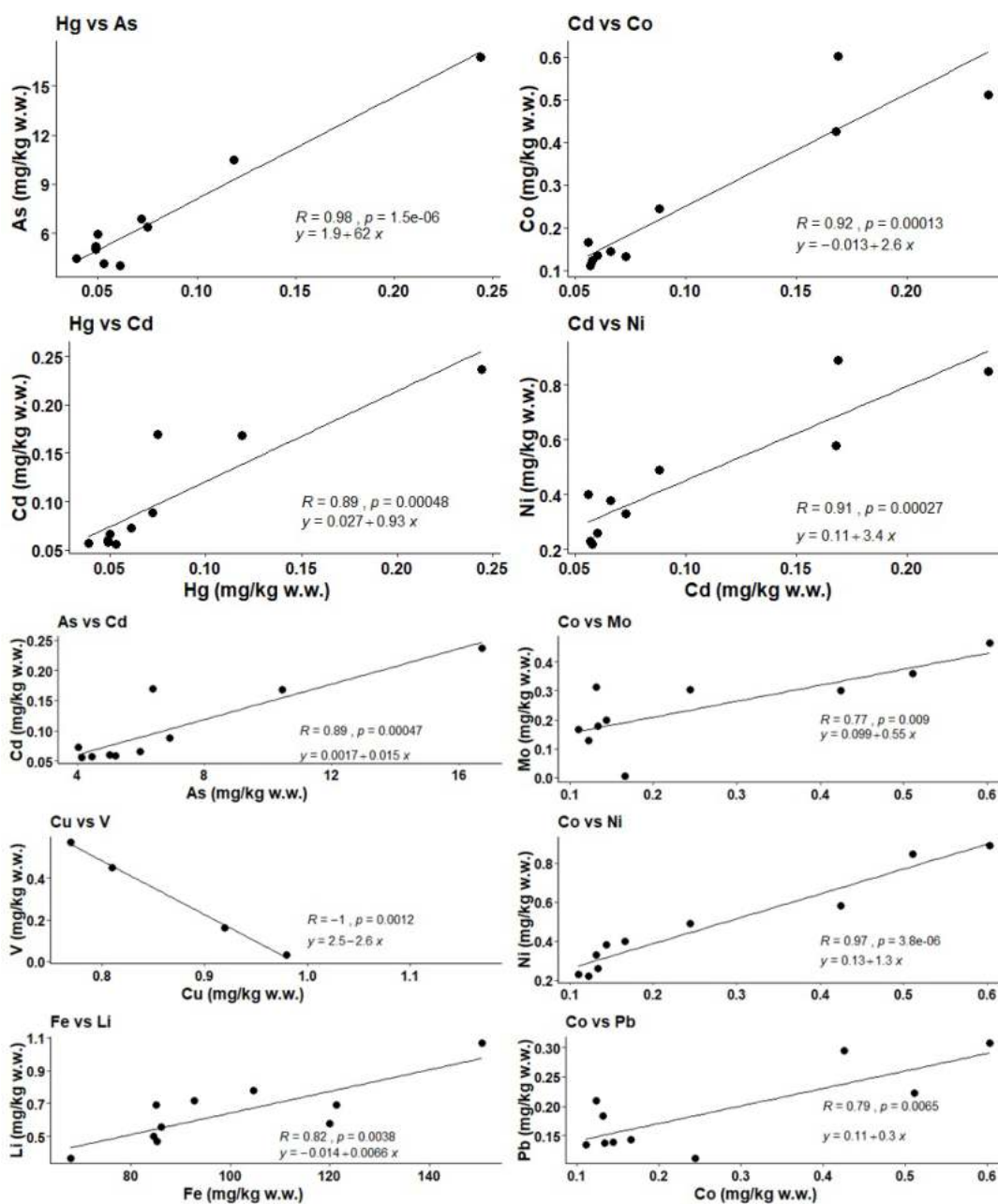


Fig 4. Elemental relationship in the digestive contents of *P. reticulata* (wet weight)

Hg-Ni, Hg-Sr, As-Co, As-Ni, As-Sr, Cd-Mo, Cd-Pb, Cd-Sr, Cu-Ti, Cu-Zn, Fe-Mg, Fe-Pb, Fe-Zn, Li-Mg, Li-Zn, Mg-Tl, Mg-Zn, Mn-Zn, Mo-Ni, Mo-Se, Ni-Pb, Ni-Se, and Se-V). A significantly positive linear correlation ($p < 0.01$) between Hg-As ($r^2 = 0.98$), Hg-Cd ($r^2 = 0.89$), Cd-Co ($r^2 = 0.92$), Cd-Ni ($r^2 = 0.91$), As-Cd ($r^2 = 0.89$), Co-Mo ($r^2 = 0.77$), Co-Ni ($r^2 = 0.97$), Fe-Li ($r^2 = 0.82$) Co-Pb ($r^2 = 0.79$) and significantly negative correlation ($p < 0.01$) for Cu-V ($r^2 = -1$) are shown in Fig. 4. Copper and Titanium showed

a positive correlation in the digestive contents of *P. reticulata*. Therefore, it indicated that these metals sources come from slow corrosion of anti-fouling coating paint in a boat [24]. Concentrations of heavy metals *P. reticulata* from Lancang Island compared to the previously reported from around the world and guidelines (NADFC, ANZFC, and JECFA/WHO) were shown in Table. 3.

In the digestive content, Cd as a toxic element was positively correlated with the most of essential metals, Mo,

Table 3. Comparison of heavy metal concentrations in muscle tissue and digestive contents of *P. reticulata* from Lancang Island and *Veniridae* clams in other area (metal concentration in mg/kg; dry weight (d.w.) or wet weight (w.w.) basis; bold indicated exceeding maximum limit from NADFC 2018)

Site	Species	Year	Hg	As	Cd	Co	Cr	Cu	Fe	Li	Mg	Mn	Mo	
Lancang Island, Indonesia	<i>Periglypta reticulata</i> (muscle)	w.w.	2018	0.03	4.41	0.04	0.14	0.49	0.47	11.59	0.39	349.70	0.71	0.03
	<i>P. reticulata</i> (digestive)	w.w.	2018	0.08	6.93	0.10	0.26	0.41	0.94	99.87	0.64	393.56	3.91	0.24
Catania Gulf	<i>D. trunculus</i> (composite)	w.w.	2012		1.53	0.01		0.25					4.26	
Cochin Area	<i>Villorita crypinoides</i> (composite)	w.w.	2011			0.34		0.26	1.4					
Shanghai	<i>Macetra chinensis</i> (composite)	d.w.	2008		0.20	0.03		0.10					5.18	
Bohai Bay	<i>Macetra veneriformis</i> (soft tissue)	w.w.	2008		1.44	0.27	0.55	1.37	2.34				23.95	0.12
Parit Jawa, Johor	<i>Polymesoda erosa</i> (total tissue)	d.w.	2009			3.26			14.1	790				
Parit Jawa, Johor	<i>Polymesoda erosa</i> (foot)	d.w.	2009			1.47			3.77	110				
Parit Jawa, Johor	<i>Polymesoda erosa</i> (gill)	d.w.					1.46		12.8	1088				
Telok Mas, Mallaca	<i>Polymesoda erosa</i> (total tissue)	d.w.	2009			4.23	2.96		15.7	1111				
Telok Mas, Mallaca	<i>Polymesoda erosa</i> (foot)	d.w.	2009				0.253		1.80	93.5				
Telok Mas, Mallaca	<i>Polymesoda erosa</i> (gill)	d.w.	2009				2.86		8.81	1620				
Coast of New Caledonia	<i>Gafrarium tumidum</i> (soft tissue)	w.w.	2008	0.42										
Coast of New Caledonia	<i>Periglypta chemnitzii</i> (soft tissue)	w.w.	2008	0.4										
Astamudi Lagoon	<i>Villorita cyprinoides</i> (soft tissue)	d.w.	2017			0.08	0.87	3.57	17.73	69.23		574.99	5.16	
Catania Fish Market	<i>D. trunculus</i> (composite)	w.w.	2013		1.52	0.005		0.24					4.25	
Marudu Bay	<i>Polymesoda expansa</i> (soft tissue)	d.w.	2017		9.12			6.07	16.6				138.1	
Rias of Pontevedra (A1)	<i>Dosiona exoleta</i> (soft tissue)	d.w.	2006			0.29			8.67					
(A2)		d.w.				0.25			9.13					
(A4)		d.w.				0.75			16.10					
Kuala Kemaman, Terengganu, Coastline of India	<i>Polymesoda expansa</i>	d.w.	2016											
Tanjung Lumpur, Malaysia	<i>Polymesoda aerosa</i>	d.w.	2013											
	<i>Polymesoda expansa</i> (soft tissue)	d.w.	2017											
	NADFC (2018)	w.w.	2018	0.50	0.25	0.10								
	ANZFC	w.w.	2000	0.5	1	2								
	JECFA/WHO	w.w.	2016	0.5		2								

Table 3. Comparison of heavy metal concentrations in muscle tissue and digestive contents of *P. reticulata* from Lancang Island and *Veniridae* clams in other area (metal concentration in mg/kg; dry weight (d.w.) or wet weight (w.w.) basis; bold indicated exceeding maximum limit from NADFC 2018) (*Continued*)

Site	Species		Year	Ni	Pb	Sb	Se	Sr	Ti	Tl	V	Zn	Ref.
Lancang Island, Indonesia	<i>Periglypta reticulata</i> (muscle)	w.w.	2018	0.26	0.04	nd	0.44	9.45	0.22	0.03	1.19	4.93	This study
	<i>P. reticulata</i> (digestive)	w.w.	2018	0.46	0.19	nd	0.66	19.26	2.57	0.03	0.30	8.76	This study
Catania Gulf	<i>D. trunculus</i> (composite)	w.w.	2012	0.33	0.07								[14]
Cochin Area	<i>Villorita crypinoides</i> (composite)	w.w.	2011	0.34	0.68							40	[26]
Shanghai	<i>Mactra chinensis</i> (composite)	d.w.	2008		0.13							14.8	[16]
Bohai Bay	<i>Mactra veneriformis</i> (soft tissue)	w.w.	2008	1.00	0.37	0.04	1.26					11.57	[17]
Parit Jawa, Johor	<i>Polymesoda erosa</i> (total tissue)	d.w.	2009	5.07	17.9							67.1	[27]
Parit Jawa, Johor	<i>Polymesoda erosa</i> (foot)	d.w.	2009		2.18							92.1	[27]
Parit Jawa, Johor	<i>Polymesoda erosa</i> (gill)	d.w.			2.56							263	[27]
Telok Mas, Mallaca	<i>Polymesoda erosa</i> (total tissue)	d.w.	2009	4.29	6.80							343	[27]
Telok Mas, Mallaca	<i>Polymesoda erosa</i> (foot)	d.w.	2009		0.937							105	[27]
Telok Mas, Mallaca	<i>Polymesoda erosa</i> (gill)	d.w.	2009		6.51							263	[27]
Coast of New Caledonia	<i>Gafrarium tumidum</i> (soft tissue)	w.w.	2008										[28]
Coast of New Caledonia	<i>Periglypta chemnitzii</i> (soft tissue)	w.w.	2008										[28]
Astamudi Lagoon	<i>Villorita cyprinoides</i> (soft tissue)	d.w.	2017	2.42	1.46							76.79	[29]
Catania Fish Market	<i>D. trunculus</i> (composite)	w.w.	2013	0.32	0.07							7.62	[14]
Marudu Bay	<i>Polymesoda expansa</i> (soft tissue)	d.w.	2017	5.71	2.31							377.1	[22]
Rias of Pontevedra (A1)	<i>Dosiona exoleta</i> (soft tissue)	d.w.	2006		4.65							203	[30]
		d.w.			2.45							176	[30]
		d.w.			7.89							301	[30]
Kuala Kemaman, Terengganu,	<i>Polymesoda expansa</i>	d.w.	2016		6.9				15.9			12.8	[34]
Coastline of India	<i>Polymesoda aerosa</i>	d.w.	2013	14	1.1							91.7	[35]
Tanjung Lumpur, Malaysia	<i>Polymesoda expansa</i> (soft tissue)	d.w.	2017		1.94							269	[36]
	NADFC (2018)	w.w.	2018		0.20								[31]
	ANZFC	w.w.	2000		2								[32]
	JECFA/WHO	w.w.	2016										[33]

Sr, Pb ($p < 0.05$) and As, Co, Ni ($p < 0.01$). Cd had only a significant correlation with Se in the muscle ($p < 0.05$), whereas Pb was negatively correlated with V in muscle but had a strong correlation between essential metals, Fe, Ni ($p < 0.05$) and Co ($p < 0.01$) in digestive. Arsenic had strong correlations with Co, Ni, Sr ($p < 0.05$), and Cd in digestive but only had a positive correlation with Co in muscle. Mercury (Hg) also had a strong association with Co, Ni, Sr ($p < 0.05$) and with As and Cd ($p < 0.01$) in digestive but only strongly influenced As in muscle. Alonso et al. reported that there was a significant correlation between metal and essential metal, for example, Cd and was positively associated with most of the essential metals analyzed in the digestive, the organ that accumulates in higher concentrations, compared to muscle [25]. These interactions probably indicate that essential metals for homeostatic mechanisms in organisms, to regulate mineral balance in the body, could be interfered with or competed with toxic elements. This fact would bring a threat to the normal function of metal in the body. So, monitoring of toxic metals in the main compartment like sediment that transfers metals into marine organisms should be done regularly and intensively [26].

■ CONCLUSION

This study investigated the concentrations of nineteen metals in muscle tissues and digestive contents of *P. reticulata* from Lancang Island, part of Seribu Islands. Concentrations of total Arsenic in muscle and digestive were found to exceed permissible limit from the National Agency of Drug and Food Control. Cadmium, Lead, and Mercury have shown under the permissible limit in muscle tissues and digestive contents, but Cd and Pb in the digestive contents should be a concern because it nearly reaches permissible limit from NADFC. Toxic metals (Pb, Hg, Cd, and As) showed strong correlations with several essential metals, so monitoring for particular metals must be done intensively. Because of the high accumulation in digestive content, the elimination of this part was suggested when consuming this clam to reduce bioaccumulation of heavy metals in the human body.

■ ACKNOWLEDGMENTS

This research was financially funded by Demand Driven Research Grant (DDRG LIPI - COREMAP CTI) No: B-1191/IPK.2/KS.02/III/2018 the fiscal year 2018. The authors also acknowledge the financial support from *Riset Prioritas* COREMAP-CTI No.: B-5006/IPK.2/KP.06/I/2019 year fiscal 2019 for the publication support.

■ AUTHOR CONTRIBUTION

S as main contributor responsible for on data analysis, and drafted the manuscript. RP and ZP executed sampling and drafted the manuscript, while NS performed laboratory analysis.

■ REFERENCES

- [1] Tchounwou, P.B., Yedjou, C.G., Patlolla A.K., and Sutton, D.J., 2012, Heavy metal toxicity and environment, *Exp. Suppl.*, 101, 133–164.
- [2] WHO/FAO/IAEA, 1996, *Trace elements in human nutrition and health*, World health organization, Geneva, Switzerland.
- [3] Chang, L.W., Magos, L., and Suzuki, T., 1996, *Toxicology of Metals*, CRC Press, Boca Raton, FL, USA, 233–254.
- [4] Inoue, K.I., 2013, Heavy metal toxicity, *J. Clin. Toxicol.*, S3, 007.
- [5] Ibrahim, N.K., and Abu El-Regal, M.A., 2014, Heavy metals accumulation in marine edible molluscs, Timsah Lake, Suez Canal, Egypt, *ARPJ. Sci. Technol.*, 4 (4), 282–288.
- [6] Hu, S., Su, Z., Jiang, J., Huang, W., Liang, X., Hu, J., Chen, M., Cai, W., Wang, J., and Zhang, X., 2016, Lead, cadmium pollution of seafood and human health risk assessment in coastline of the southern China, *Stochastic Environ. Res. Risk Assess.*, 30 (5), 1379–1386.
- [7] Langston, W.J., Bebianno, M.J., and Burt, G.R., 1998, “Metal handling strategic in mollusk” in *Metal Metabolism in Aquatic Environments*, Eds. Langston, W.J., and Bebianno, M.J., Chapman & Hall, London, 219–283.

- [8] Abdallah, M.A.M., and Abdallah, A.M.A., 2008, Biomonitoring study of heavy metals in biota and sediments in South Eastern coast of Mediterranean sea, Egypt, *Environ. Monit. Assess.*, 146, 139–145.
- [9] Richard, G.P., 1988, Microbial purification of shellfish: A review of depuration and relaying, *J. Food Prot.*, 51 (3), 218–251.
- [10] Shirnesan, G., Bakhtiari, A.R., Seyfabadi, S.J., and Mortazavi, S., 2013, Environmental geochemistry of Cu, Zn and Pb in sediment from Qeshm Island-Persian Gulf, Iran: A comparison between the northern and southern coast and ecological risk, *Geochem. Int.*, 51 (8), 670–676.
- [11] Dsikowitzky, L., Dwiytino, Heruwati, E., Ariyani, F., Irianto, H.E., and Schwarzbauer, J., 2014, Exceptionally high concentrations of the insect repellent *N,N*-diethyl-*m*-toluamide (DEET) in surface waters from Jakarta, Indonesia, *Environ. Chem. Lett.*, 12 (3), 407–411.
- [12] SNI, 2006, *Cara uji kimia-bagian 2: Penentuan kadar air pada produk perikanan*, Badan Standardisasi Nasional-BSN, Jakarta, 1–12.
- [13] USEPA, 2007, *Method 3051A: Microwave assisted acid digestion of sediments, sludge, soils, and oils*, <https://www.epa.gov/sites/production/files/2015-12/documents/3051a.pdf>.
- [14] Copat, C., Arena, G., Fiore, M., Ledda, C., Fallico, R., Sciacca, S., and Ferrante, M., 2013, Heavy metals concentrations in fish and shellfish from eastern Mediterranean Sea: Consumption advisories, *Food Chem. Toxicol.*, 53, 33–37.
- [15] Sivaperumal, P., Sankar, T.V., and Viswanathan Nair, P.G., 2007, Heavy metal concentrations in fish, shellfish and fish products from internal market of India vis-à-vis international standards, *Food Chem.*, 102 (3), 612–620.
- [16] Lei, B.L., Chen, L., Hao, Y., Cao, T.H., Zhang, X.Y., Yu, Y.G., and Fu, J.M., 2013, Trace elements in animal-based food from Shanghai markets and associated human daily intake and uptake estimation considering bio accessibility, *Ecotoxicol. Environ. Saf.*, 96, 160–167.
- [17] Li, Y., Liu, H., Zhou, H., Ma, W., Han, Q., Diao, X., and Xue, Q., 2015, Concentration distribution and potential health risk of heavy metals in *Macra veneriformis* from Bohai Bay, China, *Mar. Pollut. Bull.*, 97 (1-2), 528–534.
- [18] Peto, M.V., 2010, Aluminium and iron in humans: Bioaccumulation, pathology and removal, *Rejuvenation Res.*, 13 (5), 589–598.
- [19] Dhanakumar, S., Solaraj, G., and Mohanraj, R., 2015, Heavy metals partitioning in sediments and bioaccumulation in commercial fish species of three major reservoirs of river cauvery delta region, India, *Ecotoxicol. Environ. Saf.*, 113, 145–151.
- [20] Moiseenko, T.I., and Kurdyasvtseva, L.S., 2001, Trace metal accumulation and fish pathologies in area affected by mining and metallurgical enterprises in the Kola Region, Russia, *Environ. Pollut.*, 114 (2), 285–297.
- [21] Waykar, B., and Deshmukh, G., 2012, Evaluation of bivalves as bio indicators of metal pollution in fresh water, *Bull. Environ. Contam. Toxicol.*, 88, 48–53.
- [22] Harsono, N.D.B.D., Ransangan, J., Denil, D.J., and Soon, T.K., 2017, Heavy metals in marsh clam (*Polymesoda expansa*) and green mussel (*Perna viridis*) along the northwest coast of Sabah, Malaysia, *Borneo J. Mar. Sci. Aquacult.*, 01, 25–32.
- [23] Liu, J., Cao, L., and Dou, S., 2017, Bioaccumulation of heavy metals and health risk assessment in three benthic bivalves along the coast of Laizhou Bay, China, *Mar. Pollut. Bull.*, 117 (1-2), 98–110.
- [24] Wei, H., Hou, L., Cui, Y., and Wei, Y., 2018, Effect of Ti content on corrosion behavior of Cu-Ti alloys in 3.5% NaCl solution, *Trans. Nonferrous Met. Soc. China*, 28 (4), 669–675.
- [25] Alonso, M.L., Montaña, F.P., Miranda, M., Castillo, C., Hernández, J., and Benedito, J.L., 2004, Interactions between toxic (As, Cd, Hg and Pb) and nutritional essential (Ca, Co, Cr, Cu, Fe, Mn, Mo, Ni, Se, Zn) elements in the tissues of cattle from NW Spain, *BioMetals*, 17, 389–397.
- [26] Kalogeropoulos, N., Karavoltos, S., Sakellari, A., Avramidou, S., Dassenakis, M., and Scoullou, M.,

- 2012, Heavy metals in raw, fried and grilled Mediterranean finfish and shellfish, *Food Chem. Toxicol.*, 50 (10), 3702–3708.
- [27] Edward, F.B., Yap, C.K., Ismail, A., and Tan, S.G., 2009, Interspecific variation of heavy metal concentrations in the different parts of tropical intertidal bivalves, *Water Air Soil Pollut.*, 196, 297–309.
- [28] Chouvelon, T., Warnau, M., Churlaud, C., and Bustamante, P., 2009, Hg concentrations and related risk assessment in coral reef crustaceans, molluscs and fish from New Caledonia, *Environ. Pollut.*, 157 (1), 331–340.
- [29] Ragi, A.S., Leena, P.P., Cheriyan, E., and Nair, S.M., 2017, Heavy metal concentrations in some gastropods and bivalves collected from the fishing zone of South India, *Mar. Pollut. Bull.*, 118 (1-2), 452–458.
- [30] Sánchez-Marín, P., and Beiras, R., 2008, Lead concentrations and size dependence of lead accumulation in the clam *Dosinia exoleta* from shellfish extraction areas in the Galician Rias (NW Spain), *Aquat. Living Resour.*, 21 (1), 57–61.
- [31] NADFC, 2018, *Batas maksimum cemaran logam berat dalam pangan olahan*, Peraturan Badan Pengawas Obat dan Makanan No. 5, Jakarta, 1–15.
- [32] ANZFC, 2012, *Standard 1.4.1. Contaminants and natural toxicants*, Australia New Zealand Food Standards Code, 1–7, <https://www.legislation.gov.au/Details/F2011C00542/Download>.
- [33] CODEX ALIMENTARIUS, 2016, General standard for contaminants and toxin in food and feed, CODEX STAND 193-1995, 1–65.
- [34] Dabwan, A.H.A., and Taufik, M., 2016, Bivalves as bio-indicators for heavy metals detection in Kuala Kemaman, Terengganu, Malaysia, *Indian J. Sci. Technol.*, 9 (9), 88708.
- [35] Gawade, L., Chari, N.V.H., Sarma, V.V., and Ingole, B.S., 2013, Variation in heavy metals concentration in the edible oyster *Crassostrea madrasensis*, clam *Polymesoda erosa* and grey mullet *Liza aurata* from coastline of India, *Indian J. Sci.*, 2 (4), 59–63.
- [36] Chuan, O.M., and Ibrahim, A., 2017, Determination of selected metallic elements in marsh clam, *Polymesoda expansa*, collected from Tanjung Lumpur Mangrove Forest, Kuantan, Pahang, *Borneo J. Mar. Sci. Aquacult.*, 01, 65–70.

Proteins Pre-concentration Using Glycidyl Methacrylate-co-stearyl Methacrylate-co-ethylene Glycol Dimethacrylate Monolith

Ahmed Ali Alkarimi^{1,*} and Kevin Welham²

¹Department of Chemistry, College of Science, University of Babylon, Hilla 51002, Iraq

²Department of Chemistry, Faculty of Science and Engineering, University of Hull, Cottingham Road, Hull HU6 7RX, United Kingdom

*** Corresponding author:**

tel: +964-7803717179

email: sci.ahmed.alkarimi@gmail.com

Received: September 16, 2019

Accepted: December 4, 2019

DOI: 10.22146/ijc.49479

Abstract: Solid-phase extraction technique is considered as a vital tool in a pre-treatment of different samples. Therefore, it was used as a beneficial and alternative extraction method over the liquid-liquid extraction in diverse applications such as food, environmental, and biological analyses. Glycidyl methacrylate-co-stearyl methacrylate-co-ethylene glycol dimethacrylate (GMA-co-SMA-co-EDMA) monolithic sorbent was prepared as strong cationic-reversed phase sorbent for solid-phase extraction of different proteins. The monolithic sorbent was prepared inside two moulds such as glass microchip device and borosilicate. The morphological properties have been investigated using the Brunauer-Emmett-Teller (BET) model analyzer and scanning electron microscope (SEM), and the formation of the monolithic sorbent was examined using the FT-IR. Eight proteins (cytochrome C, insulin, myoglobin, lysozyme, β -lactoglobulin, trypsin, albumin chicken egg white, and apo-transferrin) with different molecular weight and isoelectric point were investigated for pre-concentration using the SCX/RP sorbent. It was found that the highest extraction recovery was obtained with three proteins cytochrome C, lysozyme, and myoglobin compared with the other proteins. These three proteins were chosen for pre-concentration using the glass microchip. Sorbent performance showed significant results in terms of stability and reproducibility.

Keywords: stearyl methacrylate; solid-phase sorbent; glycidyl methacrylate; extraction

■ INTRODUCTION

Solid-phase extraction was used as a beneficial and alternative extraction method. Therefore, it has been used in laboratories for concentrating and purifying different samples. In addition, it could be used for cleaning-up or isolating a wide range of analytes in the matrices such as animal tissue, blood, beverage, water, urine and soil [1-3].

Liquid-solid extraction media were invented in the mid of 1970s. Meanwhile, the extraction methodology was published firstly in 1998. Since then, many further developments have been applied to form the SPE cartridges or disks in addition to newer sorbents, such as molecularly imprinted polymers (MIPs), and immunosorbents (IMs) [4]. Similar to the developments in the sorbent and materials, the solid phase extraction technique over the last few years has been developed and

modified, toward automation and miniaturization. According to the Environmental Protection Agency (EPA), this technique has been accepted and used for more than two decades as an alternative procedure for sample preparation over the liquid-liquid extraction technique for the determination of various organic compounds in waste and drinking water [5-6].

The principle of SPE is based on a partitioning of a sample between the liquid mobile phase and the solid stationary phase. Therefore, the extraction occurs when the sample has a high affinity for the solid phase compared with the sample matrix. The samples will be retained on the solid phase and can be eluted at a later stage using an appropriate solvent(s) that has a higher affinity for the sample in the desorption step [7]. The intermolecular forces between the sample and the active

sites on the sorbent surface, besides, the solid phase nature (hydrophobic RP, hydrophilic NP, ion-exchange IE) could determine the retention mechanism of the extraction process [8]. However, different mechanisms for elution or retention may occur, and these mechanisms are similar to those in column liquid chromatography mechanism. So far, the partitioning mechanism and/or adsorption mechanism are demonstrated to be the suitable mechanism for solid-phase extraction [1,8].

SPE sorbents should have some properties to achieve significant results, such as high contact surface area to increase the loading ability, selectivity, and reduce the risk of losing the target analyte. In addition, they should have high stability toward elevated temperature and solvents that used in the extraction steps. Moreover, an excellent permeability to reduce the analysis time and backpressure when high flow is applied, are required. And they do not degrade during the storage periods [9-10].

Nowadays, there are a variety of solid-phase extraction sorbents that have been used according to the analyte target. Several examples of these sorbents are, (i) silica based; such as octadecyl bonded silica, octyl bonded silica, and butyl dimethyl bonded silica, and (ii) copolymers or crosslinked polymers depending on the sorbent material properties, which can be hydrophobic, hydrophilic, ion exchange, and mixed-mode copolymers [11].

Monolithic materials were used in the last decades as an innovative and valued generation of polymers that could be utilized in a wide range of applications. However, they could be prepared easily inside mold (s) that contain a heterogeneous or homogenous mixture. Monolithic materials morphology can be seen as a large interconnected pores or channels, consequently, these channels permit using high flow rates with suitable back pressures [12]. The appropriate surface area with significant convective mass-transfer led to consider the organic monolithic materials as ideal media to separate large molecules, for example, proteins, peptides, nucleic acids, and synthetic polymers [13-16].

The key factor for significant extraction is choosing appropriate solid phase materials. Currently, SPE materials could be selected based on the properties of the sample and the sorbent for retaining the interested sample

or analyte and eluting the interfering materials [17]. This work aims to prepare a solid-phase sorbent based on a monolithic polymer that was investigated using in situ polymerization inside a glass microchip and borosilicate tube for pre-concentration of proteins.

■ EXPERIMENTAL SECTION

Materials

All chemicals were purchased from Sigma-Aldrich, Poole, UK, and Fisher Scientific, Loughbrouh 3-(trimethoxysilyl) propylmethacrylate (γ -MAPS), glycidyl methacrylate, stearyl methacrylate, ethylene glycol dimethacrylate, proteins, 2,2-dimethoxy-2-phenyl acetophenone, ammonium acetate, acetonitrile, sodium phosphate dibasic, 1-propanol, methanol, acetic acid, Acetone, sodium hydroxide, hydrochloric acid. Milli-q water 18 m Ω was used in all experiments.

Stainless steel union 1/8" to 1/16" adapter (Kinesis, Cambs, UK), borosilicate tube (1.5 mm I.D and 3.0 mm O.D) (Smith Scientific, Kent, UK), polyetheretherketone (PEEK) tubing (Thames Restek Ltd., Saunderton, UK), microtight adapter (Kinesis, Cambs, UK), glass syringe (SGE, Kinesis, Cambs, UK), glass microchip B-270 crown glass (SKAN) UK were used for the preparation of the SPE sorbent.

Instrumentation

The instruments used were FT-IR 380 spectra (Thermo Scientific, Hemel Hempstead, UK), syringe pump (Bioanalytical System Inc., USA), scanning electron microscope images (Zeiss EVO 60 USA), UV light lamp (Cambridge UK), stirrer VWR (West Chester, PA, USA), HPLC-UV system (20 A Shimadzu, USA), Brunauer-Emmett-Teller (BET) model (Surface Area and Porosity Analyser, Micromeritics Ltd., DunsTable, UK), C4 phenomenex aeris wide pore column, 2.1 \times 100 mm packed with silica particles (size 3.6 μ m) (USA).

Procedure

Fabrication of the monolithic materials

Silanization step [18]. In the first step, the molds were washed with acetone, then by water. After that, the activation of the inner surface of the molds was achieved by pumping the sodium hydroxide solution (0.2 M) at

5.0 $\mu\text{L min}^{-1}$ for 1 h using a syringe pump, then purged with water. Hydrochloric acid solution (0.2 M) was pumped at 5.0 $\mu\text{L min}^{-1}$ for 1 h, then flushed with water and ethanol. The final step was silanized the molds using 3-(trimethoxysilyl) propylmethacrylate (γ -MAPS) 20% in ethanol at pH of 5.0 that was adjusted with acetic acid through pumping at 5.0 $\mu\text{L/min}$ for 1 h. The molds were dried with nitrogen gas and left for 12 h; then, the molds will be ready for in-situ polymerization.

In-situ polymerization of the monolith [19]. The photo polymerization reaction was utilized to investigate the formation of the monolith inside the molds at room temperature. The preparation method was based on Ueki et al. [19] method with some modifications. The polymerization mixture contains two monomers of stearyl methacrylate and glycidyl methacrylate with the ratio of 70:30. The crosslinker used was ethylene glycol dimethacrylate, while 2,2-dimethoxy-2-phenyl acetophenone was used as an initiator (0.1% corresponding to the monomers).

The binary porogenic solvent consisted of methanol and 1-propanol was used with the ratio of 40:60, respectively, to dissolve monomers, crosslinker, and initiator. After dissolving all the components, an ultra-wave sonicator was used to sonicate the mixture for 10 min. The next step was removing the oxygen from the mixture by purging with nitrogen stream for 5 min.

The molds were filled with the polymerization mixture using a syringe then closed from both sides and exposed to UV light lamp for UV polymerization at 365 nm for anticipated irradiation time (23 min for borosilicate tube and 18 min for microchip). The final step was flushing the polymer with ethanol followed by water to eliminate any residual starting materials.

Solid-phase extraction for pre-concentration

The prepared monolithic sorbent was used for pre-concentration of proteins. However, the performance of the monolithic sorbent was evaluated using albumin from chicken egg white cytochrome C from bovine heart, human insulin, myoglobin from horse heart, β -lactoglobulin from bovine milk, apo-transferrin human, and lysozyme from the chicken egg white. All the proteins used were standard proteins. 10 μM of each protein was

prepared by dissolving in 100 mM ammonium acetate at room temperature around 20 $^{\circ}\text{C}$.

The procedure of the pre-concentration was based on the methods published elsewhere [20] with some modifications. Initially, the monolithic sorbent was conditioned by pumping 500 μL acetonitrile. After that, it was equilibrated using 500 μL sodium phosphate dibasic at a suitable pH for each protein. The next step was loading the protein sample by pumping 500 μL of proteins, and then the solid phase sorbent was washed with 500 μL milli-q water. The final step was eluting the protein using 250 μL 30:70 acetonitrile and sodium phosphate dibasic.

Microchip devise for pre-concentration

The microchip has been fabricated for pre-concentration of proteins. The design of the chip contains three glass layers with the thickness of each layer is 3 mm, while the length and width are 30 and 15 mm, respectively.

The first layer consists of a channel with the dimension of 1 mm width, 5 mm length, and 150 mm depth. In addition, it contains two access holes with a diameter of 1.5 mm. The second layer consists of the hole with the diameter of 6.5 mm and 1 mm in depth. The third layer consists of a channel with 5 mm length and 1 mm width, and 150 mm with two access holes (1.5 mm). All the layers have been prepared thermally using a custom-made oven at 585 $^{\circ}\text{C}$ for 3 h.

■ RESULTS AND DISCUSSION

Investigation of Strong Cationic Exchange/Reversed Phase Sorbent for Pre-concentration of Proteins

Organic monolith could be regarded as appropriate sorbent materials because these materials do not need frit

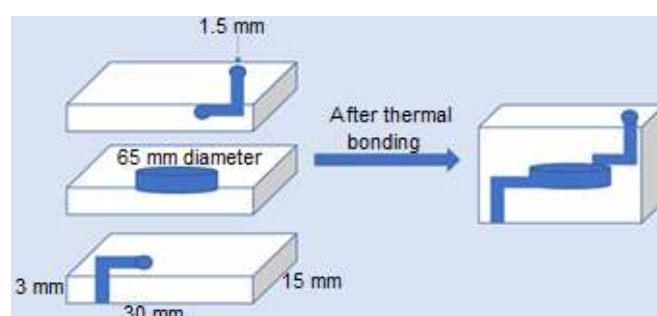


Fig 1. Microchip devise for pre-concentration

fabrication or packing. In addition, they are easily prepared. Therefore, the prepared solid-phase sorbent was changed to strong cationic exchange/reversed phase (SCX/RP) sorbent by sulfonation of epoxy ring [21] on the surface of the monolith. The FT-IR technique was used to characterize the formation of the monolith and open epoxy ring and the transformation to SO_3Na group, which could be utilized for strong cationic exchange. From the FT-IR spectrum, it can be noticed that several main prominent peaks could be used to confirm the formation of the monolithic sorbent as summarized in Table (1).

The prepared sorbent was for the pre-concentration of proteins. As mentioned elsewhere, the organic monoliths do not suffer from residual silanol interaction problems; consequently, it could be used over the wide pH range [23]. Therefore, the SCX/RP monolithic columns were used for the pre-concentration of the proteins with high pH value according to the pI of the protein. So far, the interfering materials could be removed, and lower detection limits could be achieved.

The Morphological Properties of the SCX/RP Sorbent

The morphological properties for the SCX/RP sorbent have been investigated using a SEM and BET analyzer. The data exhibited that the solid phase sorbent has an average surface area of $71 \text{ m}^2/\text{g}$. This surface area could provide sufficient interactions between proteins and the functional groups on the sorbent surface due to the micro and mesopores. In addition, the average pore size was 8.13 nm , which allows the sample molecules to move through the sorbent with a suitable backpressure. The morphology of the sorbent is shown in Fig. 2.

Pre-Concentration of Proteins Using Solid Phase Sorbent that was Fabricated inside the Borosilicate Tube

The SCX/RP monolithic sorbent has been used for pre-concentration of proteins. Eight standard proteins that differ in molecular weight and isoelectric point (pI), as shown in Table 2, have been used for the pre-concentration study.

The pre-concentration method was adapted from the method published elsewhere [26]. The process consisted of several different steps. Initially, conditioning of the sorbent was performed by pumping $500 \mu\text{L}$ acetonitrile using syringe pump and discard it. This process was followed by equilibrating with $500 \mu\text{L}$ of 55 mM Na_2HPO_4 at suitable pH for each protein. The next step was loading the sample by pumping $600 \mu\text{L}$ of proteins. After that, the sorbent was washed using $500 \mu\text{L}$ of milli-q water. The Final step was eluting the proteins using $300 \mu\text{L}$ of $20:80 \text{ ACN}$ ($0.1\% \text{ TFA}$)/ Na_2HPO_4 . The flow rate was $10 \mu\text{L min}^{-1}$ for all the steps except the sample loading step which was $5 \mu\text{L min}^{-1}$ to allow more time for proteins to interact with the sorbent.

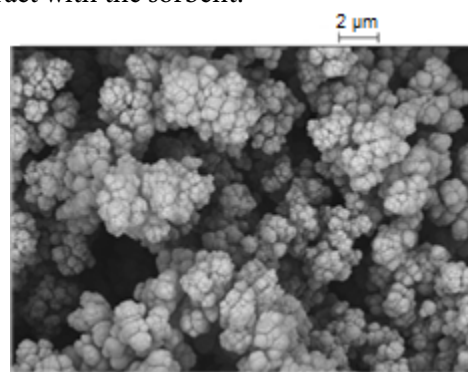


Fig 2. SEM images of the sorbent

Table 1. The FT-IR data for the main peaks of the co-polymer and the monomers before and after ring opening reaction

Monomers/Polymers	C=O [22]	C=C [22]	Epoxy group [22]	R-SO ₃ [23]	S-O [24]	-OH [25]
GMA [22]	1717.53 cm^{-1}	1637.94 cm^{-1}	907.79 cm^{-1}			
SMA [22]	1720.59 cm^{-1}	1639.13 cm^{-1}				
EDMA [22]	1716.89 cm^{-1}	1637.86 cm^{-1}				
GMA-co-SMA-co-EDMA polymer	1726.41 cm^{-1}	Disappeared	910.07 cm^{-1}			
Formation of SCX/RP monolithic sorbent	1724.34 cm^{-1}	Disappeared	Disappeared	1032.23 cm^{-1}	995.96 cm^{-1}	$3600-3100 \text{ cm}^{-1}$

Table 2. Standard proteins utilized in the pre-concentration analysis

No.	Proteins	Isoelectric point	Molecular weight (Da)
1	Apo-Transferrin	5.8	80000
2	Albumin chicken egg white	5.3	42700
3	Trypsin	4.5	23300
4	β -Lactoglobulin	5.3	18363
5	Myoglobin	6.8	17199
6	Lysozyme	11.35	14307
7	Cytochrome C	10.2	12384
8	Insulin	5.3	5805

The efficiency of protein pre-concentration has been investigated depending on the extraction recovery percentage. HPLC-UV system was used to calculate the peak area of protein before and after pre-concentration, and then, to calculate the extraction recovery (ER) % as shown in Eq. (1):

$$\text{Extraction recovery (\%)} = (I_{\text{eluent}}/I_{\text{total}}) \times 100 \quad (1)$$

where I_{eluent} is the peak area of eluted protein, and I_{total} is the peak area of injected protein before pre-concentration. The result of the extraction recovery for each protein is shown in Table (3).

It can be seen from Table 3 that the extraction recovery was varied for each protein. However, cytochrome C, lysozyme, and myoglobin have a higher extraction recovery compared with other proteins. Basically, the mechanism of interactions is strong cationic and reverse phase interactions. Eventually, the electrostatic interaction will be more significant over other interactions, because the charged molecules have stronger electrostatic interactions in ion exchange chromatography and can be operated longer over the distances than other interactions. Cytochrome C, lysozyme, and myoglobin, according to Table 3 have higher pI value; therefore, these proteins could interact with the ionic exchanger more than other proteins due to higher charge density of these proteins. Therefore, more samples could interact with the solid phase sorbent and released the unwanted materials from the sample. Consequently, when these proteins are eluted in less solvent volume, the peak area will increase. The cytochrome C chromatograms before and after pre-concentration are shown in Fig. 3 and 4.

It can be seen from the two figures that the peak intensity after the pre-concentration process increased, which indicates that SCX/RP sorbent could be used to purify, and pre-concentrate of cytochrome C. Cytochrome C was used as an example because it has higher extraction recovery compared with other proteins.

Table 3. Proteins extraction recovery using SCX/RP sorbent that fabricated inside borosilicate tube (n = 3)

Proteins	Extraction recovery (%)
Insulin	28.42
Cytochrome C	86.76
Lysozyme	79.64
Myoglobin	68.13
β -Lactoglobulin	47.93
Trypsin	44.88
Albumin chicken egg white	49.41
Apo-Transferrin	35.83

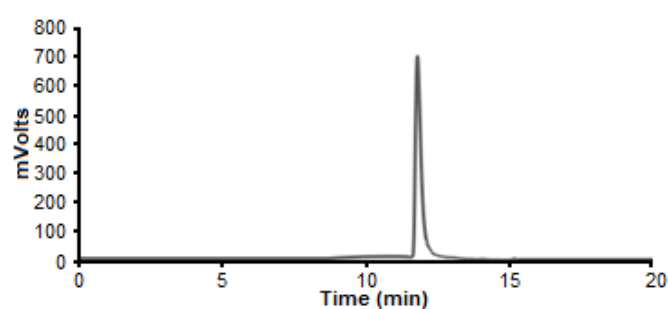


Fig 3. Cytochrome C chromatogram before injection to the SCX/RP sorbent using HPLC UV system (20 A Shimadzu, USA), wide pore column C4 phenomenex aeris, 2.1 \times 100 mm packed with silica particles (size 3.6 μ m), purified water/acetonitrile in the presence of 0.1% (TFA) was used as a mobile phase using gradient analysis, 0.2 mL min⁻¹ flow rate, sample injection volume (20 μ L), and the column temperature 40 $^{\circ}$ C

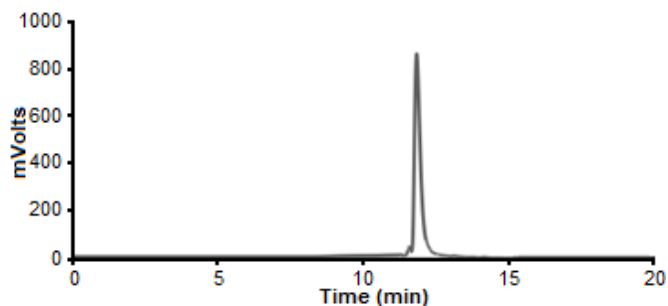


Fig 4. Cytochrome C chromatogram after elution from the SCX/RP sorbent using HPLC UV system (20 A Shimadzu, USA), wide pore column C4 phenomenex aeris, 2.1×100 mm packed with silica particles (size $3.6 \mu\text{m}$), purified water/acetonitrile in the presence of 0.1% (TFA) was used as a mobile phase using gradient analysis, 0.2 mL min^{-1} flow rate, sample injection volume ($20 \mu\text{L}$), and the column temperature $40 \text{ }^\circ\text{C}$

Pre-concentration of Proteins Using Glass Microchip

The monolithic sorbent was fabricated and used as a solid-phase sorbent for proteins pre-concentration inside the glass microchip. The main reason for using the microchip was to reduce the sample and solvent volumes, ultimately lead to reducing the waste. The pre-concentration process was followed the same steps as previously described, yet, the volume of the samples and solvents was reduced.

Three proteins of cytochrome C, lysozyme, and myoglobin were chosen for pre-concentration using a glass microchip because a higher recovery ratio was obtained with these proteins. So far, after conditioning the sorbent by pumping $300 \mu\text{L}$ of acetonitrile using a syringe pump and it was discarded, it was equilibrated with $300 \mu\text{L}$ of $55 \text{ mM Na}_2\text{HPO}_4$ at suitable pH for each protein. The

different volumes of the protein sample, i.e., 200 , 250 , 300 , and $350 \mu\text{L}$ were loaded in each experiment to the solid phase sorbent and washed with $300 \mu\text{L}$ of milli-q water to investigate the maximum loading volume that can be used without losing of protein. The final step was eluting the proteins using $100 \mu\text{L}$ of $20:80 \text{ CAN}$ ($0.1\% \text{ TFA}$)/ Na_2HPO_4 . A flow rate of $12 \mu\text{L min}^{-1}$ was used for all steps, except for the loading step that was $6 \mu\text{L min}^{-1}$.

It was found that $250 \mu\text{L}$ of protein samples was the maximum volume that can be utilized without losing the protein sample. The extraction recovery of the cytochrome C, lysozyme, and myoglobin using the sorbent that investigated inside the glass microchip is shown in Table 4.

It can be seen from Table 4 that the extraction recovery for the three proteins increased compared to the extraction recovery of the same proteins using the borosilicate tube as shown in Table 3. Moreover, it can be concluded that the SCX/RP sorbent prepared inside the glass microchip could be utilized for the pre-concentration of proteins.

The native state of protein before and after the pre-concentration process was investigated using MS spectrometer, the results showed that the protein still in the native state without any change as given in Fig. 5.

Table 3. The extraction recovery ratio for the proteins using SCX/RP sorbent that fabricated inside the glass microchip ($n = 3$)

Proteins	Extraction recovery (%)
Cytochrome C	98.39
Lysozyme	93.15
Myoglobin	90.97

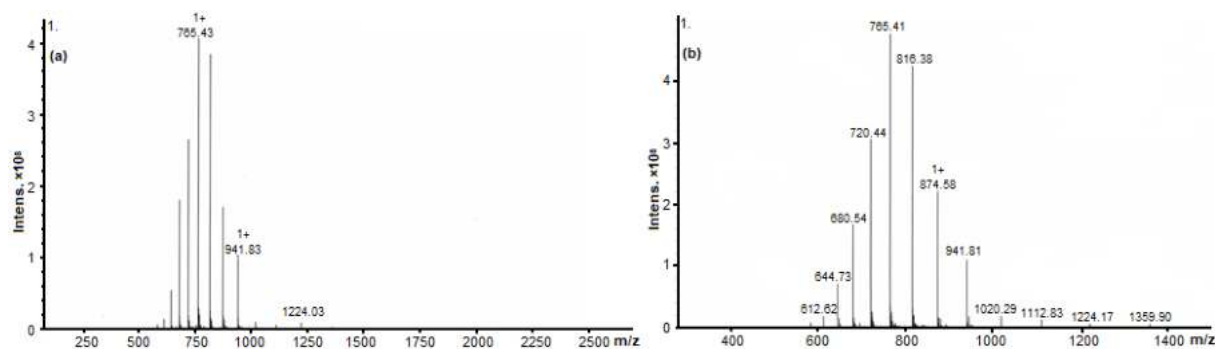


Fig 5. Mass spectra of cytochrome c (a) before and (b) after the pre-concentration process

Evaluation of Monolithic Sorbent Performance in Pre-concentration

The extraction performance for the solid phase sorbent fabricated inside the microchip device was evaluated using the reproducibility and long-term stability. Three proteins that have higher extraction recovery, cytochrome C, lysozyme, and myoglobin, were used in this step. Batch-to-batch reproducibility was calculated by extracting these proteins for three times using a different microchip, while run-to-run reproducibility was evaluated through extracting these proteins for three times utilizing the same microchip. The evaluation results for the solid phase sorbent are shown in Table 5.

It can be seen from Tables 5 that the extraction reproducibility using microchip was achieved due to the acceptable range of RSD% values, which could be due to the low volume of the sample that loaded to the solid phase sorbent. Consequently, it will reduce the extraction error and improve performance.

It was found that the SCX/RP monolithic sorbent could be used for several times due to the stability of the sorbent with the time. Therefore, it could be used for 15 times when it was prepared inside the borosilicate tube. While, it could be utilized for 9 times when it was investigated inside the microchip.

Moreover, the lifetime for the monolithic sorbent was examined. The results showed that it was 20 days for the solid phase sorbent that was prepared inside the borosilicate tube, by calculating the back pressure of the experiment each time. After 20 days, the borosilicate tube was failed to keep the same performance. Therefore, it was not used after 20 days. These results were carried out for the sorbents that were stored in a mixture of water and acetonitrile with the ratio of 50:50.

Table 5. The RSD for the extraction recovery for the batch-to-batch, and for the run-to-run analysis (n = 3)

	RSD (%)		
	Cytochrome C	Myoglobin	Lysozyme
Batch-to-Batch	1.82	3.19	3.02
Run-to-Run	2.13	1.95	2.05

CONCLUSION

A strong cationic/reversed phase monolithic sorbent was successfully prepared inside a glass microchip device and borosilicate using UV polymerization method. The final product was used as a solid phase extraction sorbent for the pre-concentration of proteins. Various proteins with different isoelectric point and molecular weight have been investigated. The results showed that the higher extraction recovery was obtained for three proteins cytochrome C, lysozyme, and myoglobin compared with the other proteins using the sorbent that was prepared inside a borosilicate tube. These three proteins have been chosen for pre-concentration test using the glass microchip. The extraction recovery for these proteins showed a significant increase compared to the same extraction recovery for the same proteins using the borosilicate tube. According to the RSD% value of extraction recovery of proteins using the SCX/RP sorbent that was fabricated inside the glass microchip, it can be concluded that the sorbent can be used for the pre-concentration of proteins.

REFERENCES

- [1] Schley, C., Swart, R., and Huber, C.G., 2006, Capillary scale monolithic trap column for desalting and preconcentration of peptides and proteins in one- and two-dimensional separations, *J. Chromatogr. A*, 1136 (2), 210–220.
- [2] Slabospitskaya, M.Y., Vlach, E.G., Saprykina, N.N., and Tennikova, T.B., 2009, Synthesis and investigation of a new macroporous monolithic material based on an *N*-hydroxyphthalimide ester of acrylic acid-*co*-glycidyl methacrylate-*co*-ethylene dimethacrylate terpolymer, *J. Appl. Polym. Sci.*, 111 (2), 692–700.
- [3] Yu, C., Davey, M.H., Svec, F., and Fréchet, M.J., 2001, Monolithic porous polymer for on-chip solid-phase extraction and preconcentration prepared by photoinitiated in situ polymerization within a microfluidic device, *Anal. Chem.*, 73 (21), 5088–5096.

- [4] Lingeman, H., and Hoekstra-Oussoren, S.J.F., 1997, Particle-loaded membranes for sample concentration and/or clean-up in bioanalysis, *J. Chromatogr. B*, 689 (1), 221–237.
- [5] Ulrich, S., 2000, Solid-phase microextraction in biomedical analysis, *J. Chromatogr. A*, 902 (1), 167–194.
- [6] Arrua, R.D., Moya, C., Bernardi, E., Zarzur, J., Strumia, M., and Igarzabal, C.I.A., 2010, Preparation of macroporous monoliths based on epoxy-bearing hydrophilic terpolymers and applied for affinity separations, *Eur. Polym. J.*, 46 (4), 663–672.
- [7] Armenta, J.M., Gu, B., Humble, P.H., Thulin, C.D., and Lee, M.L., 2005, Design and evaluation of a coupled monolithic pre-concentrator-capillary zone electrophoresis system for the extraction of immunoglobulin G from human serum, *J. Chromatogr. A*, 1097 (1-2), 171–178.
- [8] Wei, Y., Chen, X., Yang, S.C., Lv, Q.H., Ye, F.G., and Zhao, S.L., 2014, Preparation and characterization of polymer solid-phase extraction monolith immobilized metal affinity ligands, *Chin. J. Anal. Chem.*, 42 (4), 495–500.
- [9] Płotka-Wasyłka, J., Szczepańska, N., de la Guardia, M., and Namieśnik, J., 2016, Modern trends in solid phase extraction: New sorbent media, *TrAC, Trends Anal. Chem.*, 77, 23–43.
- [10] Gilart, N., Borrull, F., Fontanals, N., and Marcé, R.M., 2014, Selective materials for solid-phase extraction in environmental analysis, *Trends Environ. Anal. Chem.*, 1, e8–e18.
- [11] Andrade-Eiroa, A., Canle, M., Leroy-Cancellieri, V., and Cerdà, V., 2016, Solid-phase extraction of organic compounds: A critical review (Part I), *TrAC, Trends Anal. Chem.*, 80, 641–654.
- [12] Arrua, R.D., Strumia, M.C., and Alvarez Igarzabal, C.I., 2009, Macroporous monolithic polymers: Preparation and applications, *Materials*, 2 (4), 2429–2466.
- [13] Oberacher, H., and Huber, C.G., 2002, Capillary monoliths for the analysis of nucleic acids by high-performance liquid chromatography–electrospray ionization mass spectrometry, *TrAC, Trends Anal. Chem.*, 21 (3), 166–174.
- [14] Tanaka, N., Nagayama, H., Kobayashi, H., Ikegami, T., Hosoya, K., Ishizuka, N., Minakuchi, H., Nakanishi, K., Cabrera, K., and Lubda, D., 2000, Monolithic silica columns for HPLC, Micro-HPLC, and CEC, *J. High. Resolut. Chromatogr.*, 23 (1), 111–116.
- [15] Trojer, L., Lubbad, H., Bisjak, P., Wieder, W., and Bonn, K., 2007, Comparison between monolithic conventional size, microbore and capillary poly(*p*-methylstyrene-*co*-1,2-bis(*p*-vinylphenyl)ethane) high-performance liquid chromatography columns: Synthesis, application, long-term stability and reproducibility, *J. Chromatogr. A*, 1146 (2), 216–224.
- [16] Jančo, M., Sýkora, D., Svec, F., Fréchet, J.M.J., Schweer, J., and Holm, R., 2000, Rapid determination of molecular parameters of synthetic polymers by precipitation/redissolution high-performance liquid chromatography using “molded” monolithic column, *Journal of Polymer Science Part A: Polymer Chemistry*, 38 (15), 2767–2778.
- [17] Huck, C.W., and Bonn, G.K., 2000, Recent developments in polymer-based sorbents for solid-phase extraction, *J. Chromatogr. A*, 885 (1-2), 51–72.
- [18] Peterson, D.S., Rohr, T., Svec, F., and Fréchet, J.M., 2003, Dual-function microanalytical device by in situ photolithographic grafting of porous polymer monolith: Integrating solid-phase extraction and enzymatic digestion for peptide mass mapping, *Anal. Chem.*, 75 (20), 5328–5335.
- [19] Ueki, Y., Umemura, T., Li, J., Odake, T., and Tsunoda, K., 2004, Preparation and application of methacrylate-based cation-exchange monolithic columns for capillary ion chromatography, *Anal. Chem.*, 76 (23), 7007–7012.
- [20] Alzahrani, S., 2012, Investigation of monolithic materials for protein sample preparation, *Dissertation*, Department of Chemistry, University of Hull, United Kingdom.
- [21] Paul, S., and Rånby, B., 1976, Methyl methacrylate (MMA)-glycidyl methacrylate (GMA) copolymers.

- A novel method to introduce sulfonic acid groups on the polymeric chains, *Macromolecules*, 9 (2), 337–340.
- [22] Safa, K.D., and Nasirtabrizi, M.H., 2006, Ring opening reactions of glycidyl methacrylate copolymers to introduce bulky organosilicon side chain substituents, *Polym. Bull.*, 57 (3), 293–304.
- [23] Wang, L., Su, Y., Zheng, L., Chen, W., and Jiang, Z., 2009, Highly efficient antifouling ultrafiltration membranes incorporating zwitterionic poly([3-(methacryloylamino)propyl]-dimethyl(3-sulfopropyl) ammonium hydroxide), *J. Membr. Sci.*, 340 (1-2), 164–170.
- [24] Liu, Y., and Laskin, A., 2009, Hygroscopic properties of $\text{CH}_3\text{SO}_3\text{Na}$, $\text{CH}_3\text{SO}_3\text{NH}_4$, $(\text{CH}_3\text{SO}_3)_2\text{Mg}$, and $(\text{CH}_3\text{SO}_3)_2\text{Ca}$ particles studied by micro-FTIR spectroscopy, *J. Phys. Chem. A*, 113 (8), 1531–1538.
- [25] Refat, M.S., Ismail, L.A., and Adam, A.M.A., 2013, Synthesis and structural characterization of charge-transfer complexes derived from three symmetrically substituted 4,4'-bis-(1,3,5-triazinylamino)stilbene-2,2'-disulfonate derivatives with some π -acceptors. Part one: Chloranilic acid, *Int. J. Chem. Sci.*, 11 (4), 1647–1658.
- [26] Miyazaki, S., Morisato, K., Ishizuka, N., Minakuchi, H., Shintani, Y., Furuno, M., and Nakanishi, K., 2004, Development of a monolithic silica extraction tip for the analysis of proteins, *J. Chromatogr. A*, 1043 (1), 19–25.

Myristica fragrans Shells as Potential Low Cost Bio-Adsorbent for the Efficient Removal of Rose Bengal from Aqueous Solution: Characteristic and Kinetic Study

**Azal Shakir Waheeb¹, Hassan Abbas Habeeb Alshamsi²,
Mohammed Kassim Al-Hussainawy³, and Haider Radhi Saud^{1,*}**

¹Department of Chemistry, College of Science, University of Al-Muthanna, Al-Samawa, Iraq

²Department of Chemistry, College of Education, University of Al-Qadisiyah, Diwaniya, Iraq

³Directorate of Al Muthanna Education, Al-Samawa, Iraq

*** Corresponding author:**

tel: +964-7822505228

email: hiader.radee@gmail.com

Received: October 2, 2019

Accepted: December 16, 2019

DOI: 10.22146/ijc.50330

Abstract: In the present study, the *Myristica fragrans* shells (MFS) was used as low-cost bio adsorbent for the removal of Rose Bengal (RB) dye from aqueous solutions. The characteristics of MFS powder were studied before and after adsorption using different techniques such as Fourier transform Infrared spectroscopy (FTIR), Thermal Gravimetric Analysis (TGA), BET and BJH surface area analysis, Atomic Force Microscopy (AFM) and Scanning Electron Microscopy (SEM). Batch adsorption was adopted to evaluate the effect of various parameters on the removal of RB such as; time of contact (5–75 min), initial dye concentration (10–50 mg L⁻¹), adsorbent dose (0.1–1.7 g L⁻¹) and pH (3–12). The results revealed that the coverage of MFS surface by RB molecules involved the formation of ester bond (esterification), and the pore diameter decreased from 190.55 to 2.43 nm when adsorption of RB onto MFS surface occurred. Experimental adsorption data were modelled using isotherm models including Langmuir, Freundlich, and Temkin. Temkin isotherm demonstrated to be the best isothermal model, and the results indicate that the adsorption of Rose Bengal on MFS surface follows pseudo second-order kinetics model. The adsorption of dye at different pH media showed that the esterification process was more preferred in acidic solution.

Keywords: *Myristica fragrans*; chemical adsorption; Rose Bengal; isotherms; FESEM; BET

■ INTRODUCTION

The spread of huge quantities of toxic contaminants in surface water and groundwater has a potential effect on human health [1]. There are numerous toxic contaminants found in wastewater such as, heavy metals, Radiological contaminants, synthetic organic and inorganic contaminants (i.e., dyes, pesticides, phenolic compounds, petrochemicals, pharmaceuticals, etc.) [2-5]. Water contaminated with untreated dyes can cause a serious environmental impendence to aquatic and human life [6]. Many type of dyes are non-biodegradable in nature and under anaerobic conditions might decompose into carcinogenic aromatic amines [7]. Rose Bengal dye is a fluorescent compound that is widely used in early-stage

diagnosis of keratoconjunctivitis sicca (KCS) in vivo effect on the human corneal epithelium [8]. Xanthene dyes have toxicity which cause a series of risks on the human health especially by inhibition of human drug-metabolizing enzymes and can cause eye redness and itching [9].

Among waste water treatments such as, ozonation, photochemical degradation, reverse osmosis, membrane separation and coagulation, the adsorption process is the most effective, low cost and most easily available method that has been successfully employed for removing pollutants from the waste water [10]. Kaur et al. used UV light for the degradation of dyes and found that under UV light, very small degradation was observed [11].

Numerous studies have focused on the utilization of natural materials, such as egg shells [12], bean peels [13], and marble waste [14], as adsorbents for the removal of pollutants from aqueous mediums. Activated carbon is the most widely used adsorbent for the removal of dyes from waste water effluents, due to its high capacity for organic compounds, however its application is still limited due to the high cost [15].

Myristica fragrans shell (MFS) is a waste product of the nutmeg industry. In the present study, MFS have been utilized for the removal of toxic materials from water. The adsorption dye on MFS surface was evaluated using different variable parameters. In addition, techniques such as AFM, FESEM, FTIR, BET/BJH, and TGA/DTA were used to elucidate the effect of dye adsorption on the surface characteristics of the adsorbent.

■ EXPERIMENTAL SECTION

Materials

Hydrochloric acid (HCl, 37%), and Sodium hydroxide (NaOH, 99.5%) were purchased from BDH. Rose Bengal ($C_{20}H_2Na_2O_5I_4Cl_4$, Dye content 95%) was purchased from Sigma-Aldrich. The chemical structure of RB dye is present in Fig. 1. It is well-known that RB possess high solubility in water, and its $\lambda_{max} = 549$ nm.

Procedure

Preparation of adsorbent

The MFS powder was obtained from MFS waste, and was ground and sieved through 150 mesh sieve. After sieving, the collected fine powder was washed several times with distilled water to remove contaminants and soluble materials. The clean powder was then dried in an oven at

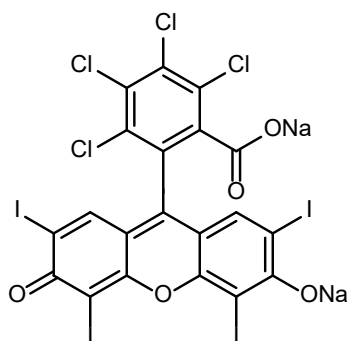


Fig 1. Rose Bengal chemical structure

100 °C for 4 h and it was placed in a desiccator to keep dry until use.

Batch mode adsorption studies

The adsorption studies were done by batch experiments which aimed to determine the adsorption parameters such as contact time initial dye concentration, initial pH solution, and adsorbent dose by changing one parameter under study, while other parameters were set in a fixed value. Different concentrations (10, 20, 30, and 40 ppm) were obtained by successive dilution of a dye stock solution of 50 ppm. Five conical flasks (250 mL) containing 100 mL of dye solution and 1.7 g of MFS surface were stirred on a shaker water bath at the rate of 120 rpm for the required time of equilibrium. The equilibrium concentration of the solution were determined by using UV-Visible technique (Shimadzu, UV-1650PC) at λ_{max} (nm), after separation of the supernatant. The quantity and the removal percentage of the adsorbed dye on the adsorbent at the equilibrium time (q_e) were calculated using Eq. (1) and (2) respectively.

$$q_e = \frac{V(C_0 - C_e)}{m} \quad (1)$$

$$q_e = \frac{V(C_0 - C_e)}{m} \quad (2)$$

where C_0 and C_e are RB concentrations (ppm) at the initial and the equilibrium time, respectively. q_e ($mg\ g^{-1}$), is the amount of RB adsorbed on a fixed adsorbent mass (g) at the time of equilibrium. V is the volume (in L) of the initial RB solution.

Characterization

MFS before and after dye adsorption were characterized by Shimadzu 8400S FTIR with wavenumber range of 400–4000 cm^{-1} at a scan resolution of 4 cm^{-1} . Field emission scanning electron microscope (FESEM, MIRA3 TESCAN) with accelerating voltage 10 kV and angstrom AFM (SPMAA3000) were used to study the surface morphology of MFS surface. Under nitrogen atmosphere at 20 mL/min gas flow rate and heating at the rate of 20 min^{-1} , the thermogravimetric analysis (TGA) was done by Perkin Elmer (TGA 4000). Surface area and pore analysis were carried out using Nova

2000e, (Quantachrome, Instruments Limited, USA) and the methods of the multipoint Brunauer, Emmett, and Teller (BET) method and BJH method.

RESULTS AND DISCUSSION

Characterization of MFS Before and After Adsorption

Functional groups

The FTIR spectrum of MFS before and after dye adsorption are shown in Fig. 2, in which the MFS spectrum shows a broad peak centered at 3385 cm^{-1} due to the intramolecular and intermolecular hydrogen bonding of the $-\text{OH}$, $-\text{NH}_2$ groups. Stretching and bending vibration of the C-H band is shown in the MFS FTIR spectrum at 2930 , 2884 , 1427 , 1381 , and 1321 cm^{-1} . A strong peak located at 1653 cm^{-1} is indexed to the carbonyl group (C=O) stretching vibration, while a weak band with multiple peaks at 1040 , 1123 , 1238 and 1267 cm^{-1} is assigned to alcohols, carboxylic acids and ethers (1000 –

1320 cm^{-1} attributed to C–O stretch) [16]. As reported in the literatures, the carbonyl stretching vibration of free RB is shown at 1614 cm^{-1} [17]. The FT-IR spectra of MFS after dye adsorption shows the carbonyl frequency at wavenumber, 1734 cm^{-1} , which confirms that the dye has been covalently attached to the MFS, and also the formation of an ester bond between alcoholic and carboxylic groups [18]. In addition, a broadband of 3385 cm^{-1} was shifted to higher wavenumber of 3419 cm^{-1} due to the weakness of the MFS intermolecular hydrogen bonding between its molecules after adsorption of the RB dye.

Surface topology

AFM image of the MFS before adsorption is depicted in Fig. 3(a). As AFM technique reveals, the morphology of MFS to be a porous surface with roughness average of about 5.35 nm and surface skewness of about -0.234 . Fig. 3(b) depicts the AFM images of the

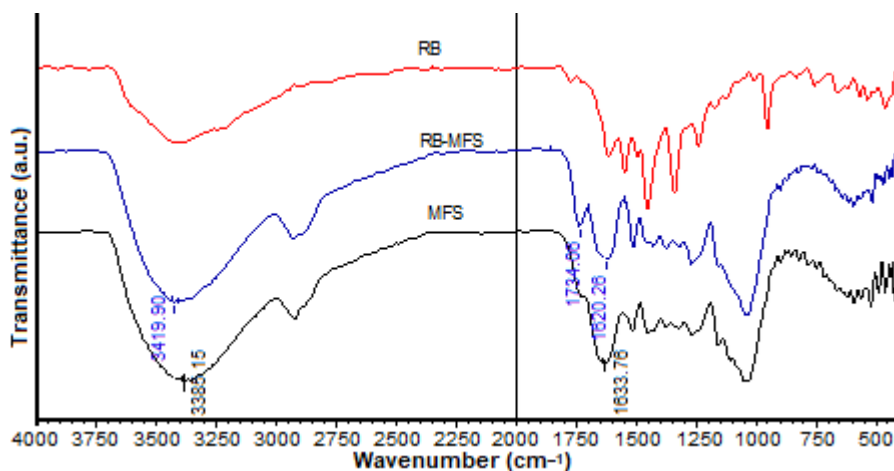


Fig 2. FTIR spectra of RB dye and MFS before and after dye adsorption

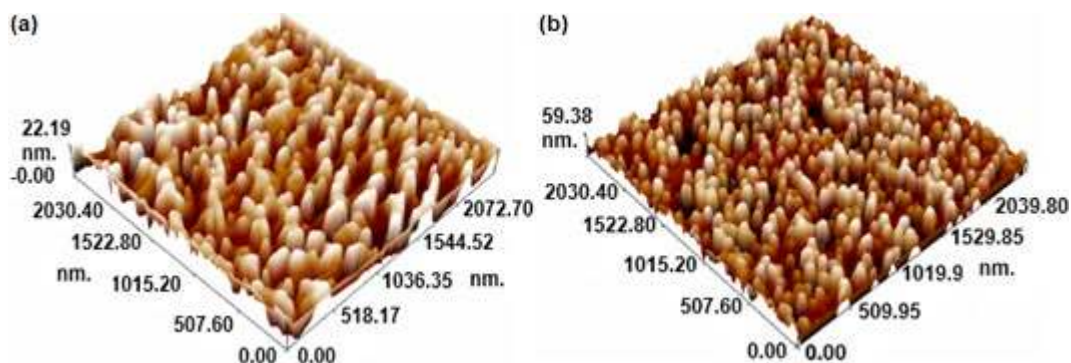


Fig 3. AFM images of MFS (a) before) and (b) after dye adsorption

MFS after adsorption of the dye. Dye adsorption causes the lowering of porosity of the MFS surface and increasing of thickness in comparison with the state before adsorption. The AFM rough analysis of the MFS negative Skewness is due to the number of surface valleys that were higher than the peaks [19], and after adsorption of the dye, the skewness value became positive due to the decrease in the number of valleys and enclosed by dye molecules [20].

Surface morphology

The surface morphology of MFS before and after adsorption were examined by scanning electron

microscopy, as presented in Fig. 4. MFS image shows irregular particle shapes with large scale of pores. After dye adsorption, the surface of MFS was smooth and had no sharp edges with small scale pores in comparison with MFS, and the coated surface clearly shows that dye particles were accumulated on the surface of MFS.

Surface area and porosity

Fig. 5 shows BET adsorption-desorption isotherms of MFS before and after adsorption. The obtained surface properties such as the BET surface area, and the BJH pore volumes are summarized in Table 1. According to

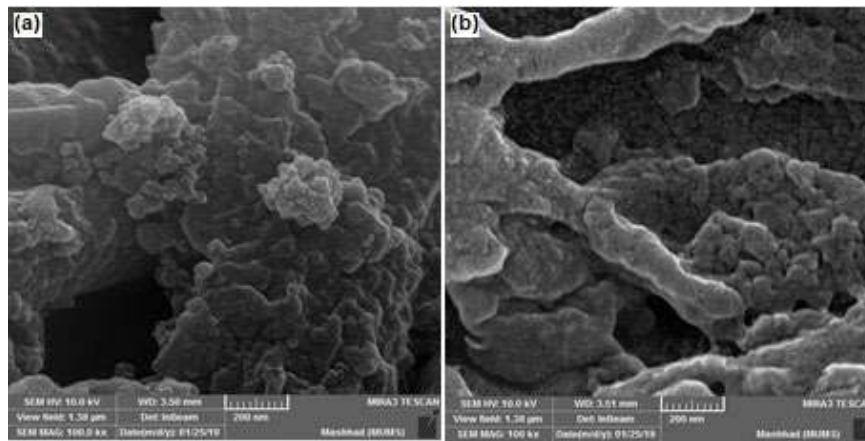


Fig 4. SEM images of MFS (a) before and, (b) after dye adsorption

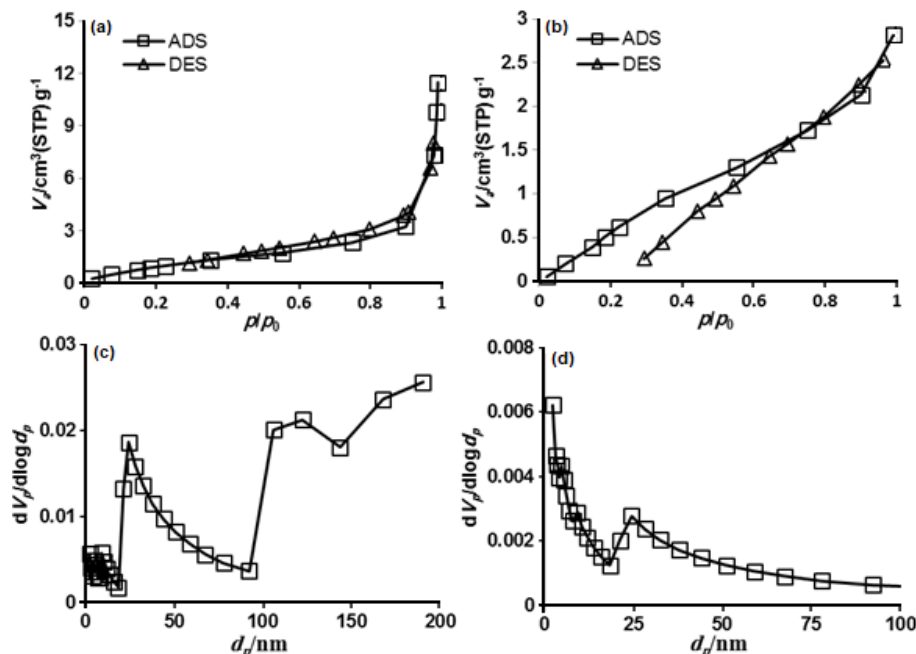


Fig 5. (a) and (b) BET isotherms of Nitrogen adsorption–desorption before and after dye adsorption respectively, (c) and (d) BJH pore size distribution curves before and after adsorption respectively

Table 1. Surface area, pore size and average diameter of MFS and MFS-RB

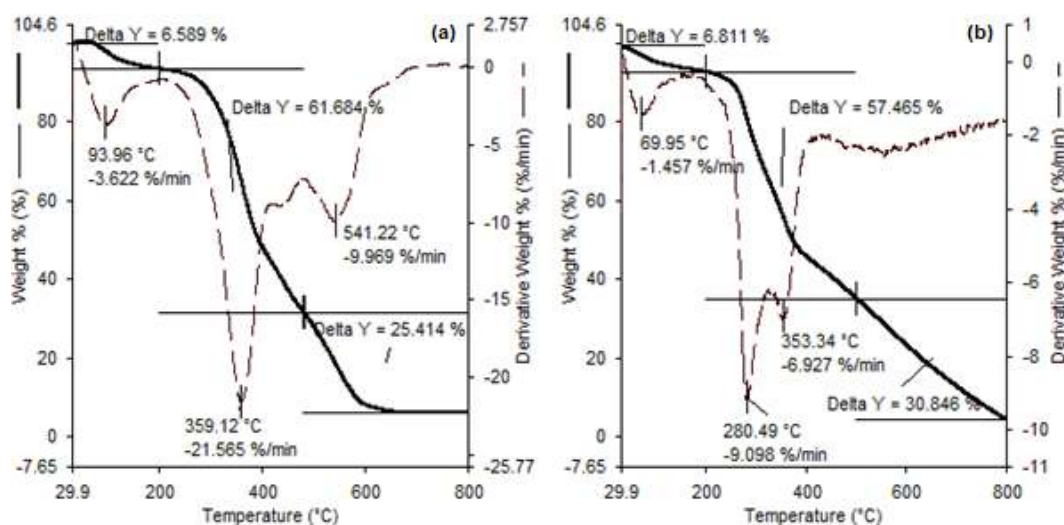
	Surface area (m ² /g)	Pore volume (cc/g)	Average pore diameter (nm)
MFS	4.4	0.0177	190.55
MFS-RB	-	0.0050	2.43

the classification proposed by (IUPAC), the isotherms of MFS can be classified as type III, where the adsorbate uptake increases exponentially due to the weak interaction between the adsorbate (N₂ gas) and the adsorbent and to the microporous nature [21]. In reference to literature, the hysteresis loops of MFS is H3 type which is indexed to the presence of non-rigid aggregates of sheet-like particles or assemblages of slit-shaped pores [22]. The surface area of MFS was 4.4 m²/g. whereas MFS after the adsorption of RB have schematically undefined curves and cannot be applied to the BET sorption isotherm models which may be due to

lower surface area of the sample. This results complies with their morphology (Fig. 3 and Fig. 4). The pore volume and pore diameter of the MFS surface decreased with the adsorption of molecules due to the filling of the pore voids with the dye molecules. Results show that the pore volume decreased by 71.29%, and the average diameter decreased from 190.55 to 2.43 nm due to the dye adsorption on the MFS surface.

Thermal Analysis

The Thermogravimetric analysis results of MFS before and after dye adsorption are shown in Fig. 6. TGA and DTA curves of MFS show three steps in weight loss (Table 2); The first stage of weight loss in the temperature range of 30 to 200 °C represents the removal of physically adsorbed water [23]. The second step of weight loss in the temperature range of 200–500 °C can be attributed to the organic breakdown of MFS biomass and the loss of the organic volatile compounds. The third

**Fig 6.** TGA/DTA curves of MFS (a) before and (b) after dye adsorption**Table 2.** TGA/DTA data of MFS and MFS-RB before and after adsorption of RB

	DTG peak (°C)	TG range (°C)	Mass loss (%)	Remaining mass	Possible explanation
MFS	93.96	30–200	6.589	93.411	Dehydration
	359.12	200–480	61.684	31.727	Volatilization of organic compounds
	541.22	480–800	25.414	6.313	Carbonation
MFS-RB	160.38	30–200	6.811	93.189	Dehydration
	237.76	200–500	57.465	35.724	Volatilization of organic compounds
	-	500–800	30.846	4.878	Carbonation and Volatilization of RB dye

stage occurred in the range of temperature of 500–800 °C which corresponds to the carbonization of the material and formation of charcoal [24]. The charcoal residues after MFS and MFS-RB were heated to 800 °C, were 6.313 and 4.878%, respectively. The decrease in the residues percentage (1.435%) of MFS-RB was due to the pyrolysis of the RB dye in the third stage of the TGA analysis, in accordance to the data obtained from the lookchem supplier web, in which the RB dye boiling point is 741.8 °C at 760 mmHg [25].

Effect of Contact Time and Adsorption Kinetics

The time-dependent behavior of the dye adsorption was investigated by varying the contact time between the RB dye and the MFS in the range of 5–75 min. The concentrations of the dye was kept at 50 ppm and MFS mass was kept at 1.7 g. The result for the removal of RB versus contact time is presented in Fig. 7. More than 80% of dye was adsorbed at contact time of 10 min and adsorption increased with time reaching to a maximum value in 65 min and afterwards remained constant. In context, the adsorption equilibrium time of the RB dye was 65 min for MFS.

To investigate the kinetic mechanism of adsorption, the experimental data was fitted to the pseudo-first order, the pseudo-second order, and intraparticle diffusion models. The three models are generally expressed as follows:

Pseudo-first order model (linear form) [26]:

$$\ln(q_e - q_t) = \ln q_e - k_1 t \quad (3)$$

Pseudo-second order model (linear form) [27]:

$$\frac{t}{q_t} = \frac{1}{k_2 q_e^2} + \frac{1}{q_e} t \quad (4)$$

Intraparticle diffusion model (linear form) [28]:

$$q_t = k_p t^{0.5} + I \quad (5)$$

where q_e and q_t = the amount of RB adsorbed at equilibrium and at t time, respectively ($\text{mg} \cdot \text{g}^{-1}$), k_1 = the overall rate constant of pseudo-first order kinetics ($\text{min}^{-1} \text{mg} \cdot \text{g}^{-1}$), k_2 = the rate constant of pseudo-second order ($\text{mg} \cdot \text{g}^{-1} \text{min}^{-1}$), K_p = the rate constant of intraparticle diffusion ($\text{mg} \cdot \text{g}^{-1} \text{min}^{-1/2}$) and I = the intercept reflecting the thickness of boundary layer.

Fig. 7(b), (c) and (d) show the kinetic models of RB adsorption on the MFS surface. The adsorption kinetic pseudo-second order was more linear with R^2 of 0.999

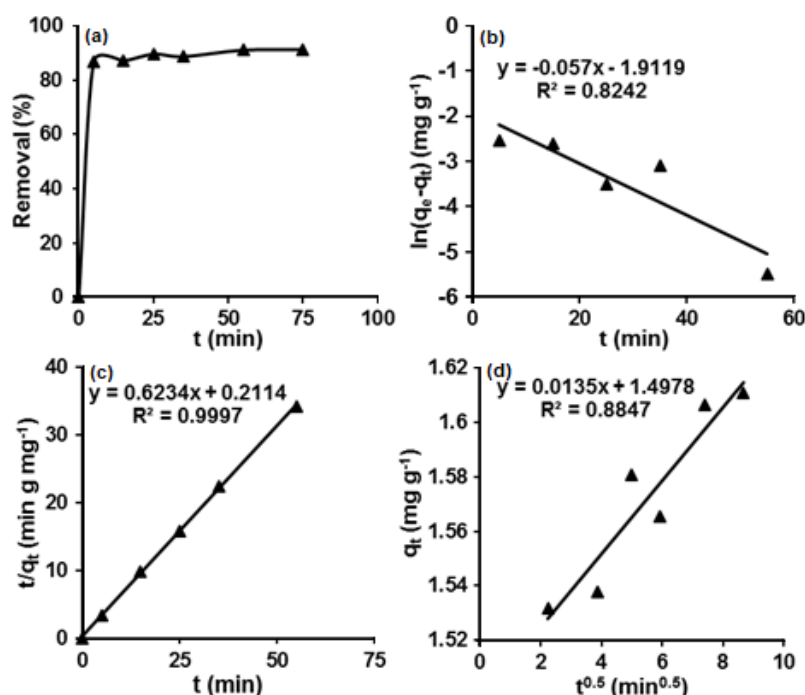


Fig 7. The removal and kinetics graphs models: (a) the removal (b) pseudo-first order (c) pseudo-second order and diffusion kinetics models of (d) intraparticle diffusion of RB using MFS

Table 3. Kinetic data of adsorption RB onto MFS

First order		Second order			Intraparticle diffusion				
$q_{e,exp}$ (mg/g)	k_1 ($\text{min}^{-1} \text{mg g}^{-1}$)	$q_{e,cal}$ (mg/g)	R^2	k_2 (min. g/mg)	$q_{e,cal}$ (mg/g)	R^2	k_p ($\text{mg g}^{-1} \text{min}^{-1/2}$)	C (mg/g)	R^2
1.610	0.057	0.147	0.824	0.902	1.622	0.999	0.013	1.497	0.884

compared to the pseudo-first order plot and intraparticle diffusion plot (see Table 3). In addition, the value of ($q_{e,cal}$) in this model is closer and more accurate than the other models. This result confirmed that the adsorption process followed the pseudo-second order which assumed that chemisorption occurred, which involved chemical reactions between adsorbent and adsorbate [29].

Adsorption Isotherm Studies

Fig. 8(a) shows the adsorption isotherm of RB dye. Referring to the theoretical basis of Giles's classification of adsorption isotherms, the isotherm of RB was of S-type, which assumed that the adsorbent is possibly mesoporous or is not porous and has a high energy of adsorption. The reaction between adsorbent and adsorbate can be determined by isotherm study. There are different isotherm equations available for studying the experimental sorption equilibrium data. However, the

most common types of isotherms are the Langmuir, Temkin and Freundlich models:

Langmuir isotherm model [30]:

$$\frac{C_e}{q_e} = \frac{C_e}{q_m} + \frac{1}{K_a q_m} \quad (6)$$

Freundlich isotherm model [31]:

$$\log q_e = \log K_f + 1/n(\log C_e) \quad (7)$$

Temkin isotherm model [32]:

$$q_e = B_1 \ln K_T + B_1 \ln C_e \quad (8)$$

where q_e = the amount of RB adsorbed (mg/g) at C_e (equilibrium concentration), q_m and k_a are Langmuir constants related to adsorption efficiency and energy of adsorption, respectively. K_f and $1/n$ are constants incorporating the factors affecting the adsorption capacity and intensity of adsorption, respectively. $\beta = RT/b$, (T) is the thermodynamic temperature in Kelvin degrees and (R) is the universal gas constant, $8.314 \text{ J mol}^{-1} \text{ K}^{-1}$. The constant (b) is identified as the adsorption heat.

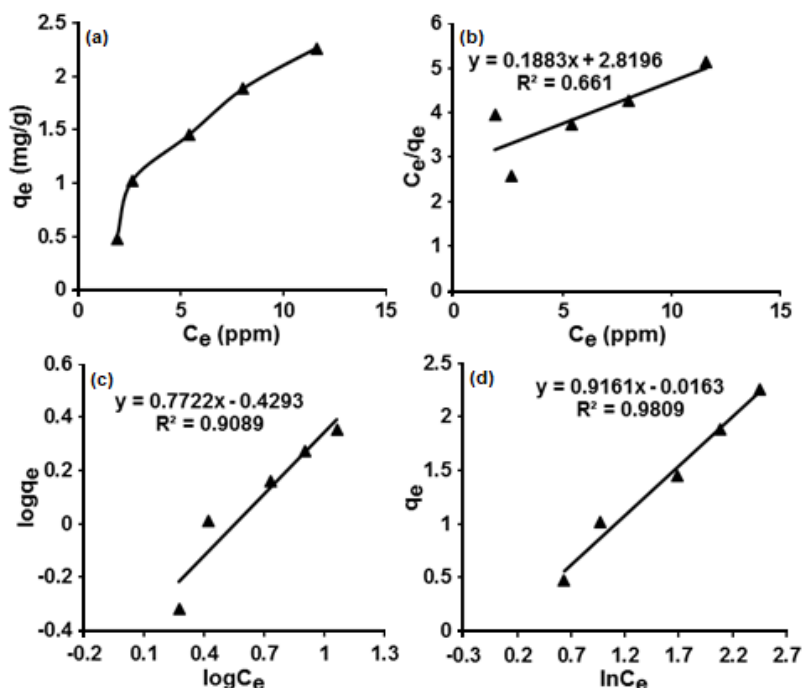


Fig 8. (a) Adsorption isotherm, (b) Langmuir model, (c) Freundlich model and, (d) Temkin model of dye at pH 7 and 25 °C

Table 4. Isotherm models data of adsorption RB onto MFS

Langmuir isotherm			Freundlich isotherm			Temkin isotherm		
K_a (L mg ⁻¹)	q_m (mg/g)	R^2	K_F (mg/g (L/mg) ^{1/n})	n	R^2	K_T (L g ⁻¹)	B	R^2
0.066	5.310	0.661	0.372	1.295	0.908	0.982	0.916	0.980

Fig. 8(b), (c) and (d) show the isotherm models of RB adsorption on the MFS surface. It is clearly seen that plot of Temkin isotherm is more linear with R^2 of 0.980 in comparison to other models of isotherms (show Table 4). Temkin isotherm contains a factor that explicitly taking into the account of adsorbent-adsorbate interactions and assumes that heat of adsorption of all molecules in the layer would decrease linearly rather than in logarithmic manner with the coverage [33].

Adsorbent dosage

To optimize the MFS dosage, the effect of adsorption amount on removal of RB dye was carried out. Fig. 9(a) shows the dependence of MFS mass on RB adsorption percentage. It was observed that RB removal increased with the increase of the amount of MFS adsorbent. The maximum removal of dyes was observed with the dosage (1.7 g) used for all subsequent experiments the results are shown in Fig. 9(a).

Initial pH effect

Different pH values (3, 4, 9 and 12) were used to study the pH effect on adsorption of RB dye onto MFS. Initial pH dye solutions were adjusted by using 0.1 N of HCl and 0.1 N of NaOH. Fig. 9(b) depicts the relationship between RB removal percentages with the initial pH values of the RB solutions. It is clearly seen that the amount of dyes removed at pH 3 produced a large adsorbate quantity. The dye removal was expected to

increase due to the esterification process that was found to be more favorable at acidic solution (pH < 3). The IR spectral lines proves the occurrence of esterification by the appearance of a peak at 1734 cm⁻¹.

Effect of Temperature

The effect of temperature on RB adsorption on MFS surface at (35–55) °C is shown in Fig. 10(a). It shows that the adsorption process decreased with the rise in temperature due to the reduced attractive forces between the RB molecules and MFS [34]. The enthalpy variation (ΔH), and other thermodynamic parameters such as free energy variation (ΔG), and entropy variation (ΔS) follows the following equations [35]:

$$\ln X_m = \frac{-\Delta H}{RT} + C \quad (9)$$

$$\Delta G = -RT \ln K \quad (10)$$

$$\Delta G = \Delta H - T\Delta S \quad (11)$$

where X_m is the maximum amount adsorbed (q_m) at a certain value of concentration equilibrium (C_e), and (K) is the distribution coefficient. The value of ΔH° was determined from the slope value of the straight line of plotting $\ln X_m$ versus $1/T$ (Fig. 10(b)). The negative value of enthalpy ($\Delta H = -42.447$ kJ/mol) and entropy ($\Delta S = -147$ J mol⁻¹ K⁻¹), confirmed the exothermic process and that the RB molecules have ordered arrangement on MFS surface [36]. On the other hand, the positive value of free energy ($\Delta G = +3065$ kJ/mol) indicated that the adsorption

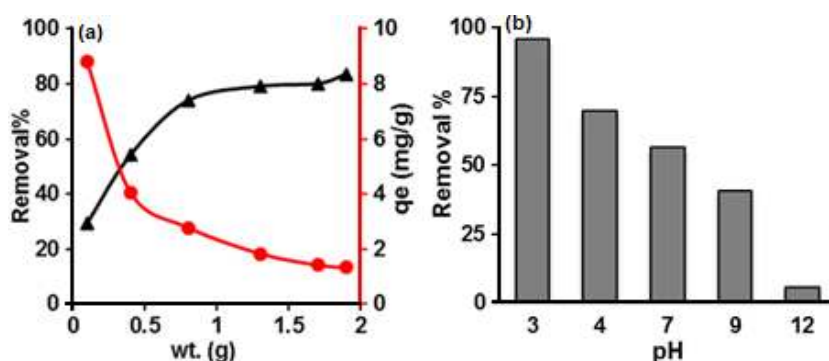


Fig 9. (a) Effect of adsorbent dosage and, (b) pH effect on adsorption of RB

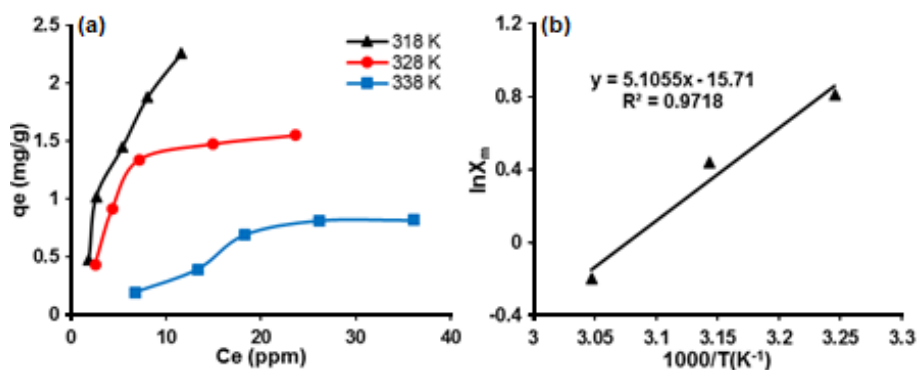


Fig 10. (a) Effect of temperature and, (b) Van't Hoff plots for the adsorption of RB onto MFS surface

process was thermodynamically non-spontaneous [35]. The value of ΔH was more than 40 kJ/mol which indicates that the uptake of RB dye onto MFS could be attributed to a chemisorption process [37].

CONCLUSION

In the present study, we examined the adsorption of Rose Bengal onto *Myristica fragrans* shells. We strongly suggest that chemisorption by ester bond formation between adsorbate and adsorbent occurred. This result was confirmed by FTIR and adsorption study.

REFERENCES

- [1] Tang, S.K., Teng, T.T., Alkarkhi, A.F.M., and Li, Z., 2012, Sonocatalytic degradation of Rhodamine B in aqueous solution in the presence of TiO₂ coated activated carbon, *APCBEE Procedia*, 1, 110–115.
- [2] Alwan, S.H., Alshamsi, H.A.H., and Jasim, L.S., 2018, Rhodamine B removal on A-rGO/cobalt oxide nanoparticles composite by adsorption from contaminated water, *J. Mol. Struct.*, 1161, 356–365.
- [3] Busquets, R., Kozynchenko, O.P., Whitby, R.L.D., Tennison, S.R., and Cundy, A.B., 2014, Phenolic carbon tailored for the removal of polar organic contaminants from water: A solution to the metaldehyde problem?, *Water Res.*, 61, 46–56.
- [4] Soliman, E.M., Ahmed, S.A., and Fadl, A.A., 2011, Reactivity of sugar cane bagasse as a natural solid phase extractor for selective removal of Fe(III) and heavy-metal ions from natural water samples, *Arabian J. Chem.*, 4 (1), 63–70.
- [5] Sorensen, J.P.R., Lapworth, D.J., Nkhuwa, D.C.W., Stuart, M.E., Goody, D.C., Bell, R.A., Chirwa, M., Kabika, J., Liemisa, M., Chibesa, M., and Pedley, S., 2015, Emerging contaminants in urban groundwater sources in Africa, *Water Res.*, 72, 51–63.
- [6] Jayanthi, V., Geetha, R., Rajendran, R., Prabhavathi, P., Sundaram, S.K., Kumar, S.D., and Santhanam, P., 2014, Phytoremediation of dye contaminated soil by *Leucaena leucocephala* (subabul) seed and growth assessment of *Vigna radiata* in the remediated soil, *Saudi J. Biol. Sci.*, 21 (4), 324–333.
- [7] Saggiaro, E.M., Oliveira, A.S., Pavesi, T., Maia, C.G., Ferreira, L.F.V., and Moreira, J.C., 2011, Use of titanium dioxide photocatalysis on the remediation of model textile wastewaters containing azo dyes, *Molecules*, 16 (12), 10370–10386.
- [8] Tabery, H.M., 1998, Toxic effect of Rose Bengal dye on the living human corneal epithelium, *Acta Ophthalmol. Scand.*, 76 (2), 142–145.
- [9] Vinuth, M., Naik, H.S.B., Vinoda, B.M., Pradeepa, S.M., Kumar, G.A., and Sekhar, K.S., 2016, Rapid removal of hazardous Rose Bengal dye using Fe(III) – Montmorillonite as an effective adsorbent in aqueous solution, *J. Environ. Anal. Toxicol.*, 6 (2), 1000355.
- [10] De Gisi, S., Lofrano, G., Grassi, M., and Notarnicola, M., 2016, Characteristics and adsorption capacities of low-cost sorbents for wastewater treatment: A review, *Sustainable Mater. Technol.*, 9, 10–40.
- [11] Kaur, J., and Singhal, S., 2014, Heterogeneous photocatalytic degradation of Rose Bengal: Effect of operational parameters, *Physica B*, 450, 49–53.

- [12] Bhaumik, R., Mondal, N.K., Das, B., Roy, P., Pal, K.C., Das, C., Banerjee, A., and Datta, J.K., 2012, Eggshell powder as an adsorbent for removal of fluoride from aqueous solution: Equilibrium, kinetic and thermodynamic studies, *E-J. Chem.*, 9 (3) 1457–1480.
- [13] Alshamsi, H.A.H., and Alwan, S.H., 2015, Adsorptive removal of Cd(II) from aqueous solution onto beans peel powder as low cost adsorbent, *Res. J. Pharm. Biol. Chem. Sci.*, 6 (6), 985–996.
- [14] Bouamra, F., Drouiche, N., Abdi, N., Grib, H., Mameri, N., and Lounici, H., 2018, Removal of phosphate from wastewater by adsorption on marble waste: Effect of process parameters and kinetic modeling, *Int. J. Environ. Res.*, 12, 13–27.
- [15] Abdel-Salam, O.E., Reiad, N.A., and ElShafei, M.M., 2011, A study of the removal characteristics of heavy metals from wastewater by low-cost adsorbents, *J. Adv. Res.*, 2 (4), 297–303.
- [16] Syahiddin, D.S., and Muslim, A., 2018, Adsorption of Cu(II) ions onto *Myristica fragrans* shell-based activated carbon: Isotherm, kinetic and thermodynamic studies, *J. Korean Chem. Soc.*, 62 (2), 79–86.
- [17] Uppal, A., Jain, B., Gupta, P.K., and Das, K., 2011, Photodynamic action of Rose Bengal silica nanoparticle complex on breast and oral cancer cell lines, *Photochem. Photobiol.*, 87 (5), 1146–1151.
- [18] Bodîrlău, R., and Teacă, C.A., 2009, Fourier transform infrared spectroscopy and thermal analysis of lignocellulose fillers treated with organic anhydrides, *Rom. J. Phys.*, 54 (1-2), 93–104.
- [19] Kumar, B.R., and Rao, T.S., 2012, AFM studies on surface morphology, topography and texture of nanostructured zinc aluminum oxide thin films, *Dig. J. Nanomater. Bios.*, 7 (4), 1881–1889.
- [20] Altaa, S.H.A., Alshamsi, H.A.H., and Al-Hayder, L.S.J., 2018, Synthesis and characterization of rGO/Co₃O₄ composite as nanoadsorbent for Rhodamine 6G-dye removal, *Desalin. Water Treat.*, 114, 320–331.
- [21] Kshirsagar, A.S., and Khanna, P.K., 2019, CuSbSe₂/TiO₂: Novel type-II heterojunction nanophotocatalyst, *Mater. Chem. Front.*, 3 (3), 437–449.
- [22] Al-Taweel, S.S., Saud, H. R., Kadhun, A.A.H., and Takriff, M.S., 2019, The influence of titanium dioxide nanofiller ratio on morphology and surface properties of TiO₂/chitosan nanocomposite, *Results Phys.*, 13, 102296.
- [23] Ali, A.S., Mohammed, A.J., and Saud, H.R., 2018, Hydrothermal synthesis of TiO₂/Al₂O₃ nanocomposite and its application as improved sonocatalyst, *Int. J. Eng. Technol.*, 7 (4), 22–25.
- [24] Cao, J., Xiao, G., Xu, X., Shen, D., and Jin, B., 2013, Study on carbonization of lignin by TG-FTIR and high-temperature carbonization reactor, *Fuel Process. Technol.*, 106, 41–47.
- [25] lookchem, 2019, *Rose Bengal lactone*, <https://www.lookchem.com/Rose-Bengal-lactone/>.
- [26] Lagergren, S., 1898, Zur theorie der sogenannten adsorption gelöster stoffe, *Kungl. Sven. Vetenskapsakad. Handl.*, 24, 1–39.
- [27] Ho, Y.S., and McKay, G., 1999, Pseudo-second order model for sorption processes, *Process Biochem.*, 34 (5), 451–465.
- [28] Kushwaha, J.P., Srivastava, V.C., and Mall, I.D., 2010, Treatment of dairy wastewater by commercial activated carbon and bagasse fly ash: Parametric, kinetic and equilibrium modelling, disposal studies, *Bioresour. Technol.*, 101 (10), 3474–3483.
- [29] Rahman, M.S., and Sathasivam, K.V., 2015, Heavy metal adsorption onto *Kappaphycus* sp. from aqueous solutions: The use of error functions for validation of isotherm and kinetics models, *BioMed. Res. Int.*, 2015, 126298.
- [30] Langmuir, I., 1918, The adsorption of gases on plane surfaces of glass, mica and platinum, *J. Am. Chem. Soc.*, 40 (9), 1361–1403.
- [31] Freundlich, H.M.F., 1906, Over the adsorption in solution, *J. Phys. Chem.*, 57, 385–470.
- [32] Tempkin, M.J., and Pyzhev, V., 1940, Recent modification to Langmuir isotherms, *Acta Physiochem. USSR*, 12, 217–222.
- [33] Nechifor, G., Pascu, D.E., Pascu, M., Traistaru, G.A., and Albu, P.C., 2015, Comparative study of Temkin and Flory-Huggins isotherms for

- adsorption of phosphate anion on membranes, *U.P.B. Sci. Bull., Ser. B*, 77 (2), 63–72.
- [34] Umoren, S.A., Etim, U.J., and Israel, A.U., 2013, Adsorption of methylene blue from industrial effluent using poly (vinyl alcohol), *J. Mater. Environ. Sci.*, 4(1), 75–86.
- [35] Al-Taweel, S.S., 2015, Equilibrium isotherm and kinetic studies of adsorption of basic Green-4 on titanium dioxide nanoparticles, *Int. J. ChemTech Res.*, 8 (10), 116–125.
- [36] Sharifipour, F., Hojati, S., Landi, A., and Faz Cano, A., 2015, Kinetics and thermodynamics of lead adsorption from aqueous solutions onto Iranian sepiolite and zeolite, *Int. J. Environ. Res.*, 9 (3), 1001–1010.
- [37] Adelodun, A.A., Ngila, J.C., Kim, D.G., and Jo, Y.M., 2016, Isotherm, thermodynamic and kinetic studies of selective CO₂ adsorption on chemically modified carbon surfaces, *Aerosol Air Qual. Res.*, 16, 3312–3329.

Synthesis, Characterization and Docking Study of Novel Pyrimidine Derivatives as Anticancer Agents

Manal Mohamed Talaat El-Saidi¹, Ahmed Ali El-Sayed^{1,2,*}, Erik Bjerregaard Pedersen², Mohamed Abdelhamid Tantawy^{3,4}, Nadia Ragab Mohamed¹, and Wafaa Ahmed Gad¹

¹Photochemistry Department, Chemical Research Division, National Research Center, Dokki, Giza, 12622, Egypt

²Department of Physics, Chemistry, and Pharmacy, University of Southern Denmark, Campusvej 55, 5230 Odense M, Denmark

³Hormones Department, Medical Research Division, National Research Center, Dokki, Giza, 12622, Egypt

⁴Stem Cells Lab, Center of Excellence for Advanced Sciences, National Research Centre, Dokki, Giza, 12622, Egypt

* **Corresponding author:**

email: ahmedcheme4@yahoo.com

Received: October 15, 2019

Accepted: November 18, 2019

DOI: 10.22146/ijc.50582

Abstract: New compounds **5** and **9** using DNA bases e.g. Adenine **1** and Guanine **6** derivatives have been synthesized. The use of simple methods to synthesize compounds **5** and **9** were done using pyrimidine as an alternative DNA base ring. Another design to synthesize new simple pyrimidine rings utilizing thiourea and ethylcyano acetate to afford 6-amino-2-thiouracil was adopted. The reaction of thiouracil **10** with chloro cyano or chloro ester and ketone, resulted in the formation of adduct compounds **18-21**, rather than the formation of compound **17**. All the synthesized compounds were subjected to docking study, in order to gain insights into their binding modes against cyclin-dependent protein kinase 2 (CDK-2) that is involved heavily in cell cycle regulation and receptor protein B-cell lymphoma 2 (BCL-2) which is involved in cell apoptosis. These targets were selected based on their key roles in cancer progression via the regulation of the cell cycle and DNA replication. Molecular-docking analyses showed that compound **14e** was the best docked ligand against both targets, as it displayed the lowest binding energy, critical hydrogen bonds and hydrophobic interactions with the targets.

Keywords: DNA; guanidine; adenine; 6-aminothiouracil; hydrazonoyl halides; thiadiazole; phenylisocyanate; molecular docking

■ INTRODUCTION

Modification of DNA and RNA oligonucleotides with new synthesized heterocyclic compounds have drawn significant interest owing to their ability to imitate new gene chemical probes that play an important role in the drug discovery process [1-7]. Gene-therapy in recent research was based on DNA and its modification [8-10]. The thymidine ring is a DNA building block that interests many researchers to focused their research on the synthesis of new pyrimidine rings as anti-cancer agents such as 5-fluorouracil [1-14], and anti-HIV like AZT, D4T, Nikavir [15-21], Lamivudina [22] and Emtricitabina [16,23-24]. The Nitrogen containing heterocycles like pyrimidines and their derivatives have received great

attention for their considerable exciting biological activities [25-28]. Several pyrimidines have been isolated from the nucleic acid hydrolysis. The nucleic acids are an essential constituent of cells. So, pyrimidines are found to be present in RNA and DNA [29]. In addition to this, the pyrimidine ring is also found in vitamin B₁ and other derivatives are used as hypnotics [30]. The literature survey indicated that compounds having pyrimidine nucleus possess a broad range of biological activities [31-35]. On the other hand, hydrazonoyl halides (pyrimidine nucleobase) are versatile synthons for many heterocycles that have found many applications in both the industrial and pharmaceutical fields [36-38]. As a precursor of bioactive heterocycles

[39-40], this report is concerned with the synthesis of new types of bioactive heterocycles using thiouracils.

This work is carried out in order to further modify our previously prepared pyrimidine ring bases heterocyclic compounds in order to increase their bioactivity. The main strategy is the chemical synthesis is described technically; while the biological activity is accomplished by molecular docking. This technique provides a rapid way to evaluate the likely binders from large chemical libraries with minimal costs and it is being widely used as a vital component of the drug discovery process [41]. Molecular docking study has been utilized to determine the possible mechanism action of the tested compounds against two proteins cyclin-dependent protein kinase 2 (CDK-2) and receptor protein B-cell lymphoma 2 (BCL-2) that are implicated significantly in cancer progression.

■ EXPERIMENTAL SECTION

Chemistry

All solvents were purified and dried before use. All melting points were uncorrected and measured using Electro-Thermal IA 9100 apparatus (Shimadzu, Japan). Infrared spectra were recorded as potassium bromide pellets on a Perkin-Elmer 1650 spectrophotometer, National Research Centre, Cairo, Egypt. ¹H-NMR spectra were recorded on a Jeol-Ex-500 NMR spectrometer and chemical shifts were expressed as part per million; (δ values, ppm) against TMS as an internal reference, National Research Centre, Cairo, Egypt. Mass spectra were recorded on EI + Q1 MSLMR UPLR, National Research Centre, Cairo, Egypt. Microanalyses were operated using the Mario Elmentar apparatus, Organic Microanalysis Unit, National Research Center, Cairo, Egypt.

Procedure

General procedure for compounds 3 and 7

To a solution of 8-bromo-2'-deoxyguanosine (**1**) or 8-bromo-2'-deoxyadenosine (**6**) (0.478 mmol) in dry DMF (30 mL), N-(4-pentynyl)-phthalimide (1.71 mmol) was added under argon gas and then copper iodide (0.25 mmol), Pd(PPh₃)₄ (0.0515 mmol) and triethylamine (1.43 mmol) were added to the reaction mixture. The

reaction was stirred at 55 °C under argon till the reaction was finished according to TLC analysis. The product was separated by evaporation of the solvent and the residue was purified by silica gel (size 230–400 mesh) column chromatography, and carried out starting from dichloromethane and increasing the polarity until the product was collected using TLC and the column was washed with MeOH.

2-{5-[2-Amino-9-(4-hydroxy-5-hydroxymethyl-tetrahydro-furan-2-yl)-6-oxo-6,9-dihydro-1H-purin-8-yl]-pent-4-ynyl}-isoindole-1,3-dione **3.** Yellow foam (silica column DCM/MeOH 7:3) yield 90%. IR spectrum (KBr, ν, cm⁻¹): 3432 (–OH); 3098 (C–H, aromatic); 1690 (–C=O); 1675 (–C=O). ¹H NMR (CDCl₃-d, δ ppm): 10.75 (s, 1H, –OH, sugar); 7.79–7.87 (m, 4H, aromatic protons); 6.48 (s, 1H, –NH); 6.23–6.27 (t, *J* = 6.25, 2H, –CH₂); 5.21–5.20 (d, *J* = 5.21, 2H, –CH₂); 4.84–4.87 (t, *J* = 4.85, 2H, –CH₂); 2.89 (s, 2H, NH₂); 2.56–2.62 (t, *J* = 5.26, 1H, sugar proton); 2.99–3.06 (m, 1H, sugar proton); 2.08–2.14 (m, 1H, sugar proton); 3.38–3.62 (m, 1H, sugar proton); 3.85–3.62 (m, 1H, sugar proton); 2.73 (s, 1H, –CH₂–OH, sugar); 1.13–1.18 (m, 2H, –CH₂); ¹³C-NMR (CDCl₃-d, δ ppm) 16.43 (–CH₂–CH₂–), 34.06 (–N–CH₂–CH₂–), 38.81 (–N–CH₂–CH₂–), 40.06 (–CH–CH₂–CH–), 61.58 (–CH–O–), 63.81(–CH₂–O–), 65.66 (–CH₂–OH), 81.48 (–C≡C–), 85.45 (–C≡C–), 87.51 (–N–CH–O–), 120.14, 122.40, 125.43, 122.88, 131.62, 134.13 (aromatic carbon), 148.08 (–N–C–C=O), 149.90 (–N–C–N–), 153.77 (–N=C–N), 167.90 (NH₂–C=N–), 168.31(–C=O), 180.10 (–C=O), 182.22 (NH–C=O). MS, *m/z* (%): 464. Anal. Calcd. for C₂₃H₂₂N₆O₆ (464.43): C, 57.74; H, 4.63; N, 17.56. Found: C, 57.60; H, 4.55; N, 17.43.

2-{5-[6-Amino-9-(4-hydroxy-5-hydroxymethyl-tetrahydro-furan-2-yl)-9H-purin-8-yl]-pent-4-ynyl}-isoindole-1,3-dione **7.** Brown foam (silica column DCM/MeOH, 6:4) yield 95%. IR spectrum (KBr, ν, cm⁻¹): 3445 (–NH₂); 3432 (–OH); 3098 (C–H, aromatic); 1700 (–C=O); 1680 (–C=O). ¹H-NMR (CDCl₃-d, δ ppm): 8.31 (s, 1H, –OH); 7.84–7.90 (m, 1H, aromatic protons); 7.70–7.73 (m, 1H, aromatic protons); 7.29 (s, 1H, pyrimidine proton); 6.78–6.87 (m, 2H, aromatic protons); 6.47 (s, 2H, –NH₂); 4.30 (s, 1H, –OH); 3.90–

3.93 (t, $J = 3.91$, 2H, $-\text{CH}_2$); 4.49 (d, $J = 3.21$, 2H, $-\text{CH}_2$); 3.82–3.85 (t, $J = 3.91$, 2H, $-\text{CH}_2$); 2.73 (s, 1H, $-\text{OH}$); 2.56–2.62 (t, $J = 5.26$, 1H, sugar proton); 2.99–3.06 (m, 1H, sugar proton); 2.08–2.14 (m, 1H, sugar proton); 3.38–3.62 (m, 1H, sugar proton); 3.85–3.62 (m, 1H, sugar proton); 2.06–2.11 (m, 2H, $-\text{CH}_2$). ^{13}C -NMR (CDCl_3 -d, δ ppm): 16.99 ($-\text{CH}_2$), 26.51 ($-\text{CH}_2$), 36.76 ($-\text{CH}_2$, sugar), 40.54 ($-\text{CH}_2$), 50.54 ($-\text{CH}_2$ -OH), 63.66 (CH-OH), 70.31 ($-\text{C}\equiv\text{C}$ -), 70.66 ($-\text{CH}$ -N, sugar), 87.51 ($-\text{CH}$, sugar), 90.14 ($-\text{C}\equiv\text{C}$ -), 97.21, 120.02, 123.50 (aromatic carbon), 131.75 ($-\text{C}-\text{NH}_2$), 134.78 ($-\text{N}-\text{C}-\text{N}$, imidazole), 148.22 ($-\text{N}-\text{C}-\text{N}$, Pyrimidine), 152.58 (C-N, pyrimidine), 155.67 (C-N, pyrimidine), 168.83 (2-C=O). MS, m/z (%): 462. Anal. Calcd. for $\text{C}_{23}\text{H}_{22}\text{N}_6\text{O}_5$ (462.46): C, 59.73; H, 4.79; N, 18.17. Found: C, 59.62; H, 4.59; N, 18.01.

General procedure for compounds 4 and 8

The compounds 3 and 7 were co-evaporated with anhydrous pyridine (3 × 4 mL) and dissolved in dry pyridine (2 mL). The resulting solution was protected from moisture, purged with argon and placed in an ice bath. TMS-Cl (0.55 mL) was added dropwise *via* syringe. The mixture was stirred for 2 h at room temperature. After that, the solution was cooled in an ice bath and isobutyric anhydride (0.13 mL) was added dropwise. The solution was stirred for 2 h in room temperature, and the product was purified from the mixture by silica gel (size 230–400 mesh) column chromatography. Columns were carried out starting from dichloromethane and increasing the polarity until the product was collected using TLC and the column was washed with MeOH.

N-[8-[5-(1,3-Dioxo-1,3-dihydro-isoindol-2-yl)-pent-1-ynyl]-9-(4-hydroxy-5-hydroxymethyl-tetrahydro-furan-2-yl)-6-oxo-6,9-dihydro-1H-purin-2-yl]-isobutyramide 4.

White ppt. (column DCM/MeOH, 8:2) yield 95%. IR spectrum (KBr, ν , cm^{-1}): 3432 ($-\text{OH}$); 3145 ($-\text{NH}$); 3098 (C-H, aromatic); 2895 (C-H, aliphatic), 1700 ($-\text{C}=\text{O}$); 1690 ($-\text{C}=\text{O}$); 1680 ($-\text{C}=\text{O}$). ^1H -NMR (CDCl_3 -d, δ ppm): 12.16 (s, 1H, $-\text{OH}$, sugar); 7.79–7.86 (m, 4H, aromatic protons); 6.63 (s, 1H, $-\text{NH}$); 6.35–6.31 (t, $J = 6.34$, 2H, $-\text{CH}_2$); 5.25, 5.24 (d, $J = 5.25$, 2H, $-\text{CH}_2$); 4.74 (s, 1H, NH); 4.84–4.87 (t, $J = 4.85$, 2H, $-\text{CH}_2$); 4.43 (s, 1H $\text{CH}(\text{CH}_3)_2$); 3.85–3.62 (m, 1H, sugar proton); 3.38–3.62 (m, 1H, sugar proton); 2.99–3.06 (m, 1H, sugar proton); 2.73 (s, 1H,

CH_2 -OH); 2.56–2.62 (t, $J = 5.26$, 1H, sugar proton); 2.08–2.14 (m, 1H, sugar proton); 1.13–1.18 (m, 2H, $-\text{CH}_2$); 1.05 (s, 3H, CH_3); 1.07 (s, 3H, CH_3). ^{13}C -NMR (CDCl_3 -d, δ ppm): 7.89 ($-\text{CH}_3$), 10.24 ($-\text{CH}_3$), 18.50 ($-\text{CH}_2$ - CH_2 -), 35.16 ($-\text{N}-\text{CH}_2$ - CH_2 -), 39.91 ($-\text{N}-\text{CH}_2$ - CH_2 -), 42.06 ($-\text{CH}-\text{CH}_2$ - CH -), 52.02 ($-\text{CH}-\text{CH}_3$), 62.08 ($-\text{CH}-\text{O}$ -), 66.91 ($-\text{CH}_2$ -O-), 65.09 ($-\text{CH}_2$ -OH), 80.41 ($-\text{C}\equiv\text{C}$ -), 85.95 ($-\text{C}\equiv\text{C}$ -), 88.21 ($-\text{N}-\text{CH}-\text{O}$ -), 120.14, 122.40, 122.88, 125.43, 131.62, 134.13 (aromatic carbon), 147.08 ($-\text{N}-\text{C}-\text{C}=\text{O}$), 149.02 ($-\text{N}-\text{C}-\text{N}$ -), 153.90 ($-\text{N}=\text{C}-\text{N}$), 167.11 (NH_2 - $\text{C}=\text{N}$ -), 168.31 ($-\text{C}=\text{O}$), 180.10 ($-\text{C}=\text{O}$), 182.02 ($\text{NH}-\text{C}=\text{O}$), 183.90 ($\text{NH}-\text{C}=\text{O}$). MS, m/z (%): 549. Anal. Calcd. for $\text{C}_{27}\text{H}_{28}\text{N}_6\text{O}_7$ (548.55): C, 59.12; H, 5.14; N, 15.32. Found: C, 59.01; H, 5.03; N, 15.12.

N-[8-[5-(1,3-Dioxo-1,3-dihydro-isoindol-2-yl)-pent-1-ynyl]-9-(4-hydroxy-5-hydroxymethyl-tetrahydro-furan-2-yl)-9H-purin-6-yl]-isobutyramide 8.

Yellow foam (column DCM/MeOH 6:4) yield 86%. IR spectrum (KBr, ν , cm^{-1}): 3401 ($-\text{OH}$); 3090 (C-H, aromatic); 1690 ($-\text{C}=\text{O}$); 1679 ($-\text{C}=\text{O}$). ^1H NMR (CDCl_3 -d, δ ppm): 8.88 (s, 1H, $-\text{OH}$); 8.70 (s, 1H, pyrimidine proton); 7.72–7.74 (m, 2H, aromatic protons); 7.85–7.87 (m, 2H, aromatic protons); 7.26 (s, 1H, $-\text{NH}$); 6.91–6.95 (m, 1H, sugar); 4.79, 4.80 (d, $J = 4.80$, 1H, sugar); 4.33 (s, 2H, CH_2 -OH); 3.83–3.99 (t, $J = 4.96$, 2H, $-\text{CH}_2$); 3.82–3.85 (t, $J = 3.91$, 2H, $-\text{CH}_2$); 3.38–3.62 (m, 1H, sugar proton); 3.85–3.62 (m, 1H, sugar proton); 2.73 (s, 1H, $-\text{OH}$); 2.56–2.62 (t, $J = 5.26$, 1H, sugar proton); 2.06–2.11 (m, 2H, $-\text{CH}_2$); 1.29 (s, 1H, $\text{CH}(\text{CH}_3)_2$); 1.21 (s, 3H, CH_3); 1.18 (s, 3H, CH_3). ^{13}C -NMR (CDCl_3 -d, δ ppm): 17.04 ($-\text{CH}_2$ - $\text{C}\equiv\text{C}$ -), 26.40 (2- CH_3), 33.76 ($-\text{CH}_2$, sugar), 36.70 ($-\text{CH}_2$ -N), 43.63 ($-\text{CH}_2$ -OH), 63.62 (CH -OH), 70.11 ($-\text{C}\equiv\text{C}$ -), 87.71 ($-\text{CH}-\text{N}$, sugar), 90.29 ($-\text{CH}$, sugar), 98.91 ($-\text{C}\equiv\text{C}$ -), 122.36, 123.57, 131.74, 134.42, 136.57, 147.89, 149.34, 152.57 (aromatic carbon), 168.89 ($-\text{C}=\text{O}$), 175.92 ($-\text{C}=\text{O}$), 180.00 ($-\text{C}=\text{O}$). MS, m/z (%): 532. Anal. Calcd. for $\text{C}_{27}\text{H}_{28}\text{N}_6\text{O}_6$ (532.21): C, 60.89; H, 5.30; N, 15.78. Found: C, 60.71; H, 5.21; N, 15.65.

General procedure for compounds 5 and 9

The compounds 4 and 8 were co-evaporated with anhydrous pyridine (3 × 3 mL) and dissolved in dry pyridine (10 mL). The DMT-Cl (3.6 mmol) was dissolved in dry pyridine (3 mL) and added to the

nucleoside solution dropwise in an ice bath over 2.5 h and the reaction mixture was stirred in an ice bath until the TLC was finished. The product was separated and purified with flash column silica gel (size 230–400 mesh) column chromatography. The column was carried out starting from dichloromethane with a few drops of triethylamine (Et₃N) and increasing the polarity until the product was collected using TLC and the column was washed with methanol.

N-{9-[5-[Bis-(4-methoxy-phenyl)-phenyl-methoxymethyl]-4-hydroxy-tetrahydro-furan-2-yl]-8-[5-(1,3-dioxo-1,3-dihydro-isoindol-2-yl)-pent-1-ynyl]-6-oxo-6,9-dihydro-1H-purin-2-yl]-isobutyramide 5. White ppt. (column DCM/MeOH 7:3) yield 55%. IR spectrum (KBr, ν , cm⁻¹): 3432 (–OH); 3140 (–NH); 3098 (C–H, aromatic); 2895 (C–H, aliphatic), 1710 (–C=O); 1697 (–C=O); 1681 (–C=O). ¹H-NMR (CDCl₃-d, δ ppm): 8.34 (s, 1H, NH); 7.79–7.86 (m, 5H, aromatic protons); 7.13–7.17 (m, 4H, aromatic protons); 7.27, 7.31 (d, J = 6.68, 2H, aromatic protons); 7.35, 7.38 (d, J = 6.68, 2H, aromatic protons); 6.67, 6.69 (d, J = 6.68, 2H, aromatic protons); 6.73, 6.76 (d, J = 6.68, 1H, aromatic protons); 6.63 (s, 1H, –NH); 6.35–6.31 (t, J = 6.35, 2H, –CH₂); 6.40–6.43 (t, J = 6.42, 1H, –CH, sugar); 5.39, 5.36 (d, J = 5.28, 1H, sugar); 5.34 (s, 1H, –OH, sugar); 4.84–4.87 (t, J = 4.85, 2H, –CH₂); 4.43 (s, 1H, CH(CH₃)₂); 3.85–3.62 (m, 1H, sugar proton); 3.68 (s, 3H, –OCH₃); 3.70 (s, 3H, –OCH₃); 2.73 (s, 2H, CH₂-ODMT); 2.56–2.62 (t, J = 5.26, 1H, sugar proton); 2.08–2.14 (m, 1H, sugar proton); 1.13–1.18 (m, 2H, –CH₂); 1.05 (s, 3H, CH₃); 1.07 (s, 3H, CH₃). ¹³C-NMR (CDCl₃-d, δ ppm) 7.89 (–CH₃), 10.24 (–CH₃), 18.50 (–CH₂–CH₂–), 35.16 (–N–CH₂–CH₂–), 39.91 (–N–CH₂–CH₂–), 42.06 (–CH–CH₂–CH–), 52.02 (–CH–CH₃), 58.72 (2–OCH₃); 62.08 (–CH–O–), 66.91 (–CH₂–O–), 65.09 (–CH₂–OH), 80.41 (–C≡C–), 85.95 (–C≡C–), 88.21 (–N–CH–O–), 90.79 (Ph–C–O), 120.14, 123.25, 123.01, 122.40, 122.88, 125.43, 131.62, 134.13, 136.35, 137.60, 138.37, 139.37, 141.09, 140.17, 142.84 (aromatic carbons), 147.08 (–N–C–C=O), 149.02 (–N–C–N–), 153.90 (–N=C–N), 167.11 (NH₂–C=N–), 168.31 (–C=O), 180.10 (–C=O), 182.02 (NH–C=O), 183.90 (NH–C=O). MS, m/z (%): 850. Anal. Calcd. for C₄₈H₄₆N₆O₉ (850.91): C, 67.75; H, 5.45; N, 9.88. Found: C, 67.51; H, 5.22; N, 9.65.

N-{9-[5-[Bis-(4-methoxy-phenyl)-phenyl-methoxymethyl]-4-hydroxy-tetrahydro-furan-2-yl]-8-[5-(1,3-dioxo-1,3-dihydro-isoindol-2-yl)-pent-1-ynyl]-9H-purin-2-yl]-isobutyramide 9. White foam (column DCM/MeOH 4:6) yield 60%. IR spectrum (KBr, ν , cm⁻¹): 3401 (–OH); 3090 (C–H, aromatic); 1675 (–C=O); 1673 (–C=O). ¹H-NMR (CDCl₃-d, δ ppm): 8.44 (s, 1H, –NH); 7.84 (s, 1H, pyrimidine proton); 7.83–7.78 (m, 2H, aromatic protons); 7.70–7.72 (m, 2H, aromatic protons); 7.39–7.41 (m, 2H, aromatic protons); 7.27–7.30 (m, 2H, aromatic protons); 7.17–7.23 (m, 4H, aromatic protons); 6.73–6.80 (m, 5H, aromatic protons); 4.79, 4.80 (d, J = 4.80, 1H, sugar); 4.33 (s, 2H, CH₂); 4.23–4.30 (m, 1H, sugar); 3.83–3.99 (t, J = 4.96, 2H, –CH₂); 3.82–3.85 (t, J = 3.91, 2H, –CH₂); 3.77 (s, 3H, –OCH₃); 3.76 (s, 3H, –OCH₃); 3.38–3.62 (m, 1H, sugar proton); 3.85–3.62 (m, 1H, sugar proton); 2.73 (s, 1H, –OH); 2.56–2.62 (t, J = 5.26, 1H, sugar proton); 2.06–2.11 (m, 2H, –CH₂); 1.29 (s, 1H, CH(CH₃)₂); 1.21 (s, 3H, CH₃); 1.18 (s, 3H, CH₃). ¹³C-NMR (CDCl₃-d, δ ppm): 17.04 (–CH₂–C≡C–), 19.19 (–CH₃), 26.40 (–CH₃), 33.76 (–CH₂, sugar), 36.70 (–CH₂–N), 43.63 (–CH₂–ODMT), 55.72 (2–OCH₃); 63.62 (CH–OH), 70.11 (–C≡C–), 87.71 (–CH–N, sugar), 98.11 (–CH, sugar), 100.00 (–C≡C–), 122.36, 123.57, 126.76, 127.72, 128.22, 129.99, 130.08, 131.84, 134.27, 136.00, 136.07, 144.77, 147.89, 148.84, 150.37, 152.37 (aromatic carbon), 168.89 (–C=O), 175.92 (–C=O), 180.00 (–C=O). MS, m/z (%): 834. Anal. Calcd. for C₄₈H₄₆N₆O₈ (834.91): C, 69.05; H, 5.55; N, 10.07. Found: C, 68.98; H, 5.40; N, 9.90.

General procedure for 14a-f

Sodium hydride (2 mmol) and carbon disulphide (1 mmol) was added to uracil (1 mmol) in 15 mL DMF; the reaction mixture was stirred overnight to have compound **11** (not isolated from the reaction mixture). The hydrazonyl halides (1 mmol) was added to the non-isolated compound **11**. The reaction mixture was stirred overnight then added with 15 mL of 1 M HCl to obtain crude solid of **14a-f**.

5-(6-Oxo-2-thioxo-1,2,3,6-tetrahydro-pyrimidin-4-ylimino)-4-tolyl-4,5-dihydro[1,3,4]thiadiazole-2-carboxylic acid phenylamide 14a. Yellow crystal (crystallization from benzene/petroleum ether), yield

72%; m.p. 250–252 °C. IR spectrum (KBr, ν , cm^{-1}): 3332 (–NH); 3098 (C–H, aromatic); 1672 (C=O), 1664 (C=O). $^1\text{H-NMR}$ (DMSO- d_6 , δ ppm): 2.63 (s, 3H, –CH₃); 5.34 (s, 1H, pyrimidine proton); 7.15–7.62 (m, 5H, aromatic-H); 7.82 (d, 2H, Ar-H); 7.96 (d, 1H, Ar-H); 11.74 (s, 1H, NH); 12.08 (s, 1H, NH); 14.02 (s, 1H, NH). $^{13}\text{C-NMR}$ (DMSO- d_6 , δ ppm): 26.56 (–CH₃); 103.56 (O=C–C–C, pyrimidine ring); 129.75, 130.25, 131.71, 137.21, 139.40, 141.50, 144.22, 149.2 (aromatic carbons); 161.22 (S–C–N); 173.98 (N=C–S); 178.83 (HN–C–N); 180.21 (C=O), 185.11 (C=S), 198.23 (C=O). MS, m/z (%): 436, 331, 316. Anal. Calcd. for $\text{C}_{20}\text{H}_{16}\text{N}_6\text{O}_2\text{S}_2$ (436.51): C, 55.03; H, 3.69; N, 19.25, S, 14.69. Found: C, 54.98; H, 3.59; N, 19.01, S 14.58.

6-(5-Acetyl-3-phenyl-3H-[1,3,4]thiadiazol-2-ylidene amino)-2-thioxo-2,3-dihydro-1H-pyrimidin-4-one 14b.

Yellow crystal (crystallization from ethanol), yield 77%; m.p. 220–222 °C. IR spectrum (KBr, ν , cm^{-1}): 3298 (–NH); 3118 (C–H, aromatic); 2980 (C–H, aliphatic); 1680 (C=O); 1670 (C=O). $^1\text{H-NMR}$ (DMSO- d_6 , δ ppm): 2.58 (s, 3H, –CH₃); 5.60 (s, 1H, pyrimidine proton); 7.11–7.66 (m, 5H, aromatic-H); 11.84 (s, 1H, NH); 12.04 (s, 1H, NH). $^{13}\text{C-NMR}$ (DMSO- d_6 , δ ppm): 25.91 (–CH₃); 106.56 (O=C–C–C, pyrimidine ring); 120.75, 122.25, 149.2 (aromatic carbons); 160.22 (S–C–N); 170.98 (N=C–S); 178.83 (HN–C–N); 182.21 (C=O), 188.11 (C=S), 198.23 (C=O). MS, m/z (%): 345 (77%); 268 (100%). Anal. Calcd. for $\text{C}_{14}\text{H}_{11}\text{N}_5\text{O}_2\text{S}_2$ (345.40): C, 48.68; H, 3.21; N, 20.28; S, 18.57. Found: C, 48.42; H, 3.02; N, 20.07, S, 18.38.

6-(5-Benzoyl-3-p-tolyl-3H-[1,3,4]thiadiazol-2-ylidene amino)-2-thioxo-2,3-dihydro-1H-pyrimidin-4-one 14c.

Brown crystal (crystallization from toluene), yield 68%; m.p. 210–212 °C. IR spectrum (KBr, ν , cm^{-1}): 3350 (–NH); 3009 (C–H, aromatic); 2920 (C–H, aliphatic); 1700 (C=O); 1668 (C=O). $^1\text{H-NMR}$ (DMSO- d_6 , δ ppm): 1.59 (s, 3H, –CH₃); 5.57 (s, 1H, pyrimidine proton); 7.14–7.66 (m, 5H, aromatic-H); 7.92–7.95 (d, 2H, aromatic CH); 8.29–8.32 (d, 2H, aromatic CH); 11.44 (s, 1H, NH); 12.15 (s, 1H, NH). $^{13}\text{C-NMR}$ (DMSO- d_6 , δ ppm): 29.50 (–CH₃); 101.75 (O=C–C–C, pyrimidine ring); 132.72, 135.21, 138.81, 139.21, 140.49, 146.56, 147.88, 151.21 (aromatic carbons); 165.26 (S–C–N); 170.78 (N=C–S); 177.89 (HN–C–N); 181.98 (C=O), 187.36 (C=S), 205.40 (C=O). MS, m/z (%): 424 (23%); 423 (3.6%); 422 (26%); 421 (50%). Anal.

Calcd. for $\text{C}_{20}\text{H}_{15}\text{N}_5\text{O}_2\text{S}_2$ (421.49): C, 56.99; H, 3.59; N, 16.62; S, 15.22. Found: C, 56.74; H, 3.44; N, 16.51; S, 15.01.

6-[3-Phenyl-5-(thiophene-2-carbonyl)-3H-[1,3,4]thiadiazol-2-ylideneamino]-2-thioxo-2,3-dihydro-1H-pyrimidin-4-one 14d.

Ball yellow crystal (benzene), yield 72%; m.p. 155–157 °C. IR spectrum (KBr, ν , cm^{-1}): 3384 (–NH); 3097 (C–H, aromatic); 2921 (C–H, aliphatic); 1680 (C=O); 1672 (C=O). $^1\text{H-NMR}$ (DMSO- d_6 , δ ppm): 5.64 (s, 1H, pyrimidine proton); 6.90–7.26 (m, 3H, thiophene-H); 7.42–7.80 (m, 5H, aromatic-H); 11.35 (s, 1H, NH); 12.13 (s, 1H, NH). $^{13}\text{C-NMR}$ (DMSO- d_6 , δ ppm): 105.96 (O=C–C–C, pyrimidine ring); 120.65, 125.32, 129.71, 137.40 (aromatic carbons); 138.60, 139.89, 147.51, 149.56 (Thiophene ring); 167.20 (HN–C–N); 175.98 (N=C–S); 183.21 (C=O), 187.11 (C=S), 198.23 (C=O). MS, m/z (%): 413 (23%); 412 (3.6%). Anal. Calcd. for $\text{C}_{17}\text{H}_{11}\text{N}_5\text{O}_2\text{S}_3$ (413.50): C, 49.38; H, 2.68; N, 16.94; S 23.26. Found: C, 49.18; H, 2.45; N, 16.75; S, 23.07.

6-[5-(Naphthalene-2-carbonyl)-3-phenyl-3H-[1,3,4]thiadiazol-2-ylideneamino]-2-thioxo-2,3-dihydro-1H-pyrimidin-4-one 14e.

Ball yellow (crystallization from benzene) yield 67%; m.p. 230–232 °C. IR spectrum (KBr, ν , cm^{-1}): 3390 (–NH); 3085 (C–H, aromatic); 2940 (C–H, aliphatic); 1690 (C=O); 1667 (C=O). $^1\text{H-NMR}$ (DMSO- d_6 , δ ppm): 5.72 (s, 1H, pyrimidine-H); 7.36–7.68 (m, 5H, aromatic -H); 7.79–8.98 (m, 7H, naphthalene-H); 11.04 (s, 1H, NH); 12.20 (s, 1H, NH). $^{13}\text{C-NMR}$ (DMSO- d_6 , δ ppm): 102.85 (O=C–C–C, pyrimidine ring); 127.32, 128.29, 129.70, 130.11, 131.71, 133.28, 134.91, 137.79, 139.59, 142.76, 146.81, 150.63 (aromatic carbons); 163.15 (S–C–N); 173.08 (N=C–S); 175.19 (HN–C–N); 182.18 (C=O), 189.86 (C=S), 203.58 (C=O). MS, m/z (%): 457 (23%). Anal. Calcd. for $\text{C}_{23}\text{H}_{15}\text{N}_5\text{O}_2\text{S}_2$ (457.53): C, 60.38; H, 3.30; N, 16.31. Found: C, 60.14; H, 3.18; N, 16.21.

6-(5-Benzoyl-3-phenyl-3H-[1,3,4]thiadiazol-2-ylidene amino)-2-thioxo-2,3-dihydro-1H-pyrimidin-4-one 14f.

Brown ppt. (crystallization from methanol) yield 66%; m.p. 209–212 °C. IR spectrum (KBr, ν , cm^{-1}): 3310 (–NH); 3090 (C–H, aromatic); 2950 (C–H, aliphatic); 1685 (C=O); 1661 (C=O). $^1\text{H-NMR}$ (DMSO- d_6 , δ ppm): 5.67 (s, 1H, pyrimidine proton); 7.04–8.12 (m, 10H, aromatic-H); 11.34 (s, 1H, NH); 12.01 (s, 1H, NH). $^{13}\text{C-NMR}$ (DMSO- d_6 , δ ppm): 105.65 (O=C–C–C, pyrimidine

ring); 129.70, 131.71, 134.91, 137.79, 139.59, 142.76, 146.81, 150.63 (aromatic carbons); 165.26 (S–C–N); 170.78 (N=C–S); 177.89 (HN–C–N); 181.98 (C=O), 187.36 (C=S), 205.40 (C=O). MS, *m/z* (%): 410 (10.2%); 408 (24.6%); 407 (23%). Anal. Calcd. for C₁₉H₁₃N₅O₂S₂ (407.47): C, 56.01; H, 3.22; N, 17.19. Found: C, 55.94; H, 3.02; N, 17.03.

General procedure for 18-21

Phenylisocyanate (1 mmol) was added to a solution of uracil (1 mmol) and potassium hydroxide (1 mmol) in 15 mL DMF; stirred overnight to afford non-isolated **16**. The non-isolated compound **16** was reacted with halo-compounds. After being stirred for 24 h, adducts **18-21** were precipitated as crude after treatment of the solution with 15 mL of iced 2 M HCl.

1-[6-Oxo-2-thioxo-1,2,3,6-tetrahydro-pyrimidin-4-yl]-3-phenyl-isothiourea 18. Dark brown (crystallization from benzene), Yield 55%; m.p. 210–211 °C. IR spectrum (KBr, ν , cm⁻¹): 3335 (–NH); 3031 (C–H, aromatic); 2976 (C–H, aliphatic); 1675 (C=O). ¹H-NMR (DMSO-d₆, δ ppm): 2.01 (s, 1H, SH); 5.42 (s, 1H, pyrimidine-H); 7.15–7.29 (m, 5H, aromatic-H); 7.89 (s, 1H, –NH); 10.79 (s, 1H, NH); 12.01 (s, 1H, NH). ¹³C-NMR (DMSO-d₆, δ ppm): 105.32 (O=C–C=C); 119.21, 125.21, 135.25, 142.21 (aromatic carbons); 171.64 (N=C–SH); 175.23 (C=O); 196.63 (C=S). MS, *m/z* (%): 280 (6.5%); 279 (22.4%); 278 (100%). Anal. Calcd. for C₁₁H₁₀N₄O₂S₂ (278.35): C, 47.46; H, 3.62; N, 20.13. Found: C, 47.25; H, 3.21; N, 20.07.

1-[6-Oxo-5-(2-oxo-2-phenyl-ethyl)-2-thioxo-1,2,3,6-tetrahydro-pyrimidin-4-yl]-3-phenyl-isothiourea 19. White crystals (crystallization from benzene/*n*-hexane), yield 75%; m.p. 239–241 °C. IR spectrum (KBr, ν , cm⁻¹): 3330 (–NH); 3029 (C–H, aromatic); 2986 (C–H, aliphatic); 1669 (C=O). ¹H-NMR (DMSO-d₆, δ ppm): 1.90 (s, 1H, –SH); 3.02 (s, 1H, –NH, pyrimidine, D₂O exchangeable); 3.55 (s, 2H, CH₂); 4.59 (s, 1H, –NH, D₂O exchangeable); 6.98–7.80 (m, 5H, aromatic-H); 7.82–8.52 (m, 5H, aromatic-H); 10.19 (s, 1H, –NH, pyrimidine). ¹³C-NMR (DMSO-d₆, δ ppm): 35.21 (–CH₂); 109.72 (O=C–C=C); 119.21, 125.21, 130.21, 142.75, 147.29, 149.33, 151.28, 159.98 (aromatic carbons); 168.22 (HN–C=C); 175.69 (HN–C–SH); 177.93 (C=O); 194.69 (C=S). MS, *m/z* (%): 398 (2.4%); 397 (22.4%); 396 (60.5%). Anal. Calcd. for C₁₉H₁₆N₄O₂S₂

(396.49): C, 57.56; H, 4.07; N, 14.13. Found: C, 57.35; H, 3.91; N, 14.09.

[4-Oxo-6-(3-phenyl-isothioureido)-2-thioxo-1,2,3,4-tetrahydro-pyrimidin-5-yl]-acetic acid ethyl ester 20. Dark red (crystallization from benzene), yield %; m.p. 203–205 °C. IR spectrum (KBr, ν , cm⁻¹): 3320 (–NH); 3055 (C–H, aromatic); 2985 (C–H, aliphatic); 1710 (C=O); 1670 (C=O). ¹H-NMR (DMSO-d₆, δ ppm): 1.18–1.25 (t, 3H, –CH₃); 2.08 (s, 1H, SH); 3.01 (s, 2H, CH₂); 4.10–4.20 (q, 2H, CH₂); 7.20–7.52 (m, 5H, aromatic-H); 8.28 (s, 1H, –NH); 11.34 (s, 1H, NH); 12.01 (s, 1H, NH). ¹³C-NMR (DMSO-d₆, δ ppm): 20.62 (–CH₃); 29.35 (–CH₂); 66.35 (–CH₂); 108.75 (O=C–C=C); 122.23, 128.21, 135.90, 150.89 (aromatic carbons); 163.72 (HN–C=C); 179.32 (C=O); 195.59 (S=C). MS, *m/z* (%): 366 (10.2%); 365 (24.6%); 364 (23%). Anal. Calcd. for C₁₅H₁₆N₄O₃S₂ (364.44): C, 49.43; H, 4.43; N, 15.37. Found: C, 49.12; H, 4.15; N, 15.10.

1-[6-Oxo-5-(2-oxo-2-propyl)-2-thioxo-1,2,3,6-tetrahydro-pyrimidin-4-yl]-3-phenyl-isothiourea 21. Dark brown ppt. (crystallization from benzene-*n*-hexane), yield 52%; m.p. 275–277 °C. IR spectrum (KBr, ν , cm⁻¹): 3285 (–NH); 3025 (C–H, aromatic); 2980 (C–H, aliphatic); 1702 (C=O); 1663 (C=O). ¹H-NMR (DMSO-d₆, δ ppm): 2.01 (s, 1H, SH); 2.61 (s, 3H, –CH₃); 2.98 (s, 2H, CH₂); 7.31–7.48 (m, 5H, aromatic-H); 7.95 (s, 1H, –NH); 9.86 (s, 1H, NH); 11.74 (s, 1H, NH). ¹³C-NMR (DMSO-d₆, δ ppm): 30.67 (–CH₃); 39.96 (–CH₂); 110.95 (O=C–C=C); 123.29, 130.98, 146.92, 152.99 (aromatic carbons); 178.77 (HN–C–N); 180.39 (C=O); 187.63 (HS–C–NH); 197.29 (S=C). MS, *m/z* (%): 336 (10.2%); 335 (24.6%); 334 (23%). Anal. Calcd. for C₁₄H₁₄N₄O₂S₂ (334.42): C, 50.28; H, 4.22; N, 16.75. Found: C, 50.02; H, 4.10; N, 16.35.

Molecular docking study

The structures of all tested compounds were modeled using the Chemsketch software (<http://www.acdlabs.com/resources/freeware/>) (Fig 1). The structures were optimized and energy minimized using the VEGAZZ software [43]. The optimized compounds were used to perform molecular docking. The three-dimensional structures of the two molecular targets (receptors) were obtained from the Protein Data Bank (PDB) (www.rcsb.org): CDK-2 (PDB: 1DI8,

<https://www.rcsb.org/pdb/explore/explore.do?structureId=1di8>), and BCL-2 (PDB:2O2F, <https://www.rcsb.org/pdb/explore/explore.do?structureId=2o2f>). The steps for receptor preparation included the removal of heteroatoms (solvent and ions), the addition of polar hydrogen and the assignment of Kollman charges. The active sites were defined using grid boxes of appropriate sizes around the bound cocystal ligands as is shown in Table 4. These compounds were docked into the active site of the CDK-2, and BCL-2 to study their interaction in silica and to correlate their anti-cancer activity. The docking study was performed using Auto dock vina, [44] and Chimera for visualization [45].

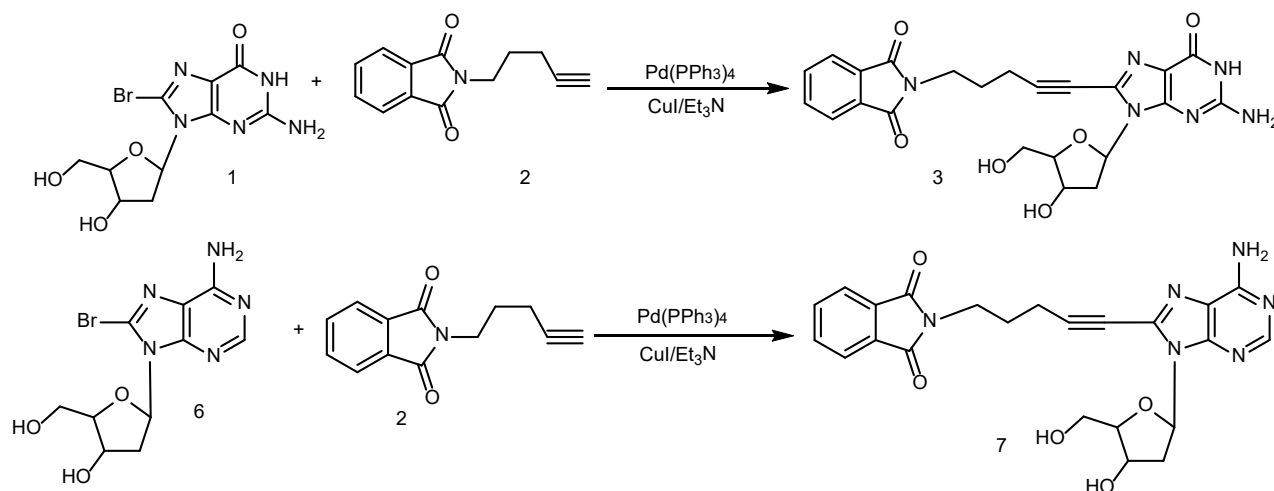
■ RESULTS AND DISCUSSION

From the modern therapeutic organic synthesis point of view and our previous work to modify DNA, [4-6] synthesis of modified DNA bases guanosine **1** and adenosine **6** derivatives was carried out. The Sonogashira reaction was carried out on the 2-pent-4-ynyl-isoindole-1,3-dione **2** with bromoguanosine **1** and bromoadenosine **6** using copper iodide and tetrakis(triphenylphosphine) palladium(0) Pd(PPh₃)₄ in the presence of triethyl amine to synthesize compound **3** and **7** (Scheme 1). The IR spectrum of compound **3** shows the amide carbonyl group at 1675 cm⁻¹, and the ¹H-NMR spectrum shows two triplets and one multiplet for the aliphatic -CH₂ groups at δ , ppm. 4.84–4.87 (t, *J* = 4.85, 2H, -CH₂); 1.13–1.18 (m, 2H, -CH₂); 6.23–6.27 (t, *J* = 6.25, 2H, -CH₂) and the

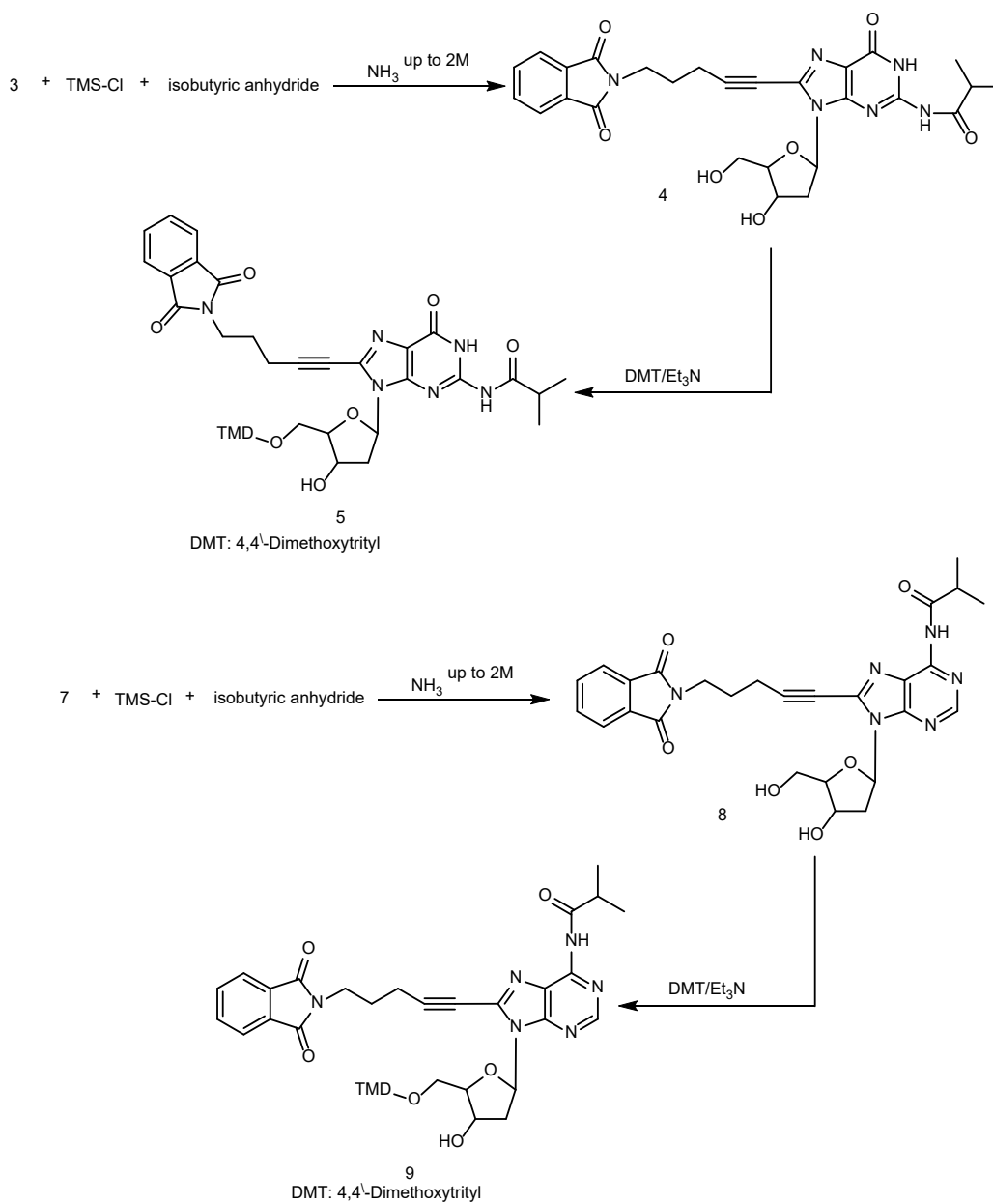
elemental analysis confirms the disappearance of bromine. The IR spectrum of compound **7** shows the amino group and the hydroxyl groups at 3445; 3432 cm⁻¹; and amide carbonyl group at 1680, and the ¹H-NMR shows singlet for the new -NH₂ at δ , ppm. 6.47 (s, 2H, -NH₂) and two triplets and one multiplet for the aliphatic -CH₂ groups at δ , ppm. 2.56–2.62 (t, *J* = 5.26, 1H, sugar proton); 2.99–3.06 (m, 1H, sugar proton); and the elemental analysis confirms the disappearance of bromine.

After that, the protection of -NH₂ groups of adenine and guanine with isobutyric anhydride in the presence of trimethylsilyl chloride (TMS-Cl) was carried out to have compounds **4** and **8**. On the other hand, the protection of the free hydroxyl sugar group (-CH₂OH) was carried out using 4,4'-dimethoxytrityl chloride (DMT-Cl) in the presence of triethyl amine to obtain the final corresponding modified DNA bases **5** and **9** (Scheme 2). The IR spectrum for compound **4** confirms the disappearance of -NH₂ peak and a carbonyl group at 1700 cm⁻¹. The ¹H-NMR spectrum shows two singlets at 1.05 ppm (s, 3H, -CH₃) and 1.07 ppm (s, 3H, -CH₃) for the new two methyl groups. The IR spectrum of compound **5** confirms the disappearance of -OH. The ¹H-NMR also confirms the disappearance of OH proton and it shows two singlets at δ ppm, 3.68 ppm (s, 3H, -OCH₃) and 3.70 ppm (s, 3H, -OCH₃) for the two methoxy groups of DMT.

6-Amino-thiouracile **10** synthesized with a known procedure [28] was allowed to react with carbon disulphide



Scheme 1



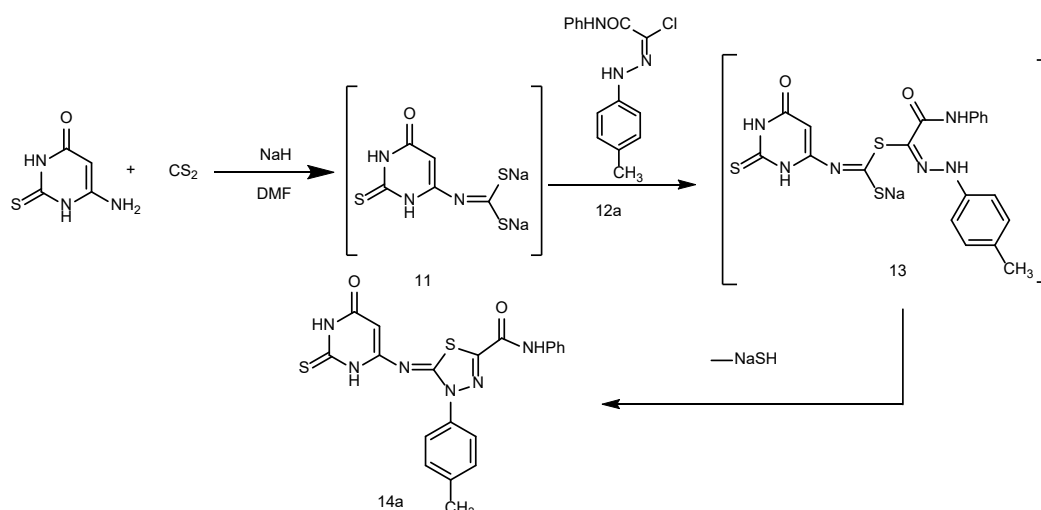
Scheme 2

in the presence of sodium hydride to yield the non-soluble disodium salt **11**. The addition of hydrazonoyl halide [29] **12a** to the formed salt **11** furnished the final isolated product **14a** (Scheme 1). The $^1\text{H-NMR}$ spectrum of **14a** revealed the presence of a singlet signal at $\delta = 5.34$ ppm corresponding to the pyrimidine hydrogen besides the characteristic signals of the aromatic protons at $\delta = 7.15$ – 7.62 , 7.82 , 7.96 ppm and three signals attributed to the $-\text{NH}$ protons at $\delta = 11.74$, 12.08 and 14.02 ppm (c.f. exp. Section). All the other spectroscopic and analytical data were in

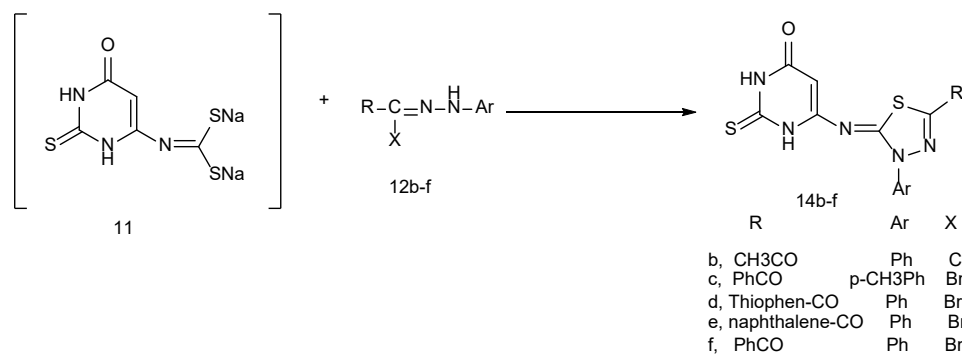
accordance with the suggested structure **14a** (Scheme 3).

It is believed that the addition of hydrazonoyl halide **12a** to the dithioimidacarbonate salt **11** led to the intermediate adduct **13**. The latter intermediate was cyclized *via* loss of NaSH to form the final cyclized product **14a**.

To generalize such methodology, the previous reaction was carried out by the use of different hydrazonoyl halide derivatives **12b-f** to yield the corresponding isolated products **14b-f** (Scheme 4). The



Scheme 3



Scheme 4

structures of all products were confirmed by spectroscopic and analytical data (c.f. experimental section).

Treatment of 6-amino-2-thiouracil with phenyl isothiocyanate in DMF containing KOH with stirring afforded the non-isolated potassium salt **16**. Interaction of **16** with different halogenated reagents did not produce the expected thiazole derivatives. The reaction yielded the products **18** upon using CH₃COCl or chloroacetonitrile that revealed the fast hydrolysis of the salt before addition. Use of benzoylchloride produced the open addition product **19** (Scheme 5).

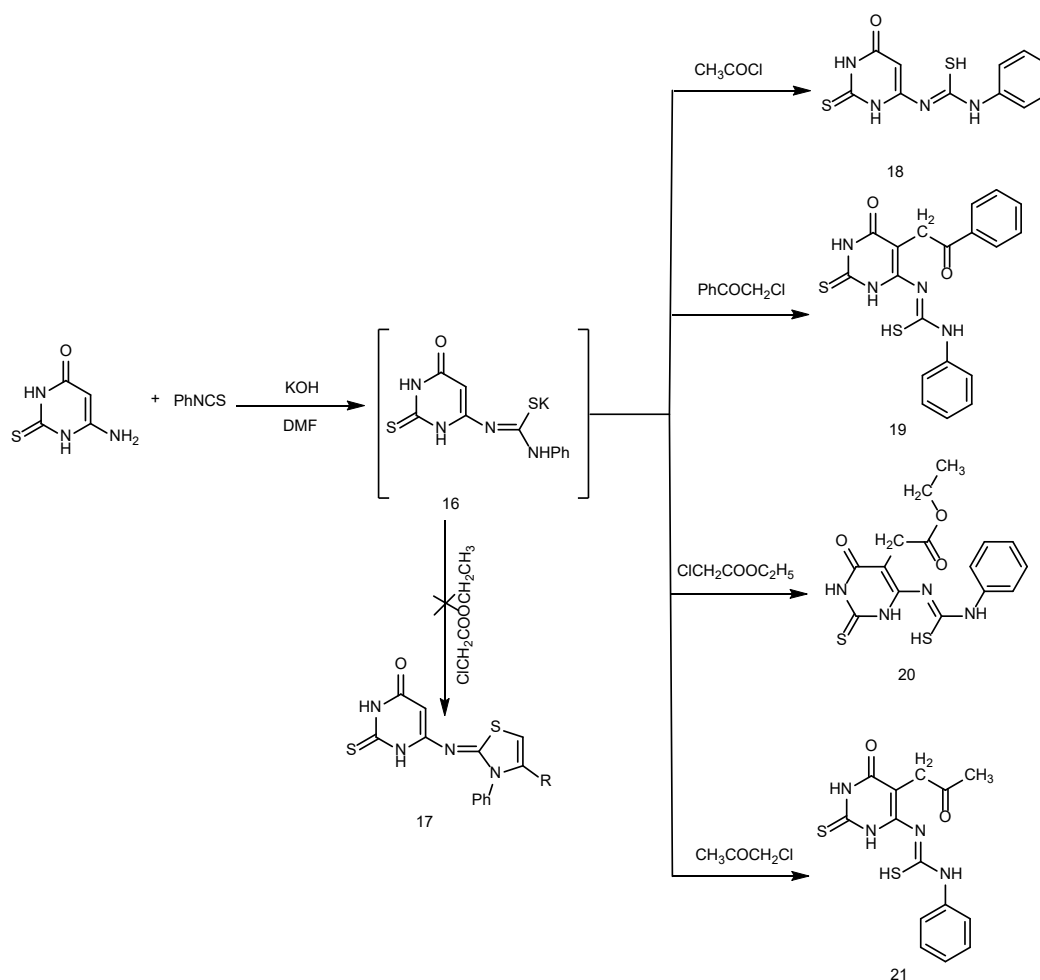
All the spectroscopic data confirmed the suggested structure (c.f. experimental section).

Molecular Docking Results

To test our docking proposal and to ensure that the binding poses of the docked ligands represented favorable and valid potential binding modes, the docking parameters

and methods were validated by redocking the cocrystal ligand in order to determine the ability of Auto Dock vina to reproduce the orientation and position of the ligand observed in the crystal structure. The redocking of cocrystal ligands to their respective molecular targets exhibited an RMSD value of < 2 Å between the original cocrystal ligand position and the docked poses, as the RMSD were 1.047 Å for 1DI8 receptor and 1.343 Å for 2O2F receptor (Fig. 1). This confirmed that the ligands were closely bound to the true conformation of their targets indicating the reliability of the docking protocols and parameters [42].

The molecular docking studies revealed that the compounds **14e**, **14f**, **14c**, **14a**, **19**, and **14d** were the most promising compounds, which is explained by their low binding energies (-9.6, -9.5, -9.0, -8.9, -8.8, and -8.6 kcal/mol, respectively), hydrogen bonding and hydrophobic interactions with the active site residues of



Scheme 5

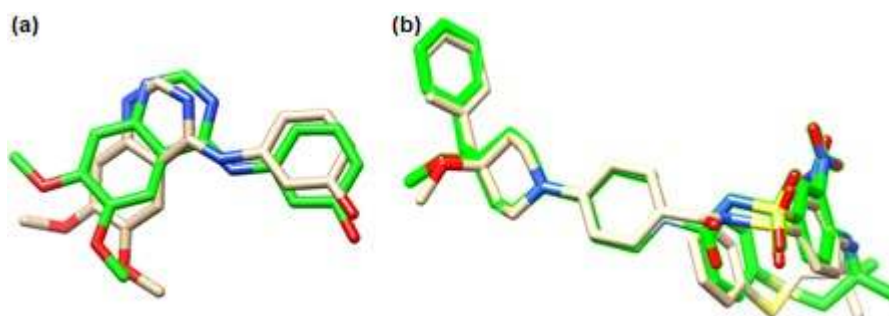


Fig 1. Docking was validated by redocking the cocrystal ligands to their corresponding receptors. The original conformation of each cocrystal ligands is displayed in a green stick, while docked poses are represented in a grey stick. The root means square deviation (RMSD) was calculated between the original and docked poses of the cocrystal ligands. (a) RMSD: 1.047Å (PDB ID: 1DI8); (b) RMSD: 1.343Å (PDB ID: 2O2F) using Chimera software

CDK-2 shown in Table 1 and 2, and Fig. 2. While compounds **14e**, **14c**, **19**, and **14a** were the most active compounds against BCL-2, which is depicted by the low binding energies (-8.2, -8.1, -8.1, and -8.1 kcal/mol,

respectively) shown in Table 1 and 3, and Fig. 3. Our molecular analysis revealed that compound **14e** was the most active compound against both proteins and that might be due to the incorporation of the free sulphur

atom (C=S) and the two nitrogens (2NH) in the pyrimidine ring. This lead to better binding of compound **14e** with the pocket of CDK-2, as depicted by 7 hydrogen bonds formation with the amino acids residues in the pocket GLN131.A (bond length 3.909 Å), ASN132.A (bond length 3.452 Å), ASN131.A (bond length 3.226 Å), GLN131.A (bond length 3.516 Å), THR14.A (bond length 2.922 Å), ASP145.A (bond length 3.461 Å), and LYS33.A (bond

length 3.133 Å).

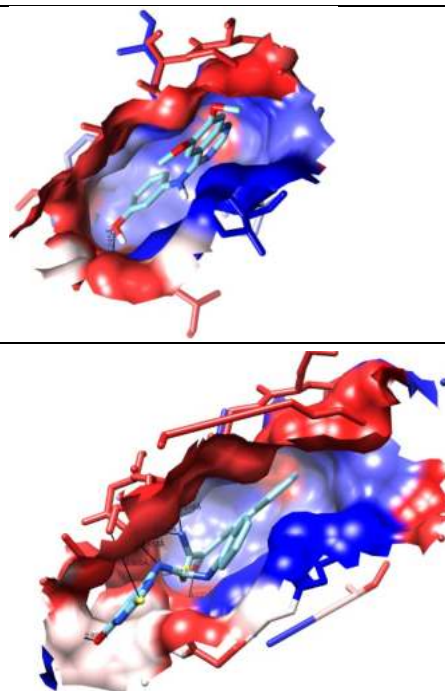
Moreover, compound **14c** was able to form 2 hydrogen bonds with the amino acids residues in the pocket of BCL-2 protein ALA97.A (bond length 3.031 Å), and TRP141.A (bond length 2.471 Å). These results shed a light on compound **14e** as a promising anticancer agent, and further wet lab experiments should be done to verify its activity.

Table 1. The results of molecular docking of best conformer with CDK-2 (1di8) receptor

Drugs	Free energy of binding (Kcal/mol)	
	CDK2	BCL2
Reference ligand	-8.3	-10.6
14a	-8.9	-8.1
14b	-8.1	-6.7
14c	-9.0	-8.1
14d	-8.6	-7.3
14e	-9.6	-8.2
14f	-9.5	-7.7
18	-7.5	-6.4
19	-8.8	-8.1
20	-7.5	-6.3
21	-8.0	-6.8

Table 2. The Hydrophobic interactions of best conformer with CDK-2 (1di8) receptor

Compounds	Hydrophobic interactions
Reference ligand	ILE10, VAL18, LEU148, VAL64, LEU134, LEU83
14e	ILE10, VAL18, LEU148, VAL64, LEU134, LEU83, PHE82, LEU298



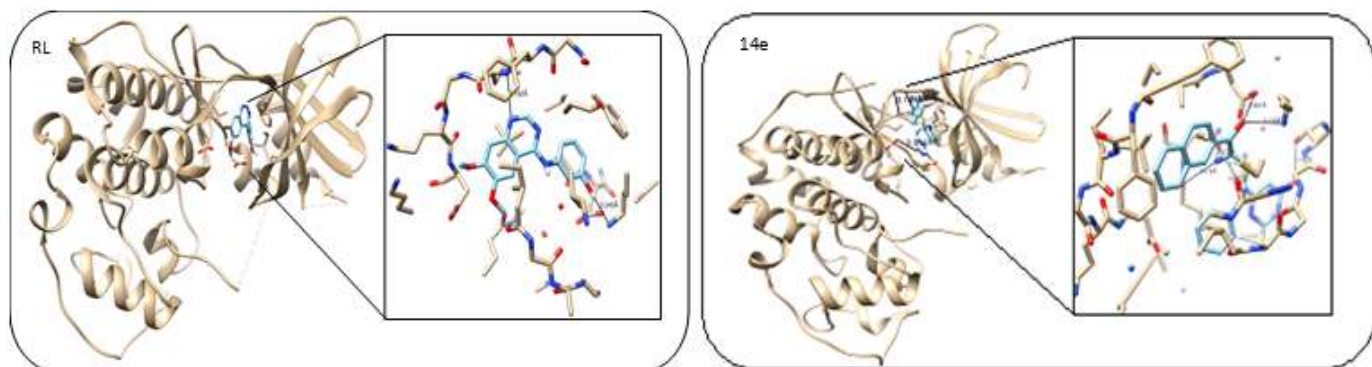


Fig 2. 3D of hydrogen bond interaction between reference ligand (RL), and the most promising compound (**14e**) with CDK-2 protein

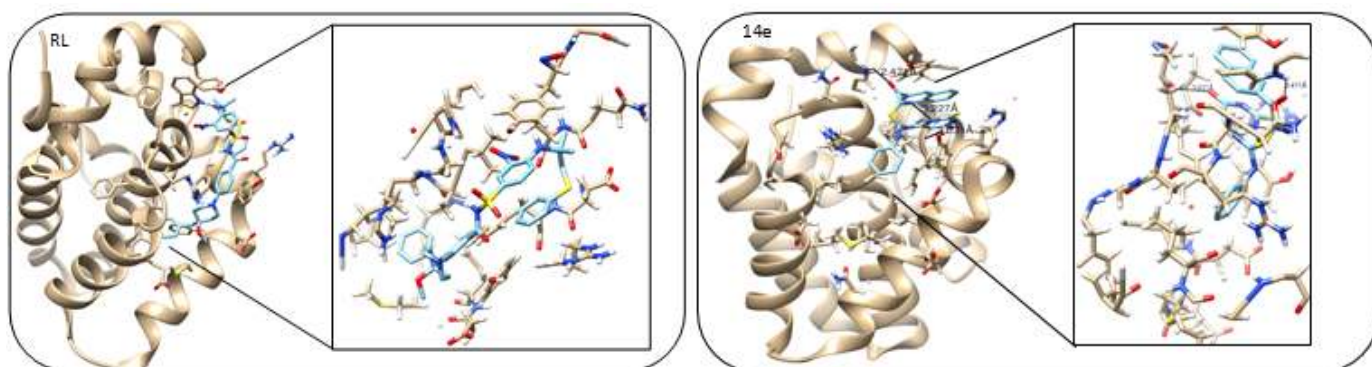


Fig 3. 3D of hydrogen bond interaction between reference ligand (RL), and the most promising compound (**14e**) with BCL-2 protein

Table 3. The Hydrophobic interactions of best conformer with BCL-2 (2O2F) receptor

Compounds	Hydrophobic interactions
Reference ligand	MET112, VAL130, VAL145, LEU134, ALA146, PHE101, PHE109, PHE150
14e	MET112, VAL130, VAL145, LEU134, PHE101, PHE109, PHE150, PHE147

■ CONCLUSION

The presented work has described the chemical modification of the pyrimidine ring base of heterocyclic biologically active compounds. Docking studies for these compounds as anticancer agents have been carried out, in order to gain insights into their binding modes against cyclin-dependent protein kinase 2 (CDK-2) that is involved in cell cycle and receptor protein B-cell lymphoma 2 (BCL-2) that is involved in cell apoptosis. These targets have been selected based on their key roles in cancer progression via the regulation of the cell cycle and DNA replication.

■ REFERENCES

- [1] Cogoi, S., Ferino, A., Miglietta, G., Pedersen, E.B., and Xodo, L.E., 2018, The regulatory G4 motif of the Kirsten ras (KRAS) gene is sensitive to guanine oxidation: Implications on transcription, *Nucleic Acids Res.*, 46 (2), 661–676.
- [2] Kosbar, T.R., Sofan, M.A., Waly, M.A., and Pedersen, E.B., 2015, Anti-parallel triplexes: Synthesis of 8-aza-7-deazaadenine nucleosides with a 3-aminopropynyl side-chain and its corresponding LNA analog, *Bioorg. Med. Chem.*, 23 (10), 2458–2469.
- [3] Müller, P., Rößler, J., Schwarz-Finsterle, J., Pedersen, E.B., Géci, I., Schmitt, E., and Hausmann, M., 2017, Corrigendum to “PNA-COMBO-FISH: From combinatorial probe design in silico to vitality compatible, specific labelling of gene targets in cell nuclei” [Exp. Cell Res., 345 (2016), 51–59], *Exp. Cell Res.*, 355 (2), 194–195.
- [4] Gouda, A.S., Amine, M.S., and Pedersen, E.B., 2017, Synthesis and molecular modeling of thermally stable DNA G-quadruplexes with anthraquinone insertions, *Eur. J. Org. Chem.*, 2017 (21), 3092–3100.
- [5] El-Sayed, A.A., Pedersen, E.B., and Khaireldin, N.Y., 2016, Thermal stability of modified i-motif oligonucleotides with naphthalimide intercalating nucleic acids, *Helv. Chim. Acta*, 99 (1), 14–19.
- [6] El-Sayed, A.A., Pedersen, E.B., and Khaireldin, N.A., 2012, Studying the influence of the pyrene intercalator TINA on the stability of DNA i-motifs, *Nucleosides Nucleotides Nucleic Acids*, 31 (12), 872–879.
- [7] Cogoi, S., Jakobsen, U., Pedersen, E.B., Vogel, S., and Xodo, L.E., 2016, Lipid-modified G4-decoy oligonucleotide anchored to nanoparticles: Delivery and bioactivity in pancreatic cancer cells, *Sci. Rep.*, 6, 38468.
- [8] Pabon-Martinez, Y.V., Xu, Y., Villa, A., Lundin, K.E., Geny, S., Nguyen, C.H., Pedersen, E.B., Jørgensen, P.T., Wengel, J., Nilsson, L., Smith, C.I.E., and Zain, R., 2017, LNA effects on DNA binding and conformation: From single strand to duplex and triplex structures, *Sci. Rep.*, 7 (1), 11043.
- [9] Bredy, T.W., 2017, *DNA Modifications in the Brain*, Academic Press, USA.
- [10] Khan, Z.U., and Muly, E.C., 2014, *Molecular Basis of Memory*, Progress in Molecular Biology and Translational Science Series, Vol. 122, Academic Press, USA.
- [11] Mohamed, N.R., Khaireldin, N.Y., Fahmy, A.F., and El-Sayed, A.A., 2010, Facile synthesis of fused nitrogen containing heterocycles as anticancer agents, *Der Pharma Chem.*, 2 (1), 400–417.
- [12] Hu, C., Chen, X., Zhao, W., Chen, Y., and Huang, Y., 2016, Design and modification of anticancer peptides, *Drug Des.*, 5 (3), 1000138.
- [13] Fan, J., Wang, S., Sun, W., Guo, S., Kang, Y., Du, J., and Peng, X., 2018, Anticancer drug delivery systems based on inorganic nanocarriers with fluorescent tracers, *AIChE J.*, 64 (3), 835–859.
- [14] Qian, Y., Bi, L., Yang, Y., and Wang, D., 2018, Effect of pyruvate kinase M2-regulating aerobic glycolysis on chemotherapy resistance of estrogen receptor-positive breast cancer, *Anticancer Drugs*, 29 (7), 616–627.
- [15] Caton-Williams, J., Lin, L., Smith, M., and Huang, Z., 2011, Convenient synthesis of nucleoside 5'-triphosphates for RNA transcription, *Chem. Commun.*, 47 (28), 8142–8144.
- [16] Lin, C.X., Fu, H., Tu, G.Z., and Zhao, Y.F., 2004, Synthesis of AZT/d4T boranophosphates as anti-HIV prodrug candidates, *Synthesis*, 2004 (4), 509–516.
- [17] Lin, C.X., Fu, H., Tu, G.Z., and Zhao, Y.F., 2010, Novel and convenient approach to synthesis of

- AZT/d4T H-phosphonates, *Chin. J. Chem.*, 22 (3), 225–227.
- [18] Gadthula, S., Chu, C.K., and Schinazi, R.F., 2005, Synthesis and anti-HIV activity of β -D-3'-azido-2',3'-unsaturated nucleosides and β -D-3'-azido-3'-deoxyribofuranosylnucleosides, *Nucleosides Nucleotides Nucleic Acids*, 24 (10-12), 1707–1727.
- [19] Sun, X.B., Kang, J.X., and Zhao, Y.F., 2002, One-pot synthesis of hydrogen phosphonate derivatives of d4T and AZT, *Chem. Commun.*, 20, 2414–2415.
- [20] Loksha, Y.M., Pedersen, E.B., Loddo, R., and La Colla, P., 2016, Synthesis and anti-HIV-1 evaluation of some novel MC-1220 analogs as non-nucleoside reverse transcriptase inhibitors, *Arch. Pharm.*, 349 (5), 363–372.
- [21] Flefel, E.M., Tantawy, W.A., El-Sofany, W.I., El-Shahat, M., El-Sayed, A.A., and Abd-Elshafy, D.N., 2017, Synthesis of some new pyridazine derivatives for anti-HAV evaluation, *Molecules*, 22 (1), E148.
- [22] El-Sayed, A.A., Tamara Molina, A., Álvarez-Ros, M.C., and Alcolea Palafox, M., 2015, Conformational analysis of the anti-HIV Nikavir prodrug: Comparisons with AZT and Thymidine, and establishment of structure-activity relationships/tendencies in other 6'-derivatives, *J. Biomol. Struct. Dyn.*, 33 (4), 723–748.
- [23] Yaqub, G., Hussain, E.A., and Mateen, B., 2010, Synthetic approaches to lamivudine: An anti-HIV AIDs and anti-hepatitis B drug, *Asian J. Chem.*, 22, 4962–4968.
- [24] Caso, M.F., D'Alonzo, D., D'Errico, S., Palumbo, G., and Guaragna, A., 2015, Highly stereoselective synthesis of lamivudine (3TC) and emtricitabine (FTC) by a novel N-glycosidation procedure, *Org. Lett.*, 17 (11), 2626–2629.
- [25] Hu, Y.Q., Zhang, S., Xu, Z., Lv, Z.S., Liu, M.L., and Feng, L.S., 2017, 4-Quinolone hybrids and their antibacterial activities, *Eur. J. Med. Chem.*, 141, 335–345.
- [26] Rizk, S.A., El-Naggar, A.M., and El-Badawy, A.A., 2018, Synthesis, spectroscopic characterization and computational chemical study of 5-cyano-2-thiouracil derivatives as potential antimicrobial agents, *J. Mol. Struct.*, 1155, 720–733.
- [27] Sahu, M., Siddiqui, N., Iqbal, R., Sharma, V., and Wakode, S., 2017, Design, synthesis, and evaluation of newer 5,6-dihydropyrimidine-2(1H)-thiones as GABA-AT inhibitors for anticonvulsant potential, *Bioorg. Chem.*, 74, 166–178.
- [28] Bhalgat, C.M., Ali, M.I., Ramesh, B., and Ramu, G., 2014, Novel pyrimidine and its triazole fused derivatives: Synthesis and investigation of antioxidant and anti-inflammatory activity, *Arabian J. Chem.*, 7 (6), 986–993.
- [29] Zhang, Q., Luo, J., Ye, L., Wang, H., Huang, B., Zhang, J., Wu, J., Zhang, S., and Tian, Y., 2014, Design, synthesis, linear and nonlinear photophysical properties and biological imaging application of a novel Λ -type pyrimidine-based thiophene derivative, *J. Mol. Struct.*, 1074, 33–42.
- [30] Sukach, V.A., Tkachuk, V.M., Rusanov, E.B., Rösenthaler, G.V., and Vovk, M.V., 2012, Heterocyclization of N-(1-chloro-2,2,2-trifluoroethylidene)carbamates with β -enaminoesters—a novel synthetic strategy to functionalized trifluoromethylated pyrimidines, *Tetrahedron*, 68 (40), 8408–8415.
- [31] Mohamed, M.F., Hassaneen, H.M., and Abdelhamid, I.A., 2018, Cytotoxicity, molecular modeling, cell cycle arrest, and apoptotic induction induced by novel tetrahydro-[1,2,4]triazolo[3,4-a]isoquinoline chalcones, *Eur. J. Med. Chem.*, 143, 532–541.
- [32] Yahya, S.M.M., Abdelhamid, A.O., Abd-Elhalim, M.M., Elsayed, G.H., and Eskander, E.F., 2017, The effect of newly synthesized progesterone derivatives on apoptotic and angiogenic pathway in MCF-7 breast cancer cells, *Steroids*, 126, 15–23.
- [33] Brahmachari, G., 2015, *Green Synthetic Approaches for Biologically Relevant Heterocycles*, Elsevier, Boston, USA.
- [34] Mohamed, N.R., El-Saidi, M.M.T., Ali, Y.M., and Elnagdi, M.H., 2007, Utility of 6-amino-2-thiouracil as a precursor for the synthesis of

- bioactive pyrimidine derivatives, *Bioorg. Med. Chem.*, 15 (18), 6227–6235.
- [35] El-Sayed, A.A., Khaireldin, N.Y., El-Shahat, M., Elhefny, E.A., El-Saidi, M.M.T., Ali, M.M., and Mahmoud, A.E., 2016, Anti proliferative activity for newly heterofunctionalized pyridine analogues, *Ponte*, 72 (7), 106–18.
- [36] Patel, H.V., Vyas, K.A., Pandey, S.P., and Fernandes, P.S., 1996, Facile synthesis of hydrazonyl halides by reaction of hydrazones with *N*-halosuccinimide-dimethyl sulfide complex, *Tetrahedron*, 52 (2), 661–668.
- [37] Shawali, A.S., Farag, A.M., Albar, H.A., and Dawood, K.M., 1993, Facile syntheses of bi-1,2,4-triazoles via hydrazonyl halides, *Tetrahedron*, 49 (13), 2761–2766.
- [38] El-Gohary, N.S., and Shaaban, M.I., 2018, Design, synthesis, antimicrobial, antiquorum-sensing and antitumor evaluation of new series of pyrazolopyridine derivatives, *Eur. J. Med. Chem.*, 157, 729–742.
- [39] Sebeka, A.A.H., Osman, A.M.A., El Sayed, I.E.T., El Bahanasawy, M., and Tantawy, M.A., 2017, Synthesis and antiproliferative activity of novel neocryptolepine-hydrazides, *J. Appl. Pharm. Sci.*, 7 (10), 9–15.
- [40] Nasab, M.J., Kiasat, A.R., and Zarasvandi, R., 2018, β -Cyclodextrin nanosponge polymer: A basic and eco-friendly heterogeneous catalyst for the one-pot four-component synthesis of pyranopyrazole derivatives under solvent-free conditions, *React. Kinet. Mech. Catal.*, 124 (2), 767–778.
- [41] Saeidi, Z., and Vatandoost, H., 2018, Aquatic insect from Iran for possible use of biological control of main vector-borne disease of malaria and water indicator of contamination, *J. Arthropod Borne Dis.*, 12 (1), 1–15.
- [42] Bursulaya, B.D., Totrov, M., Abagyan, R., and Brooks, C.L., 2003, Comparative study of several algorithms for flexible ligand docking, *J. Comput. Aided Mol. Des.*, 17 (11), 755–763.

Structural Change of Apoferritin as the Effect of pH Change: DLS and SANS Study

Arum Patriati^{1,*}, Nadi Suparno¹, Grace Tjungirai Sulungbudi¹, Mujamilah Mujamilah¹, and Edy Giri Rachman Putra²

¹Center for Science and Technology of Advanced Materials, National Nuclear Energy Agency, Puspiptek Area Serpong, Tangerang Selatan 15310, Indonesia

²Polytechnic Institute of Nuclear Technology, National Nuclear Energy Agency, Jl. Babarsari Kotak POB 6101/YKKB, Yogyakarta, Indonesia

*** Corresponding author:**

tel: +62-85643516165

email: arum@batan.go.id

Received: October 16, 2019

Accepted: December 17, 2019

DOI: 10.22146/ijc.50630

Abstract: Apoferritin is a complex protein potential for drug delivery application. The advantage of apoferritin lies in its core-shell structure, its nano size, and its pH-sensitivity. This study was aimed to characterize the structure of apoferritin due to the pH alteration effect in a solution using dynamic light scattering (DLS) and small-angle neutron scattering (SANS). Both DLS and SANS can observe protein size in solution near its physiological condition. The results show that apoferritin possesses a core-shell structure with a diameter of around 12–13 nm at pH 7. The dissociation of apoferritin occurs at pH 1.9. The SANS data shows the apoferritin at pH 1.9 was dissociated into the smaller oligomer. The structure of this smaller oligomer has a different configuration than the configuration of apoferritin subunits at pH 7. It can cause the failure of reassembly of apoferritin if the apoferritin is neutralized back to pH 7 after dissociation from pH 1.9.

Keywords: apoferritin; dissociation; pH change; SANS; DLS

■ INTRODUCTION

Ferritin is a core-shell complex protein that has a role in iron storage and detoxification in mammalian and maintains the iron excess in the body [1-2]. Without iron inside, ferritin is called apoferritin. The inner space of apoferritin can be used to transport some organic or inorganic compounds in the body. Apoferritin is non-toxic, biodegradable, and biocompatible in the body, has a nano-size inner core, and high thermal stability [3-4]; thus, promising for a drug delivery application. Moreover, the apoferritin structure has a sensitivity to pH conditions, which can be used to develop a controlled released drug delivery system [5-6].

Apoferritin dissociates into its monomers at pH 2 and can reversibly associate in neutral pH, which is used to encapsulate a cancer drug called doxorubicin [7]. However, a native-PAGE test of apoferritin and apoferritin-doxorubicin at pH 4 and pH 7 showed that the molecular weight for both remained the same after the dissociation process through pH 2. The molecular weight

data of the native-PAGE test did not show the mechanism of the dissociation itself.

This work will observe the structural change of the apoferritin in various pH using dynamic light scattering (DLS) and small-angle neutron scattering (SANS). Analysis of protein using DLS allows us to know the general size of protein in solution via its dynamic light scattering characteristic [8-10]. Meanwhile, SANS analysis will give more detail about the low-resolution three-dimensional structure of the protein in the solution based on the small-angle scattering phenomenon. The observation of protein structure in the solution provides important information to reveal its structure near its native condition [11]. Therefore, the structural change of apoferritin regarding its dissociation-association properties can be better understood.

■ EXPERIMENTAL SECTION

Materials

Apoferritin in 25 mg/mL saline solution (no. A3641)

and deuterium oxide/D₂O (no. 151882) were purchased from Sigma-Aldrich. Potassium dihydrogen phosphate/KH₂PO₄ (no. 104873), potassium hydrogen phosphate/K₂HPO₄ (no. 105104), sodium chloride/NaCl (no. 106400), and hydrochloride acid/HCl (no. 100317) were purchased from Merck. All chemicals were used without further purification.

Instrumentation

Dynamic Light Scattering (DLS) measurements were carried out using Particle Size Analyzer (Zetasizer Nano ZS-Malvern) with light of wavelength 633 nm. This instrument provides the ability to measure particle size and zeta potential of particles or molecules in a liquid medium. The Zetasizer system determines the size by measuring the Brownian motion of the particles in a sample. The fundamental principle is that small particles move more quickly in a liquid than larger particles. Therefore, measuring the Brownian motion of particles or molecules, it can interpret their size.

Small Angle Neutron Scattering (SANS) measurements were carried out using the SANS BATAN spectrometer [12]. SANS is a technique which utilizes the scattered neutron from particles or molecules in small angle region. The neutron scattering data provides information about size, distribution of particles or molecules in 1–100 nm. Since neutron can deeply penetrate into material, SANS can measure any form of sample such as gel, liquid or solid.

Procedure

Sample preparation

Apoferitin was dialyzed in K₂HPO₄-KH₂PO₄ buffer (pH 7.4) for 24 h as an apoferitin native state. Apoferitin in pH 1.9 was prepared by dialyzed it in a KCl-HCl buffer for 24 h. The apoferitin for the DLS experiment was dissolved in H₂O. Meanwhile, for SANS, the apoferitin was dissolved in D₂O to gain contrast match.

DLS measurement

The DLS measurements were conducted by set the detector at 173° in order to avoid the direct beam scattering interference. All samples were measured at room temperature.

SANS measurement

All samples were measured using neutron with a wavelength of 3.9 Å at room temperature. Each measurement was conducted at two detector positions, i.e., at 2 m for 8 h and 6 m for 20 h. This configuration was set to cover q range from 0.01 Å⁻¹ to 0.2 Å⁻¹. All measured samples were corrected from its background and electronic noise.

Experimental scattering data were corrected with GRASP [13] and analyzed with Igor SANS Analysis [14]. The ab initio molecular shape determination programs GNOM, DAMMIF, and DAMAVER [15] were used to reconstruct molecular shapes of the proteins in solution. This reconstruction undergoes the Fourier-transform calculation and gains the pair distribution function of the small-angle neutron scattering data. The pair distribution function represents the distribution of each pair scattering body in the protein. Furthermore, the three-dimensional model of the protein can be reconstructed.

RESULTS AND DISCUSSION

Apoferitin consists of 24 protein subunits arranged in several symmetries to create a core-shell structure with eight hydrophilic channels from three-fold symmetry and six hydrophobic channels from four-fold symmetry [16]. The interactions between all of its protein subunits are physical interaction without any chemical covalent bonding [17]. Due to its subunits interaction, the stability of the apoferitin structure depends on its environment, such as pH conditions. DLS experimental data of apoferitin at pH 7 show a sharp peak on 13 nm (Fig. 1). The peak was observed to be shifted to 7 nm when the environment of apoferitin is set to an acidic solution at pH 1.9. This data indicated that the apoferitin had been dissociated into a smaller part of its oligomer. When the solution becomes acidic (at pH 2 or lower), the protonation occurs in the carboxyl group at the surface of the apoferitin [18]. The protonation disturbs the stability of the tertiary structure of the subunits through the stability of the whole apoferitin core-shell structure. The protonation to carboxyl groups goes further to the hydroxyl group at tryptophan residue, which has an important role in the

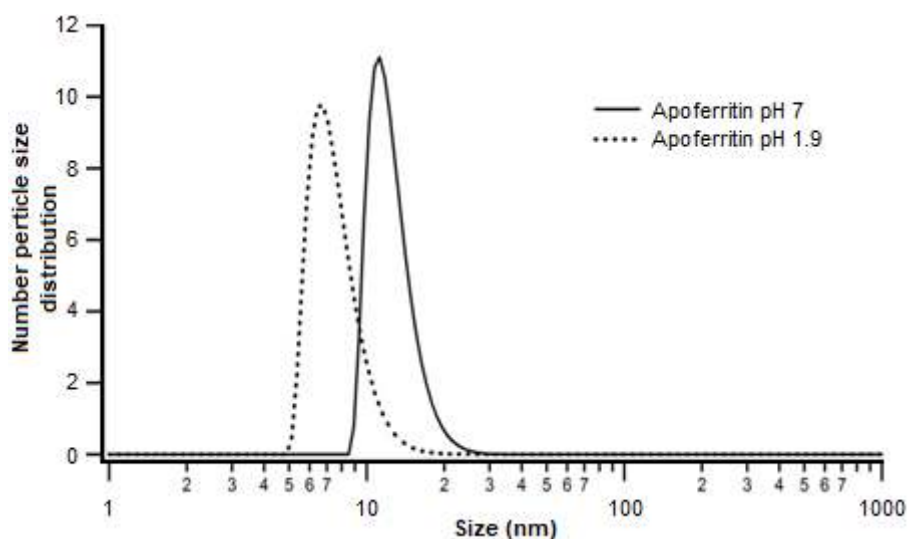


Fig 1. DLS data of the apoferritin size at pH 7 (solid line) and pH 1.9 (dot line)

hydrophobic channel structure [18]. As the hydroxyl group is being exposed by solution, it gives the dissociation effect for the apoferritin.

The alteration of the hydroxyl group, which has a role on the hydrophobic channel, break the four-fold symmetry of the apoferritin. The break of interaction between subunits in this four-fold symmetry initiated the dissociation of the apoferritin into the smaller part. This smaller part of the apoferritin was confirmed by DLS measurement from the decreasing of the particle size shown in Fig. 1.

The dissociation of apoferritin in acidic solution was also confirmed by SANS. The SANS scattering profile of apoferritin at pH 7 shows the typical ripple of the core-shell structure (Fig. 2). Data analysis using a spherical core-shell model with Igor SANS Analysis results in the core size of apoferritin of 7.98 nm and the shell thickness of 2.06 nm, suggesting that the overall diameter of apoferritin is 12.1 nm, which are coincided with the DLS data. The analysis of apoferritin at pH 1.9 was well-fitted with the triaxial ellipsoid model and gained 1.2, 3.5, and 6.7 nm for the three-axis of the ellipsoid.

Further analysis of the SANS scattering profile was conducted to construct the three-dimension low-resolution model of the apoferritin at pH 7 and pH 1.9. The SANS scattering data were Fourier-transformed into pair distribution function as the real space function from SANS scattering data. The pair distribution function

expresses the distance of each scattering body (r) of the apoferritin and the probability of each value. This analysis was done using the GNOM program. The information on the distribution of the r values extracted from the function in the GNOM is then modeled into three-dimensional form. The reconstruction of three-dimensional models from the data is built by dummy atoms and a dummy particle with a volume using DAMMIF and DAMAVER program. The program will arrange the dummy atoms in a certain position and volume based on the pair distribution function.

The pair distribution function of the apoferritin at pH 7 and pH 1.9 show that D_{\max} of the apoferritin is larger at pH 7 than at pH 1.9 (Fig. 2(c)). Since the D_{\max} in pair distribution function represents the longest distance of the two-scattering body, it indicates that apoferritin was disassembled in an acidic solution. Apoferritin at neutral pH (pH 7) has D_{\max} of 12 nm and decreases to 7 nm at pH 1.9. The D_{\max} of apoferritin at pH 7 represents the apoferritin core-shell structure diameter, while at pH 1.9, the D_{\max} represents the longest distance of its structure.

The three-dimensional structure of the apoferritin at pH 7 and pH 1.9 generated by the DAMMIF program and visualized by pyMOL [19-20] are shown in Fig. 3 and Fig. 4, respectively. The three-dimensional model structure of the apoferritin at pH 7 corresponds with the other work [16-17,21].

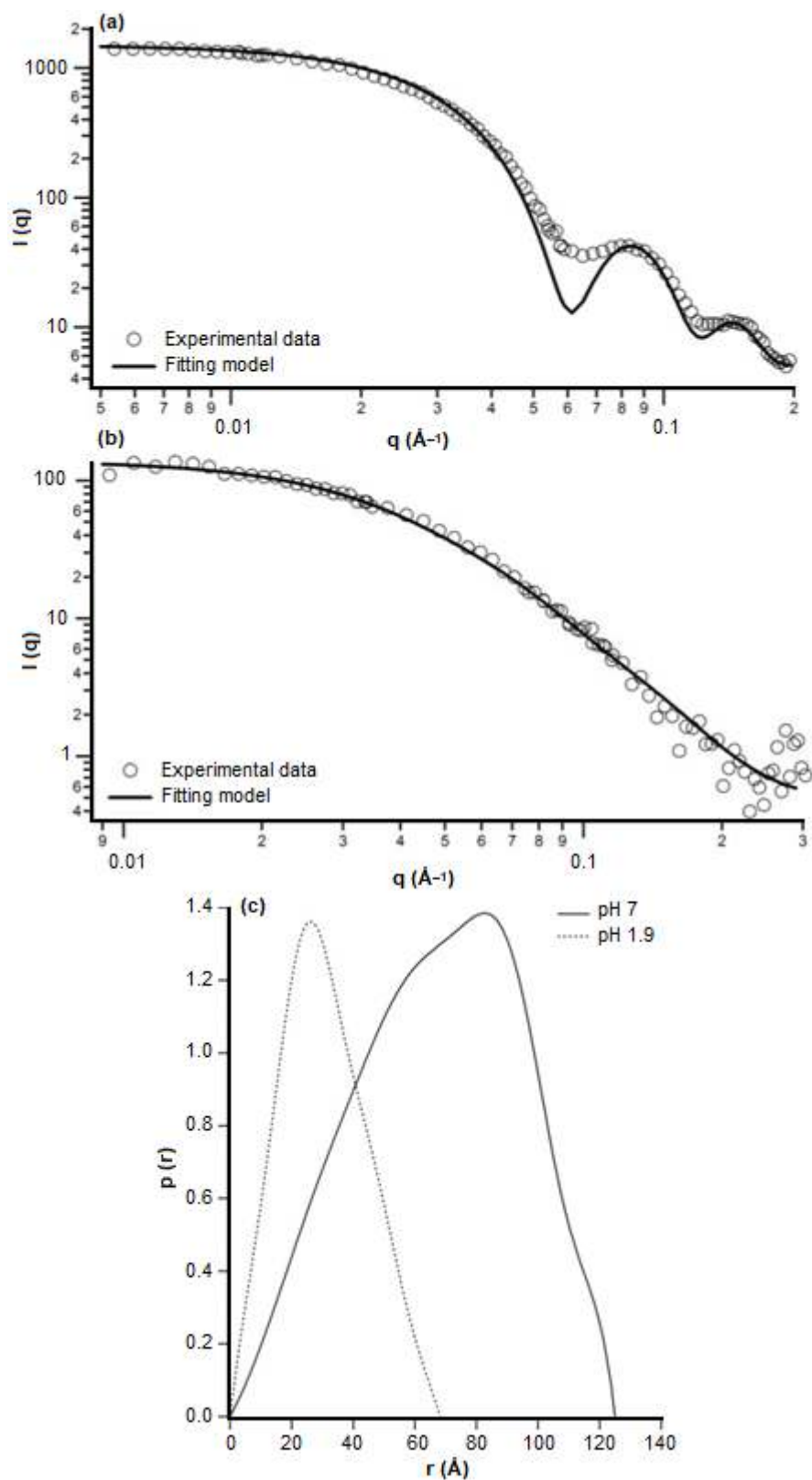


Fig 2. SANS scattering profile of apoferritin at (a) pH 7 and (b) pH 1.9. (c) The pair distribution function of apoferritin at pH 7 and pH 1.9

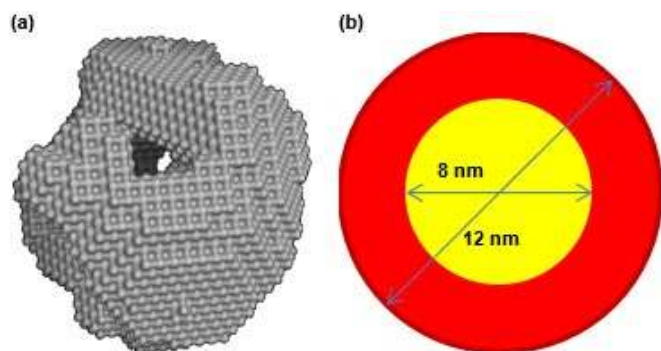


Fig 3. (a) The three-dimensional model of apoferritin at pH 7 generated by DAMMIF and visualized by pyMOL and (b) the core-shell model based on Igor SANS analysis data

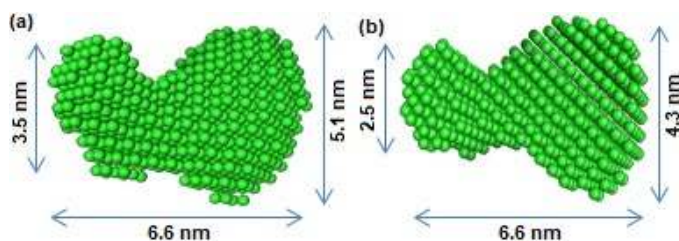


Fig 4. The three-dimensional model of apoferritin at pH 1.9 based on SANS data from (a) side view and (b) top view after 90° rotation

The core-shell structure of the apoferritin is disrupted at acid condition, which is depicted in its three-dimensional model. The molecular weight of the dissociated apoferritin at pH 1.9 cannot be confirmed since the SANS data is not analyzed by absolute scale. However, the model generated from SANS is still reliable as the structure of protein depends on the profile of the neutron scattering intensity at certain scattering vector (q).

The $R_{g,p(r)}$ of apoferritin at pH 7 is 5.25 nm, while the $R_{g,p(r)}$ of apoferritin at pH 1.9 is 3.66 nm. This result is similar to the $R_{g,p(r)}$ of apoferritin at pH 1.9 and pH 7 that was reported by Kim et al. [22]. However, the three-dimensional structure of apoferritin at pH 1.9 is not consistent with the one proposed in Ref. 22. In this work, the three-dimensional model of apoferritin at pH 1.9 shows the smaller part of instead of maintains its diameter with semi-circle structure which is showed in Ref. 22. This dissociation is due to the protonation of the apoferritin to its four-fold symmetry subunits. They exist at six positions in all around of the apoferritin core-shell structure. Therefore, the alteration of those sites at a very

rich proton condition, pH 1.9, makes the apoferritin dissociated into the smaller oligomer.

The dimension of the small oligomer of the apoferritin at pH 1.9 obtained by SANS data analysis is about three times of its monomer (PDB:5erk) [23]. As the SANS analysis is not conducted by absolute intensity mode, this dimension does not represent its molecular weight. Therefore, it cannot conclude the number of subunits in this small oligomer. However, the arrangement of the apoferritin subunits oligomer at pH 1.9 is different with four-fold, three-fold or four-fold symmetry in its core-shell oligomer at pH 7. It indicates that the protonation induces the disruption of the tertiary structure of the apoferritin subunit and changes its configuration. Furthermore, it can cause failure in the reassembly of the apoferritin from acidic to neutral pH. This assumption should be further studied to clarify the reassembly ability of apoferritin from acidic conditions to neutral pH conditions.

■ CONCLUSION

The data from DLS and SANS revealed the dissociation process of apoferritin as the effect of the change of pH. Instead of being dissociated into its monomers, the dissociation of apoferritin at pH 1.9 was like small oligomers with the dimension of three times of apoferritin's monomer. The three-dimensional structure of this small oligomer, which indicated a configuration change, can cause the failure of apoferritin to reassembly in neutral pH.

■ ACKNOWLEDGMENTS

Authors acknowledge to Nuclear Energy Agency of Indonesia (BATAN) for the funding of this research under research project (DIPA) term 2014-2019.

■ REFERENCES

- [1] Bulvik, B.E., Berenshtein, E., Meyron-Holtz, E.G., Konijn, A.M., and Chevion, M., 2012, Cardiac Protection by preconditioning is generated via an iron-signal created by proteasomal degradation of iron proteins, *PLoS One*, 7 (11), e48947.
- [2] Theil, E.C., 2011, Ferritin protein nanocages use ion channels, catalytic sites, and nucleation channels to

- manage iron/oxygen chemistry, *Curr. Opin. Chem. Biol.*, 15 (2), 304–311.
- [3] Heger, Z., Skalickova, S., Zitka, O., Adam, V., and Kizek, R., 2014, Apoferritin applications in nanomedicine, *Nanomedicine*, 9 (14), 2233–2245.
- [4] Dostálová, S., Konečná, R., Blažková, I., Vaculovičová, M., Kopel, P., Křížková, S., Vaculovič, T., Adam, V., and Kizek, R., 2013, Apoferritin as a targeted drug delivery system, *MendelNet 2013*, 908–912.
- [5] Balamuralidhara, V., Pramodkumar, T.M., Srujana, N., Venkatesh, M.P., Gupta, N.V., Krishna, K.L., and Gangadharappa, H.V., 2011, pH Sensitive drug delivery systems: A review, *Am. J. Drug Discovery Dev.*, 1 (1), 24–48.
- [6] Wang, X., Dong, J., Liu, X., Liu, Y., and Ai, S., 2014, A novel pH-controlled immunosensor using hollow mesoporous silica and apoferritin combined system for target virus assay, *Biosens. Bioelectron.*, 54, 85–90.
- [7] Kilic, M.A., Ozlu, E., and Calis, S., 2012, A novel protein-based anticancer drug encapsulating nanosphere: Apoferritin-doxorubicin complex, *J. Biomed. Nanotechnol.*, 8 (3), 508–514.
- [8] Stetefeld, J., McKenna, S.A., and Patel, T.R., 2016, Dynamic light scattering: A practical guide and applications in biomedical sciences, *Biophys. Rev.*, 8 (4), 409–427.
- [9] Hawe, A., Hulse, W.L., Jiskoot, W., and Forbes, R.T., 2011, Taylor dispersion analysis compared to dynamic light scattering for the size analysis of therapeutic peptides and proteins and their aggregates, *Pharm. Res.*, 28 (9), 2302–2310.
- [10] Li, Y., Lubchenko, V., and Vekilov, P.G., 2011, The use of dynamic light scattering and Brownian microscopy to characterize protein aggregation, *Rev. Sci. Instrum.*, 82 (5), 053106.
- [11] Blanchet, C.E., and Svergun, D.I., 2013, Small-angle X-ray scattering on biological macromolecules and nanocomposites in solution, *Annu. Rev. Phys. Chem.*, 64 (1), 37–54.
- [12] Putra, E.G.R., Bharoto, and Seong, B.S., 2010, Recent development of a 36 meter small-angle neutron scattering BATAN spectrometer (SMARTer) in Serpong Indonesia, *J. Phys. Conf. Ser.*, 247, 012010.
- [13] Dewhurst, C., 2003, *GRAS_{ANS}P User Manual*, Institut Laue Langevin, Grenoble, France, ILL03DE01T.
- [14] Kline, S.R., 2006, Reduction and analysis of SANS and USANS data using IGOR Pro, *J. Appl. Crystallogr.*, 39 (6), 895–900.
- [15] Petoukhov, M.V., Franke, D., Shkumatov, A.V., Tria, G., Kikhney, A.G., Gajda, M., Gorba, C., Mertens, H.D.T., Konarev, P.V., and Svergun, D.I., 2012, New developments in the ATSAS program package for small-angle scattering data analysis, *J. Appl. Crystallogr.*, 45 (2), 342–350.
- [16] Uchida, M., Kang, S., Reichhardt, C., Harlen, K., and Douglas, T., 2010, The ferritin superfamily: Supramolecular templates for materials synthesis, *Biochim. Biophys. Acta, Gen. Subj.*, 1800 (8), 834–845.
- [17] Zhang, Y., and Orner, B.P., 2011, Self-assembly in the ferritin nano-cage protein superfamily, *Int. J. Mol. Sci.*, 12 (8), 5406–5421.
- [18] Crichton, R.R., and Bryce, C.F., 1973, Subunit interactions in horse spleen apoferritin. Dissociation by extremes of pH, *Biochem. J.*, 133 (2), 289–299.
- [19] Hagelueken, G., Ward, R., Naismith, J.H., and Schiemann, O., 2012, MtsslWizard: In silico spin-labeling and generation of distance distributions in PyMOL, *Appl. Magn. Reson.*, 42 (3), 377–391.
- [20] Baugh, E.H., Lyskov, S., Weitzner, B.D., and Gray, J.J., 2011, Real-time PyMOL visualization for Rosetta and PyRosetta, *PLoS One*, 6 (8), e21931.
- [21] Russo, C.J., and Passmore, L.A., 2015, Ultrastable gold substrates for electron cryomicroscopy, *Science*, 346 (6215), 1377–1380.
- [22] Kim, M., Rho, Y., Jin, K.S., Ahn, B., Jung, S., Kim, H., and Ree, M., 2011, pH-Dependent structures of ferritin and apoferritin in solution: Disassembly and reassembly, *Biomacromolecules*, 12 (5), 1629–1640.
- [23] Pontillo, N., Pane, F., Messori, L., Amoresano, A., and Merlino, A., 2016, Cisplatin encapsulation within the ferritin nanocage: A high-resolution crystallographic study, *Chem. Commun.*, 52 (22), 4136–4139.

Supplementary Data

This supplementary data is a part of paper entitled "Employing an R Software Package rsm for Optimizing of Genistein, Daidzein, and Glycitein Separation and Its Application for Soy Milk Analysis by HPLC Method".

S1. R formula for analyzing genistein data

```
library(rsm)
gen = read.csv("gen2.csv")
gen

##setting up coded levels for genistein model
gen.rsm <- coded.data(gen, x1 ~ (methanol - 65)/5,
                      x2 ~ (flowrate - 0.8)/0.2,
                      x3 ~ (temp - 40)/10)

gen.rsm

##RSM for analyzing retention time for genistein
gen.ret.rsm <- rsm(retention ~ SO(x1, x2, x3), data = gen.rsm)
gen.ret.rsm
summary(gen.ret.rsm)

par(mfrow = c(1,3))
persp(gen.ret.rsm, ~ x1 + x2 + x3, at = summary(gen.ret.rsm)$canonical$xs,
      contours = "col", col = rainbow(40),
      zlab = "Retention Time",
      xlabs = c("Methanol Concentration (%)", "Flowrate (mL/min)", "Temperature
(°C)"))

##RSM for analyzing resolution for genistein
gen.res.rsm <- rsm(resolution ~ SO(x1, x2, x3), data = gen.rsm)
gen.res.rsm
summary(gen.res.rsm)

par(mfrow = c(1,3))

persp(gen.res.rsm, ~ x1 + x2 + x3, at = summary(gen.res.rsm)$canonical$xs,
      contours = "col", col = rainbow(40),
      zlab = "Resolution",
      xlabs = c("Methanol Concentration (%)", "Flowrate (mL/min)", "Temperature
(°C)"))

##RSM for analyzing tailing factor for genistein
gen.tai.rsm <- rsm(tailing ~ SO(x1, x2, x3), data = gen.rsm)
gen.tai.rsm
summary(gen.tai.rsm)

par(mfrow = c(1,3))
persp(gen.tai.rsm, ~ x1 + x2 + x3, at = summary(gen.tai.rsm)$canonical$xs,
      contours = "col", col = rainbow(40),
      zlab = "Tailing Factor",
```



```
      xlabs = c("Methanol Concentration (%)", "Flowrate (mL/min)", "Temperature
(°C)"))

##RSM for analyzing N for genistein
gen.n.rsm <- rsm(n ~ SO(x1, x2, x3), data = gen.rsm)
gen.n.rsm
summary(gen.n.rsm)

par(mfrow = c(1,3))
persp(gen.n.rsm, ~ x1 + x2 + x3, at = summary(gen.n.rsm)$canonical$xs,
      contours = "col", col = rainbow(40),
      zlab = "Theoretical Plates Number",
      xlabs = c("Methanol Concentration (%)", "Flowrate (mL/min)", "Temperature
(°C)"))
```

S2. R formula for analyzing daidzein data

```
library(rsm)
dai = read.csv("dai2.csv")
dai

##setting up coded levels for daidzein model
dai.rsm <- coded.data(dai, x1 ~ (methanol - 65)/5,
                     x2 ~ (flowrate - 0.8)/0.2,
                     x3 ~ (temp - 40)/10)
dai.rsm

##RSM for analyzing retention time for daidzein
dai.ret.rsm <- rsm(retention ~ SO(x1, x2, x3), data = dai.rsm)
dai.ret.rsm
summary(dai.ret.rsm)

par(mfrow = c(1,3))
persp(dai.ret.rsm, ~ x1 + x2 + x3, at = summary(dai.ret.rsm)$canonical$xs,
      contours = "col", col = rainbow(40),
      zlab = "Retention Time",
      xlabs = c("Methanol Concentration (%)", "Flowrate (mL/min)", "Temperature
(°C)"))

##RSM for analyzing resolution for daidzein
dai.res.rsm <- rsm(resolution ~ SO(x1, x2, x3), data = dai.rsm)
dai.res.rsm
summary(dai.res.rsm)

par(mfrow = c(1,3))
persp(dai.res.rsm, ~ x1 + x2 + x3, at = summary(dai.res.rsm)$canonical$xs,
      contours = "col", col = rainbow(40),
      zlab = "Resolution",
      xlabs = c("Methanol Concentration (%)", "Flowrate (mL/min)", "Temperature
(°C)"))
##RSM for analyzing tailing factor for daidzein
dai.tai.rsm <- rsm(tailing ~ SO(x1, x2, x3), data = dai.rsm)
```

```
dai.tai.rsm
summary(dai.tai.rsm)

par(mfrow = c(1,3))
persp(dai.tai.rsm, ~ x1 + x2 + x3, at = summary(dai.tai.rsm)$canonical$xs,
      contours = "col", col = rainbow(40),
      zlab = "Tailing Factor",
      xlabs = c("Methanol Concentration (%)", "Flowrate (mL/min)", "Temperature
(oC)"))

##RSM for analyzing N for daidzein
dai.n.rsm <- rsm(n ~ SO(x1, x2, x3), data = dai.rsm)
dai.n.rsm
summary(dai.n.rsm)

par(mfrow = c(1,3))
persp(dai.n.rsm, ~ x1 + x2 + x3, at = summary(dai.n.rsm)$canonical$xs,
      contours = "col", col = rainbow(40),
      zlab = "Theoretical Plates Number",
      xlabs = c("Methanol Concentration (%)", "Flowrate (mL/min)", "Temperature
(oC)"))
```

S3. R formula for analyzing glycitein data

```
library(rsm)
gly = read.csv("gly2.csv")
gly

##setting up coded levels for glycitein model
gly.rsm <- coded.data(gly, x1 ~ (methanol - 65)/5,
                     x2 ~ (flowrate - 0.8)/0.2,
                     x3 ~ (temp - 40)/10)

gly.rsm

##RSM for analyzing retention time for glycitein
gly.ret.rsm <- rsm(retention ~ SO(x1, x2, x3), data = gly.rsm)
gly.ret.rsm
summary(gly.ret.rsm)

par(mfrow = c(1,3))
persp(gly.ret.rsm, ~ x1 + x2 + x3, at = summary(gly.ret.rsm)$canonical$xs,
      contours = "col", col = rainbow(40),
      zlab = "Retention Time",
      xlabs = c("Methanol Concentration (%)", "Flowrate (mL/min)", "Temperature
(oC)"))

##RSM for analyzing resolution for glycitein
gly.res.rsm <- rsm(resolution ~ SO(x1, x2, x3), data = gly.rsm)
gly.res.rsm
summary(gly.res.rsm)
par(mfrow = c(1,3))
persp(gly.res.rsm, ~ x1 + x2 + x3, at = summary(gly.res.rsm)$canonical$xs,
```

```
contours = "col", col = rainbow(40),
zlab = "Resolution",
xlabs = c("Methanol Concentration (%)", "Flowrate (mL/min)", "Temperature
(oC)"))

##RSM for analyzing tailing factor for glycitein
gly.tai.rsm <- rsm(tailing ~ SO(x1, x2, x3), data = gly.rsm)
gly.tai.rsm
summary(gly.tai.rsm)

par(mfrow = c(1,3))
persp(gly.tai.rsm, ~ x1 + x2 + x3, at = summary(gly.tai.rsm)$canonical$xs,
contours = "col", col = rainbow(40),
zlab = "Tailing Factor",
xlabs = c("Methanol Concentration (%)", "Flowrate (mL/min)", "Temperature
(oC)"))

##RSM for analyzing N for glycitein
gly.n.rsm <- rsm(n ~ SO(x1, x2, x3), data = gly.rsm)
gly.n.rsm
summary(gly.n.rsm)

par(mfrow = c(1,3))
persp(gly.n.rsm, ~ x1 + x2 + x3, at = summary(gly.n.rsm)$canonical$xs,
contours = "col", col = rainbow(40),
zlab = "Theoretical Plates Number",
xlabs = c("Methanol Concentration (%)", "Flowrate (mL/min)", "Temperature
(oC)"))
```